THE MODULATION OF SUBMILLIMETRE RADIATION

A thesis submitted to the Faculty of Science of the University of London for the degree of Doctor of Philosophy

by

Martin Wynford BOOTON

BSc(London)

Department of Physics
The Royal Holloway College

May 1979

ABSTRACT

An investigation is undertaken into methods of fast modulation and detection of submillimetre radiation. Detection at room temperature was achieved with travelling wave antennae coupled to a crystal rectifier. Metal-oxide-metal and metal-oxide-semiconductor rectifying junctions were studied. Generation of submillimetre radiation was performed by means of a hydrogen cyanide laser, operating primarily at a wavelength of 337 μm. The investigation was motivated by a need for an increase in output power from the laser which requires a fast switch operative at submillimetre wavelengths. Evaluation of a Q-switching technique, utilizing the near coincidences between absorption features in various vapours and the 337 μm emission line of the HCN laser was made. Further investigations were carried out on the transient properties of the plasma that forms the active medium of a pulsed excited HCN laser. Shift of the resonance condition by means of an ancillary discharge is undertaken as a Q-switching technique.

Magneto-optical modulation as an alternative switching technique was also studied. To this end, the temperature-dependence of the magneto-optical constants of seven different rare-earth iron garnets were studied at a wavelength of 337 μm. The properties investigated include the Faraday rotation, absorption coefficient and the room temperature refractive index. The theory of the magneto-optical effects at microwave and optical frequencies is reviewed and extended into the submillimetre region. Effects of magnetic anisotropy are discussed.

CONTENTS

FIGURES

CHAPTER ONE

INTRODUCTION

Investigation of the submillimetre region of the electromagnetic spectrum started in the late nineteenth century when Rubens and Aschkinass[1] isolated long wavelength radiation from a thermal source. Loosely defined as the wavelength range from 1 to 0.1 millimetres, the submillimetre band has remained relatively unexplored compared to the optical and microwave regions. This has occurred mainly because until the invention of the hydrogen cyanide laser in 1964[2], thermal emission continued to be the only source of radiation in this region. The early work of Rubens and Aschkinass employed Reststrahlen plates to select the long wavelength radiation. The power obtained was inadequate for further experimentation, but in 1911 Rubens and Wood[3] obtained higher intensities by using the dispersion in quartz lenses to focus only far infra-red radiation on to a thermocouple. By using light from a sodium flame to determine the spacing between the plates of an interferometer, the technique was shown to produce submillimetre radiation with a peak in its distribution near 110 μm wavelength and measurable amounts at 200 μm. Sufficient power was obtained by this method to perform a series of measurements on the absorption and reflectivity of various vapours, liquids and solid materials.

Development in a spectral region depends not only on the radiation sources but also on the available detectors. For many applications, a detector with a fast rise time is required. It is therefore significant to note that in 1957 Happ et al.[4] reported detecting submillimetre radiation from a mercury arc lamp by contacting a tungsten antenna on to a semiconductor crystal. With the antenna mounted in waveguide, Happ et al. were able to observe the response of silicon and germanium point-contact diodes over the wavelength range 100 to 1000 μm.

An increase in activity in the submillimetre region started with the invention of the HCN, H_2O and CO_2 gas discharge lasers. Other lasers, DCN, D_2O, H_2S and SO_2 added to the available emission lines and, more recently, this number has been increased by work initiated by Chang et al.[5] on optically pumping organic molecules by radiation from a CO_2 laser. Recent advances have also been made from the microwave approach. The most successful to date is the backward wave tube,which is available

giving milliwatt powers up to 480 GHz, and research is continuing to extend its range to 1500 GHz[6].

Further development of the submillimetre region will largely depend on the advantages the region possesses and the applications it has to offer. Investigations are currently being pursued in the field of far infra-red spectra of molecules using Fourier transform spectroscopy[6,7]. This may have direct application to work carried out at the National Physical Laboratory on the composition of the atmosphere[7]. Plasma diagnostic techniques using far infra-red radiation are well established, this frequency band being optimum for measurements of the transient properties of high temperature and high density plasmas that are produced in fusion reactors[5,6,7].

Possible future applications of the submillimetre band may be predicted by examination of its merits relative to other spectral regions. The far infra-red has advantages over the microwave region of greater bandwidth and either higher resolution or smaller antenna size. Strong atmospheric attenuation, however, limits the wavelength range over which submillimetre radiation may be propagated at low altitude. The transmission measurements of Hall[7] and of Williams and Foster[8] show that, although atmospheric windows exist, attenuation within these bands of less than 10 dB per kilometre is unlikely for most weather conditions. This factor is possibly another contributor to the slow exploitation of the region. Accepting the limitation of short range, submillimetre waves potentially have a resolving power superior to systems operating at microwave frequencies, while being able to function in adverse weather conditions which would prevent the use of conventional optical techniques. Future applications may also include space to space communications[7] where the wider beam widths usually employed at lower frequencies are preferable to the narrow beams used in most optical systems.

Future uses of submillimetre waves are likely to require high power sources, sensitive low noise detectors and, in many cases, the ability to modulate the beam. This aspect of submillimetre technology has been studied in the present programme by investigating techniques of fast modulation. This first involved developing techniques for Q-switching a gas laser and, secondly, by undertaking an investigation of the magneto-optical properties of several magnetic materials with the eventual aim of producing external modulation of a submillimetre source.

Development of a Q-switching technique has been undertaken on the HCN laser. In order to understand more fully the Q-switching action, part of the programme involved a detailed investigation of gas discharge phenomena in the HCN laser plasma. However, the modulation technique developed can, in principle, be applied to many submillimetre laser sources.

The work embarked upon is introduced in Chapter Two with a theoretical description of far infra-red gas discharge lasers. A review of the known properties of the HCN laser reported in the literature is given in Chapter Three. The theory cited in these chapters is extended in Chapter Four and used to analyse the switching techniques. Experimental investigation of these techniques and of other properties of the laser necessary to understand the switching processes, particularly the pump mechanism, is described in Chapter Five with further evaluation in Chapter Six.

As previously stated, submillimetre systems depend not only on the power from the source, but also on the performance of the available detectors. Far infra-red detectors are of three basic types, photoconductive, bolometers, and rectifying junctions. Bolometers have high sensitivities and low noise levels, but are limited in their application by their slow response times. The most common of these, the Golay cell, was used throughout much of this work. Good sensitivity, low noise and fast response, are obtained from photoconductive detectors, the most widely used in the submillimetre region being the Putley[9] and Rollin[10] detectors, and from rectifying junctions using the Josephson effect[5,6]. However, the necessity for these devices to operate at liquid-helium temperatures is generally inconvenient. In the present programme fast detection, required to observe the Q-switched output from the laser, was carried out at room temperature using the rectifying properties of point-contacts made between a tungsten wire antenna and metal and semiconductor electrodes. These detectors have a fast response and operate at room temperature, but suffer from low sensitivity and are subject to damage by vibration. An investigation into the first of these shortcomings, the sensitivity, is described in Chapter Seven. The problem was approached experimentally by observing the performance of several diodes under different conditions, and obtaining a better understanding of the device by developing an improved theoretical model of the diode junction.

The final aspect of the programme was an investigation of the properties of materials suitable for magneto-optical beam modulation. The feasibility of magneto-optical modulation in the far infra-red was demonstrated by Birch and Jones[11] who obtained modulation frequencies in excess of 2 MHz from a Faraday effect device. Although modulation greater than 10 MHz has been achieved in the submillimetre region by impact ionisation of impurity atoms in doped semiconductors[12], the liquid-helium temperatures required prohibit wide applications of this technique. Development of this field in the present programme was therefore restricted to magneto-optical methods which, although limited by the rate at which the applied magnetic field can be reversed, can be utilized at much higher temperatures. This study has involved an experimental survey of magneto-optical effects in garnets at a discrete frequency of 891 GHz and a theoretical investigation of the observed properties.

A theoretical account of the Faraday effect is presented in Chapter Eight and extended to take account of the various properties considered to be important. Seven different rare-earth iron garnets have been studied. Some of these materials have already been studied in the near infra-red and some have also been shown to possess considerable Faraday rotation at 337 μm[13]. The physical properties of the garnets necessary for evaluation, primarily the magnetisation and anisotropy, are outlined in Chapter Nine and are followed in Chapter Ten by the experimental data obtained on Faraday rotation, refractive index and reflection and absorption coefficients. Although the aim of the work is to produce information from which modulators and non-reciprocal devices may be constructed for room temperature operation, measurements were made over a range of temperatures in order to aid theoretical interpretation of the optical parameters in terms of the documented magnetic properties. This analysis and evaluation of the relative merits of the different garnets are presented in Chapter Eleven.

CHAPTER TWO

GENERAL THEORY OF GAS LASERS

2.1. Introduction

As a foundation to the analysis in later chapters, a description will be given of the physical principles of far infra-red gas lasers. The HCN laser is typical of submillimetre gas discharge sources as the refractive index of the inter-cavity medium is not only dependent on the lasing species, but also on the electron density, both of which are time-dependent.

The account will first consider output coupling techniques, the associated losses and the modes of oscillation. This is followed by a description of the processes which occur in the ionised gas column. Finally, a description of the Q-switching mechanism is given.

2.2. Output coupling techniques

A number of different methods can be employed to couple radiation from the laser cavity. An uncommon technique for the submillimetre region is the use of partially transmitting mirrors. However, this will be discussed along with hole coupling, beam splitter coupling and 'Michelson coupling'.

2.2.1. Transmission through mirrors

Partially transmitting mirrors are often used at optical frequencies, but the requirement for high transparency of the substrate on which the reflective film is deposited, restricts their use in the far infra-red. The low gain and consequent large size of many submillimetre lasers necessitates the use of large diameter mirrors which usually limits the choice of material to Melinex film. Curved reflecting surfaces can be produced, as demonstrated by McCaul[14], by using the mirror to form part of a pressurized cell. However, in order to produce a concave mirror, the cell must be placed within the laser cavity, which requires a second Melinex film to be placed across the cavity. The subsequent reduction in Q due to reflections from this additional surface is undesirable and so the technique is essentially limited to the use of plane mirrors.

2.2.2. Hole coupling

A coupling technique often employed in far infra-red lasers is to derive the output beam by means of diffraction at the edge of a small hole in

the centre of one of the cavity mirrors. The laser power incident at such a mirror surface has been represented by Bradley[15] as

$$P = P_0 \int 2\pi r \exp\left\{ \frac{-2r^2}{w} \right\} . \, dr$$

where P_0 is the power per unit area at the centre of the mirror, r is the radial distance from the centre and w is the mode radius. w is defined as the radius at which the amplitude of the radiation at the mirror surface has fallen to $1/e$ of that at the optic axis. The total integrated power is given by

$$P = P_0 \frac{\pi w^2}{2}$$

so, with a hole at the centre of the mirror of radius a_0, and with $a_0 << w$, the fraction of the total power lost by the mirror is

$$T = \frac{2a_0^2}{w^2} \qquad \ldots(2.1)$$

2.2.3. Beam splitter coupling

Beam splitter coupling utilises a dielectric film mounted in the laser cavity at an angle of 45^o to the optic axis. This arrangement produces two output beams, one reflected from each side of the film. Chamberlain et al.[16] have calculated the intensity coefficient of reflection of a dielectric film inclined at 45^o to the incident radiation when multiple interference is taking place. For a material of refractive index n and thickness t, the reflection coefficient r for radiation of frequency ν is given by

$$r = R_{s,p}^{\frac{1}{2}} \frac{1 - \exp\{2i\varepsilon\}}{1 - R_{s,p} \exp\{2i\varepsilon\}} \qquad \ldots(2.2)$$

where

$$\varepsilon = 2\pi\nu tn \cos\theta'$$

θ' is the angle of refraction and $R_{s,p}$ are the single surface reflectivities when the electric vector is respectively polarised perpendicular and parallel to the plane of incidence. The different reflectivities experienced by the two polarisations will present different losses and hence a different cavity Q for the two polarised modes. Unlike the previous coupling techniques, the beam splitter will tend to produce a degree of polarisation of the output beam.

2.2.4. Michelson coupling

This coupling technique, described by Wells et al.[17], also incorporates a beam splitter in the laser cavity at 45° to the optical axis. A third mirror is used to return one of the output beams to the beam splitter. Denoting the amplitude of each of the beams normally reflected out of the cavity as a, then translation of the third mirror towards or away from the beam splitter will alter the intensity of the output beam from zero to $4a^2$.

2.3. Cavity losses

It will be useful for the analysis of Chapter Six to derive an equation for the cavity losses. Consider the cavity represented by Figure 2.1 which has been formed by two mirrors of reflectivities r_1 and r_3 and a beam splitter of reflectivity r_2. Absorption in the laser will be represented by the intensity coefficient A and loss due to diffraction by D, both parameters being defined for one transit of the cavity by a wavefront.

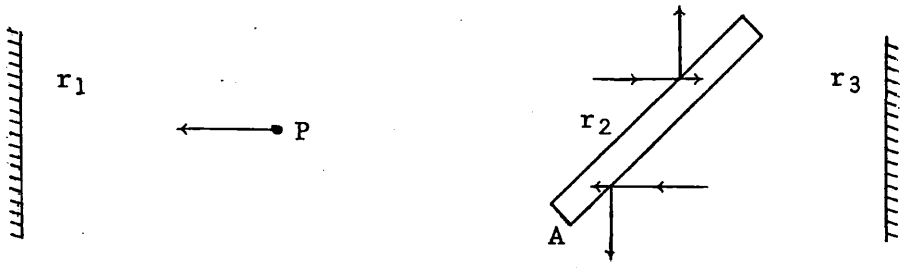

Figure 2.1. Schematic representation of a laser cavity in which beam splitter output coupling is employed. Mirror reflectivities r_1 and r_3, beam splitter reflectivity r_2, fractional absorption loss A.

Following the analysis of Birch and Bradley[18], a beam of unit intensity at a point P in a cavity with no active medium will have an intensity

$$r_1 r_3 (1 - r_2)^2 (1 - A)^2 (1 - D)^2$$

when returning to P after a double pass between the mirrors. The fractional losses in a double pass are therefore expressed as

$$f = 1 - r_1 r_3 (1 - r_2)^2 (1 - A)^2 (1 - D)^2 \qquad \ldots(2.3)$$

2.4. Resonator modes

A theoretical investigation of the diffraction losses in a Fabry-Pérot cavity has been made by Fox and Li[19]. It was found that after many transits of the cavity by the wave-front, a constant field distribution is produced. Many modes can exist in this steady state, the lowest order mode having its greatest intensity on the optical axis and therefore experiencing the lowest diffraction loss. The analysis found the losses in confocal cavities to be, in some cases, orders of magnitude less than those of plane parallel systems. Fox and Li's data showing the power lost per cavity transit plotted against Fresnel number are reproduced in Figure 2.2. For radiation of wavelength λ, incident on a circular mirror of radius a, the Fresnel number is defined as

$$N = \frac{a^2}{L\lambda}$$

L being the length of the cavity. The angle of diffraction from the mirror can be approximated as $\phi = \lambda/2a$ and after travelling a distance L, the energy lost from the wave-front is $2L\phi/a$, which is $L\lambda/a^2$. Hence it is seen that the higher the Fresnel number the lower are the diffraction losses.

It is noted from Figure 2.2 that the nomenclature for modes in hollow waveguides is applied to laser cavities. Using this notation, Kneubühl and Steffen[20] produced an approximate expression for the resonant cavity length L_{qmn} corresponding to the $TEM_{q+1,m,n-1}$ mode as

$$L_{qmn} = \left\{\frac{\lambda}{2}\right\}\left[q + \left\{\frac{1}{N}\right\}\left\{\frac{P_{mn}}{2\pi}\right\}^2\right]$$

q being the longitudinal mode number, P_{mn} the n^{th} zero of the Bessel function of order m, and λ and N are respectively the wavelength and Fresnel number.

The above expression shows that a number of modes can be established within a Fabry-Pérot cavity, but not all will simultaneously oscillate. By geometrical optics, Kogelnik and Li[21] analysed the paths of rays passing between spherical mirrors. Those resonators in which a periodic refocusing of the rays occurs were termed stable oscillators, while those in which a nett divergence takes places were unstable. For an infinite number of passes along a cavity of length L, it was found that stable oscillation occurred when

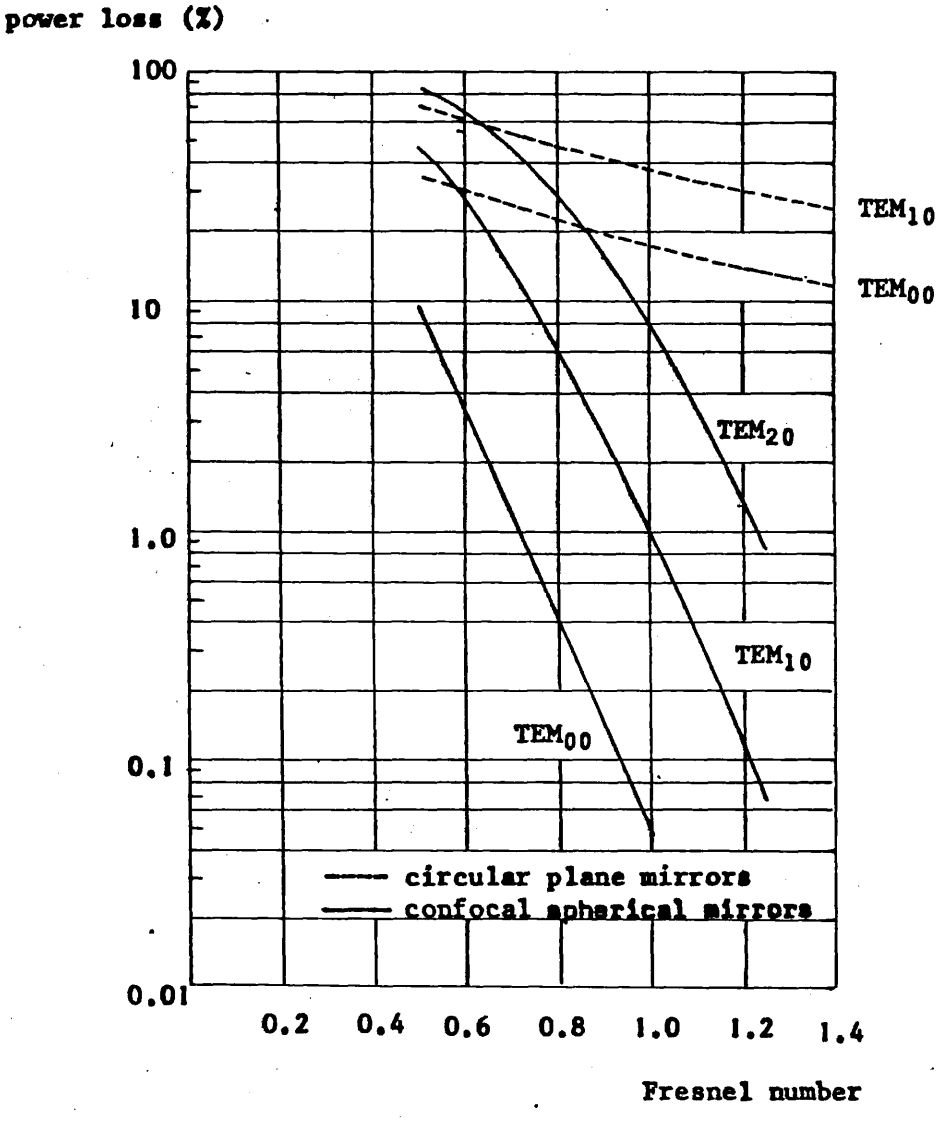

Figure 2.2. Theoretical power loss per cavity transit against Fresnel number. Solid lines for confocal spherical mirrors, dashed lines for circular plane mirrors. After Fox and Li[19].

$$0 < \{1 - \frac{L}{R_1}\}\{1 - \frac{L}{R_2}\} < 1$$

R_1 and R_2 being the radii of curvature of the two mirrors. Kogelnik and Li's diagram depicting stable and unstable formations is reproduced in Figure 2.3, the unstable conditions being shown by the shaded regions. Continuing the investigation by wave analysis, the fundamental mode was found to have a Gaussian radial profile and that the wave-front is coincident with the radius of curvature of the mirrors. This showed that the width of the beam, 2w, must vary along the length of the cavity. The definition of w given in section 2.2.2 for the mirror surfaces is applicable to any position inside the resonator.

An expression, derived by Kogelnik and Li, which will be useful in later chapters, is for the beam radius w at the mirror surface in a cavity with mirrors of equal curvature. Letting $R = R_1 = R_2$, this is

$$w = \{\frac{\lambda R}{\pi}\}^{\frac{1}{2}}\{\frac{2R}{L} - 1\}^{-\frac{1}{4}} \qquad \ldots(2.4)$$

As before, λ is the wavelength of the radiation. It is noted that this relationship was derived for a cavity with an infinite aperture. Because of the rapid slope of a Gaussian curve, the expression is considered to be a good approximation provided that w is less than the radius of the cavity.

2.5. The propagation of electromagnetic radiation through a plasma

The active medium of an HCN laser is formed by an electrical discharge in a vapour or gaseous mixture. The theory of electromagnetic wave propagation in an unmagnetised plasma will now be reviewed in order to evaluate the effect of the plasma on the laser system.

The term 'plasma' is applied to an ionised gas containing equal numbers of negative and positive charges. Each positive ion will be surrounded by a cloud of electrons whose nett charge is equal and opposite to that of the ion. The potential which controls the distribution of particles about the ion is given by the 'screened Debye interaction'[22]

$$v(r) = \frac{Ze}{\varepsilon r} \exp\{\frac{-r}{\lambda_D}\}$$

r represents the distance of the electron from the ion, Z is the number of charges on the ion, e is the electronic charge, ε the permittivity of the medium and λ_D is the Debye length. When $r << \lambda_D$, the interaction

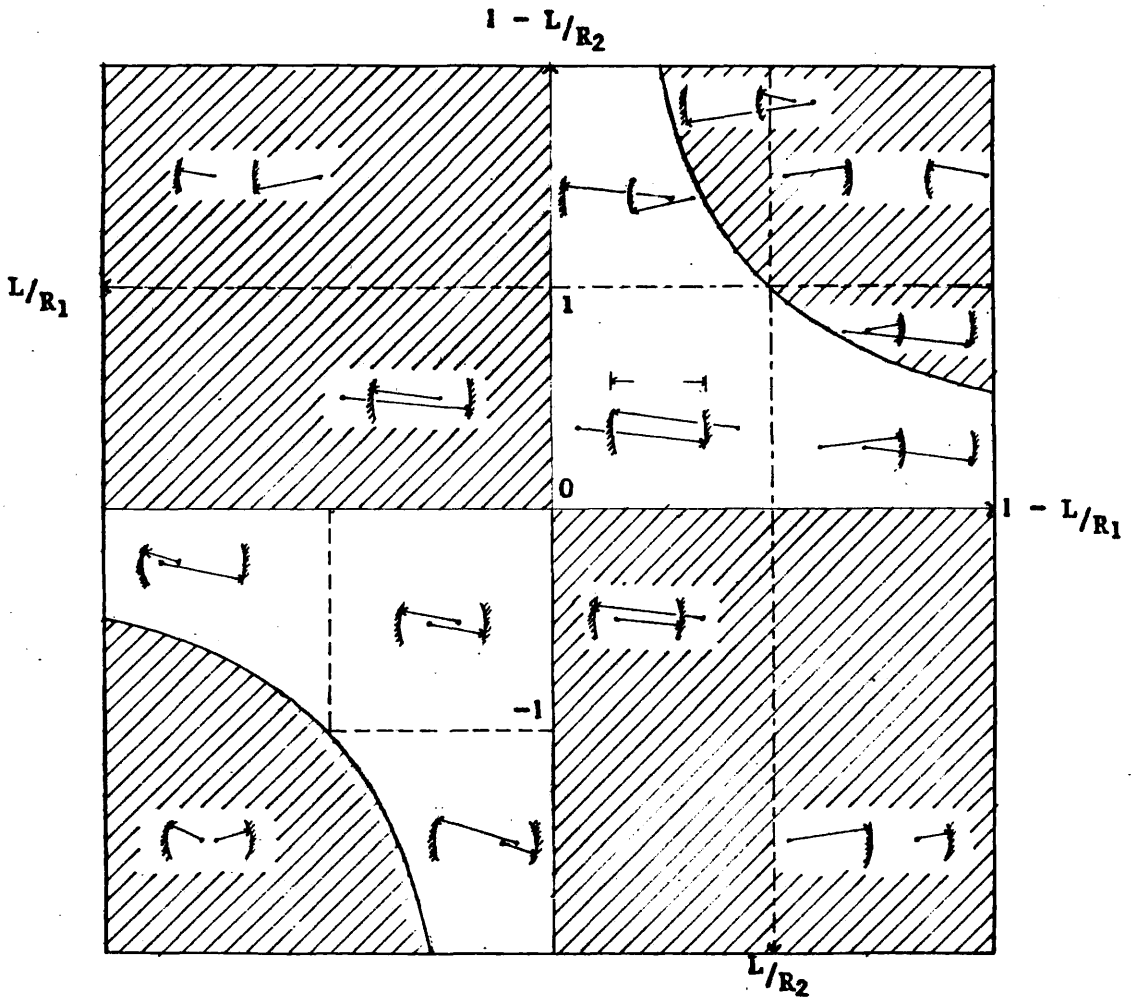

Figure 2.3. Stability diagram of laser cavities. Unstable cavities occur in shaded regions. After Kogelnik and Li[21].

between the electron and ion approximates to that of the Coulomb law; however, for $r \geq \lambda_D$, the field tends to zero exponentially, due to screening by the electron cloud. The Debye length in plasmas that form the active medium of an HCN laser is less than 10 μm[14] and hence less than the 337 μm wavelength of the laser radiation. For these conditions, the contribution of the 'free' electrons to the refractive index μ of the plasma is given by[22]

$$\mu^2 = 1 - \left\{\frac{\omega_p}{\omega}\right\}^2 = 1 - \frac{n}{n_c} \qquad \ldots(2.5)$$

Here ω is the angular frequency of the radiation, n the electron density and ω_p is termed the plasma frequency given by

$$\omega_p = \left\{\frac{ne^2}{\varepsilon m_e}\right\}^{\frac{1}{2}}$$

m_e being the mass of an electron. n_c is the highest electron density through which the radiation can propagate and is often referred to as the 'cut-off' density. The 'cut-off' condition corresponds to $\omega = \omega_p$ from which the critical density is given by

$$n_c = \omega\left\{\frac{m_e}{e^2}\right\}^{\frac{1}{2}} \qquad \ldots(2.6)$$

At least two electron decay mechanisms occur in the laser plasma. Firstly, diffusion to the walls of the tube which, in the absence of electric and magnetic fields, is described by[23]

$$n_e(t) = n_0 \exp\left\{-\frac{D.t}{\Delta^2}\right\} \qquad \ldots(2.7)$$

where n_0 is the density at a time t = 0, D is a diffusion coefficient and Δ is known as the characteristic diffusion length and is dependent on the geometry of the plasma tube as

$$\frac{1}{\Delta^2} = \left\{\frac{\pi}{L}\right\}^2 + \left\{\frac{2.405}{r}\right\}^2$$

L and r being the tube length and radius respectively.

At the magnitude of electron density observed in the plasma of a pulse-excited HCN laser[14,24], space charge effects between electrons and ions would be expected to produce ambipolar diffusion[14,25]. Mutual attraction

between oppositely charged particles would tend to restrain the more rapidly moving electrons while increasing the velocity of the ions. Hence, D in equation 2.7 becomes the ambipolar diffusion coefficient.

The second electron decay mechanism is electron-ion recombination. This takes place under conditions of nett charge neutrality. Denoting the ion density by n_+, space charge neutrality requires

$$n_+ = n_e$$

A recombination coefficient α is defined by[26]

$$\frac{dn_+}{dt} = \frac{dn_e}{dt} = -\alpha\, n_e n_+$$

or
$$\frac{dn_e}{dt} = -\alpha n_e^2$$

If α is a constant, the solution becomes

$$\frac{1}{n_e} - \frac{1}{n_0} = \alpha t \qquad \ldots(2.8)$$

where $n_e = n_0$ at $t = 0$.

In a later examination, a recombination coefficient will be determined for the plasma that forms the active medium of the hydrogen cyanide laser. A number of different types of ion constitute such a discharge, so an effective recombination coefficient α_{EFF} is introduced to represent the overall recombination loss.

Equation 2.5 shows that during the transient conditions of a pulse-excited laser, the refractive index of the plasma will vary, altering the optical path length of the cavity. It is therefore expected that during the ionisation and afterglow periods, the cavity will be disturbed from its resonant condition. Provided that the variation of electron density is large enough, the laser may be swept through several 'gain profiles'. This situation can be analysed by equating the optical path length in the cavity to an integral number of half wavelengths which represents a resonant condition. Regarding the cavity to be composed from a non-ionised region of length L_v and a plasma of length L_p, then

$$L_v + L_p\left\{1 - \frac{n}{n_c}\right\}^{\frac{1}{2}} = q \cdot \frac{\lambda}{2} \qquad \ldots(2.9)$$

q being the longitudinal mode number. Differentiating yields

$$\frac{dq}{dn} = \frac{-L_p}{n_c\lambda\left\{1 - \frac{n}{n_c}\right\}^{\frac{1}{2}}} \qquad \ldots(2.10)$$

At a particular value of n, this equation is seen to be constant for a laser of specified frequency and active length. This result will be of use in later analysis in which the time dependence of the output power of the laser is explained in terms of the phenomenon of 'mode sweeping' by the decaying plasma. For a laser of total cavity length L operating at a centre frequency ν, the change in optical path ΔL necessary to sweep through the gainwidth $\Delta\nu$ is obtained from the relationship[24]

$$\frac{\Delta L}{L} = \frac{\Delta\nu}{\nu}$$

Differentiating the path length in equation 2.9 with respect to time gives the rate of change of path length

$$\frac{-1}{\left\{1 - \frac{n}{n_c}\right\}^{\frac{1}{2}}} \cdot \frac{L_p}{2n_c} \cdot \frac{dn}{dt}$$

This result permits the time taken by the plasma to sweep the laser through its gain profile to be calculated from

$$\Delta t = \frac{\frac{-\Delta\nu}{\nu} \cdot \left[L_v + L_p\left\{1 - \frac{n}{n_c}\right\}^{\frac{1}{2}}\right]\left\{1 - \frac{n}{n_c}\right\}^{\frac{1}{2}}}{\frac{L_p}{2n_c} \cdot \frac{dn}{dt}} \qquad \ldots(2.11)$$

As the build-up of the laser output must take place within this period, this parameter introduces a fundamental limitation to the power generated by the laser. Its effect on Q-switching and on the unmodulated laser will be examined in later chapters.

It was stated earlier that the decay of a plasma was due, in part, to diffusion of charged particles. McCaul[14] has analysed the situation in which diffusion to the walls produces a radial electron distribution which creates a divergent plasma lens. The variation of the density along the radius r of a tube of radius r_0 was represented in an

approximate form by the parabola

$$n(r) = n_0\left[1 - \beta\left\{\frac{r}{r_0}\right\}^2\right]$$

n_0 being the electron density on the axis of the tube, and β an empirical constant of a value in the range $0 < \beta < 1$. The effect of this distribution on the path of a ray has been given by McCaul in the form of a matrix equation. The position r_2 and slope r_2' of a ray with respect to the optical axis after travelling a distance L in a plasma from a point r_1 from the axis at a slope r_1' can be calculated from

$$\begin{bmatrix} r_2 \\ r_2' \end{bmatrix} = \begin{bmatrix} \cosh \alpha L & \frac{\sinh \alpha L}{\alpha} \\ \alpha \sinh \alpha L & \cosh \alpha L \end{bmatrix} \begin{bmatrix} r_1 \\ r_1' \end{bmatrix} \qquad \ldots(2.12)$$

where $\alpha = \left[\frac{\beta n_0}{r_0^2 n_c}\right]^{\frac{1}{2}}$

Assuming the entire length of the cavity to be filled with plasma, McCaul presented the conditions required for stable oscillation by

$$0 < \left[\cosh \alpha L - \frac{\sinh \alpha L}{\alpha R_1}\right]\left[\cosh \alpha L - \frac{\sinh \alpha L}{\alpha R_2}\right] < 1 \qquad \ldots(2.13)$$

R_1 and R_2 are the radii of curvature of the laser mirrors. This shows that at high electron densities, losses through refraction could be sufficiently large to prevent the build-up of radiation. A stability diagram produced by McCaul to include the electron lens effects is reproduced in Figure 2.4. Over a range of conditions the plasma can render the laser unstable, but as the density decays after pulsed excitation, the position of the system on the diagram moves from the lower left to the upper right. The cavity can therefore be swept from an unstable condition to one which may support oscillation. The effect of such action on the build-up of radiation in the laser cavity must depend on the rate of reduction of the refractive losses. An investigation into this process will be described in Chapter Four.

It is evident that the variation of the electron density in the active medium of a laser can play a dominant rôle in determining the temporal output characteristics of the device. It would therefore be of interest

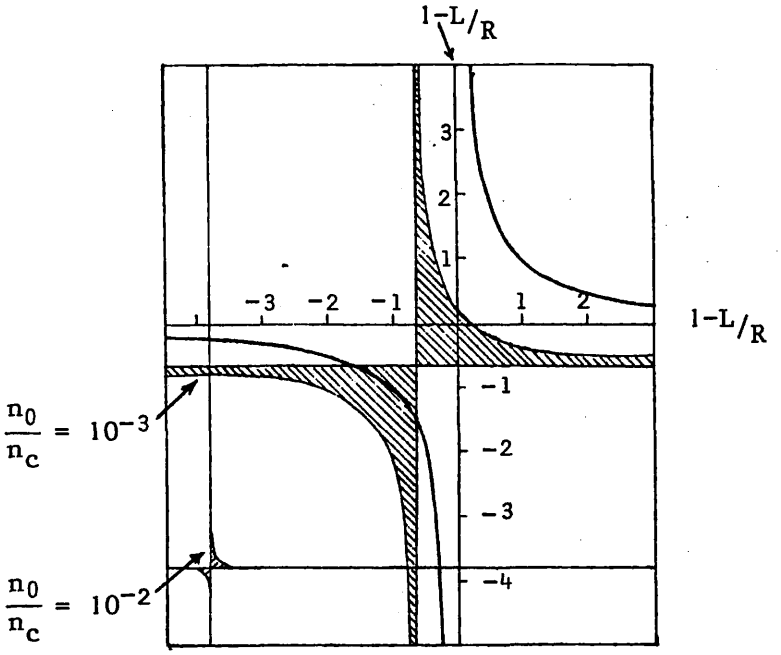

Figure 2.4. Stability diagram of a laser cavity in which the electron lens effect is included. $L/r_0 = 60$. Stable conditions are represented by shaded areas (after McCaul, reference 14).

to determine this variation experimentally. This can be achieved by recording the output from an interferometer as it passes through successive conditions of constructive interference due to the changing optical path in a plasma located in one of the interferometer arms. The phase shift incurred in counting either N minima or N maxima at the output is given by

$$\Delta\phi = 2\pi N$$

This can be expressed in terms of the difference in phase which occurs with the plasma present in the tube and then in the absence of the plasma after its decay. Using equation 2.5, this is

$$\Delta\phi = \frac{2\pi}{\lambda} x\left[1 - \left\{1 - \frac{n}{n_c}\right\}^{\frac{1}{2}}\right]$$

where x is the geometrical length of path in the plasma. Equating the two expressions enables the density to be calculated directly as

$$n = n_c\left[1 - \left\{1 - \frac{N\lambda}{x}\right\}^2\right] \qquad \ldots(2.14)$$

2.6. Rate equations

Transitions between vibration-rotation energy levels of the active molecule of a far infra-red laser are depicted in Figure 2.5 as part of a series of cascading levels.

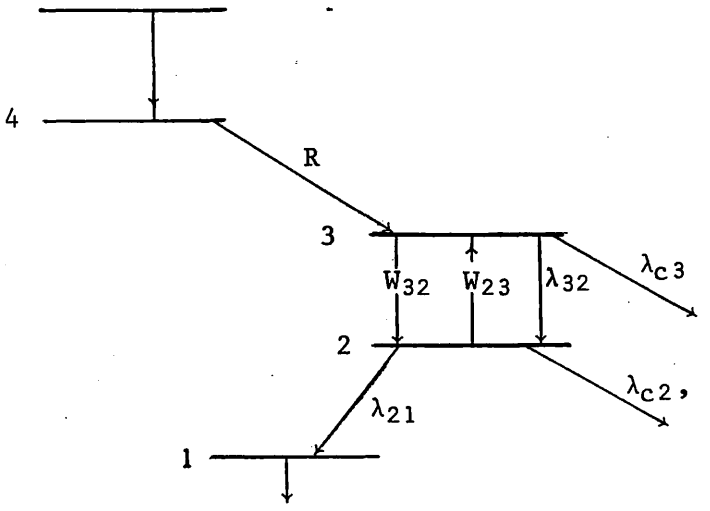

Figure 2.5. Diagram of a simplified model of the energy levels in a far infra-red laser active molecule. Pump rate R, stimulated transition probabilities W_{32} and W_{23}, spontaneous radiative probabilities λ_{32} and λ_{21}, and collisional de-excitation probabilities λ_{c3} and λ_{c2}.

This simplified model considers only one stimulated transition to be present. It has thus been assumed that the laser operates at a single frequency. A more complex situation will be described in Chapter Three for the HCN molecule where simultaneous emission of several lines involves tight coupling between the various levels. Of the four levels shown in the diagram, stimulated emission takes place from level 3 to level 2. The rate at which molecules are populated in level 3 by decay from level 4 will be assigned as the pump rate R. For a gas discharge laser in which the active species are created during the ionisation period, the pump rate is expected to be a function of the overall recombination rate. If K is the fraction of the recombined particles which become 'active' molecules, then

$$R = R(K\alpha_{EFF} n_e^{\,2})$$

Following the analysis of Frayne[27], the effective transition probability in the absence of stimulated emission for the upper λ_3, and lower λ_2, energy levels of the lasing transition will be considered to be formed respectively from a radiative contribution λ_{32}, λ_{21} and a collisional contribution λ_{c3}, λ_{c2} such that

$$\lambda_3 = \lambda_{32} + \lambda_{c3}$$

and

$$\lambda_2 = \lambda_{21} + \lambda_{c2}$$

Representing the probabilities for stimulated emission from level 3 to level 2 as W_{32} and from level 2 to level 3 by W_{23}, then the rates of population of the two energy levels can be expressed as

$$\frac{dN_3}{dt} = R + W_{23}N_2 - (\lambda_3 + W_{32})N_3$$

and

$$\frac{dN_2}{dt} = (W_{32} + \lambda_{32})N_3 - (W_{23} + \lambda_2)N_2$$

N_3 and N_2 are the number densities of the molecules in the upper and lower states. If we now consider the steady state situation necessary for CW operation, then

$$\frac{dN_3}{dt} = \frac{dN_2}{dt} = 0$$

which gives

$$R + W_{23}N_2 = (\lambda_3 + W_{32})N_2$$

and

$$(W_{23} + \lambda_2)N_2 = (W_{32} + \lambda_{32})N_3$$

By combining these two equations, the expressions for the population of the upper and lower states are given by

$$N_3 = \frac{(W_{23} + \lambda_2)R}{W_{23}(\lambda_3 + \lambda_2 - \lambda_{32}) + \lambda_3\lambda_2}$$

and

$$N_2 = \frac{(W_{32} + \lambda_{32})R}{W_{23}(\lambda_3 + \lambda_2 - \lambda_{32}) + \lambda_3\lambda_2}$$

Two parameters of importance in later analysis are the population inversion $N = N_3 - N_2$ and the density of molecules available to interact with the laser radiation $N_3 + N_2$. For a steady state condition, these may be written as

$$N = \frac{R(\lambda_2 - \lambda_{32})}{W_{23}(\lambda_3 + \lambda_2 - \lambda_{32}) + \lambda_3\lambda_2} \qquad \ldots(2.15)$$

and

$$N_3 + N_2 = \frac{R(\lambda_2 + \lambda_{23} + 2W_{23})}{W_{23}(\lambda_3 + \lambda_2 - \lambda_{32}) + \lambda_3\lambda_2} \qquad \ldots(2.16)$$

2.7. Q-switching

The gain of a laser medium is proportional to the population inversion and may be written

$$\alpha = \sigma(N_3 - N_2) \qquad \ldots(2.17)$$

The parameter σ is referred to as the peak absorption cross-section and is defined by[28]

$$\sigma = \frac{\alpha_0}{N_3 + N_2}$$

where α_0 is the peak absorption of the transition. For many lasers, α_0 can be determined by measuring the absorption in the laser medium at a low pump intensity, which ensures that the majority of particles are in their ground state. At a fixed value of $N_3 + N_2$, σ is then a measurable constant. For the type of laser described in section 2.6, the lower energy level of the transition is not the ground state and so a direct attenuation measurement cannot be made. It is also evident that $N_3 + N_2$ is not constant and is dependent on the pump rate. For a gas discharge laser, α_0 will be regarded as the gain at low intensity for specified conditions of pressure and pump rate.

In the Q-switching technique, stimulated emission is prevented from taking place by temporarily reducing the 'Q' of the cavity whilst maintaining a high pump rate. This enables the population inversion to build up above the threshold value necessary for laser action. The subsequent rise and decay of radiation in the laser resulting from switching the cavity from a low to a high Q condition passes through the phases illustrated in Figure 2.6. After the switching action, a period of slow build-up of radiation occurs, τ_D, followed by a faster

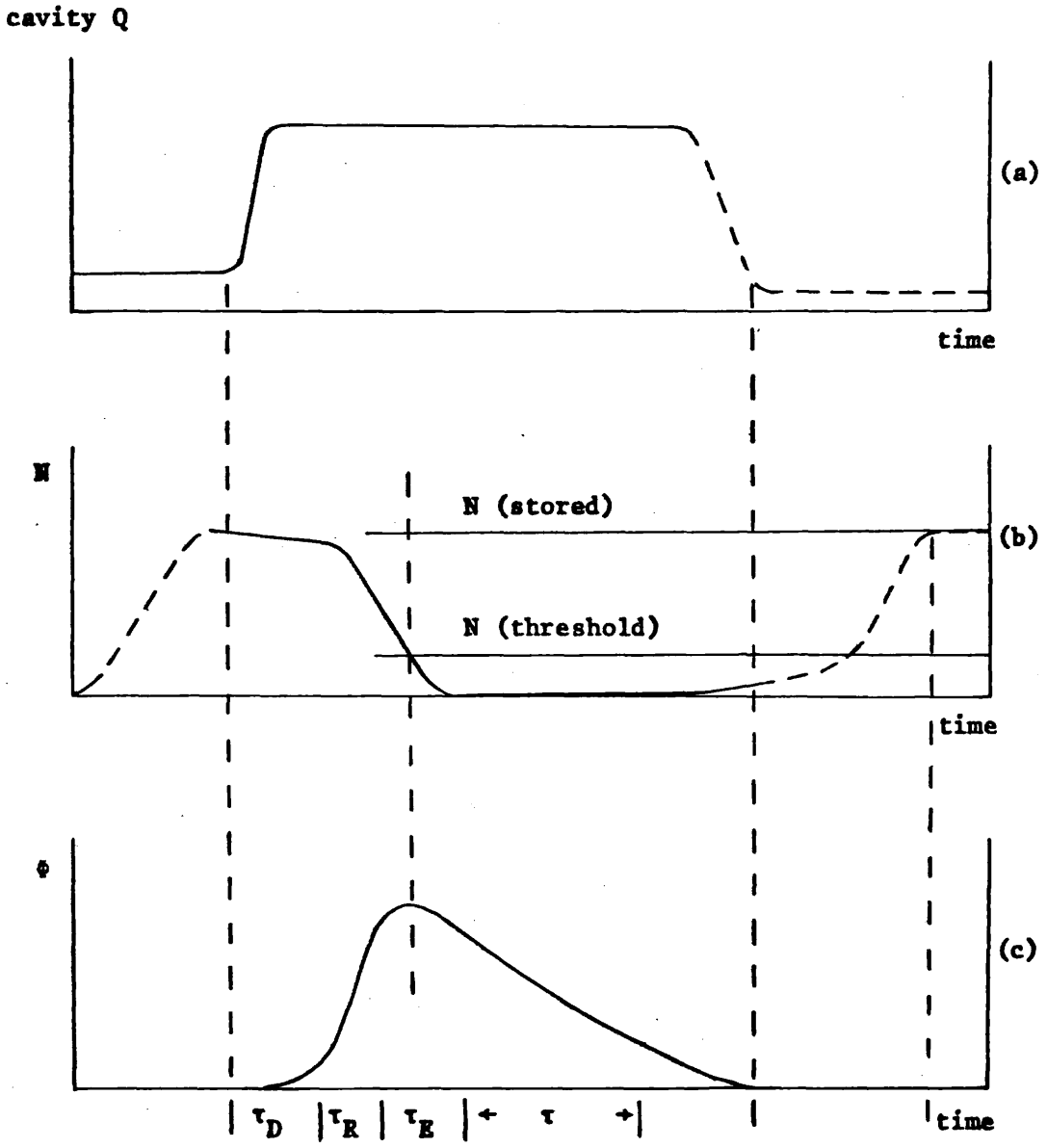

Figure 2.6. The variation with time of (a) the cavity Q, (b) the population inversion, and (c) the photon density in a fast Q-switched laser

increase in a time τ_R, the pulse rise time. The radiation trapped in the cavity undergoes a rapid rise in intensity until a fall in the gain results from a significant reduction in the population inversion. Following this rapid rise, a time τ_E elapses in which the large photon density depletes the inversion. Due to the finite losses in the cavity, the radiation then decays in a time τ, the cavity decay time. When analysing Q-switched pulses, it is useful to express τ in terms of these losses by

$$\tau \simeq \frac{-2t_L}{\log_e(1 - f)} \qquad \ldots(2.18)$$

where t_L is the transit time of a wavefront between the ends of the cavity and f the fractional losses described in section 2.3. It will be seen in Chapter Four that τ, α, t_L and the cavity length L, determine the overall rise of the output pulse. This includes τ_D, which sets a limit to the time in which the switching action must be completed to take advantage of the large population inversion when the photon density is rising at its maximum rate.

Consider a wavefront in a laser with a gain sufficiently small that changes in the energy distribution may be ignored. The fractional increase per second $\dot{\Phi}/\Phi$ of the photon density is approximately $\alpha L/t_L$. Expressing the fractional loss rate as $\gamma(t)/\tau$, then

$$\frac{d\Phi}{dt} = \left[\frac{\alpha L}{t_L} - \frac{\gamma(t)}{\tau}\right] \Phi \qquad \ldots(2.19)$$

$\gamma(t)$ is a time-dependent loss term which represents the Q-modulation.

The time dependence of the population inversion N is evaluated in terms of the pump rate and loss rates due to stimulated and spontaneous emission and collisional depopulation. Emission of a photon reduces N by two units, which produces a contribution to the inversion rate of $-2\alpha L/t_L$. The effect of collisional and radiative decay of both the upper and lower levels of the transition will be taken into account by a single probability λ. Evaluation of this parameter will be undertaken in Chapter Six. Using equation 2.17, the rate of change of population inversion may be expressed as

$$\frac{dN}{dt} = -2\Phi\sigma N \frac{L}{t_L} + R - \lambda N \qquad \ldots(2.20)$$

To facilitate the use of equations 2.19 and 2.20 in later chapters, the term 'threshold inversion' will be defined. A laser is said to be at its threshold condition when the gain is exactly balanced by the losses such that

$$\frac{\alpha L}{t_L} = \frac{\gamma(t)}{\tau}$$

Equation 2.19 shows this to occur when $d\phi/dt = 0$ and, as illustrated in Figure 2.6, threshold inversion is attained at the peak of the Q-switched output pulse. The threshold inversion is obtained from equation 2.17 to determine the population inversion corresponding to α in the above expression as

$$N_p = \frac{t_L}{\tau\sigma L} \qquad \ldots(2.21)$$

CHAPTER THREE

THE HYDROGEN CYANIDE LASER

3.1. The active molecule

Stimulated emission at a wavelength of 337 microns was first observed in 1964 by Gebbie, Stone and Findlay[2] when pulse ionising each of the gaseous compounds HCN, CH_3CN and C_2H_5CN in a 6 metre long plane optical cavity. CW emission was performed by Gebbie et al.[29] in 1966. Identification of the active species was advanced by Stafsudd et al.[30] when showing that the laser line could only be generated when hydrogen or deuterium was added to a carbon-nitrogen mixture. As the emission lines did not fit the then known spectrum of the HCN molecule, Stafsudd suggested that a molecule of the form H_xCN, where $x > 1$, was being produced. However, Lide and Maki[31] theoretically calculated the vibration-rotation energy levels in the HCN molecule, shown in Figure 3.1, which agreed with accurate frequency measurements in Table 3.1 made by Hocker and Javan[32].

Table 3.1

Accurate frequency measurements of CW HCN laser emission lines

(after Hocker and Javan, reference 32; calculated values after Lide and Maki, reference 31)

Frequency (GHz)	Wavelength (microns)	Calculated wavelength (microns)
804.7509	372.5283	372.55
890.7607	336.5578	336.50
894.4142	335.1831	335.24
964.3134	310.8870	311.83
967.9658	309.7140	309.70
(unmeasured)	284	284.01

The measurement technique was to harmonically mix the submillimetre radiation with the output from an 'O-band' klystron. The frequencies of the five main lines from 310 to 373 μm were obtained to an estimated accuracy of 1 part in 10^6. Further frequency measurement was carried out by Bradley et al. [33] producing a value for the 337 μm line

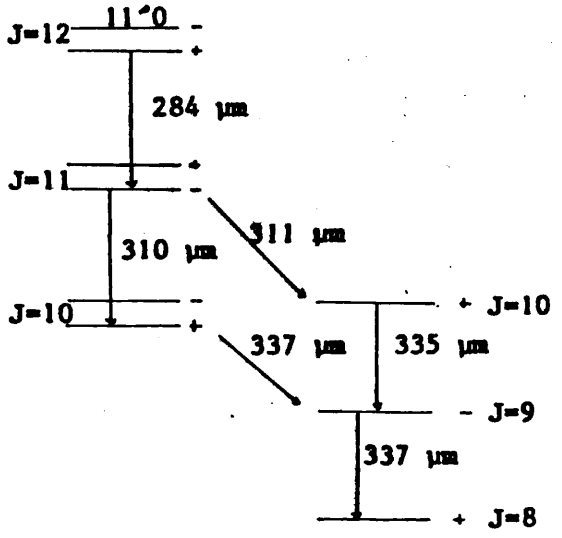

Figure 3.1. Energy level diagram for the HCN molecule. After Lide and Maki[31].

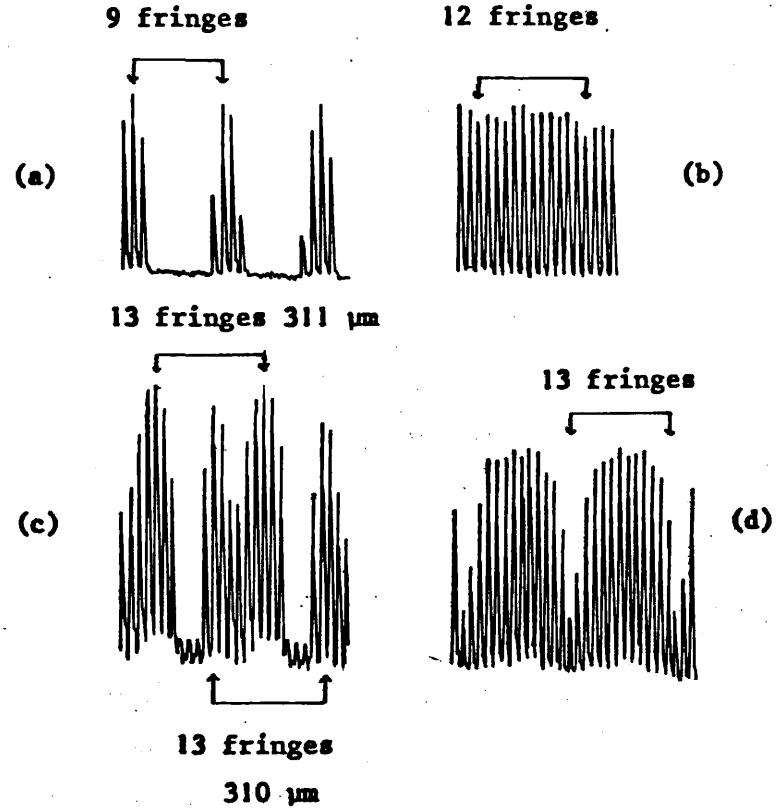

Figure 3.2. Recorded modulations with cavity length of (a) 373 μm, (b) 337 μm, (c) 311 μm and 310 μm, and (d) 311 μm wavelength radiation from the HCN laser. After Frayne[27].

of 890760.2 ± 0.2 MHz.

Also by harmonic mixing with an 'Q-band' klystron, Hocker et al.[34] measured the gain width of the 337 μm line from a CW laser to be 8±2 MHz. To obtain maximum output from the laser with such narrow line widths, the length of the cavity requires optimization for each axial mode. Making use of this property to observe successive modes by linearly varying the optical cavity length, Frayne[27] provided additional confirmation of the energy level scheme of Lide and Maki. The interferograms obtained and reproduced in Figure 3.2 were filtered with a grating spectrometer in order to study the modes of each wavelength separately. It was found that tight coupling between the J=10($04^{o}0$) and the J=9($04^{o}0$) rotational levels produced competition between modes oscillating at 337 μm and 311 μm. The population of the J=9($04^{o}0$) level increases when the laser is operating at 337 μm and because of the coupling of successive levels, the population of level J=10($04^{o}0$) also increases, resulting in a less intense line at 311 μm than would have occurred had there been no emission at 337 μm. It was also found that when a length of cavity had been selected that should allow simultaneous oscillation at both 310 μm and 311 μm, then emission took place at 311 μm when neither the 310 μm nor the 337 μm lines oscillated. This is explained by cascade from J=10(11'0) to J=9(11'0) being inhibited every 12.54 fringes of 310 μm, observed experimentally by Frayne every 13 fringes. This observation suggests that cascading transitions are tightly coupled and that, under the conditions of the experiment, collisional depopulation is not a dominant process. This is considered to be a necessary, although insufficient, condition for a worthwhile increase in power by Q-modulation.

3.2. The CW HCN laser

Stimulated emission at a wavelength of 337 μm can be obtained by ionisation of several different compounds and gaseous mixtures. The gain of these media has been measured by Stafsudd and Yeh[35] by operating a d.c. discharge in an amplifier tube through which submillimetre radiation was directed. The maximum intensity of the input beam to the tube was 7.2×10^{-4} watts cm^{-2}, the gain measurements being found to be independent of the signal power at these levels. The largest gain measured by Stafsudd was in a methane-nitrogen mixture. Two sets of data for this mixture are reproduced in Figure 3.3(a) for a pressure ratio methane:nitrogen of 2:1 and in Figure 3.3(b) for a 1:1 ratio. The gain is seen to be a function of pressure and discharge current and is observed to decrease with increased tube diameter.

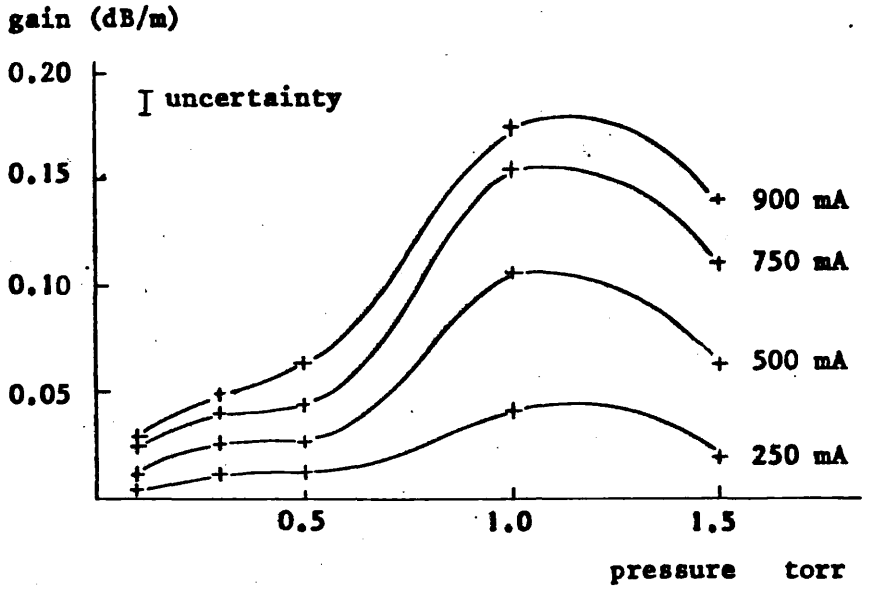

(a)

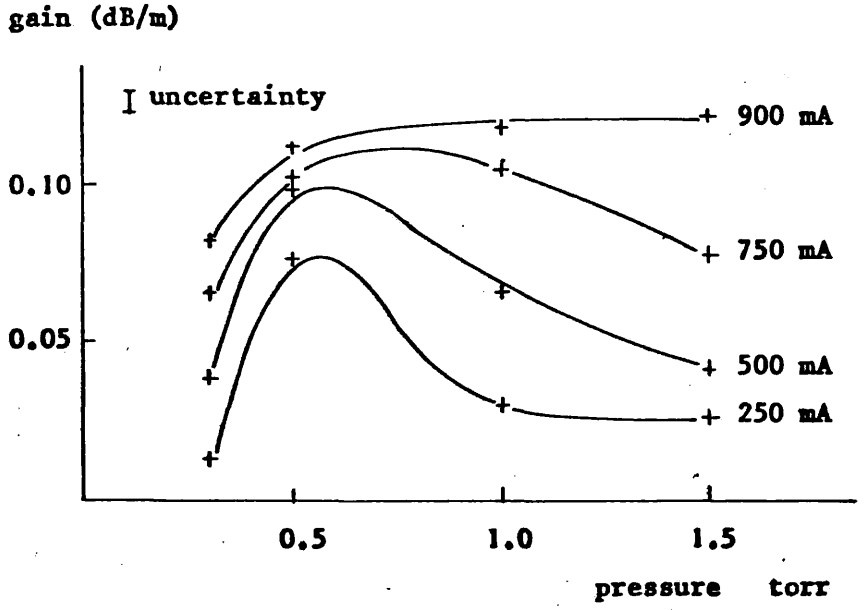

(b)

Figure 3.3. Gain at 337 μm wavelength against pressure in d.c. discharges in (a) a 2:1 ratio of N_2 to CH_4 in a 5 cm diameter tube, and (b) a 1:1 ratio of N_2 to CH_4 in a 7.5 cm diameter tube. After Stafsudd and Yeh[35].

With a 1:1 mixture of methane and nitrogen, Fuller[33] found that by restricting the range of gas pressures and limiting the current, a striated discharge can be produced. This was found to be necessary in order to obtain a narrow output line which, with very stable striations, could be reduced to a few kilohertz in width at 891 GHz. Increasing the current would, at some point, produce a non-striated discharge and although, in general, higher powers could be generated, the line width would increase by almost one hundred times.

A CW power of 60 mW from a 2.5 metre long 7.5 cm diameter HCN laser has been reported by Stafsudd[35]. Lasers with a longer cavity and larger diameter have been built by Sharp and Wetherell[36] and by Bradley et al.[33]. Sharp and Wetherell reported 42 mW from a 3.4 metre long, 14 cm diameter hole coupled laser, while Bradley obtained 75 mW from an 8.5 metre long, 10 cm diameter cavity, using the Michelson coupling technique described in section 2.2.4.

3.3. The pulse-excited HCN laser

Submillimetre radiation in the form of one or more pulses is generated when ionising the gaseous medium of an HCN laser by means of a high current pulsed discharge. This radiation can be emitted during the current flow period or in the afterglow, and peak powers of 450W have been reported by Sharp and Wetherell[36] from a discharge current of 560 amperes.

A decaying plasma can sweep a laser through its gain profile as described in section 2.5. This phenomenon has been observed experimentally by Whitbourn et al.[24]. The duration of pulses generated in the afterglow was seen to increase with the time elapsed from the current discharge and showed agreement with equation 2.11 as the plasma decay rate decreased throughout this period. Equation 2.9 shows that for an increase in cavity length, a greater electron density is necessary to maintain the resonant condition. A pulse of radiation emitted from a decaying plasma is therefore expected to occur at an earlier time after lengthening the cavity. This effect was also observed by Whitbourn et al. Agreement was obtained between measured and calculated mirror displacements, which provided further confirmation of the mode scanning mechanism.

With pulse-excited far infra-red lasers, a period of time can exist between the end of the current pulse and the onset of oscillation. This

delay has been observed in the HCN[37,38,39,40,41,42] and other gas discharge lasers[43,44,45,46], and under the same conditions of laser configuration and plasma density has been found to be shorter at higher radiation frequency[43,46,47]. This characteristic has been attributed by McCaul[14] to the refractive lens effect described in section 2.5. The finite time taken by a decaying plasma to sweep the cavity from an unstable condition to one in which stimulated emission may build up is suggested by McCaul to constitute a self Q-switching mechanism. Equation 2.13 shows the period of instability to be determined by the radial distribution of the electron density, the geometry of the cavity, and the cut-off density. The latter term is a function of the frequency of the radiation and hence support for McCaul's theoretical analysis is given by the experimentally observed frequency dependence.

In all the investigations reported above, the gaseous media were excited by an axial discharge along the laser cavity. Stimulated emission from a transversely excited HCN laser has been obtained by Lam et al.[48] but only peak powers of 9W were produced. Although the technique of transverse excitation has been improved by Kneubühl et al.[6] to include u.v. pre-ionisation, an assessment of whether any notable advantage was attained cannot be made as only the energy of the output pulses was reported, which was found to be in the range 1 to 10 mJ.

3.4. Active Q-switching of the HCN laser

Active Q-switching of the HCN laser has been performed by Jones et al.[42] and by Frayne[27], using the rotating mirror technique. Jones et al. separated the rotating mirror from the active medium by a polyethylene film, while Frayne incorporated the rotating mirror into the vacuum system thus eliminating the need for a window across the optical cavity. Pulses of radiation with peak intensity two to three times the CW level were produced by Jones et al. when modulating a d.c. excited laser, and slightly larger values of five times were reported by Frayne. However, when Q-switching a pulse-excited laser, increases of two to three times the non-modulated output were again produced by Jones et al., while an improvement of twenty-five times was reported by Frayne. Both investigations showed that an optimum rotation rate of the mirror exists for maximum output. Decrease in peak power and pulse width at rotation rates greater than the optimum value were attributed by Jones et al. to the time of alignment of the cavity being too short to allow the radiation to build up.

Plasma decay modulation has been used by Tait et al.[49] as a Q-switching technique. Fast modulation of the optical path of the cavity was produced by locating a separate discharge within the laser cavity which was ionised by means of a separate pulsed power supply. This discharge, directed transversely to the axis of the laser, was separated from the active medium by a polythene diaphragm to enable experiments to be performed with gases other than the methane-nitrogen mixture. It was found that with d.c. excitation of the active medium, the transient conditions of the ancillary discharge caused the laser to generate pulses of 337 μm and 311 μm radiation. Experiments were performed by pulse ionising hydrogen, nitrogen, argon and helium. Hydrogen had the faster rate of decay and argon and helium the slower. Laser action took place after the peak density of the pulsed discharge had been reached, after a delay which was greatest for the more slowly decaying plasmas. Two possible reasons are forwarded by Tait et al. for this result. The collision frequency in the plasma may have been high, thus keeping the laser below its threshold gain level, or the radial plasma density profile may have prevented oscillation, due to refraction. It was found that the rise of the radiation pulses was composed of a rapid build up in intensity followed by a more gradual increase. Tait et al.'s interpretation of this is that laser action commences within the gain profile of the laser and is then swept round the profile by the transient discharge. During the earliest pulses, when the phase shift was most rapid, the switching plasma swept the laser towards its line centre and beyond before a significant build-up of radiation could take place. Tait et al. suggested that this indicates that the plasma sweeping was sufficiently fast for useful Q-switching but in practice, even under the most rapid switching conditions, the shortest pulses lasted approximately 5 microseconds and no enhancement of the laser power was observed.

Without prior knowledge of the work of Tait et al., an auxiliary pulsed discharge placed within the optical cavity of a laser was included as one of the Q-switching techniques evaluated as part of this investigation. A larger ratio of the optical path length in the switching plasma to that in the active medium was produced by orientating the auxiliary discharge longitudinally to the optic axis of the laser. A more rapidly changing phase condition, and hence a faster switching action, were thus obtained. However, increasing the speed of an optical switch produced by a transient discharge can have the detrimental effect of

reducing the time available for the laser radiation to build up. This situation will be considered further as part of a theoretical evaluation in Chapter Four.

CHAPTER FOUR

MODULATION OF THE HCN LASER

4.1. Introduction

A brief account of previous investigations into Q-switching the HCN laser by plasma phase shift and by the rotating mirror technique was given in Chapter Three. A theoretical analysis will now be described in which the merits of these and of other switching techniques will be compared.

4.2. Fast cavity Q-switching

Figure 2.6 illustrates the behaviour of a high inversion fast switched laser. A more detailed analysis of this situation will follow after describing two techniques by which a step change in the cavity Q may be produced by actively modulating the losses of the system. Initially an infinitely fast switch will be assumed; however, the effect on the radiation output from finite switching times set by the limitations of practical techniques will be assessed in section 4.3.

4.2.1. Gaseous absorber switch

Gases and vapours producing strong attenuation of the emission lines of the HCN laser have been reported by Bradley et al.[50] and by Duxbury et al.[51] and a further investigation into such absorption properties will be described in Chapter Five. A switching technique is proposed whereby stimulated emission is suppressed by introducing a cell containing such a gas into the laser cavity. High Q conditions are then established by ionising the absorbing medium my means of a subsidiary discharge.

4.2.2. Polarisation switch

It was stated earlier that a Faraday rotation device has been produced by Birch and Jones[11] from which modulation frequencies in excess of 2MHz were obtained. The availability of such a device makes possible modulation of the polarisation within a laser cavity. The hemispherical resonator formation used by Birch and Bradley[18] might reduce the beam diameter sufficiently to pass through the aperture of a practicable device. Beam splitter output coupling ensures that only modes with the electric field perpendicular to the plane of the beam splitter oscillate. Q-switching is achieved by rotating the beam

through 90^{o} per double pass, thus preventing oscillation, and then switching the magnetic field of the rotator so that no net rotation is produced.

4.2.3. Output from a fast switched laser

Analysis of the laser output produced by fast Q-switching is obtainable from the rate equations 2.19 and 2.20 by assuming a step change in the loss parameter $\gamma(t)$. Following the method used by Hellworth[28], the rate equations will be divided by the threshold inversion

$$N_p = \frac{t_1}{\tau\sigma\ell}$$

and defining

$$n = \frac{N}{N_p}\ ,\ \phi = \frac{\Phi}{N_p} \quad \text{and} \quad r = \frac{R}{N_p}$$

enables the equations to be expressed in a more convenient form for computation as

$$\frac{d\phi}{dt} = (n - \gamma)\ \phi \qquad \ldots(4.1)$$

and

$$\frac{dn}{dt} = -2n\phi + r - \lambda n \qquad \ldots(4.2)$$

where t is measured in units of the cavity decay time as

$$t \rightarrow \frac{t}{\tau}$$

An indication of the value of the lifetime of the upper excited state was given by Jones et al.[42] as 6 μs, obtained from their experiments on Q-switching. They stated that this figure may be too low due to the approximations made in the derivation of the formula used. However, using this value, the variation of the photon density and population inversion, normalised with respect to the threshold inversion in a laser cavity, are shown in Figure 4.1. The solution of equations 4.1 and 4.2 were obtained numerically, as described in Appendix I, for a laser 6.5 metres long with losses due to a diagonal beam splitter of reflectivity 0.1. These values were chosen to be representative of the experimental lasers described in Chapter Five. For this initial investigation into fast switching, the term $r - \lambda n$ has been given an approximate form, λ being expressed in terms of the lifetime of the

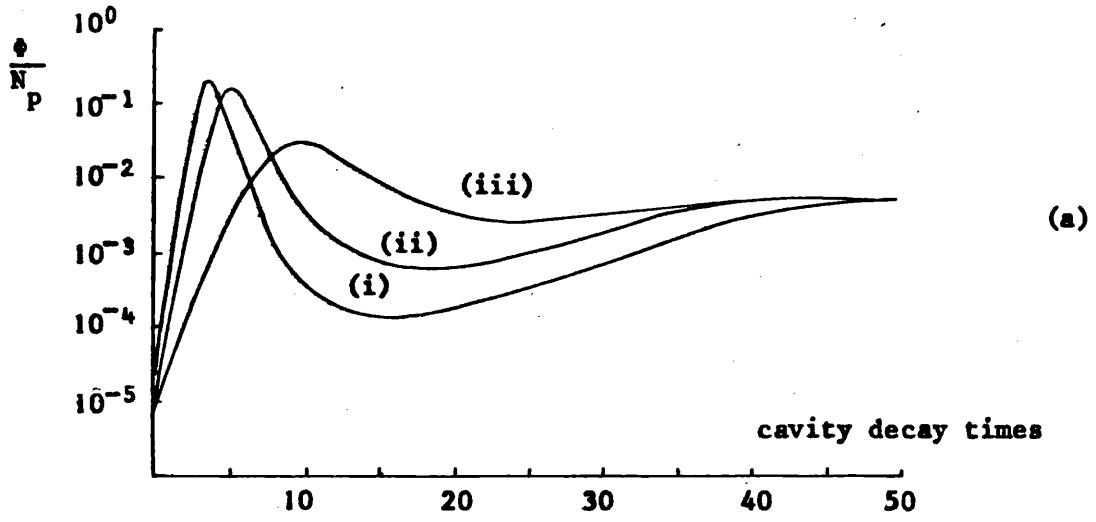

(a)

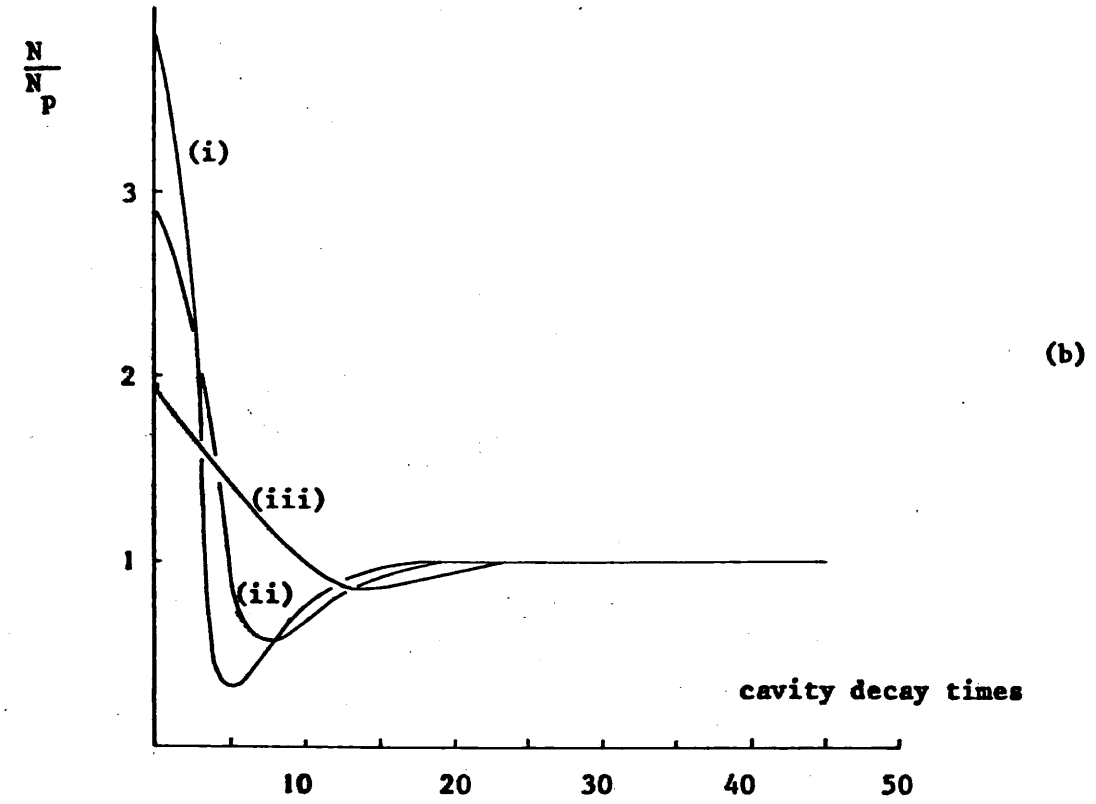

(b)

Figure 4.1. Variation of (a) photon density and (b) population inversion with time in a fast Q-switched laser for initial population inversions of (i) 4 N_p, (ii) 3 N_p and (iii) 2 N_p. Pump rate at a nominally constant value of $r = N_p/\tau$. The switch remains open after operating.

upper state only, as

$$\lambda \simeq 1 - \exp\{-\frac{\Delta t}{6\times10^{-6}}\}$$

and the pump rate as a nominally low value of

$$r = \frac{N_p}{\tau}$$

Δt represents the time expended between successive calculations required by the numerical technique. The figure shows the situation in which the Q-switch remains open after a step reduction in the cavity losses. It clearly indicates that the higher the population inversion before switching, the greater will be the peak intensity of the radiation pulse and the faster will be its rise and decay. These pulse shapes will be useful in a later section when comparing switching techniques. However, constant pump rate and continuous high Q after switching are seldom realized with gas laser systems, so a study will first be made of these conditions.

4.3. Finite cavity Q-switching periods

The two Q-modulation experiments with the rotating mirror technique described in Chapter Three showed that enhancement of the output power of the HCN laser can be achieved in this manner. The technique has the disadvantage however, that the cavity mirrors are only aligned for a finite time and that the period of high Q can only be extended by decreasing the switching speed. A situation can thus exist in which the cavity is not aligned for a time long enough for a radiation pulse to build up to its otherwise maximum intensity. A similar situation may also exist when a pulse excited laser is periodically swept through conditions of high and low Q by the variation of the plasma density.

Periodic switching will be studied by examining the mode scanning process. A more realistic model of the pumping mechanism than that used in the previous section will be formulated from the proposals of section 2.5. It was suggested that the pump rate is proportional to the recombination rate, which in turn can be obtained from the overall rate of plasma decay and the rate of electron loss through diffusion. A comparison of the magnitudes of these two parameters using the value for the diffusion constant measured by Schötzau and Kneubühl[5,52] and the decay rates indicated by Whitbourn et al.[24] show the contribution to the pump rate by diffusion to be of secondary importance. An expression for the pump rate in the numerical calculations, again

described in Appendix I, will thus be

$$r = \frac{K}{N_p} \cdot \frac{dn_e}{dt} \div \Delta t$$

K being the pumping fraction described in section 2.6.

The sweeping of a cavity through its resonant condition can be taken into account by using equation 2.5 for the electronic contribution to the refractive index. Appendix I describes this for a Lorentzian gain profile[53] in which the variation of the plasma density over a short period has been approximated to a linear decay.

Comparison is made between the build-up of photon density in the cavity for situations in which continuous phase change takes place and that which would occur if the cavity were to remain in a static resonant condition. Using as typical values those plasma densities and decay rates indicated by Whitbourn et al.[24] and the same parameters for cavity length, output coupling and probability of de-excitation of the population inversion previously employed, Figure 4.2 shows the calculated photon densities produced with pumping fractions of 10^{-8}, 10^{-9} and 10^{-10}. It is seen that for a pump rate of 4×10^{-2} Np sec^{-1}, the peak intensity produced when mode scanning takes place is less than that obtained when the laser is continuously resonant, and so the output is inhibited by the slow switching rate and the finite switching time. Although a greater output is obtained at the higher pumping rate of 4×10^{-1} Np sec^{-1}, the modulation mechanism again prevents the radiation from building up to its otherwise optimum level. It should also be noted that for the lower pumping rate of 4×10^{-3} Np sec^{-1}, very little build-up of radiation occurs under modulated conditions. The unmodulated case shows this to be due to the rise time of the radiation pulse being greater than the mode scanning time.

4.4. Refractive plasma lens

The refractive lens effect described in Chapter Two resulting from radial diffusion in the plasma of gas lasers has been proposed by McCaul[14] as a further self-switching mechanism. The implication of the high electron density on the axis of the discharge in the early part of the afterglow is that a divergent lens is produced of sufficient power to place the laser in an unstable cavity region of the type illustrated in Figure 2.4. In this situation energy storage will occur, producing a system with a high inversion when oscillation takes place

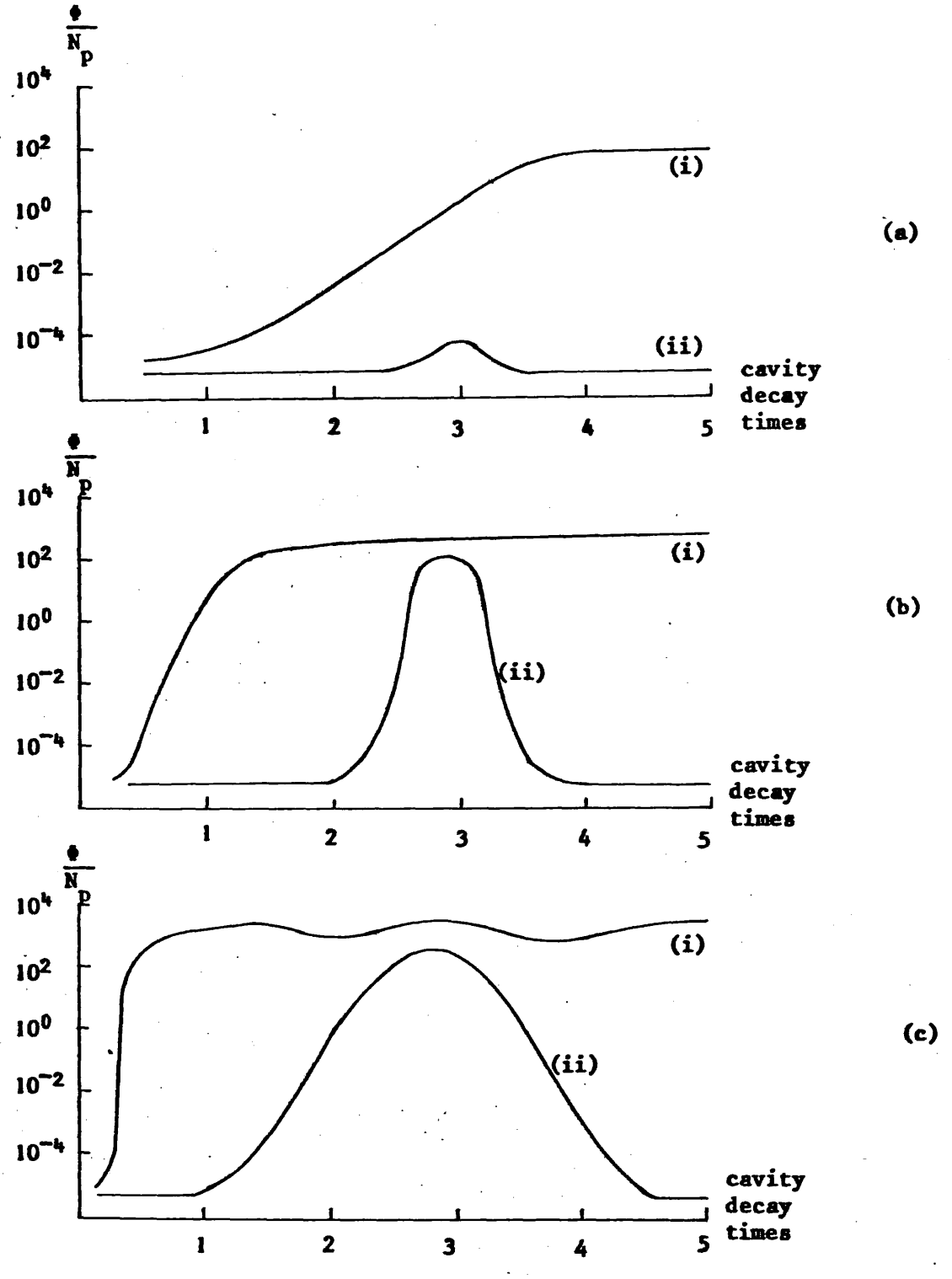

Figure 4.2. Theoretical variation of photon density in a laser against time for (i) a continually resonant cavity, and (ii) mode sweeping, for pump rates of (a) $4 \times 10^{-3}\ N_p$, (b) $4 \times 10^{-2}\ N_p$ and (c) $4 \times 10^{-1}\ N_p\ sec^{-1}$

later in the afterglow. To distinguish between the behaviour of this and other switching mechanisms, it is imperative that the speed at which the change of cavity Q takes place is calculated. To do this, the radial gain profile will be assumed to be Gaussian, a situation suggested by Kogelnik and Li[21] to be representative of the active plasma medium of gas lasers. The energy of a wavefront with a Gaussian intensity profile will be calculated using the expression for the beam width given by equation 2.4. Assuming an approximate expression for the profile to be

$$I = ae^{-br^2}$$

r representing a point on the radius of the mirror with a and b as constants, the following relationship is obtained

$$I = I_0 e^{(-2r^2)/w^2} \qquad \ldots(4.3)$$

where I_0 is the intensity at the centre of the mirror (r=0).

Equation 4.3 may be differentiated as

$$\frac{dI}{dr} = \frac{-4r}{w^2} e^{(-2r^2)/w^2} \cdot I_0$$

This permits an expression for the power of the wavefront

$$P = \int_{r=0}^{r=r} I(r) \cdot 2\pi r \cdot dr$$

to be calculated as

$$P = \frac{\pi w^2 I_0}{2} \left\{1 - e^{(-2r^2)/w^2}\right\} \qquad \ldots(4.4)$$

This equation represents the power of the beam passing through a circle of radius r at the mirror surface. The total power of an unrefracted beam is thus found by inserting $r = r_0$, the mirror radius. Figure 4.3 shows two possible situations in which a ray at a radial position r_1 at one mirror surface becomes refracted to the circumference of the second mirror after one pass along the cavity. The fraction of the energy lost per cavity transit due to the introduction of the plasma lens can be found after calculating the energy remaining in the cavity by placing $r = r_1$ in equation 4.4. To obtain a value for r_1, the matrix equation 2.12 is represented as

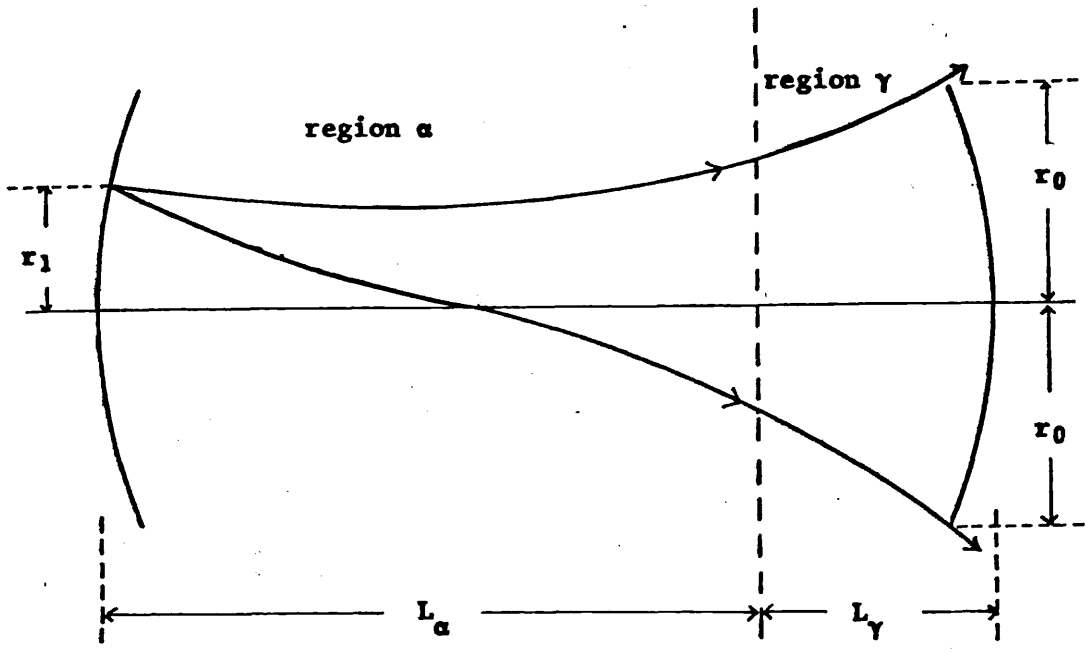

Figure 4.3. Schematic representation of a laser cavity filled by two distinct regions of different optical density. For the situation in which at least one region, α, is a coaxial plasma with a radial variation in its electron density, two conditions are shown whereby an infra-red ray passes out of the cavity after one transit between the mirrors. r_1 is the radial position of a ray on reflection from the first mirror, r_0 the cavity radius, L_α the length of region α and L_γ is the length of region γ.

$$\begin{bmatrix} r_2 \\ r_2' \end{bmatrix} = \begin{bmatrix} \alpha_{11} & \alpha_{12} \\ \alpha_{21} & \alpha_{22} \end{bmatrix} \begin{bmatrix} r_1 \\ r_1' \end{bmatrix}$$

then the solution

$$r_2 = \alpha_{11} r_1 + \alpha_{12} r_1'$$

can be evaluated by substituting

$$r_2 = \pm r_0$$

The analysis of Kogelnik and Li[21] showed that for the fundamental mode the mirror surfaces are coincident with the curvature of the wavefront. This enables the initial gradient of the ray to be expressed as $r_1' = (r_1)/R$, R being the common radii of curvature of the two mirrors. In order to take account of the effect of a beam splitter or switching device, a situation is considered, which is represented in Figure 4.3, in which the cavity comprises two regions of lengths L_α and L_γ of different optical density. For this analysis, the region of length L_γ is considered to be evacuated so that the corresponding matrix is

$$\begin{bmatrix} \gamma_{11} & \gamma_{12} \\ \gamma_{21} & \gamma_{22} \end{bmatrix} = \begin{bmatrix} 1 & L_\gamma \\ 0 & 1 \end{bmatrix}$$

r_1 can now be calculated from

$$r_1 = r_0 \left\{ \alpha_{11} - \frac{\alpha_{12}}{R} + L_\gamma \left[\alpha_{21} - \frac{\alpha_{22}}{R} \right] \right\}^{-1} \qquad \ldots(4.5)$$

The fraction of energy lost per cavity transit due to refraction can now be calculated from equations 4.4 and 4.5. Appendix II describes this for a cavity containing two separate optical density regions as shown in Figure 4.3, represented by two ray matrices. The losses incurred in a laser 750 cm long containing a plasma of length 700 cm with mirrors of radii of curvature of 750 cm are respectively shown in Figures 4.4(a) and (b) for cavity diameters of 7.6 and 15 cm. The figures are plotted for different parabolas representing the plasma density gradient described by constants $\beta = 0.25, 0.5, 0.75$, β having been defined in section 2.5. This range contains the value of $\beta = 0.65$ considered by McCaul[14] to account for his experimental observations. The figures show that the wider diameter laser is stable at electron densities approximately an order of magnitude higher than the narrower

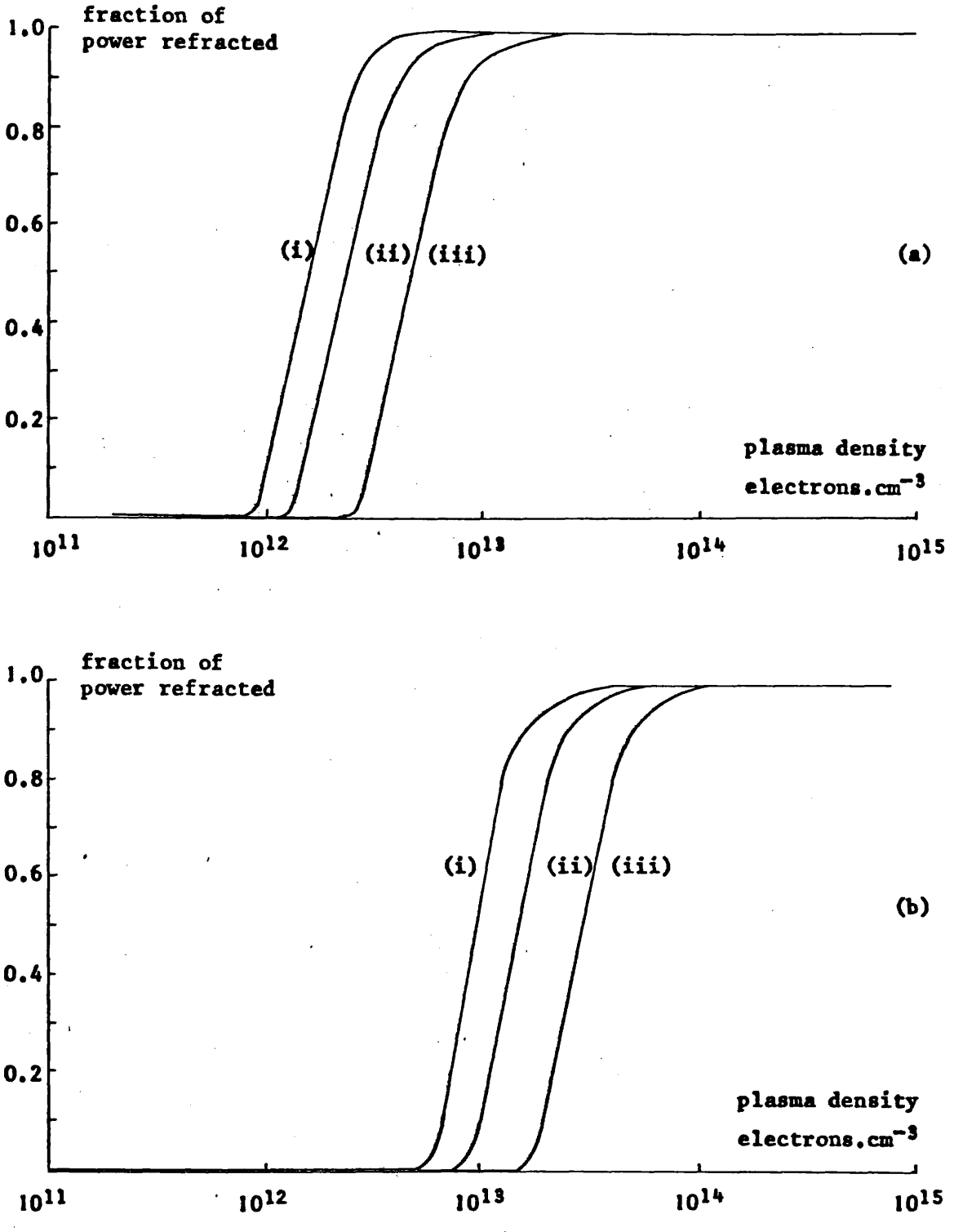

Figure 4.4. Fraction of power lost from a laser due to refraction against plasma density in (a) a 7.6 cm diameter cavity, and (b) a 15 cm diameter cavity. Radiation density profile constant β = (i) 0.75, (ii) 0.5, (iii) 0.25. Cavity length = R = 750 cm. Plasma length = 700 cm.

one. A model of the cavity was derived containing two regions of different optical density so that allowance can be made for a beam splitter or switching device. The effect of introducing a non-refractive length of cavity is illustrated for constant electron density in Figure 4.5, showing that the greater the length of plasma the higher are the refraction losses. This situation implies that the greater the plasma length the longer must be the decay of the afterglow before laser action takes place and hence the slower will be the rate of decay. The plasma length thus affects the speed of the Q-switch whether refractive or mode scanning. Comparison of the speeds of the two effects can be made for the laser configurations chosen, using the curves of Figure 4.4. Assuming the refractive switch to operate in the time required for the fraction of energy lost to change from F = 0.9 to F = 0.1 and that over this short period the plasma decay can be approximated to a linear variation, then the time taken for the switch to operate will be

$$\Delta t \simeq 4 \times 10^{12} / \left\{\frac{dn_e}{dt}\right\}$$

for the 7.6 cm diameter laser and

$$\Delta t \simeq 2 \times 10^{13} / \left\{\frac{dn_e}{dt}\right\}$$

for the 15 cm diameter laser. Comparing this with the mode scanning time given by equation 2.11 as

$$\Delta t \simeq 4.8 \times 10^{11} / \left\{\frac{dn_e}{dt}\right\}$$

calculated for a laser with a gain profile of width 10 MHz[34] and assuming $n_e << n_c$, then the phase shift is seen to be the dominant mechanism.

4.5. Q-switch with Michelson cavity formation

Analysis performed in this chapter has shown that Q-switching action is limited by both the speed at which the switch operates and the time for which the cavity remains in a high Q condition. It was also shown in Figure 4.1 that, for the conditions in which build-up of population inversion is performed by suppressing stimulated emission, a minimum time exists for the rise of the Q-switched pulse. An investigation will now be made of an alternative switching technique whereby these limitations may be overcome by placing the switch outside the resonant cavity. The Michelson output coupling system described in section 2.2.4 is arranged as shown in Figure 4.6 so that a discharge may be located

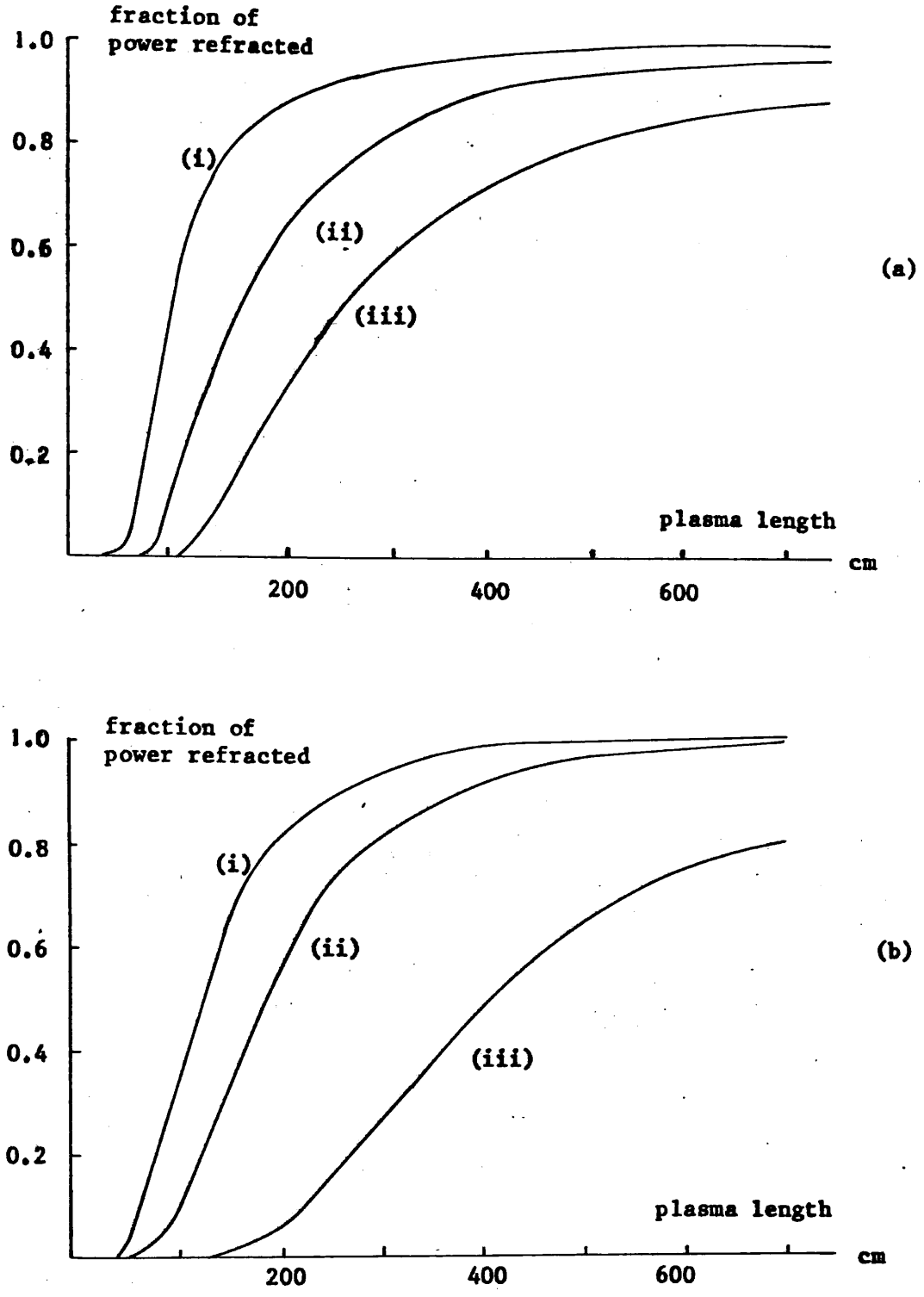

Figure 4.5. Fraction of power lost from a laser due to refraction against length of plasma in (a) a 7.6 cm diameter cavity, and (b) a 15 cm diameter cavity. Plasma density for (a) = (i) $1\times10^{13}cm^{-3}$, (ii) $6\times10^{12}cm^{-3}$, (iii) 4×10^{12} cm^{-3}. Radial density profile constant $\beta = 0.5$. Cavity length=R=750 cm.
PLASMA DENSITY FOR (b) = (i) $6\times10^{13}cm^{-3}$, (ii) $4\times10^{13}cm^{-3}$, (iii) $2\times10^{13}cm^{-3}$.

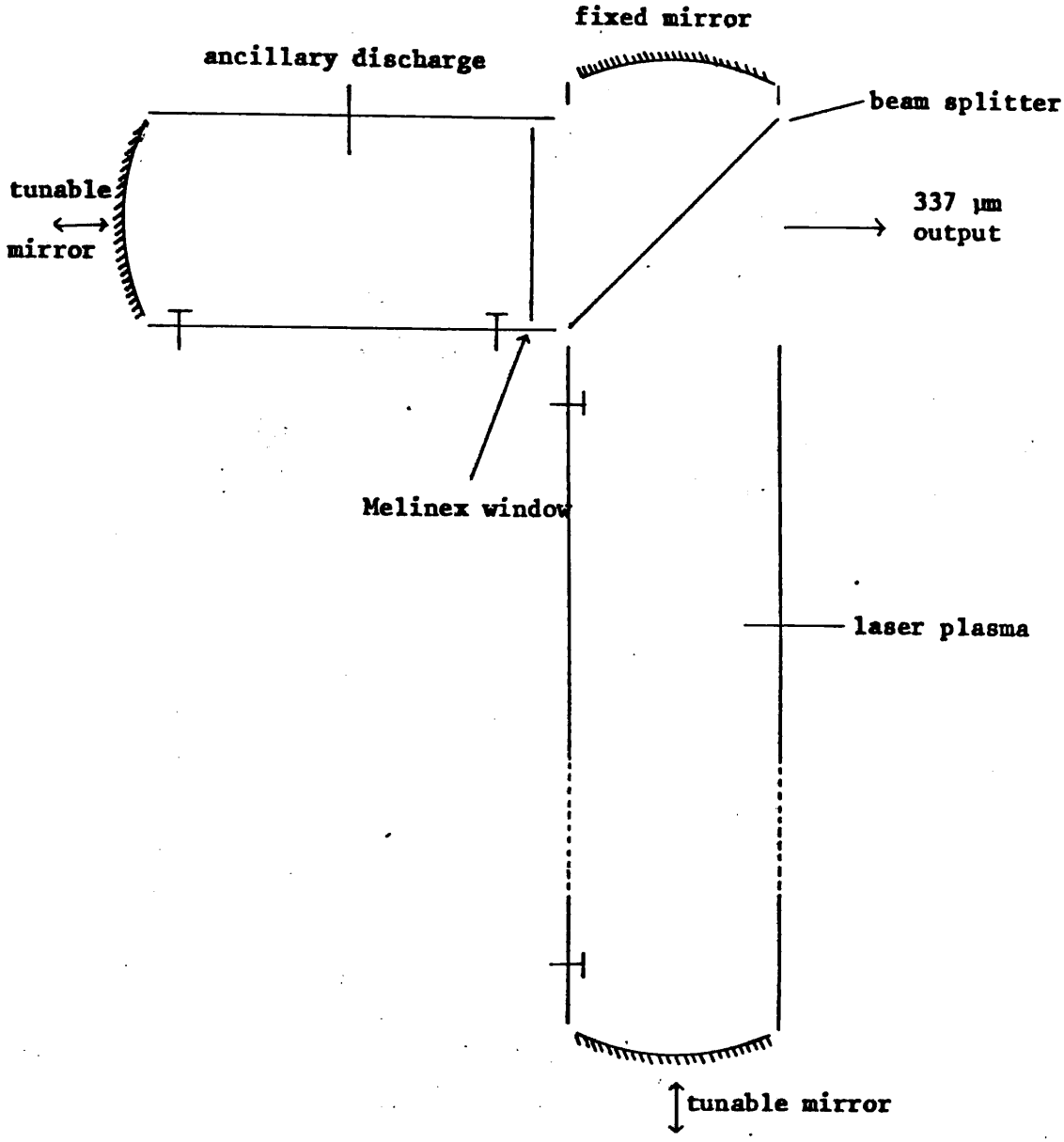

Figure 4.6. Schematic representation of a gas discharge laser employing the 'Michelson' output coupling technique with an ancillary plasma for Q-switching

between the beam splitter and the ancillary mirror. By tuning the Fabry-Pérot cavity to resonance and reducing the output to zero by translation of the third mirror, it is proposed that a Q-switched radiation pulse may be obtained by pulse ionisation of the side-arm. A numerical investigation of this switching action has been undertaken by equating the reflection coefficient of the beam splitter to zero before excitation of the plasma. Assuming the output coupling to be the dominant loss mechanism, equation 2.3 shows that the loss parameter γ approaches zero prior to switching and unity afterwards. The calculations undertaken to represent these conditions are given in Appendix I and the results shown in Figure 4.7. Unlike the switching mechanisms considered previously, the period of storage allows build-up of both the population inversion and the internal photon density. The rise time of the switched radiation pulse under these conditions is therefore limited only by the speed of operation of the switch.

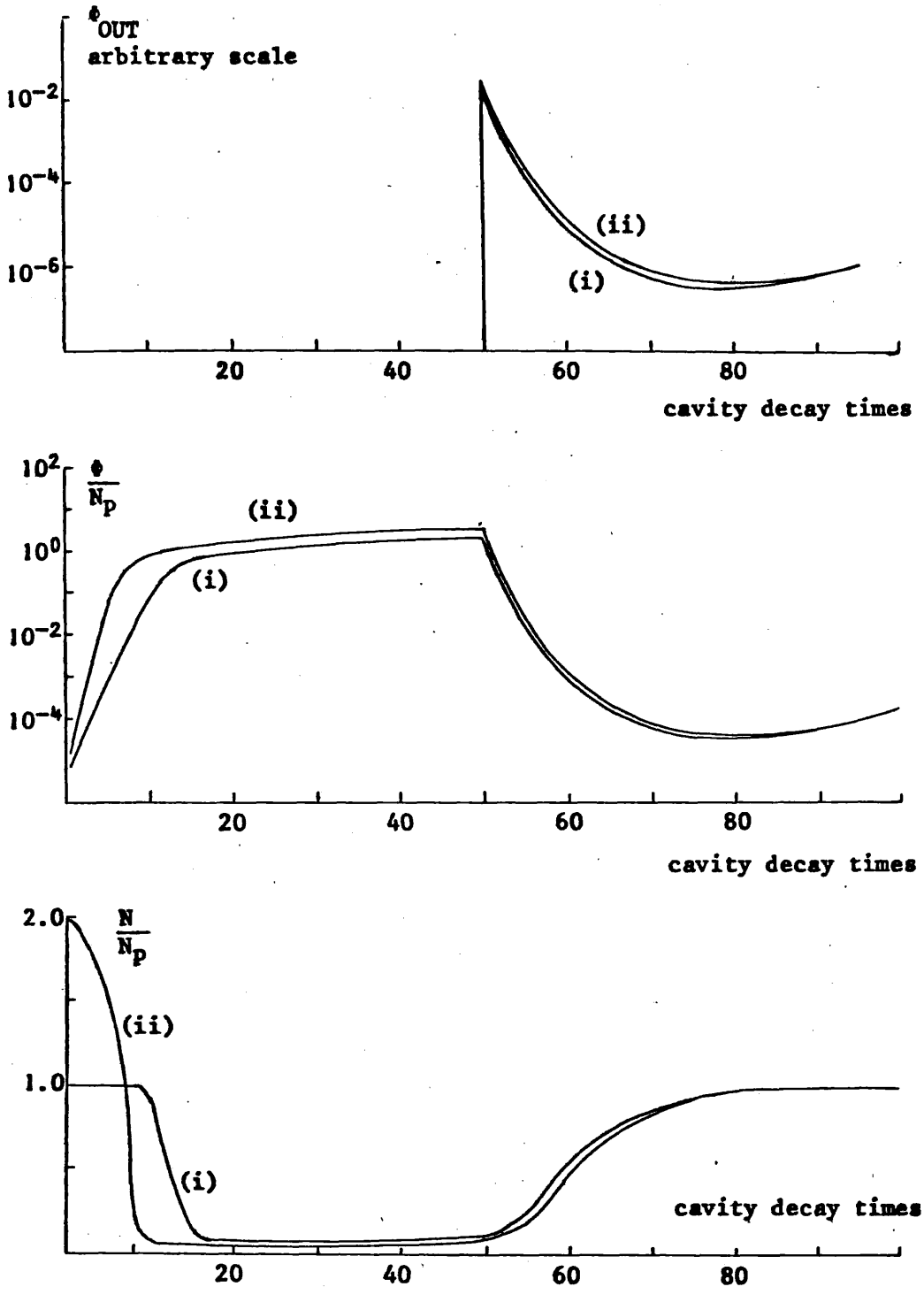

Figure 4.7. Variation of (a) radiation output ϕ_{OUT}, (b) inter-cavity photon density $\frac{\phi}{N_p}$, and (c) population inversion $\frac{N}{N_p}$, against cavity decay time for a fast Q-switched laser using the Michelson technique. Initial population inversion (i) N_p and (ii) $2N_p$. Pump rate = N_p

CHAPTER FIVE

EXPERIMENTAL INVESTIGATION OF THE HCN LASER

5.1. Introduction

An account is given of experimental investigations into the following modulation techniques:

(i) gaseous absorber ionisation
(ii) plasma phase shift
(iii) the'Michelson' switching system.

It has been shown that the output from a Q-switched laser is affected by the gain profile of the laser and the characteristics of the plasmas which form both the optical switch and the active medium. A description of these properties will therefore be given along with observations on the performance of the lasers. Firstly, the configurations and operational conditions of the HCN lasers used in the investigations will be discussed.

5.2. The HCN lasers

Modulation experiments were performed using an HCN laser system with a volume of active medium 7.6 cm in diameter and 480 cm in length. Two configurations of this laser are shown schematically in Figure 5.1, (a) employing beam splitter output coupling and (b) hole coupling. Both versions incorporated a cell in the optical cavity to contain a switching plasma. In some experiments the gas in the switching cell was kept separate from the rest of the laser by placing a Melinex window across the cavity at the position denoted by W in the figure.

Large powers generated by large diameter HCN lasers have been reported[36]. The properties of a 15 cm diameter laser were therefore studied with a view to Q-switching such a system. The output from this laser was observed using hole coupling and beam splitter coupling techniques. Both arrangements are shown in Figure 5.1(c).

The cavities were separately filled with a continuous flow of ethylenediamine vapour, propylamine vapour, a methane-nitrogen mixture, and a methane-ammonia mixture. The lasers were then energised by ionising these gaseous media using the power supply described in Appendix III. When operating with a matched load of forty ohms, this supply produced a pulse of current forty microseconds in duration with

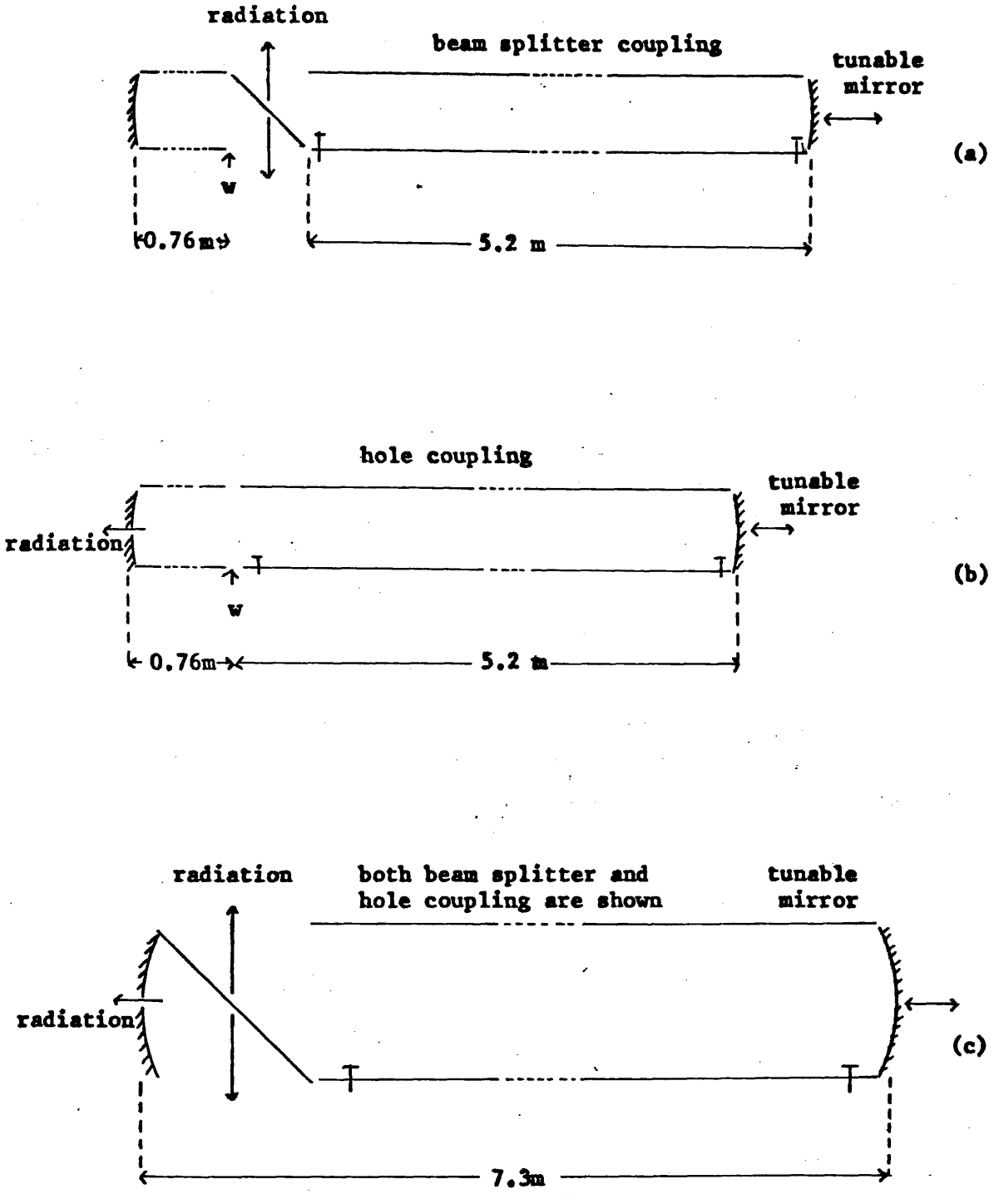

Figure 5.1. Schematic representations of the formations of the cavities of the various HCN lasers. Cavity diameter = (a) and (b) 7.6 cm, (c) 15 cm. A Melinex window can be inserted across the cavity at position w in lasers (a) and (b).

a rise and fall of approximately a microsecond. A close approximation to this square current pulse was obtained when ionising a methane-nitrogen or methane-ammonia mixture, n-propylamine and ethylenediamine vapour and the attenuating vapours of deuterium oxide and dichloromethane. However, a much slower build up and decay of the current, 15 to 20 μs, occurred in difluoroethylene.

The fractional loss associated with each cavity configuration is a necessary parameter for the evaluation of the laser characteristics. Approximate values were calculated by assuming that the major contributor to the loss of a confocal cavity is that due to the output coupling mechanism. Using equation 2.1, an estimate of the fractional loss of the hole-coupled laser was found to be

$$f = 0.4$$

To obtain the value for the beam splitter coupler, measurements were made of the reflectivity at normal incidence of several standard manufactured thicknesses of Melinex film. Figure 5.2 indicates that by assuming a symmetrical fringe pattern, a maximum value of the reflectivity may be obtained as 0.21 ± 0.02 at a film thickness of 55 ± 5 μm. The reflectivity is expressed by

$$r = \frac{4R \sin^2 \delta/2}{(1 - R)^2 + 4R \sin^2 \delta/2}$$

a form of Airy's formula arranged by Tolansky[54] to take into account multiple reflections within the film. R is the single surface reflectivity and

$$\delta = 4\pi \frac{\mu t}{\lambda} \cos \phi$$

where μ is the refractive index of the film, t the film thickness and λ the wavelength of the radiation. This formula, applicable to plane wavefronts at small angles φ to the normal of the film, is a maximum when $\sin^2 \delta/2 = 1$. Hence the above figure for the maximum value of r enables a value of

$$R = 0.056 \pm 0.008$$

to be calculated. The corresponding film thickness substituted into

$$2\mu t \cos \phi = (n + \tfrac{1}{2})\lambda$$

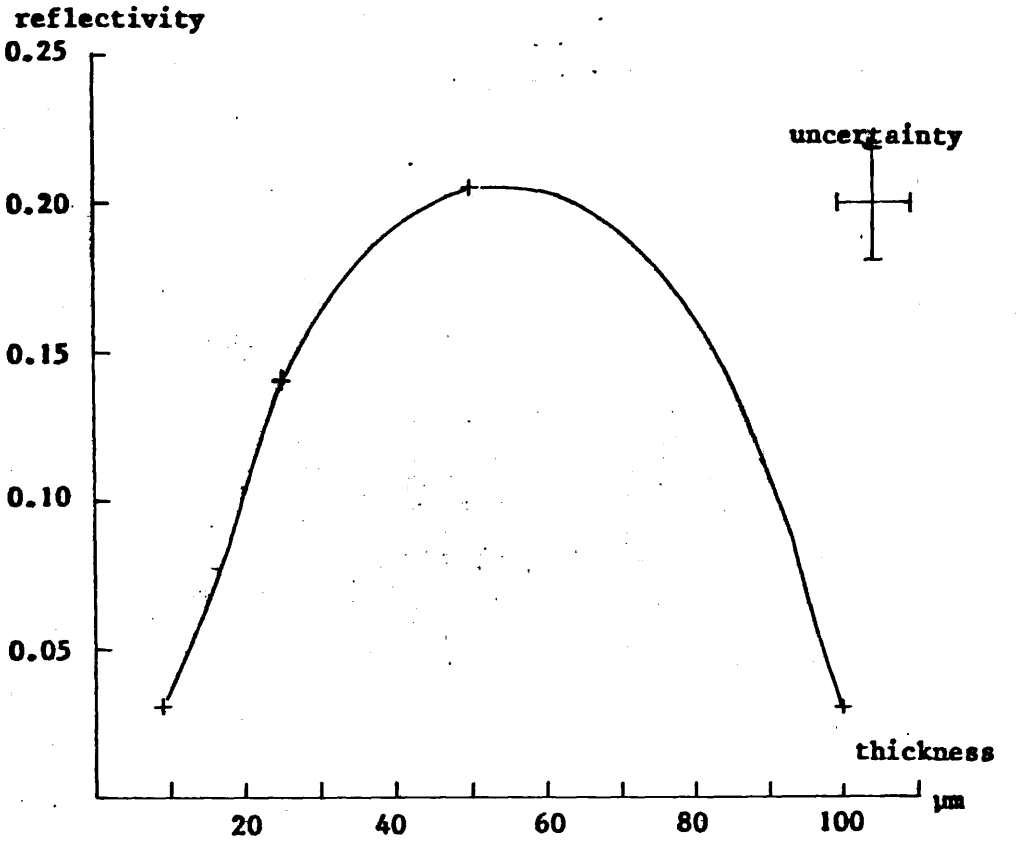

Figure 5.2. Reflectivity of Melinex film at 891 GHz against thickness for radiation at normal incidence

which is the phase condition for maximum reflectivity, yields, for normal incidence and for an integer n = 0

$$\mu = 1.68 \pm 0.15$$

Close agreement with this value, and thus confirmation of the choice of n, is obtained by inserting R into the Fresnel equation for reflection giving

$$\mu = 1.62 \pm 0.32$$

Using a polarisation analyser composed of a series of parallel 140 μm wide gold lines spaced 110 μm apart on a Melinex film, the output from the laser was observed to be polarised parallel to the plane of incidence with the beam splitter. Hence for a film at 45° to the optical axis, the appropriate Fresnel equation enables the single interface reflectivity to be calculated. This in turn allows the reflectivity of the beam splitter to be obtained from equation 2.2 as r = 0.25 ± 0.09. Taking into account reflection from both sides of the beam splitter, equation 2.3 gives the fractional loss due to the coupler as

$$f = 0.56 \pm 0.07$$

5.3. Power measurements

5.3.1. CW HCN laser

The CW output powers from the lasers were measured by mechanically chopping the beam and focusing the radiation into a calibrated Golay cell. The manufacturer of the Golay cell, Pye Unicam, would quote the temperature stability of the device to no better than 1% per °C.

The four different media were ionised in turn in the 15 cm diameter system by the d.c. power supply described in Appendix III. In common with the observations of Fuller[33] outlined in Chapter Three, a stable CW output from the lasers necessitated limiting the current, and hence the output power, to produce a discharge with stationary striations. At higher currents the striations became less stationary until their fluctuating motions filled the tube, producing a continuous glow discharge. Under these conditions, diode detection showed the laser output to contain a level of noise composed of harmonics of 50 Hz. Producing a stable discharge at the lower pressures was facilitated by employing a water-cooled hollow cathode.

The different media required different gas pressures in order to maintain

a stable striated discharge. Figure 5.3 shows the variation of the CW output power with discharge current for three of the media using the hole-coupling technique. Stable discharges at pressures greater than 1 torr were obtained with a methane-nitrogen mixture, but as the figure implies, lower pressures were necessary for a methane-ammonia mixture, 0.4 torr, and ethylenediamine vapour 0.2 torr. Stimulated emission was only obtained using propylamine vapour at current levels which produced an unstable discharge. An indication of the output level obtainable in this state is given in Table 5.1.

By employing beam splitter output coupling, higher powers than obtained previously were produced with the methane-ammonia and methane-nitrogen mixtures, as shown in Figure 5.4. However, no radiation was generated with this laser configuration using propylamine or ethylenediamine vapour. This result was considered to be due to the higher loss conditions of the beam splitter coupled cavity which requires a threshold gain greater than could be produced by either of the low pressure vapours.

Similar tests were performed with the 7.6 cm diameter laser system. Figure 5.5 shows the variation of output power with discharge current from a methane-nitrogen mixture and coupled out by a beam splitter. The figure shows the output generated in the absence of a Melinex window inside the cavity. The introduction of a window into the cavity required increasing the current to a level at which an unstable discharge was produced before stimulated emission occurred. An indication of the reduction of CW power caused by the window is given by the level shown in Table 5.2 which is 9 dB lower than that obtained without the window at the same current. This high loss figure indicates a serious limitation to the use of an absorption cell as a switching device. This situation will be discussed further in section 5.6.3.

To enable the photon density in the laser cavity to be ascertained for evaluation of the switching techniques in Chapter Six, the profiles of the output beams from the lasers were measured for both coupling techniques. Figure 5.6(a) shows the cross-section of the output from the beam splitter in the 15 cm diameter system, and Figure 5.6(b) that obtained from the hole-coupled arrangement.

5.3.2. Pulse-excited HCN laser

Stimulated emission from each of the laser systems was observed while energised with current pulses generated by the Blumlein modulator described in Appendix III. Detection using point-contact diodes showed

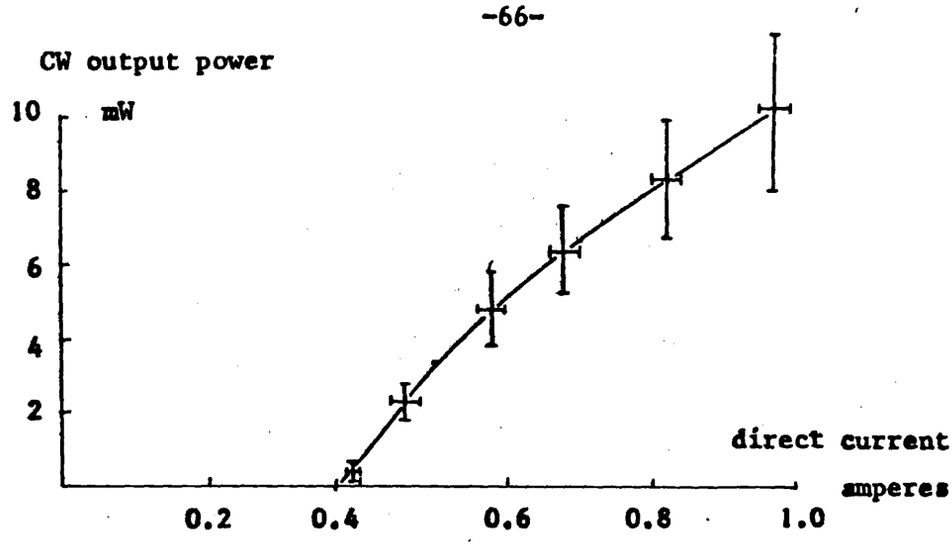

(a)

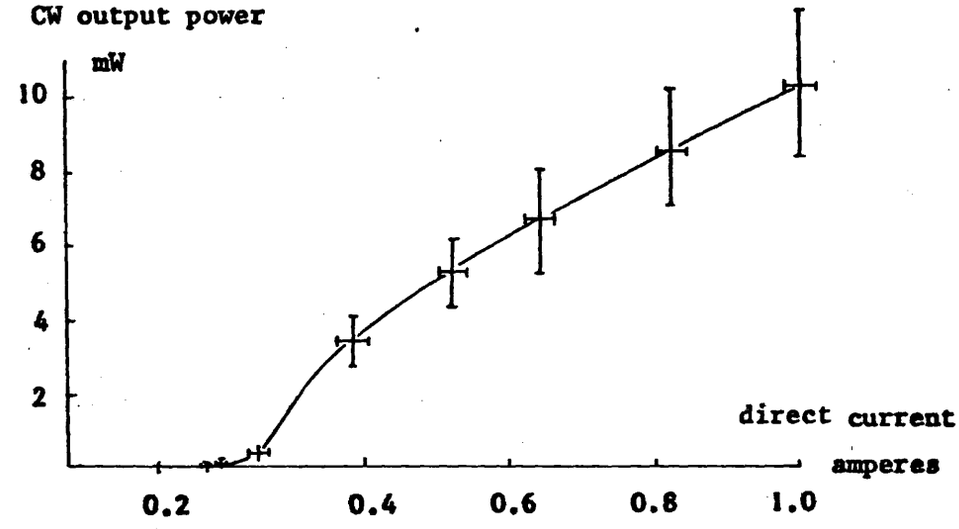

(b)

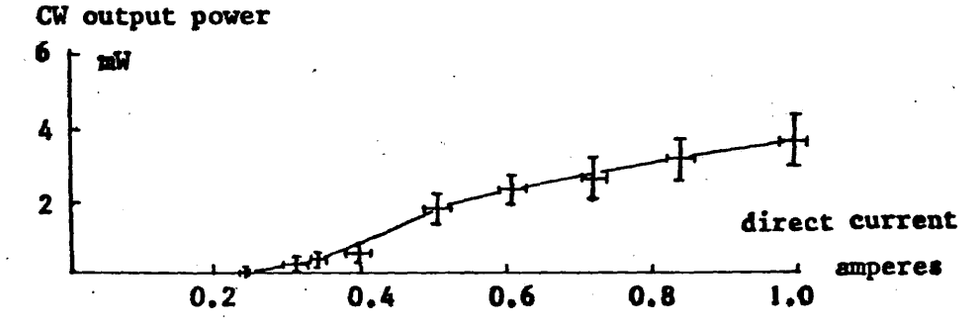

(c)

Figure 5.3. CW output power from the 15 cm diameter hole-coupled laser against current for (a) 0.4 torr of methane-ammonia mixture, (b) 1.0 torr of a methane-nitrogen mixture, and (c) 0.2 torr of ethylenediamine vapour. Crossed bars indicate uncertainty.

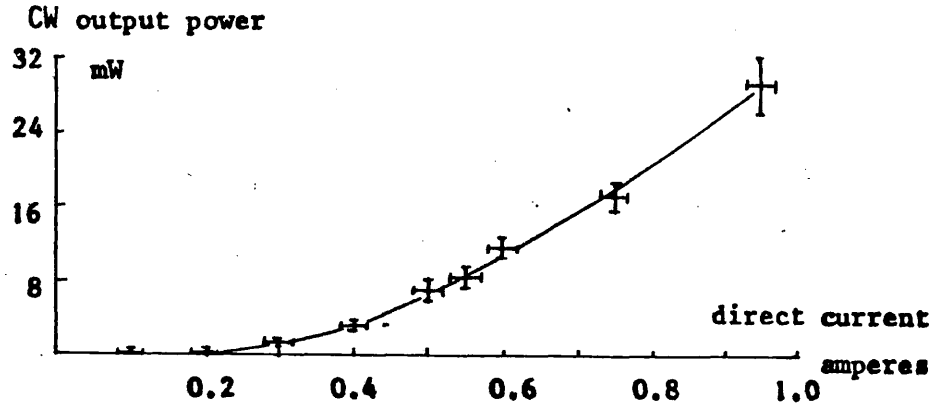

(a)

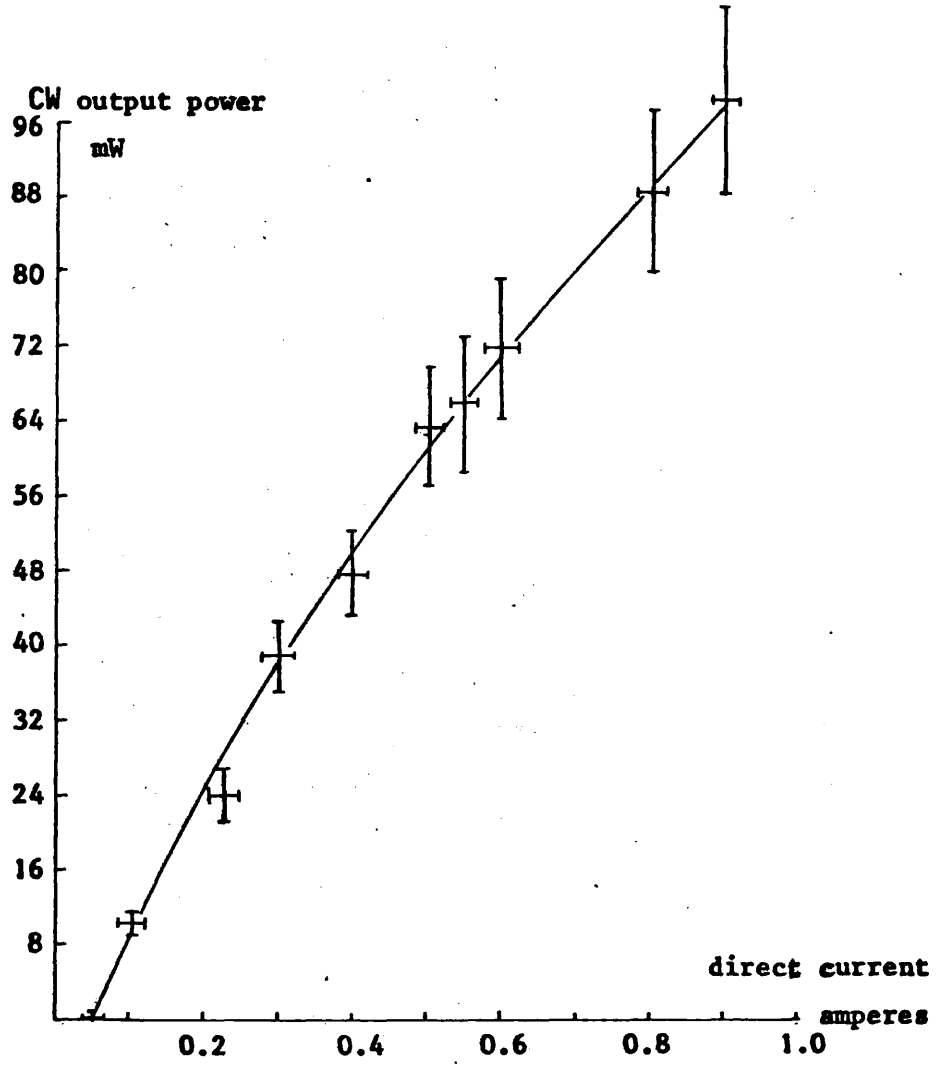

(b)

Figure 5.4. Total CW output power from the 15 cm diameter beam splitter coupled laser against current for (a) 0.4 torr of a methane-ammonia mixture, and (b) 1 torr of a methane-nitrogen mixture. Crossed bars indicate uncertainty.

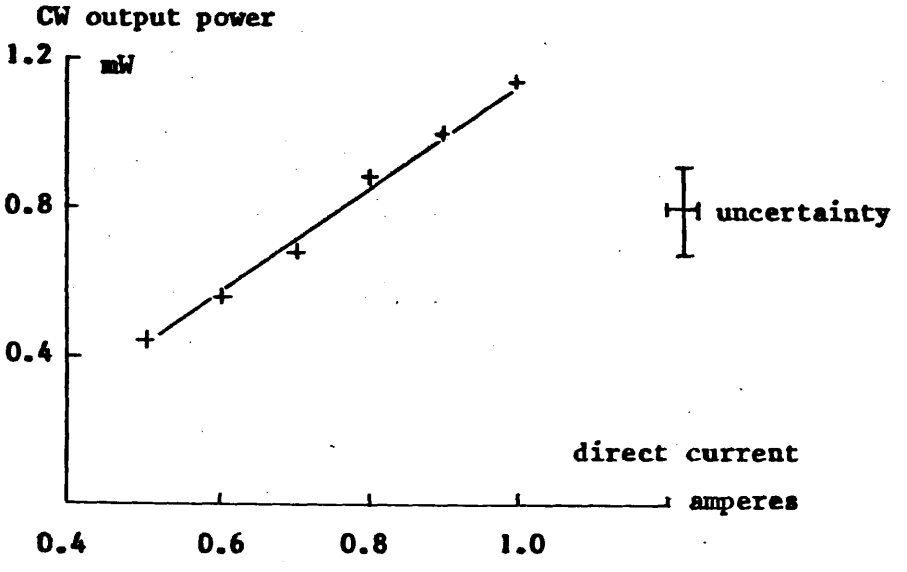

Figure 5.5. Total CW output power against discharge current for a 7.6 cm diameter beam splitter coupled HCN laser. Discharge in 1.2 torr of a methane-nitrogen mixture. No window inside cavity.

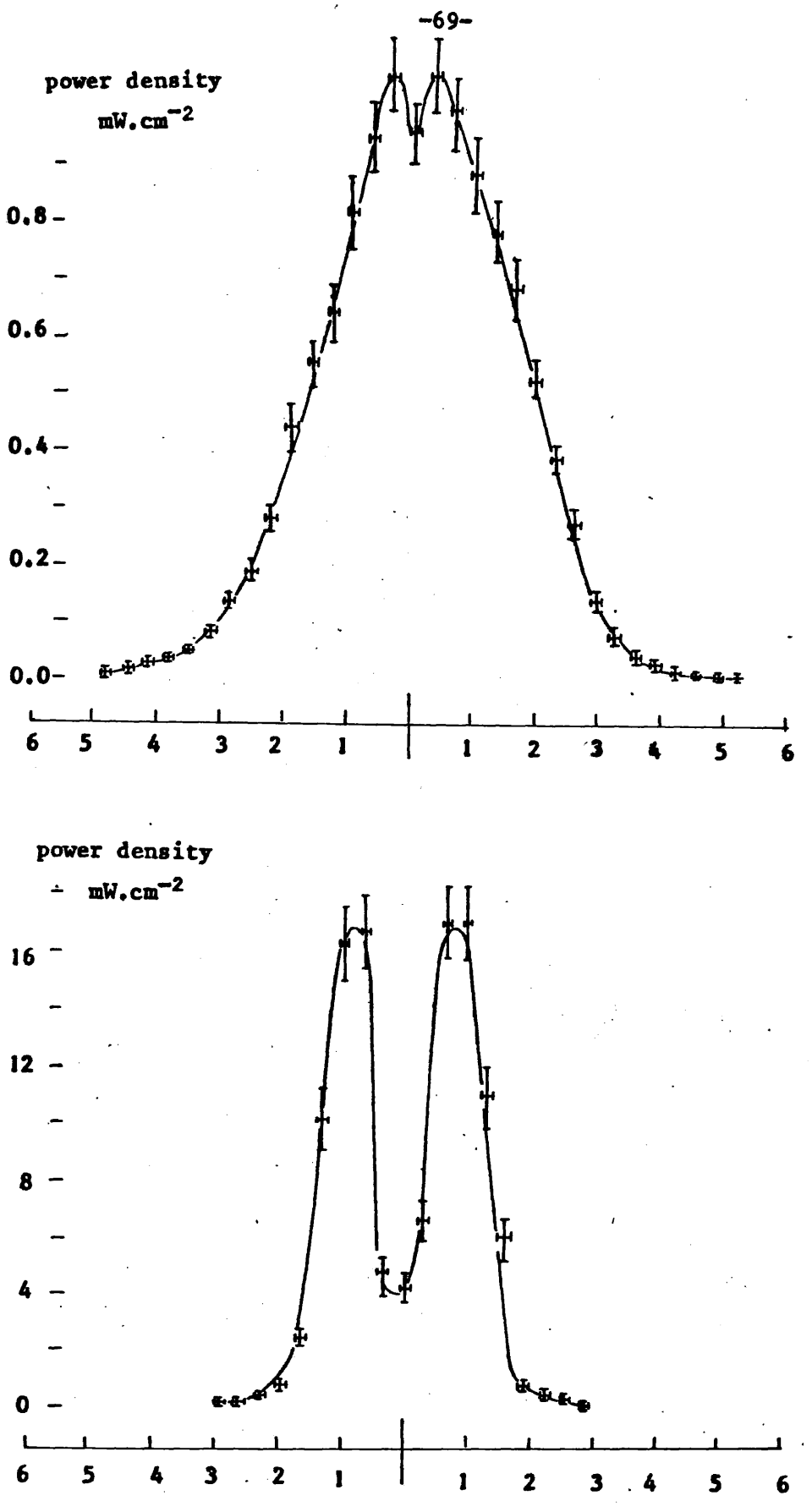

Figure 5.6. Beam profiles of the outputs from the 15 cm diameter laser for (a) a beam splitter coupled output, and (b) a hole-coupled output. Crossed bars indicate uncertainty.

the output to consist of a chain of radiation pulses. The duration of these pulses was short in comparison with the rise of a Golay cell which could therefore be used to measure the radiation energy. The output from the diode detectors was displayed as voltage against time. Hence, equating the total energy with the area under the pulses enabled the diode output to be calibrated in terms of radiation power.

The variation of the submillimetre energy generated by the 15 cm diameter laser in which a mixture of methane and nitrogen at a pressure of 1 torr was pulse ionised, is shown against discharge current in Figure 5.7. The gradient of this curve is seen to decrease at high currents. An explanation in terms of a shortened period of laser action through enhancement of refraction in the plasma is supported by observing the radiation pulses. Figure 5.8(a) shows simultaneous outputs from both beam splitter and hole coupling after an initial discharge current of 800 amperes. No radiation was generated by the main current pulses,

Table 5.1

15 cm diameter laser

length of optical cavity = 7.3 metres
length of active medium = 7.0 metres
radii of curvature of mirrors, R1 = R2 = 760 cm

Medium		Pressure (torr)	Current (amperes)	Output
Hole-coupled laser				
Pulsed	methane-ammonia mixture	0.4	470	0.21±0.04 mJ
Pulsed	ethylenediamine vapour	0.25	600	11.7±1.5 mJ
Pulsed	methane-nitrogen mixture	1.0	340	13.4±1.5 mJ
Pulsed	propylamine vapour	0.4	460	5.8±0.8 mJ
CW	propylamine vapour	0.3	>1	2.1±0.4 mW
Beam splitter coupled laser				
Pulsed	methane-ammonia mixture	0.4	380	1.7±0.3 mJ

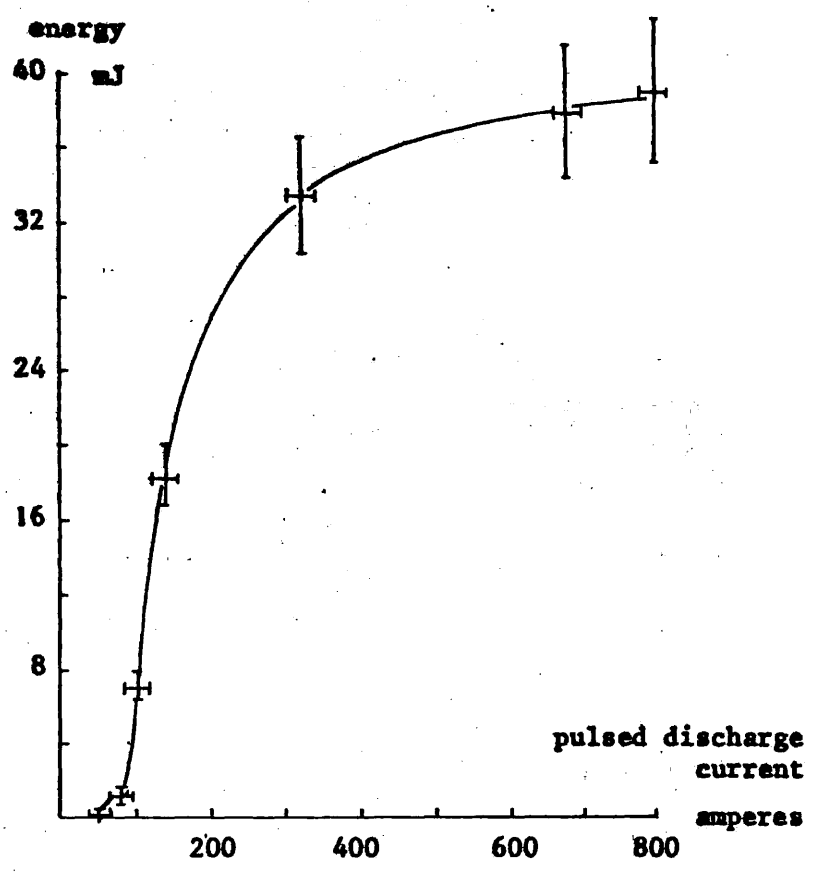

Figure 5.7. Energy of output radiation per discharge against discharge current for the 15 cm diameter, beam splitter coupled, HCN laser. Discharge in a 1 torr methane-nitrogen mixture. Pulse repetition frequency = 3 pulses per second. Crossed bars indicate uncertainty.

upper trace: hole-coupled output

lower trace: beam splitter coupled output

(a)

horizontal scale, 2 ms per large division

upper trace: hole-coupled output
lower trace: current monitor
vertical scale 800A per large div.

(b)

horizontal scale, 20 μs per large division

hole-coupled output

vertical scale, approx. 80W per large division (c)

horizontal scale, 20 μs per large division

hole-coupled output

vertical scale, approx. 75W per large division

(d)

horizontal scale, 50 μs per large division

Figure 5.8. Pulsed outputs from the 15 cm diameter laser using 1 torr of a CH_4-N_2 mixture

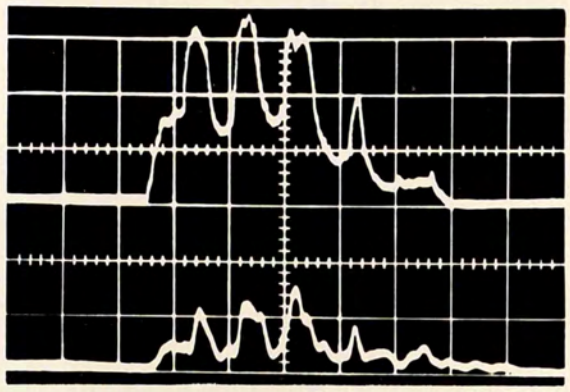

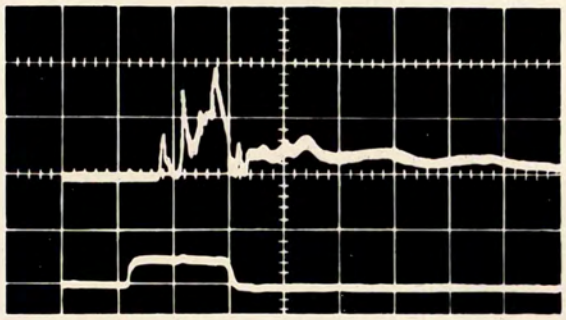

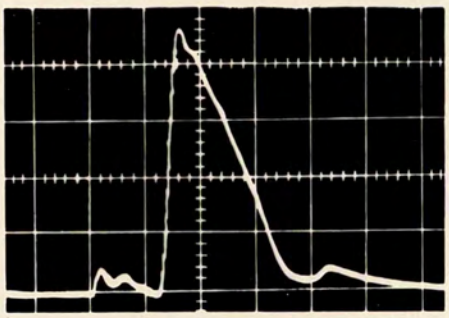

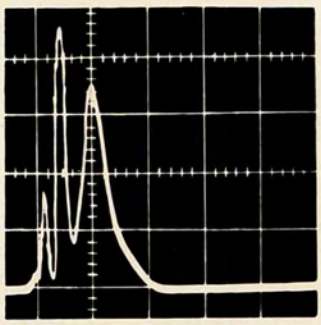

Table 5.2

7.6 cm diameter laser

length of active medium = 4.8 metres

radii of curvature of mirrors, R1 = R2 = 452 cm

Medium		Pressure (torr)	Current (amperes)	Output
Hole-coupled laser (length of optical cavity = 5.9 metres)				
Pulsed	propylamine vapour	0.7	380	0.01±0.002 mJ with window
Pulsed	propylamine vapour	0.7	380	0.035±0.005 mJ without window
Beam splitter coupled laser (length of optical cavity = 5.7 metres)				
Pulsed	methane-nitrogen mixture	1.0	215	0.585±0.06 mJ without window
Pulsed	methane-nitrogen mixture	1.0	250	0.13±0.02 mJ with window
CW	methane-nitrogen mixture	1.0	0.8	0.05±0.005 mW with window

only by the smaller recharging pulses of the mismatched Blumlein power supply. However, Figure 5.8(b) shows that by reducing the initial discharge to 400 amperes, oscillation takes place during and after the first current pulse. Maximum peak output power was obtained by adjustment of both the path length of the cavity and the discharge current. An optimized output obtained by hole coupling is shown in Figure 5.8(c). Oscillation is mostly suppressed during the current flow and then builds up during the decay of the current pulse to a peak power of 380 ± 40W. Figure 5.8(d) demonstrates a situation in which the discharge was not of sufficient magnitude to prevent laser action. The first radiation pulse was emitted during the current flow and the optical path length was such that destructive interference prevented further build-up. The cavity was then swept through two more resonant conditions. The maximum power produced in this case was 340 ± 30W.

The characteristics of the 7.6 cm diameter laser were found to differ from those of the larger system. Pulse ionisation of a methane-nitrogen mixture normally produced submillimetre radiation only from the

recharging pulses as shown respectively for beam splitter and hole coupling in Figure 5.9(a) and Figure 5.9(b). This suggests that divergence introduced by the plasma has a greater effect in the narrower cavity. To test for the existence of an electronic lens, its 'power' was reduced by decreasing the magnitude of the current pulse from the usual operating level of approximately 300A to 130A. At 130A stimulated emission was generated by the initial excitation after increasing the length of the cavity from the value optimised for emission from the recharging pulses. The cavity tuning was required because the magnitude of the forward current pulse was greater than the former level of the recharging pulses. However, the radiation power obtained in this way was inferior to that produced previously. Two possible explanations for this can be put forward. One is that plasma refraction produced by the initial current pulse still reduced the Q of the cavity to a level significantly lower than that of the recharging pulses. This situation could not be examined as no laser action occurred on further reduction of the level of the current pulse. A second mechanism may be deduced by reference to the experiments of Robinson and Whitbourn[55] and Schötzau and Kneubühl[56] on pulse ionising a static mixture of methane and nitrogen. Laser action was seen to commence only after several discharges, reach maximum power after a definite number of pulses, and then reduce to zero with continued ionisation. An explanation of these observations may be obtained from the work of Schötzau and Kneubühl[56]. It was found that hydrogen was necessary to obtain laser action and that build-up during successive excitations increased the ratio of hydrogen to hydrogen cyanide which passed through an optimum condition. A similar build-up of hydrogen and other dissociated constituents will occur in a continuously flowing gas system. The constant removal of these components ensures that laser action need not decrease with continued excitation and that an optimum pulse-repetition-rate should exist. This situation was demonstrated with the 7.6 cm diameter laser by observing the total radiated energy generated by the recharging pulses, while varying the pulse-repetition-rate of the forward current pulse. Figure 5.10 shows that an optimum pulse-repetition-rate was found for most values of discharge current. The proportions of the products of the discharge therefore depend on the overall pulse-repetition-rate in addition to build-up during the succession of recharging pulses. This last factor is inferred from Figures 5.9(a) and (b) which showed that the first and largest recharging pulse did not produce the greatest peak power, but that the output increased during the first few pulses and then decreased with the later pulses. It is also noted that a finite time is required

upper trace: current monitor
vertical scale 20A per large division
lower trace: hole-coupled output
horizontal scale, 2 ms per large division (a)

beam splitter coupled output
horizontal scale, 1 ms per large division (b)

hole-coupled output
horizontal scale, 20 μs per large division (c)

hole-coupled output
horizontal scale, 20 μs per large division (d)

Figure 5.9. Pulsed outputs from the 7.6 cm diameter laser. (a) and (b) 1 torr CH_4-N_2 mixture, (c) propylamine vapour and (d) propylamine vapour with a Melinex window inside the cavity

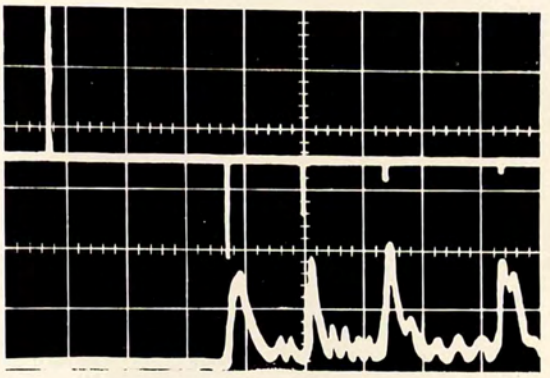

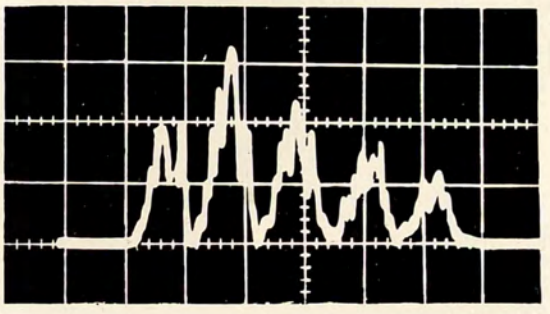

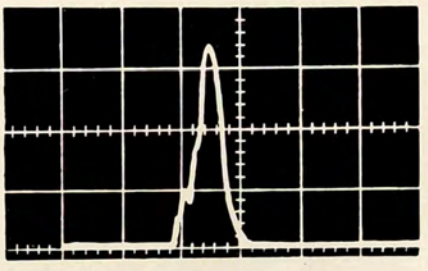

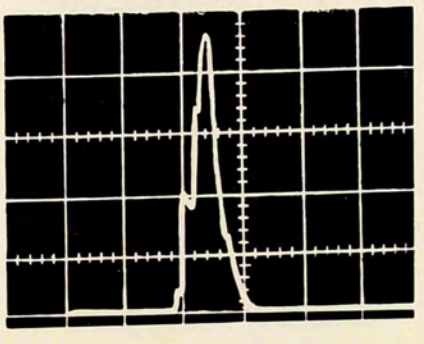

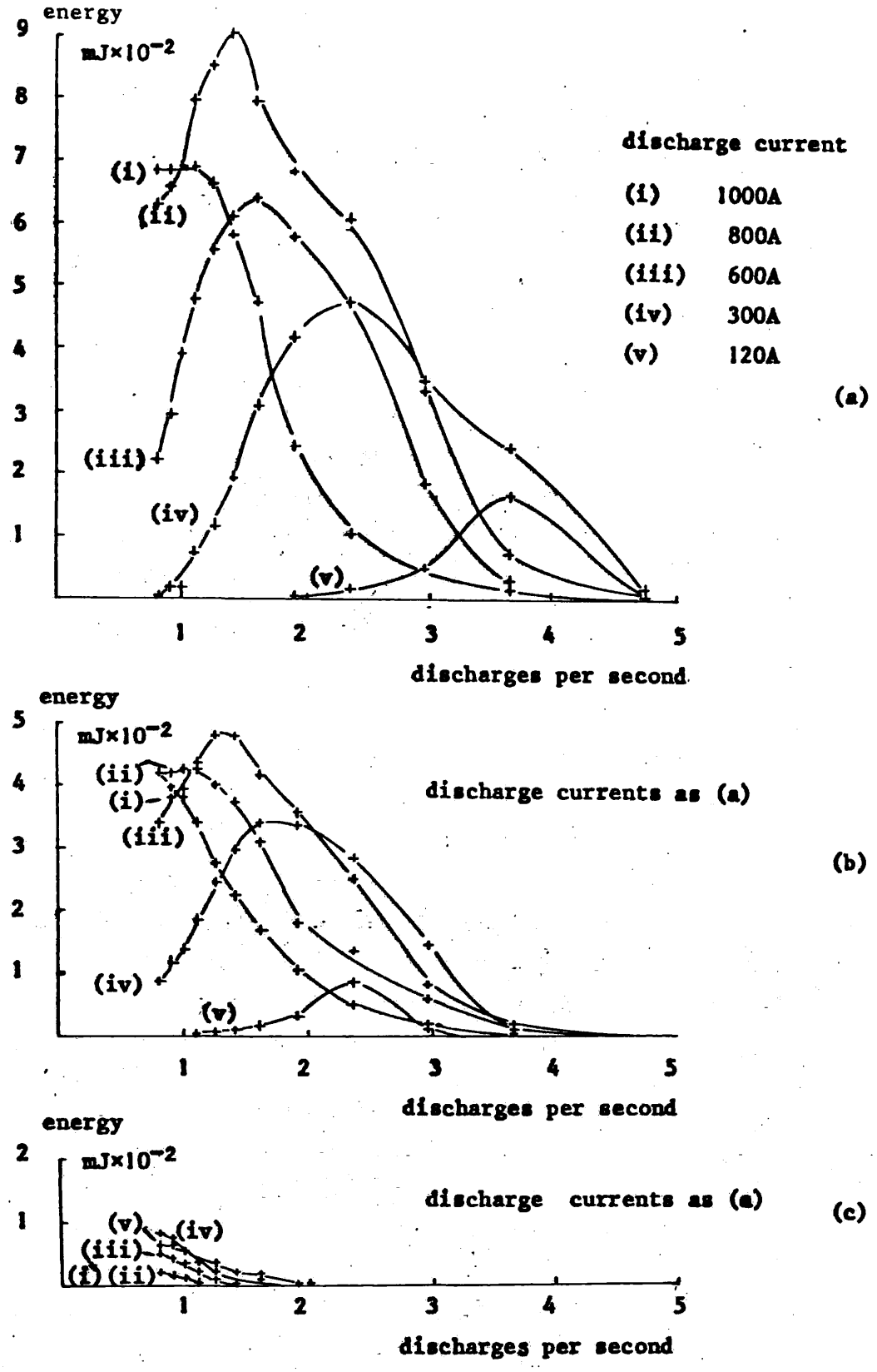

Figure 5.10. Energy of output radiation per discharge against the number of discharges per second from the 7.6 cm diameter, hole-coupled laser, using (a) 1 torr, (b) 0.85 torr, and (c) 0.45 torr of a methane-nitrogen mixture. No window across cavity. Error in measurement of energy, approx. ±10%, and in discharge repetition, approx. ±4%.

to produce conditions necessary for laser action. This is shown by the outputs from the 15 cm diameter laser given in Figures 5.8(b) and (c). Although this cavity configuration allowed stimulated emission to occur during the forward current pulse, an output was not observed until 10 to 15 μs after the start of the pulse.

Both the 7.6 cm and 15 cm diameter laser systems show that with a discharge of sufficient magnitude, no stimulated emission was produced during either the current pulse or the afterglow even though the electron density would decay to a level at which laser action would take place with smaller current pulses. This feature of the hydrogen cyanide laser implies that the pump mechanism is not simply related to the overall rate of recombination as suggested earlier, but that discharge products created during ionisation are essential to the operation of the laser and that they decay at a faster rate than the rest of the discharge. These properties of the plasma will be considered again in Chapter Six when analysing the pumping mechanism.

The lack of a large radiation output from the initial current pulse from the Blumlein supply when using the 7.6 cm diameter laser was found to be a specific property of the ionised methane-nitrogen mixture. Figures 5.9(c) and (d) show radiation pulses generated in similar circumstances from propylamine vapour. As with the 15 cm diameter laser, stimulated emission was produced during the late part of the current pulse and in the early afterglow, although the duration of the output was noticeably shorter than obtained previously. Again, an analysis of these characteristics will be made in Chapter Six.

To aid an investigation into Q-switching a pulse-excited laser, the output power of the 7.6 cm diameter laser was recorded with a Melinex window across the cavity. Table 5.2 shows that a reduction occurs in the energy emitted from the hole-coupled laser by a factor of 3.5, due to the presence of a window. A similar reduction in the peak power also resulted whilst the duration of the pulses, shown by Figures 5.9(c) and (d), undergoes little change. Similarly, Table 5.2 shows that a window inside the beam splitter coupled laser causes a reduction in the far infra-red energy of 4.5 times.

5.3.3. Beam splitter vibrations

Simultaneous detection of the beam splitter and hole-coupled outputs from the 15 cm diameter laser, as seen in Figure 5.12(b), showed that the two radiation pulse shapes differed, and that the peak of the

outputs occurred at different times. It was considered that the detected output from the beam splitter could be perturbed by an acoustic disturbance from the discharge causing the Melinex film to vibrate. To test for the existence of these vibrations, light from a helium-neon laser was reflected from the beam splitter on to a photo-sensitive transistor, as illustrated in Figure 5.11. Pulse excitation of the hydrogen cyanide laser led to a variation in the output from the transistor, shown by the upper trace of Figure 5.12(a), as movement of the beam splitter altered the orientation of the visible beam. The far infra-red radiation coupled from the beam splitter, shown by the lower trace of Figure 5.12(a), is seen to be emitted whilst the Melinex film is in motion. As with CW operation, the highest peak powers were obtained using beam splitter coupling; however, the movement of the Melinex film will seriously limit its use in the Michelson Q-switching configuration. This will be discussed further, later in the chapter.

5.4. Cavity interferograms

In order to analyse the output characteristics of pulse-excited lasers and to facilitate active Q-switching, the mode structures of the various laser configurations were studied. The output powers from the lasers were recorded whilst driving one of the cavity mirrors along the optical axis at a constant rate.

An investigation of the 15 cm diameter laser was made using plane-parallel cavity mirrors. For both d.c. and pulse excitation it was found that variation of the cavity length made little difference to the output intensity. This behaviour was attributed to successive cavity modes being excited by reflection from the tube walls. Replacement by spherical mirrors produced a laser with an output which was highly dependent on the mirror spacing. Two mirrors of radius of curvature of 760 cm produced a similar variation of the output with cavity length from the hole and beam splitter coupling. The interferograms obtained from these configurations, shown respectively in Figures 5.13(a) and (b) for d.c. excitation, are seen to consist of a series of modes of 337 μm radiation superimposed on lower intensity modes at other frequencies. Pulsed excitation produced wider fringes than did a d.c. discharge and, as seen in Figure 5.13(c), pulse-excited 337 μm lines tended to swamp the weaker emissions. Examination of the CW interferograms shows that the structures interspaced between the 337 μm fringes exhibit characteristics reported by Frayne[27] of minimum activity every 12 fringes of 337 μm radiation corresponding to 13 fringes of 311 or

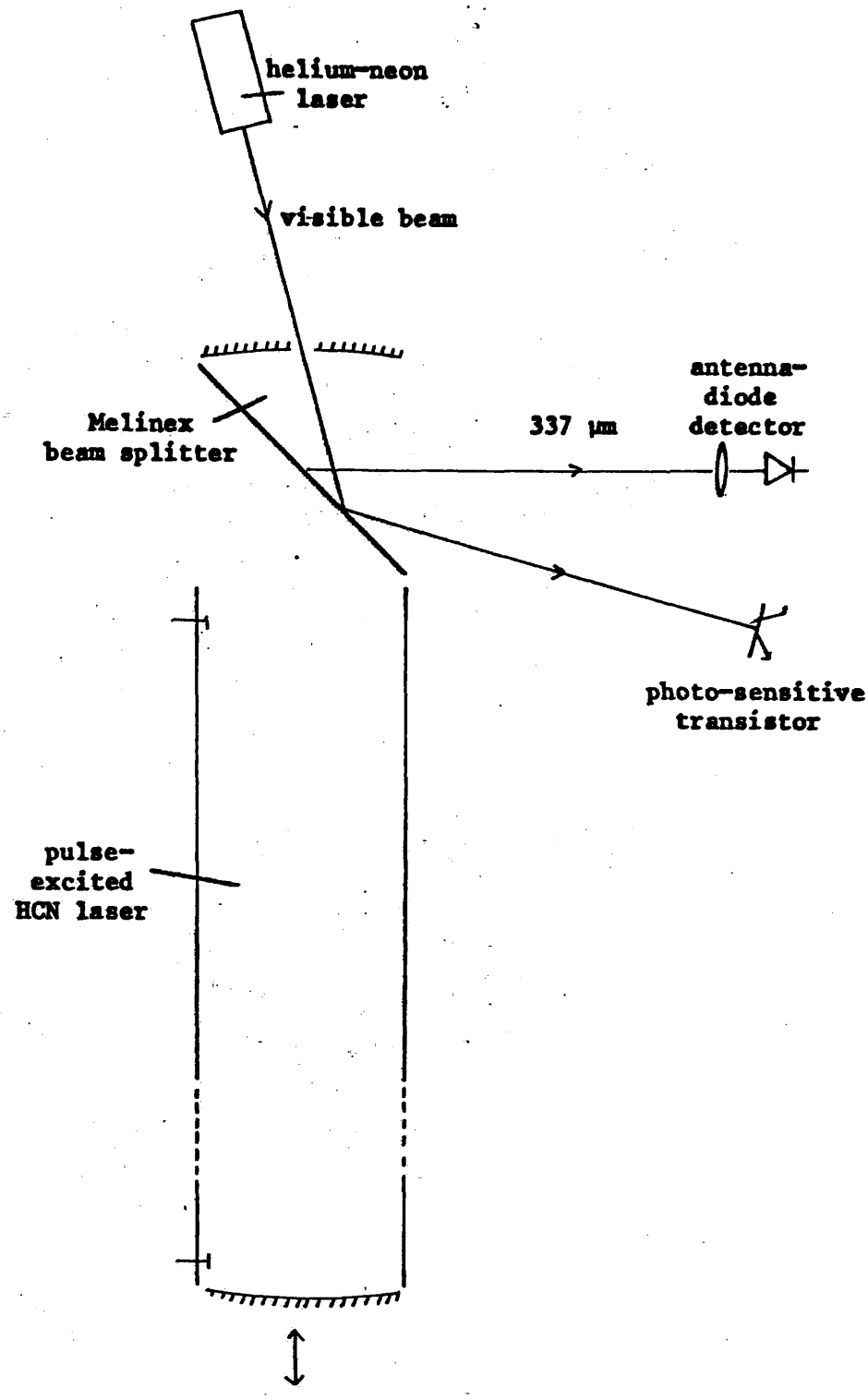

Figure 5.11. Experimental arrangement to monitor the laser radiation output and beam splitter movement

upper trace: output from a photo-transistor

lower trace: beam splitter coupled output (a)

horizontal scale, 100 μs per large division

upper trace: beam splitter coupled output

lower trace: hole-coupled output (b)

horizontal scale, 20 μs per large division

Figure 5.12. Pulsed excitation of the 15 cm diameter laser using 1 torr of a CH_4-N_2 mixture. (a) Comparison of the laser output with that from a photo-transistor responding to a visible beam reflected from the laser's beam splitter and (b) comparison of simultaneous beam splitter and hole-coupled laser outputs.

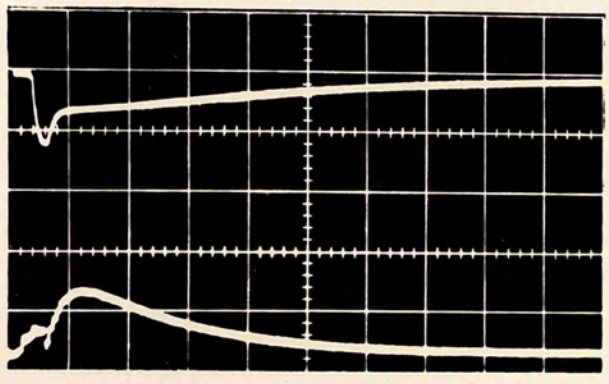

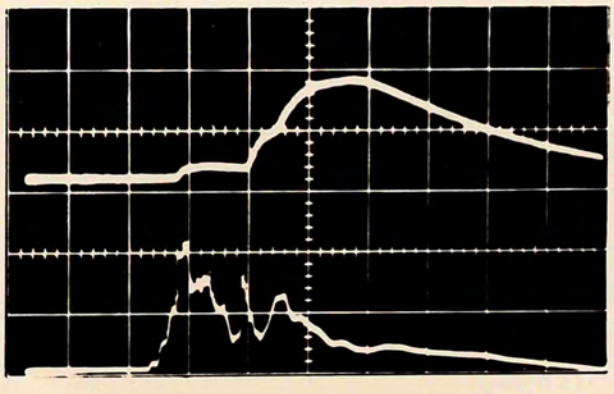

(a)

CW hole-coupled laser

cavity length increasing →

(b)

CW beam splitter coupled laser

cavity length increasing →

pulse-excited beam splitter coupled laser

(c)

cavity length increasing →

Figure 5.13. Cavity interferograms for the 15 cm diameter laser. Radii of curvature of mirrors $R_1=R_2=760$ cm.

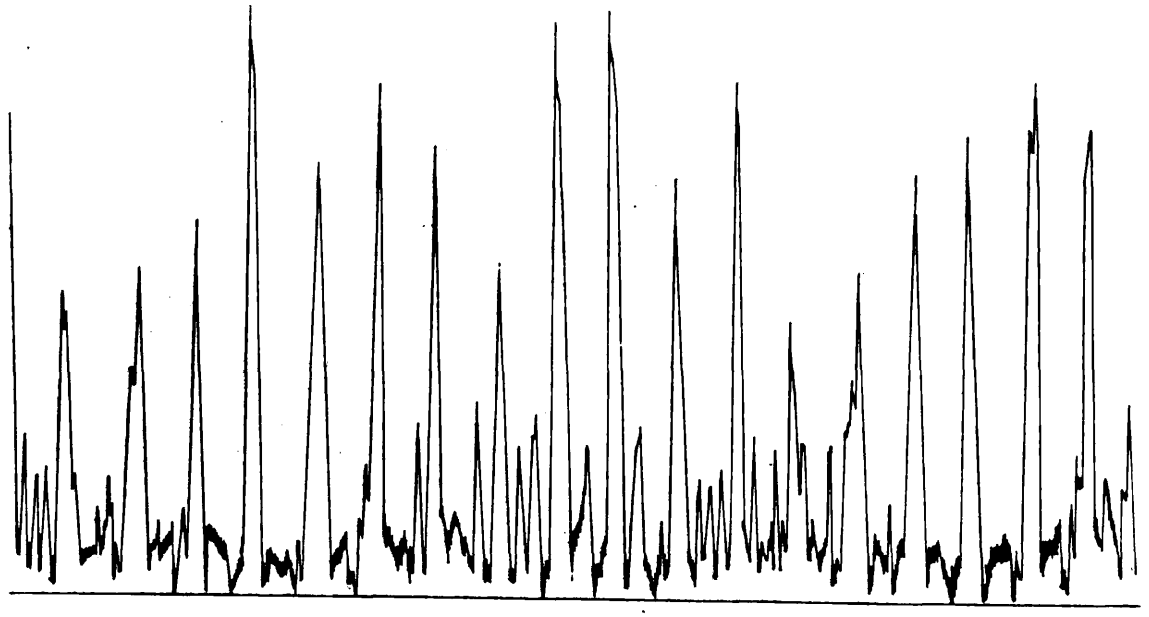

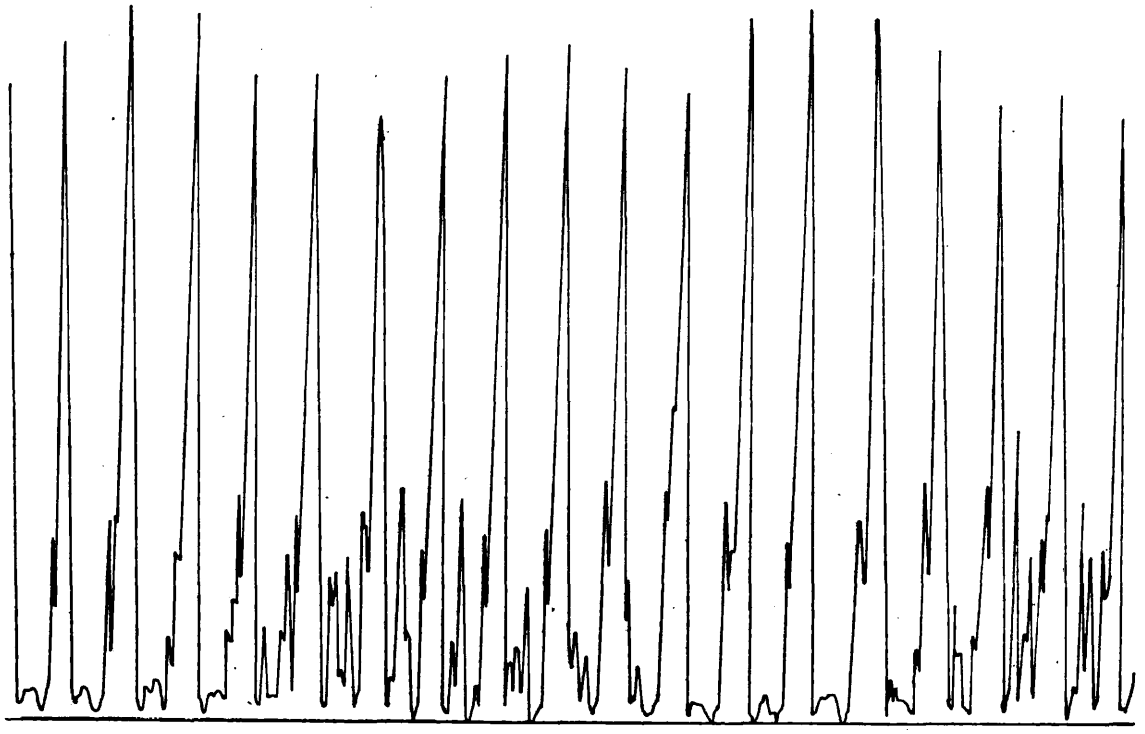

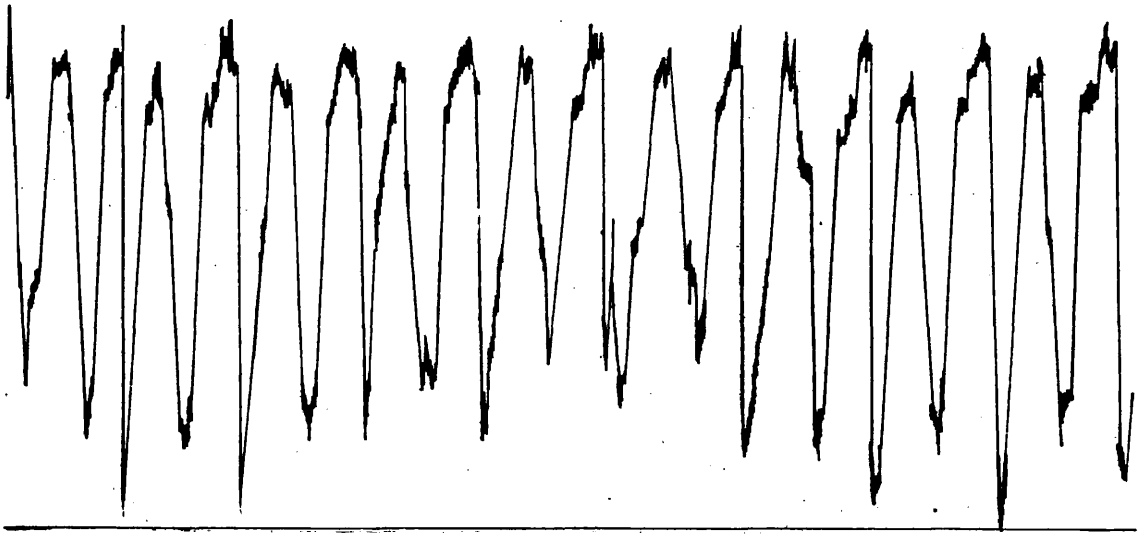

310 μm. The existence of a similar mechanism in the pulsed laser is indicated by the lowest minima of Figure 5.13(c) occurring every 12 fringes. The absence of the weaker modes at certain cavity lengths is an essential requirement for Q-switching. The technique of modulating the cavity path length by an ancillary plasma requires the ability to tune the cavity from a position of zero output to the peak of the 337 μm fringe without passing through other minor modes. It would also be necessary, when using the Michelson configuration, to ensure that the laser was not in a condition to oscillate at other frequencies because tuning the side mirror would then not inhibit all stimulated emission. As the mode structure of the pulsed laser is not resolved because of the large mode widths, examination of the proximity of the fringes is undertaken using the CW data. Figure 5.13(b) shows a mode situated on the short cavity side of the main 337 μm fringe which remained in this position over the observed path change of 100 fringes. A second 337 μm line is therefore generated by the laser, although it is not so easily distinguishable in the output from the hole-coupled cavity, and cannot be extinguished, as can other lines, by selecting an appropriate cavity length. Modulation of the gain profile of the laser by an ancillary discharge in the cavity would take place on the long cavity length side of the fringe and so this mode would not cause undue depopulation of the upper level. Further examination of the spectral purity of the main output line was carried out by tuning a Michelson interferometer so that the main 337 μm fringe from the CW beam splitter coupled laser was reduced in magnitude relative to modes at other frequencies. Under such conditions, the interferogram of Figure 5.14(a) was obtained for a region of minimum activity of the subsidiary modes. This exaggerated record of laser lines other than the 337 μm line was used to resolve the modes present within the envelope of the main fringe by calculating the second differential of the interferogram. This technique, developed by Keighley and Rhodes[33], locates the positions of the components of the fringes at the minima of the second derivative. This second derivative, seen inverted in Figure 5.14(b), shows that in regions of minimum activity of lines other than 337 μm, the main fringes are still composed of several different modes. It is evident that the success of shifting the resonant condition of the laser to the peak of a single gain profile by an ancillary discharge is limited. Some loss of inversion through excitation of minor modes would appear inevitable.

Observation of the mode structure of the beam splitter coupled 7.6 cm diameter laser with mirrors of radii of curvature 4.1 metres and cavity

(a)

cavity length decreasing →

(b)

cavity length decreasing →

Figure 5.14. (a) Expanded portion of the cavity interferogram for the 15 cm diameter CW laser and (b) the corresponding inverted second differential.

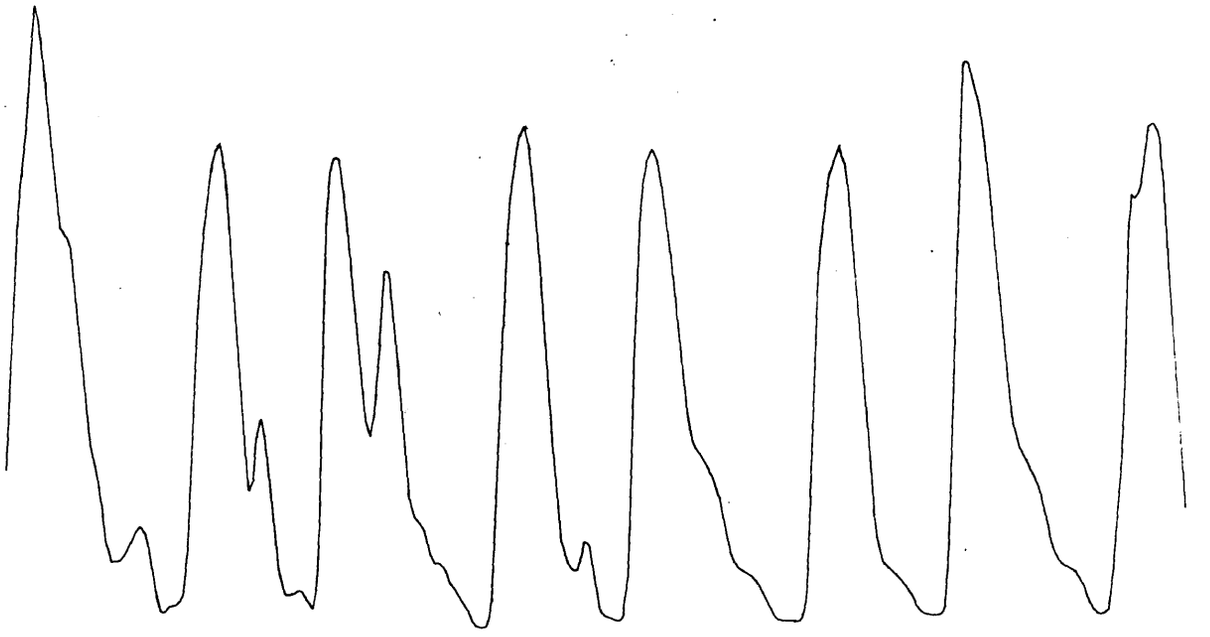

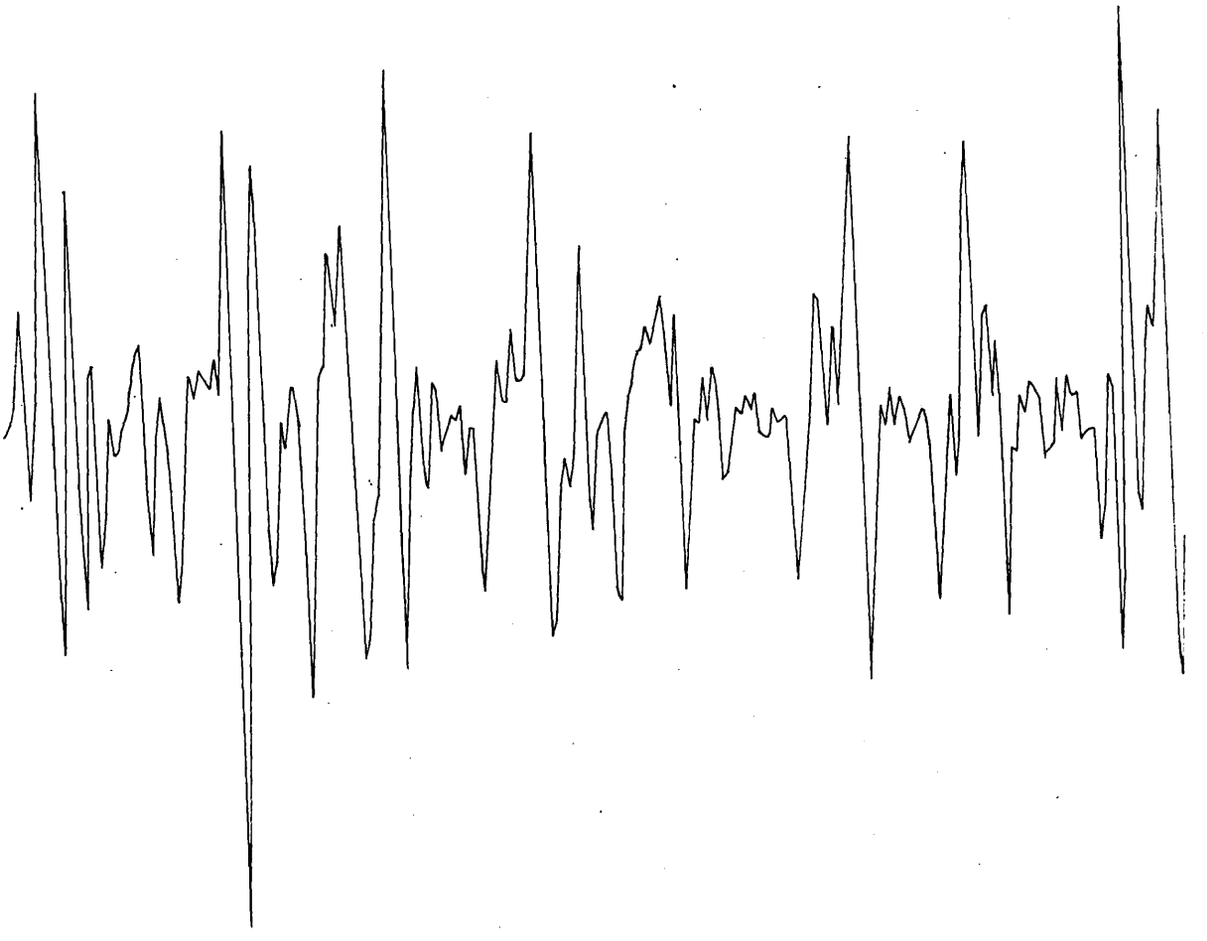

length 6.2 metres was first made without the Melinex window in the cavity. Two modes were generated, one at 337 μm and one at 310 μm which, as seen in Figure 5.15(a) for CW operation, became superimposed at some mirror separations but could be separated by altering the cavity length. This property could be utilized when the Q-switching experiments were to be performed. Insertion of a window into the laser prevented oscillation at 310 μm and introduced a second 337 μm mode overlapping the main fringe on its short cavity length side. Q-switching a single mode of this laser by an inter-cavity discharge should therefore be possible but must suffer from the loss introduced by the window.

5.5. Determination of transient plasma densities

Q-switching techniques incorporating discharges in gaseous media were proposed in Chapter Four. A necessary property of the ancillary plasma is that the required phase shift may be effected in a time sufficiently short compared with that produced by the transient electron density of the active media. In order to obtain optimum Q-switching conditions, the time variation of the plasma densities created by discharges in the various laser active media was measured and compared with those of other gases.

Electron densities were measured by directing the radiation in one arm of a Mach-Zehnder interferometer axially through a 50 cm long, 7.6 cm diameter plasma tube. This orientation was chosen as no assumption is necessary to describe the radial variation of the plasma density. The investigation was first undertaken using radiation from an HCN laser. The arrangement of the interferometer, shown in Figure 5.16, utilized both outputs from a beam splitter coupled laser for the signal and reference arms which were combined by a second beam splitter and detected using a point contact diode. On entry to a screened room, the signal radiation passed through a 2 cm diameter tube in order to sample the plasma over a limited area of its cross-section. The diameter of the reference beam was reduced with an iris to ensure good visibility of the interference fringes. An example of these fringes is shown in Figure 5.17(a) which resulted from a plasma produced by a discharge from a capacitor ionising 0.35 torr of air in a 7.6 cm diameter tube. Modulating the phase of a pulse-excited laser by creating a plasma in a short section of the cavity would require a discharge of a higher and more rapidly varying electron density than that of the active medium. An examination was therefore made of high density ionisation produced by an electrical discharge from a capacitor triggered by means of a

(a)

cavity length decreasing

→

(b)

cavity length decreasing

→

Figure 5.15. Cavity interferograms for the 7.6 cm diameter CW beam splitter coupled laser (a) without a window inside the cavity and (b) with a Melinex window across the cavity

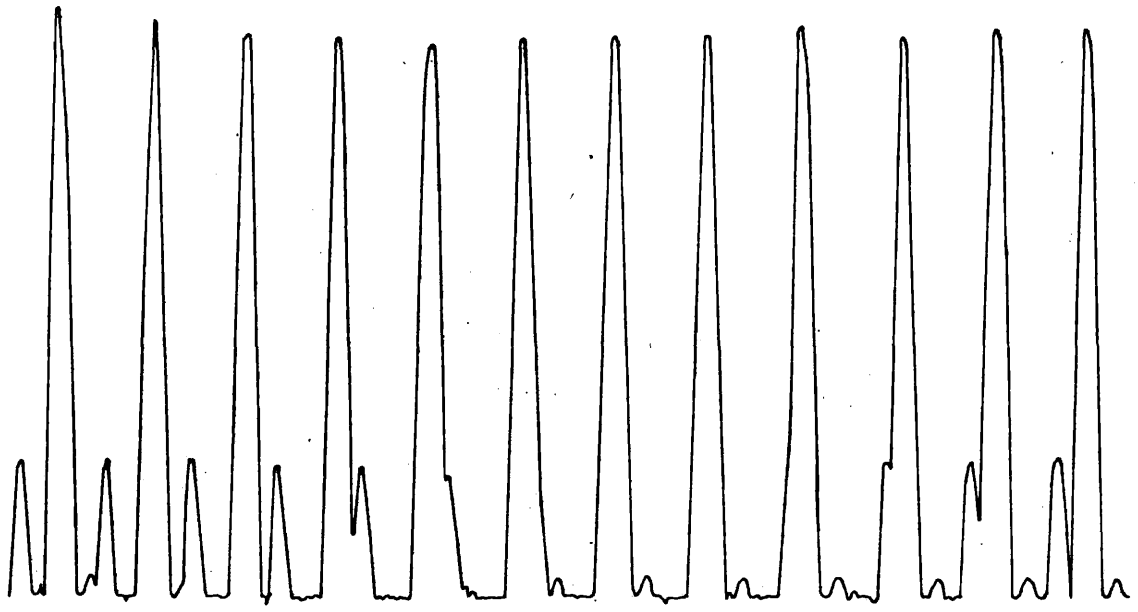

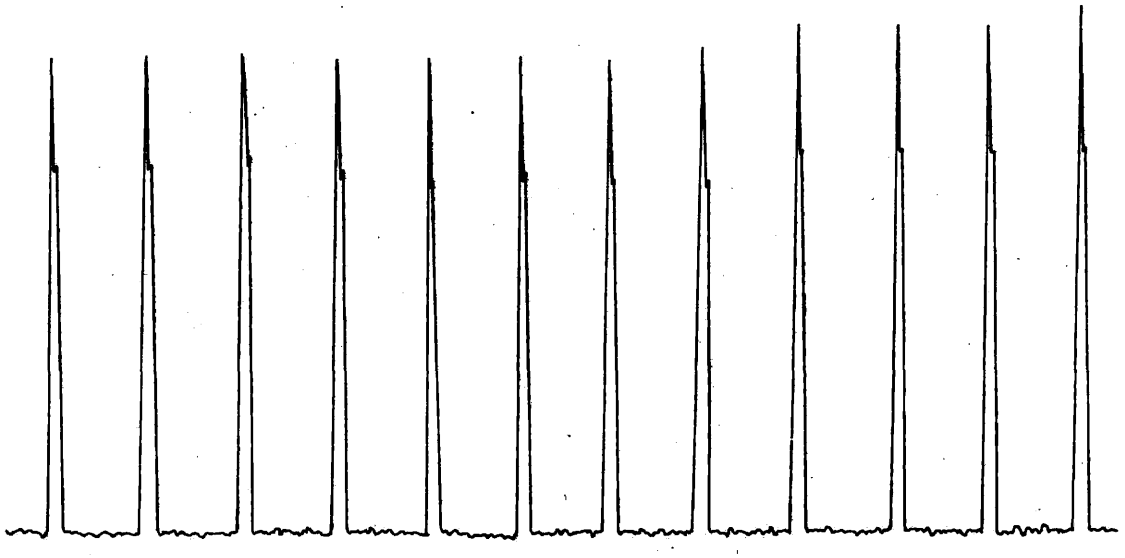

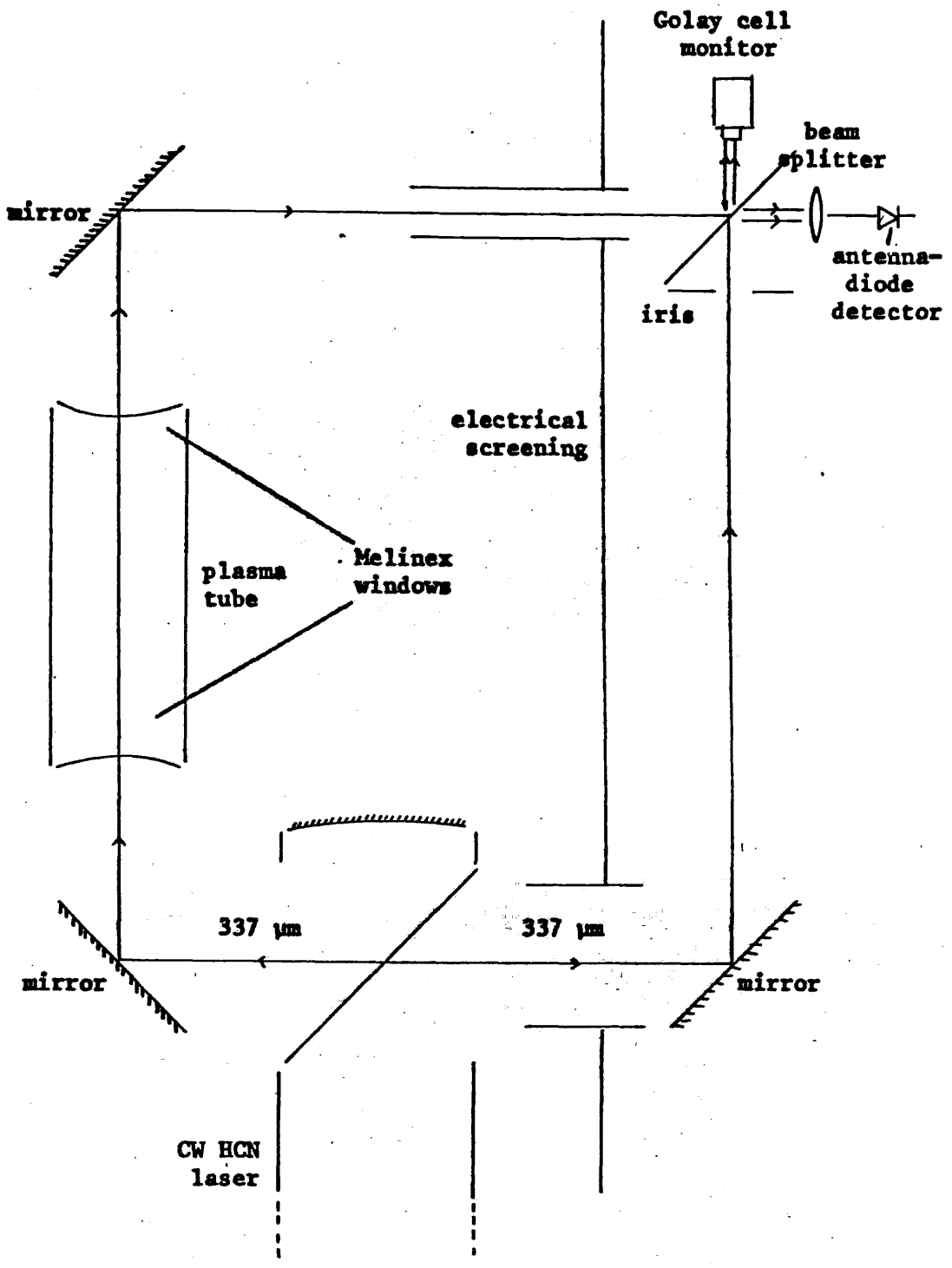

Figure 5.16. Arrangement of the Mach-Zehnder interferometer

horizontal scale, 100 μs per large division (a)

horizontal scale, 100 μs per large division (b)

Figure 5.17. Interference fringes produced by (a) the laser interferometer for 0.35 torr of air ionised by the Marx generator and (b) the microwave interferometer for 0.5 torr of helium ionised by the Blumlein supply

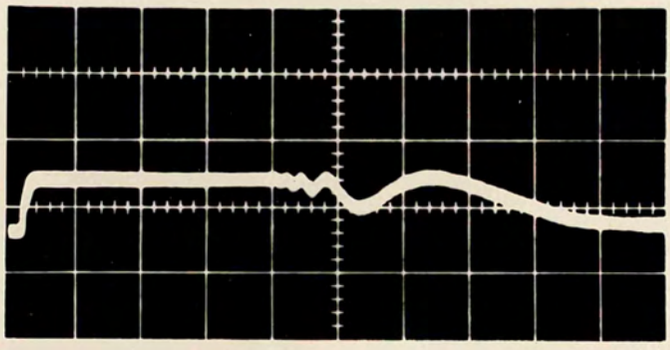

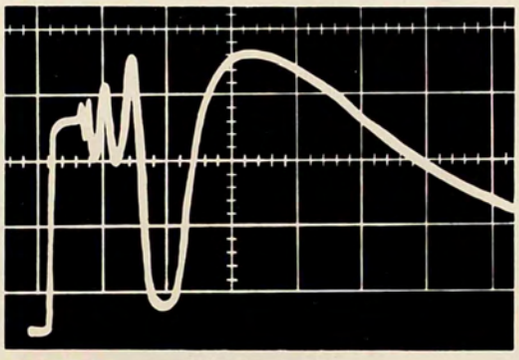

spark gap. Before initiating the discharge, the relative phase of the two beams was adjusted to give either a maximum output or complete cancellation by translation of one of the interferometer mirrors. This enabled the nett losses incurred in the plasma to be measured. The trace in Figure 5.17(a) shows high losses in the early part of the afterglow which prevent resolution of the fringes. It was only in the late afterglow, when the electron decay had fallen to the levels depicted in Figure 5.18, that transmission would be sufficient for laser action. The figure also shows the variation of the plasma density in the late afterglow in 1 torr of a methane-nitrogen mixture ionised under similar conditions. Similar rates of electron decay were recorded when ionising helium gas, both by discharge from the capacitor or Marx generator, Figure 5.19(a), or by the thyratron modulator, Figure 5.19(b). The effectiveness of these discharges for modulation purposes is assessed by comparison with the rates of decay of the electron density in active media. Such conditions were simulated by ionising a methane-nitrogen mixture using the thyratron modulator. Plasma density was measured at several gas pressures and plotted against time in Figure 5.20. The decay rates shown in the two figures are seen to be similar, indicating that insufficient phase shift can be produced in the comparatively short length of cavity allowable for a non-active plasma. Electron density measurements were also made using deuterium oxide vapour in order to realize the degree of phase shift introduced while Q-switching the laser by ionising an absorbing medium. The results are seen in Figure 5.21 again to be similar to that of the laser medium and so will only alter the phase according to the ratio of the length of the ancillary plasma to that of the active discharge. The vapour was ionised by the Marx generator to obtain maximum dissociation. Figure 5.22 shows the transmission of 337 μm radiation through the several plasmas, and that in the case of deuterium oxide vapour, a peak in transmission occurs as the decreasing loss due to ionisation becomes superseded by an increasing number of recombined molecules.

Ionised conditions produced in a 15 cm diameter system were investigated using a 65 cm length of tube. A lower frequency radiation was required in order to measure electron density, as insufficient phase shift was produced for the laser interferometer.

Power from a klystron at 9.3 GHz was coupled into two waveguide runs by a magic tee, one beam being radiated axially through a plasma tube, the other supplying the phase reference as illustrated in Figure 5.23. A

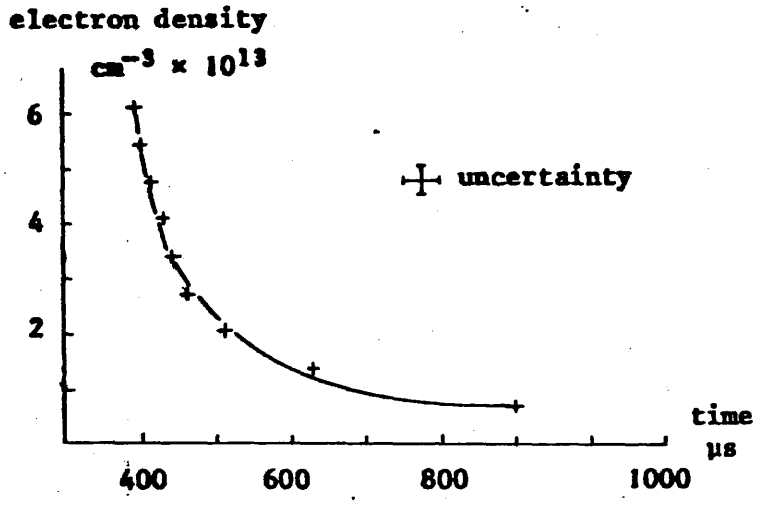

(a)

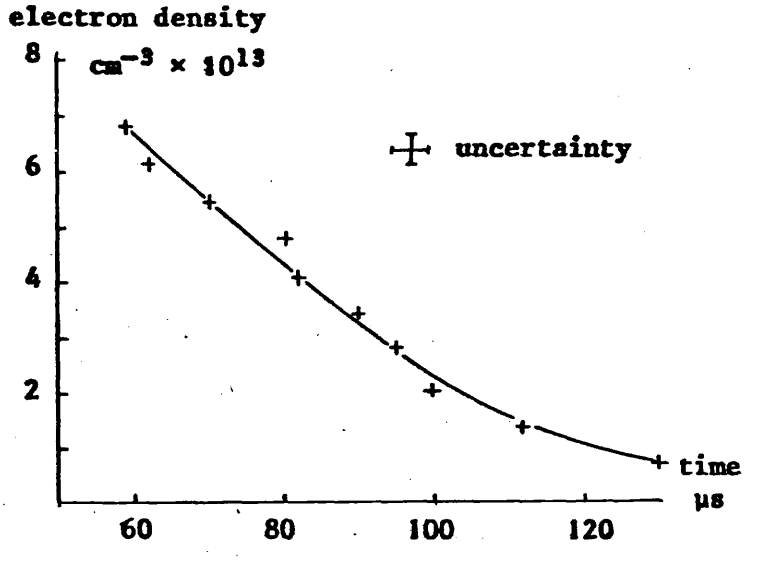

(b)

Figure 5.18. Electron density against time after initiating discharge in (a) 0.35 torr of air, and (b) 1 torr of a methane-nitrogen mixture using the Marx generator. 7.6 cm diameter plasma tube.

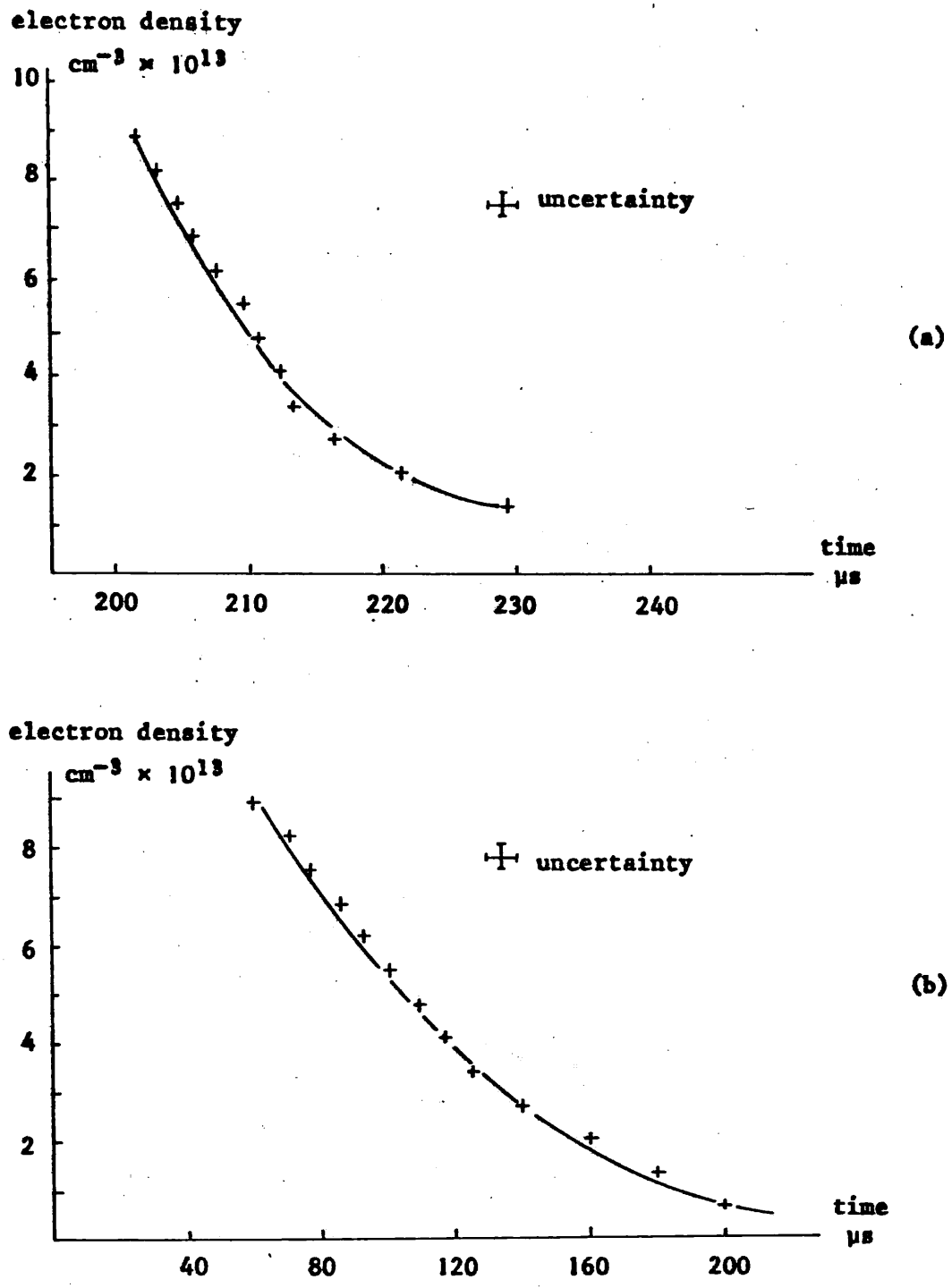

Figure 5.19. Electron density against time after initiating discharge in 1 torr of helium in a 7.6 cm diameter tube using (a) the Marx generator, and (b) the Blumlein power supply

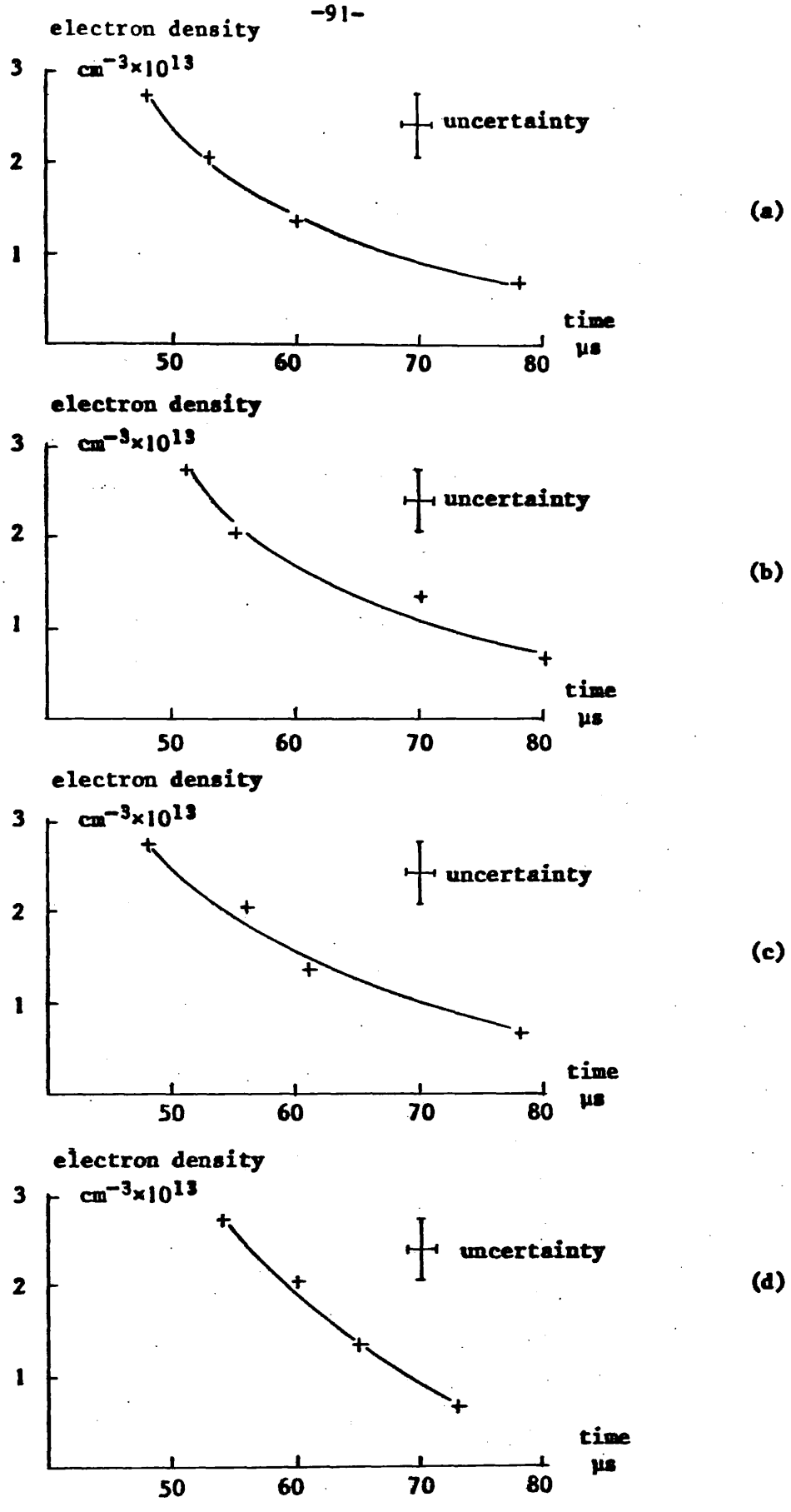

Figure 5.20. Electron density against time after initiating a discharge in a methane-nitrogen mixture at (a) 1.2 torr, (b) 1.0 torr, (c) 0.6 torr, and (d) 0.5 torr. 7.6 cm diameter discharge tube. Blumlein power supply.

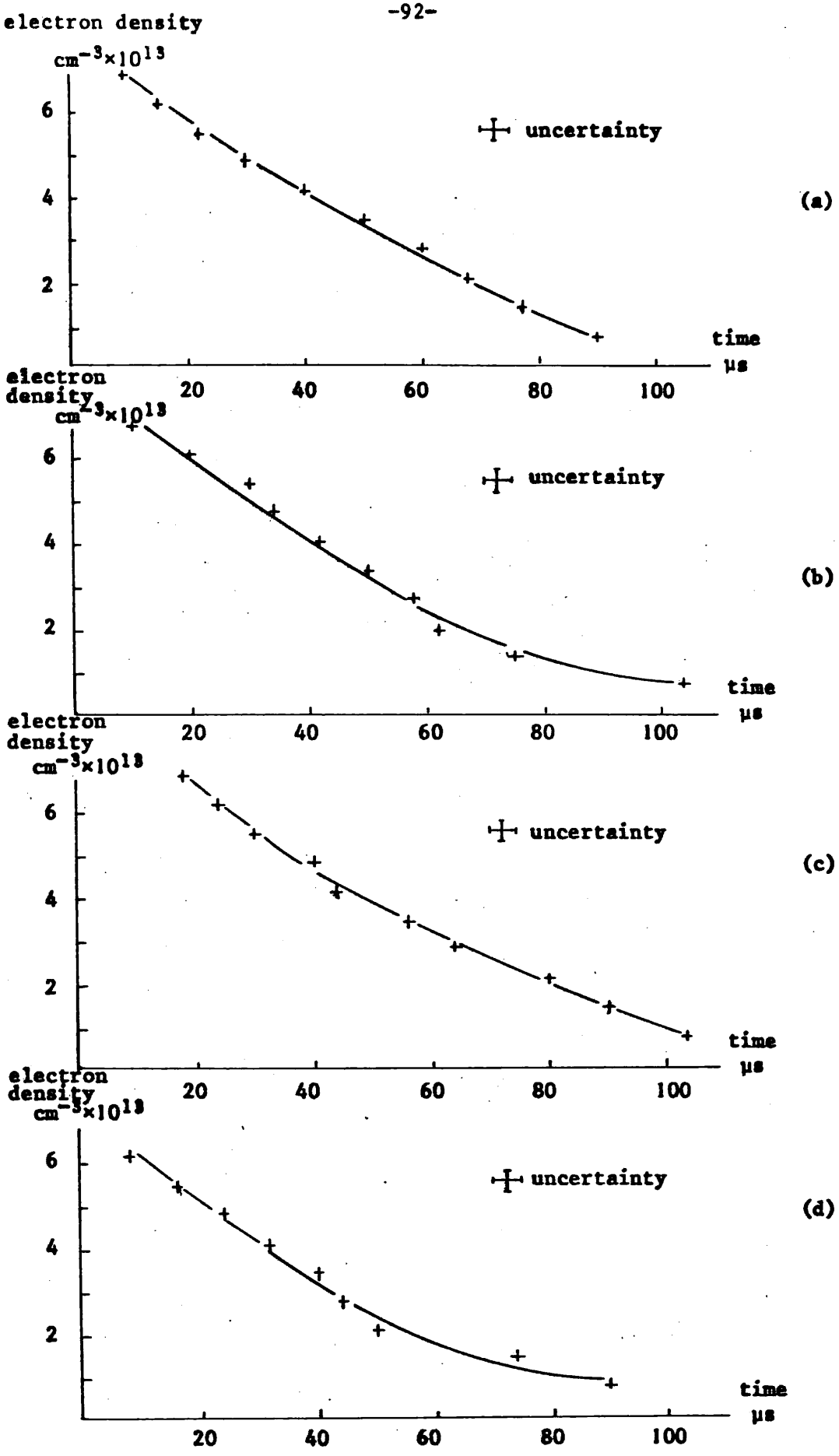

Figure 5.21. Electron density against time after initiating a discharge in deuterium oxide vapour at (a) 5 torr, (b) 3.5 torr, (c) 2.5 torr, and (d) 1 torr. 7.6 cm diameter discharge tube. Discharge from Marx generator.

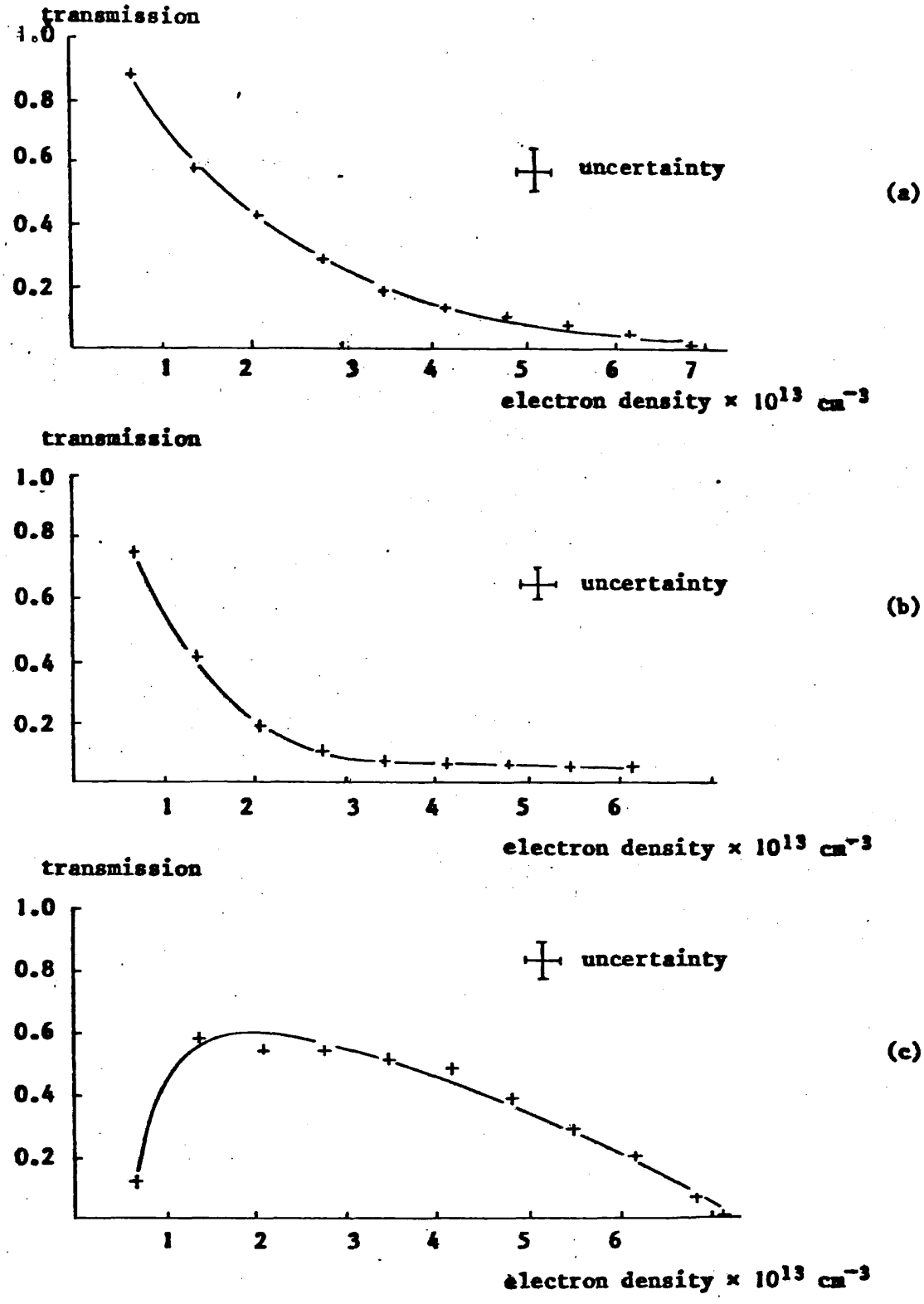

Figure 5.22. Transmission at 891 GHz against electron density in ionised media of (a) 0.35 torr of air, (b) 1 torr of helium, and (c) 5 torr of deuterium oxide in a 60 cm long, 7.6 cm diameter tube

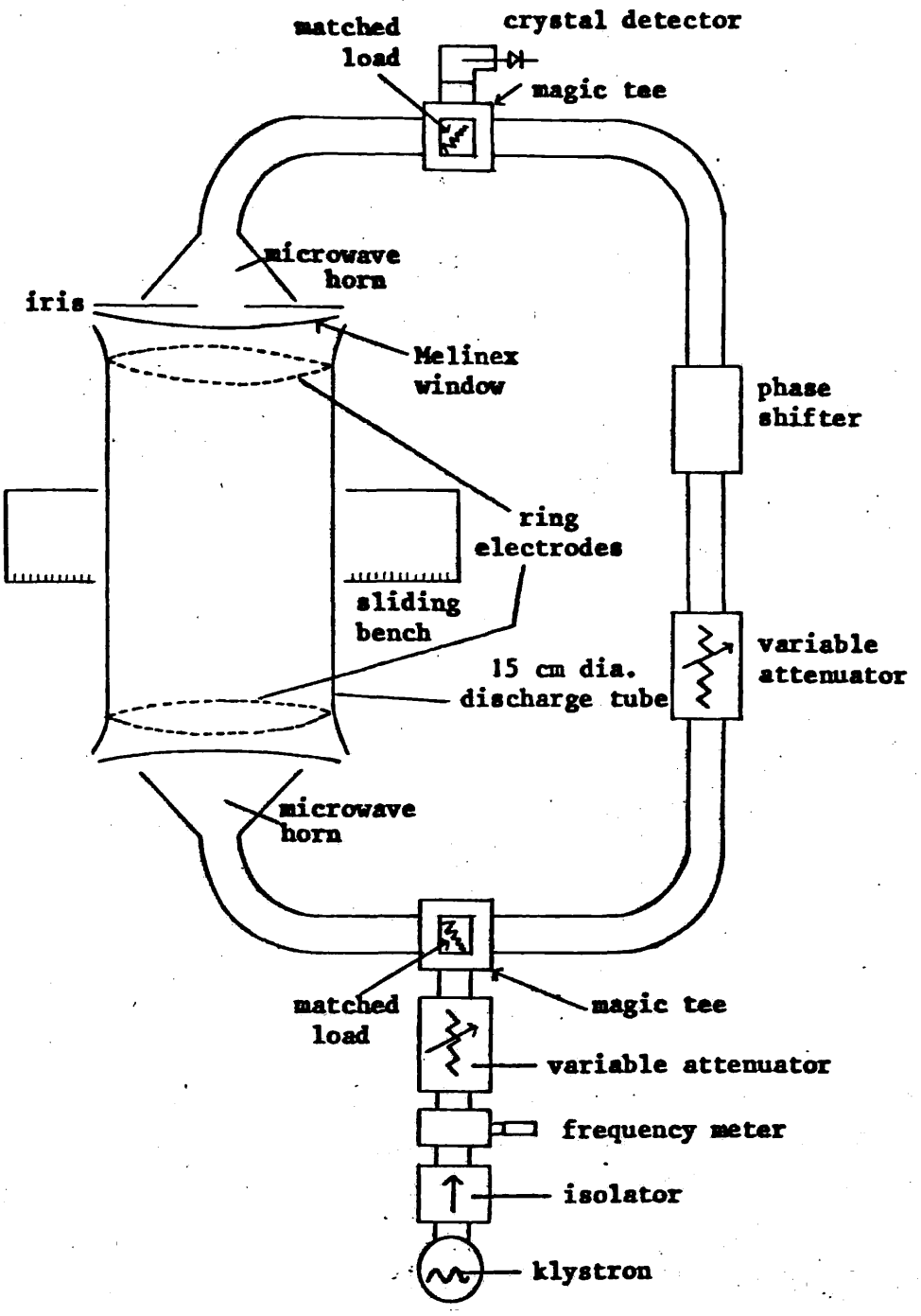

Figure 5.23. Arrangement of the microwave interferometer

limited region of the plasma was observed by collecting radiation from the plasma through a 2 cm diameter iris. This enabled the electron density to be measured at any radial position by transverse movement of the tube on a sliding bench. Two microwave beams were combined by a second magic tee and coupled into a detector. An attenuator and a phase shifter in the reference arm were used to equalize the two beams in intensity and adjust the relative phase to produce either maximum or zero output.

In order to simulate the conditions in the active medium of a 15 cm diameter laser, a methane-nitrogen mixture was ionised by the Blumlein supply. Electron densities were measured over a range of gas pressures and are seen in Figure 5.24 to be lower and less rapidly decaying than those produced in the 7.6 cm diameter tube. This gives some support to the proposal made previously that stimulated emission only occurred after the high current pulse in the larger diameter laser because of plasma-induced refraction. Figure 4.4 illustrated that over the range of radial electron density profiles selected for computation, the plasma densities measured in the 7.6 cm diameter tube would produce a high loss cavity while those in the wider system would add little to the loss mechanisms. Measurements obtained from the 15 cm diameter tube using propylamine and ethylenediamine vapour are seen respectively in Figures 5.25 and 5.26 to be similar in magnitude and rate of decay to those of the methane-nitrogen mixture.

High losses in the laser interferometer system prevented measurement of the radial density profile in the 7.6 cm diameter tube. However, using the microwave interferometer movement of the 15 cm diameter tube across the beam showed that the electron density varies across the diameter of the tube. The electron density profiles obtained for three active media are displayed in Figure 5.27 at selected times after the end of the current pulse. With the exception of ethylenediamine vapour near the tube walls, values of the parameter β, defined in section 2.5, have been calculated at each point on the curves, the average values of which are shown in Table 5.3.

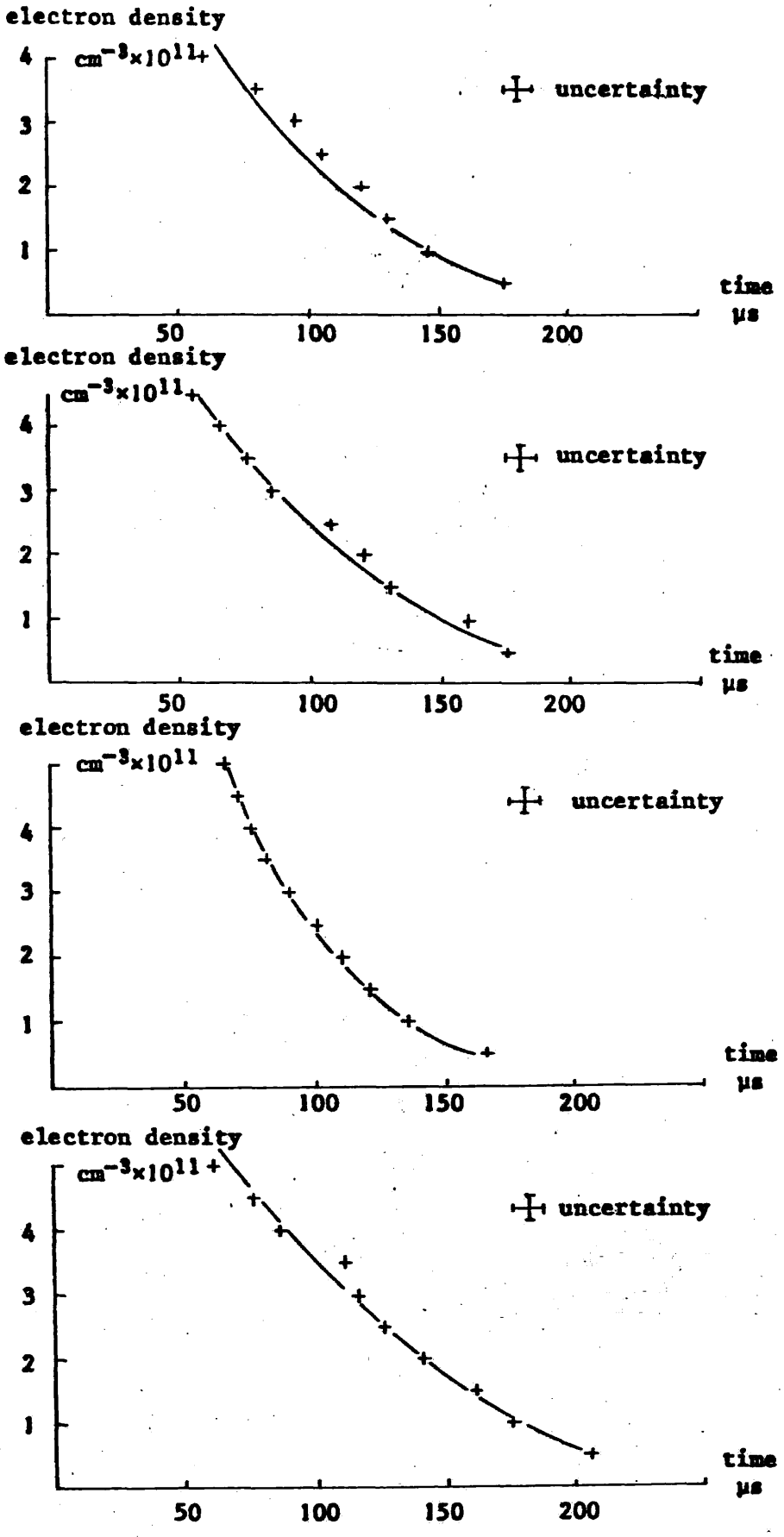

Figure 5.24. Electron density against time after initiating a discharge in a methane-nitrogen mixture at (a) 1.0 torr, (b) 0.8 torr, (c) 0.65 torr, and (d) 0.4 torr. 15 cm diameter discharge tube. Blumlein power supply.

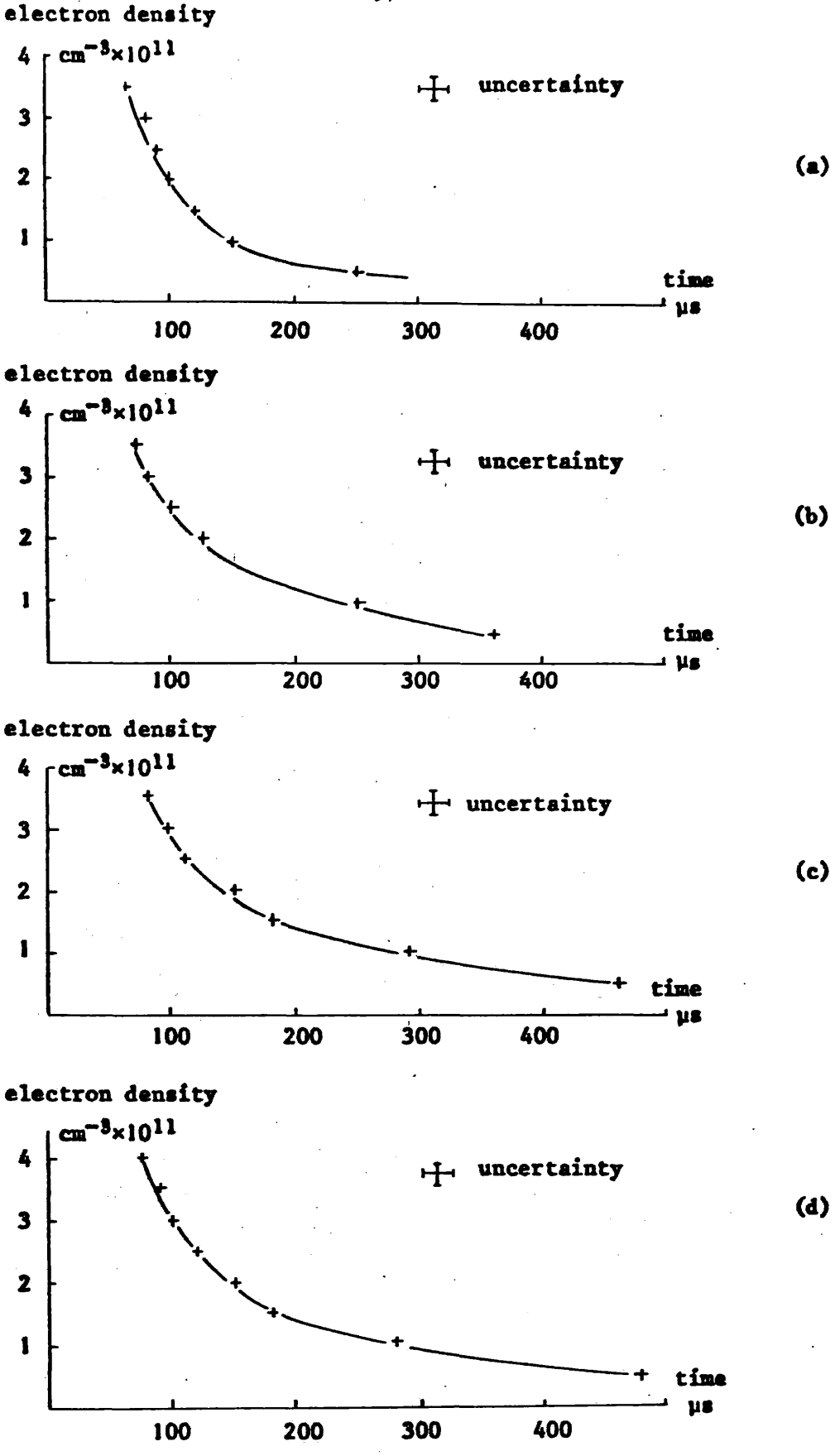

Figure 5.25. Electron density against time after initiating a discharge in propylamine vapour at (a) 0.9 torr, (b) 0.75 torr, (c) 0.5 torr, and (d) 0.35 torr. 15 cm diameter discharge tube. Blumlein power supply.

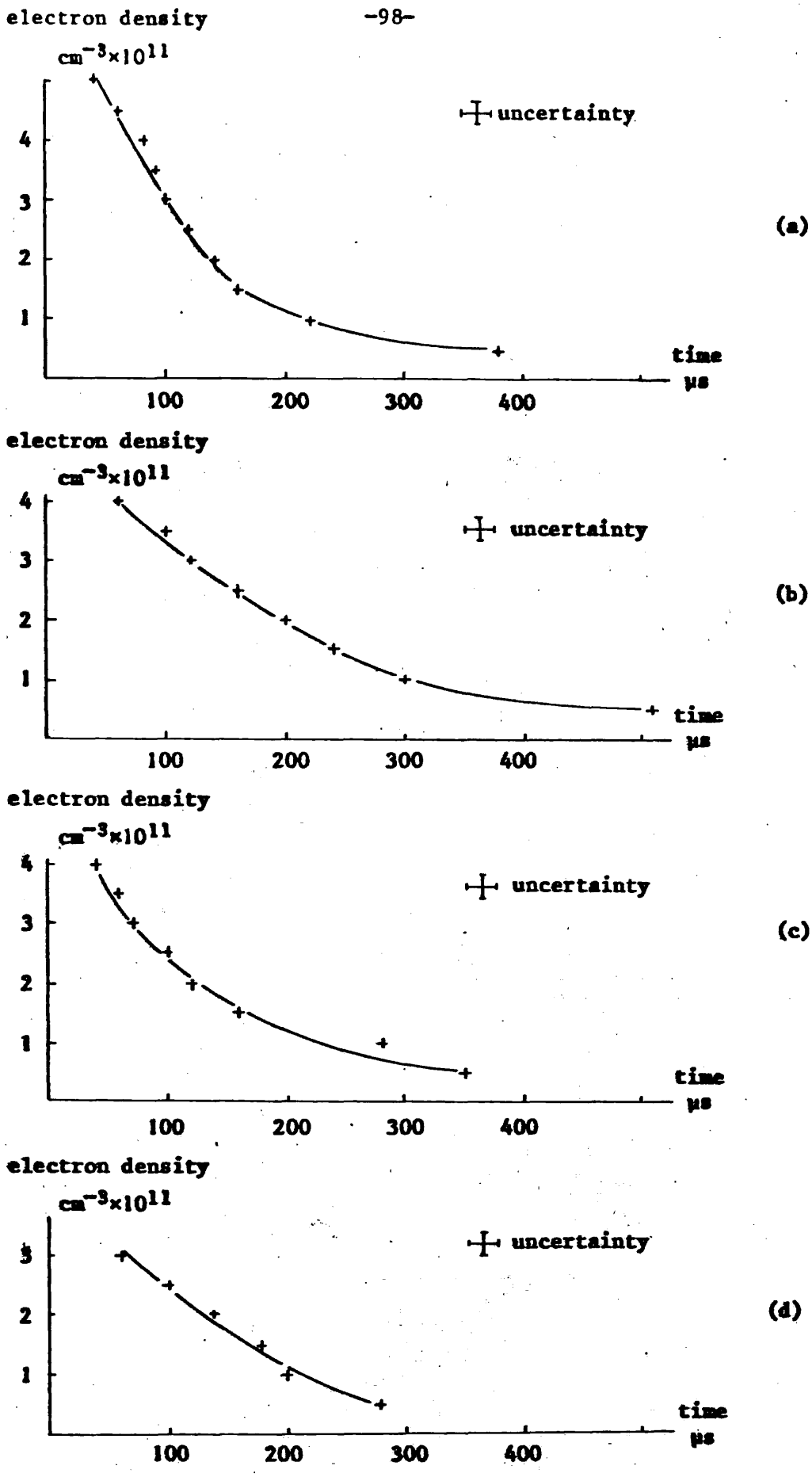

Figure 5.26. Electron density against time after initiating a discharge in ethylenediamine vapour at (a) 0.9 torr, (b) 0.6 torr, (c) 0.35 torr, and (d) 0.2 torr. 15 cm diameter discharge tube. Blumlein power supply.

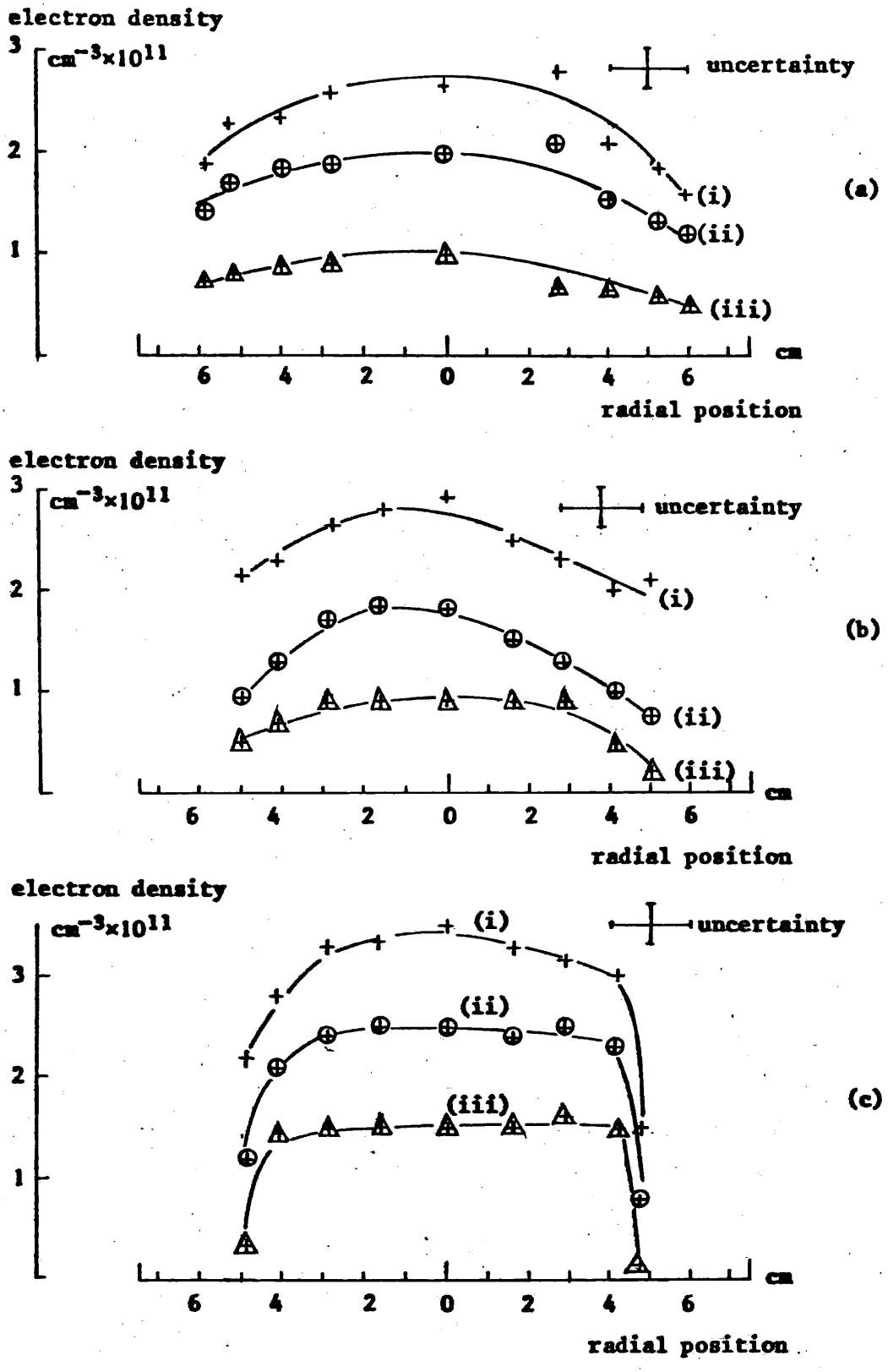

Figure 5.27. Radial electron density profiles of ionisations in (a) 0.75 torr of a methane-nitrogen mixture, (b) 0.75 torr n-propylamine vapour, and (c) 0.2 torr of ethylenediamine vapour at (i) 5 μs, (ii) 30 μs, and (iii) 70 μs after the end of the current pulse from the Blumlein supply.

Table 5.3

Values of β describing the radial electron density profile in three different ionised media in a 15 cm diameter tube

Time after end of current pulse (μs)	Methane-nitrogen mixture	Propylamine vapour	Ethylenediamine vapour
5	0.55 ± 0.1	0.55 ± 0.1	0.5 ± 0.1
30	0.55 ± 0.1	0.8 ± 0.1	0.4 ± 0.05
70	0.7 ± 0.1	0.9 ± 0.1	0.3 ± 0.05

The modulation experiments of Tait et al.[49] described in Chapter Three involved pulse excitation of gases inside the resonant cavity of a CW laser. It was found that several different ionised gases, separated from the active medium, decayed at different rates and produced output pulses of differing widths. Measurements made in the 15 cm diameter tube agreed with Tait's findings that ionised nitrogen decayed at a faster rate than helium. However, observing the afterglow in nitrogen, methane and helium over a range of pressures, displayed respectively in Figures 5.28, 5.29 and 5.30, showed that none decayed at a faster rate than the methane-nitrogen mixture. The investigations of both Frayne[27] and Belland et al.[53] demonstrated that an HCN laser may operate while introducing helium into the methane-nitrogen mixture. As reducing the rate of decay of the active medium would produce longer periods in which an active Q-switching may be performed, the effect of the addition of this third gas was therefore studied. Progressively increasing the proportion of helium is seen in Figure 5.31 to lengthen the decay time. However, an alteration of the decay rate during the laser active period immediately after the current pulse is insignificant.

5.6. Modulation of the HCN laser

An investigation into ionised absorber switching, the first of the three modulation techniques listed at the beginning of the chapter, commenced by examining the attenuating properties of difluoroethylene, deuterium oxide vapour, and dichloromethane vapour. With the exception of dichloromethane, these media[50,51] have been reported to possess strong attenuating properties at 337 μm. Because of the need to Q-switch a pulse-excited laser, the relative merits of these materials as attenuators of the pulsed laser output were measured. To study the modulation technique in isolation from the effects of mode scanning

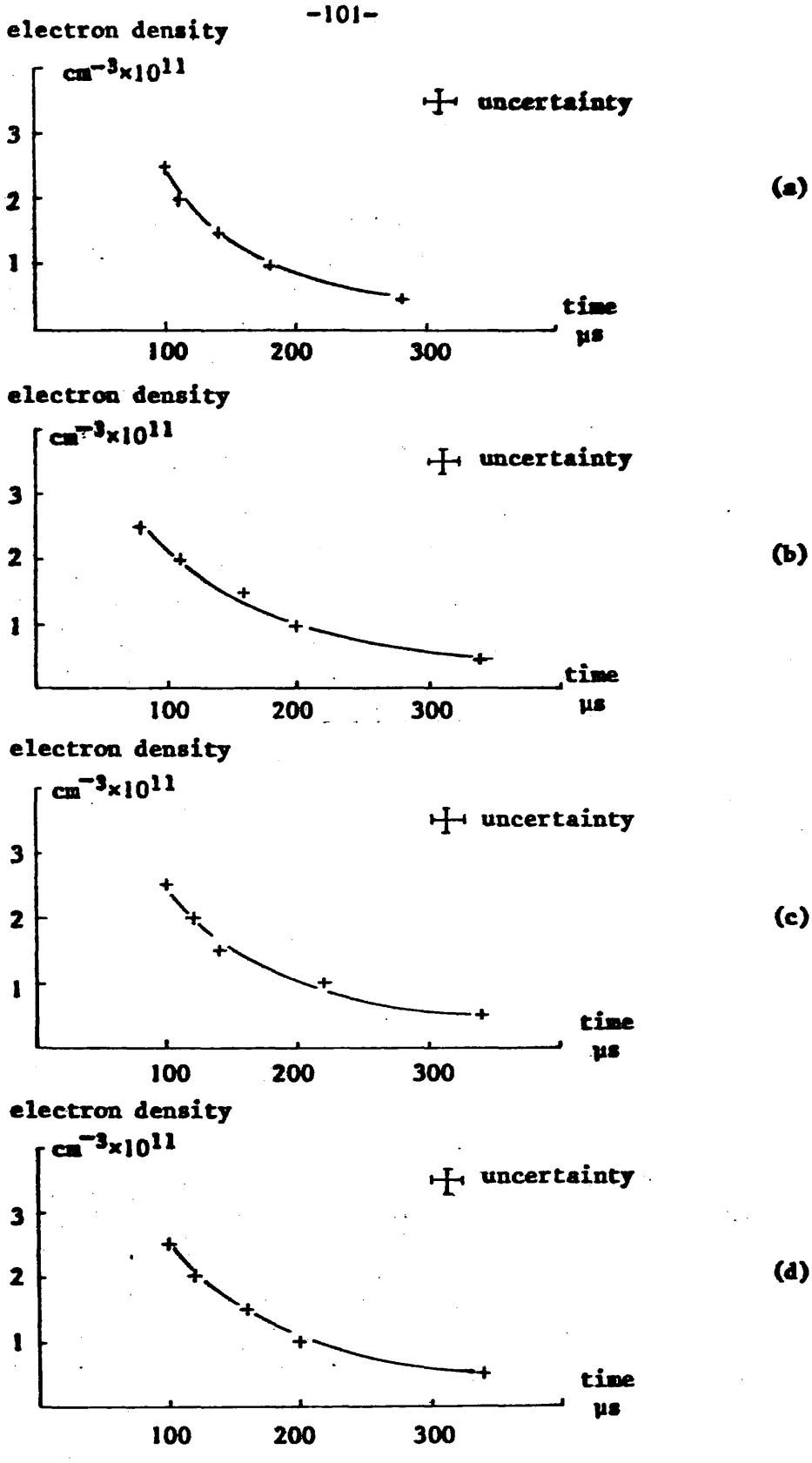

Figure 5.28. Electron density against time after initiating a discharge in nitrogen at (a) 1.0 torr, (b) 0.5 torr, (c) 0.4 torr, and (d) 0.2 torr. 15 cm diameter discharge tube. Blumlein power supply.

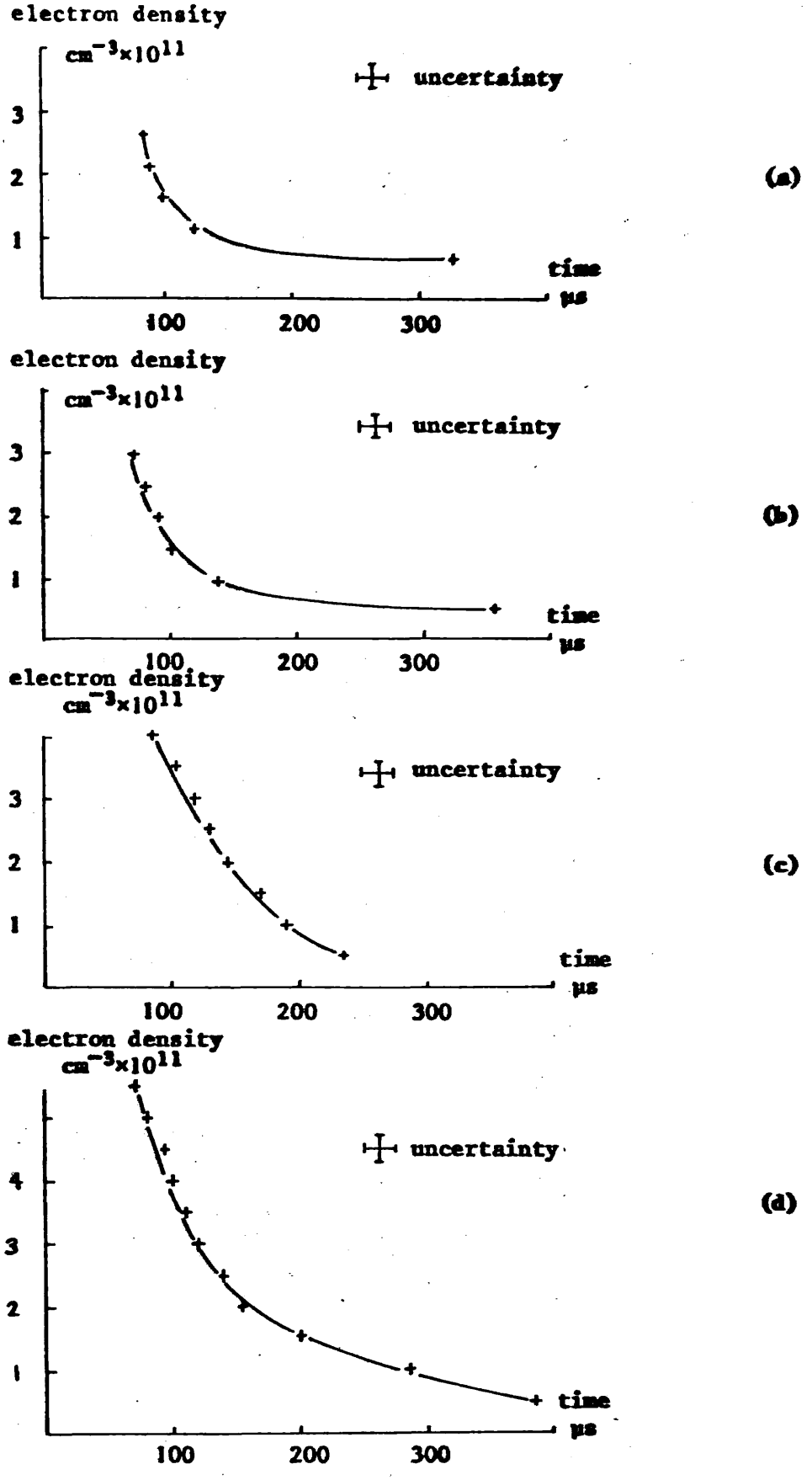

Figure 5.29. Electron density against time after initiating a discharge in methane at (a) 0.9 torr, (b) 0.7 torr, (c) 0.4 torr, and (d) 0.2 torr. 15 cm diameter discharge tube. Blumlein power supply.

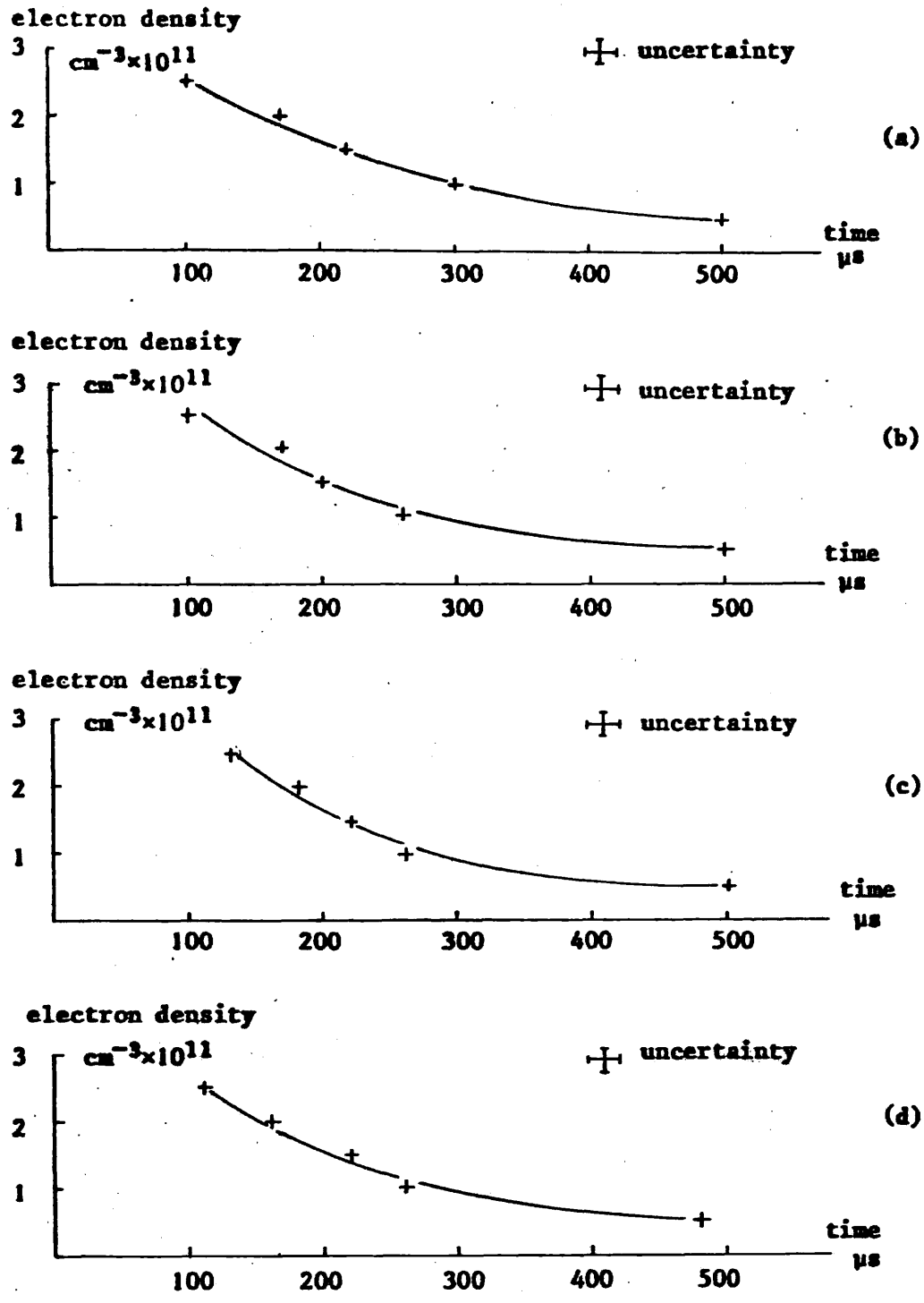

Figure 5.30. Electron density against time after initiating a discharge in helium at (a) 1.0 torr, (b) 0.75 torr, (c) 0.5 torr, and (d) 0.4 torr. 15 cm diameter discharge tube. Blumlein power supply.

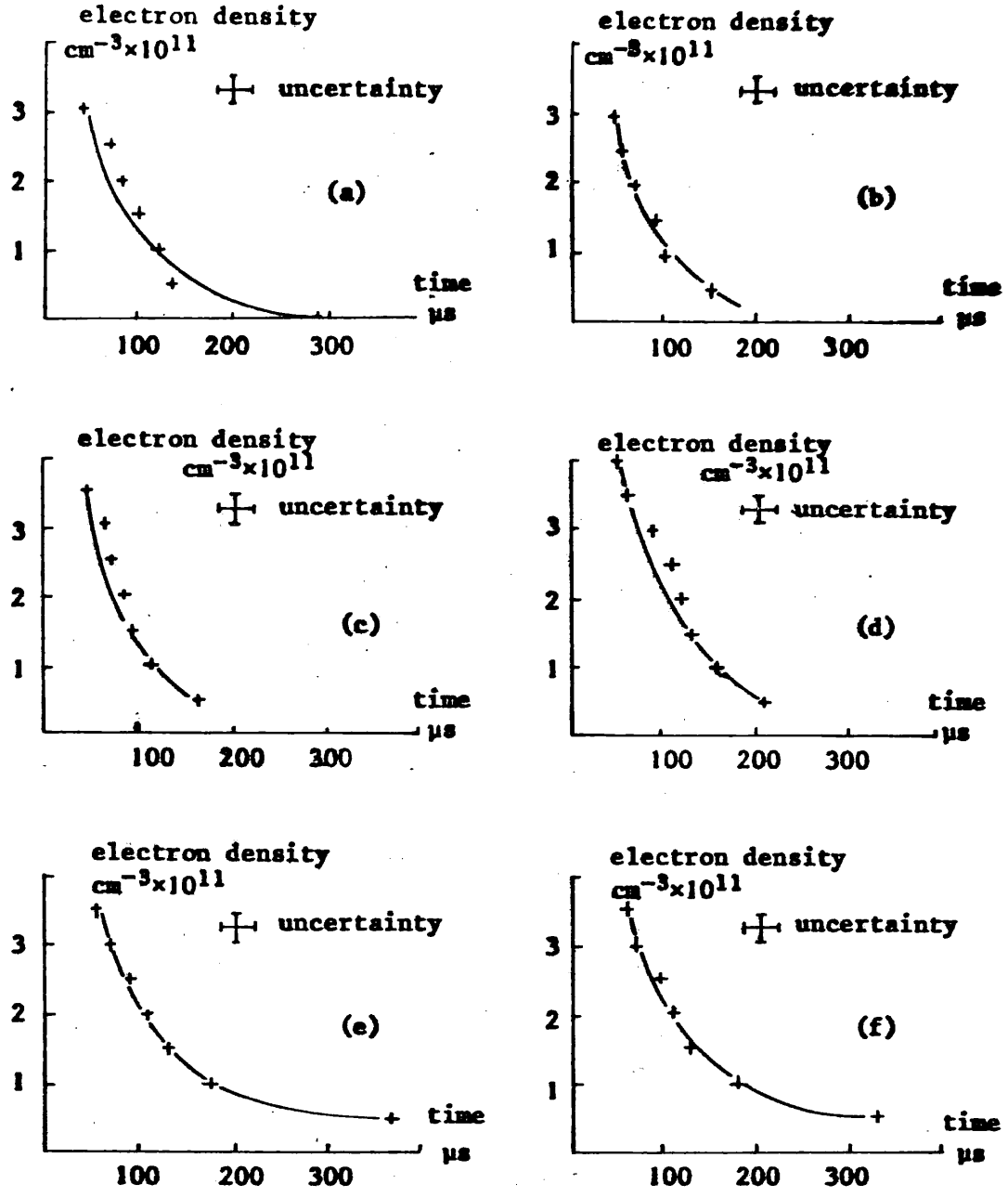

Figure 5.31. Electron density against time after initiating a discharge in:

pressure, torr	(a)	(b)	(c)	(d)	(e)	(f)
CH_4-N_2	0.5	0.4	0.3	0.2	0.1	0.0
He	0.0	0.1	0.2	0.3	0.4	0.5

15 cm diameter discharge tube. Blumlein power supply.

and plasma refraction, modulation experiments were performed with a d.c. excited laser. For this purpose, comparison was also made of the attenuation of CW radiation in the three media.

5.6.1. Gaseous attenuation at 337 μm

The experimental arrangement is shown in Figure 5.32. The two outputs from a beam splitter coupled laser were focused on to separate Golay cells, one beam having passed through an absorption tube. After equalising the intensity of the two beams by an attenuator, a differential pre-amplifier of an oscilloscope was used to cancel the electrical signals from the two detectors. Admitting an absorbing vapour into the tube produced an imbalance in the two signals which was restored by attenuating the output from the appropriate detector. This provided a direct measurement of the absorption in the tube. Attenuation in the different gases was measured over a range of pressures, as seen respectively in Figures 5.33 and 5.34, for CW and pulsed radiation. At low pressures, the greatest absorption is obtained from dichloromethane vapour, but is superseded by deuterium oxide vapour at high pressure. However, it was found to be difficult to maintain pressures greater than 10 torr in deuterium oxide vapour so that a requirement for a level of attenuation greater than 19 dB m^{-1} would necessitate the use of difluoroethylene or dichloromethane vapour.

It is noted from the low pressure measurements, up to 10 torr, that in both difluoroethylene and dichloromethane vapour, attenuation is greater for pulsed laser radiation than for a continuous output. This suggests that like difluoroethylene[51], dichloromethane possesses an absorption feature close to the 337 μm laser line. This may be investigated by scanning the laser cavity through its gain profile, which was demonstrated by Hocker et al.[34] to alter the centre frequency of the laser output. The data shown in Figures 5.33 and 5.34 were made while observing a chart recording of the cavity interferogram and making measurements at the peak of the output. Measuring attenuation in the gases at other points on the profile of the interferogram fringe showed, as expected, higher absorption at the longer, and therefore lower frequency, cavity positions in difluoroethylene. It was also seen from the readings shown in Figure 5.35 that dichloromethane possesses an absorption feature similarly spaced from the centre of the laser's gain profile.

To examine the suitability of the absorbing media for modulation purposes, the gases were separately admitted into the sealed cell of the 7.6 cm

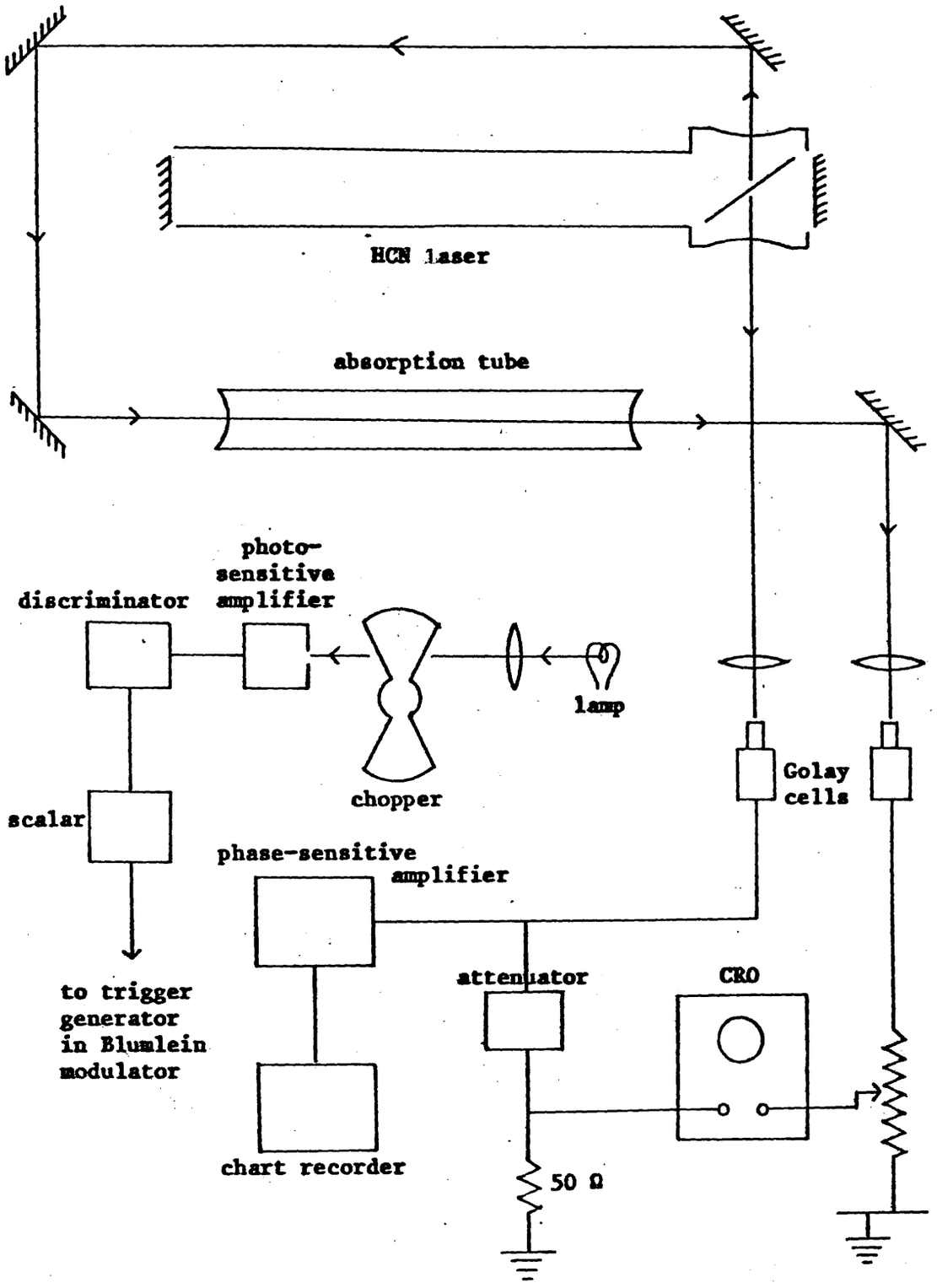

Figure 5.32. Experimental arrangement for measuring attenuation of laser radiation in gases

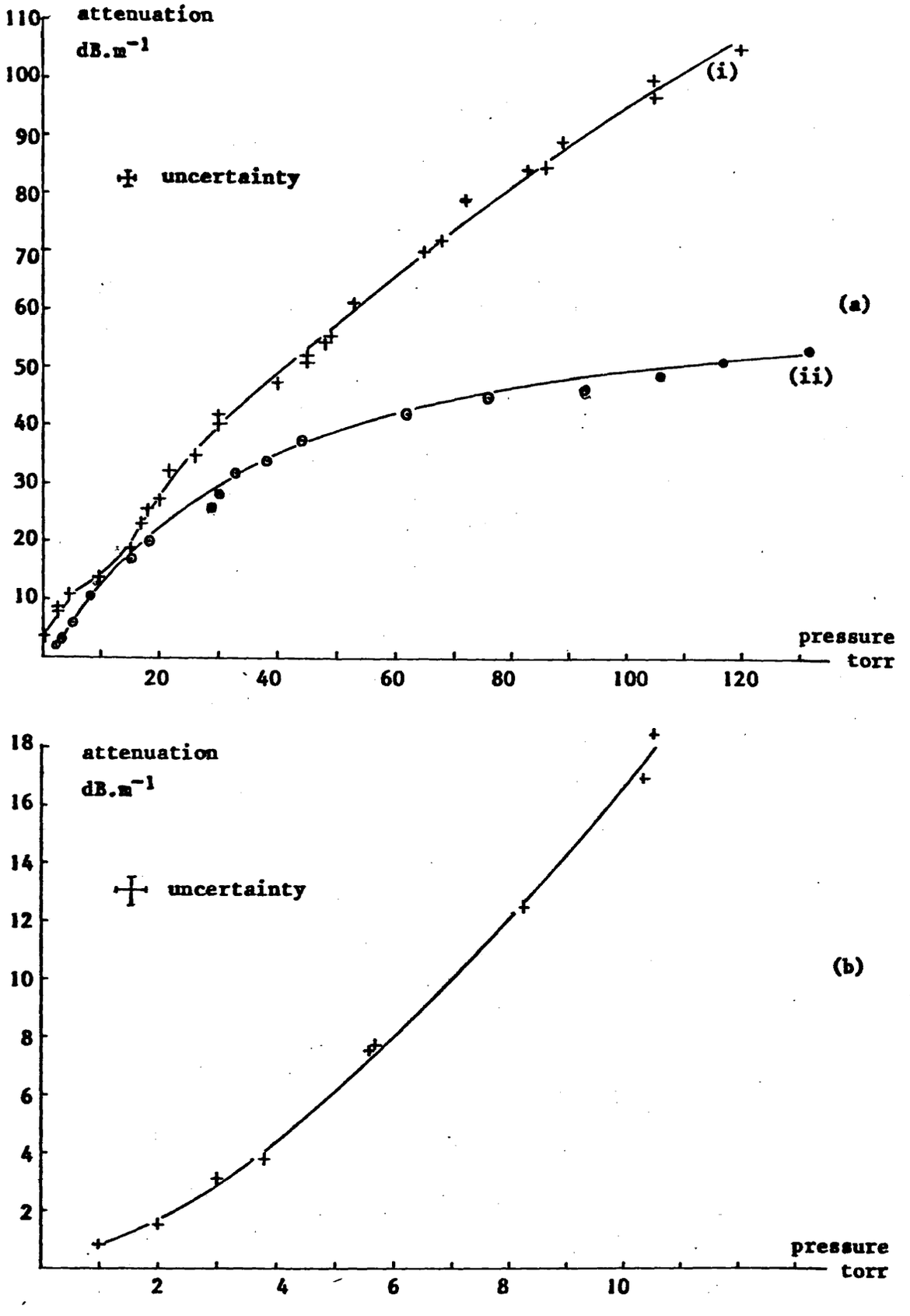

Figure 5.33. Attenuation of 891 GHz radiation from a CW HCN laser in (a), (i) dichloromethane vapour, (ii) difluoroethylene, and (b) deuterium oxide vapour, against pressure

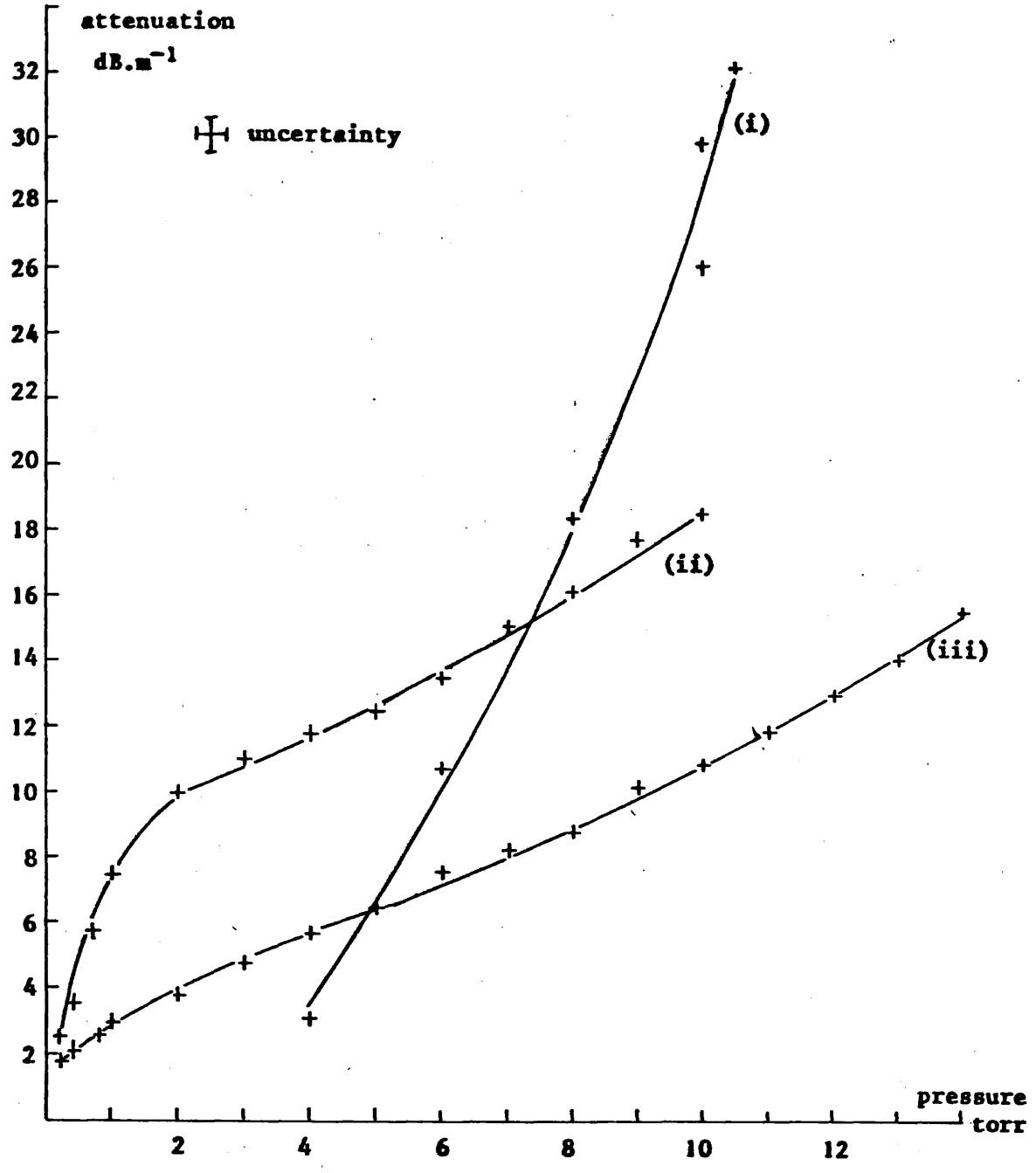

Figure 5.34. Attenuation of 891 GHz radiation from a pulse-excited HCN laser in (i) deuterium oxide vapour, (ii) dichloromethane vapour, and (iii) difluoroethylene, against pressure

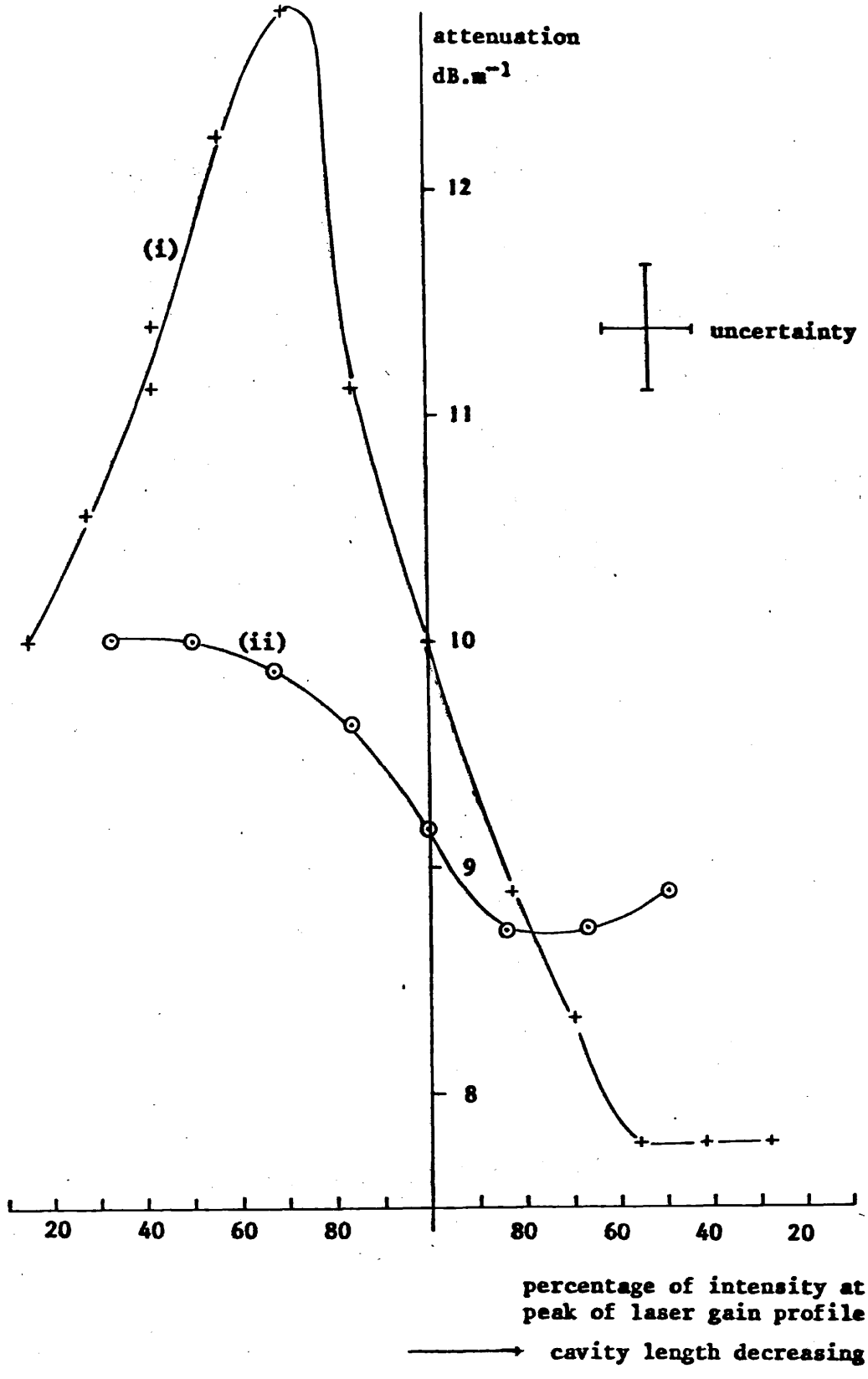

Figure 5.35. Attenuation of radiation from HCN laser in (i) 1 torr of dichloromethane vapour, and (ii) 8 torr of difluoroethylene, as cavity length is tuned through a 337 μm gain profile. Laser pulse excited.

diameter laser illustrated in Figure 5.1(a). The cell, separated from the active medium by a 400 gauge Melinex window, took up 32 cm of the 5.7 metre long optical cavity. CW laser action ceased when only small quantities of absorbing vapour were present in the cell which indicated that less than 0.5 dB of attenuation was required to extinguish the emission. However, greater absorption was required for the pulse-excited laser. This is shown in Figure 5.36 where the reduction of the output is plotted against pressure for each of the three vapours introduced into the cell. Laser action was inhibited at minumum pressures of 2.5 torr of dichloromethane vapour, 6 torr of deuterium oxide vapour and 10 torr of difluoroethylene, each approximately corresponding to 3.5 dB of attenuation in 32 cm of path length. This initial observation suggests that dichloromethane vapour is the better medium for Q-switching.

5.6.2. Active absorber switching

It was found that stimulated emission could be obtained on ionising the absorbing vapour which had been admitted into the cavity to suppress laser action. Using ring electrodes, uniform breakdown across the diameter of the tube in difluoroethylene at the required pressure of 10 torr for a pulse-excited laser was not feasible except at the high current densities produced by the Marx generator. However, ionisation of dichloromethane and deuterium oxide vapour proved to be more successful. The discharge, applied axially in the absorption cell, was produced by a 2 MW Blumlein supply which generated 5 μs pulses of approximately 1 μs rise time. Switching experiments were first performed with an active medium produced from a methane-nitrogen mixture excited by the recharging pulses from the main Blumlein supply. No increase in the output from the laser could be produced, and the maximum switched output power obtained was -2 dB of that generated with an evacuated cell. It was apparent that the losses of the absorption tube were not reduced to a sufficiently low level. Repeating the experiment on the initial current pulse in propylamine vapour produced a similarly reduced output which was maximized by operating the switch at a time corresponding to the peak of the unmodulated output pulse. This observation indicates that no build up of population inversion occurred with this technique.

The losses remaining in the absorption tube after ionisation were also too large to enable a modulated output to be obtained from a d.c. excited laser.

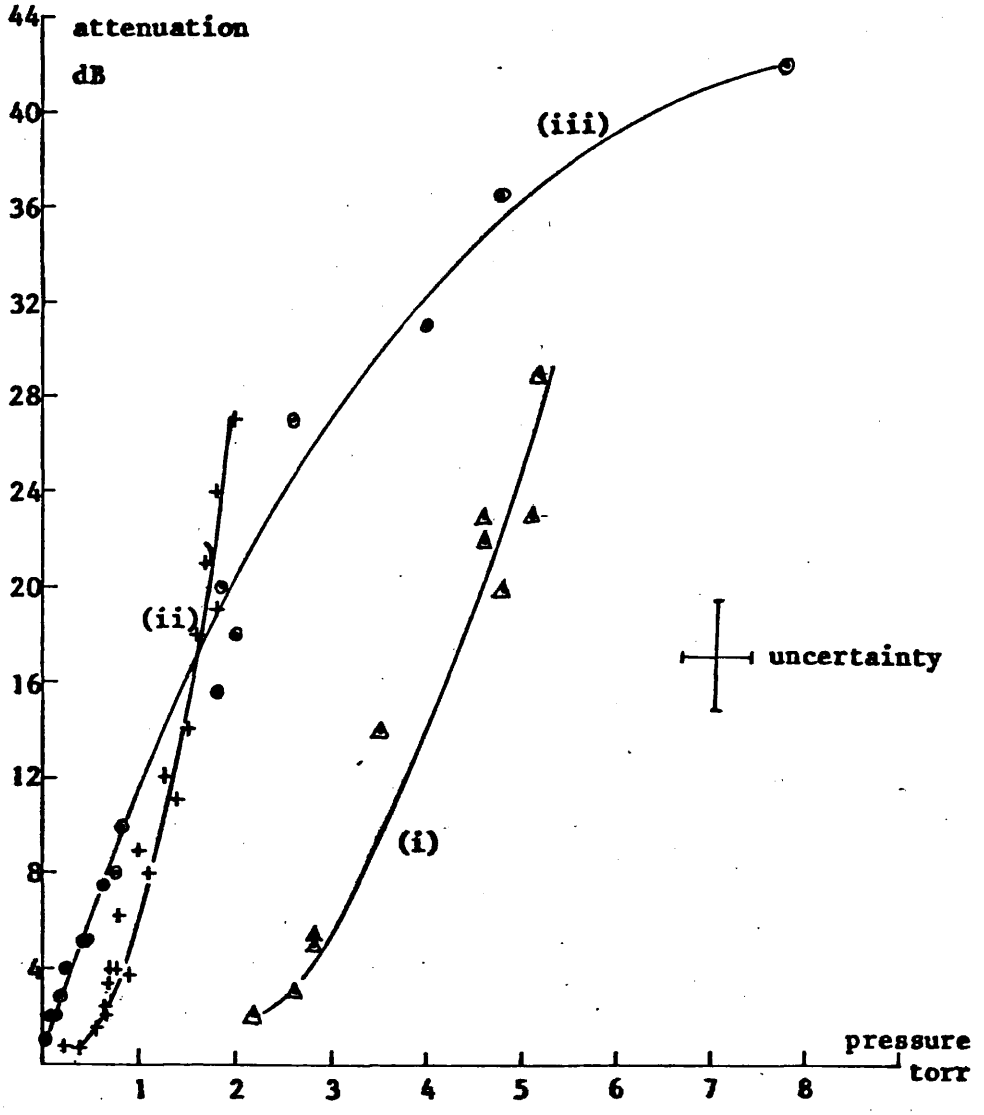

Figure 5.36. Attenuation of the output from the pulse-excited 7.6 cm diameter, beam splitter coupled HCN laser against the pressure of an attenuating gas admitted into a 32 cm long cell within the laser cavity. Absorbing gases are (i) deuterium oxide vapour, (ii) dichloromethane vapour, and (iii) difluoroethylene.

5.6.3. Plasma phase shift switching

In common with the observation of Tait et al.[49], it was found that the output from a d.c. excited laser could be modulated by pulse ionising transparent gases within the optical cavity. By operating discharges separately in methane, helium, air and nitrogen in the sealed cell, the stimulated emission could be inhibited or, if the cavity length had been increased beyond the resonant condition, the signal could be recovered. As with the work of Tait et al., no enhancement of the laser power was produced. To reduce the losses of the system, the Melinex window was removed from the cavity. Further switching experiments were carried out by pulse-ionising the products of the discharge from the active region which were now free to diffuse into the cell. Modulating a fully tuned CW laser again resulted in reducing the output. However, detuning the cavity on the long side of the resonant position, so that the pulsed plasma would recover the optimum condition, produced an output pulse of greater intensity than the CW level. An example is shown in Figure 5.37(a) where the pulse of radiation is seen to precede a series of oscillations caused by vibrations in the beam splitter instigated by the pulsed discharge. This Q-switched output is seen in greater detail in Figure 5.37(b), the peak intensity being 1.7 dB greater than that of the fully tuned CW output. Maximum energy storage was obtained by further detuning the cavity so that CW emission was extinguished. Ionising the cell then produced the radiation pulse of Figure 5.37(c) with a peak intensity 3 dB greater than the optimum CW level. The trace shown is seen to possess two components, the first produced by the current pulse sweeping the laser through the resonant condition, and the second as the current decays and the cavity passes back around the same gain profile. An example of stimulated emission being inhibited by the current pulse is shown in Figure 5.37(d) where the CW emission was partially reduced by tuning the cavity on the short side of the optimum length. Two structures are seen as the resonator path length was swept into the wings of a second, closely adjacent gain profile.

No modulation of a pulse-excited laser was observed. This was expected as higher density plasmas than those produced by a Blumlein supply would be necessary in the short cell to produce the required phase shift. At higher densities created using the Marx generator, transmission through the cell became low and reduced the Q of the cavity. This effect is shown in Figure 5.17(a). The requirement for a high density low loss plasma was not pursued in this investigation.

horizontal scale, 2 ms per large division (a)

horizontal scale, 100 μs per large division (b)

horizontal scale, 100 μs per large division (c)

horizontal scale, 100 μs per large division (d)

Figure 5.37. Q-switched outputs from the 7.6 cm diameter, beam splitter coupled, d.c. excited laser. Switching cell inside optical cavity. (a) and (b) show Q-switched pulse followed by acoustic vibrations; cavity partially detuned from maximum CW output; (c) CW level fully detuned, (d) CW level partially detuned.

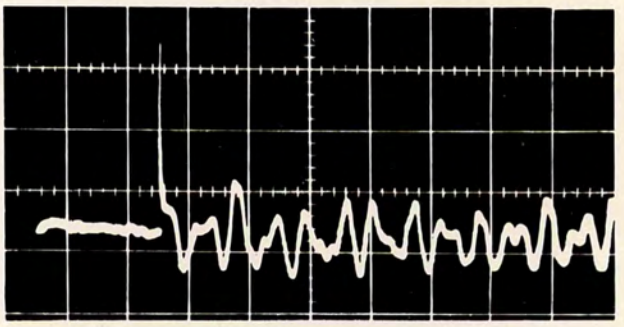

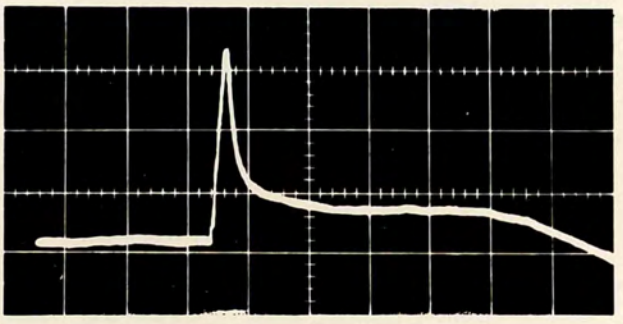

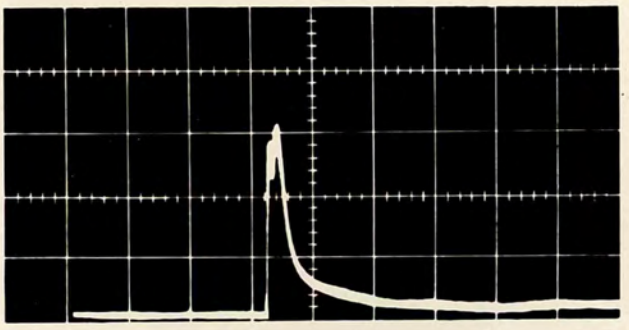

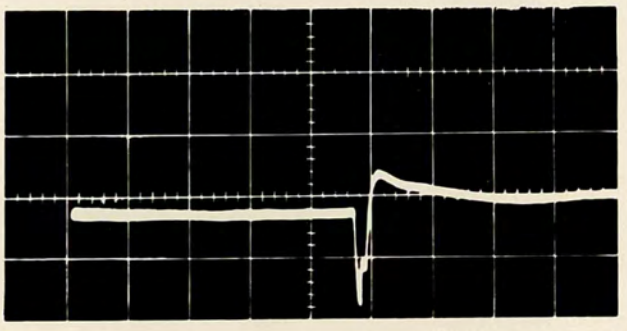

5.6.4. Michelson configuration

An examination was made of the Q-switching technique proposed in Chapter Four where a third mirror is introduced into the beam splitter coupled laser system. Following the arrangement shown in Figure 4.6, a mirror was mounted on the end of a discharge tube which was placed on one of the output ports of the 7.6 cm diameter laser. As with the previous cell, ring electrodes were incorporated and a Melinex window inserted across the cavity at the position W in the figure, to isolate the pulsed discharge from the beam splitter. When operating the laser by d.c. excitation, maximum CW output was obtained by optimizing both the Fabry-Pérot cavity length and the position of the mirror on the side arm. Translation of this additional mirror produced a variable output power ranging, as described in section 2.2.4, from zero to a level four times that of a single output from the conventional beam splitter arrangement. As before, ionising the cell with the laser tuned to give maximum output inhibited laser action. This is demonstrated in Figure 5.38(a) where the fully tuned condition has been perturbed by both the initial and recharging current pulses from the Blumlein supply. Producing radiation pulses with the side mirror tuned to reduce the CW output to zero proved to be critically dependent on both the mirror position and the magnitude of the current pulse. An example of two such pulses is shown in Figure 5.38(b). The recharging current pulse was of sufficient magnitude to produce constructive interference in the cell and allowed the second and larger pulse to build up. The initial current flow altered the path length in the tube to a second condition of field cancellation and hence terminated the build-up of radiation. Further adjustment of the current flow and the mirror position enabled greater output intensities to be obtained, typified by Figure 5.38(c). Here the magnitude of the current has been increased to obtain the next condition of constructive interference. The output commenced with a small radiation pulse generated during the build-up of the ionisation and was followed by the rise of the main radiation output during the current flow. The largest Q-switched output obtained by this technique had a peak intensity 6 dB greater than that of the CW output, providing an improvement of 12 dB over that of the single beam output.

After removal of the Melinex window from the cell, vibrations in the beam splitter, initiated by the pulsed discharge, produced a continuous alteration of the path length in the side arm. A similar situation was produced when pulse-exciting the active medium. It was seen that translation of the side mirror now made little difference to the laser

horizontal scale, 10 μs per large division (a)

horizontal scale, 20 μs per large division (b)

horizontal scale, 5 μs per large division (c)

Figure 5.38. Q-switched outputs from the 7.6 cm diameter, d.c. excited laser using the Michelson switching arrangement. (a) CW level fully tuned, (b) and (c) CW level detuned

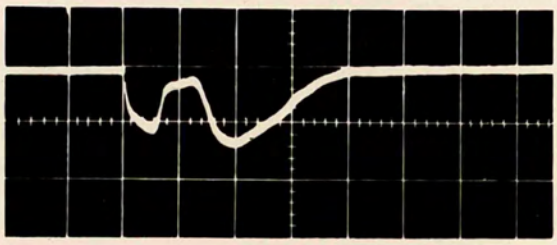

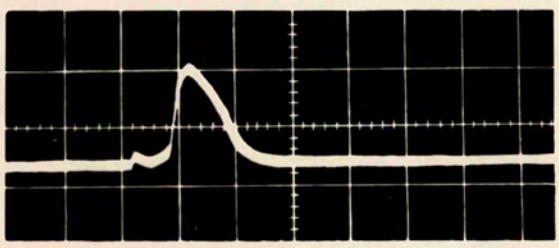

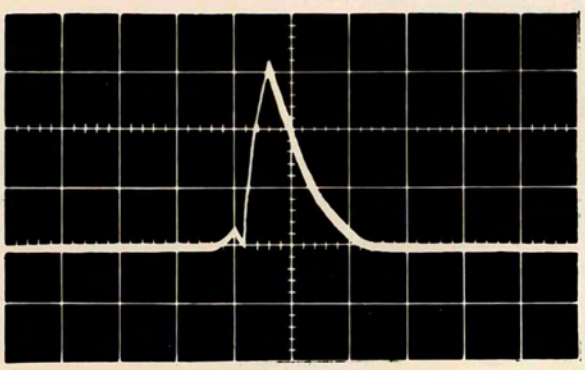

output, showing that the phase condition in the side arm was changing at a rate too rapid to allow the conditions necessary for Q-switching to be set up.

It is evident that the successful use of the Michelson coupling arrangement must depend on employing a low loss rigid beam splitter. Suitable materials for this are suggested in Chapter Twelve. A discussion of the properties of the HCN laser and of the feasibility of Q-switching the 15 cm diameter system is given in Chapter Six.

CHAPTER SIX

EVALUATION OF THE Q-SWITCHING MECHANISM OF THE HCN LASER

6.1. Introduction

The experiments described in the previous chapter on plasma phase shift switching and on switching with the laser in the Michelson configuration showed some degree of success. These techniques produced enhancement of the output when the laser was d.c. excited but none when pulse excited. It is noted that the active switching experiments were performed with the 7.6 cm diameter laser in which high plasma densities were produced causing fast mode scanning. An analysis is carried out into the suitability of the 15 cm diameter laser system for active switching and whether advantage can be taken of the slower mode scanning which results from laser action occurring at lower electron densities. The data obtained enable an evaluation to be made of the pumping rate into the upper excited level of the HCN molecules and hence whether a fast switching mechanism can produce a build-up of radiation in a period shorter than the mode scanning time. First confirmation of the mode scanning theory is given.

6.2. Mode scanning

The output from the 7.6 cm diameter laser is shown in Figure 5.9(b) taking place in the afterglow of a discharge in a methane-nitrogen mixture. A plot of the number of the modes scanned against the corresponding plasma density yields the graph shown in Figure 6.1. The slope of this graph for the afterglow period has a value

$$\frac{dq}{dn} = -(1.4 \pm 0.15) \times 10^{-12} \text{ cm}^3$$

This is in good agreement with the prediction of equation 2.10 which, over the same density range, gives a value of -1.5×10^{-12} cm^3. Mode scanning was also observed from the 15 cm diameter laser in a methane-nitrogen discharge but mainly during the excitation current pulse. The measured values of electron density show the time taken to scan through one mode in the afterglow period to be longer than the duration of the output pulses shown in Figures 5.8(c) and 5.8(d). A possible explanation for these two different output characteristics is that during the current pulse, high gain conditions produced multimode operation and so complete cancellation of the field did not take place. As the gain falls in the afterglow, fewer modes become excited, resulting in the more complete cancellation shown in Figure 5.8(d). However, Figure 5.8(c) indicates that stimulated emission in the afterglow can take place while the phase

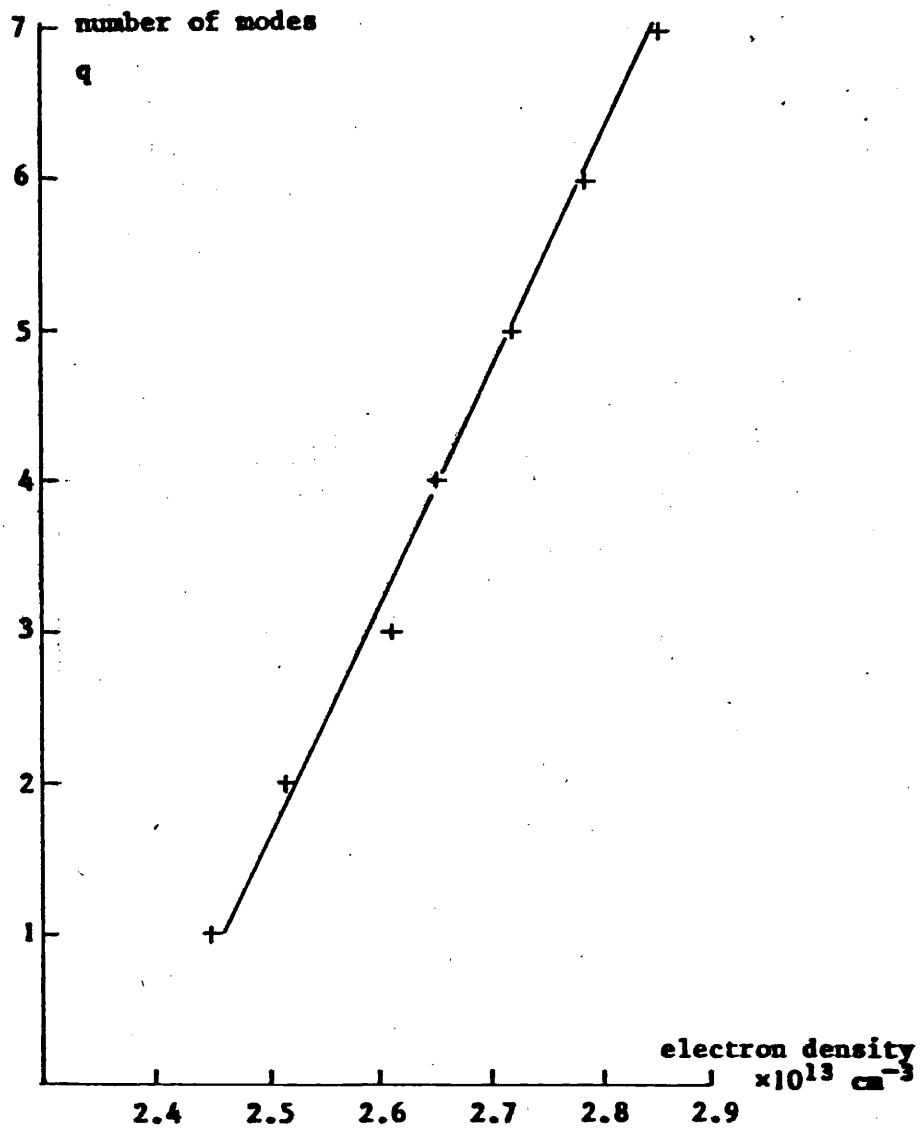

Figure 6.1. Number of modes q scanned in the 7.6 cm diameter laser against the corresponding electron density in the methane-nitrogen mixture.

of the cavity is largely constructive. This in-phase condition provides a finite time in which active switching could take place. To gain an understanding of the necessary value of the pump rate, an arbitrary period is chosen for the switching to occur to be within -3 dB of the peak of the laser's gain profile. Using a value of 8 MHz[34] for the half width of this line, equation 2.11 gives a figure of 125 μs to complete the switching action. Assuming the output coupling to be the main contributor to the cavity losses after switching, equation 2.18 shows this period to be 1300 cavity decay times. The computed outputs displayed in Figure 4.1, generated by an infinitely fast Q-switching action, show this to be an adequate interval for an output pulse to build up provided the initial value of the population inversion is significantly above the threshold level. For the finite switching rate situation evaluated in section 4.3, the output characteristics illustrated in Figure 4.2 demonstrate that this period would also enable a radiation pulse to be generated, after having allowed a delay before switching sufficient for the population inversion to build up from zero. This is provided that a minimum pump rate between 4×10^{-3} and 4×10^{-2} s^{-1} times the threshold inversion is maintained. It is evident that a knowledge of the pump rates of the HCN lasers is necessary in order to investigate the feasibility of actively switching pulse-excited systems. This will be acquired by first examining the mechanism of the plasma decay in the various active media studied.

6.3. Plasma decay

Figures 6.2 and 6.3 respectively show the variation of the inverse of plasma density against time, and the log of plasma density against time for (a) a methane-nitrogen mixture, (b) n-propylamine vapour, and (c) ethylenediamine vapour ionised in a 15 cm diameter tube. The relationships 2.8 and 2.7 indicate that, if the electron decay was due purely to recombination, then the graphs shown in Figures 6.2 (a)-(c) would have a linear variation, and if diffusion was the sole process taking place, then Figures 6.3(a)-(c) would be straight line plots. The three active media under examination show different characteristics of electron removal. It appears that recombination is the dominant process in the early part of the afterglow period in the methane-nitrogen mixture, changing to diffusion later. For ethylenediamine and n-propylamine vapour it is difficult to attribute either process to be the main mechanism. An investigation of the pumping mechanism in each of the three media is facilitated by separating the effects of diffusion and recombination. This has been performed using a method described by Anisimov et al.[57]. The expression for the total rate of change of electron density

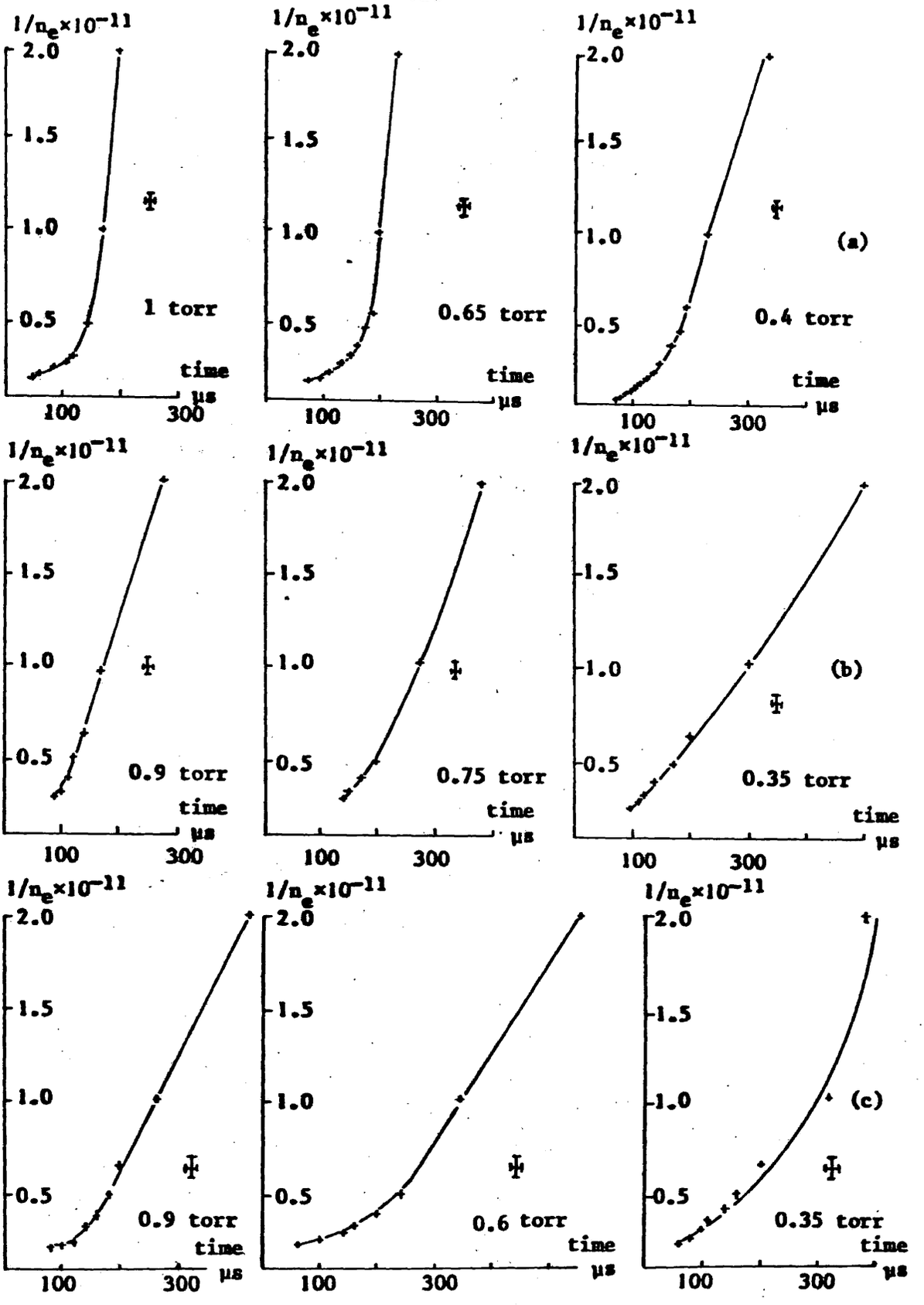

Figure 6.2. Plots of inverse of electron density, $1/n_e$, against time in (a) a methane-nitrogen mixture, (b) n-propylamine vapour, and (c) ethylenediamine vapour, in a 15 cm diameter tube. Crossed bars represent uncertainty. Units of $1/n_e$ are cm^3.

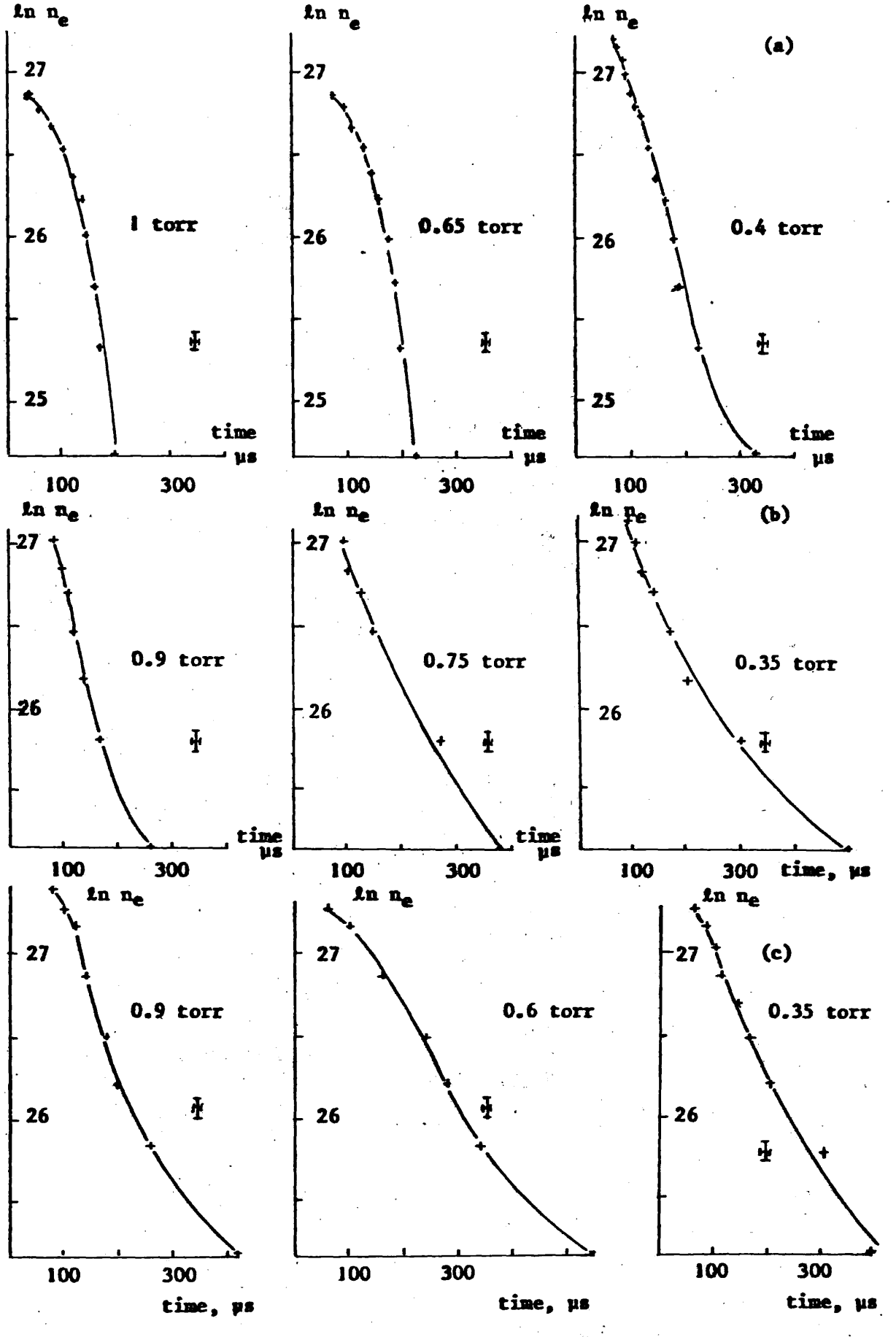

Figure 6.3. Plots of ln (n_e) against time in (a) a methane-nitrogen mixture, (b) n-propylamine vapour, and (c) ethylene-diamine vapour in a 15 cm diameter tube. Crossed bars represent uncertainty.

$$\frac{dn_e}{dt} = -\frac{D_a}{\Lambda^2} n_e - \alpha_{EFF} n_e^2$$

is multiplied by $-P/(n_e)$, P being the gas pressure, such that

$$-\frac{P}{n_e}\frac{dn_e}{dt} = \frac{D_a P}{\Lambda^2} + P\alpha_{EFF} n_e$$

Because of the pressure-dependence of the diffusion constant, $D_a P$ is assumed to be independent of pressure and so a plot of $-P/(n_e)\ dn_e/dt$ against P produces a straight line of slope $\alpha_{EFF} n_e$ and intercept $D_a P/(\Lambda^2)$ on the $-P/(n_e)\ dn_e/dt$ axis. The limitations of this technique have been discussed by Newton and Sexton[25] where any departure from the assumption that $D_a P$ is pressure-independent introduces an inaccuracy and the method must give the lowest possible value for the recombination coefficient. The values obtained in this way are shown plotted against electron density in Figure 6.4.

6.4. Pump mechanism

It is now possible to calculate the rate of removal of electrons from the plasma by recombination. Making the assumption that the pump rate of the laser is proportional to $\alpha_{EFF} n_e^2$, then Figure 6.5 indicates that throughout the period in which the 15 cm diameter laser oscillates, the pumping process is maintained at a near steady rate. It would be instructive to compare this proposal with values of pump rate that may be deduced from the measurement of a laser pulse. To do this, assumptions must be made about the peak absorption cross-section σ, and the probability of de-excitation λ, of the population inversion during pulsed conditions. The expression for σ given in Chapter Two

$$\sigma = \frac{\alpha_0}{N_3 + N_2}$$

shows that σ is not the simple parameter that exists for a solid state medium. In the case of the chemical production of HCN, α_0 must be measured in terms of unsaturated gain rather than absorption and hence will be a function of the inversion density. Its value will therefore vary throughout the afterglow period, as will the total number of active particles, $N_3 + N_2$. It was shown earlier that the population inversion and the total number of molecules in the upper and lower levels of the laser transition may be expressed by equations 2.15 and 2.16. Taking both quantities to be directly proportional to the pump rate R, the assumption will be made that to a first approximation, σ may be considered

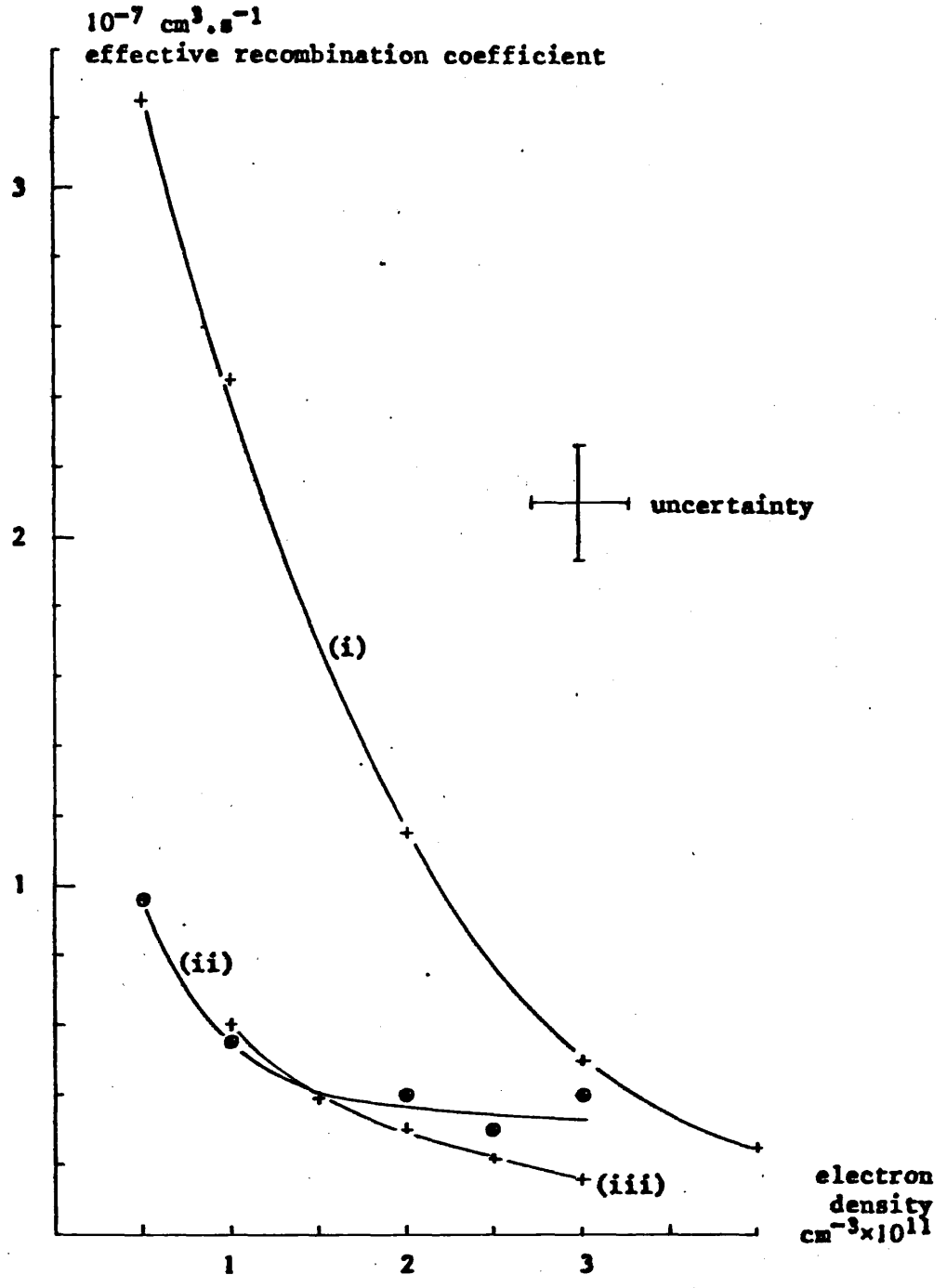

Figure 6.4. Effective recombination coefficients in (i) a methane-nitrogen mixture, (ii) n-propylamine vapour, and (iii) ethylenediamine vapour, against electron density. 15 cm diameter tube.

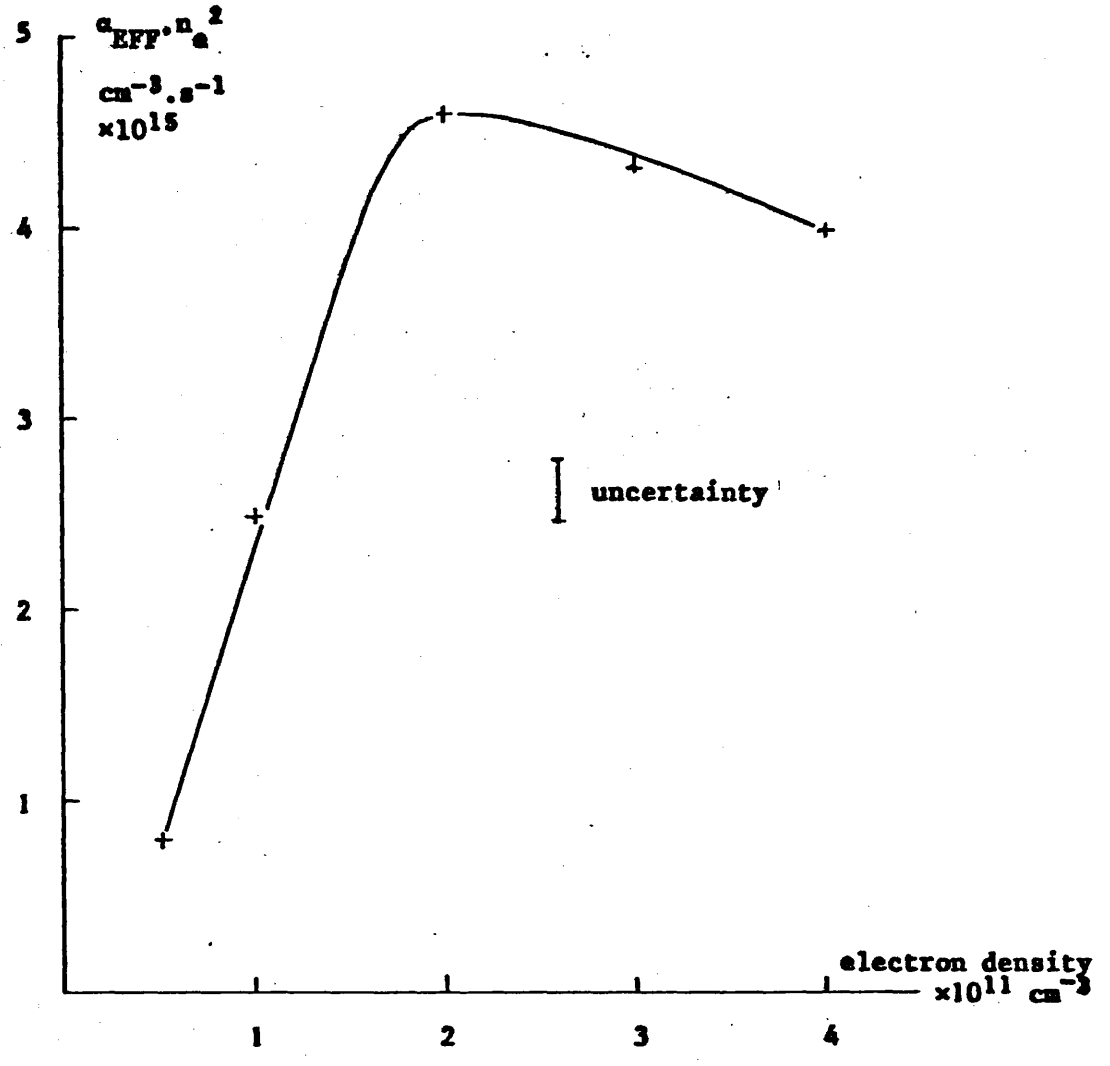

Figure 6.5. $\alpha_{EFF}.n_e^2$ against electron density for a discharge in a methane-nitrogen mixture in a 15 cm diameter tube

to be independent of R. Experimental confirmation at low plasma density that α_0 is directly proportional to R is obtained from the measurements of Stafsudd and Yeh[35], reproduced in Figure 3.3. Using their measurements of the gain of a d.c. excited methane-nitrogen mixture in a 7.6 cm diameter tube, straight line graphs of gain against current are obtained, as shown in Figure 6.6 at the gas pressure normally employed in the present work of 1 torr. However, this linear relationship is not obtained at all gas pressures, indicating that the collisional de-excitation components of the probabilities λ_3 and λ_2 produce a significant effect on the inversion level. To decide whether increased collisional activity during pulsed excitation seriously perturbs λ_3 and λ_2 from their d.c. excited values, estimates of the electron temperature have been made.

6.4.1. Electron temperature

The radial density measurements made in the 15 cm diameter tube indicated that some loss of intensity of the microwave beam was caused by refraction. This loss was estimated using the method described in section 4.4 and the electron density measurements of section 5.5 with the values of β in Table 5.3. Reflection from the plasma at the electron densities incurred is considered to be insignificant. Attenuation of the X-band radiation due to absorption in the interferometer experiments was calculated from the amplitude of the interference fringes after allowing for refraction. The intensity of the beam emerging from the plasma I_2 after attenuation was calculated from the unattenuated intensity I_1 and from the intensity of the in-phase condition of the fringes I' as

$$I_2 = I_1 + I' - 2\sqrt{I_1 I'}$$

The attenuation length d, defined as the distance in the plasma in which the amplitude of the microwave radiation is reduced by a factor of $1/e$, was calculated from

$$d = \frac{-2x}{\log_e\left(\frac{I_2}{I_1}\right)}$$

x being the path length in the plasma. An expression for the attenuation length given by Heald and Wharton[22] as

$$d = \frac{2c}{\nu}\left[\frac{\omega}{\omega_p}\right]^2 \left[1 - \left(\frac{\omega_p}{\omega}\right)^2\right]^{\frac{1}{2}}$$

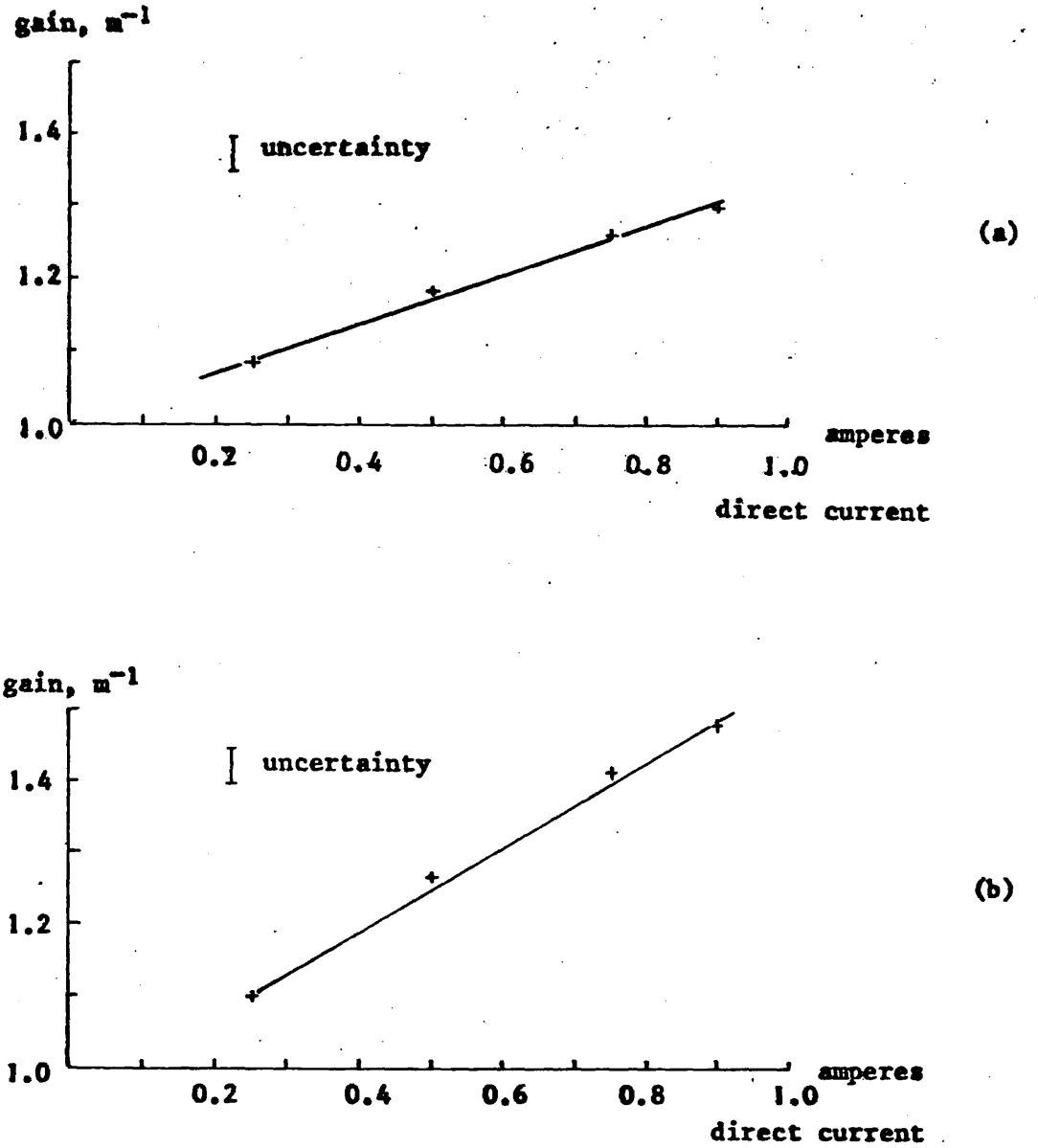

Figure 6.6. Gain against direct current in (a) 1:1 ratio, and (b) 1:2 ratio of methane:nitrogen at 1 torr. Data obtained from Stafsudd and Yeh[35].

where ω is the angular frequency of the probing radiation, ω_p the plasma frequency and c the velocity of light, enables a value to be obtained for the particle collision frequency ν. At the low plasma densities encountered, Coulomb collisions between electrons and ions are assumed to be the dominant process and so the expression for the electron-ion collision frequency[58]

$$\nu = 2.63\ n_e Z (T_e)^{-3/2} \log_e \Lambda \qquad \ldots(6.1)$$

was used to calculate the electron temperature T_e from the calculated value of ν, the electron density n_e, the ionic charge Z, which was assumed to be unity, and the Coulomb logarithm $\log_e \Lambda$. The parameter Λ, defined by Spitzer[59] as the ratio of the Debye length to the mean impact parameter producing a 90° deflection, is expressed by Heald and Wharton[22] as

$$\Lambda_{sp} = \frac{\lambda_D}{\tilde{b}_{90}} = \frac{1.55 \times 10^{10} (kT\{ev\})^{3/2}}{Z (n_{e\{cm^{-3}\}})^{\frac{1}{2}}}$$

Because of the low plasma densities, a correction to the Coulomb logarithm, again described by Heald and Wharton, for the condition $\omega >> \omega_p$ was made such that

$$\log_e \Lambda = \log_e (0.45) \frac{\omega_p}{\omega} \Lambda_{sp} \qquad \ldots(6.2)$$

Expressing 6.1 as

$$(T_e)^{3/2} = X = b \log_e \Lambda$$

and 6.2 as

$$\log_e \Lambda = \log_e a + \log_e X$$

values for T_e were obtained graphically by plotting $\log_e X$ and $(X/b) - \log_e a$ against X. The values calculated for T_e and ν are shown in Figure 6.7 plotted against n_e for discharges in (a) a methane-nitrogen mixture, (b) ethylenediamine vapour, and (c) n-propylamine vapour. T_e is seen to be low and the small variation in both T_e and ν suggests that little change occurs in the de-excitation processes during the laser active period of the afterglow.

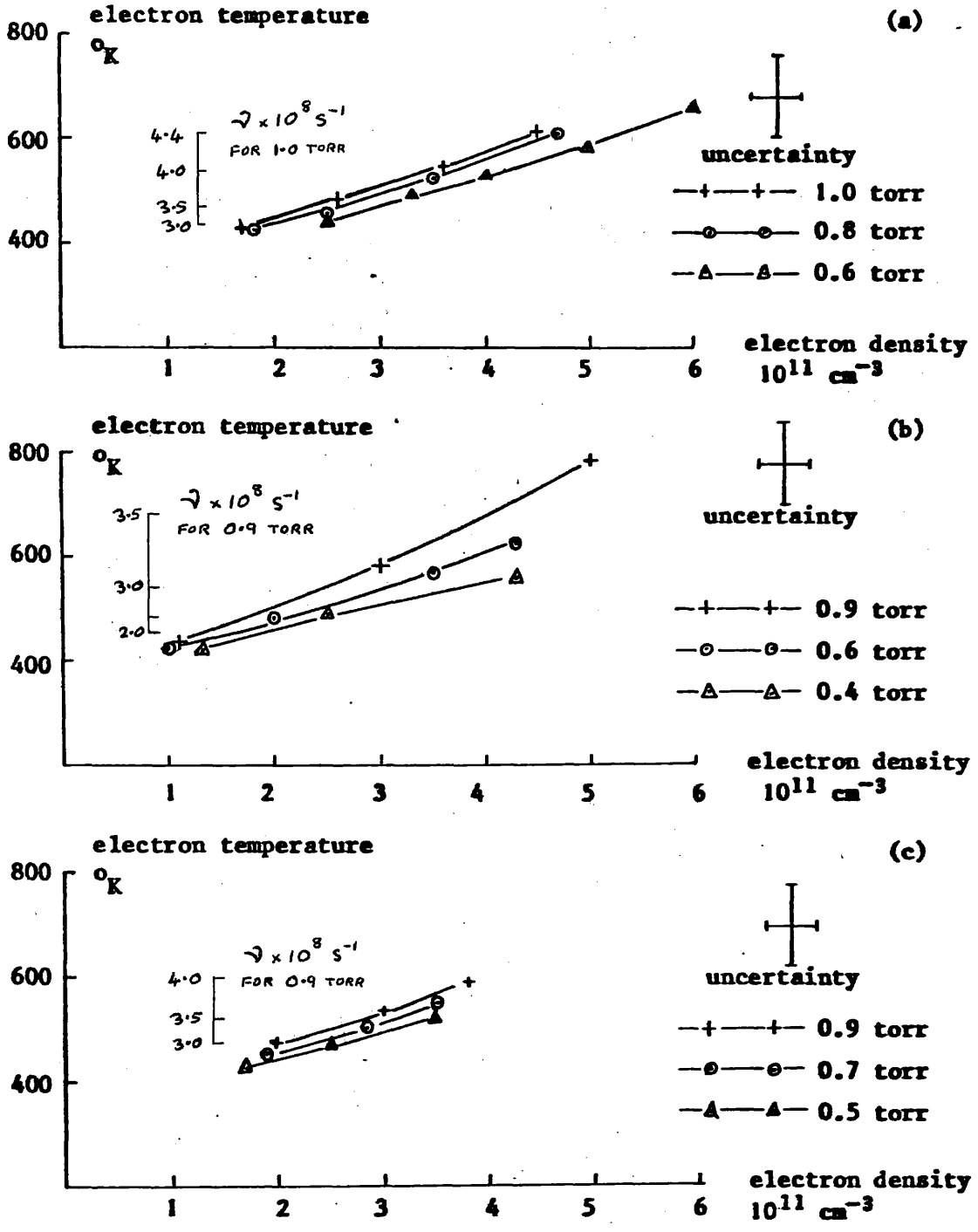

Figure 6.7. Variation of electron temperature with electron density in the afterglow of plasmas formed using the Blumlein power supply in (a) a methane-nitrogen mixture, (b) ethylenediamine vapour, and (c) n-propylamine vapour.

6.4.2. Molecular formation

It was shown earlier that neither the process of diffusion nor recombination could account solely for the plasma decay in the three media investigated. It will be useful at this stage to examine the variation of the plasma conditions during the laser active period in order to correlate these with the chemical processes taking place.

The mass spectroscopy experiments of Schötzau and Kneubühl[56] showed that molecular hydrogen is essential to the operation of the HCN laser. Observation showed that for a methane-nitrogen discharge, maximum stimulated emission occurred when the highest concentration of hydrogen molecules was present, which did not correspond to the maximum concentration of HCN molecules. Their studies of a pure HCN atmosphere showed that hydrocyanic acid is dissociated by electron impact, while hydrogen molecules tend to suppress this action. Although CW operation could not be obtained from an HCN gas, laser emission occurred under pulsed excitation, the output intensity building up over several pulses. This corresponded to a build-up of hydrogen and proved that electron impact is not the dominant excitation mechanism of the HCN molecules, since the concentration of HCN decreased after each pulse. Schötzau and Kneubühl[52] presented an energy level diagram for the C/H/N system which is reproduced in Figure 6.8. This shows that H_2 is produced in the plasma at an energy near that of the formation of HCN, while HCN molecules are unstable at the dissociation energy of nitrogen molecules. From these observations, Schötzau and Kneubühl proposed a mechanism whereby excited HCN molecules may be produced by a chemical reaction in a methane-nitrogen discharge

$$CH_4 + e^- \rightarrow CH_3 + H + e^-$$

followed by the formation of hydrogen cyanide as

$$CH_3 + N \rightarrow HCN + 2H$$

and that a metastable vibration state of the hydrogen molecule transfers energy to the HCN molecule.

The nitrogen to hydrogen ratio, determined by the discharge current, must be optimum for HCN production. HCN will not be stable if nitrogen dominates but will decompose if atomic hydrogen dominates, due to the difference of the energy levels of H and HCN.

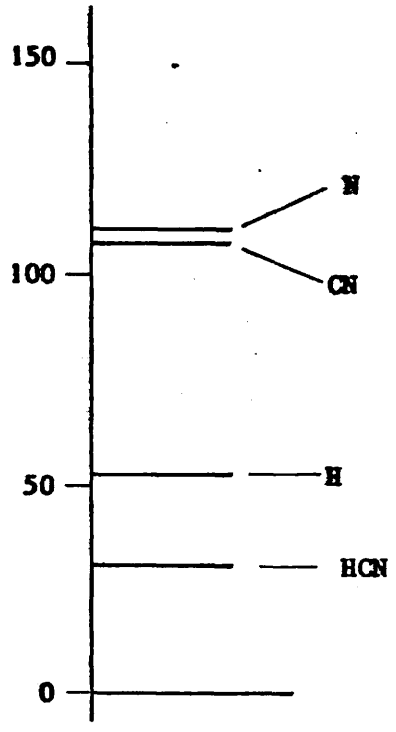

Figure 6.8. Energy levels in the C/H/N system in an HCN laser medium. After Schötzau and Kneubühl[52].

The measurements of electron temperature shown in Figure 6.7 for the present work with a 15 cm diameter discharge tube, indicate a low probability of CH_3 production by electron collision with methane molecules during the afterglow. It would be instructive to discover whether the treatment adopted in this text, where an effective recombination coefficient has been defined for the ionic mixture, can be used to explain the recombination process in terms of more complete dissociation of the CH_4 and N_2 molecules into C, H and N ions. The mass-spectrometric analysis of Schötzau and Kneubühl[56] showed that the concentration of HCN molecules was small compared to the concentration of hydrogen. Assuming that this situation existed in the lasers operated in the present work, and that the production of hydrogen masks other processes, then three-body recombination would be expected to occur, where two oppositely charged particles collide with a third body. A test of this assumption can be performed using an expression for the recombination coefficient of this process derived by D'Angelo[60] of

$$\alpha = 3.9 \times 10^{-9}\, n_e (T_e)^{-4.5}$$

Plotting $\log_{10}\left[\frac{\alpha_{EFF}}{n_e}\right]$ against $\log_{10}(T_e)$ in Figure 6.9 for the three media produced straight line graphs, the slopes of which are shown in Table 6.1.

Table 6.1

Gradients of straight line plots of $\log_{10}\left[\frac{\alpha_{EFF}}{n_e}\right]$ against $\log_{10}(T_e)$ for (a) methane-nitrogen mixture, (b) ethylenediamine vapour, (c) n-propylamine vapour

	Pressure torr	Gradient
(a)	1.0	-8.3 ± 0.5
	0.8	-6.6 ± 0.5
	0.6	-7.0 ± 0.8
(b)	0.9	-7.5 ± 0.4
	0.7	-8.0 ± 0.4
	0.5	-8.8 ± 0.5
(c)	1.0	-3.0 ± 0.5
	0.7	-2.9 ± 0.6
	0.5	-4.0 ± 0.9

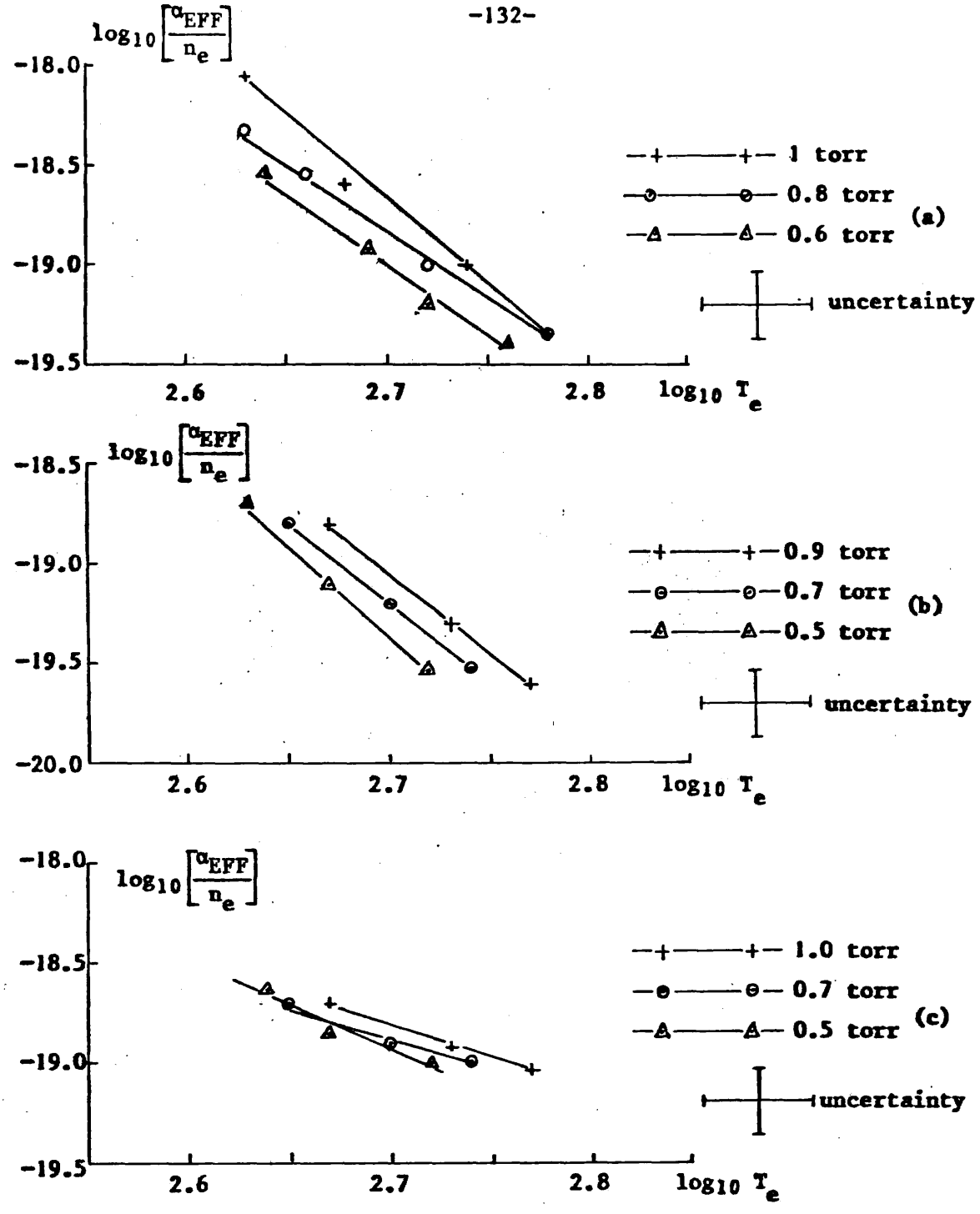

Figure 6.9. Plots of $\log_{10}\left[\frac{\alpha_{EFF}}{n_e}\right]$ against $\log_{10} T_e$ for the afterglow periods of discharges in

(a) methane-nitrogen mixture
(b) ethylenediamine vapour, and
(c) n-propylamine vapour

The values of these gradients do not agree with the power of T_e in the expression of -4.5. It must be concluded that hydrogen production does not dominate other processes in the laser studied and that collisions with other molecules and ions cannot be ignored. However, the situation in which atomic ions of C, H and N recombine into molecular ions can be represented by the ion conversion relationship given by Cronin and Sexton[61] as

$$\frac{d}{dt}N_{ai} = \beta P_0^2 N_{ai}$$

where N_{ai} = atomic ion density

β = ion conversion constant

P_0 = gas pressure reduced to 0^oC

Plots of $\frac{dn_e}{dt}$ against n_e in Figure 6.10 for the methane-nitrogen mixture, n-propylamine vapour and ethylenediamine vapour all reveal straight line graphs for different pressures. Making the assumption that the original molecules are dissociated into ions of their constituent atoms so that the electron density numerically represents the ion density, then ion conversion as described by Cronin and Sexton appears operative throughout the decay period under investigation.

At the low electron densities produced in the 15 cm diameter tube, the ion temperature will be taken as approximately equal to the gas temperature. Considering this in conjunction with the low electron temperatures and the apparent continuous mechanism of ion conversion, little change is indicated in the conditions of the chemical process throughout the afterglow. The assumption will therefore be made that the collisional contribution to the upper and lower transition probabilities, λ_{c3} and λ_{c2} respectively, varies little throughout the laser active period. It is also assumed that the values of λ_{c3} and λ_{c2} for the 15 cm diameter laser when pulse-excited are close to those when d.c. excited. Support for this supposition is obtained from the experiments of Schötzau and Kneubühl[52]. From their work on a d.c. excited laser at an electron density of 2.7×10^{10} cm^{-3}, a value for the the electron-ion collision frequency is calculated to be $2 \times 10^{+8}$ s^{-1}. This is seen to be close to the values displayed in Figure 6.7. Further confirmation is provided by Frayne[27] who obtained values for the transition probabilities in a 7.6 cm diameter laser. From the present work, a much greater difference between the electron densities produced in a pulse-excited and in a d.c. excited 7.6 cm diameter laser is

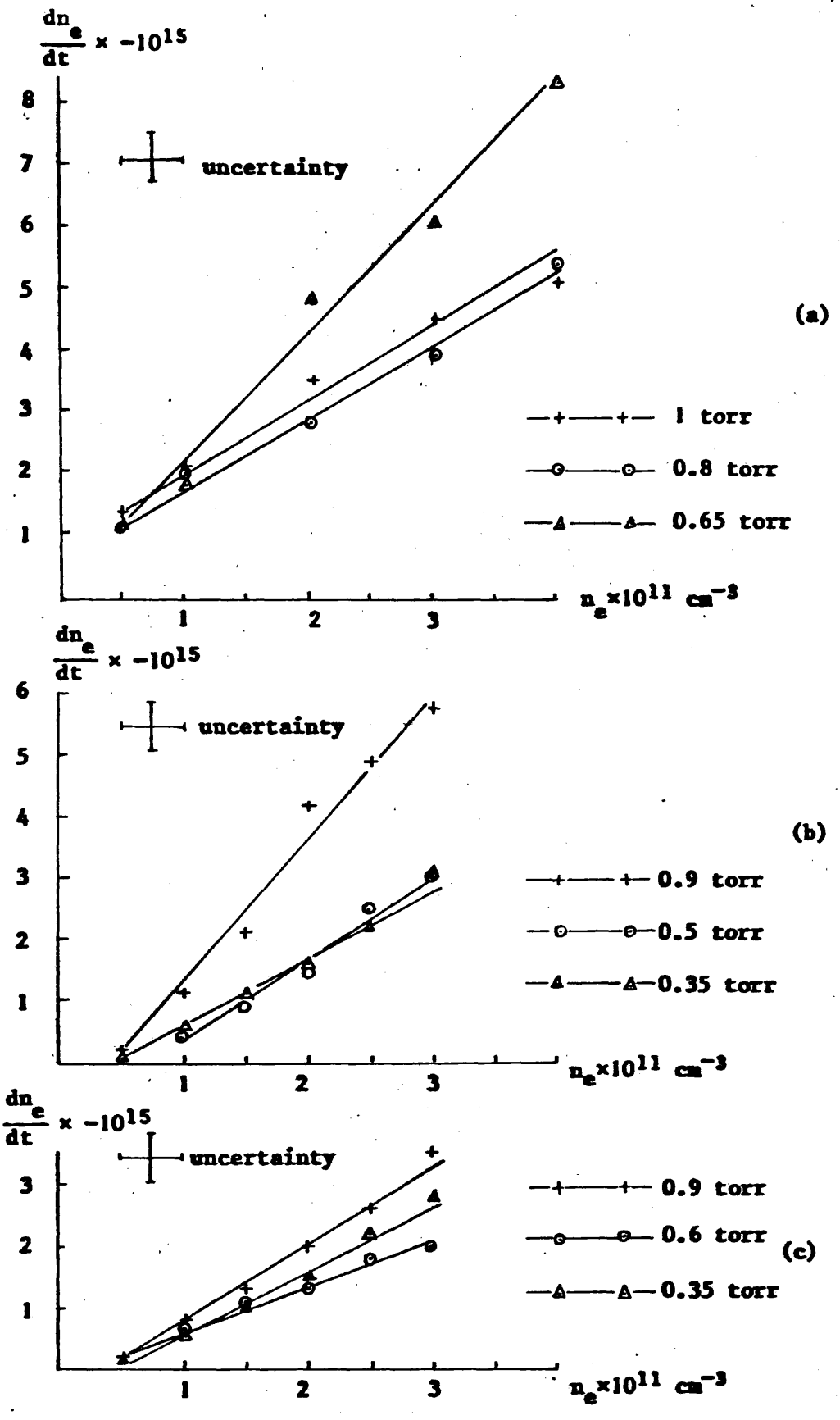

Figure 6.10. $\frac{dn_e}{dt}$ against n_e for (a) methane-nitrogen mixture, (b) n-propylamine vapour, and (c) ethylenediamine vapour ionised in a 15 cm diameter tube

expected than between those produced in the 15 cm diameter pulsed laser and those of the d.c. laser of Schötzau and Kneubühl. Nevertheless, Frayne obtained a close agreement between $\lambda_3 = 8.1 \times 10^3\ s^{-1}$ for a pulse-excited laser and $\lambda_3 = 7.7 \times 10^3\ s^{-1}$ for a d.c. laser.

From the work of Frayne[27], the probability of the de-excitation of the population inversion may be expressed as

$$\lambda \simeq \left[\frac{1}{\lambda_3}\left\{1 - \frac{\lambda_{32}\lambda_2}{\lambda_2\{\lambda_3 - \lambda_2\}}\right\}\right]^{-1}$$

where, as in Chapter Two, λ_3 is the transition probability of the upper level with radiative contribution λ_{32}, and λ_2 the transition probability of the lower level. From observations of the transient output from a rotating mirror Q-switched laser, Frayne estimated that $\lambda_{32} \sim {}^4/_5\ \lambda_2$. Using this with his values obtained for the 337 μm emission line of

$$\lambda_3 = 7.7 \times 10^3\ s^{-1} \text{ and } \lambda_2 = 1.64 \times 10^2\ s^{-1}$$

a value for λ is calculated to be

$$\lambda \simeq 4.2 \times 10^4\ s^{-1}$$

An estimate of the peak absorption cross-section σ may now be made using the variation of CW output power from the hole-coupled laser with discharge current shown in Figure 5.3(b). Setting $\frac{dN}{dt} = 0$ in equation 2.20 for the CW case, the expression

$$-2\Phi\sigma N \frac{L}{t_L} + R - \lambda N_p = 0 \qquad \ldots(6.3)$$

is obtained. As gain and population inversion are constant during CW operation and equal to that for the threshold case, the near linear relationship in Figure 5.3(b) implies that over the region investigated, the pump rate is approximately proportional to the discharge current I_{DC}. Hence expressing

$$R \simeq KI_{dc} \qquad \ldots(6.4)$$

K being a constant, the slope of the curve enabled a value of K to be calculated as

$$K = 1.6 \times 10^{16} \text{ coulombs cm}^{-3}$$

To obtain this result, an average photon density inside the laser was calculated from the cavity losses and by assuming an effective radius to be that of the mode radius. A value of the mode radius of the 15 cm diameter laser system obtained using equation 2.4 is w = 2.79 cm. This is in good agreement with the mode radius measured from the beam profile of the beam splitter coupled laser in Figure 5.6(a) of w = 2.85 ± 0.30 cm. Having obtained a value for K, the discharge current at the intercept of the current axis $I_{\Phi=0}$ can be used in equations 6.3 and 6.4 to give a value for the threshold population inversion of

$$N_p = \frac{KI_{\Phi=0}}{\lambda} = 5.6 \times 10^9 \text{ cm}^{-3}$$

Using the value for the fractional losses of the hole-coupled laser given in section 5.2 of f = 0.4, the cavity decay time is calculated from equation 2.18 as $\tau \simeq 9.4 \times 10^{-8}$ s.

The threshold gain of the laser system is found by setting $\frac{d\Phi}{dt} = 0$ in equation 2.19 for CW operation, which gives

$$\alpha_p = \frac{1}{\tau} \cdot \frac{t_1}{\ell} = 3.6 \times 10^{-4} \text{ cm}^{-1}$$

A value can now be calculated for the peak absorption cross-section under conditions of CW action of

$$\sigma = \frac{\alpha_p}{N_p} = 6.4 \times 10^{-14} \text{ cm}^2$$

Again, taking into account the diagnostics of the laser plasma, namely the low electron temperature and the apparently continuous process of ion conversion, the assumption will be made that the above value of σ may be used as an indication of its value during pulsed excitation. It was stated earlier that the radiation output taking place in the afterglow shown in Figure 5.8(c) was largely unaffected by mode scanning. This situation allows equation 2.19 to be used to calculate the gain of the system and the population inversion as shown in the afterglow period in Figure 6.11(a). This in turn enables values for $R - \lambda N$ to be obtained. However, the de-excitation λN is found to be negligible and so approximate values of R have been calculated and are plotted in Figure 6.11(b). For an indication of whether these pumping rates are sufficient to produce a Q-switched output in the limited period in which the gain profile is scanned, further reference is made to the numerical

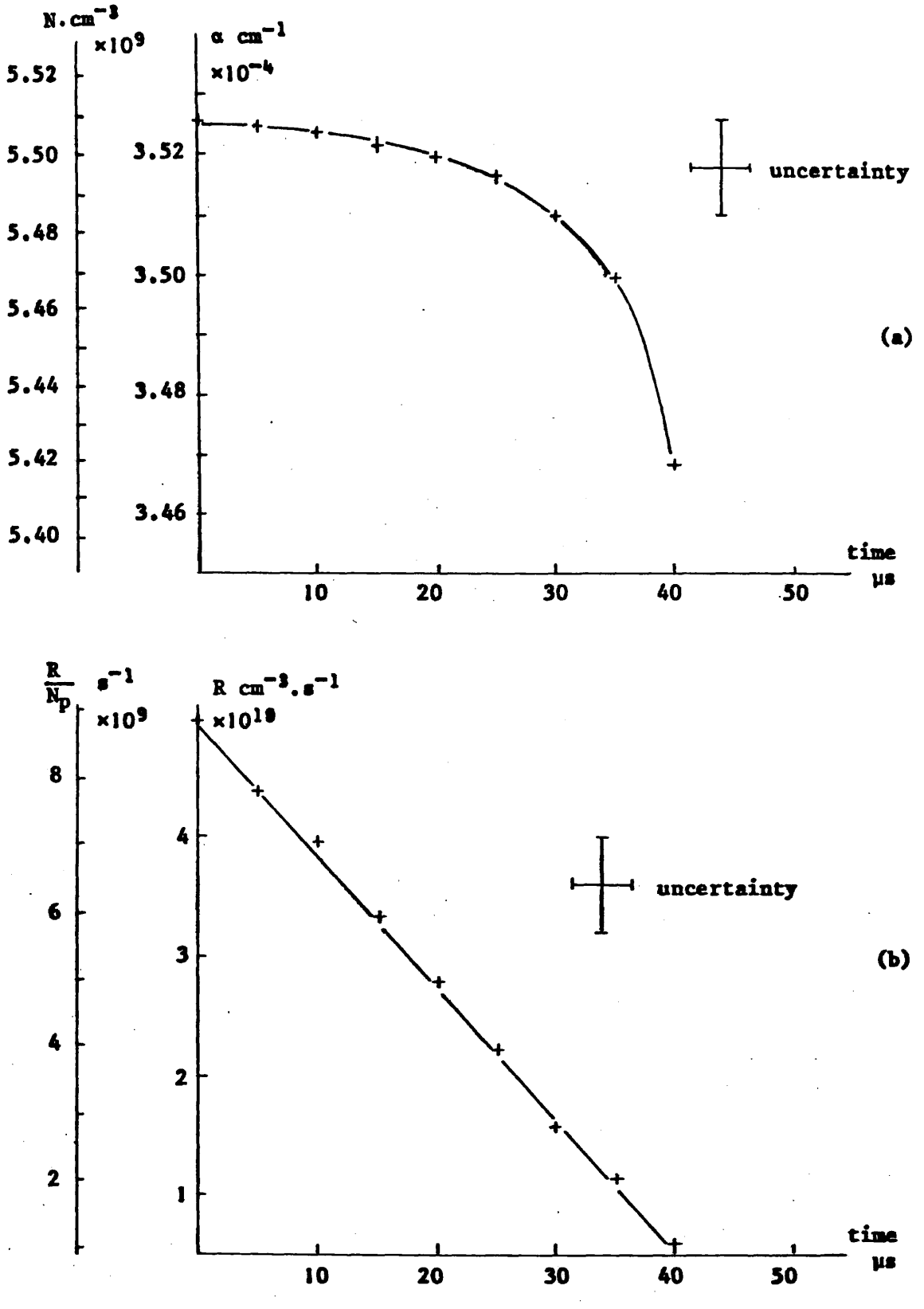

Figure 6.11. (a) Gain and population inversion and (b) pump rate, against time after threshold inversion for the afterglow of a discharge in 1 torr of a methane-nitrogen mixture in the 15 cm diameter laser

calculations described in Chapter Four. The photon density Φ in the cavity after a fast Q-switch was calculated for a range of pump rates. The time taken to attain the maximum rate of increase in Φ, which occurs in the period denoted by τ_R in section 2.7, is plotted against pump rate in Figure 6.12. It is considered more informative to calculate this parameter than the rise time of the pulse which may be large under conditions of high pump rate whereas, in a practical system, the pump rate would not remain constant and the high Q condition could not be maintained over long periods. The extrapolated graph of Figure 6.12 indicates that for the values of pump rate encountered in Figure 6.11(b), a Q-switched output may be expected to reach its most rapid rise in approximately seven cavity decay times.

It is therefore indicated that on initiating the Q-switch at the -3 dB point of the gain profile, the period τ_R would be reached before the decaying plasma had swept the laser to the peak of the profile. This suggests that conditions in the 15 cm diameter system are such that further increase in power may be obtained by active Q-switching.

6.5. Discussion

The experiments described in section 5.6 showed pulsed ionisation of the side arm of a laser built in the Michelson configuration to be the most successful of the Q-switching techniques investigated. The least insertion loss was introduced into the cavity by this method and the fastest rising pulses were produced which provide confirmation of the theoretical analysis of Chapter Four. However, to generate high intensity radiation from the HCN laser, the Q-switching technique must be applied to a pulse-excited system. To do this, the vibration of the beam splitter incurred in the present work must be eliminated by using a rigid material. The observations reported in section 5.3.2 showed that much higher powers can be produced by increasing the diameter of the cavity; therefore, of the two systems investigated, the greatest potential for producing high peak intensity would be to apply the Q-switching technique to the 15 cm diameter laser.

The analysis in this chapter indicated that higher pulsed powers may be generated in the wider laser by a sufficiently fast Q-switch provided suitable conditions exist in the cavity. With the Michelson switching technique, the pumping action may increase the population inversion while the output coupling remains zero, but the field will only build up when the cavity is swept through a gain profile. It is therefore

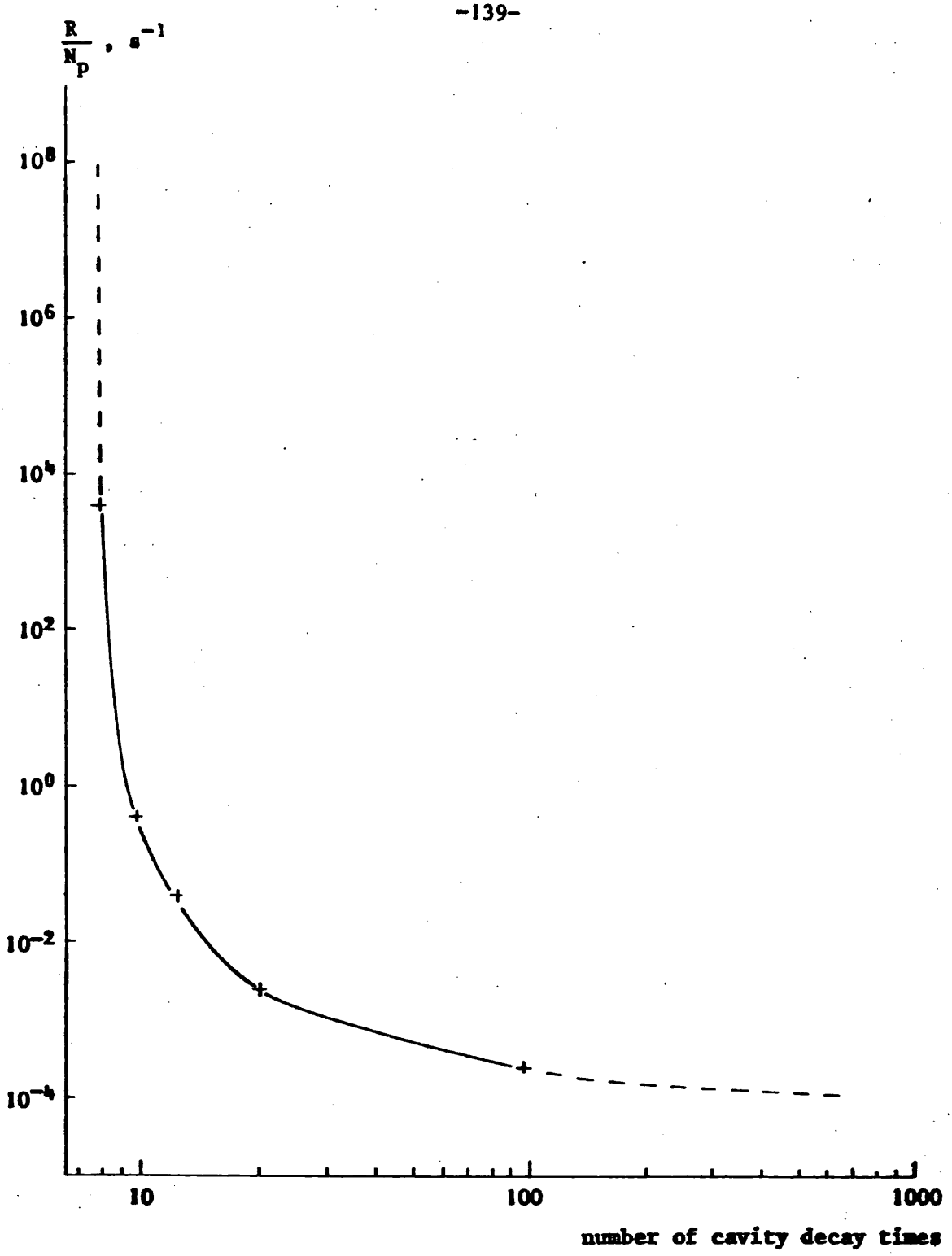

Figure 6.12. Theoretical pump rate $\frac{R}{N_p}$ against the number of cavity decay times taken to reach the maximum value of $\left(\frac{d\phi}{dt}\right)$

essential to arrange for the magnitude of the current pulse to give the correct phase condition at the time that laser action would commence in an unmodulated cavity. Figures 5.8(c) and 5.8(d) demonstrated that the wrong ionising current reduces the time available for both the internal wavefront to build up and for the switching action to be completed. The second parameter noted above, the population inversion, would also require optimisation for successful Q-switching. Figures 6.5 and 6.11(b) show the pumping rate to be greater than the overall recombination rate and so it is evident that the pumping mechanism is not as simple as suggested in Chapter Four. It is recalled that with the 7.6 cm diameter laser, the main current pulse could be so large that the stimulated emission was inhibited and that little or no laser action occurred when the plasma density decayed to a lower value, even though emission took place at a similar density on the rapid succession of recharging current pulses. An explanation is put forward by proposing that the molecular hydrogen which excites the HCN molecules, as described by Schötzau and Kneubühl[56], is itself de-excited during the afterglow. Optimum conditions are therefore found by adjusting the magnitude of the current pulse and the pulse repetition frequency which at a fixed gas flow rate will determine the level to which the hydrogen builds up. The dependence of the output on both these parameters is demonstrated by the measurements displayed in Figure 5.10.

CHAPTER SEVEN

SUBMILLIMETRE DETECTION

7.1. Introduction

Throughout the present work, the laser radiation was detected with a Golay cell and with antenna point-contact diodes. A Golay cell was used because of its reliability and high sensitivity, but its usefulness was limited by its slow response time. Pulses of radiation were observed using antenna point-contact diode detectors because of their fast response. As stated in Chapter One, an investigation was undertaken to endeavour to improve the sensitivity of these diode detectors. A theoretical model of the diode junction was developed from continued joint discussions with Mr. Nicholas Chandler of this department. For the experimental work, the fabrication of plane metal electrodes and the measurements of work functions were also carried out by Mr. Chandler.

7.2. Detector parameters

In the following discussion, three quantities will be used to describe the performance of the detectors:

(i) the voltage responsivity, $\gamma = \frac{\Delta V}{\Delta P}$, where a change in radiation power ΔP, at the detector produces a corresponding change in the output voltage ΔV, from the detector;

(ii) the noise equivalent power (n.e.p.), defined as the amount of radiation power necessary to produce an output from the detector equal to the root mean square of the noise output voltage;

(iii) the response time t_r, defined as the period in which an output from a detector, produced by a step change in the input radiation intensity, rises from 0.1 to 0.9 of the peak output. This is limited by the bandwidth B of the detector and output circuit such that $t_r = 0.35/_B$.

7.3. The Golay cell

The Golay cell responds to a change in infra-red radiation incident on a thin absorbing film. The gas in contact with the film is heated and increases in pressure. The rise in pressure distorts the cell containing the gas, which in turn changes the geometry of an optical system, part of which is in contact with the cell, subsequently altering the intensity of optical radiation incident on a photocell. The output from the

detector is derived from this photocell. A result of the mechanical nature of the Golay cell is its slow response. The time which elapses from the initial change in intensity of the incident radiation to the peak of the output from a commercial detector is nominally 30 ms[62]. Relaxation of the pneumatic cell, by a slow leakage of gas to a reservoir on the other side of the mirror membrane, has a recovery period of approximately 1.5 seconds. These large response and recovery times cause the responsivity to vary with the modulation frequency of the incident radiation. At optimum modulation frequencies, the responsivity of the cell[62] is usually between 10^5 and 10^6 volts per watt and is approximately linear up to 10^4 times the root mean square noise level.

7.4. Antenna point-contact diode detectors

Ever since Happ et al.[4] demonstrated the ability of the point-contact diode to detect submillimetre waves, these detectors have been formed by bringing a fine pointed tungsten whisker into contact with a metal or semiconductor base. The whisker, when placed in an electromagnetic field, acts as a travelling wave antenna and rectification of the induced current occurs at the junction of the whisker and the base. Matarrese and Evenson[63] demonstrated that long-wire antenna theory is applicable to the whisker, which in practice is many wavelengths long, and that as a consequence there exists an optimum angle between the antenna and the radiation for coupling power into the detector. Green et al.[7,64] showed that rectification at a junction with a metal base can, to some extent, be explained by considering electrons to tunnel through a metal-insulator-metal barrier. Further investigations were performed on tungsten to n-doped semiconductor diodes by Payne and Prewer[65] and by Becklake et al.[66] who obtained their best results from a tungsten whisker and n-type germanium base. They also showed that a Schottky barrier could be used in the submillimetre region. Evenson et al.[67,68] obtained higher responsivities from detectors mounted in free space rather than cavity mounted diodes as used by Payne and Prewer, and Becklake et al.

7.4.1. Circuit theory of point-contact junctions

The current-voltage characteristic of a diode can be expressed as a general polynomial

$$I = aV + bV^2 + cV^3 + \ldots \qquad \ldots(7.1)$$

where I is the current in the diode corresponding to a voltage V across

the junction and a, b and c are constants. Green[64] showed that the current-voltage characteristic of a metal-oxide-metal (M-O-M) diode is nearly linear, so $^1/_a$ can be used as a good approximation to the resistance R of the junction. Hence, for a low power level P of angular frequency ω coupled into the junction, the voltage across the diode can be approximated to

$$V = (2PR)^{\frac{1}{2}} \sin \omega t = \left(\frac{2P}{a}\right)^{\frac{1}{2}} \sin \omega t \qquad \ldots(7.2)$$

Inserting 7.2 into 7.1, a d.c. component of the current is obtained as

$$I_{dc} = \frac{b}{a} \cdot P$$

The d.c. component of the voltage detected across the diode is therefore

$$V_{dc} = I_{dc}R = \frac{I_{dc}}{a} = \frac{b}{a^2} \quad P$$

so the voltage responsivity is

$$\gamma = \frac{b}{a^2} \quad \text{volts . watt}^{-1} \qquad \ldots(7.3)$$

A useful parameter for describing the rectification of a diode is the rectification ratio, defined as

$$\eta(V) = \left| I(V)/_{I(-V)} \right|$$

$$= \frac{(aV + bV^2 + cV^3)}{(aV - bV^2 + cV^3)} \qquad \ldots(7.4)$$

which, for a nearly linear I-V characteristic, can be written as

$$\eta(V) \simeq 1 + \frac{2bV}{a}$$

Hence 7.3 gives the relationship

$$\gamma = \{\frac{b}{a}\}R = \{[\eta(V) - 1] \; / _{2V}\}R \quad \text{volts . watt}^{-1} \qquad \ldots(7.5)$$

The response time of an isolated barrier has been quoted by Becklake et al.[66] to be in the picosecond region for metal-semiconductor junctions and of the order of 10^{-16} seconds for metal-insulator-metal diodes by Hartman[69]. Both types of barrier are therefore capable of operating at far infra-red frequencies. The limiting factors in a practical device are the capacitance and resistances involved.

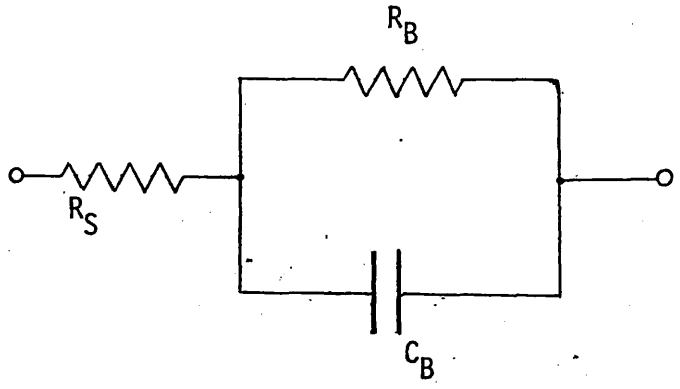

Figure 7.1. Equivalent circuit of a point-contact diode. Barrier capacitance C_B, barrier resistance R_B, spreading resistance R_S

Figure 7.1 shows a passive equivalent circuit of a diode where the dielectric barrier has a capacitance C_B and resistance R_B, in series with a parasitic spreading resistance R_S. In addition to the resistance of the antenna and any contacts involved with the construction of the detector, the spreading resistance represents the resistance encountered as the current moves away from the junction and into the bulk of the substrate; a term particularly important when considering semiconductor devices. To obtain an expression for the performance of a diode, it is assumed that part of the power transferred to the device is absorbed in the non-linear resistance R_B, and part in the spreading resistance. If P_{RF} represents the total power dissipated and P_B is the power absorbed by R_B, then analysis of the circuit in Figure 7.1 yields

$$\frac{P_B}{P_{RF}} = \frac{1}{\left(1 + \frac{R_S}{R_B}\right)\left(1 + \frac{\omega^2 C_B R_B R_S}{1 + \frac{R_S}{R_B}}\right)}$$

$$= \frac{1}{\left(1 + \frac{R_S}{R_B}\right)\left(1 + \left\{\frac{\omega}{\omega_c}\right\}^2\right)} \qquad \ldots(7.6)$$

where the -3 dB point, often referred to as the corner frequency, is expressed as

$$\omega_c = \frac{\left(1 - \frac{R_S}{R_B}\right)^{\frac{1}{2}}}{C_B\left(R_B R_S\right)^{\frac{1}{2}}} \qquad \ldots(7.7)$$

These relationships show that for high frequency response both the barrier capacitance and the spreading resistance must be kept as low as is possible. Becklake et al.[70] have given a value of the corner frequency point-contact semiconductor devices as ∿150 GHz. For faster response the semiconductor should be replaced by a metal.

7.4.2. Tunnel and electric field emission in M-O-M junctions

The simple potential distribution between two plane-parallel metal surfaces separated by a thin insulating material can be represented diagrammatically as in Figure 7.2(a). Two metals with work functions Ψ_1 and Ψ_2, Fermi levels η_1 and η_2 and separated by a distance S, create a potential barrier in the dielectric medium of height $\xi(x)$. The barrier can be expressed as $\phi(x)$ above the Fermi level, with values ϕ_1 and ϕ_2 at the metal-insulator interfaces. An asymmetric barrier potential of this kind can be assumed to represent most practical configurations. A symmetric junction is difficult to fabricate even with similar metals[71].

Current can flow through a M-O-M junction by electronic tunnelling. If the electrons in the electrodes have sufficient thermal energy, they cam surmount the surface barrier and flow in the conduction band of the oxide. Simmons[72,73] has examined these processes for a parallel metal-dielectric-metal structure while taking into account the image forces present within the insulator. These forces arise because electrons approaching an electrode polarise the metal surface and create an attractive force between the electron and electrode. The potential of the electron resulting from this image force requires that the height of the potential barrier is no longer the value represented by $\phi(x)$ in Figure 7.2(a), but more accurately illustrated by the smoothly changing curve of Figure 7.2(b).

Electron tunnelling occurs because electrons of energy E_x have a finite probability $D(E_x)$ of penetrating a potential barrier $\xi(x)$ where

$$D(E_x) = \exp\left[\frac{-4\pi}{h} (2m)^{\frac{1}{2}} \int_{S_1}^{S_2} \{ \xi(x) - E_x \} \, dx \right]$$

thus producing an electron current density of

$$J = \int_0^{\infty} D(E_x) N(E_x) dE_x$$

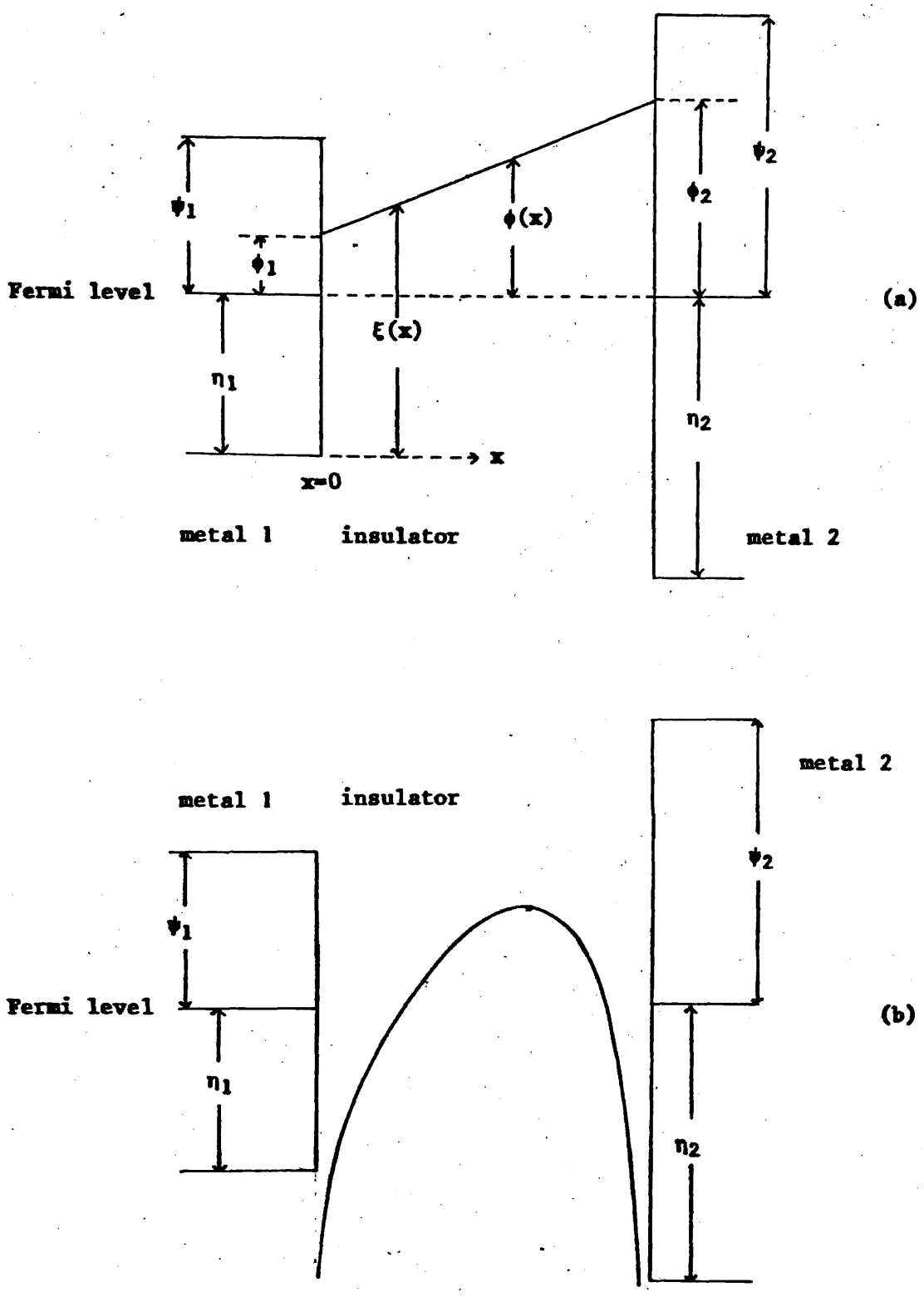

Figure 7.2. Energy diagram of potential barrier between dissimilar electrodes (a) ignoring image forces, and (b) with image forces taken into account. After Simmons[72].

$N(E_x)$ being the electron supply function, h Planck's constant, and m the mass of an electron.

For the case of negative bias applied to the electrode of lower work function, Simmons[72] has calculated the nett tunnel current density flowing from this electrode to be

$$J_1 = J_0\left(\bar{\phi}_1 \exp\{-A\phi_1^{\frac{1}{2}}\} - \{\bar{\phi}_1 + eV\} \exp\{-A[\bar{\phi}_1 + eV]^{\frac{1}{2}}\}\right) \qquad \ldots(7.8)$$

in which

$$\bar{\phi}_1 = \phi_1 + \frac{S_1 + S_2}{2S}\{\Delta\Psi - eV\} - \left\{\frac{1{\cdot}15\lambda S}{\Delta S}\right\} \log_e\left[\frac{S_2(S - S_1)}{S_1(S - S_2)}\right] \qquad \ldots(7.9)$$

where

$$S_1 = \frac{9{\cdot}2\lambda S}{[3\phi_1 + 4\lambda - \{eV - \Delta\Psi\}]} - \frac{1{\cdot}2\lambda S}{[\phi_2 - eV]} \qquad \ldots(7.10)$$

and

$$S_2 = S - \frac{1{\cdot}2\lambda S}{[\phi_2 - eV]} \qquad \ldots(7.11)$$

S_1 and S_2 are expressed for a range of bias V applied to the barrier where $0 < eV \lesssim \Delta\Psi$, e being the charge on the electron and $\Delta\Psi$ the difference in the values of the work functions of the two metal surfaces such that

$$\Delta\Psi = \phi_2 - \phi_1 = \Psi_2 - \Psi_1$$

With the electrode of higher work function negatively biased, the nett tunnel current density flowing from this electrode to that of lower work function is

$$J_2 = J_0\left(\bar{\phi}_2 \exp\{-A\phi_2^{\frac{1}{2}}\} - \{\bar{\phi}_2 + eV\} \exp\{-A[\bar{\phi}_2 + eV]^{\frac{1}{2}}\}\right) \qquad \ldots(7.12)$$

where

$$\bar{\phi}_2 = \phi_2 - \left(\frac{S_1 + S_2}{2S}\right)(eV + \Delta\Psi) - \left(\frac{1{\cdot}15\lambda S}{\Delta S}\right) \log_e\left(\frac{S_2(S - S_1)}{S_1(S - S_2)}\right) \qquad \ldots(7.13)$$

S_1 and S_2 are expressed for the condition $eV \lesssim \phi_1$ as

$$S_1 = \frac{1{\cdot}2\lambda S}{\phi_2} \qquad \ldots(7.14)$$

and

$$S_2 = S - \frac{9{\cdot}2\lambda S}{[3\phi_2 + 4\lambda - 2\{eV + \Delta\Psi\}]} + S_1 \qquad \ldots(7.15)$$

In each of the relationships for J_1 and J_2, ΔS is written in terms of the respective values of S_1 and S_2 as

$$\Delta S = S_2 - S_1 \quad .$$

S_1 and S_2 being the limits of the barrier at the Fermi level. J_0 and A are expressed for each of the bias conditions as functions of the appropriate value for ΔS as

$$J_0 = \frac{e}{\{2\pi h \,.\, \Delta S^2\}}$$

and

$$A = \frac{\{4\pi\Delta S\}}{h} \{2m\}^{\frac{1}{2}}$$

is given by

$$\lambda = \frac{\{e^2 \log_e 2\}}{8\pi K\epsilon_0 S}$$

K is the dielectric constant of the insulating layer and ϵ_0 the permittivity of free space.

A second mechanism, thermal emission, has also been investigated by Simmons[73] using the Richardson-Dushman equation

$$J = AT^2 \left[e^{-\phi_1/kT} - e^{-\phi_2/kT}\right]$$

where k is Boltzmann's constant, A is the Richardson-Dushman constant and T is the absolute temperature. A is expressed as

$$A = 4\pi me \frac{k^2}{h^3}$$

Again taking into account image forces, Simmons used the Richardson-Dushman equation to obtain equations for current density as

$$J_1 = AT^2 \exp\left(\frac{eV - \phi_2}{kT}\right) \exp\left(\frac{\{14{\cdot}4[7 + KS\{\Delta\Psi - eV\}]\}^{\frac{1}{2}}}{KSkT}\right) \qquad \ldots(7.16)$$

for the range $0 \leq V \leq {}^{\Delta\Psi}/_{e}$, when the electrode of lower work function is negatively biased, and

$$J_2 = AT^2 \exp\left(\frac{-\phi_2}{kT} \right) \exp\left(\frac{14{\cdot}4\{eV + \Delta\Psi\}}{KSkT} \right)^{\frac{1}{2}} \qquad \ldots(7.17)$$

when the electrode of higher work function is negatively biased. Both equations were derived for the condition $(eV)/(kT) > 2$.

Numerical values for current density predicted by equations 7.8, 7.12, 7.16 and 7.17 have been calculated by Simmons[73] and comparison made of the tunnel and thermal effects. Figure 7.3(a) shows the current density J, through a M-O-M barrier, plotted against applied voltage V, for an electrode spacing of S = 40 Å, and an insulating layer of dielectric constant K = 3. Representing the J-V curves by dotted lines when the electrode of lower work function is positively biased and by continuous lines when the same electrode is negatively biased, then for ϕ_1 = 1 eV curves 1(a) and 1(b) are the characteristics for ϕ_2 = 1.5 eV and curves 2(a) and 2(b) for ϕ_2 = 2 eV. Thermionic J-V characteristics at 300°K with the electrode of lower work function negatively biased, are represented by curves 1(c) and 2(c) for ϕ_2 = 1.5 eV and ϕ_2 = 2 eV respectively; again ϕ_1 = 1 eV in both cases. The thermal characteristics for the case of the electrode of lower work function being positively biased are negligible when compared to the values of curves 1(c) and 2(c) and are not plotted. Figure 7.3(a) shows a situation where the thermionic current is small when compared to the tunnel current. However, by increasing the electrode spacing to 50 Å, Figure 7.3(b) shows that certain bias conditions exist in which the thermal current is the larger of the two. The observation that the dominant mechanism in an M-O-M barrier can change with the thickness of the insulating layer is important when considering a practical whisker-diode detector. The force on the tungsten wire in contact with an oxide layer on a conducting substrate is increased until sufficient rectification is observed. In this situation, the tungsten whisker can be considered to gouge into the oxide, decreasing the metal to metal spacing. Figures 7.3(a) and 7.3(b) also show that at the lower voltages, the forward direction of rectification of the tunnel current occurs when the electrode of lower work function is positively biased, while the forward direction for the thermal current is produced by negatively biasing this electrode. The two figures therefore indicate that as a whisker is forced into the dielectric, both the degree of rectification and the polarity are expected to vary as the situation changes from a region where the thermionic current is dominant to one in which the tunnel current is dominant. It is also seen that cross-over points exist for the two senses of applied bias for the tunnel currents. Thus for a

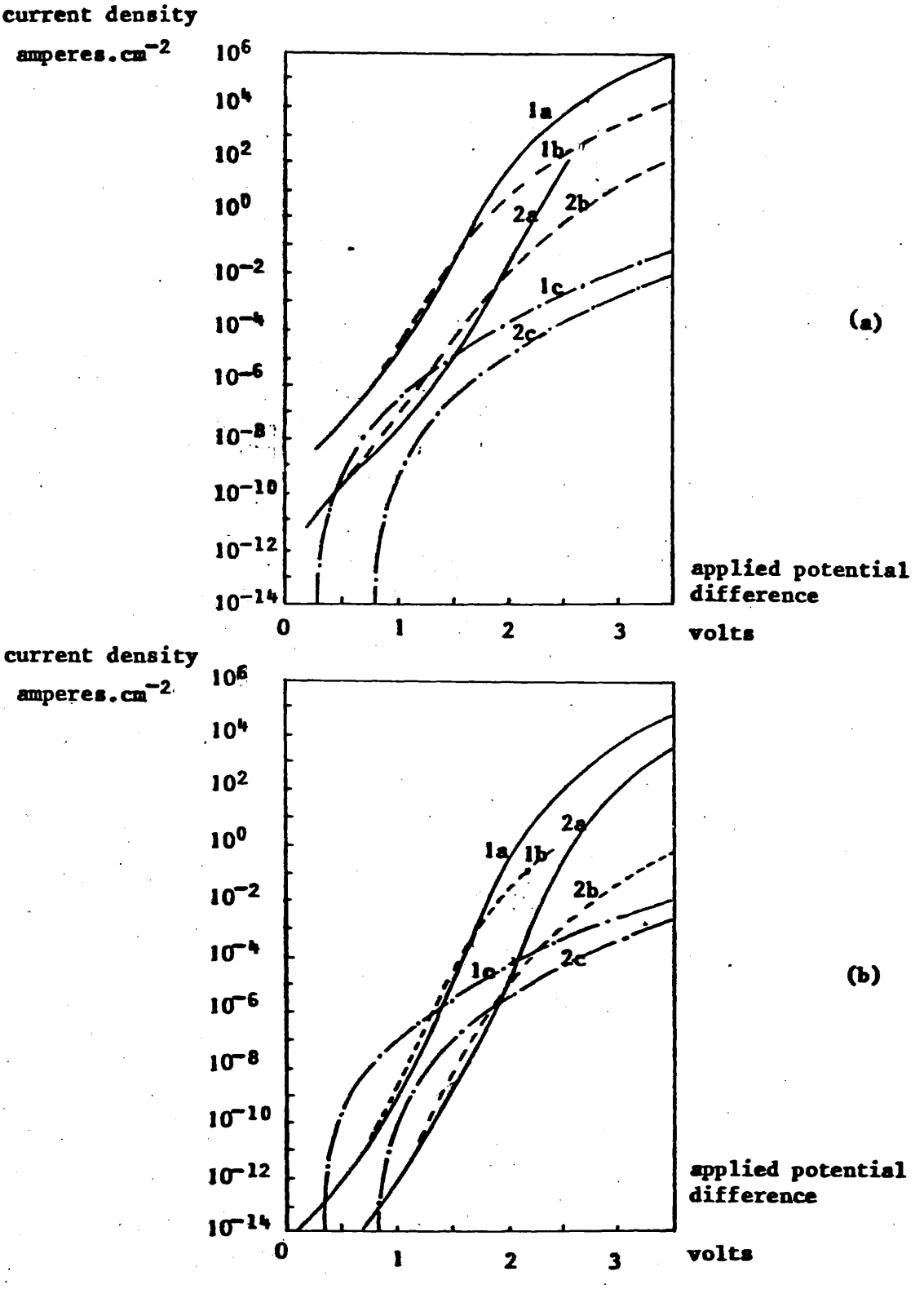

Figure 7.3. Comparison of thermal and tunnel currents flowing between plane parallel dissimilar electrodes for (a) S = 40 angstroms and (b) S = 50 angstroms. K = 3 and ϕ_1 = 1 eV.

For tunnel characteristics 1a, 1b, ϕ_2 = 1.5 eV and for 2a, 2b, ϕ_2 = 2.eV. Dotted and full lines respectively represent the electrode of lower work function positively and negatively biased. For thermionic characteristics at 300°K, curve 1c, ϕ_2 = 1.5 eV and 2 c, ϕ_2 = 2 eV. After Simmons[73].

diode of fixed barrier spacing, to which an increasing voltage is applied, variation and reversal of the rectification may be expected as a result of either effect. Applied voltage is shown to be a function of input power to the detector in equation 7.2 and experimental evidence for polarity reversal with variation in input power is obtained from the measurements of Green et al.[7] at a frequency of 75 GHz which are reproduced in Figure 7.4.

Instability and polarity reversal in point-contact whisker detectors has been reported[7,64,65] while the device was subjected to mechanical adjustment or vibration from the experimental environment. However, consistent characteristics have been observed by Marhic and Jassby[74] on bringing a pointed tungsten whisker into contact with an n-type germanium crystal. The best output was obtained at a low whisker pressure, which then reduced to zero, reversed sign and increased slowly as the pressure was increased. This variation in output could be retraced on reduction of the whisker pressure.

The observations of Marhic and Jassby are not strictly applicable to M-O-M diodes but are significant because the sensitivity of the device on insertion of the whisker was reversible on withdrawal, and the cycle repeatable. Similar observations from the present work will be reported in section 7.4.5 on the characteristics of both M-O-M and metal-oxide-semiconductor (M-O-S) diodes. This demonstrates that the variation of the output was not entirely attributable to random changes in work function, or damage to the oxide by lateral movement of the whicker, or to deformation of the tip of the whisker. The observations of Green et al.[7] give some confirmation to the M-O-M model of the detector which the theoretical work of Simmons shows to be a sensitive function of the oxide thickness. It will therefore be instructive to investigate the effect of varying the thickness of the insulating barrier on the operation of a point-contact diode.

7.4.3. A model of a point-contact junction

The equations listed above to describe electron flow through an M-O-M junction were derived by Simmons for two plane parallel metal surfaces separated by a dielectric. Chow[75] has shown that non-uniform spacing of the electrodes can significantly alter the current-voltage characteristics of a tunnel diode. For the situation where a pointed tungsten wire is considered to burrow through an oxide layer, account will now be taken of the geometry of the device[76].

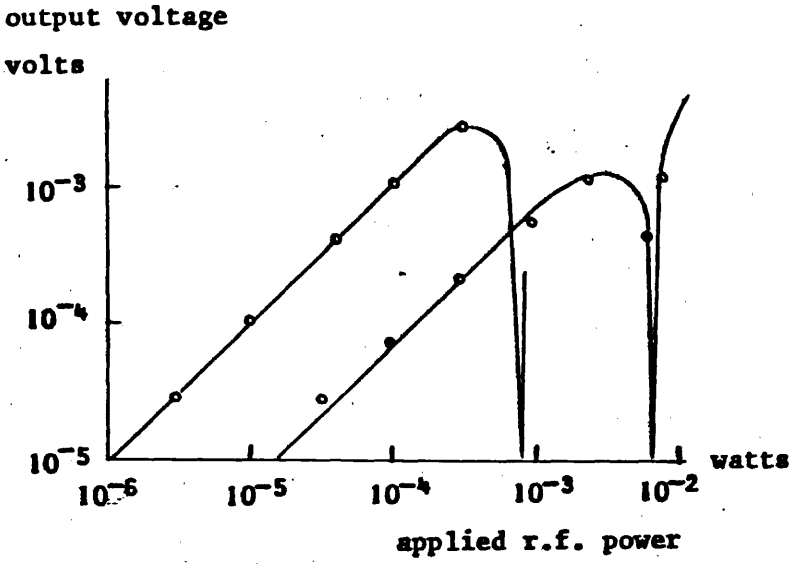

Figure 7.4. D.C. output voltage against applied r.f. power at 4 mm wavelength from a point-contact diode detector. After Green et al.[7].

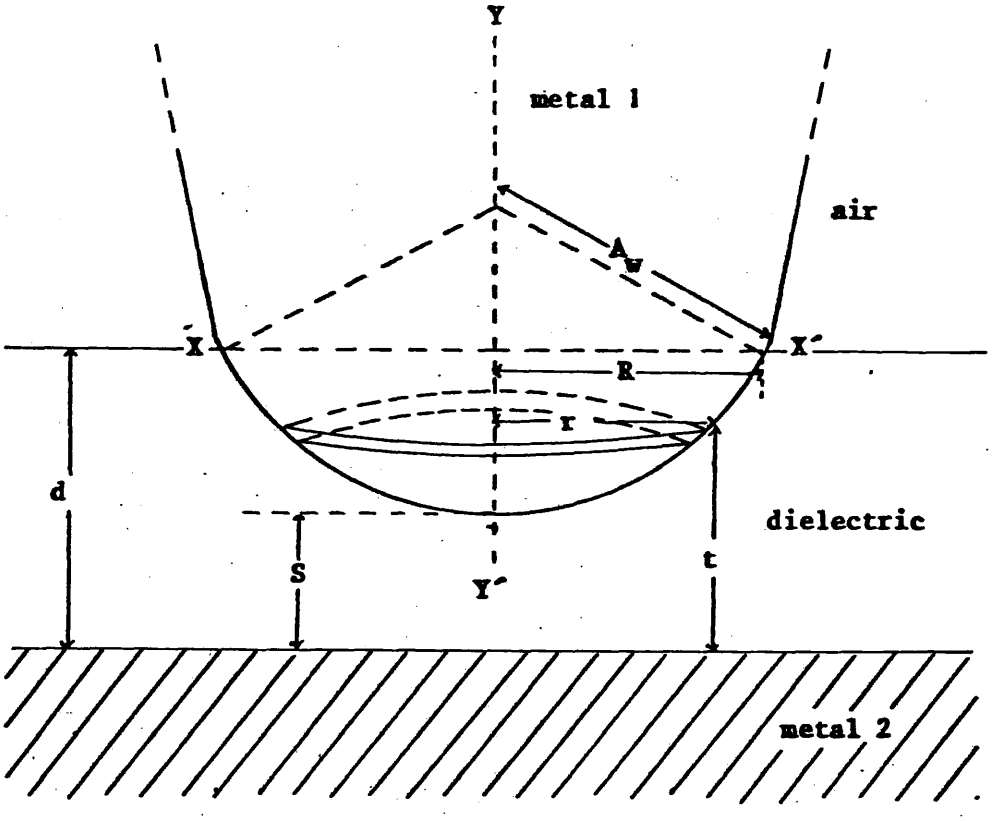

Figure 7.5. The hemispherical tip of an antenna partially embedded in the oxidised surface of a plane electrode

Consider a flat metal surface on which has formed a uniform oxide layer of thickness d; the interface between metal and oxide being clearly defined. Let the tip of the whisker be part of a sphere of radius A_w, inserted into the oxide such that the point on the sphere in closest proximity to the plane metal surface is at a distance S from this surface. Figure 7.5, drawn about an axis of symmetry YY', illustrates this model. In order to calculate the current flowing between the electrodes, the surface of the tip of the whisker may be considered to be divided into rings of width δr and radius r centered on YY' such that r = 0 at Y and r = R at the surface of the dielectric XX'. Assuming typical values for the radius of the tip of the whisker of 0.1 to 1 μm[64,74], and typical thicknesses of oxide formed in air of ∿100 Å[71], the approximation may be made that the curvature of the surface of each annulus is negligible so that the surface of the tip can be represented as a large number of rings each parallel to the plane metal surface. The distance t of a ring from the metal surface can be written as

$$t = S + A_w - (A_w^2 - r^2)^{\frac{1}{2}} \qquad \ldots(7.18)$$

This enables the current density J(t) flowing in an annulus at a distance t from the metal plane to be expressed as a function of r, J(r). The electron flow from each ring is therefore $2\pi r \cdot \delta r \cdot J(r)$, and so the current ratio for the device may be calculated as

$$\eta = \frac{\int_0^R 2\pi J_2(r) r dr}{\int_0^R 2\pi J_1(r) r dr} \qquad \ldots(7.19)$$

where the upper limit of each integration may be written

$$R = \left[2A_w\{d - S\} - \{d - S\}^2\right]^{\frac{1}{2}} \qquad \ldots(7.20)$$

$J_1(r)$ and $J_2(r)$ are the current densities for each sense of applied bias. The voltage responsivity of a diode detector may be found by using Simmons' equation to calculate current flow at specific values of instantaneous voltage. A method of numerically solving equation 7.19 for both the tunnel and thermionic effects, and calculating the corresponding responsivity is described in Appendix IV.

An example will be evaluated in which a metal has on its surface an oxide layer 101 Å thick with a dielectric constant of 8[71]. A hemispherical electrode of 10^6 Å radius is inserted into the oxide and the work function

difference between the two metals is taken to be 1 eV. The height of the potential barrier at the metal-dielectric interfaces will have a value between zero and that of the work function of the electrode. Assigning an arbitrary value of four volts to the lower of the two parameters ϕ_1 of Figure 7.2(a), and applying $V_B = 0.09$ volts across the junction, the lower limit of the range of bias applicable to Simmons' equations, tunnel and thermionic current were calculated and the results given in Figure 7.6(a). The currents generated by the two mechanisms are compared and are seen to vary in relative importance with the depth of the whisker in the oxide. The difference between the two tunnel currents for each sense of applied bias potential and the thermionic current for the reverse bias condition were both too small to show with the current scale employed. Using the above values to obtain the rectification ratio and barrier resistance, the responsivity that would result from each individual mechanism can be found and is given in Figure 7.6(b). The opposite signs of the two responsivity curves are immediately noticeable and are a result of the rectification ratio of the tunnel currents being greater than unity, while that for the thermionic currents is less than unity. The responsivity of a diode detector is produced by the combined effects of both processes and must be calculated using the total current. The rectification ratio of the combined currents is seen in Figure 7.6(c) to pass through unity. The voltage responsivity for this example and for other sphere radii and values of applied bias are plotted against the minimum barrier spacing S in Figure 7.7. For two different barrier heights defined by $\phi_1 = 4$ eV and $\phi_1 = 1$ eV, the responsivity shown in the figure undergoes a reversal in polarity at a value of S corresponding to $\eta = 1$. This condition is seen to be a function of the applied bias and that at certain values of oxide thickness the polarity of the output from a detector would change, as indicated by equation 7.2, on alteration of the input power. Confirmation of this feature of the diode model is provided by the experimentation of Green et al.[7] described earlier and displayed in Figure 7.4. The magnitude of the responsivity is seen to fall with increased whisker tip size and smaller dielectric spacing. In both cases the resistance of the barrier is decreased and so the voltage built up across it is reduced. Figure 7.7 also shows a reduction in diode response on lowering ϕ_1 from 4 to 1. A further reduction of the height of the potential barrier by assigning $\phi_1 = 0.5$ eV reduced the voltage responsivity still further, as illustrated in Figure 7.8. Plotted separately for clarity, curves for this barrier height are only shown for $V_B = 0.09$ volts in order to comply with the theoretical restriction $0 < eV \lesssim \Delta\Psi$.

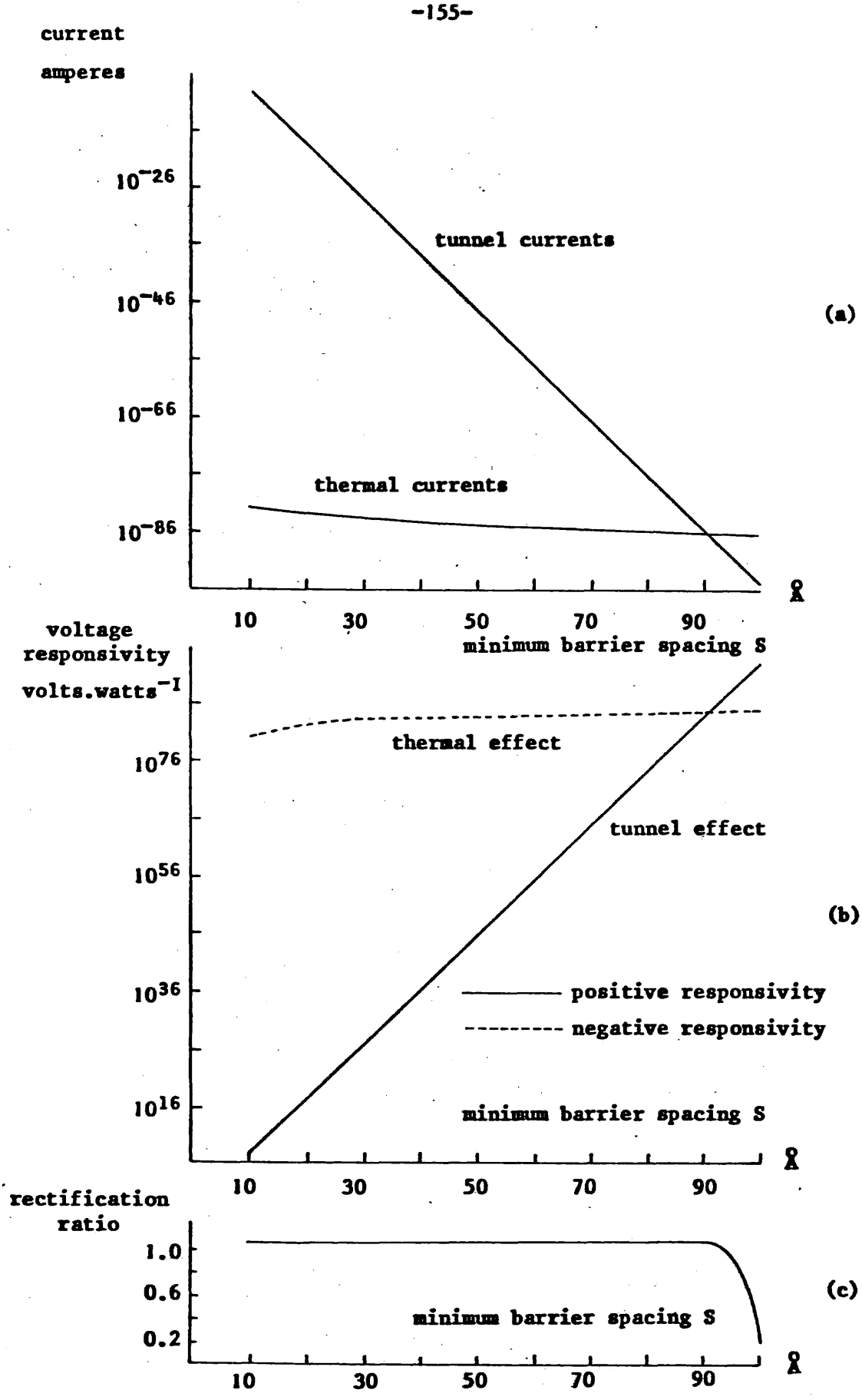

Figure 7.6. Theoretical properties of a M-O-M point-contact diode detector. $K = 8$, $\phi_1 = 1$ eV, $\phi_2 = 2$ eV, $A_w = 10^6$ amperes and $V_{dc} = 0.09$ volts.

(a) current (b) voltage responsivity (c) rectification ratio against minimum barrier spacing

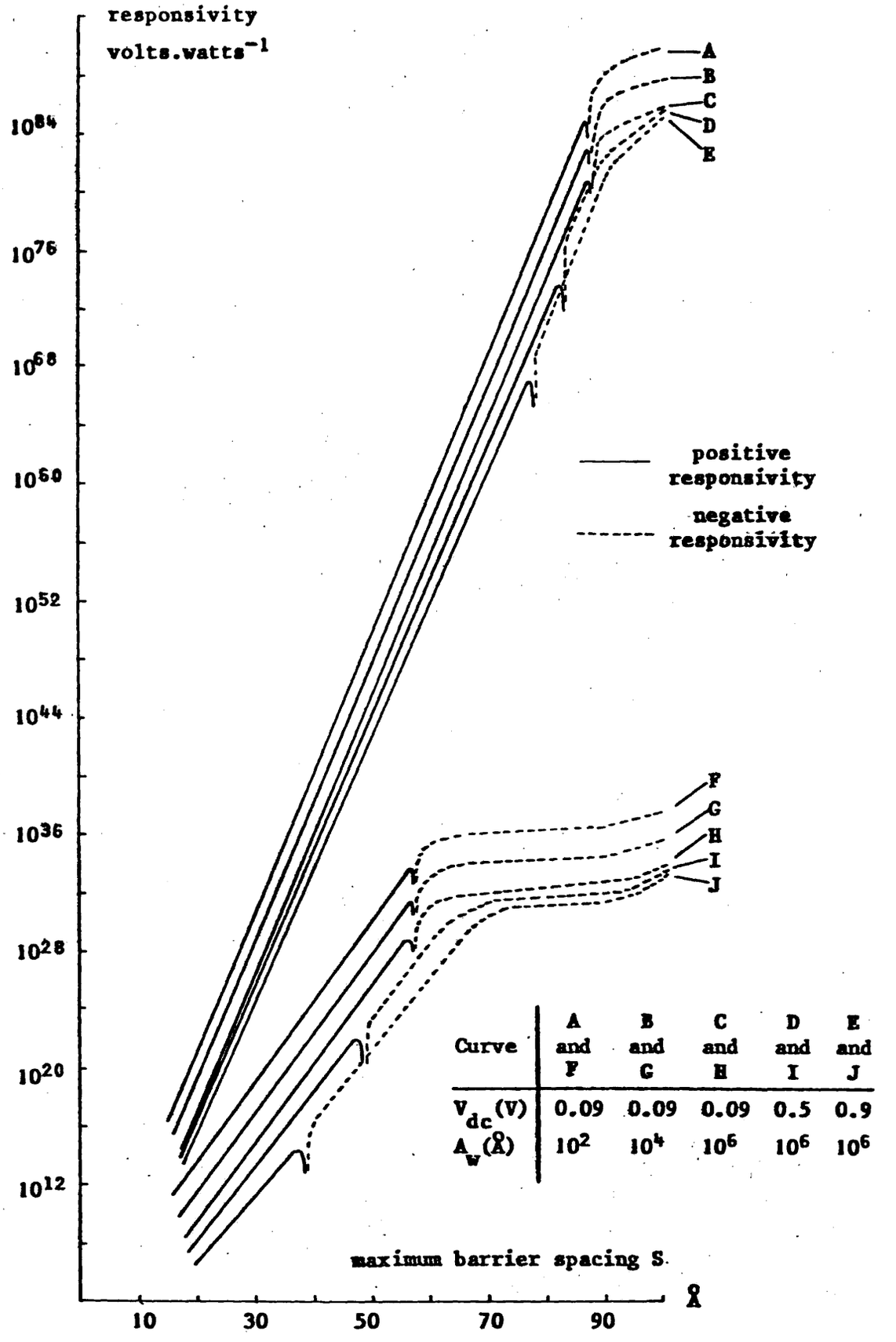

Figure 7.7. Theoretical voltage responsivity of a M-O-M point-contact diode detector. K = 8, ϕ_1 = 4 eV and ϕ_2 = 5 eV for curves A,B,C,D and E. ϕ_1 = 1 eV and ϕ_2 = 2 eV for curves F,G,H,I and J.

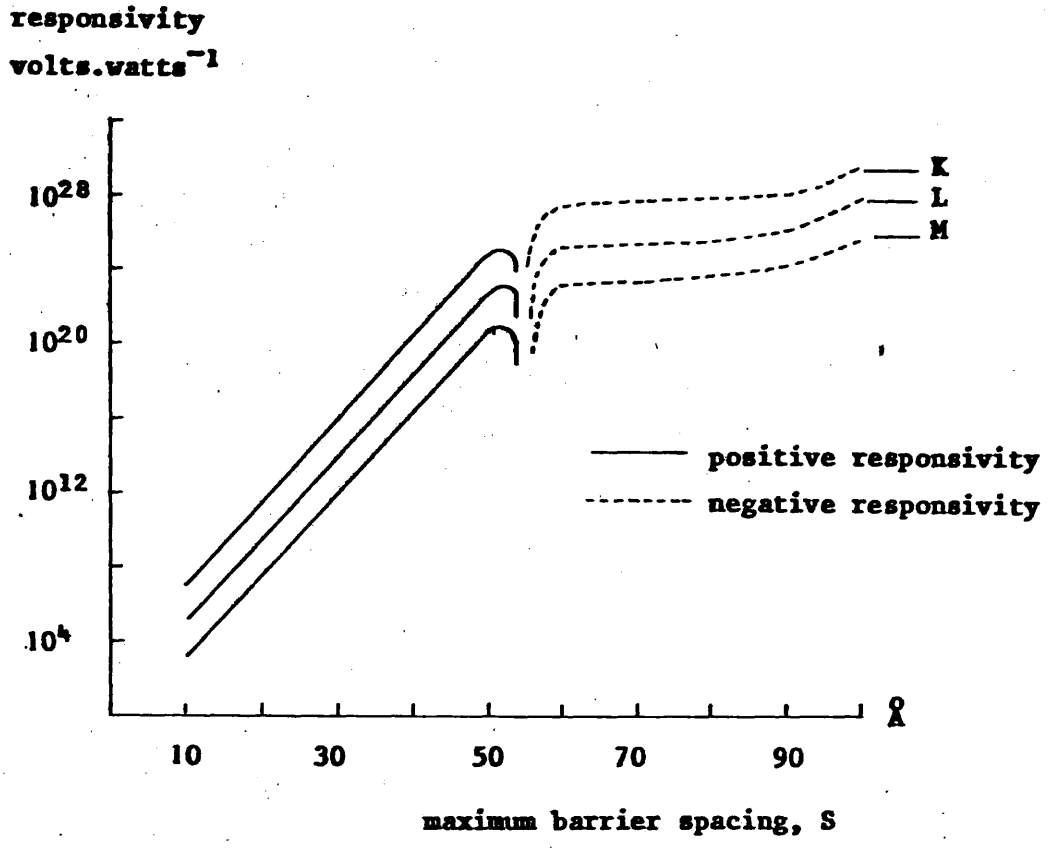

Figure 7.8. Theoretical voltage responsivity of a M-O-M point-contact diode detector. $K = 8$, $\phi_1 = 0.5$ eV, $\phi_2 = 1.5$ eV and $V_{dc} = 0.09$ volts

curve K, $A_w = 10^2$ Å

L, $A_w = 10^4$ Å

M, $A_w = 10^6$ Å

The variation of the response of devices produced from different combinations of metals has been investigated by altering the work function difference $\Delta\Psi$ from 0.1 to 2.0 eV and plotting the voltage responsivity against the minimum barrier thickness in Figure 7.9(a). Again, a value for the lower limit of the barrier height has been chosen as $\phi_1 = 1$ eV and the bias voltage was reduced to 0.09 volts in order to comply with the restriction $0 < eV < \Delta\Psi$. The figure shows similar characteristics to those of Figures 7.7 and 7.8 and demonstrates that large increases in responsivity are obtained by relatively small increase in $\Delta\Psi$. This last observation is more clearly shown by Figure 7.9(b) where the responsivity has been replotted against $\Delta\Psi$ for selected values of S.

An extensive study of the full range of the parameters involved in the model of the diode has not been undertaken, neither have the processes been examined outside the limits on $\Delta\Psi$ and V for which the equations of Simmons were derived.

7.4.4. Diode detector construction

7.4.4.1. Whisker antenna

The detector antennae were fabricated from straight sections of 20 micron diameter tungsten wire. An antenna would be supported at one end by being gripped in the bent-over end of a thin copper post. The free end of each whisker was sharpened electrolytically by lowering it into a solution of potassium hydroxide and applying several volts a.c. between the whisker and an electrode immersed in the solution. The whiskers were then rinsed in water to remove any electrolyte. An example of a fine conical point etched at the tip of a whisker is shown in Figure 7.10(a). This was observed using an optical microscope with a depth of field of 5 μm. The instrument was focused on the whisker at a point approximately half way along the length of the cone in order to show the taper produced by the electrolytic process.

7.4.4.2. Substrate material

Point contacts were made on to both metal and semiconductor substrates. Small crystals of n-doped germanium and undoped gallium arsenide were used while a sample of n-type silicon of resistivity 0.005 to 0.020 Ω cm was obtained in the form of a large disc. Uniform metal substrates were made by evaporating either gold or aluminium films on glass slides, in a vacuum system pumped down to 10^{-6} torr. Tungsten was used in rolled ribbon form.

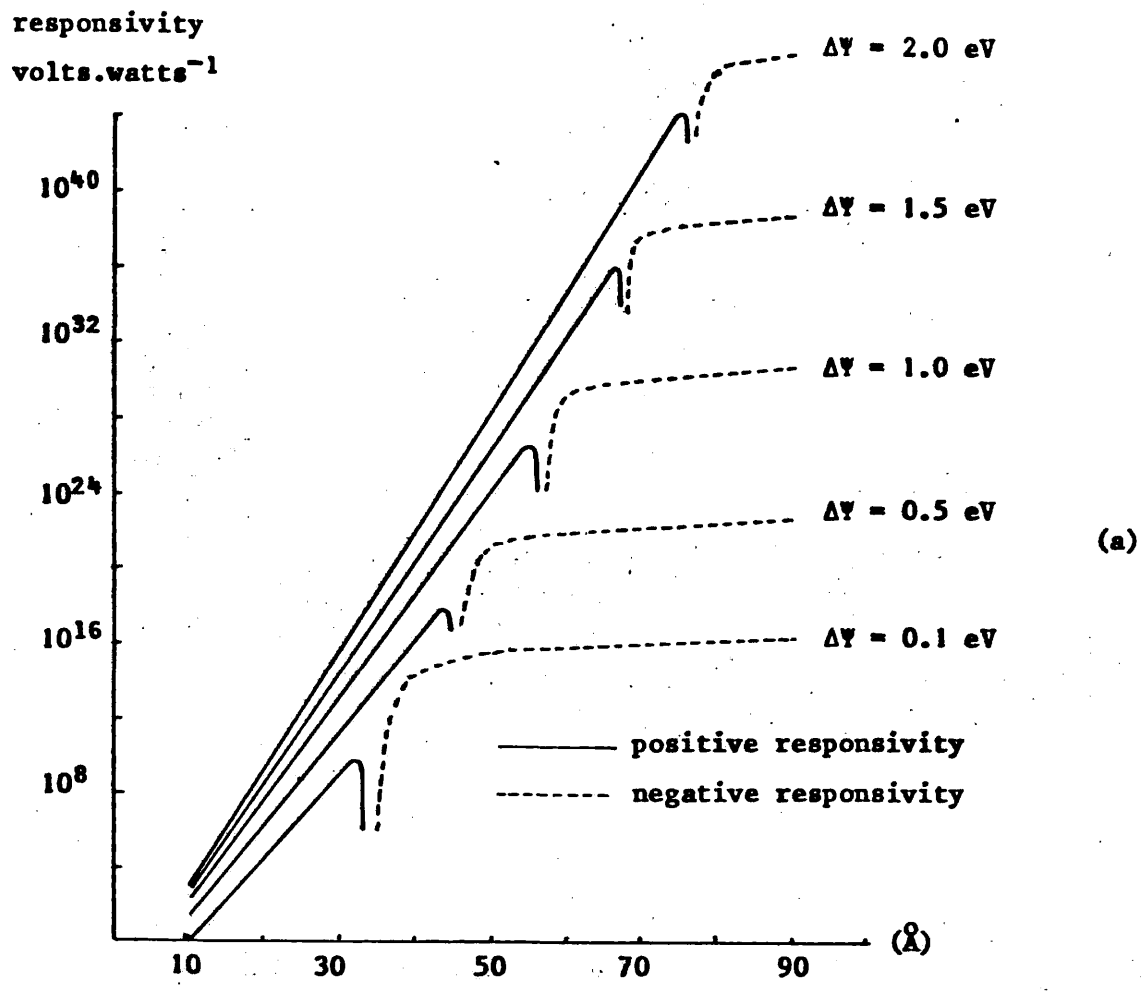

(a)

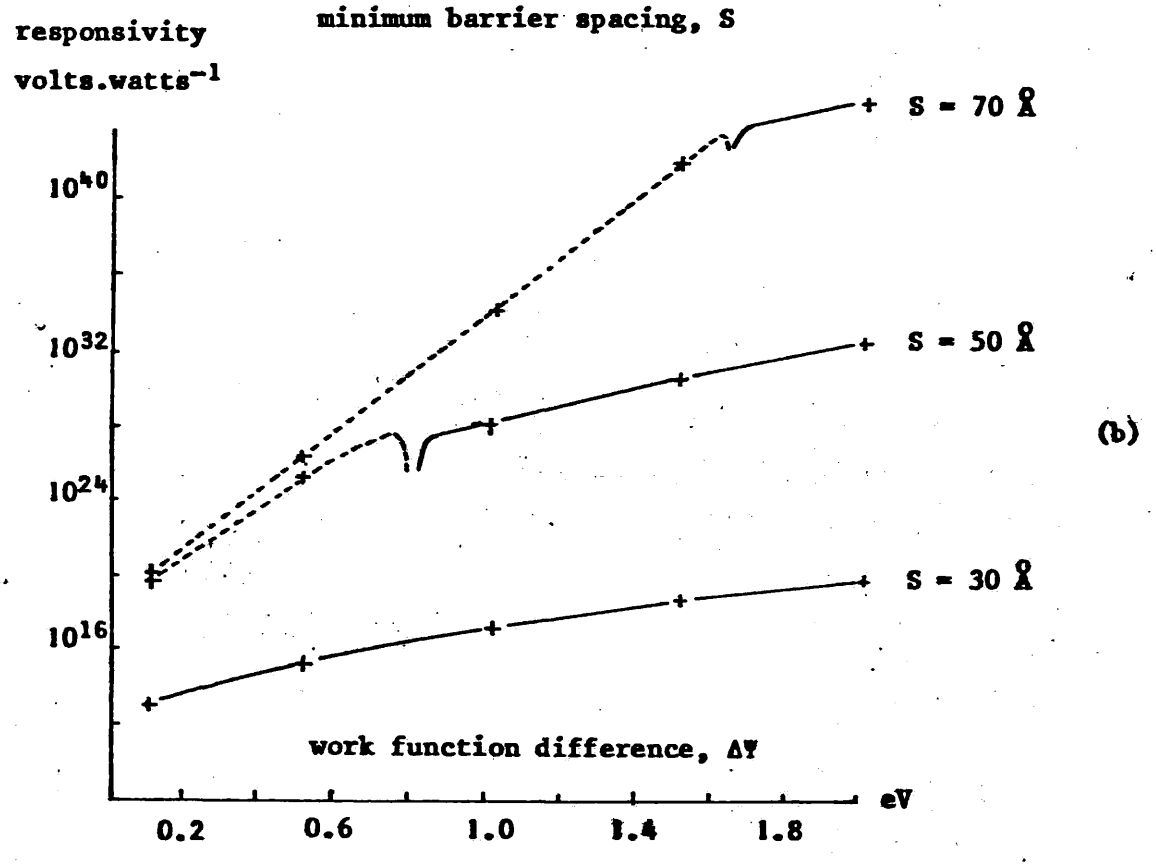

(b)

Figure 7.9. Theoretical voltage responsivity of a M-O-M point-contact diode detector, (a) against S, (b) against $\Delta\Phi$. K = 8, ϕ_1 = 1 eV, V_{dc} = 0.09 volts.

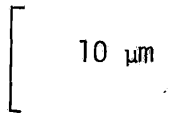

(a)

(b)

(c)

Figure 7.10. Electrolytically etched tungsten whisker, (a) freshly etched, (b) after one impact with an electrode, and (c) after two impacts

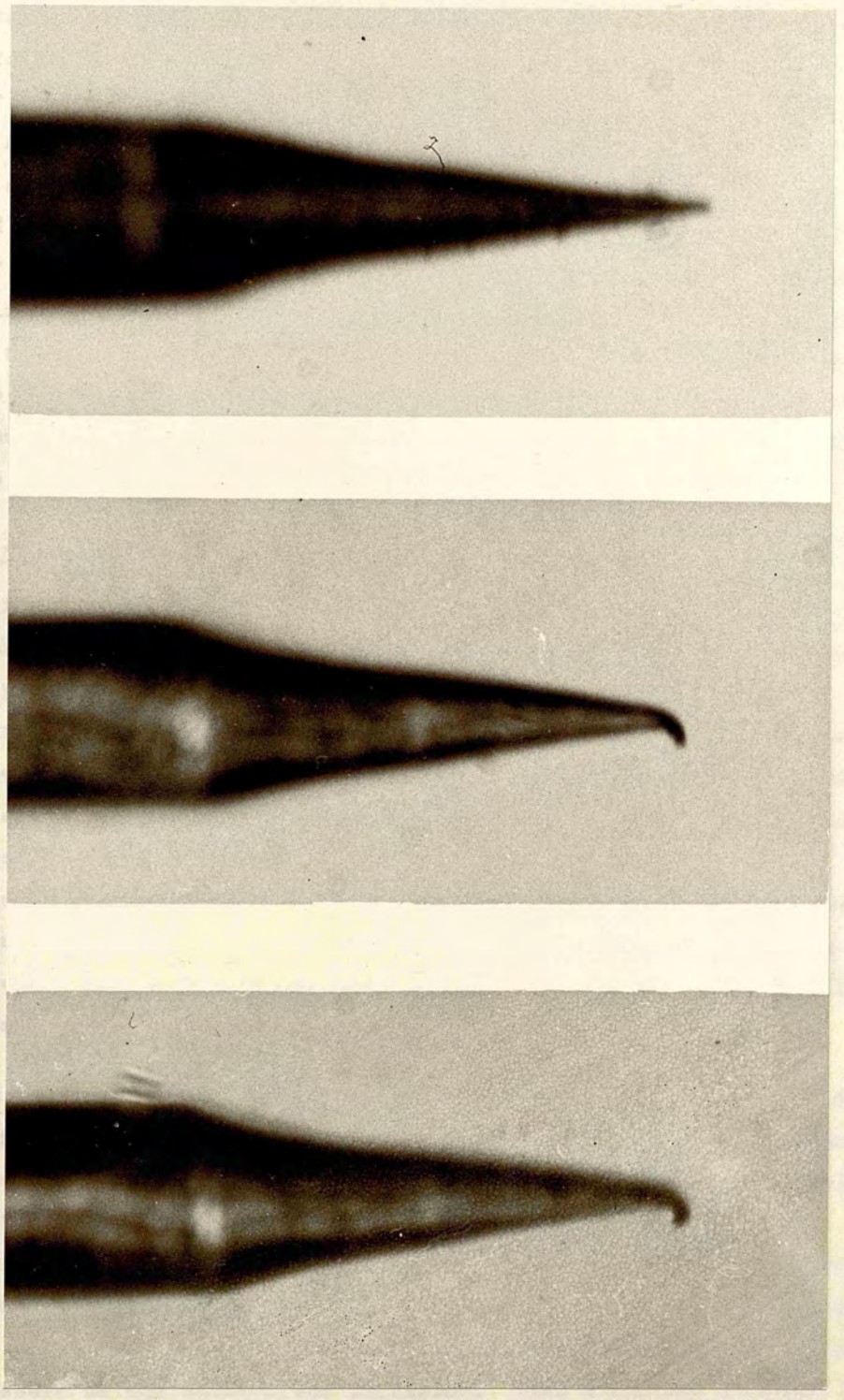

7.4.4.3. Assembly

The arrangement used for making and supporting the diode detector is illustrated in Figure 7.11. The copper post holding the tungsten whisker is retained in a chuck which is in turn connected to the centre pin of a BNC socket. The diode substrate is attached to the non-rotating centre shaft of a special micrometer with a resolution of 1 μm and earthed via the BNC connector. To make contact between the tip of the whisker and the substrate, the two are first brought into close proximity by horizontal movement of the chuck assembly. With the whisker placed in the submillimetre beam, final adjustment is made using the micrometer to move the diode substrate. Contact is made while observing the output from the detector and fine adjustment of the force on the whisker is made to optimise this signal.

7.4.5. Performance characteristics

It was found that very light pressure on the tungsten whisker was necessary to produce rectification from a metal-oxide-metal point-contact diode, particularly when using a gold substrate with its very thin dielectric surface layer. Low contact pressure often gave rise to an unstable output voltage which on occasions took the form of a periodic change of polarity. This behaviour was found to be due to mechanical vibrations continually altering the oxide barrier thickness; the condition for reversal of the output polarity sometimes being within the excursion of the vibrating whisker tip. However, by accepting a reduction in the output, it was often possible to improve the stability of the detector by increasing the whisker pressure.

Maximum output was again attained with little pressure being applied to the tungsten whisker when forming diodes with doped silicon and doped germanium substrates. Outputs higher than those from the M-O-M diodes were obtained, and hence more rugged detectors could be made by increasing the whisker pressure as larger reductions in rectification were acceptable. As was often the case with M-O-M barriers, the output voltage from silicon and germanium diodes was also reduced to zero as the pressure on the whisker was increased. With a further increase in pressure, the output returned with opposite polarity. The magnitude of the voltage obtained at high pressure was rarely as great as that obtained at low whisker pressure. However, the response could be recovered as the characteristic of output voltage with pressure was reproducible in both directions.

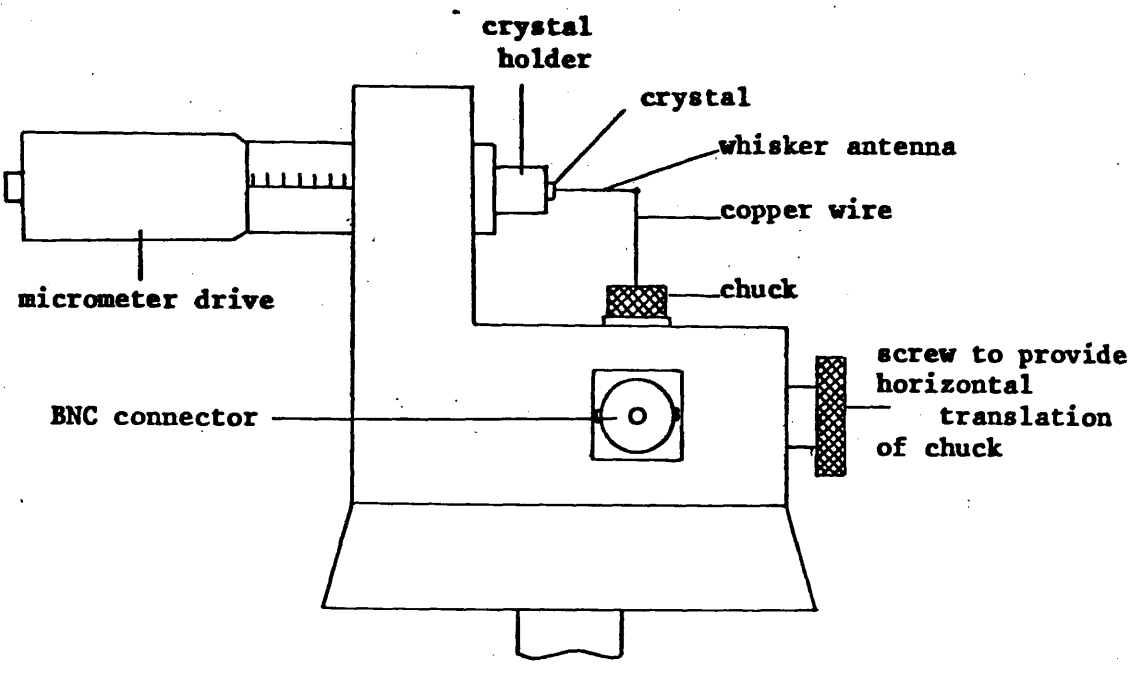

Figure 7.11. Antenna-diode detector mount

Repeated contact of the tungsten whisker on to the substrate resulted in a reduction of the output from the diode; however, the original sensitivity could be regained by resharpening the whisker point. Bending the point of the tungsten whisker, and hence increasing the area of contact on to the substrate, is demonstrated in Figure 7.10. The newly sharpened whisker is Figure 7.10(a) is shown after being brought into contact with a substrate in Figure 7.10(b), and after a further application in Figure 7.10(c). Loss of responsivity on blunting the whisker point was particularly noticeable with metal substrates, as it was usual to obtain no detectable output unless the whisker was freshly sharpened.

7.4.6. Experimental data

Forming diodes by making contact between a tungsten antenna and various samples of a particular material usually resulted in the same polarity of output on initial contact; however, some exceptions did occur. Haas and Thomas[77] have found that the work function of a polycrystalline sample of tungsten varies over its surface. This was explained by the metal surface being composed from regions of different compositions and different exposed crystal faces. The work function of the point of the tungsten wire is unknown, but by comparing its possible variation with the difference between the average values for the two electrodes would indicate whether polarity reversal may occur by contacting the whisker on different areas of the substrate. Hence, where possible, diode detectors were evaluated which had been constructed from substrates, the work functions of which had previously been measured.

7.4.6.1. Work function measurements

For substrates with a sufficiently large surface area, the work function was measured by Chandler using the vibrating capacitor method of measuring contact potential difference[78,79]. A slice of n-type silicon and evaporated films of gold and aluminium in turn formed one electrode of a parallel plate capacitor, while the second electrode was fabricated from a sheet of platinum foil. In the presence of an external circuit, the two plates acquire a potential difference equal to the work function difference of the two materials. A change in capacitance was produced by sinusoidally vibrating the substrate perpendicularly to the plane of the electrodes. This generated an alternating current in the circuit. This current was reduced to zero by application of a direct potential of opposite polarity to that across the capacitor, thus enabling the work function difference to be measured. By taking the work function of

platinum as 5.32 eV the work functions of the materials used in the present work were measured and are shown in Table 7.1. The values obtained for these samples were found to be in good agreement with published figures.

Table 7.1

Average work functions of the plane electrodes

Material	Present work	Published results	Reference
Aluminium	4.26 ± 0.02 eV	4.24 ± 0.03 eV	80
Gold	5.39 ± 0.03 eV	5.32 ± 0.1 eV	80
Silicon	4.85 ± 0.02 eV	4.85 ± 0.05 eV	80, 81

7.4.6.2. Responsivity

337 μm wavelength radiation was focused on to the window of a Golay cell of known responsivity. This enabled the power incident at the window to be calibrated against the output from a second Golay cell used as a monitor. The radiation to the monitor cell was coupled from the beam by a Melinex film. Placing the antenna of a diode detector at the point of convergence of the beam allowed values to be calculated for the voltage responsivity of the device. Plotted as a function of the resistance of a load in parallel with the diodes, Figures 7.12 and 7.13 show respectively the measured responsivities of M-O-M and M-O-semiconductor detectors. Responsivities obtained by making two separate point contacts on to a sample of n-type germanium and two contacts on to n-type silicon are displayed to illustrate the variability in performance produced by each construction of a diode. It is noted that the polarity of the output changed on re-application of the whisker to the n-silicon substrate. The output resistances of these devices were measured from the responsivity-load curves and are listed in Table 7.2.

7.4.6.3. Current-voltage characteristics

The small barrier area in point-contact diodes renders the devices susceptible to electrical damage. The current-voltage characteristics were therefore investigated by applying pulses of current to the diodes to limit the energy dissipated. The diodes were subjected to positive and negative going pulses, produced by using a transformer to differentiate a 900 Hz output from a square wave ocillator, as shown

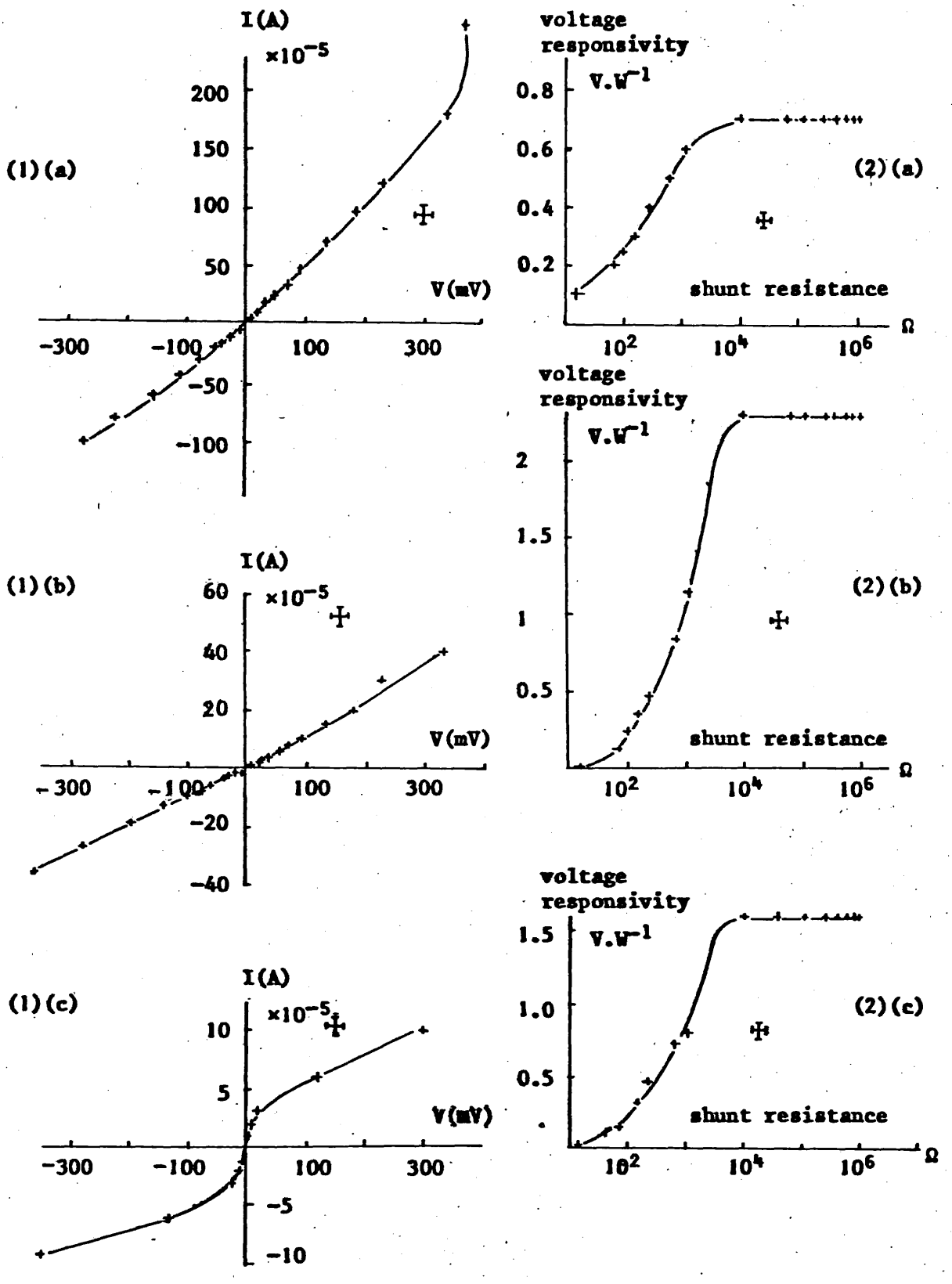

Figure 7.12. Experimentally measured properties of M-O-M point-contact diode detectors. (1) I-V characteristics, and (2) voltage responsivity for a tungsten antenna to (a) gold, (b) aluminium, and (c) tungsten. Crossed bars indicate uncertainty.

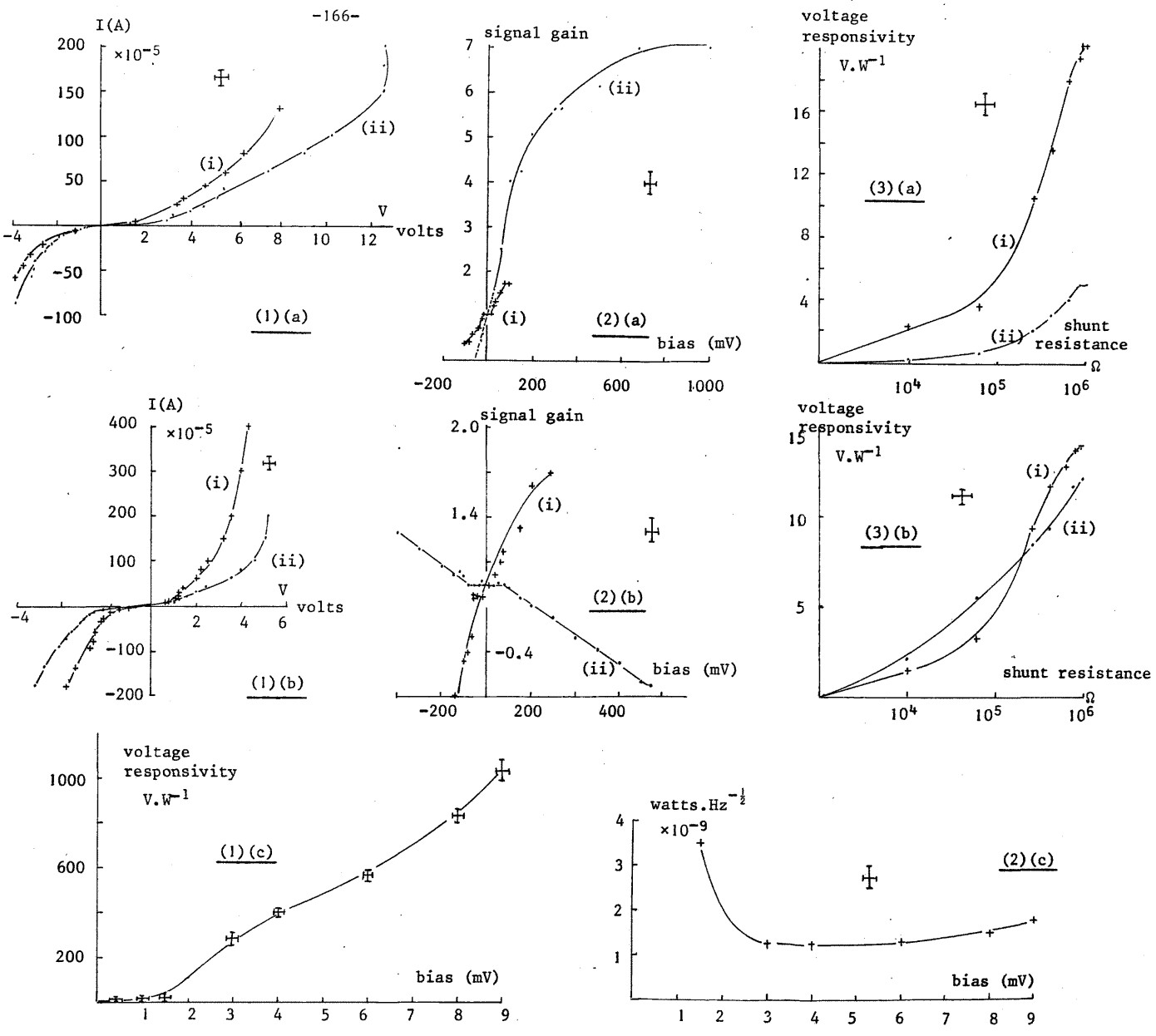

Figure 7.13. Experimentally measured properties of M-O-semiconductor point-contact diode detectors. (1) I-V characteristics; (2) voltage responsivity gain against bias; (3) voltage responsivity against shunt resistance for a tungsten antenna to (a) n-type germanium, and (b) n-type silicon. Two separate contacts, (i) and (ii), are shown for each semiconductor. Voltage responsivity against applied bias is shown in (1)(c) for a tungsten antenna to GaAs detector and the corresponding n.e.p. in (2)(c). Crossed bars indicate uncertainty.

Table 7.2

Measured zero bias resistance, output resistance and the upper limit of the n.e.p. of point-contact diode detectors

Diode	Zero bias resistance (ohms)	Output resistance (ohms)	Maximum n.e.p. (watts . $Hz^{-\frac{1}{2}}$)
W-Si	$(2.3 \pm 0.3) \times 10^4$	$(7.8 \pm 0.1) \times 10^5$	2.5×10^{-9} and 2.9×10^{-9}
W-Ge	$(4.5 \pm 0.3) \times 10^4$	$(3.2 \pm 0.1) \times 10^5$	1.5×10^{-9} and 7.2×10^{-9}
W-Au	220 ± 25	200 ± 15	5×10^{-8}
W-Al	930 ± 65	1100 ± 100	1.5×10^{-8}
W-W	770 ± 30	900 ± 30	2.2×10^{-8}

in Figure 7.14. Current-voltage characteristics obtained for tungsten-oxide-metal diodes are displayed in Figure 7.12 and tungsten-oxide-semiconductor diodes in Figure 7.13. Average values for the zero bias resistance were measured from the characteristics and are displayed in Table 7.2.

7.4.6.4. Biased diodes

The effect on the responsivity of a diode detector of applying a d.c. bias across its junction was investigated using the circuit of Figure 7.15. The variation of the response of tungsten to n-germanium and tungsten to n-silicon diodes with applied bias is given in Figure 7.13. The polarity of the bias voltage stated is that applied to the tungsten whisker and, as is shown, the incorrect polarity can reduce the diode output to an unmeasurable level. The most notable response was obtained from a detector formed by contacting a tungsten whisker on to an undoped sample of gallium arsenide. This device gave no observable output in an unbiased state, but with several millivolts of positive d.c. potential produced the largest responsivity of any of the detectors investigated, as seen from Figure 7.13.

No increase in output was obtained from the tungsten to metal diodes with applied d.c. bias.

7.4.6.5. Response time

Figures 7.12 and 7.13 show the reduction in responsivity produced by placing a shunt resistor across the detector. The addition of such a load is a useful technique for reducing the response time of the device and can be used to obtain the output resistance, as listed in Table 7.2. The tungsten to metal diodes have inherently the fastest response with

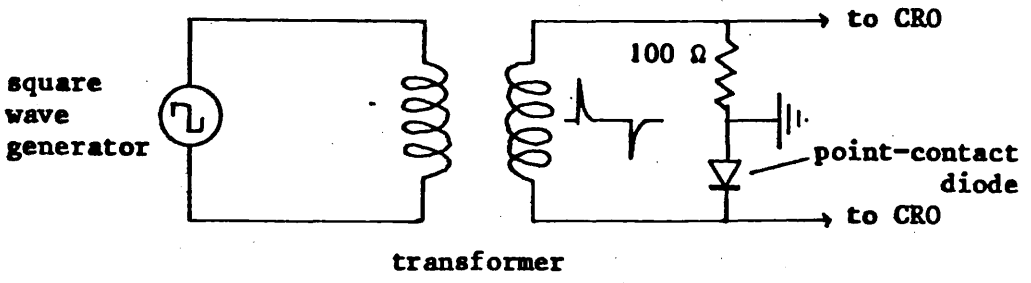

Figure 7.14. Circuit used to apply current pulses to point-contact diodes for measurements of I-V characteristics

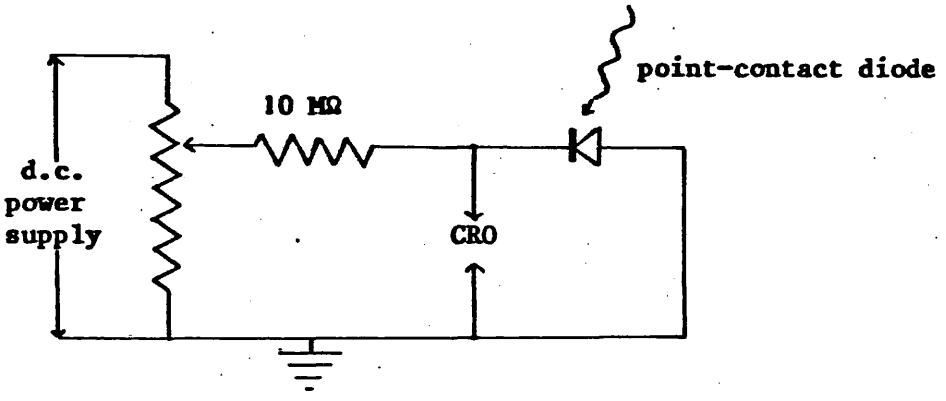

Figure 7.15. Circuit used to apply d.c. bias to point-contact diodes

an output resistance in the range 200 to 1000 ohms. When connected to an amplifier with a typical input capacitance of 10 pF, response times of 4.4×10^{-9} to 2.2×10^{-8} seconds can be expected. If greater responsivities are required, a tungsten to semiconductor diode would be necessary. With an output resistance of the order of 10^5 Ω, silicon and germanium diodes will have a response time of approximately 1 μs. However, Figure 7.13 indicates that the impedance, and hence the speed, could be reduced before the loss of responsivity became prohibitive.

7.4.6.6. Diode noise

For video detection, the observed noise is limited by the bandwidth of the system and it is usual to express the n.e.p. in terms of a 1 Hz bandwidth. The n.e.p. includes the parameters of voltage responsivity and the measured noise output voltage, the square of the latter being proportional to the bandwidth. The convention was therefore adopted of quoting the n.e.p. in units of watts . hertz$^{-\frac{1}{2}}$.

The noise output from the tungsten to metal and tungsten to silicon and germanium diodes was less than could be detected using a Tektronix 1A5 amplifier. Assuming a minimum observable signal to be 0.1 mV, the maximum possible noise values have been calculated for each diode, and listed in Table 7.2 as noise equivalent power in watts . hertz$^{-\frac{1}{2}}$. The upper limit for the values of n.e.p. quoted is greatest for the tungsten to metal diodes. This is misleading and is a result of the responsivity of the metal devices being lower than those of the semiconductor devices.

Observable noise was generated by the tungsten to undoped gallium arsenide diode. The n.e.p. is shown plotted against the bias potential in Figure 7.13, and is approximately an order of magnitude better than that reported for a tungsten to doped gallium arsenide diode[66].

7.5. Discussion

Comparison of the performance of the diode detectors with the theory reveals the similarity of reversal of the polarity of the output and the reduction in responsivity as the whisker is driven into the dielectric layer. The proposed model of a point-contact diode is supported by the experimental observations as the output is reproducible on application of the whisker to the substrate, and reversible on withdrawal. Random fluctuation of parameters affecting the diode performance during insertion of the whisker into the oxide, as for example variation in the work functions of the electrodes, are to a large extent ruled out. Further evidence for the validity of the model is

obtained from the experimental demonstration that the largest responsivity occurs at the largest barrier spacing and that once reversal has taken place, the output is smaller than that obtained previously. These observations indicate that once the whisker has made contact with the oxide, the work function of the substrate and the whisker appear reasonably constant as the tungsten tip gouges into the dielectric. The observed property that diodes made with different samples of a substrate material, and in some cases on different regions of the same sample, can produce a different output polarity on initial contact, can be explained by the analysis of Haas and Thomas[77]. As described earlier, Haas and Thomas showed that the value of the work function can vary across the surface of a material. By virtue of the nature of the technique used, the work function measurements of Chandler, described in section 7.4.6.1, are average values for the whole substrate surface. The small differences between the measured values and that of polycrystalline tungsten indicate that reversal of the polarity of the work function difference over localized regions of the substrate is probable. It must also be noted that there is a considerable difference between the values reported for the work function of the various crystal orientations of tungsten[80], as illustrated in Table 7.3

Table 7.3

Work function of tungsten at different crystal orientations

(after reference 80)

Crystal orientation	Work function (eV)
110	5.3 ± 0.12
111	4.4 ± 0.03
116	4.3 ± 0.03
100	4.6 ± 0.08

Assuming the typical size of the tip of an etched tungsten whisker[64,74] to be comparable with or smaller than the grain size[82], it is evident that with successive re-etching of the whisker, and bending of the whisker point, different crystal faces may be brought into contact with the substrate.

Although the theoretical model provides a good qualitative description of the experimental observations, the poor quantitative agreement requires explanation. Indeed, at typical input powers of several milliwatts, the high output voltages that would result from much of the range of responsivity shown in Figures 7.7 and 7.8 immediately indicate a source of error in the model. Not only would the theoretical conditions $V < (\Delta\Psi)/e$ and $V \leq (\phi_1)/e$ be invalid, but the rectified potential would exceed the dielectric strength of the barrier. The difference between the calculated and experimental values may also be attributed in part to the imperfect efficiency of the antenna. The problem of coupling the submillimetre radiation into the detector is one that has not been dealt with in this programme of work. It is also evident that the geometry of the whisker/tip will seldom be the idealized configuration depicted in Figure 7.5. A source of error may therefore exist, as Chow[75] showed that local perturbations in the electrode spacing can change the resistance by several orders of magnitude. It has also been assumed that well defined interfaces exist between the electrodes and a perfect dielectric. In a practical point-contact device the insulator is formed by atmospheric contamination and is deformed as pressure is applied to the whisker. Chen and Adler[83] showed that imperfections in the dielectric would singificantly reduce its resistance. It is also suggested that a poorly defined metal-insulator interface would reduce the height of the potential barrier and the effective width of the insulator. Figures 7.7 and 7.8 show the responsivity to be a strong function of these two parameters and indicate that further reduction in their values would predict a more realistic output. Since ϕ_1, $\Delta\Psi$ and the antenna efficiency were unmeasured, a large combination of numerical values for these parameters would be needed in order to simulate real conditions. For this reason, and that reduction of ϕ_1 and $\Delta\Psi$ is limited by the boundary conditions mentioned above, further adjustment of these parameters was not carried out. It is therefore evident that a continued evaluation of the diode model should include expressions for the tunnel and thermionic currents for lower barrier heights[72,73].

In addition to thermionic emission and quantum mechanical tunnelling, a more complete analysis should take account of thermally assisted electron tunnelling and field assisted tunnelling. Reproduced from the work of Pitt[84], Figure 7.16 shows a schematic representation of the four mechanisms. Although field assisted and thermally assisted tunnelling have not been considered in this work, it is thought probable that, if included, the model would continue to provide a qualitative description of the

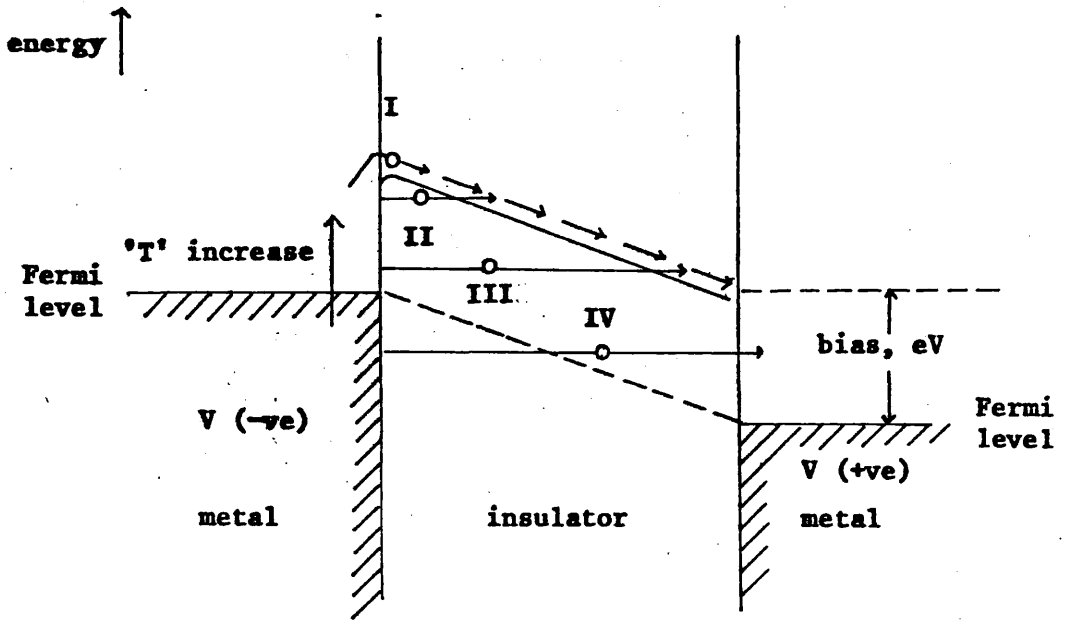

Figure 7.16. Schematic representation of a potential barrier showing current transport mechanisms. I, Schottky emission; II, thermally assisted tunnel current; III, field assisted tunnel current; IV, quantum-mechanical tunnel current. After Pitt[84].

experimentally observed characteristics. As before, this would require the rectification ratio to pass through unity as one mechanism is dominated by another. It may be postulated that both quantum mechanical tunnelling or field assisted tunnelling, enhanced by the high electric fields created at small electrode spacings, would give way at larger spacing to thermionic emission or thermally assisted tunnelling, which occur at lower fields. Thermally assisted tunnelling and thermionic emission have been shown by Roberts and Polanco[85] to possess similarly shaped current-voltage characteristics. The effect of including the additional current mechanisms would merely be to alter the shape and magnitude of the theoretical curves of Figures 7.7 and 7.8 and the thickness of the dielectric at which polarity reversal takes place.

An indication of the operational range of the various devices investigated can be obtained from the experimental data displayed in Table 7.2. The values of the zero bias resistance calculated from the slope at the origin of the current-voltage curves in Figure 7.12 are in close agreement with the output resistance found from the corresponding graphs of responsivity against load. These measurements indicate values in the region 200 to 1000 Ω as typical for M-O-M diodes. Since the spreading resistance will be low for metals, these values will be used as the resistance of the oxide barrier. Using 0.1 μm as a typical value for the diameter of an electrolytically etched tungsten wire and a spacing of 50 Å in an insulator of dielectric constant of 8, an approximate value can be assigned to the capacitance of a point-contact diode of 10^{-16} farads. Using equation 7.7 and a spreading resistance of 1 Ω for a metal substrate, the -3 dB point for an M-O-M device is calculated to be between 4.5 THz and 100 THz. Using typical output resistances of tungsten to n-silicon and n-germanium diodes, as given in Table 7.2 as the spreading resistance, and the same values for barrier resistance and capacitance as previously calculated, and a dielectric constant of 4.5[86], the corner frequency is now found to be in the region of 15 THz.

CHAPTER EIGHT

MAGNETO-OPTICS OF SOLIDS

8.1. Introduction

Reference was made in Chapter One to the work of Birch and Jones[11] who demonstrated the use of Faraday rotation to modulate 337 μm radiation. The description and analysis of sections 4.2.2 and 4.2.3 on the feasibility of using such a modulator as a Q-switching technique led to a study of magneto-optical properties of magnetic garnets at this wavelength.

The tensor components of magnetic materials at microwave frequencies were derived by Polder[87] to explain the Faraday effect in ferrites, a technique similar to that employed for the optical region. Expressions for the components of the permeability of ferrites will be extended in this chapter to include those solid state properties important at far infrared frequencies.

8.2. Electromagnetic propagation in magnetic media

Lax and Button[88] considered a plane electromagnetic wave with magnetic vector $\underline{h}$ to pass through a magnetically anisotropic medium of negligible electrical conductivity, permeability tensor $\bar{\mu}$ and a scalar dielectric permittivity ε. The propagation of an electromagnetic plane wave was then described by the Maxwell equations

$$\left.\begin{aligned} \nabla \wedge \underline{E} &= -j\omega\bar{\mu} \cdot \underline{h} \\ \text{and} \qquad \nabla \wedge \underline{h} &= j\omega\varepsilon\underline{E} \end{aligned}\right\} \qquad \ldots(8.1)$$

For a medium infinite in extent, an $e^{j\omega t}$ time dependence for $\underline{h}$ and for the electric field vector $\underline{E}$ was assumed. Removing $\underline{E}$ from the equations

$$\nabla \wedge \nabla \wedge \underline{h} = \omega^2 \varepsilon \bar{\mu} \cdot \underline{h}$$

was obtained and expressed as

$$-\nabla^2 \underline{h} + \nabla(\nabla . \underline{h}) = \omega^2 \varepsilon \bar{\mu} \cdot \underline{h} \qquad \ldots(8.2)$$

Defining a propagation constant for the wave by the complex quantity

$$\Gamma = \alpha + j\beta \qquad \ldots(8.3)$$

the magnetic vector of the wave had the solution

$$\underline{h} = \underline{h_0}\, e^{-\Gamma(\underline{n}.\underline{r})}$$

in which $\underline{r}$ was the displacement vector and $\underline{n}$ the unit vector in the direction of propagation. Substituting this solution into equation 8.2 gave

$$\Gamma^2\{-n^2\underline{h} + (\underline{n}.\underline{h})n\} = \omega^2\varepsilon\bar{\mu} \cdot \underline{h} \qquad \ldots(8.4)$$

In later analysis, a general solution of this equation will be required in which no restriction is placed on the relative orientations of the magnetisation and the direction of propagation of the electromagnetic wave. Hence, using equation 8.4 and expressing $\underline{h}$ in Cartesian coordinates and $\bar{\mu}$ as a 3 × 3 matrix, three component equations are obtained

$$h_x\left[(-n^2+n_x^2)\Gamma^2-\mu_0\omega^2\varepsilon\mu_{xx}\right]+h_y\left[n_xn_y\Gamma^2-\mu_0\omega^2\varepsilon\mu_{xy}\right]+h_z\left[n_xn_z\Gamma^2-\mu_0\omega^2\varepsilon\mu_{xz}\right] = 0$$

$$h_x\left[n_yn_x\Gamma^2-\mu_0\omega^2\varepsilon\mu_{yx}\right]+h_y\left[(-n^2+n_y^2)\Gamma^2-\mu_0\omega^2\varepsilon\mu_{yy}\right]+h_z\left[n_yn_z\Gamma^2-\mu_0\omega^2\varepsilon\mu_{yz}\right] = 0$$

$$h_x\left[n_zn_x\Gamma^2-\mu_0\omega^2\varepsilon\mu_{zx}\right]+h_y\left[n_zn_y\Gamma^2-\mu_0\omega^2\varepsilon\mu_{zy}\right]+h_z\left[(-n^2+n_z^2)\Gamma^2-\mu_0\omega^2\varepsilon\mu_{zz}\right] = 0$$

$\ldots(8.5)$

The determinant of the coefficients of these three homogeneous linear equations in h_x, h_y and h_z can be equated to zero and the evaluation simplified by defining the direction of propagation of the wave to be along the Z direction. Thus

$$n_x = n_y = 0 \quad \text{and} \quad n_z = 1$$

and the determinant reduces to

$$\mu_{zz}\Gamma^4+\mu_0\omega^2\varepsilon\left[\mu_{yy}\mu_{zz}+\mu_{xx}\mu_{zz}-\mu_{xz}\mu_{zx}-\mu_{yz}\mu_{zy}\right]\Gamma^2$$

$$-(\mu_0\omega^2\varepsilon)^2\left[\mu_{xx}\mu_{yy}\mu_{zz}+\mu_{xx}\mu_{yz}\mu_{zy}-\mu_{xz}\mu_{yx}\mu_{zy}+\mu_{xz}\mu_{yy}\mu_{zx}+\mu_{xy}\mu_{yx}\mu_{zz}-\mu_{xy}\mu_{yz}\mu_{zx}\right]=0$$

Making the substitutions B and C such that the above equation becomes

$$\mu_{zz}\,\Gamma^4 + \mu_0\omega^2\varepsilon B\Gamma^2 - (\mu_0\omega^2\varepsilon)^2\, C = 0$$

then the biquadratic equation in Γ shows two propagation modes given by

$$\Gamma^2_{\pm} = -\frac{\mu_0\omega^2\varepsilon}{2}\left[B \pm (B^2 + 4C)^{\frac{1}{2}}\right] \qquad \ldots(8.6)$$

These two modes can be represented in a form used by Lax and Button[88] by defining two complex scalar permeabilities as

$$\left.\begin{aligned} \mu_+ &= B + \left[B^2 + 4C\right]^{\frac{1}{2}} = \mu'_+ - j\mu''_+ \\ \text{and} \qquad & \\ \mu_- &= B - \left[B^2 + 4C\right]^{\frac{1}{2}} = \mu'_- - j\mu''_- \end{aligned}\right\} \qquad \ldots(8.7)$$

Using the definition of Γ expressed in equation 8.3 with the permeabilities in 8.7, Lax and Button show that the real and imaginary parts of $\Gamma_{\pm}$ yield the simultaneous equations

$$\beta^2_{\pm} - \alpha^2_{\pm} = \frac{\mu_0\omega^2\varepsilon}{2}\,\mu'_{\pm}$$

and

$$2\alpha_{\pm}\beta_{\pm} = \frac{\mu_0\omega^2\varepsilon}{2}\,\mu''_{\pm}$$

which can be solved to give

$$\left.\begin{aligned} \alpha_{\pm} &= \tfrac{1}{2}(\mu_0\omega^2\varepsilon)^{\frac{1}{2}}\left[(\mu'^2_{\pm} + \mu''^2_{\pm})^{\frac{1}{2}} - \mu'_{\pm}\right]^{\frac{1}{2}} \\ \text{and} \qquad & \\ \beta_{\pm} &= \tfrac{1}{2}(\mu_0\omega^2\varepsilon)^{\frac{1}{2}}\left[(\mu'^2_{\pm} + \mu''^2_{\pm}) + \mu'_{\pm}\right]^{\frac{1}{2}} \end{aligned}\right\} \qquad \ldots(8.8)$$

8.3. Magneto-optical effects

The optical properties of prime concern in this investigation are those of Faraday rotation and the associated losses. The necessary experimental configuration is one in which the magnetic field applied to the specimen is parallel to the propagation direction of the electromagnetic wave. In this situation, the net magnetic moment of the dipoles is often considered to be aligned along the propagation direction, which if defined as the Z-direction, leads to a simplified expression for the permeability tensor as

$$\bar{\mu} = \mu_0 \begin{bmatrix} \mu & -j\kappa & 0 \\ j\kappa & \mu & 0 \\ 0 & 0 & 1 \end{bmatrix}$$

a form referred to as the Polder tensor[87]. Introducing the elements of this matrix into equation 8.4 with the condition that $h_z = 0$, Lax and Button[88] show the relationship between h_x and h_y to be

$$h_x = \pm j h_y$$

This solution represents two circularly polarised waves, which gives a value of the propagation constant for each polarisation as

$$\Gamma_{\pm}^2 = -\omega^2 \varepsilon \mu_0 (\mu \pm \kappa)$$

The positive and negative signs denote the opposite directions of rotation of the two waves and as with the general case, two scalar permeabilities can be expressed in terms of their real and imaginary parts

$$\left.\begin{aligned} \mu_+ &= \mu_+' - j\mu_+'' = \mu + \kappa \\ \text{and} \\ \mu_- &= \mu_-' - j\mu_-'' = \mu - \kappa \end{aligned}\right\} \quad \ldots(8.9)$$

These can be used in 8.8 to calculate the components of the propagation constants which, in general, will be different for the two counter-rotating waves. Thus after travelling a distance d into the medium, each component will have rotated through a different angle θ^+ and θ^- with respect to the polarisation of the initial plane wave. The real part of the propagation constant is defined as the attenuation constant of the wave while the imaginary part is the phase constant[88]. Assuming equal attenuation for each of the two components, the net rotation of the plane polarised beam, illustrated in Figure 8.1, will be

$$\theta_F = \frac{\theta^- - \theta^+}{2} = \frac{d}{2}(\beta_- - \beta_+) \text{ radians per unit length} \quad \ldots(8.10)$$

This quantity is referred to as the Specific Faraday rotation. It is desirable to use a Faraday rotation device in a region of low absorption loss. Evaluation of the attenuation constant α cm^{-1}, and the Faraday rotation per centimetre θ_F, in a material enables a figure of merit to be calculated by defining

$$F = \left| \frac{\theta_F}{\alpha} \right| \quad \ldots(8.11)$$

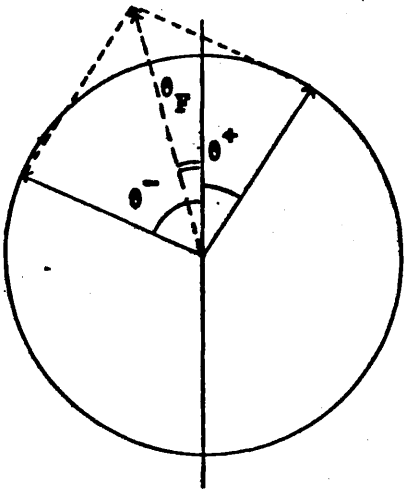

Figure 8.1. Nett rotation θ_F of the plane of polarisation of a wave due to unequal phase constants of the two counter-rotating components

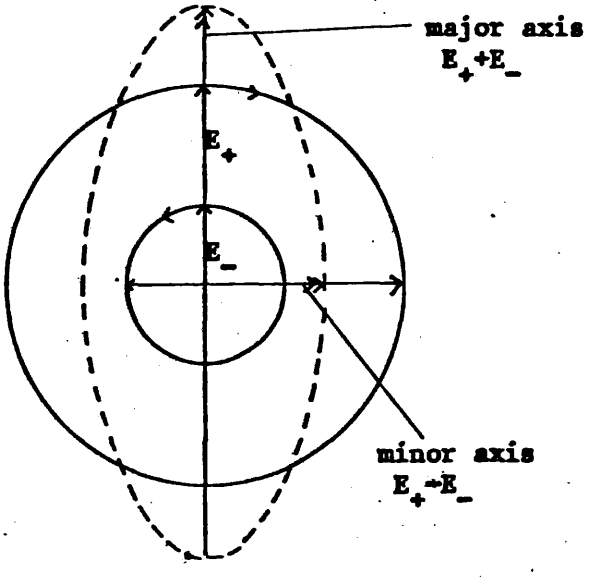

Figure 8.2. Elliptically polarised wave caused by unequal attenuation of the two counter-rotating components

A situation can arise in which the two oppositely rotating waves experience unequal attenuation which results in the production of an elliptically polarised transmitted beam, as illustrated in Figure 8.2. The existence of a component of the electric field orthogonal to the rotated polarisation will reduce the modulation depth attainable from a rotation device. Thus a measure of the ellipticity produced by a material is a further parameter necessary for evaluating the usefulness of a material for a Faraday rotation device. Ellipticity is defined in terms of the electric field components E_+ and E_- shown in Figure 8.2, as

$$\varepsilon = \frac{E_+ - E_-}{E_+ + E_-}$$

which can be expressed as

$$\varepsilon = \frac{E_0(e^{-\alpha_+ d} - e^{-\alpha_- d})}{E_0(e^{-\alpha_+ d} + e^{-\alpha_- d})} \simeq (\alpha_- - \alpha_+)\frac{d}{2} \qquad \ldots(8.12)$$

8.4. Sublattice interaction

It has been shown that ellipticity and Faraday rotation may be respectively described in terms of $\alpha_\pm$ and $\beta_\pm$, which in turn can be expressed as functions of the permeability tensor. A study will therefore be undertaken of the dependence of the elements of this tensor on the properties of magnetic materials. This will be approached by examining the action on the constituent magnetic dipoles of the medium by the various fields present. To pursue this investigation, a description and mathematical formulation of the internal magnetic fields of a solid are reviewed.

8.4.1. Internal fields

8.4.1.1. Exchange field

The Weiss molecular field[89] resulting from the interaction between the electron spins of two magnetic dipoles is explained in terms of the quantum-mechanical exchange force. The energy ε_{EX} between two ions having spins $\underline{S_i}$ and $\underline{S_J}$ was shown by Heisenberg[90] to be

$$\varepsilon_{EX} = -2J_e \, \underline{S_i} \cdot \underline{S_J}$$

J_e being the exchange integral which is interpreted as a measure of the overlap of the electronic charge distributions. The mutual electro-

static repulsion of the two distributions is responsible for the alignment of the two spins. The exchange interaction is a short range force, the wave functions of the electrons decreasing rapidly with distance from the ion, causing the exchange integral to be a sensitive function of the separation. J_e is negligible at large inter-ionic distances, the substance being paramagnetic. However, at smaller spacings, the integral increases in magnitude with the result that stronger parallel alignment ensues giving the materials a ferromagnetic character. At still smaller separations J_e becomes negative, causing the magnetic dipoles of adjacent interacting ions to align themselves anti-parallel. The exchange interaction will be taken into account here by introducing the Weiss molecular field in a form proposed by Néel[91] in which the field experienced by a dipole is proportional to the magnetisation of the dipole with which it is interacting. This will be written in the form

$$\underline{H}_E = \lambda \underline{M}$$

where λ is described as the molecular field constant, and $\underline{M}$ represents the magnetisation of the second dipole.

8.4.1.2. Magnetic anisotropy

It has been found experimentally that some materials are easier to magnetise in a certain crystallographic direction than in others. This property is called magnetic anisotropy and causes preferential alignment of the magnetic dipoles along this direction, which has the effect of presenting an additional field to the magnetic sublattice. Crystal directions which are saturated by relatively low magnetic fields are termed 'easy' directions of magnetisation, whilst directions needing higher fields are denoted as 'hard' directions of magnetisation. The difference in energy needed to saturate a material in the easy and hard directions is called the anisotropy energy. In a cubic system, the expression

$$\varepsilon_A = K_1(\alpha_1^2\alpha_2^2 + \alpha_2^2\alpha_3^2 + \alpha_3^2\alpha_1^2) + K_2\alpha_1^2\alpha_2^2\alpha_3^2$$

is used to describe this anisotropy energy ε_A[88], where α_1, α_2 and α_3 are the direction cosines of the magnetisation with respect to the [100] type directions, and K_1 and K_2 are anisotropy constants.

The concept of anisotropy field can be introduced as a field $\underline{H}_A$ which

tends to align the magnetisation $\underline{M}$ along an easy direction by creating a torque $\underline{T}_A$ on the dipoles according to the relation

$$\underline{T}_A = \frac{d\varepsilon_A}{d\theta} \cdot \hat{\underline{n}} = \underline{M} \wedge \underline{H}_A$$

where θ is the angle of rotation about an axis parallel to the $\underline{M} \wedge \underline{H}_A$ vector and $\hat{\underline{n}}$ is the unit vector in the direction of $\underline{T}_A$. This equation however does not uniquely define $\underline{H}_A$ as $\hat{\underline{n}}$ is unknown. In the current analysis, the method of Kittel[92] is used in which the anisotropy field is expressed in terms of effective demagnetisation factors, so that $\underline{H}_A$ in component form becomes

$$\underline{H}_x^A = - N_x^A M_x \hat{\underline{i}}; \quad \underline{H}_y^A = - N_y^A M_y \hat{\underline{j}}; \quad \underline{H}_z^A = - N_z^A M_z \hat{\underline{k}} \qquad \ldots(8.13)$$

8.4.1.3. Demagnetising field

A specimen placed in an external field becomes polarised and the magnetic dipoles induced on its surface reduce the effective field strength within the sample. This effect will be treated mathematically as a demagnetising field and can be expressed[92,93] as

$$\underline{H}_D = - 4\pi N \underline{M} \qquad \ldots(8.14)$$

N being the demagnetising factor, its value being dependent on the shape of the sample. A particular case which will be used in later analysis is that of the thin slab in which the Z axis, the direction of the applied field, is perpendicular to the broad face of the crystal. Here the components of the demagnetisation factor have values[88] of

$$N_x = N_y = 0 \quad ; \quad N_z = 1 \qquad \ldots(8.15)$$

8.4.2. Precessional motion

The mathematical description of the elements of the susceptibility tensor that follows is applicable to materials composed of more than one magnetic site. In such a medium, each type of magnetic ion, situated at a specific crystallographic site, forms part of a sublattice. Many magnetic media, including the ferrimagnetic garnets which will be studied later, are described by a multi-sublattice model[94].

The simple equation of the precessional motion of a magnetic dipole of magnetic moment $\underline{M}_i$ situated in a magnetic field $\underline{H}_i$ is

$$\frac{d\underline{M}_i}{dt} = \gamma_i(\underline{M}_i \wedge \underline{H}_i) \qquad \ldots(8.16)$$

This equation refers to the motion of one specific sublattice system denoted by the subscript i. The gyromagnetic ratio γ_i of the dipoles in this subsystem, defined as the ratio of the magnetic moment of the dipole to its angular momentum, is expressed in gaussian units as

$$\gamma_i = g_i \frac{e}{2mc} \qquad \ldots(8.17)$$

m being the electronic mass, e the electronic charge, c the velocity of light in free space and g_i the spectroscopic splitting factor of the sublattice. $\underline{H}_i$ is the vectorial sum of all magnetic fields acting on a dipole in the i^{th} sublattice. The components of this field which originate from the magnetisation of other sublattices produce a collection of coupled subsystems. This coupling can, in the case of ferrimagnetic media, provide the major contribution to $\underline{H}_i$.

Equation 8.16 does not allow for losses incurred by the precessing dipoles. To take this into account, a 'damping' term proportional to $\underline{M}\wedge(\underline{M}\wedge\underline{H})$ can be introduced, This is a vector orientated in the direction required to supply a retarding torque to the motion. An accurate assumption can be made for tightly coupled systems that $|\underline{M}|$ remains constant[95] so that $d\underline{M}/dt$ lies in the plane perpendicular to $\underline{M}$. This allows the vectors $\underline{M}\wedge\underline{H}$ and $\underline{M}\wedge(\underline{M}\wedge\underline{H})$ to be combined linearly and so, by introducing a damping coefficient α_i, an expression can be written

$$\frac{d\underline{M}_i}{dt} = \gamma_i(\underline{M}_i \wedge \underline{H}_i) - \alpha_i \underline{M}_i\wedge(\underline{M}_i \wedge \underline{H}_i) \qquad \ldots(8.18)$$

This equation was derived by Landau and Lifshitz[95] to represent the motion of a lossy system and it will be used here to obtain the susceptibility elements of magnetic media. The coefficient α_i has dimensions of the inverse of angular momentum and is expressed as[88]

$$\alpha_i = \frac{\gamma_i}{\omega\, T_i |M_i|} \qquad \ldots(8.19)$$

in which ω is the angular frequency of the probing radiation, and T_i is introduced as the spin lattice relaxation time of the sublattice.

For the microwave frequency region, it is possible to simplify the theory and regard a ferrimagnet to have the properties of a ferromagnet by

considering only the net magnetic moment of the system

$$\underline{M} = \sum_i \underline{M}_i$$

and by defining an effective gyromagnetic ratio as

$$\gamma_{EFF} = \frac{\sum_i M_i}{\sum_i \left(\frac{M_i}{\gamma_i} \right)}$$

Before describing a relationship for the spin lattice relaxation time in terms of parameters which are measurable at microwave frequencies, the reasons for treating multi-sublattice systems differently in different spectral regions will be outlined.

Consider the simplified undamped motion formulated in equation 8.16 for a two-sublattice system. Lax and Button[88] show that

$$\left.\begin{aligned} j\omega \underline{m}_1 &= \gamma_1 (\underline{M}_1 + \underline{m}_1) \wedge (\underline{H}_1 + \underline{h}) \\ \text{and} \\ j\omega \underline{m}_2 &= \gamma_2 (\underline{M}_2 + \underline{m}_2) \wedge (\underline{H}_2 + \underline{h}) \end{aligned}\right\} \quad \ldots(8.20)$$

where

$$\underline{H}_1 = (H_0 + H_{A_1} + \lambda M_2)\, \hat{\underline{k}}$$

and

$$\underline{H}_2 = (H_0 - H_{A_2} - \lambda M_1)\, \hat{\underline{k}}$$

The r.f. components of the gyrating magnetic dipoles and the magnetic component of the probing radiation are assumed to vary as

$$\underline{m}_i = \underline{m}_{0_i}\, e^{j\omega t}$$

$$\underline{h} = \underline{h}_0\, e^{j\omega t}$$

respectively. The magnetic fields at the dipoles, $\underline{H}_1$ and $\underline{H}_2$, result from the addition of the applied field $H_0\hat{\underline{k}}$, the anisotropy fields $H_{A_1}\hat{\underline{k}}$ and $-H_{A_2}\hat{\underline{k}}$, and the exchange fields $\lambda M_2\hat{\underline{k}}$ and $-\lambda M_1\hat{\underline{k}}$. Equations 8.20 can be expressed in terms of the x and y components of $\underline{m}_1$ and $\underline{m}_2$, resulting in four equations in m_{1x}, m_{1y}, m_{2x} and m_{2y}. A simplified mathematical interpretation of the situation is described by defining circularly rotating quantities[88]

$$m_i^{\pm} = m_{ix} \pm jm_{iy}$$

and

$$h^{\pm} = h_x \pm jh_y$$

$m_1^{\pm}$ and $m_2^{\pm}$ can be solved in terms of the common r.f. magnetic field such that

$$m_1^{\pm} = \frac{\{\omega_2 \pm \omega + \lambda\gamma_2 M_2\}\gamma_1 M_1 h^{\pm}}{\Delta\pm}$$

$$m_2^{\pm} = \frac{-\{\omega_1 \pm \omega - \lambda\gamma_1 M_1\}\gamma_2 M_2 h^{\pm}}{\Delta\pm}$$

$$\Delta_{\pm} = \{\omega \pm \omega_1\}\{\omega \pm \omega_2\} + \lambda^2\gamma_1\gamma_2 M_1 M_2 \qquad \ldots(8.21)$$

where

$$\omega_1 = \gamma_1\{H_0 + H_{A_1} + \lambda M_2\}$$

and

$$\omega_2 = \gamma_2\{H_0 - H_{A_2} - \lambda M_1\}$$

The solutions of these equations for the two senses of circular polarisation yield both negative and positive values for the frequency and are shown by Lax and Button to represent different modes of precession. Two resonance conditions are found by solving the secular equation obtained from the third relation of equations 8.21 as

$$\omega^2 \pm \{\omega_1 + \omega_2\}\omega + \omega_1\omega_2 + \lambda^2\gamma_1\gamma_2 M_1 M_2 = 0$$

The low (ω_+) and the high (ω_-) value solutions are referred to as the resonance values of the ferromagnetic and ferrimagnetic modes respectively. These two situations can be examined separately by using the equations 8.21 to obtain the ratio

$$\frac{m_1^{\pm}}{m_2^{\pm}} = \frac{-\{\omega_2 + \lambda\gamma_2 M_2 \pm \omega\}\gamma_1 M_1}{\{\omega_1 - \lambda\gamma_1 M_1 \pm \omega\}\gamma_2 M_2}$$

Considering the ferromagnetic case, the simplifications $\omega_2 \simeq -\gamma_2\lambda M_1$ and $\omega_1 \simeq \gamma_1\lambda M_2$ are made, and the low-frequency limit can be expressed by

$$\omega_+ << \lambda\gamma M$$

so $$\frac{m_1^{\pm}}{m_2^{\pm}} = -\frac{M_1}{M_2}$$

This implies that the two dipoles are aligned and precess in the same direction, so at low frequencies a ferrimagnet can be studied using the single sublattice model. This treatment enables the precession to be expressed by

$$\omega = \gamma_{EFF} H_{1,2} \qquad \ldots(8.22)$$

showing that the sense of rotation is determined by the sign of γ_{EFF}, which is generally negative and therefore counter-clockwise.

To evaluate the high frequency case let

$$\Delta_{\pm} \to 0$$

then

$$\omega_2 \pm \omega = -\frac{\lambda^2 \gamma_1 \gamma_2 M_1 M_2}{\omega_1 \pm \omega}$$

The first two equations of 8.21 now yield

$$\frac{m_1^{\pm}}{m_2^{\pm}} = -\frac{\gamma_1}{\gamma_2} = -\frac{M_2}{M_1}$$

This shows that

$$\frac{m_1}{m_2} \neq \frac{M_1}{M_2}$$

and so the angles of inclination of each of the dipoles to the direction of the field about which they gyrate are different. $\underline{M}_1$ and $\underline{M}_2$ are again rotating in the same sense, but in a clockwise direction. The two modes are illustrated vectorially in Figure 8.3.

Having shown that ferromagnetic resonance can occur at low frequencies, it is now possible to form an expression for the spin lattice relaxation time in terms of measurable quantities. The loss term is introduced by applying the Landau-Lifshitz equation, 8.18, to the simple single lattice model. Again considering the applied field $\underline{H}_0$, the magnetisation $\underline{M}$ and the propagation of the electromagnetic beam to be directed along the Z axis, but neglecting anisotropy and the shape of the specimen, 8.18 expressed in component form enables m_x and m_y to be written in terms of h_x and h_y. The elements of the susceptibility tensor obtained

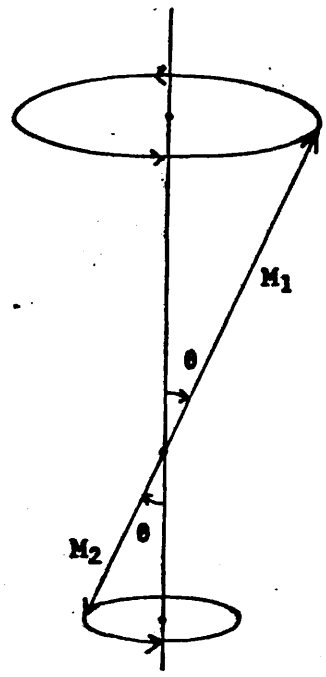

(a)

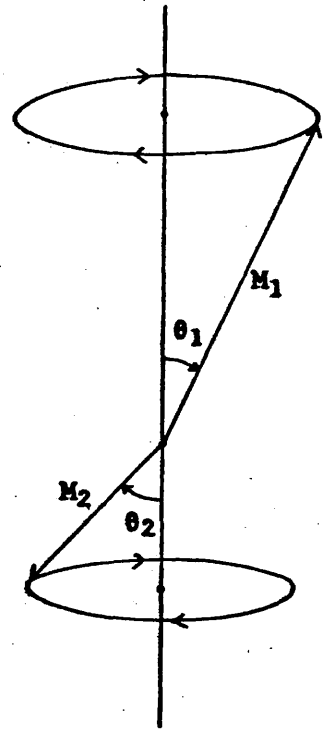

(b)

Figure 8.3. (a) The low frequency ferromagnetic mode, and (b) the high frequency exchange mode of precession in a double sublattice system. Reproduced from Geschwind and Walker[121].

in this way are shown by Lax and Button to be

$$\chi_{xx} = \chi_{yy} = \frac{\{\omega_0 + j/_T\}\omega_M}{\{\omega_0 + j/_T\}^2 - \omega^2}$$

and

$$\chi_{yx} = -\chi_{xy} = \frac{j\omega\omega_M}{\{\omega_0 + j/_T\}^2 - \omega^2}$$

in gaussian units where $\omega_M = 4\pi\gamma M$ and $\omega_0 = \gamma H_0$ and T is the spin lattice relaxation time. As with the undamped case, it is convenient to describe the situation in terms of two counter-rotating electromagnetic fields and allocate a susceptibility parameter to each polarisation. Writing the susceptibility tensor as

$$\chi_{\pm} = \chi_{xx} \pm j\chi_{xy} = \chi'_{\pm} - j\chi''_{\pm}$$

for the two senses of circular polarisation, and inserting into the expressions for χ_{xx} and χ_{xy}, χ''_{+} is found to be

$$\chi''_{+} = \frac{\omega_M T}{\{\omega_0 - \omega\}^2 T^2 + 1}$$

This is seen to have a singularity at $\omega = \omega_0$. An expression can now be found for T in terms of the change in the applied field ΔH, required to scan across the half-width of the absorption line. Substituting the definition of the half-width

$$\chi''_{+\,\omega_0 \pm \Delta\omega} = \tfrac{1}{2}\,\chi''_{+\,\omega_0}$$

in the above expression, $\chi''_{+\omega_0}$ being the peak value of χ''_{+}, and defining

$$\omega - \omega_0 = \Delta\omega/2$$

the condition

$$\Delta\omega = \frac{2}{T} = \gamma \cdot \Delta H \qquad \ldots(8.23)$$

is obtained. Reference to data obtained using this expression and whether such data are applicable at submillimetre frequencies will be be made in later chapters.

8.4.3. Susceptibility of double sublattice systems

8.4.3.1. Anti-parallel subsystems

It has been shown that interaction between ferrimagnetic media and electromagnetic radiation at high frequencies cannot be treated as a simple single lattice interaction as can the lower frequency ferromagnetic case. To derive a realistic model, loss terms must be considered while introducing the major fields acting on the magnetic dipoles. Analysis of this problem was performed by Wangsness[96] for a double sublattice system by considering only the externally applied field and the exchange fields. The equations

$$\underline{H}_1 = \underline{H}_0 + \lambda\underline{M}_2 \qquad \text{and} \qquad \underline{H}_2 = \underline{H}_0 + \lambda\underline{M}_1$$

were substituted into the Landau - Lifshitz equation 8.18 and the applied field orientated in the Z-direction so that $H_0 = H_z$ and the assumption was made that $M_{i_z} \simeq M_i$. Again the r.f. components of H_x, H_y, M_x and M_y were expressed as being proportional to $e^{j\omega t}$. To simplify his equations, Wangsness expanded his expressions in powers of λ^2, the coefficients of higher orders being zero. Frayne[13] demonstrated that including terms in λ only added H_0 to existing terms in λM which could be justified by assuming $H_0 << \lambda M$, but that the omission of certain terms of zero order of λ removed quantities involving the molecular field coefficient from the calculation. The result is that the model is accurate only at low frequencies. In a more rigorous analysis, the basic equations of Wangsness were expanded by Frayne to include the zero and first order terms in λ and expressions were derived for the real and imaginary parts of the elements of the susceptibility tensor which are shown in Figure 8.4.

8.4.3.2. Canted subsystems

The evaluation above has described a situation in which the sublattice magnetisation vectors are aligned with the externally applied field. However, for the general case, the fields present within the material may orientate the magnetic dipoles away from the external field. This concept was introduced in section 8.4.1.2 on anisotropy, where it was stated that a torque exerted on the magnetic vectors tended to rotate them towards the easy directions of magnetisation. The situation is now considered where the applied and exchange fields together with the anisotropy and demagnetisation fields are taken into account. A double sublattice system is analysed, its constituent dipole moments being

$$\chi_{xy}' = \frac{\omega\{\omega_e^2\gamma_{eff}M - \omega^2(\gamma_1M_1+\gamma_2M_2)\} + \dfrac{4\omega^3\omega_e^2M(\alpha_1\gamma_2+\alpha_2\gamma_1)\{S_1S_2/(S_1+S_2)\}^2\{\omega_e\omega_0(S_1^2\alpha_1+S_2^2\alpha_2)/S_1S_2 - \omega^2(\alpha_1+\alpha_2)\}}{\{\omega^2-\omega_e(\omega+\omega_0)\}\{\omega^2+\omega_e(\omega-\omega_0)\}}}{\{\omega^2-\omega_e(\omega+\omega_0)\}\{\omega^2+\omega_e(\omega-\omega_0)\} + \dfrac{4\omega^2\omega_e^2\{S_1S_2/(S_1+S_2)\}^2\{\omega_e\omega_0(S_1^2\alpha_1+S_2^2\alpha_2)/S_1S_2 - \omega^2(\alpha_1+\alpha_2)\}^2}{\{\omega^2-\omega_e(\omega+\omega_0)\}\{\omega^2+\omega_e(\omega-\omega_0)\}}}$$

$$\chi_{xx}' = \frac{\omega_e^2\gamma_{eff}^2MH - \omega^2H(\gamma_1^2M_1+\gamma_2^2M_2) + \dfrac{2\omega^2\omega_e\{S_1S_2/(S_1+S_2)\}\{\omega_e\omega_0(S_1^2\alpha_1+S_2^2\alpha_2)/S_1S_2 - \omega^2(\alpha_1+\alpha_2)\}\{\omega^2\gamma_{eff}^2(\alpha_1S_1^2+\alpha_2S_2^2) - \omega^2(\alpha_1M_1^2+\alpha_2M_2^2)\}}{\{\omega^2-\omega_e(\omega+\omega_0)\}\{\omega^2+\omega_e(\omega-\omega_0)\}}}{\{\omega^2-\omega_e(\omega+\omega_0)\}\{\omega^2+\omega_e(\omega-\omega_0)\} + \dfrac{4\omega^2\omega_e^2\{S_1S_2/(S_1+S_2)\}^2\{\omega_e\omega_0(S_1^2\alpha_1+S_2^2\alpha_2)/S_1S_2 - \omega^2(\alpha_1+\alpha_2)\}^2}{\{\omega^2-\omega_e(\omega+\omega_0)\}\{\omega^2+\omega_e(\omega-\omega_0)\}}}$$

$$\chi_{xy}'' = \frac{-\left(2\omega^2\left(\dfrac{\alpha_1}{\gamma_1}+\dfrac{\alpha_2}{\gamma_2}\right)\gamma_{eff}\omega_eM_1M_2 + \dfrac{2\omega^2\omega_e\{S_1S_2/(S_1+S_2)\}\{\omega_e\omega_0(S_1^2\alpha_1+S_2^2\alpha_2)/S_1S_2 - \omega^2(\alpha_1+\alpha_2)\}\{\gamma_{eff}\omega_e^2M - \omega^2(\gamma_1M_1+\gamma_2M_2)\}}{\{\omega^2-\omega_e(\omega+\omega_0)\}\{\omega^2+\omega_e(\omega-\omega_0)\}}\right)}{\text{Denominator}}$$

$$\chi_{xx}'' = \frac{-\left(\omega\omega_e^2\gamma_{eff}^2(\alpha_1S_1^2+\alpha_2S_2^2) - \omega^3(\alpha_1M_1^2+\alpha_2M_2^2) - \dfrac{2\omega\omega_e^2\{S_1S_2/(S_1+S_2)\}\omega_0\omega_M\{\omega_e\omega_0(S_1^2\alpha_1+S_2^2\alpha_2)/S_1S_2 - \omega^2(\alpha_1+\alpha_2)\}}{\{\omega^2-\omega_e(\omega+\omega_0)\}\{\omega^2+\omega_e(\omega-\omega_0)\}}\right)}{\text{Denominator}}$$

where $\gamma_{EFF} = \dfrac{\gamma_1\gamma_2M}{\gamma_2M_1 - \gamma_1M_2}$, $\omega_e \simeq \lambda(\gamma_2M_1 + \gamma_1M_2)$

$M = M_1 + M_2$ and $\omega_0 = \gamma_{FF}|H|$

Figure 8.4. Elements of the susceptibility tensor of a damped double sublattice system which include the exchange field. After Frayne[13]

represented by $\underline{M}^i$ and $\underline{M}^j$ oriented in directions defined by the direction cosines $\cos\alpha_1{}^i$, $\cos\alpha_2{}^i$, $\cos\alpha_3{}^i$, and $\cos\alpha_1{}^j$, $\cos\alpha_2{}^j$, $\cos\alpha_3{}^j$ respectively. The magnetic vectors are expressed in terms of static and oscillatory components such that the magnetisation of the i^{th} subsystem is written

$$\underline{M}^i = \left(M_{i_x}+m_{i_x}e^{j\omega t}\right)\hat{\underline{i}}+\left(M_{i_y}+m_{i_y}e^{j\omega t}\right)\hat{\underline{j}}+\left(M_{i_z}+m_{i_z}e^{j\omega t}\right)\hat{\underline{k}}$$

and similarly the magnetic field at the dipoles of the i^{th} sublattice are represented in component form as

$$\underline{H}^i = \Big[\lambda\left(m_{J_x}e^{j\omega t}+M_{J_x}\right)+H_{0_x}-N_{i_x}\left(M_{i_x}+m_{i_x}e^{j\omega t}\right) -N_x\left(M_{i_x}+m_{i_x}e^{j\omega t}+M_{J_x}+m_{J_x}e^{j\omega t}\right)+h_x e^{j\omega t}\Big]\hat{\underline{i}}$$

$$+\Big[\lambda\left(m_{J_y}e^{j\omega t}+M_{J_y}\right)+H_{0_y}-N_{i_y}\left(M_{i_y}+m_{i_y}e^{j\omega t}\right) -N_y\left(M_{i_y}+m_{i_y}e^{j\omega t}+M_{J_y}+m_{J_y}e^{j\omega t}\right)+h_y e^{j\omega t}\Big]\hat{\underline{j}}$$

$$+\Big[\lambda\left(m_{J_z}e^{j\omega t}+M_{J_z}\right)+H_{0_z}-N_{i_z}\left(M_{i_z}+m_{i_z}e^{j\omega t}\right) -N_z\left(M_{i_z}+m_{i_z}e^{j\omega t}+M_{J_z}+m_{J_z}e^{j\omega t}\right)+h_z e^{j\omega t}\Big]\hat{\underline{k}}$$

λ is the molecular field coefficient describing the exchange interaction between the two sublattices, N_x, N_y, N_z are the demagnetisation factors arising from the shape of the specimen, N_{i_x}, N_{i_y}, N_{i_z} are the effective demagnetisation factors representing the anisotropy of the i^{th} subsystem, H_{0_x}, H_{0_y}, H_{0_z} are the magnitudes of the components of the applied field which for generality is given an arbitrary orientation and $\hat{\underline{i}}$, $\hat{\underline{j}}$, $\hat{\underline{k}}$ are the unit vectors in the x, y and z directions respectively. To simplify the vector multiplication $\underline{M}^i \wedge \underline{H}^i$, it is expedient to separate the static and oscillatory components of $\underline{H}^i$ such that the orientation of the static field is along the precessional axis of $\underline{M}^i$ and so is described by the same direction cosines. The static component is represented by

$$\left\{\begin{array}{l}\left(-N_{i_x}M_{i_x}-N_x\{M_{i_x}+M_{J_x}\}+\lambda M_{J_x}+H_{0_x}\right)\cos\alpha_1{}^i \\ \qquad +\left(-N_{i_y}M_{i_y}-N_y\{M_{i_y}+M_{J_y}\}+\lambda M_{J_y}+H_{0_y}\right)\cos\alpha_2{}^i \\ \qquad\qquad +\left(-N_{i_z}M_{i_z}-N_z\{M_{i_z}+M_{J_z}\}+\lambda M_{J_z}+H_{0_z}\right)\cos\alpha_3{}^i\end{array}\right\}\ \hat{\underline{n}}_i$$

$$= \Big\}\!\!-\!\!\Big(_i\ \hat{\underline{n}}_i \qquad \ldots(8.24)$$

$\hat{\underline{n}}_i$ is the unit vector in the direction of the dipole moment and can be expressed as

$$\hat{\underline{n}}_i = \cos\alpha_1{}^i\ \hat{\underline{i}} + \cos\alpha_2{}^i\ \hat{\underline{j}} + \cos\alpha_3{}^i\ \hat{\underline{k}}$$

$\underline{H}^i$ can now be represented in a simplified form as

$$\underline{H}^i = \left(m_{i_x}\{-N_{i_x}-N_x\}+m_{J_x}\{-N_x+\lambda\}+h_x\right)e^{j\omega t}\ \hat{\underline{i}}$$

$$+\left(m_{i_y}\{-N_{i_y}-N_y\}+m_{J_y}\{-N_y+\lambda\}+h_y\right)e^{j\omega t}\ \hat{\underline{j}}$$

$$+\left(m_{i_z}\{-N_{i_z}-N_z\}+m_{J_z}\{-N_z+\lambda\}+h_z\right)e^{j\omega t}\ \hat{\underline{k}} + \Big\}\!\!-\!\!\Big(_i\ \hat{\underline{n}}_i$$

and the magnetisation can be re-arranged as

$$\underline{M}^i = \left(m_{i_x}\ \hat{\underline{i}} + m_{i_y}\ \hat{\underline{j}} + m_{i_z}\ \hat{\underline{k}}\right)e^{j\omega t} + M_i\ \hat{\underline{n}}_i$$

For ease of manipulation, the substitutions

$$\left\{\begin{array}{l}a_{i_x} = -\{N_{i_x} + N_x\}\ ,\quad \{a_{i_y} = -\{N_{i_y} + N_y\}\ ,\quad a_{i_z} = -\{N_{i_z} + N_z\} \\ \\ b_x = \lambda - N_x, \qquad b_y = \lambda - N_y, \qquad b_z = \lambda - N_z\end{array}\right. \qquad \ldots(8.25)$$

will be made. Using the expressions

$$\hat{\underline{i}} \wedge \hat{\underline{n}}_i = \cos\alpha_2{}^i\ \hat{\underline{k}} - \cos\alpha_3{}^i\ \hat{\underline{j}}$$
$$\hat{\underline{j}} \wedge \hat{\underline{n}}_i = -\cos\alpha_1{}^i\ \hat{\underline{k}} + \cos\alpha_3{}^i\ \hat{\underline{i}}$$
$$\hat{\underline{k}} \wedge \hat{\underline{n}}_i = \cos\alpha_1{}^i\ \hat{\underline{j}} - \cos\alpha_2{}^i\ \hat{\underline{i}}$$

and neglecting second order terms, the vector product $\underline{M}^i \wedge \underline{H}^i$ is found to be

$$\underline{M}^i \wedge \underline{H}^i = \left\{ \begin{array}{l} \left(\left[-\cos\alpha_2{}^i \left(m_{i_x} a_{i_x} + m_{J_x} b_x + h_x \right) + \cos\alpha_1{}^i \left(m_{i_y} a_{i_y} + m_{J_y} b_y + h_y \right) \right] M_i \right) \hat{\underline{k}} \\ \qquad + \left(\cos\alpha_2{}^i m_{i_x} - \cos\alpha_1{}^i m_{i_y} \right) \rightarrow ({}_i \\ + \left(\left[\cos\alpha_3{}^i \left(m_{i_x} a_{i_x} + m_{J_x} b_x + h_x \right) - \cos\alpha_1{}^i \left(m_{i_z} a_{i_z} + m_{J_z} b_z + h_z \right) \right] M_i \right) \hat{\underline{j}} \\ \qquad + \left(-\cos\alpha_3{}^i m_{i_x} + m_{i_z} \cos\alpha_1{}^i \right) \rightarrow ({}_i \\ + \left(\left[-\cos\alpha_3{}^i \left(m_{i_y} a_{i_y} + m_{J_y} b_y + h_y \right) + \cos\alpha_2{}^i \left(m_{i_z} a_{i_z} + m_{J_z} b_z + h_z \right) \right] M_i \right) \hat{\underline{i}} \\ \qquad + \left(m_{i_y} \cos\alpha_3{}^i - m_{i_z} \cos\alpha_2{}^i \right) \rightarrow ({}_i \end{array} \right\} e^{j\omega t}$$

Again substitutions are made to facilitate the algebra by representing the above equation as

$$\underline{M}^i \wedge \underline{H}^i = e^{j\omega t} (A\hat{\underline{k}} + B\hat{\underline{j}} + C\hat{\underline{i}})$$

The vector product $M^i \wedge (M^i \wedge \underline{H}^i)$ can now be calculated, and so again omitting second order terms

$$\underline{M}^i \wedge (M^i \wedge \underline{H}^i) = e^{j\omega t} \left\{ \begin{array}{l} M_i A \left(-\cos\alpha_1{}^i \hat{\underline{j}} - \cos\alpha_2{}^i \hat{\underline{i}} \right) \\ + M_i B \left(\cos\alpha_1{}^i \hat{\underline{k}} - \cos\alpha_3{}^i \hat{\underline{i}} \right) \\ + M_i C \left(\cos\alpha_2{}^i \hat{\underline{k}} - \cos\alpha_3{}^i \hat{\underline{j}} \right) \end{array} \right\}$$

The above expressions for $\underline{M}^i \wedge \underline{H}^i$ and $\underline{M}^i \wedge (\underline{M}^i \wedge \underline{H}^i)$ may be used to solve the Landau-Lifshitz equation, which written in the notation of this analysis is

$$\frac{d\underline{M}^i}{dt} = \gamma_i \, \underline{M}^i \wedge \underline{H}^i - \alpha_i \, \underline{M}^i \wedge (\underline{M}^i \wedge \underline{H}^i)$$

In the component form, this becomes

$$j\omega m_{i_x} = \gamma_i C - \alpha_i M_i (A \cos \alpha_2{}^i - B \cos \alpha_3{}^i)$$

$$j\omega m_{i_y} = \gamma_i B - \alpha_i M_i (-A \cos \alpha_1{}^i + C \cos \alpha_3{}^i)$$

$$j\omega m_{i_z} = \gamma_i A - \alpha_i M_i (B \cos \alpha_1{}^i - C \cos \alpha_2{}^i)$$

which can be expanded and re-arranged for i = 1, 2 and j = 2, 1 to give a matrix equation of the form

$$[D] \cdot \begin{bmatrix} m_{1_x} \\ m_{2_x} \\ m_{1_y} \\ m_{2_y} \\ m_{1_z} \\ m_{2_z} \end{bmatrix} = \begin{bmatrix} E_1 h_x + F_1 h_y + G_1 h_z \\ E_2 h_x + F_2 h_y + G_2 h_z \\ E_3 h_x + F_3 h_y + G_3 h_z \\ E_4 h_x + F_4 h_y + G_4 h_z \\ E_5 h_x + F_5 h_y + G_5 h_z \\ E_6 h_x + F_6 h_y + G_6 h_z \end{bmatrix} \qquad \ldots(8.26)$$

where $[D]$ is a 6 × 6 matrix. Treating the elements $E_{1\to6}$, $F_{1\to6}$ and $G_{1\to6}$ as 6 × 1 column matrices, Appendix VII gives expressions for these parameters and for the elements of $[D]$ and describes a technique whereby the equations are re-arranged into the form

$$\underline{m} = \chi \cdot \underline{h} \qquad \ldots(8.27)$$

Relating the elements of the susceptibility tensor χ to the permeability tensor by the equation

$$\bar{\mu} = 1 + 4\pi\bar{\chi} \qquad \ldots(8.28)$$

the phase constants and hence the Faraday rotation are calculable as described in Appendix VII.

CHAPTER NINE

MAGNETIC PROPERTIES OF THE RARE-EARTH IRON GARNETS

9.1. Introduction

As stated previously, an investigation of magneto-optical properties in the far infra-red was undertaken on a number of iron garnets. In this chapter a summary of the structure and magnetic properties of the garnets is given to facilitate interpretation of the experimental measurements.

9.2. Crystal structure

The formula unit of a rare-earth iron garnet[97,98] can be written $R_3Fe_2(FeO_4)_3$ where R represents a trivalent rare-earth ion or a diamagnetic yttrium ion. Figure 9.1(a)[99] shows the formula unit structure of such a garnet, eight of which occupy the unit cell. The iron ions form two anti-parallel sublattices, twenty-four of these ions per unit cell are located at the centre of a tetrahedron and are denoted as being situated at "d" sites, and sixteen are located at the centre of an octahedron, called "a" sites. Either rare-earth or yttrium ions occupy the centre of the eight-cornered polyhedron shown in Figure 9.1(a) on twenty-four "c" sites per unit cell. There are ninety-six oxygen ions in a unit cell on "h" sites such that each oxygen ion is surrounded by an Fe^{3+}(a) ion, an Fe^{3+}(d) ion and two R^{3+}(c) ions. Figure 9.1(b) gives a simplified view of the garnet structure showing it to be a body-centred cubic crystal of "a" type ions with "c" and "d" ions on the cube faces.

9.3. Magnetic properties

In general, the ions of each of the three magnetic sublattices can possess a spontaneous magnetic dipole moment, but the interaction between these magnetic moments depends on super-exchange interaction taking place via the oxygen ions. The oxygen ion has ten electrons, six of them in the 2p layer. The 2p electrons form three pairs, the electron of each pair being in opposite spin states and occupying orbits which overlap the electron distributions of neighbouring ions. In this state the oxygen ion cannot take part in exchange coupling as the 2p layer is filled. Kramers[101] proposed that at least one of the 2p oxygen electrons can go into a vacant level in a neighbouring ion leaving the oxygen ion in an excited state so that it is able to partake in exchange interaction. If the overlap of the wave functions is

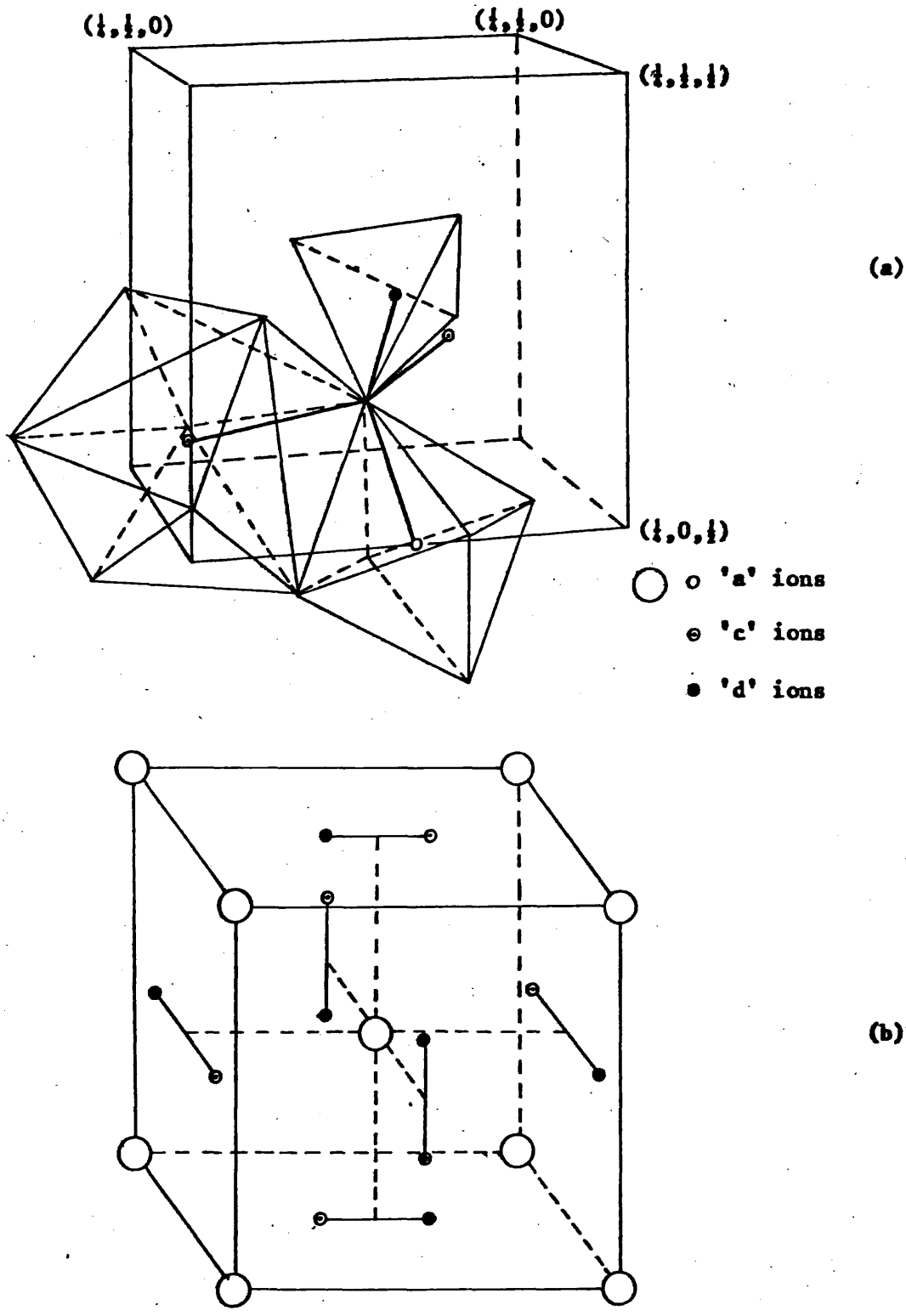

Figure 9.1. (a) Crystal structure of an iron garnet within the unit cell; after Gilleo and Geller[99], and (b) a simplified view shows the cubic structure, reproduced from Craik and Tebble[100].

sufficiently large, a p electron from an oxygen ion may go over to an adjacent ion and cause ferrimagnetic coupling. The strongest super-exchange interaction takes place when the angle the respective ions make with the interspaced oxygen is 180^{o}, corresponding to a maximum overlap of the wave functions. The Weiss molecular-field treatment can be used to explain the ferrimagnetic situation. Denoting the ions occupying the "a", "c" and "d" sites as the A, C and D sublattices respectively, the effective super-exchange field on a magnetic dipole in each of the sublattices[102] is

$$H_A = \lambda_{AA}M_A + \lambda_{AC}M_C + \lambda_{AD}M_D$$

$$H_C = \lambda_{CC}M_C + \lambda_{CA}M_A + \lambda_{CD}M_D$$

$$H_D = \lambda_{DD}M_D + \lambda_{DA}M_A + \lambda_{DC}M_C$$

where, identifying any two of the three sublattices A, C and D by ij, then λ_{ij} is the molecular field coefficient signifying an exchange field at a dipole in the i^{th} sublattice due to a magnetisation M_j in the j^{th} sublattice. The angles between the various super-exchange linkages are[88]

$Fe^{3+}(a) - O^{2-} - Fe^{3+}(d)$	126.6^{o}
$Fe^{3+}(d) - O^{2-} - R^{3+}(c)$	122.2^{o}
$R^{3+}(c) - O^{2-} - Fe^{3+}(a)$	100^{o}
$R^{3+}(c) - O^{2-} - R^{3+}(c)$	104.7^{o}

This shows the A-D interaction which aligns the A and D sublattices anti-parallel, to be relatively strong. The next strongest is the D-C alignment. It is generally considered that the A and D lattices are so tightly bound that the two subsystems can be treated as one 'equivalent sublattice' with a magnetisation corresponding to that of three $Fe^{3+}(d)$ ions minus two $Fe^{3+}(a)$ ions per formula unit. This model has been verified in yttrium iron garnet[103,104,105] and enables the rare-earth iron garnets to be treated as a two-sublattice system, the C-C interaction usually being considered negligible. Values of the molecular field coefficient have been listed by Anderson[102] for the sublattices of yttrium and gadolinium iron garnets, and by Frayne[13] for the coefficient between the rare-earth and the 'equivalent' fictitious lattices in terbium and gadolinium iron garnets displayed in Table 9.1.

Table 9.1

The Weiss molecular field coefficients in yttrium iron garnet and gadolinium iron garnet: after Anderson[102]

	λ_{ad}	λ_{aa}	λ_{dd}	λ_{cd}	λ_{dc}	λ_{ca}	λ_{ac}	λ_{cc}
YIG	71505	47820	22394					
GdIG	91060	61000	29000	4075	8150	800	800	800

The Weiss molecular field coefficient λ, between the rare-earth ion sublattice and the 'equivalent ferric sublattice' in terbium iron garnet and gadolinium iron garnet; after Frayne[13]

TbIG	1600
GdIG	1900

Yttrium has no spontaneous magnetic moment, the trivalent Y^{3+} ion having an inert krypton core so that there exists no unpaired electron spins, the 4p layer being completely filled. The magnetic properties of yttrium iron garnet are therefore often considered to be those of the iron lattice. The rare-earths have an incomplete 4f layer, which is partially screened by the 5s and 5p layers. This screening produces a partial orbital contribution to the magnetic moment which, together with the spin magnetic moments of the 4f electrons, results in a nett magnetic moment as shown calculated in Table 9.2[106]. These values are applicable at absolute zero temperature but decrease with increasing temperature due to thermal misalignment.

Table 9.2

Spin, orbital moment and magnetic moment of rare-earth ions in the iron garnets used in the present work; after Smit and Wijn[106]

	Sm	Gd	Tb	Dy	Ho	Er
S	$^5/_2$	$^7/_2$	3	$^5/_2$	2	$^3/_2$
L	-5	0	3	5	6	6
L+2S	0	7	9	10	10	9

All the rare-earth ions shown in Table 9.2, with the exception of samarium, have a magnetisation greater than that of the A-D sublattice at absolute zero. Because of the relative strengths of the super-exchange linkages, the decrease of the magnetic moment of the C sub-system with temperature is greater than the decrease of the value of the ferric sublattice; hence a condition arises where the magnitudes of the magnetisation of the two sublattices are equal. Being oppositely orientated the magnetisations cancel, producing an anti-ferromagnetic state at a temperature unique to each garnet, known as the 'compensation temperature'. The nett spontaneous magnetisations of the iron garnets studied here are shown plotted against temperature in Figure 9.2[107]. In later analysis, values for the magnetisation of the rare-earth ions will be obtained by calculating the difference between the nett magnetisation of the garnet and the corresponding value for yttrium iron garnet.

9.4. Anisotropy

The measurements of the magnetisation of rare-earth iron garnets made by Bertaut and Pauthenet[107], shown in Figure 9.2, were made with poly-crystalline specimens. The magnetisation of various garnets have been measured using single crystals, where anisotropy has been shown to be present and particularly pronounced at low temperatures.

At room temperature the garnets possess an easy direction of magnetisation, the [111] direction and a hard direction, the [100] direction. However, this does not remain the case for all the garnets over the entire ferrimagnetic temperature range. Harrison et al.[108] have shown that the relative ease of magnetisation along the different crystallographic directions in some of the garnets change rôles at certain temperatures. An example is shown in Figure 9.3 in which the easy direction of magnetisation in samarium iron garnet changes from the [111] direction at 81°K to [110] at 58.6°K, while the hard direction, usually the [100] direction, changes to the [111] direction when the temperature is lowered to 23.6°K. For the rare-earth iron garnets, the K_1 coefficient is the major contributor to the anisotropy although the K_2 term increases in importance at low temperatures. Values of K_1 measured by Pearson[109] and shown in Figure 9.4 will be discussed in Chapter Eleven when analysing the effects of anisotropy on Faraday rotation.

9.5. Far infra-red spectra of iron garnets

A brief examination of the far infra-red spectra of the garnets

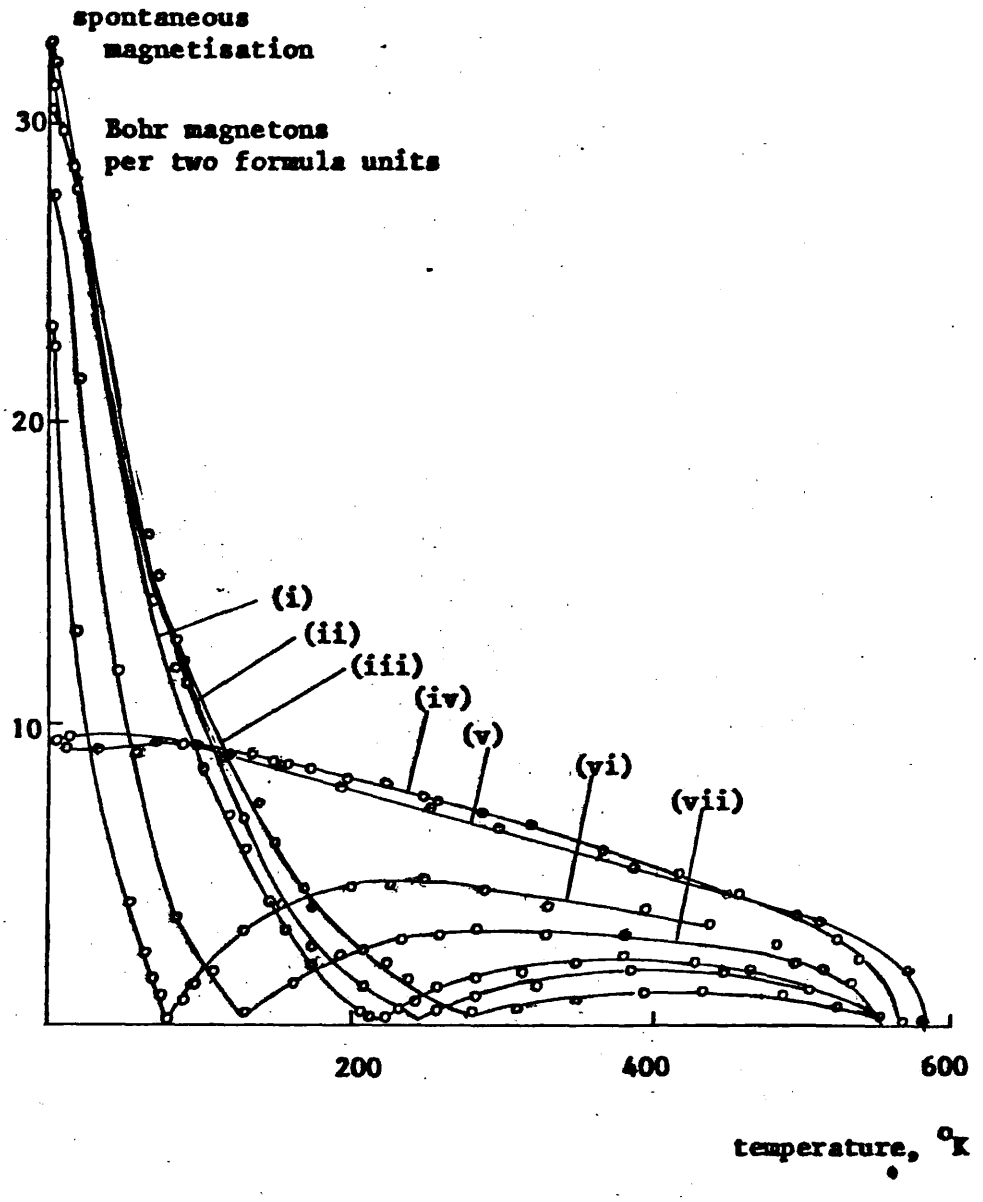

Figure 9.2. Spontaneous magnetisation in Bohr magnetons per two formula units against temperature in iron garnets of (i) dysprosium, (ii) terbium, (iii) gadolinium, (iv) yttrium, (v) samarium, (vi) erbium, and (vii) holmium. After Bertaut and Pauthenet[107].

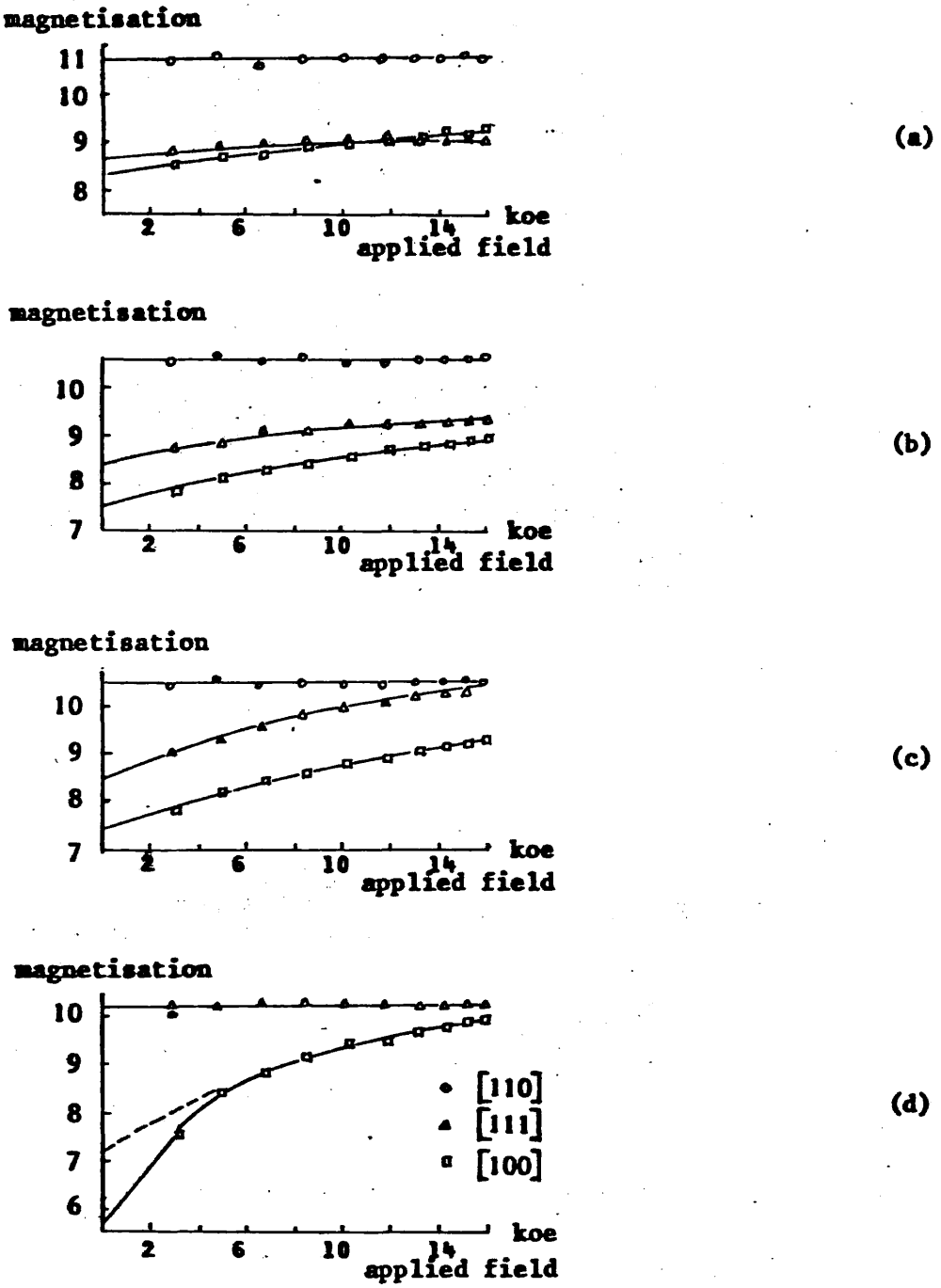

Figure 9.3. Spontaneous magnetisation in single crystal specimens of samarium iron garnet against applied magnetic field at (a) 23.6°K, (b) 43.9°K, (c) 58.6°K, and (d) 81°K. Magnetisation in Bohr magnetons per two formula units. After Harrison et al.[108].

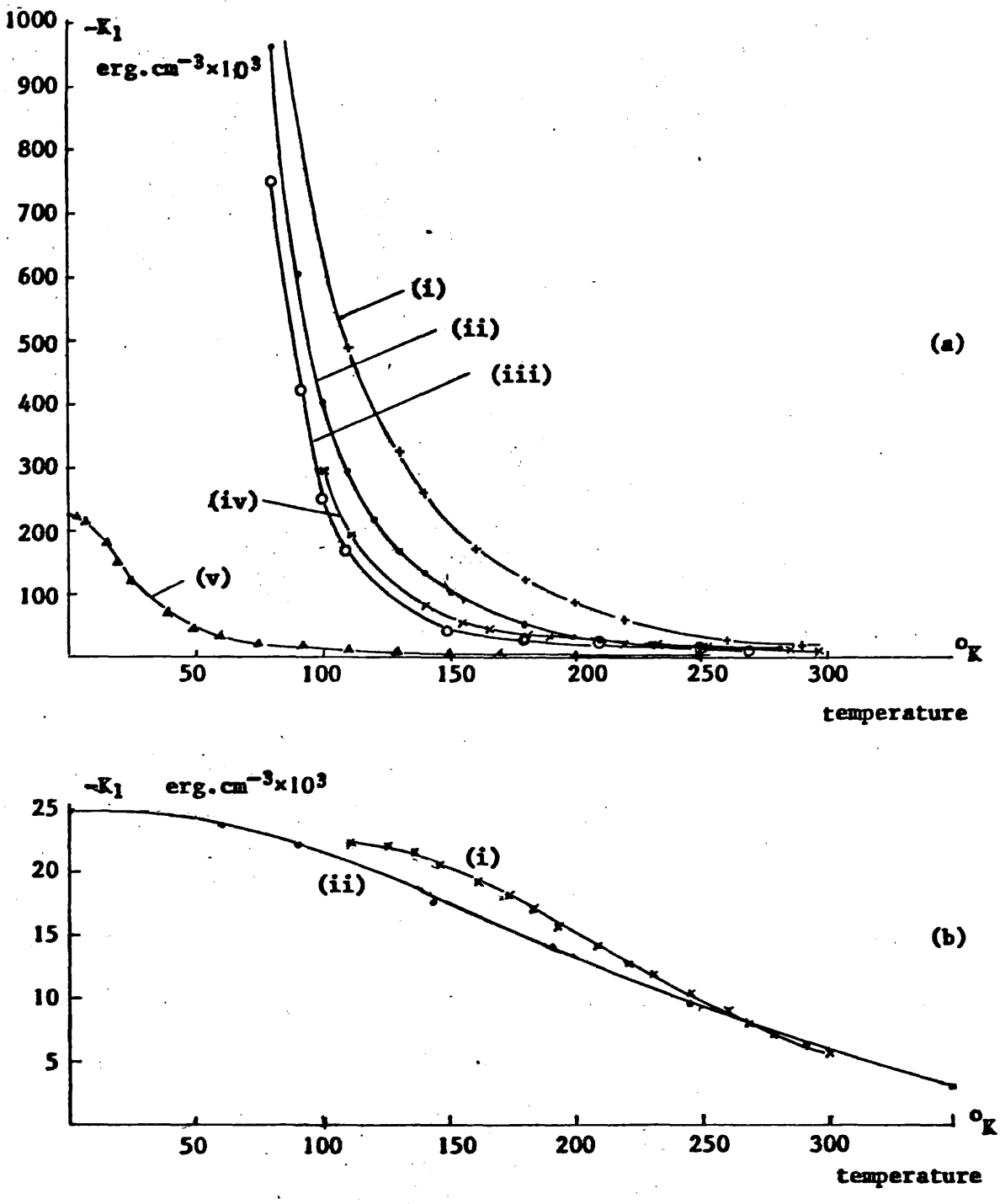

Figure 9.4. Variation of the first anisotropy constant with temperature of iron garnets of (a)(i) samarium, (ii) dysprosium, (iii) holmium, (iv) terbium, (v) gadolinium, and (b)(i) erbium, and (ii) yttrium. After Pearson[109].

investigated will be made in Chapter Eleven to assess the possible effect on the theoretical interpretation of the magneto-optical properties. The submillimetre spectra are therefore reproduced here firstly in Figure 9.5 from the work of Yamamoto, Smith and Bell[110] for dysprosium iron garnet. Figure 9.5(a) shows the frequency variation of the absorption lines with applied magnetic field at temperatures between 1.6 and 4.2°K. No significant change with temperature was observed in this range. The variation at higher temperatures is illustrated in Figure 9.5(b) for conditions of zero magnetic field. Yamamoto et al.[110] also investigated terbium iron garnet and observed the lines shown in Table 9.3. Because of limited experimentation, these absorption features were only measured at 4.2°K in the absence of an applied field, the 36 cm^{-1} absorption being described as weak.

The spectra of erbium, samarium and holmium iron garnets were measured by Sievers and Tinkham[111] and are reproduced in Figure 9.6. Only the temperature variation of the absorption lines in these garnets was measured without an applied magnetic field. Gadolinium iron garnet was also investigated and only one far infra-red line was observed which is listed in Table 9.3.

Table 9.3

Far infra-red spectral lines
in terbium and gadolinium iron garnets

Iron garnet	Wave number cm^{-1}	Temperature °K	Reference
terbium	36	4.2	110
	68.5	4.2	110
gadolinium	∿80	2	111

Electronic and ferrimagnetic resonance absorption lines in the rare-earth iron garnets are due to the rare-earth ion situated in the exchange field[111]. For the diamagnetic yttrium ion such properties do not exist and the main contributor to the spectrum of yttrium iron garnet in the far infra-red are the acoustical modes[112]. Although values for the attenuation coefficient were not obtained, the transmission measurements in yttrium iron garnet at 891 GHz described in the next chapter suggest that no strong absorption feature exists near the laser frequency.

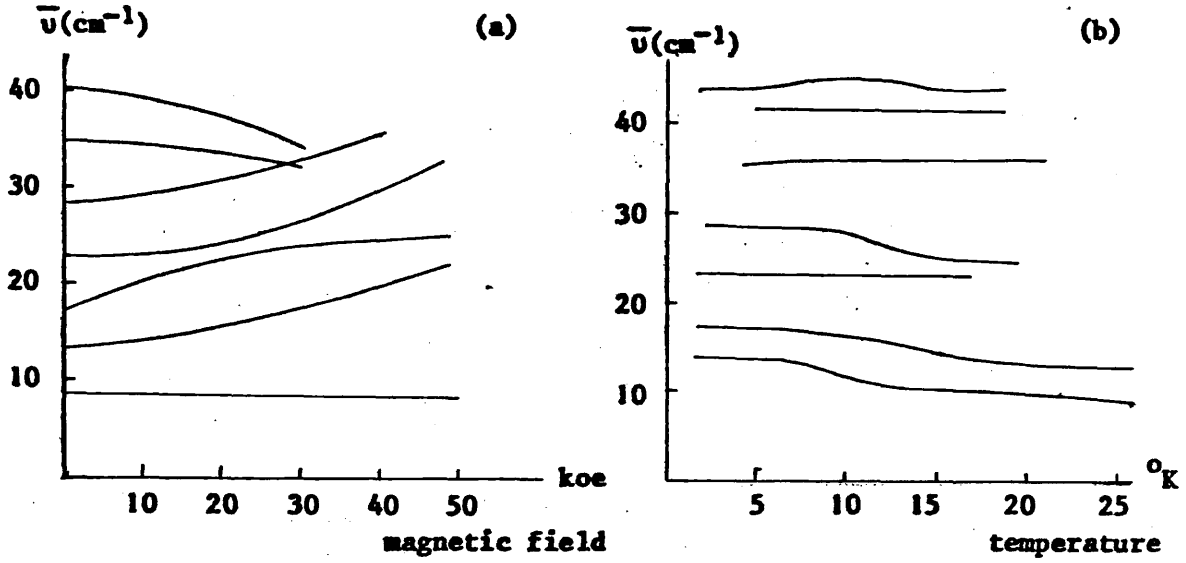

Figure 9.5. Variation of the wave numbers of absorption lines in dysprosium iron garnet with (a) magnetic field at 4.2°K, and (b) temperature at zero magnetic field. After Yamamoto et al.[110].

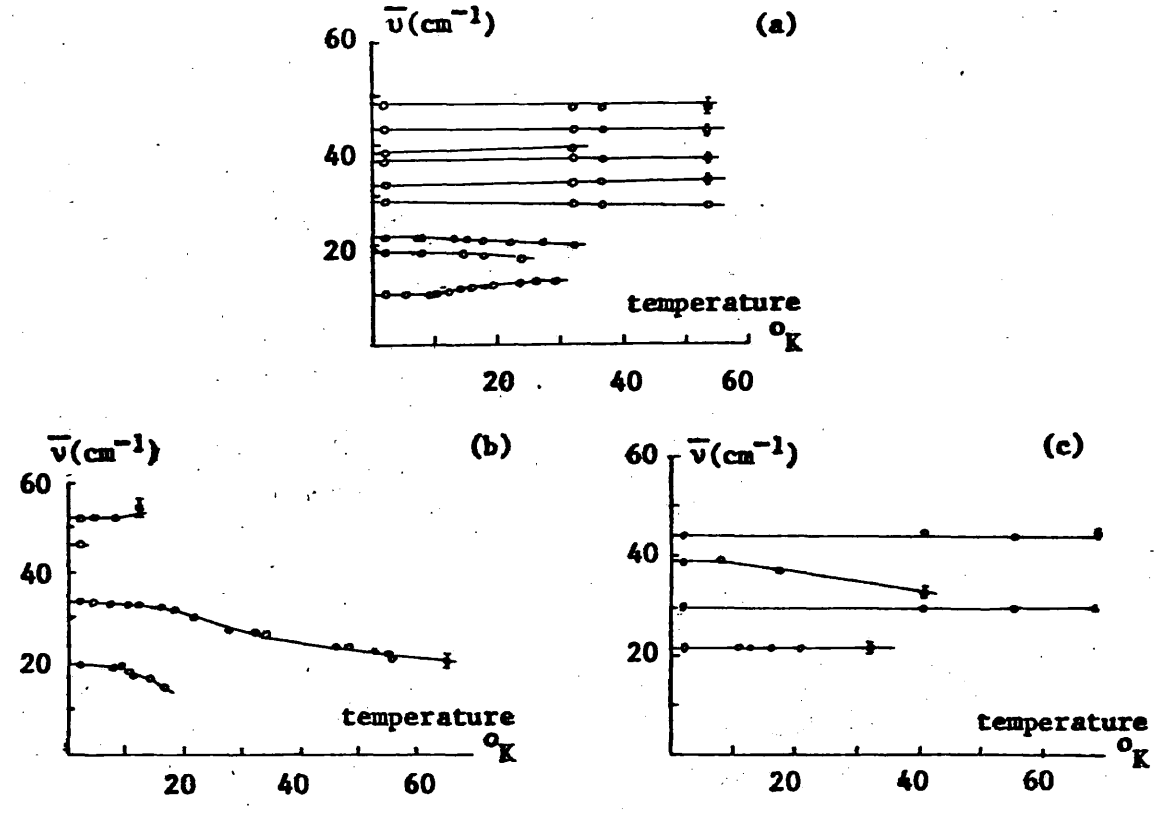

Figure 9.6. Variation with temperature of the wave numbers of absorption lines in iron garnets of (a) erbium, (b) samarium, and (c) holmium. Measurements made by Sievers and Tinkham[111] with zero magnetic field.

CHAPTER TEN

MAGNETO-OPTICAL MEASUREMENTS

10.1. Introduction

Magneto-optical parameters were observed at a wavelength of 337 μm in several iron garnets over a range of temperatures, the principal measurements made being those of Faraday rotation and attenuation. Other parameters obtained include the refractive index and reflection coefficient, and in two of the garnets the difference in attenuation of the two counter-rotating waves was sufficiently large to enable the ellipticity to be measured.

10.2. The cryostat

Controlled temperature experiments were performed using an Oxford Instruments cryostat illustrated schematically in Figure 10.1. Two concentric Dewar flasks were filled with liquid nitrogen and heat was conducted away from the garnet crystal to the inner Dewar via a column of helium gas which was surrounded by a copper shield to minimise heat radiation from the outer shell of the cryostat reaching the column and the crystal. Radiation from an HCN laser was guided through the cryostat by stainless steel light-pipes which entered the cryostat through rotatable vacuum seals.

The temperature of the crystal was measured using a gold (which contained 0.03% iron) to Chromel thermocouple, the output of which was fed to an Oxford Instruments temperature controller. This instrument maintained the garnet specimen at a selected temperature by supplying power to a heating coil situated near the crystal. Temperature stabilisation was accurate to $\pm 0.25^{o}K$ at $90^{o}K$, while increasing to $\pm 1^{o}K$ at $300^{o}K$.

10.3. Faraday rotation

Radiation from the laser was focused by a polythene lens into a tapered light-pipe connected to a tube entering the cryostat. To ensure good polarisation of the beam after passing through the light-pipe, a polariser was placed inside the cryostat across the end of the pipe. The polariser was of the type described in section 5.2 which comprised a series of gold lines on a Melinex film. To arrange for the magnetic field and the propagation direction of the beam to be parallel, the input and output light-pipes were passed through the bored-out centres of the poles of an electromagnet, as shown in Figure 10.2. To find

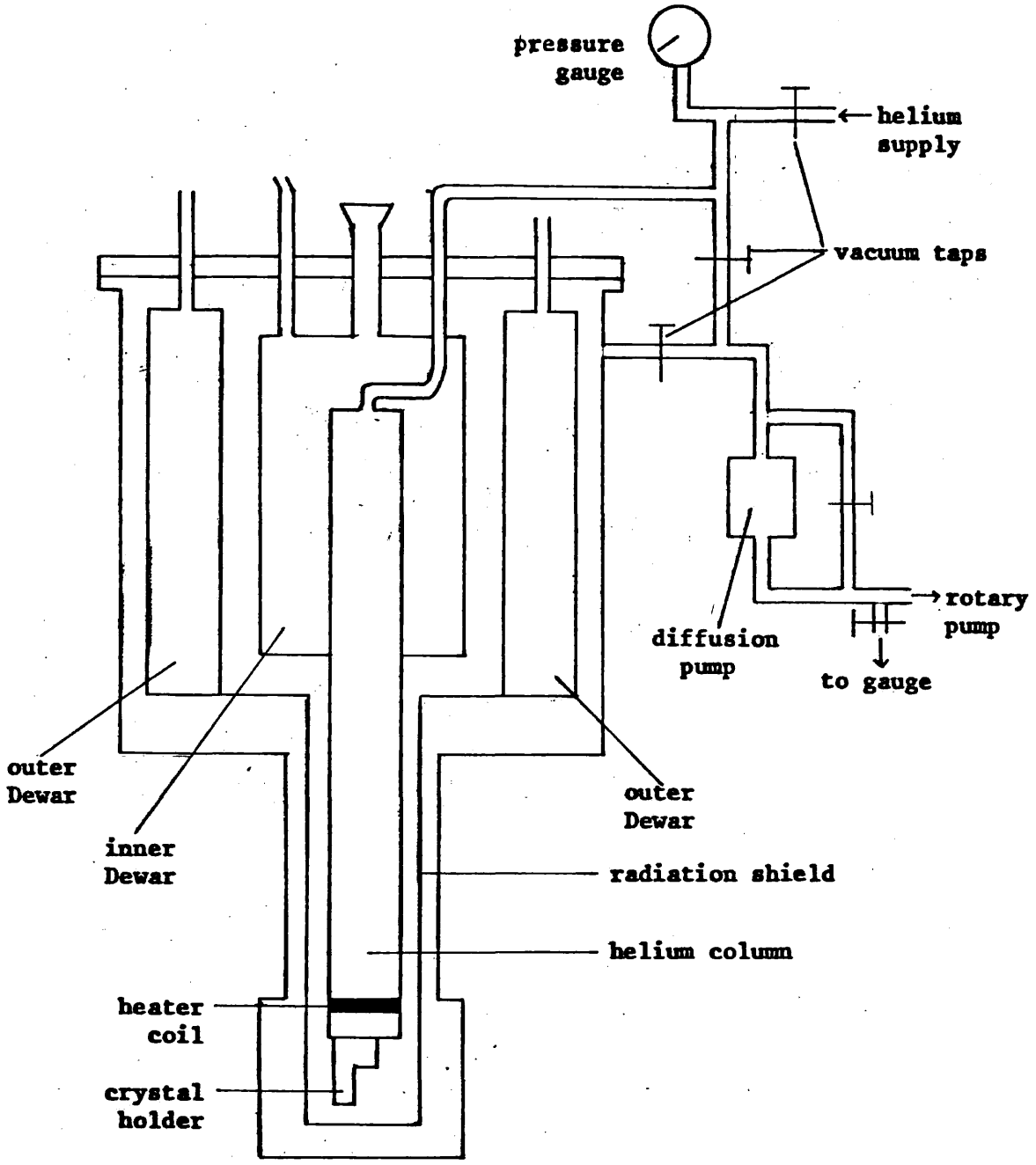

Figure 10.1. Schematic view of the cryostat showing the concentric Dewars and helium column together with the vacuum and helium admittance systems

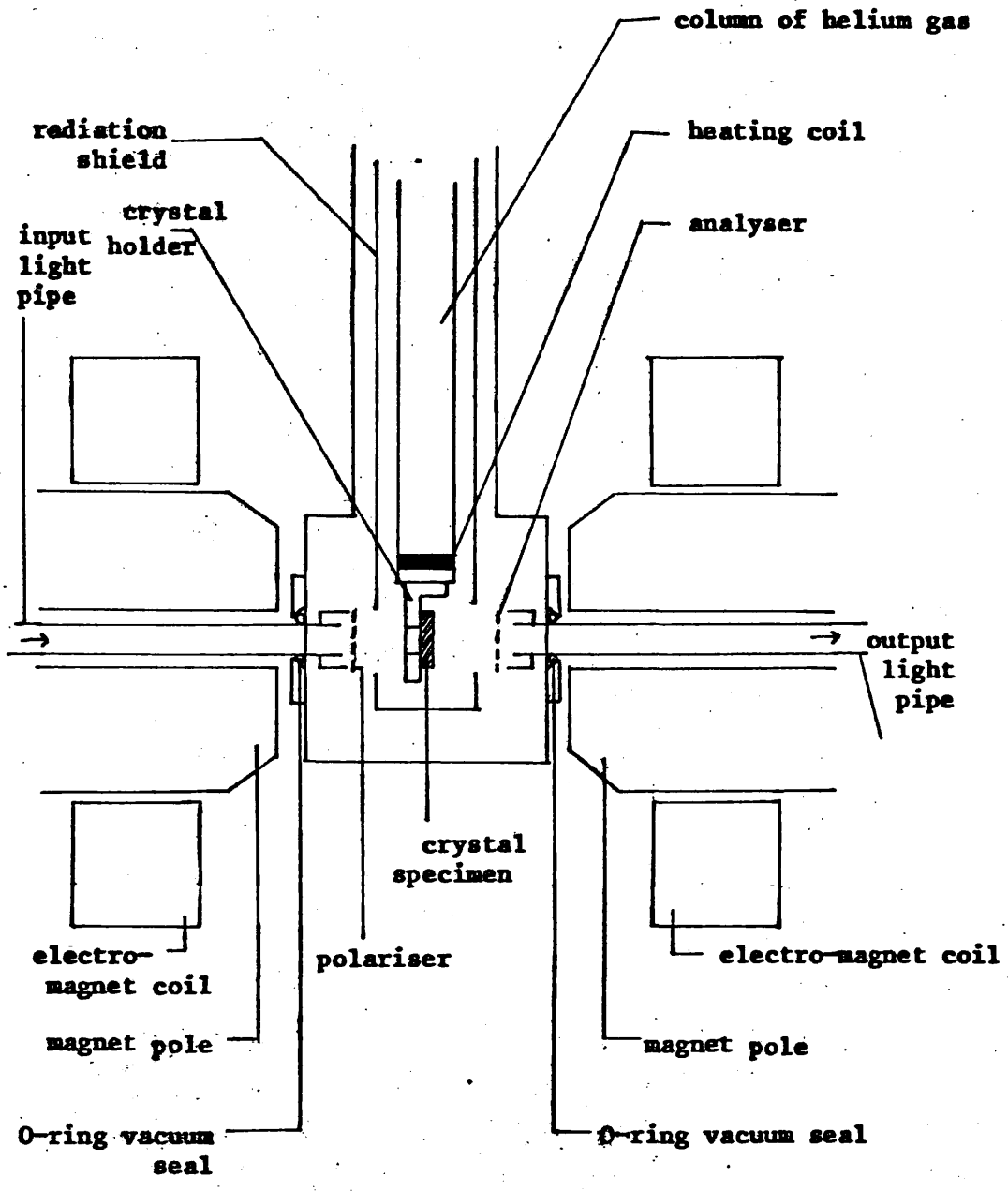

Figure 10.2. Schematic view of the experimental arrangement for measuring Faraday rotation

the polarisation of the beam transmitted through the garnet, a similar polariser was placed in the cryostat over the output light-pipe to act as an analyser. An angle corresponding to minimum transmitted signal was found by rotating the analyser to give an equal signal on either side of the minimum. Repeating this process a number of times with the applied field parallel to the propagation direction and followed by the two being anti-parallel, the Faraday rotation was measured to an accuracy of $\pm 0.5^{o}$. The convention employed was that the rotation is positive when clockwise, viewed along the propagation direction, when the propagation direction and applied field are parallel.

Faraday rotation was measured between $90^{o}K$ and $350^{o}K$ in the [111] and [110] directions in single crystals of yttrium, dysprosium, gadolinium, holmium and terbium iron garnets. These measurements, displayed in Figures 10.3 to 10.7 as specific Faraday rotation, were obtained when applying the maximum field obtainable from the electromagnet, of 4.3 koe at the specimen. This was regarded as sufficient to magnetically saturate the iron garnets at room temperature and above, but not necessarily high enough to saturate all samples at the low temperatures. To observe this property, the rotation was measured in some crystals at fixed temperatures while varying the applied field. Figures 10.8 to 10.11 show that in the region of $100^{o}K$ and below, rotation in most of the garnet specimen is still increasing with field at 4.3 koe, while saturation appears to be obtained at higher temperatures. An important factor in determining the switching speed of a modulation device is the rate of increase of rotation with field. This is seen to be greatest at the higher temperatures.

Data obtained by Frayne on Faraday rotation in samarium and erbium iron garnets with an 6.5 koe applied magnetic field are presented in Figures 10.12 and 10.13 as the attenuation constants of these materials were measured as part of the current programme to enable figures of merit to be calculated. An analysis of these Faraday rotation measurements will be pursued in the next chapter.

10.4. Transmission measurements

To measure the transmission coefficient of the various iron garnets at 337 μm, the polarisers were removed from the light-pipes and a Melinex beam splitter was placed in front of the tapered input light-pipe. Monitoring the intensity of the radiation reflected from this beam splitter in the manner shown in Figure 10.14 allowed the intensity of the beam passing through the cryostat to be calibrated in terms of

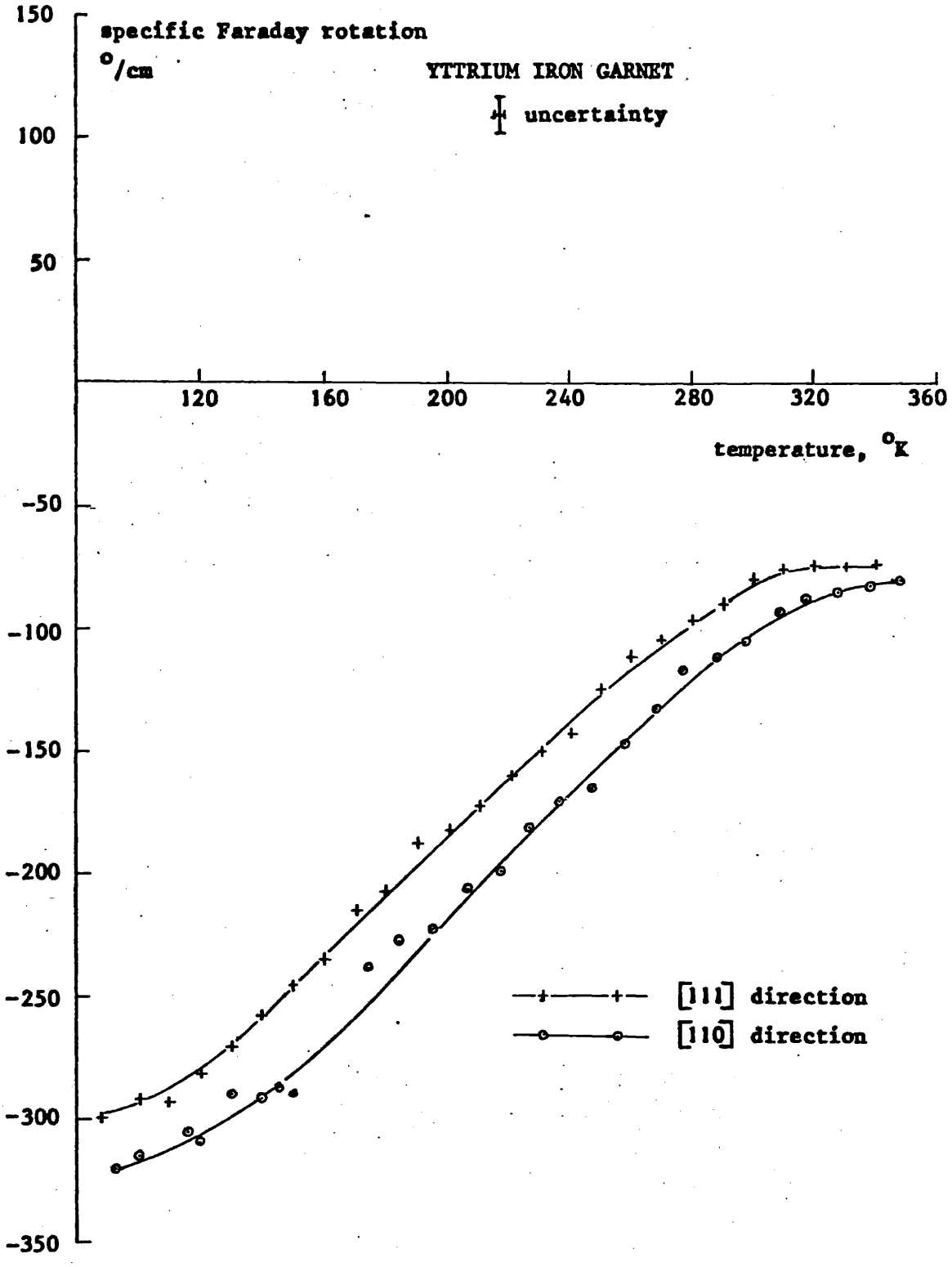

Figure 10.3. Measured Faraday rotation at 891 GHz in yttrium iron garnet against temperature. Applied magnetic field 4.3 koe.

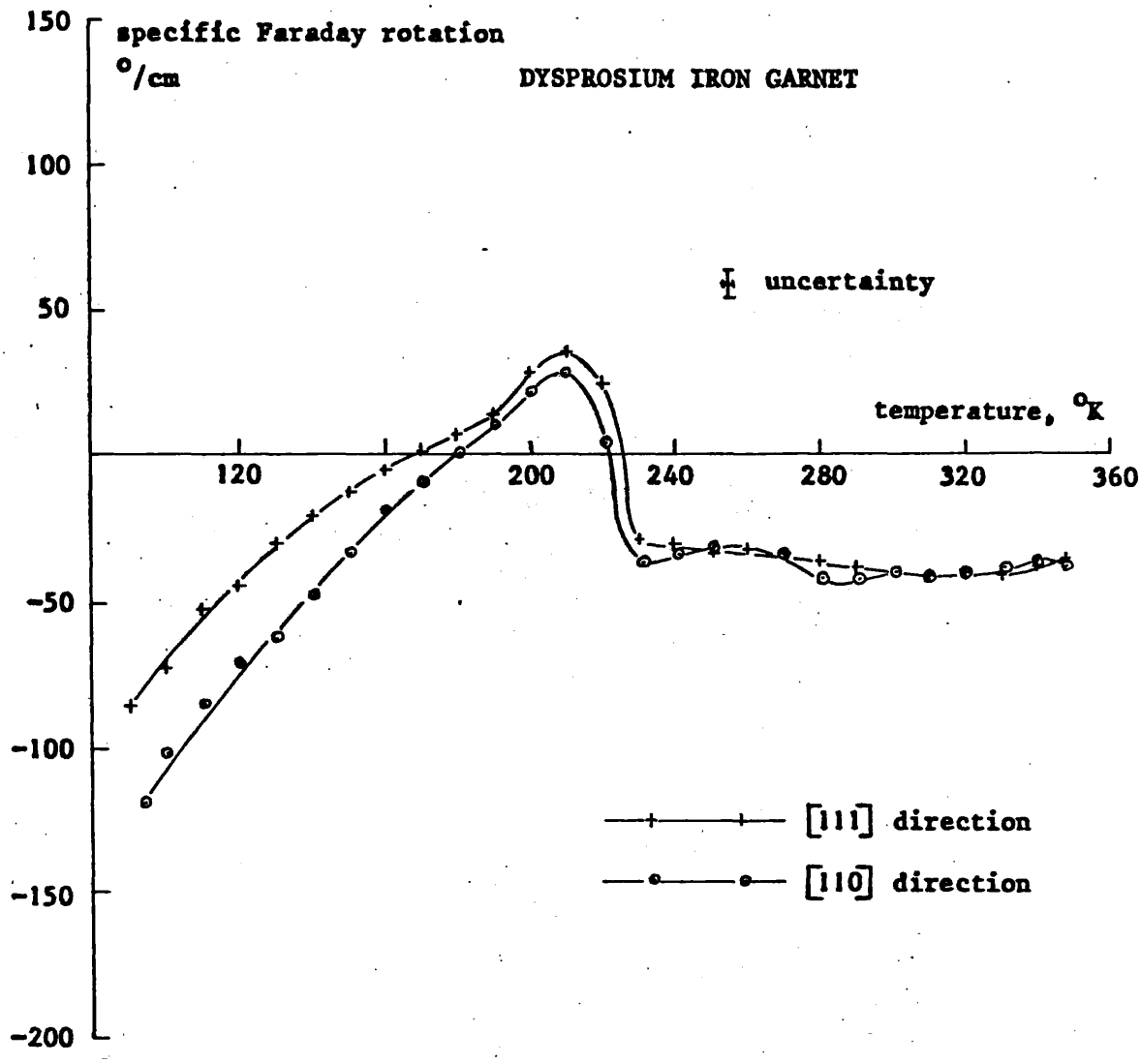

Figure 10.4. Measured Faraday rotation at 891 GHz in dysprosium iron garnet against temperature. Applied magnetic field 4.3 koe.

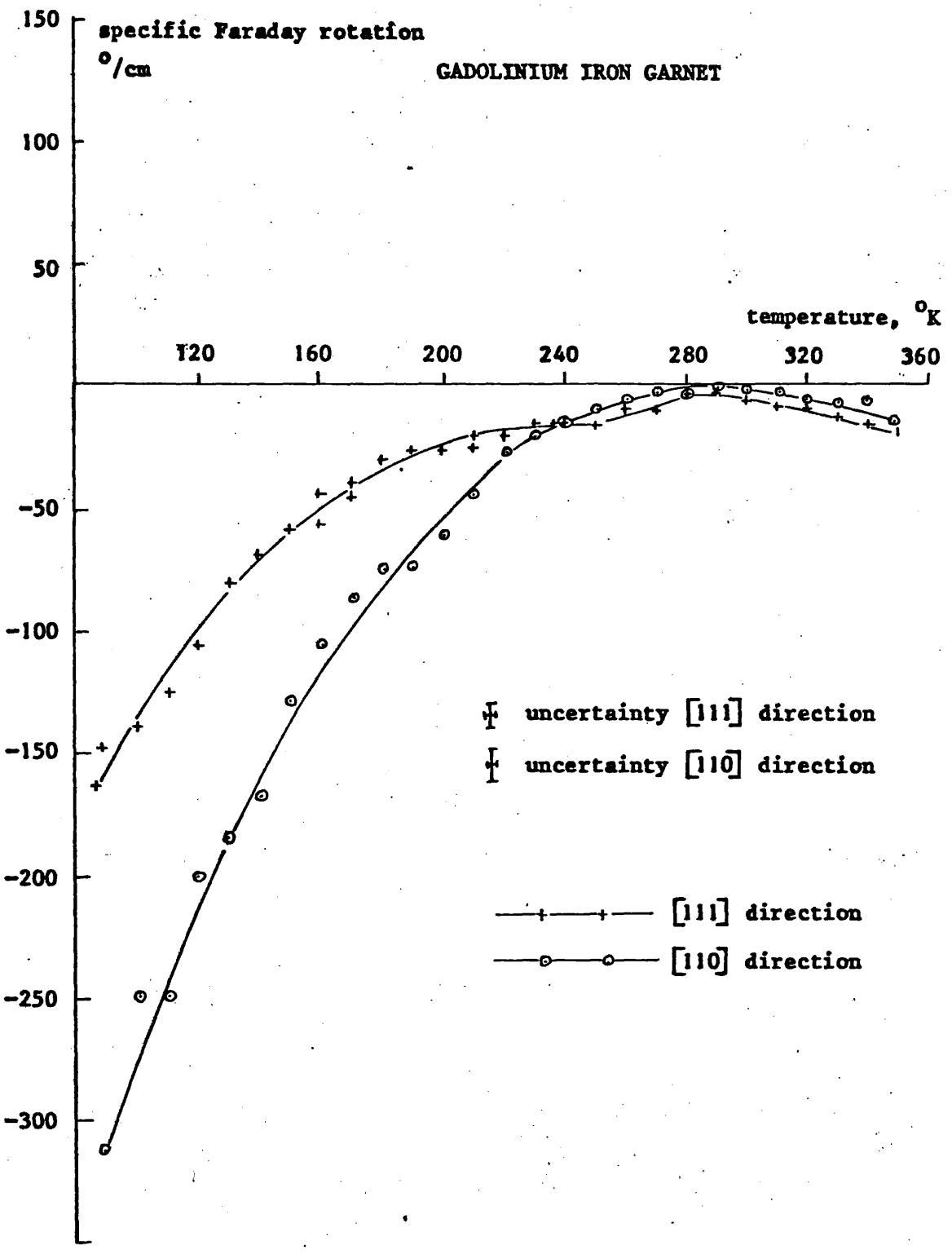

Figure 10.5. Measured Faraday rotation at 891 GHz in gadolinium iron garnet against temperature. Applied magnetic field, 4.3 koe.

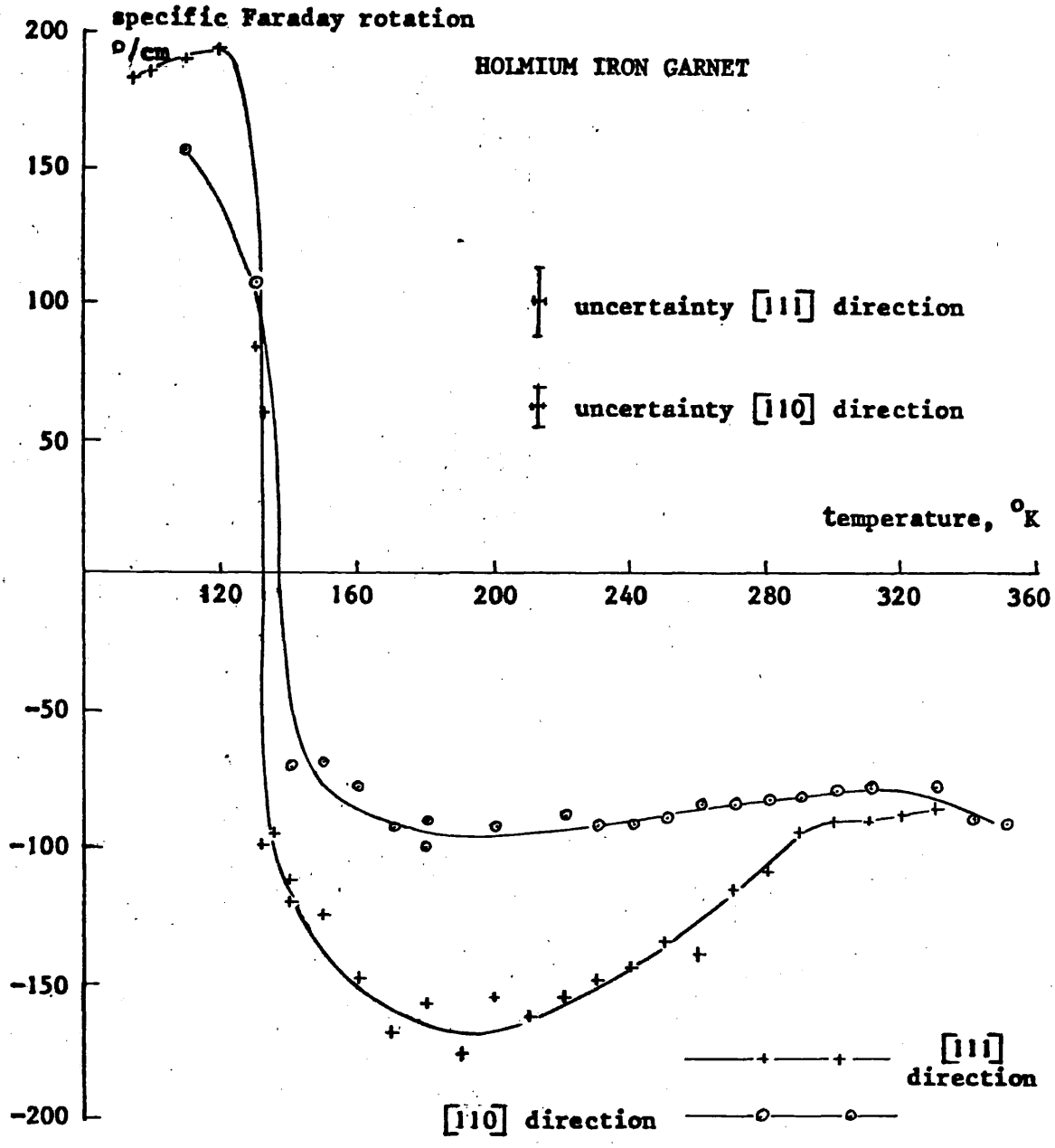

Figure 10.6. Measured Faraday rotation at 891 GHz in holmium iron garnet against temperature. Applied magnetic field 4.3 koe.

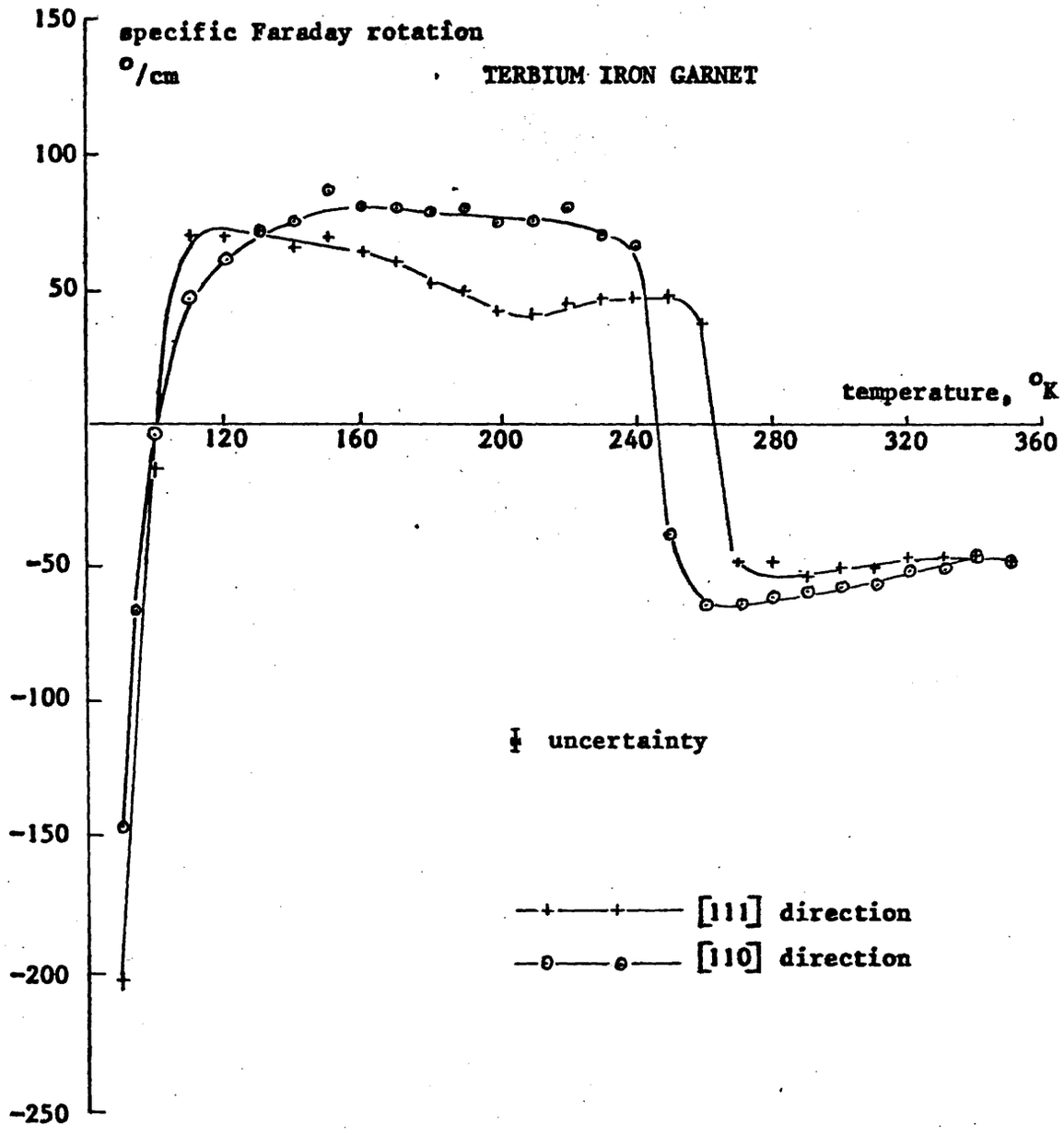

Figure 10.7. Measured Faraday rotation at 891 GHz in terbium iron garnet against temperature. Applied magnetic field 4.3 koe.

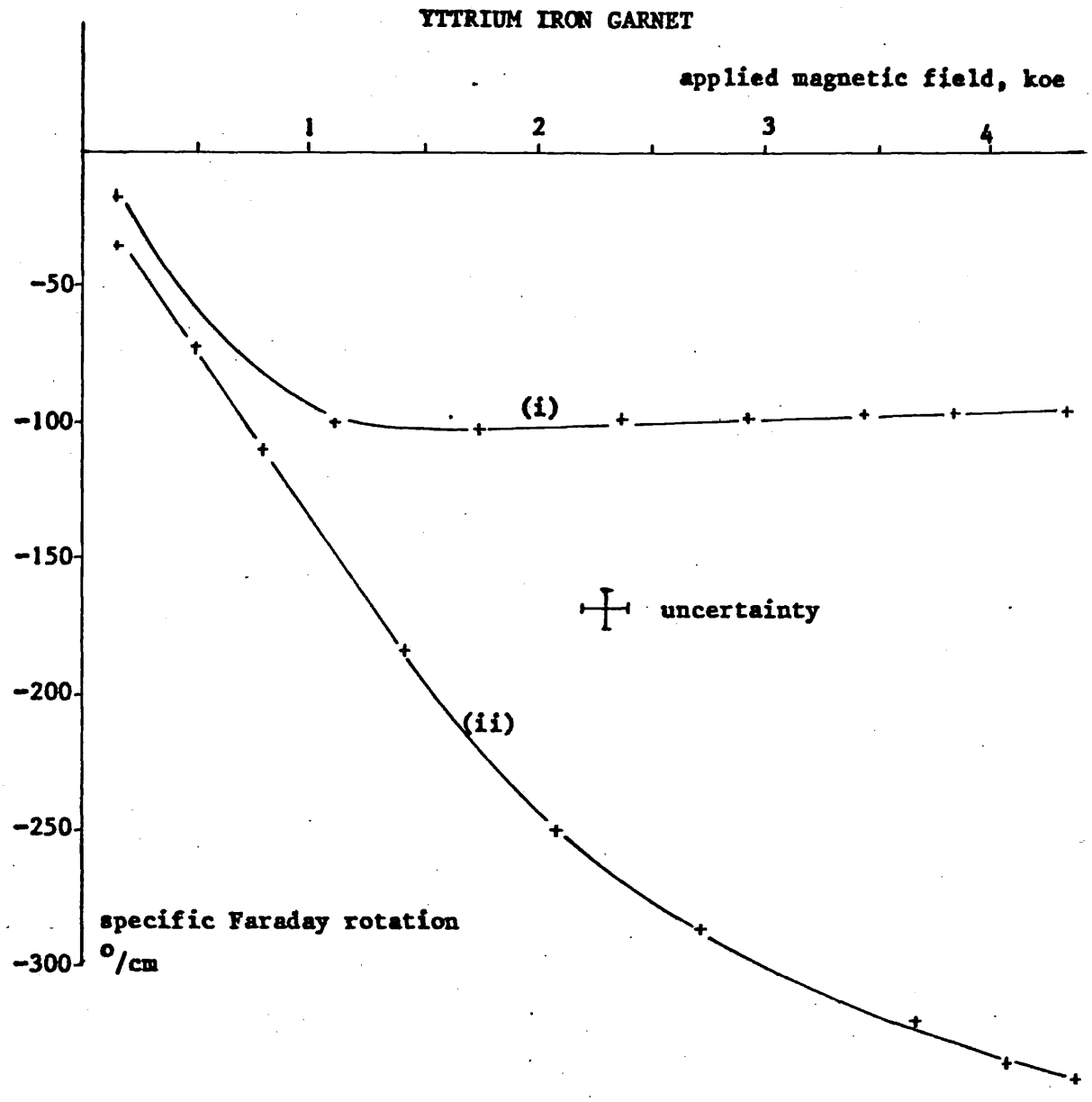

Figure 10.8. Measured Faraday rotation at 891 GHz in yttrium iron garnet against applied magnetic field. [110] direction. (i) 300°K, (ii) 95°K.

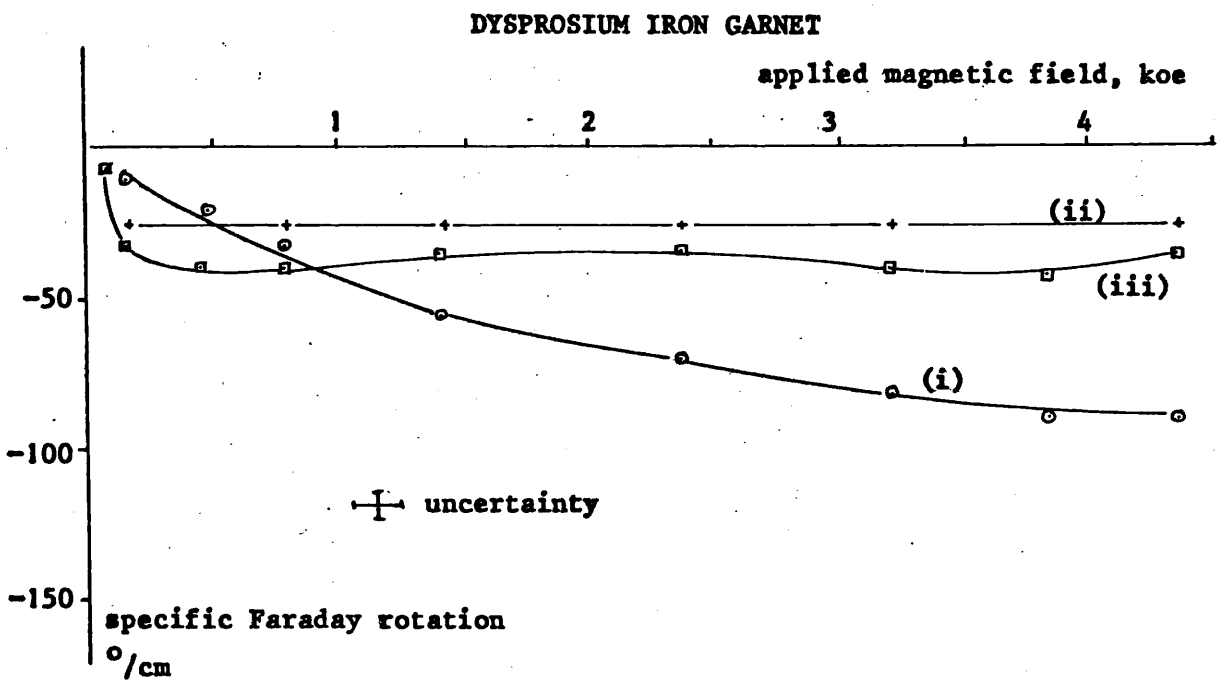

Figure 10.9. Measured Faraday rotation at 891 GHz in dysprosium iron garnet against applied magnetic field. [110] direction. (i) 100°K, (ii) 222°K, and (iii) 300°K

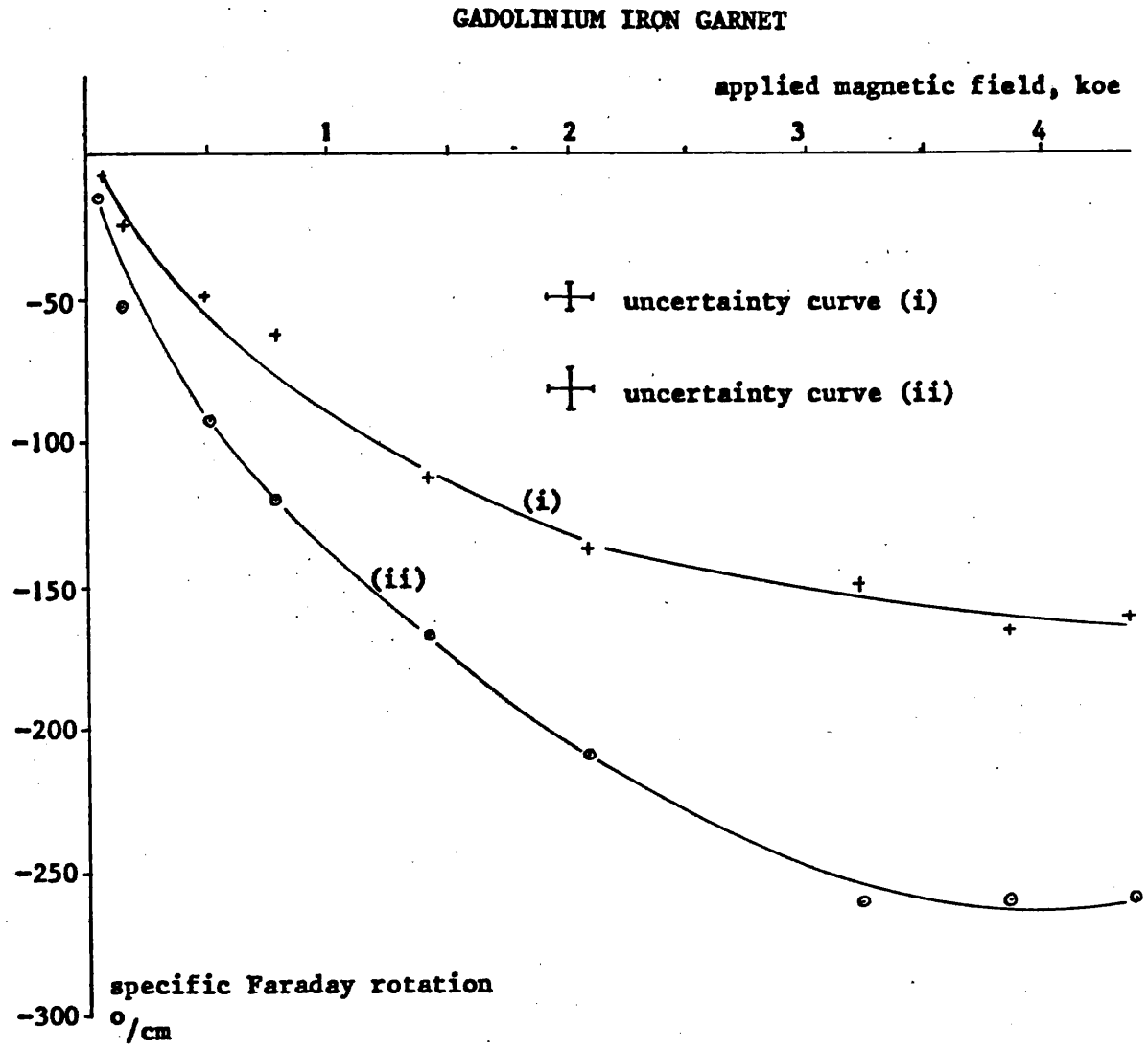

Figure 10.10. Measured Faraday rotation at 891 GHz in gadolinium iron garnet against applied magnetic field at 100°K. (i) [111] direction, (ii) [110] direction.

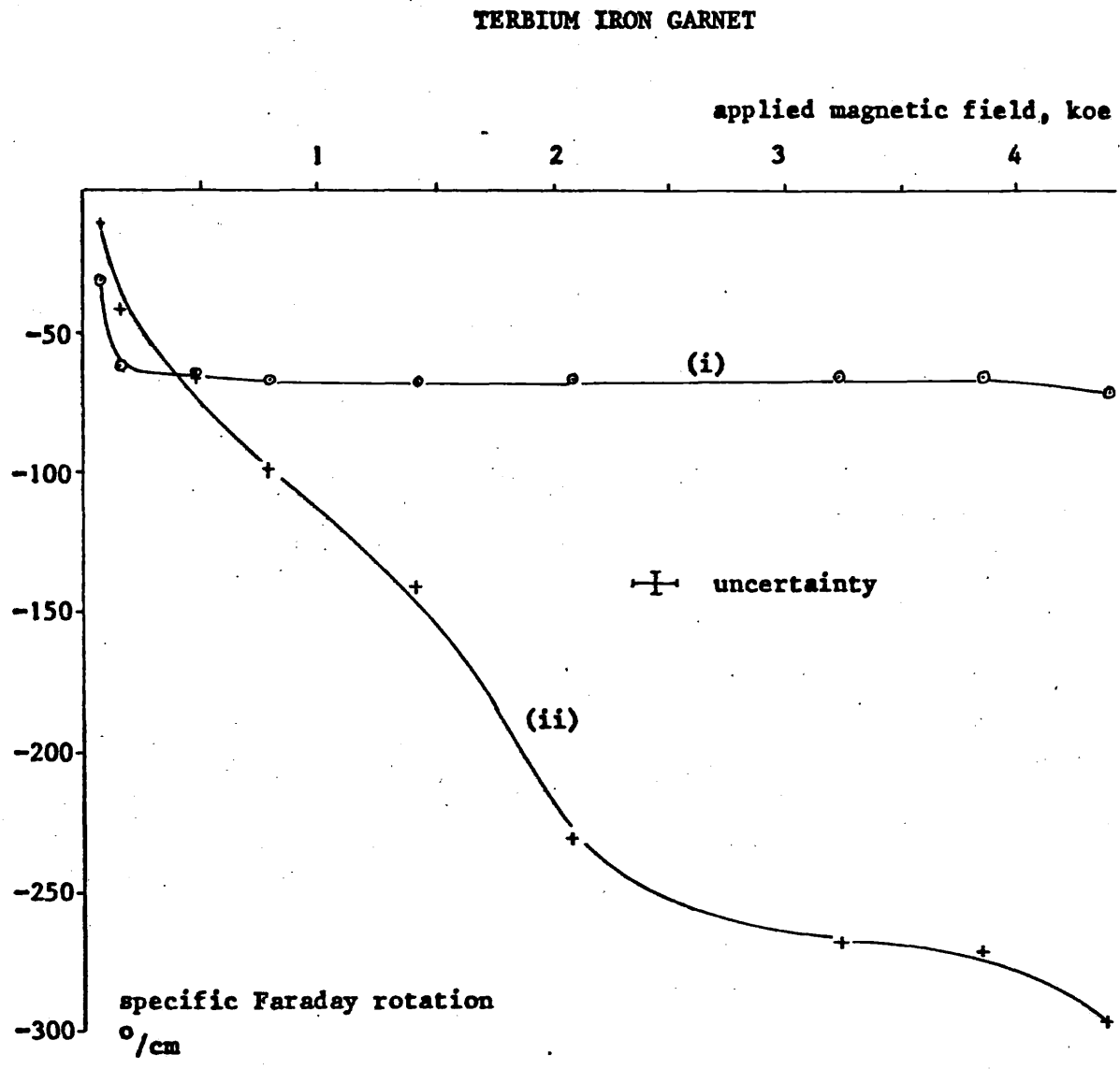

Figure 10.11. Measured Faraday rotation at 891 GHz in terbium iron garnet against applied magnetic field. [111] direction. (i) 300°K, (ii) 88°K.

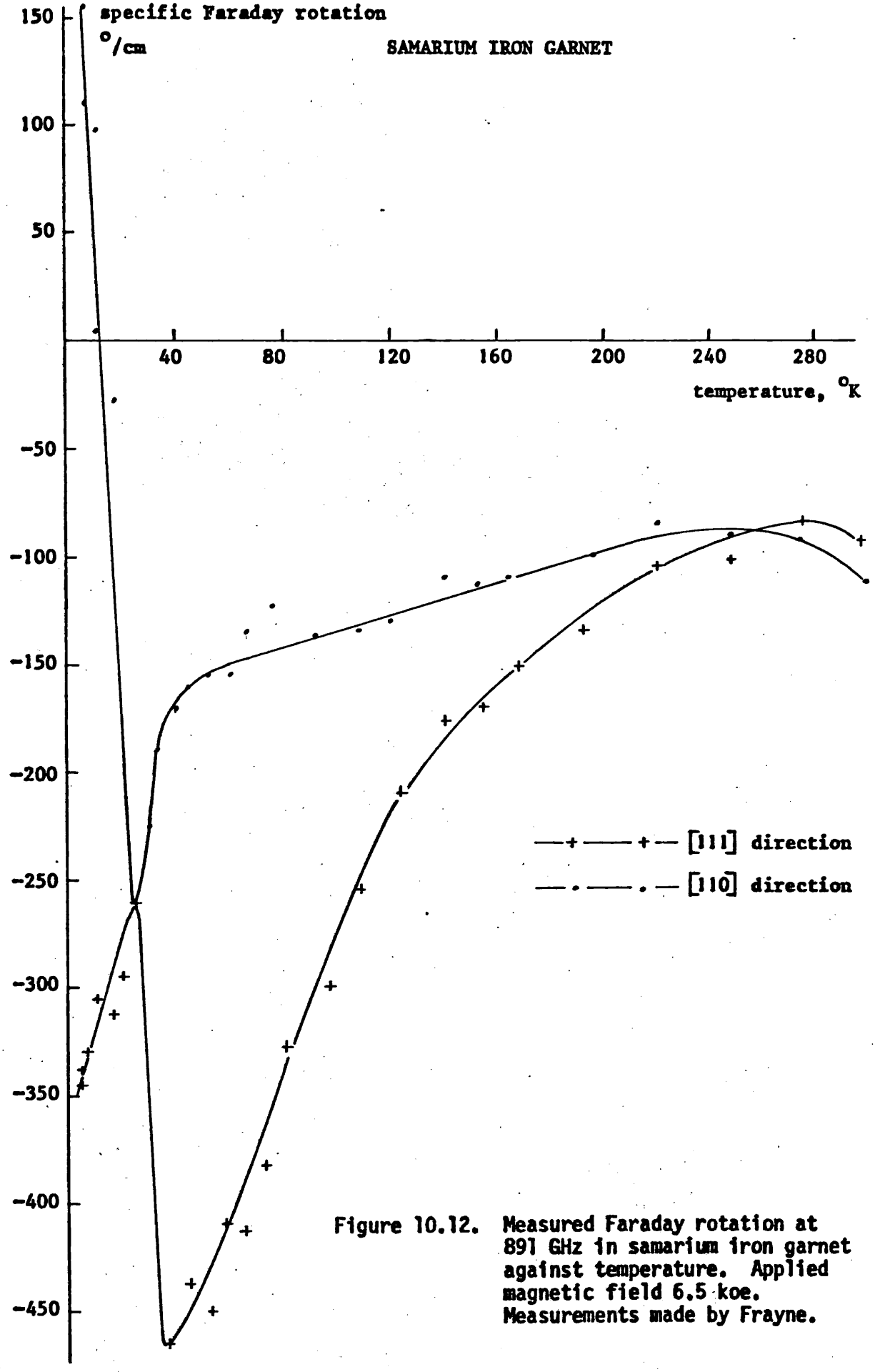

Figure 10.12. Measured Faraday rotation at 891 GHz in samarium iron garnet against temperature. Applied magnetic field 6.5 koe. Measurements made by Frayne.

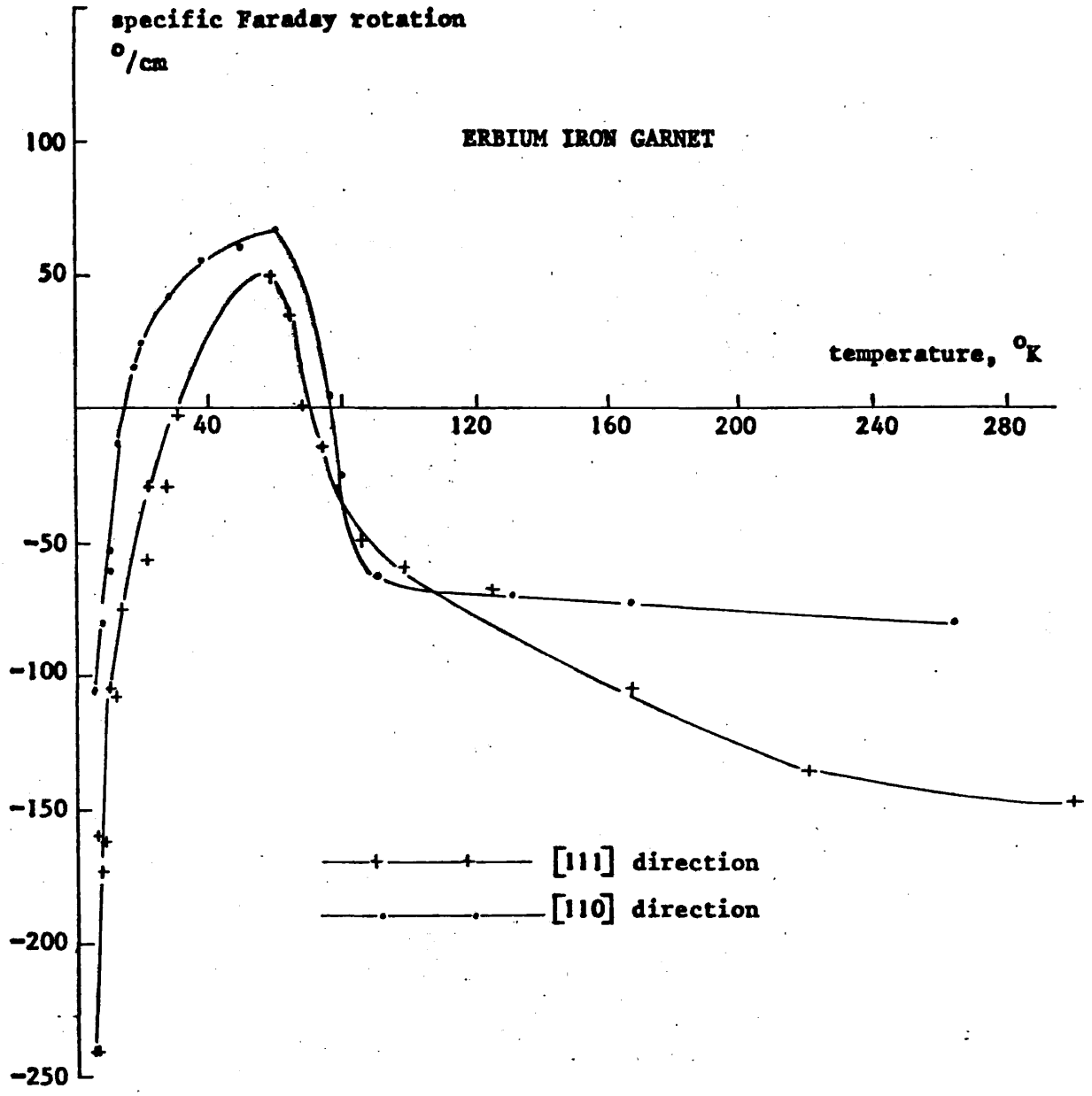

Figure 10.13. Measured Faraday rotation at 891 GHz in erbium iron garnet against temperature. Applied magnetic field 6.5 koe. Measurements made by Frayne.

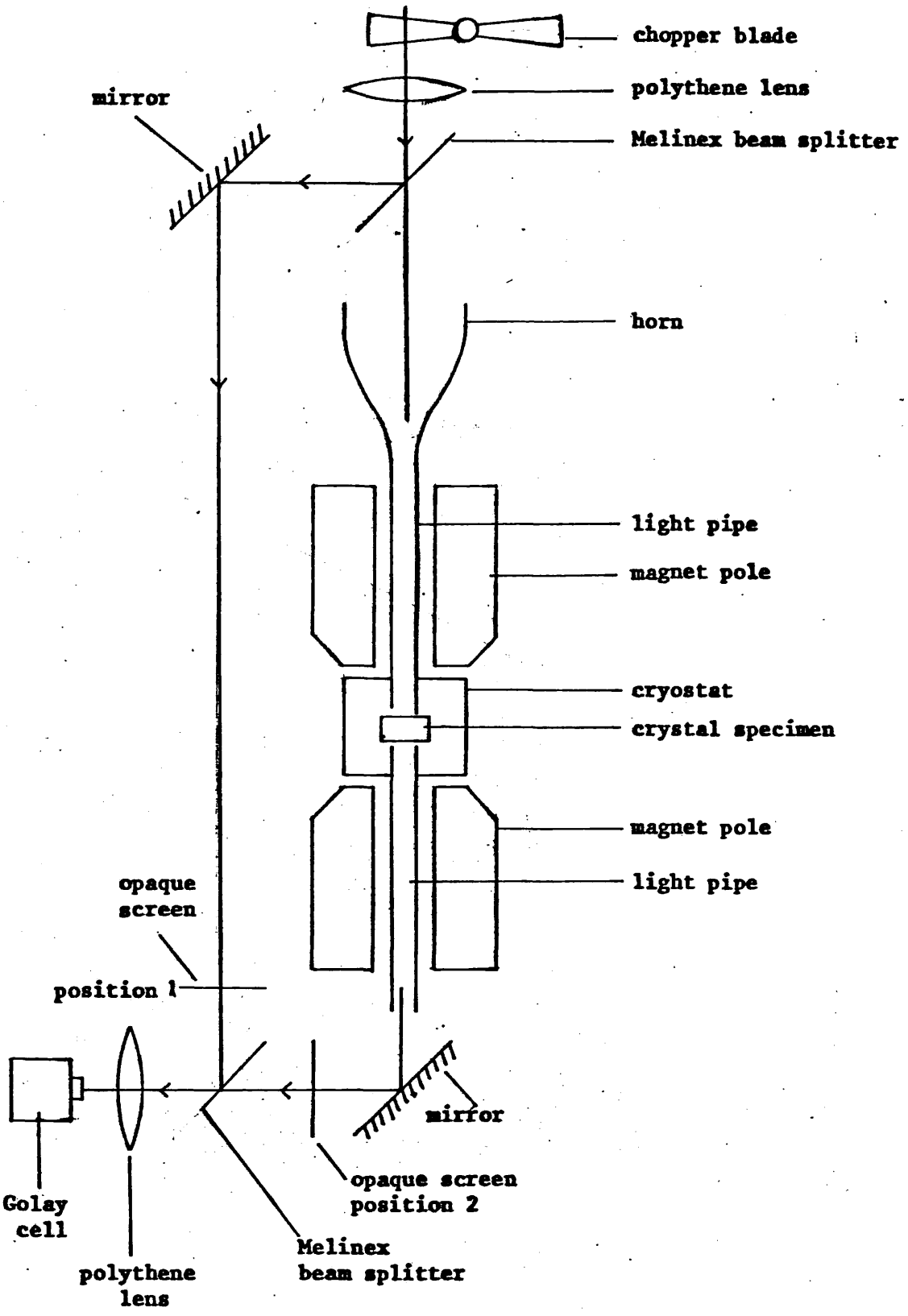

Figure 10.14. Experimental arrangement for measuring the transmission in an iron garnet specimen. To compare the intensity of the radiation from the crystal with that of the monitor, the opaque screen is moved between positions 1 and 2.

percentage transmission through a crystal. For each orientation of the garnets studied, the transmission $T_{1,2}$ was measured for two samples of different thickness $d_{1,2}$. This enabled the expressions of Borets and Grinera[113] describing transmission of electromagnetic radiation in a parallel-sided slab of lossy dielectric medium to be used as

$$T_{1,2} = (1 - r^2)e^{-\alpha d_{1,2}} \qquad \ldots(10.1)$$

where r is the intensity reflection coefficient and α is the attenuation constant calculated from

$$\alpha = \frac{\log_e\left[\frac{T_2}{T_1}\right]}{d_1 - d_2} \qquad \ldots(10.2)$$

These relationships take into account multiple reflections within the sample which must satisfy the condition $\alpha d \geqslant 1.6$. The absorption and reflection coefficients, together with the refractive index calculated from

$$\mu = \frac{1 + \sqrt{r}}{1 - \sqrt{r}} \qquad \ldots(10.3)$$

were evaluated as described in Appendix V for dysprosium, gadolinium, holmium, erbium and samarium iron garnets and are displayed in Figures 10.15 to 10.19. Large errors were incurred in the measurements shown in Figures 10.15 to 10.19, which were mainly due to the normal incidence technique that had to be employed in the cryostat. An evaluation of this method was carried out by Oswald[114]. He showed that for a specific value of d_1/d_2, an optimum value of the product αd exists for determining α, and that the accuracy falls rapidly as αd deviates from this condition.

Because two specimens of sufficiently different thickness were not available for each of the yttrium and terbium iron garnets, only transmission measurements are presented, which are shown in Figures 10.20(a) and 10.20(b) respectively. Transmission measurements made by Frayne are reproduced in Figure 10.21 for erbium and samarium iron garnets. Although attenuation and reflection coefficients are given in Figures 10.18 and 10.19 for these two garnets, Figure 10.21 is included as much lower temperatures were obtained. It must be noted that a 6.5 koe magnetic field was applied to the garnet specimens in these experiments at right angles to the propagation direction of the radiation.

DYSPROSIUM IRON GARNET

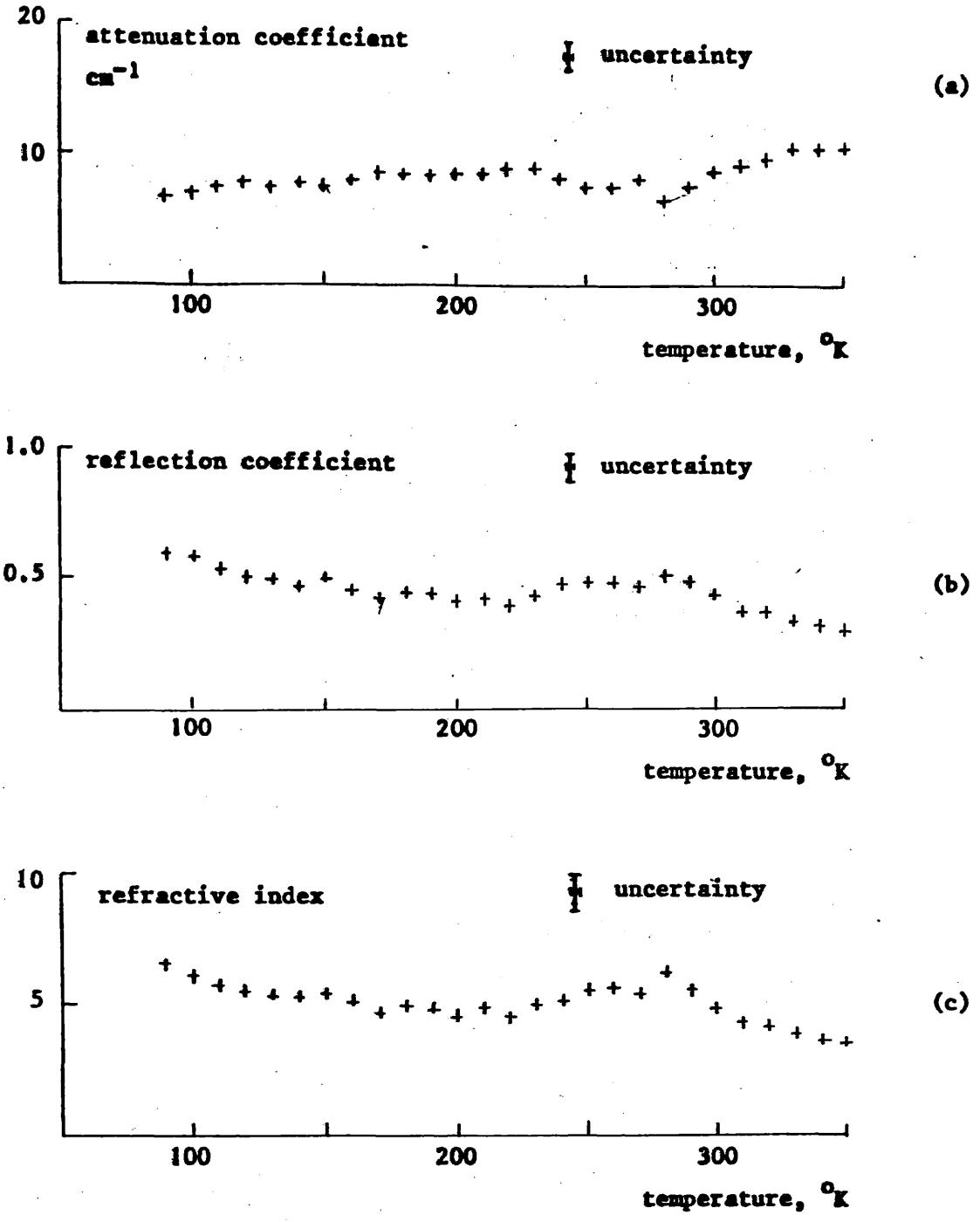

Figure 10.15. (a) Attenuation coefficient, (b) reflection coefficient, and (c) refractive index, at 891 GHz in dysprosium iron garnet against temperature. [111] direction. Applied magnetic field 4.3 koe.

GADOLINIUM IRON GARNET

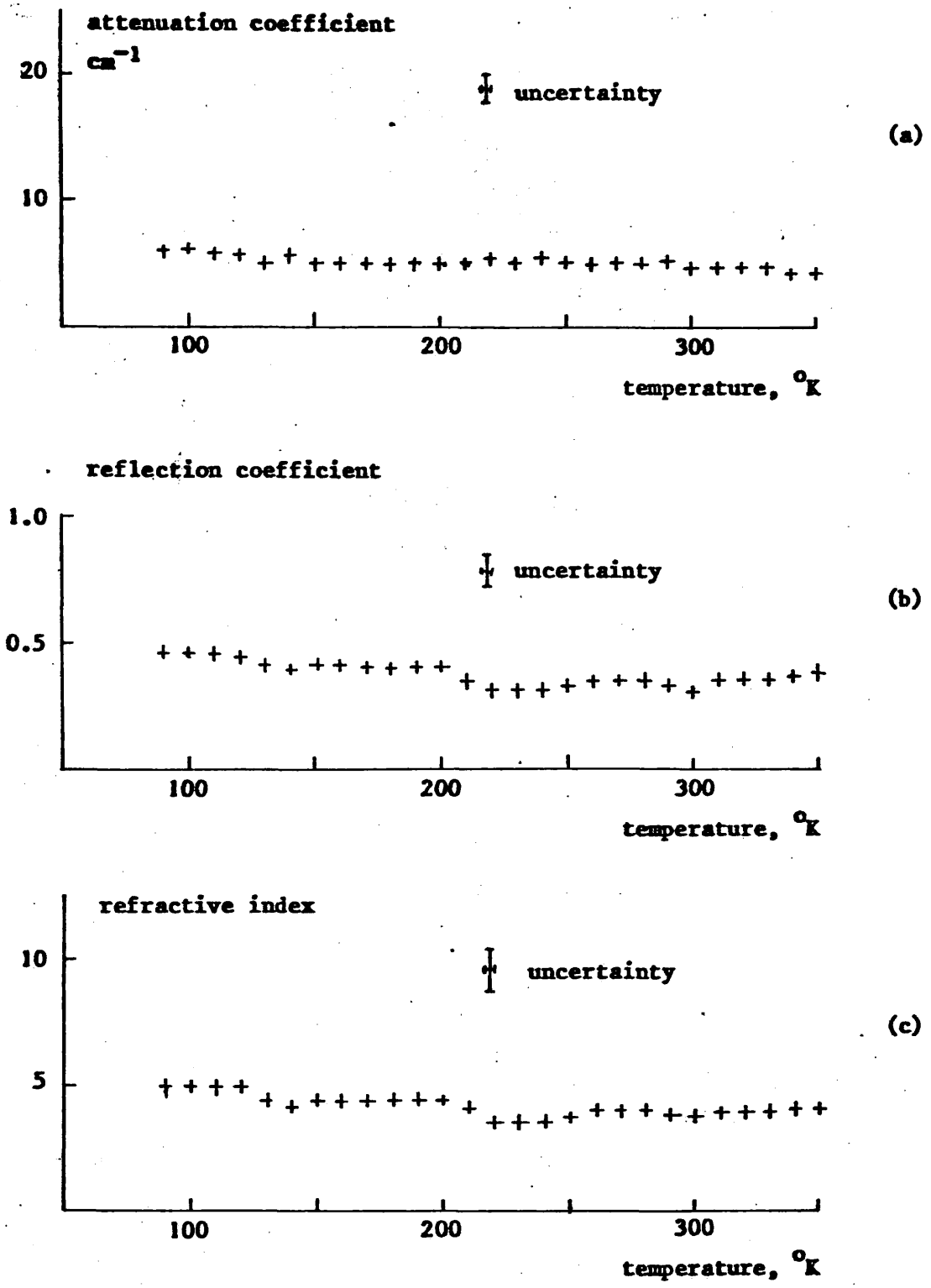

Figure 10.16. (a) Attenuation coefficient, (b) reflection coefficient, and (c) refractive index, at 891 GHz of gadolinium iron garnet against temperature. [110] direction. Applied magnetic field 4.3 koe.

HOLMIUM IRON GARNET

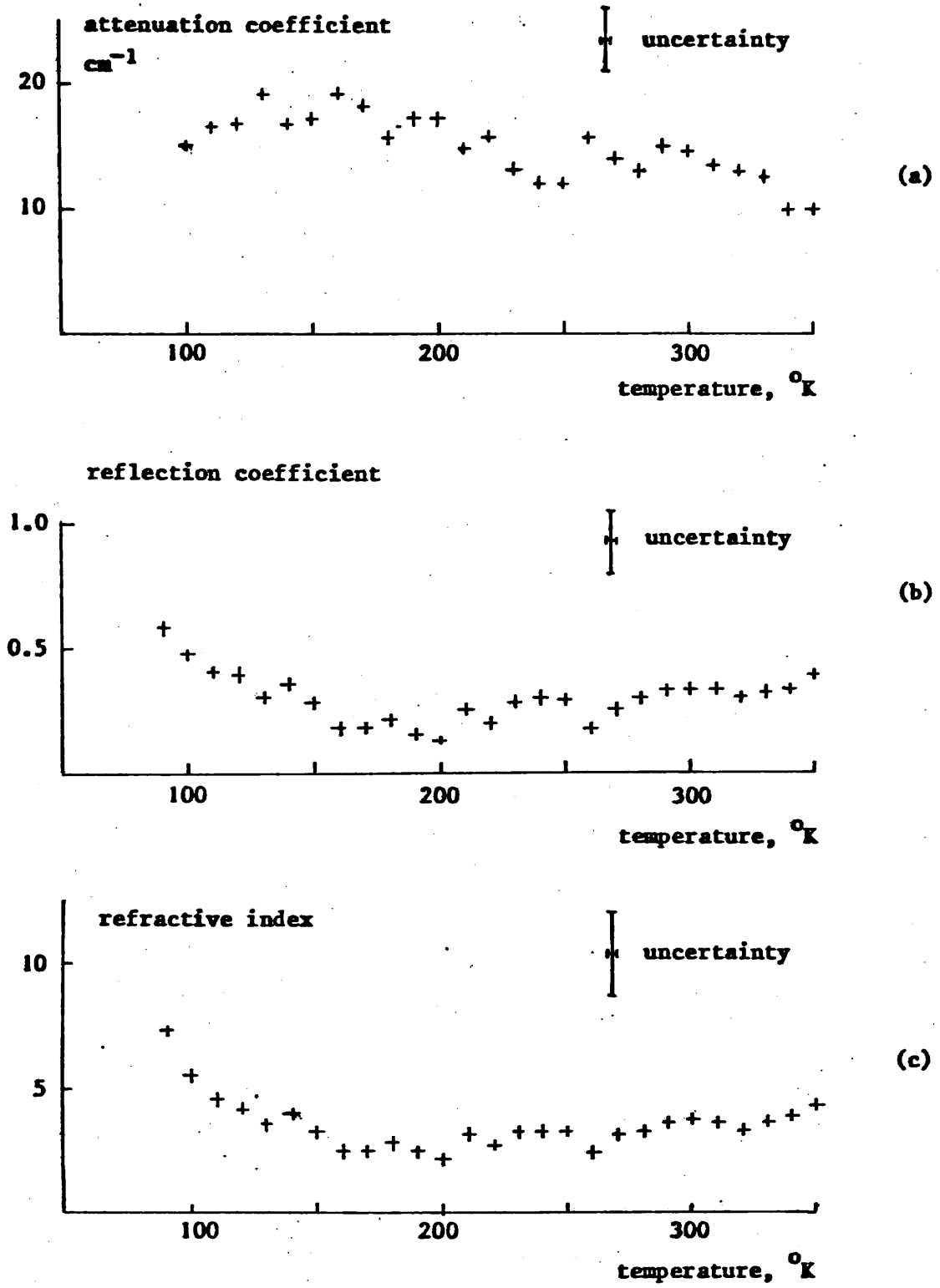

Figure 10.17. (a) Attenuation coefficient, (b) reflection coefficient, and (c) refractive index, at 891 GHz of holmium iron garnet against temperature. [111] direction. Applied magnetic field 4.3 koe.

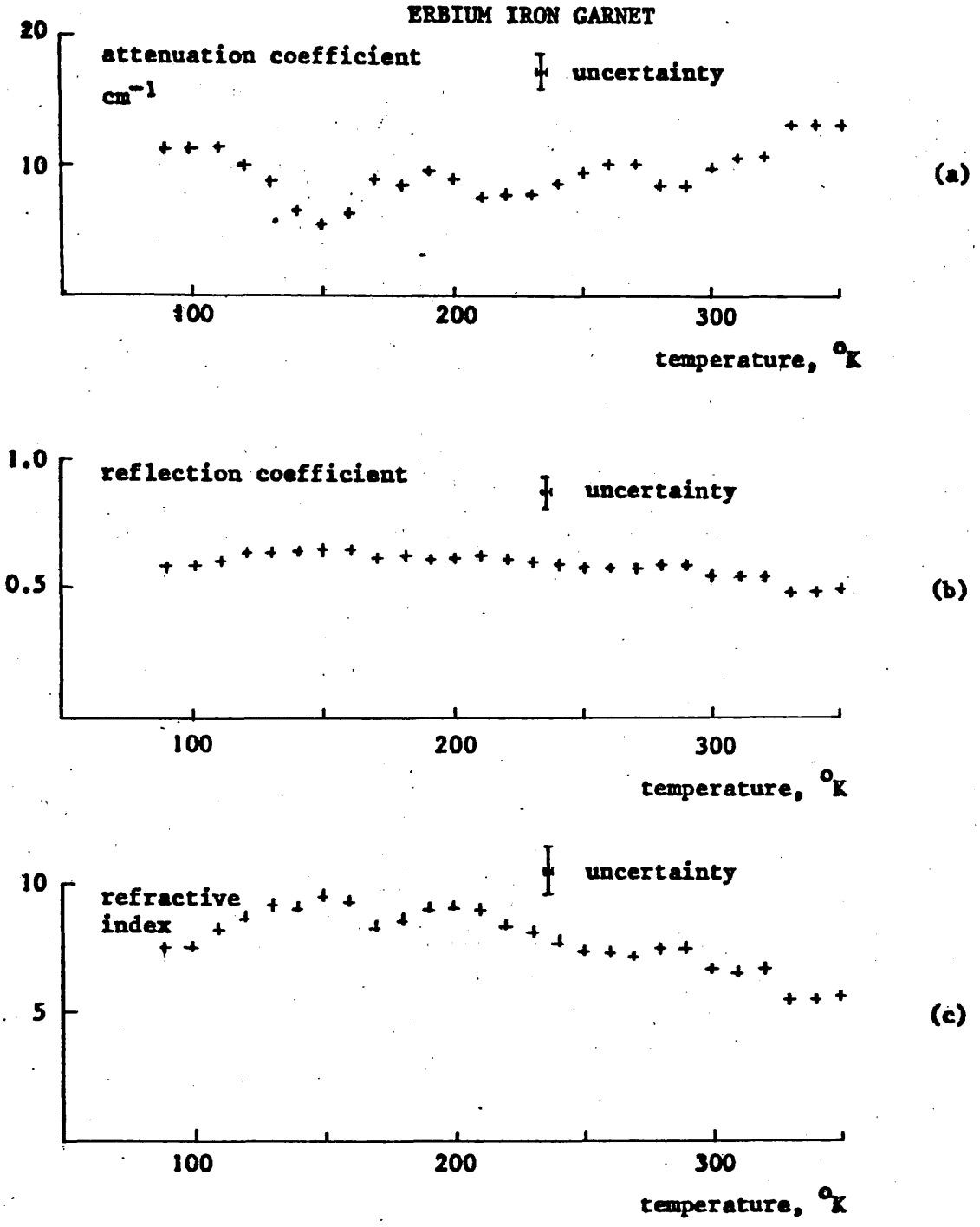

Figure 10.18. (a) Attenuation coefficient, (b) reflection coefficient, and (c) refractive index, at 891 GHz in erbium iron garnet against temperature. [110] direction. Applied magnetic field 4.3 koe.

SAMARIUM IRON GARNET

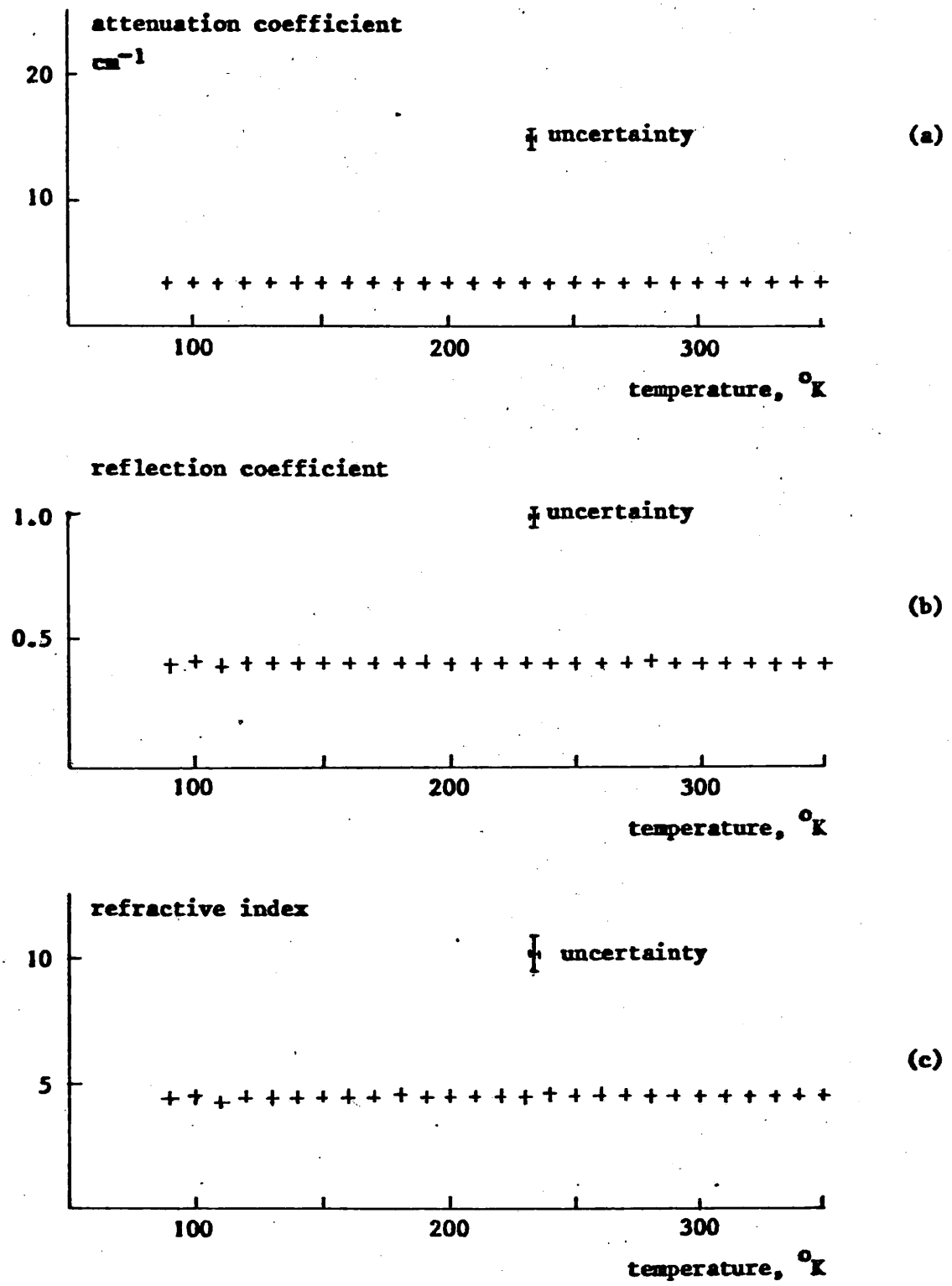

Figure 10.19. (a) Attenuation coefficient, (b) reflection coefficient, and (c) refractive index, at 891 GHz of samarium iron garnet against temperature. [111] direction. Applied magnetic field 4.3 koe.

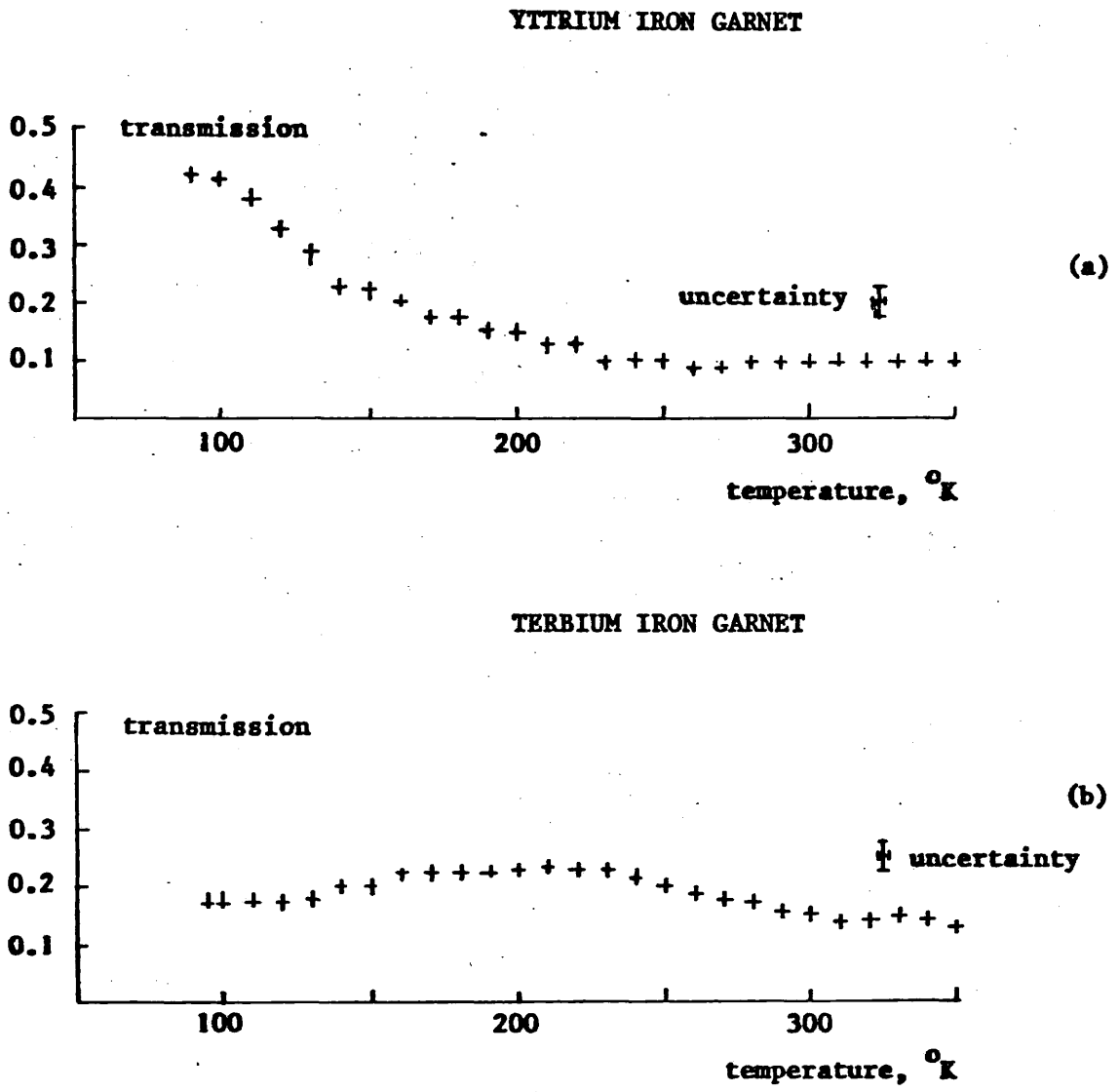

Figure 10.20. Transmission at 891 GHz against temperature in (a) a 2.6 mm thick sample of yttrium iron garnet in a [111] direction, and (b) a 2.0 mm thick sample of terbium iron garnet in a [110] direction. Applied magnetic field 4.3 koe.

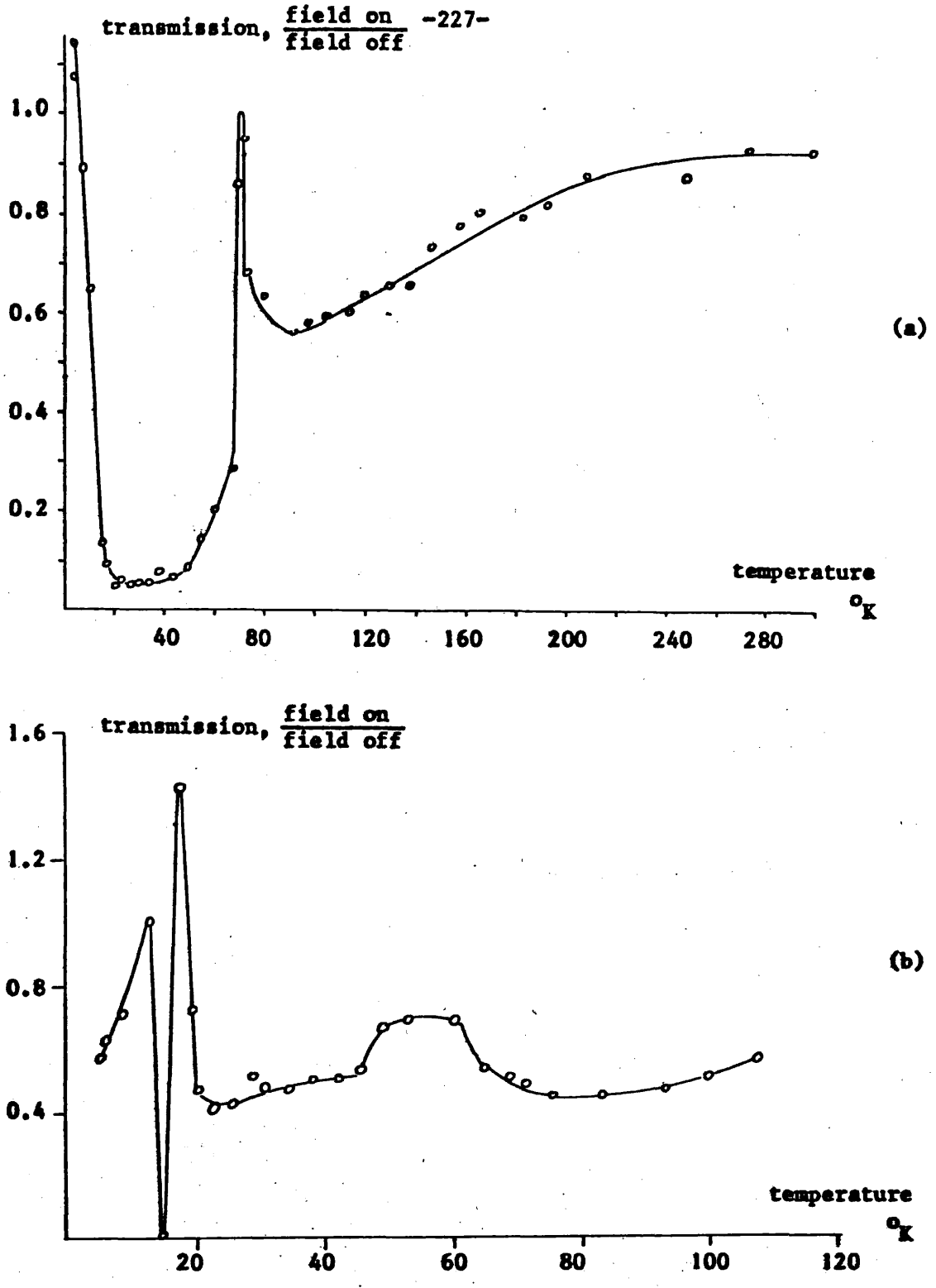

Figure 10.21. Temperature dependence of the ratio of the transmissions at 891 GHz with a transversely applied field to that with zero applied field in (a) a [100] direction in erbium iron garnet and (b) a [111] direction in samarium iron garnet. Applied field 6.5 koe. Measurements made by Frayne.

The attenuation constants, together with the corresponding value of the specific Faraday rotation, have been used to obtain a figure of merit for the garnets, the modulus of which is plotted against temperature in Figure 10.22. Of the five garnet types of which adequate information was attained, samarium iron garnet is seen to possess a superior performance over the entire experimental temperature range.

For the theoretical analysis of Faraday rotation that follows in the next chapter, the calculations performed require a knowledge of the required refractive index of the garnets. With the exception of erbium iron garnet and holmium iron garnet at low temperatures, this variation is seen to be slight over most of the experimental temperature range. Because of the large errors in the normal incidence measurement technique, an interferometric method was used to confirm the measurements of refractive index at room temperature.

10.5. Interferometric measurement of refractive index

Figure 10.23(a) shows the arrangement of a Michelson interferometer where a garnet of thickness d was mounted across an iris placed in one arm. In the second arm, a similar iris was inserted and an attenuator was introduced to balance the losses caused by the garnet. Illuminated by a plane wavefront from an HCN laser, a change of optical path created by rotating the garnet about a vertical axis as illustrated in Figure 10.23(b), enabled the number N of each minimum output from the interferometer to be plotted against the angle of rotation. The refractive index μ of the garnets was thus obtained from the relationship

$$(2N-1)\frac{\lambda}{2} = d\left[\left\{\mu^2 - \sin^2\theta\right\}^{\frac{1}{2}} - \cos\theta - \mu + 1\right]$$

where θ is the angle between the normal to the crystal face and the direction of the incident radiation, λ is the free-space wavelength and $\theta = 0^{\circ}$ corresponds to a condition of constructive interference. The values of refractive index obtained using garnet specimens that were large enough to allow an adequate transmitted intensity are shown in Table 10.1.

Reasonable agreement was obtained between the interferometric and the transmission measurements at room temperature. The largest discrepancy occurred with holmium iron garnet but all differences are within the estimated errors and it is therefore considered that the temperature varying data is sufficiently accurate to show the general trend.

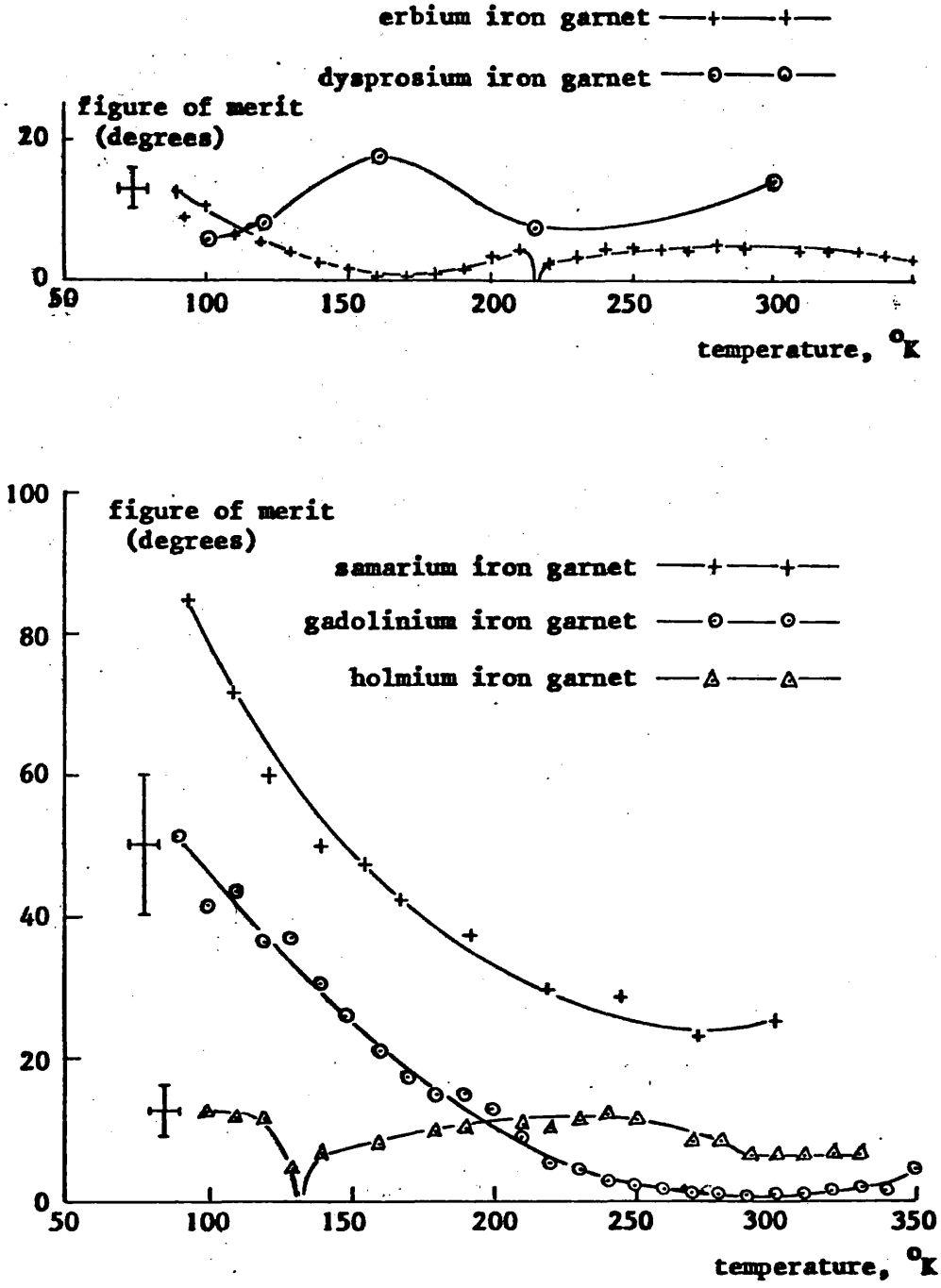

Figure 10.22. Figure of merit of rare-earth iron garnets at 891 GHz. Crossed bars to the left of the curves represent the uncertainty of the adjacent point on that curve. The fractional error for the figure of merit remains approximately constant over the remainder of the data.

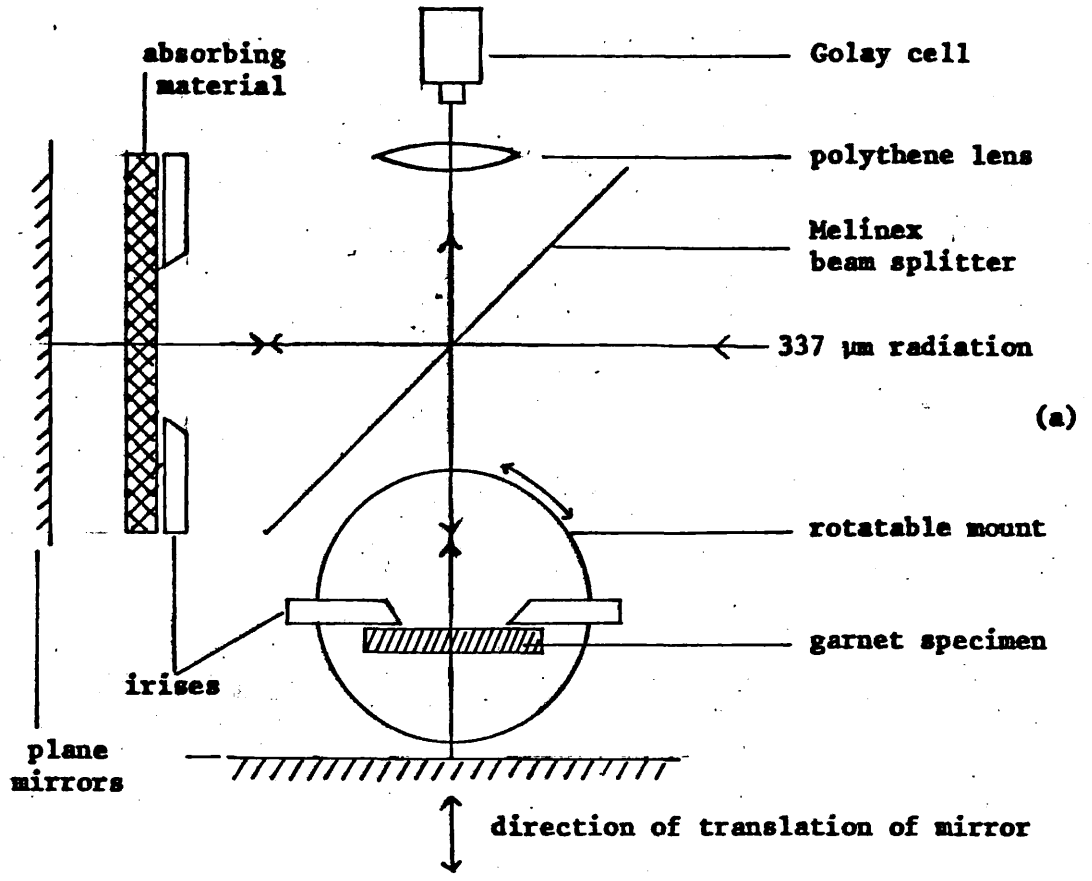

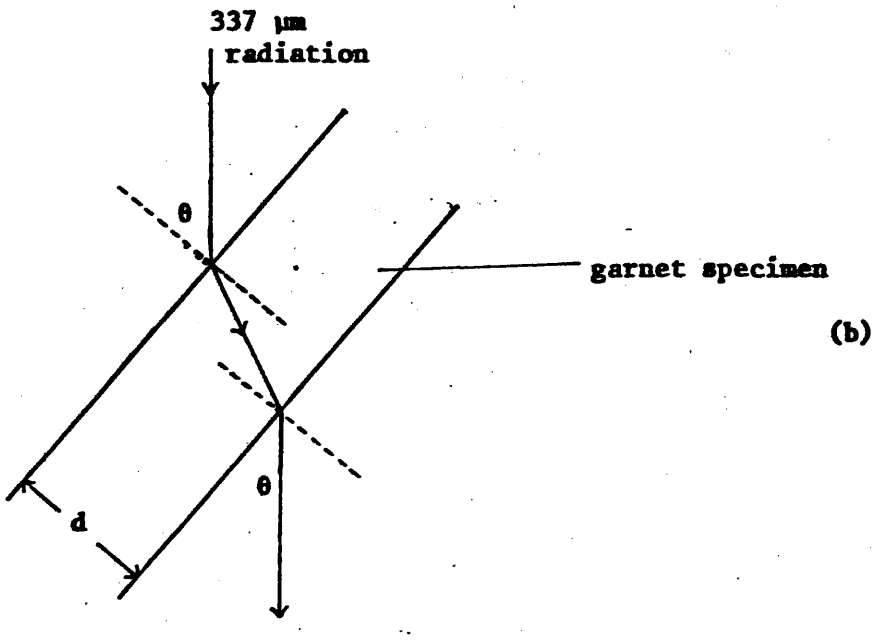

Figure 10.23. (a) Arrangement of Michelson interferometer used to measure the refractive index of the garnet specimen at room temperature; (b) garnet rotated at angle θ to radiation.

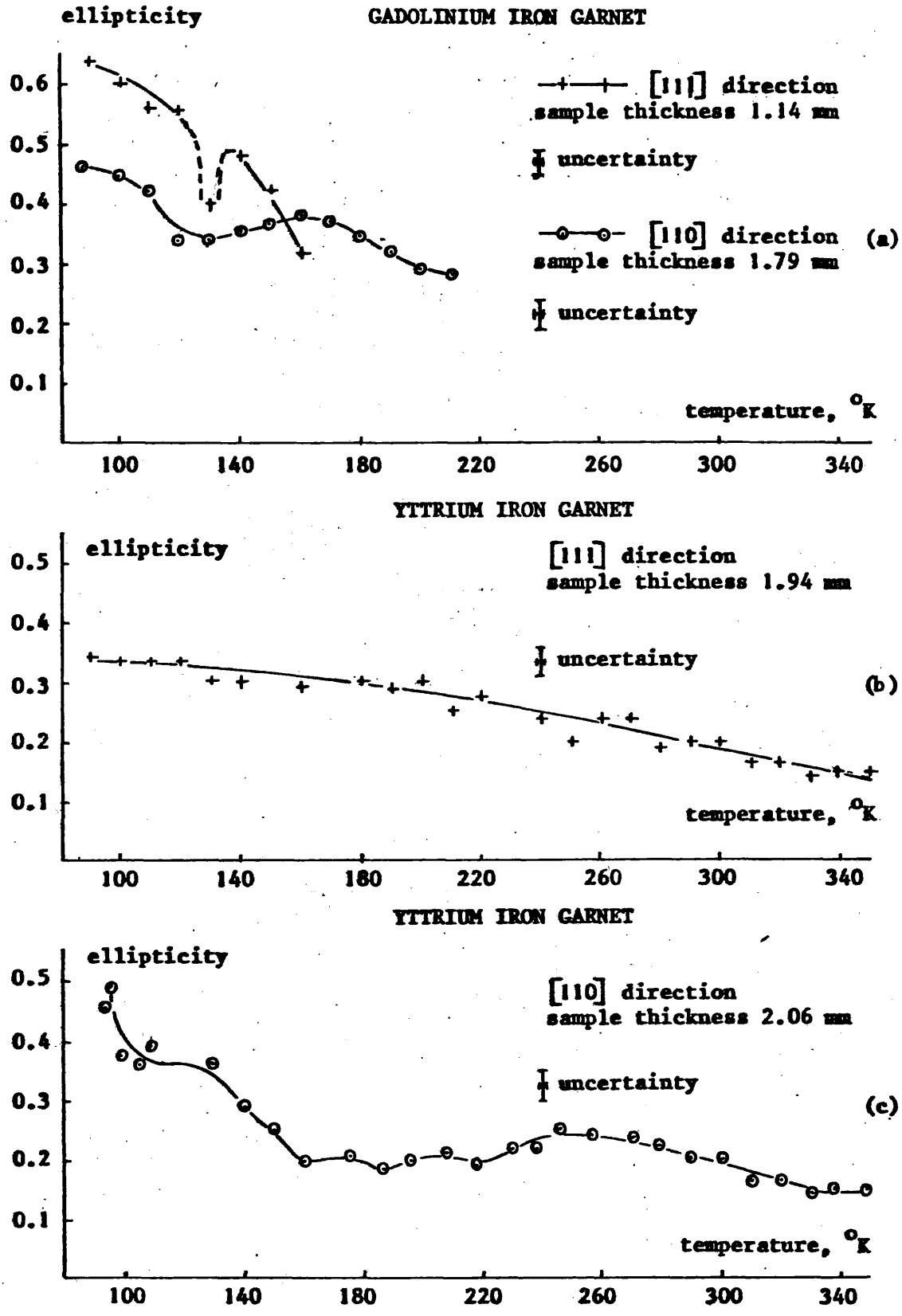

Figure 10.24. Ellipticity against temperature at 891 GHz in (a) gadolinium iron garnet in [111] and [110] directions, (b) yttrium iron garnet in [111] direction, and (c) yttrium iron garnet in the [110] direction. Applied magnetic field 4.3 koe.

Table 10.1

Refractive index of the rare-earth and yttrium iron garnets at 891 GHz at room temperature using the interferometric technique

Iron garnet	μ
DyIG [110]	4.18 ± 1.20
SmIG [111]	4.17 ± 0.80
HoIG [111]	4.48 ± 0.60
YIG [111]	4.25 ± 0.55
YIG [110]	4.32 ± 0.40

10.6. Ellipticity

In yttrium and gadolinium iron garnets, the transmitted radiation was observed to become elliptically polarised. With the same experimental arrangement as that used to observe Faraday rotation, the minimum and maximum transmitted intensity observed on rotation of the analyser were measured. The ellipticity, as defined in Chapter Eight, was thus obtained from the square root of the ratio of the two measurements and is shown in Figure 10.24 for the four crystals in which the effect was noted. The ellipticity is seen to be most pronounced at low temperatures and decreases with increase of temperature to a level below that measurable by the system.

A minimum occurring in the graph for the [111] direction of gadolinium iron garnet is signified by a broken line as the data are insufficient to locate accurately its position. Further comment on this curve is made in section 11.3.

CHAPTER ELEVEN

ANALYSIS OF MAGNETO-OPTICAL DATA

11.1. Introduction

In the previous chapter, an exploration of some of the magneto-optical properties of certain iron garnets in the submillimetre region was described. An analysis of these properties in terms of the physical processes outlined in Chapter Eight and the parameters associated with them will now be made.

11.2. Undamped systems

By ignoring loss terms, simplified expressions for the susceptibility tensor can be derived and further simplified by making approximations applicable to the low or high frequency regions. Equations 8.8, 8.10 and 8.27 enable the formulation of a relationship for the specific Faraday rotation in terms of the susceptibility elements from which two standard expressions have been derived[115]

$$\theta_F = \frac{\sqrt{\varepsilon_r}}{2C} \cdot \gamma_{EFF} \cdot \frac{\omega^2}{\omega_0^2 - \omega^2} \cdot 4\pi M \qquad \ldots(11.1)$$

for the low frequency ferromagnetic mode and

$$\theta_F = \frac{\sqrt{\varepsilon_r}}{2C} \cdot 4\pi \cdot \{\gamma_1 M_1 + \gamma_2 M_2\} \qquad \ldots(11.2)$$

for the high requency exchange mode. ε_r is the dielectric constant and the other terms are those defined in Chapter Eight.

Analysis involving each of the above equations requires a knowledge of the spectroscopic splitting factors for each sublattice. The quantum numbers shown in Table 9.2 enable the g factors to be calculated using the familiar formula[116]

$$g = 1 + \frac{J(J+1) + S(S+1) - L(L+1)}{2J(J+1)}$$

These values, displayed in Table 11.1, apply at the absolute zero temperature. A temperature-dependent variation of the g values has been assumed by Johnson and Tebble[117] and by Chetkin and Shalygin[118] who used equation 11.2 to explain their Faraday rotation measurements in the near infra-red region. The theoretical value of 2 for the g factor of the ferric sublattice agrees well with the numerical values

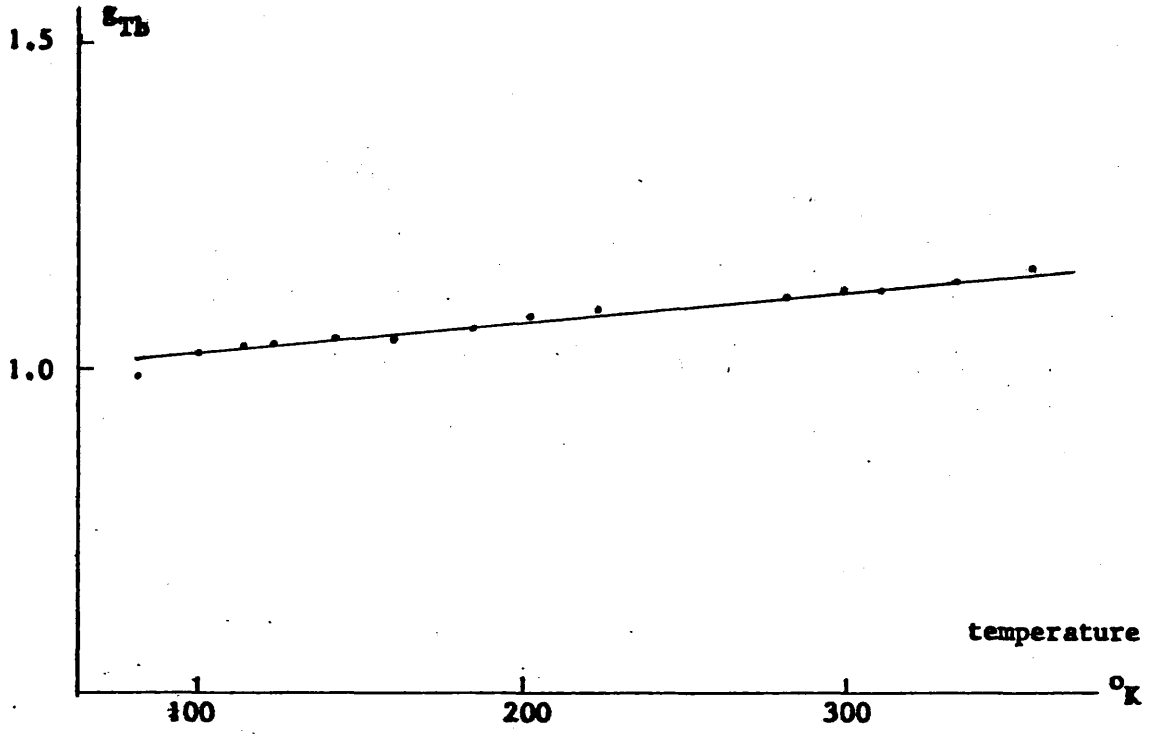

Figure 11.1. The temperature dependence of g_{Tb} in terbium iron garnet obtained from Faraday rotation measurements using 6.5 μm wavelength radiation. After Chetkin and Shalygin[118].

Table 11.1

Spectroscopic splitting factors of trivalent rare-earth ions calculated from the values of L and S in Table 9.2

Rare-earth ions	Sm	Gd	Tb	Dy	Ho	Er
g	0	2	1.5	1.33	1.25	1.2

Table 11.2

Thermal variation of spectroscopic splitting factors calculated from Faraday rotation measurements at a wavelength of 5.0 μm. After Johnson and Tebble[117]

T °K	80	100	120	140	160	180
g(Fe)	2.06	2.06	2.06	2.07	2.07	2.07
g(Gd)	2.17	2.17	2.13	2.05	1.97	1.96
g(Dy)	0.77	0.84	0.86	0.89	0.90	0.90
	200	220	240	260	280	300
g(Fe)	2.08	2.08	2.08	2.08	2.08	2.08
g(Gd)	1.96	1.96	1.96	1.97	1.99	2.00
g(Dy)	0.92	0.96	0.96	1.00	1.04	1.06

determined by Johnson and Tebble on examination of the rotation in yttrium iron garnet. Chapter Nine explained that an 'equivalent' iron lattice is composed of two separate, tightly bound sublattices. The results of Johnson and Tebble displayed in Table 11.2 assume that g is equal for the ferric ions on each type of site. Confirmation of this is shown by the measurements of Rodrigue et al.[119] who evaluated the g values for the a and d subsystems at 300°K as 2.003 and 2.005 respectively. Also working in the microwave region, Weiss[120] substantiates the small temperature variation with his measurements on the effective g factor g_{EFF}, shown in Figure 11.2. The g factor for gadolinium ions in Table 11.1 also has a value close to the observed value, and is subject to little thermal change. Again microwave data support this interpretation as Geschwind and Walker[121] found little

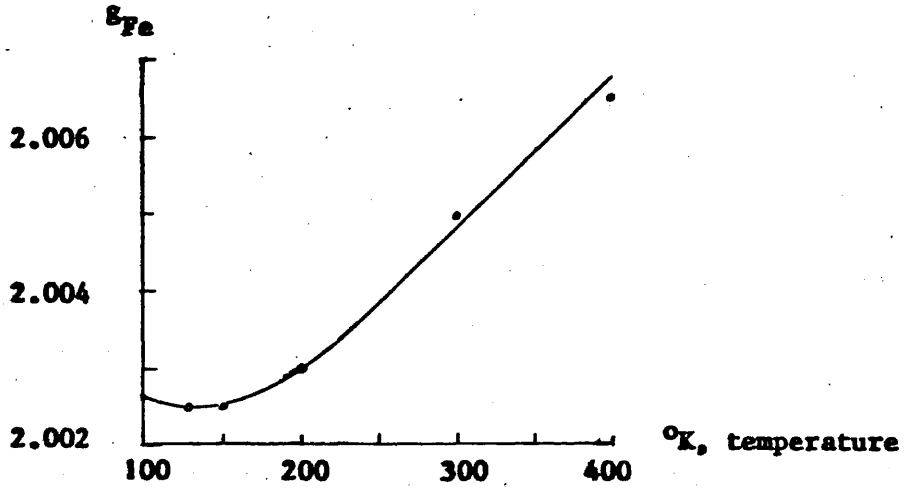

Figure 11.2. The temperature dependence of g_{Fe} for the 'equivalent' ferric lattice in yttrium iron garnet measured at 24 GHz. After Weiss[120].

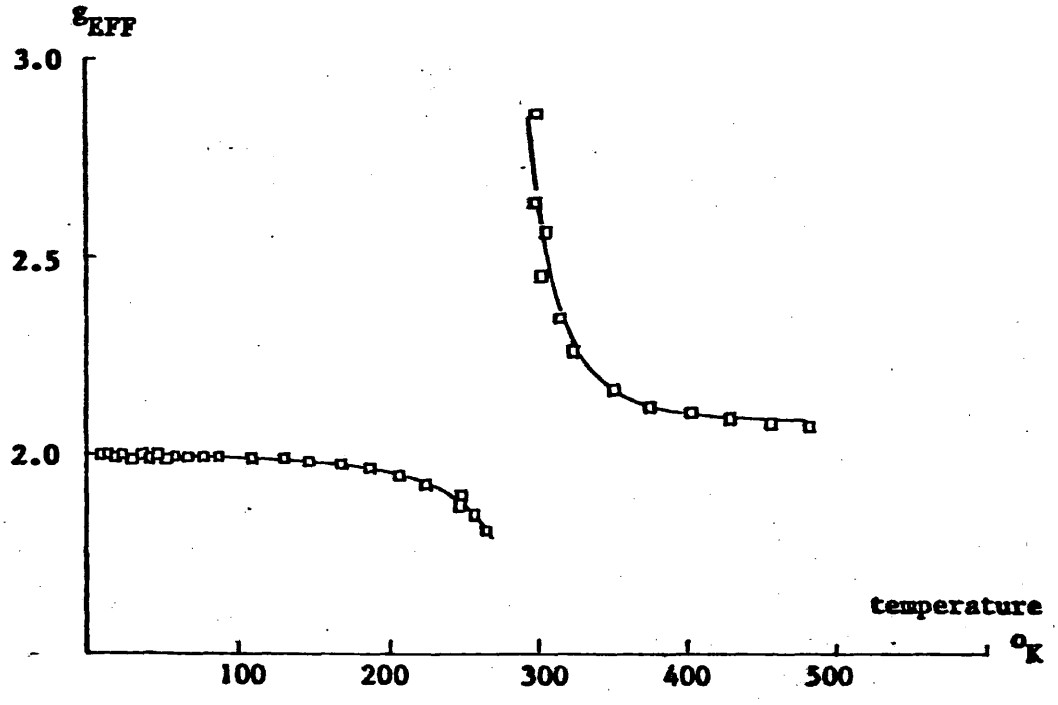

Figure 11.3. The temperature dependence of the effective g factor in gadolinium iron garnet measured at 9.2 GHz. After Rodrigue[119].

difference between the values of the g factors of the gadolinium ions and the ferric sublattice, as $g_{Fe} - g_{Gd} = 0.02$. Rodrigue et al.[119] obtained a similar result over a large temperature range, an exception being in the temperature region close to the magnetic compensation point. These results are displayed in Figure 11.3, where an effective spectroscopic splitting factor for gadolinium iron garnet has been plotted against temperature. The g factors for the dysprosium and terbium ions displayed in Table 11.1 are greater than their experimentally deduced values in Table 11.2 and Figure 11.1 respectively. With the exception of yttrium iron garnet, large linewidths observed in microwave resonance experiments[122] suggest that in many of the rare-earth iron garnets, damping effects cannot be ignored. If the spin-lattice damping quenches the angular momentum of the rare-earth ions significantly then equation 11.2, which takes no account of loss terms, will produce inaccurate values for the rare-earth ion g factors.

It is instructive to investigate the magneto-optical properties of the iron garnets using the values of g in Table 11.1 Examination of the ferromagnetic mode requires a knowledge of the effective gyromagnetic ratio on which the sense of the rotation as well as its magnitude depends. Using the magnetisation data of Bertaut and Pauthenet[107], γ_{EFF} has been calculated for five different garnets and is shown in Figure 11.4. The plots for erbium iron garnet and holmium iron garnet show two inflection points, as expected for the general case for γ_{EFF} of a two-sublattice system. The expression

$$\gamma_{EFF} = \frac{M_1 + M_2}{\frac{M_1}{\gamma_1} + \frac{M_2}{\gamma_2}}$$

shows that at the magnetic compensation temperature when $M=M_1+M_2=0$, γ_{EFF} must become zero, and that if $\gamma_1 \neq \gamma_2$, the angular momentum $S = M_1/\gamma_1 + M_2/\gamma_2$ will become zero at a different temperature, causing γ_{EFF} to become infinite. The angular momentum and magnetisation of a subsystem are oppositely orientated due to the negative electronic charge; however, in the region between the two compensation points M and S have the same sign and γ_{EFF} is positive. Using the values shown in Figure 11.4 in equation 11.1, the Faraday rotation predicted for the ferromagnetic mode has been calculated and is displayed in Figure 11.5. Although the shape of the curve for gadolinium iron garnet shows some similarity with the experimental measurements, the rotations of the other four garnets are seen to disagree. The inaccuracy of these

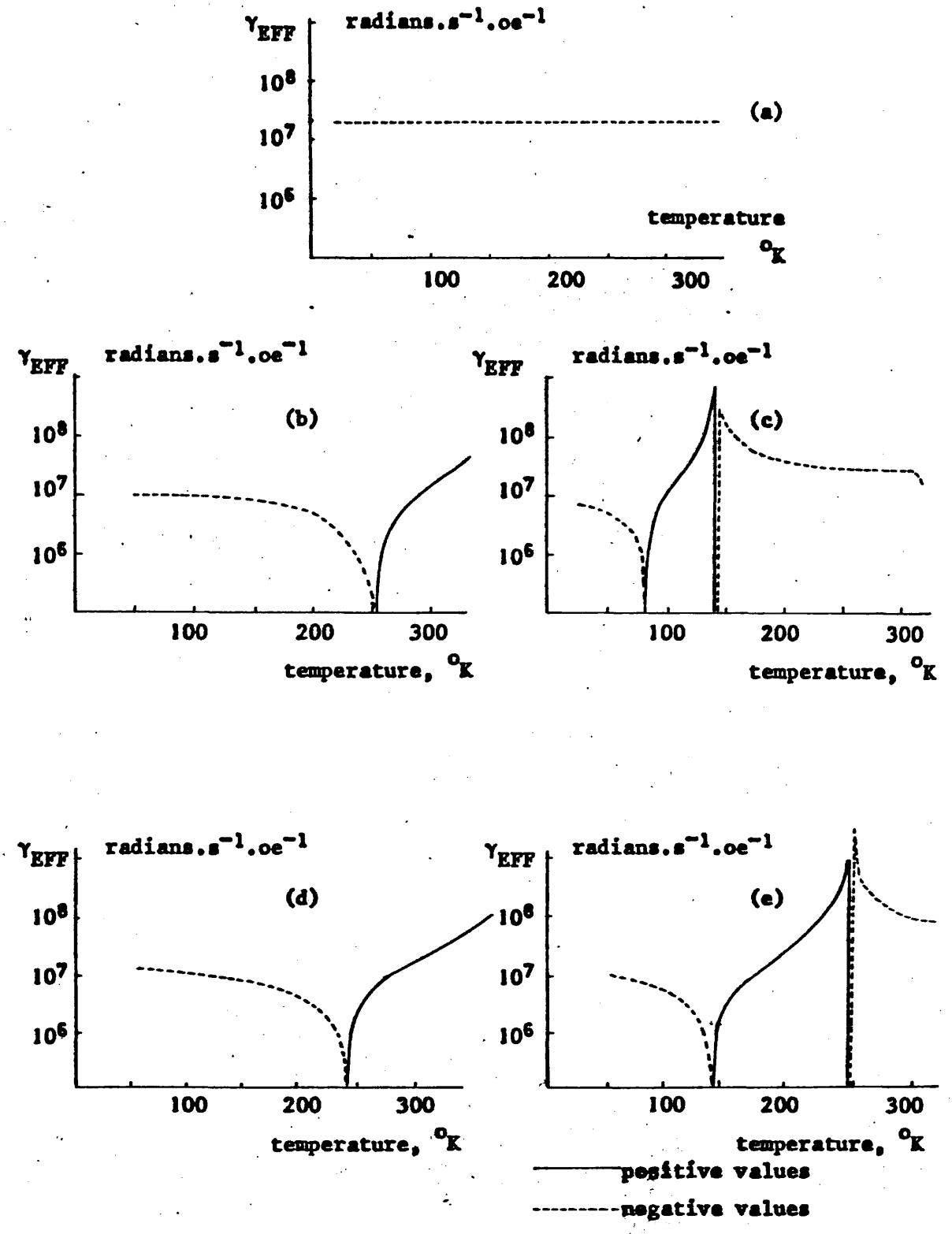

Figure 11.4. Temperature variation of the effective gyromagnetic ratio for (a) gadolinium, (b) terbium, (c) erbium, (d) dysprosium, and (e) holmium iron garnets employing values for the rare-earth g factors in Table 11.1. $g_{Fe} = 2$.

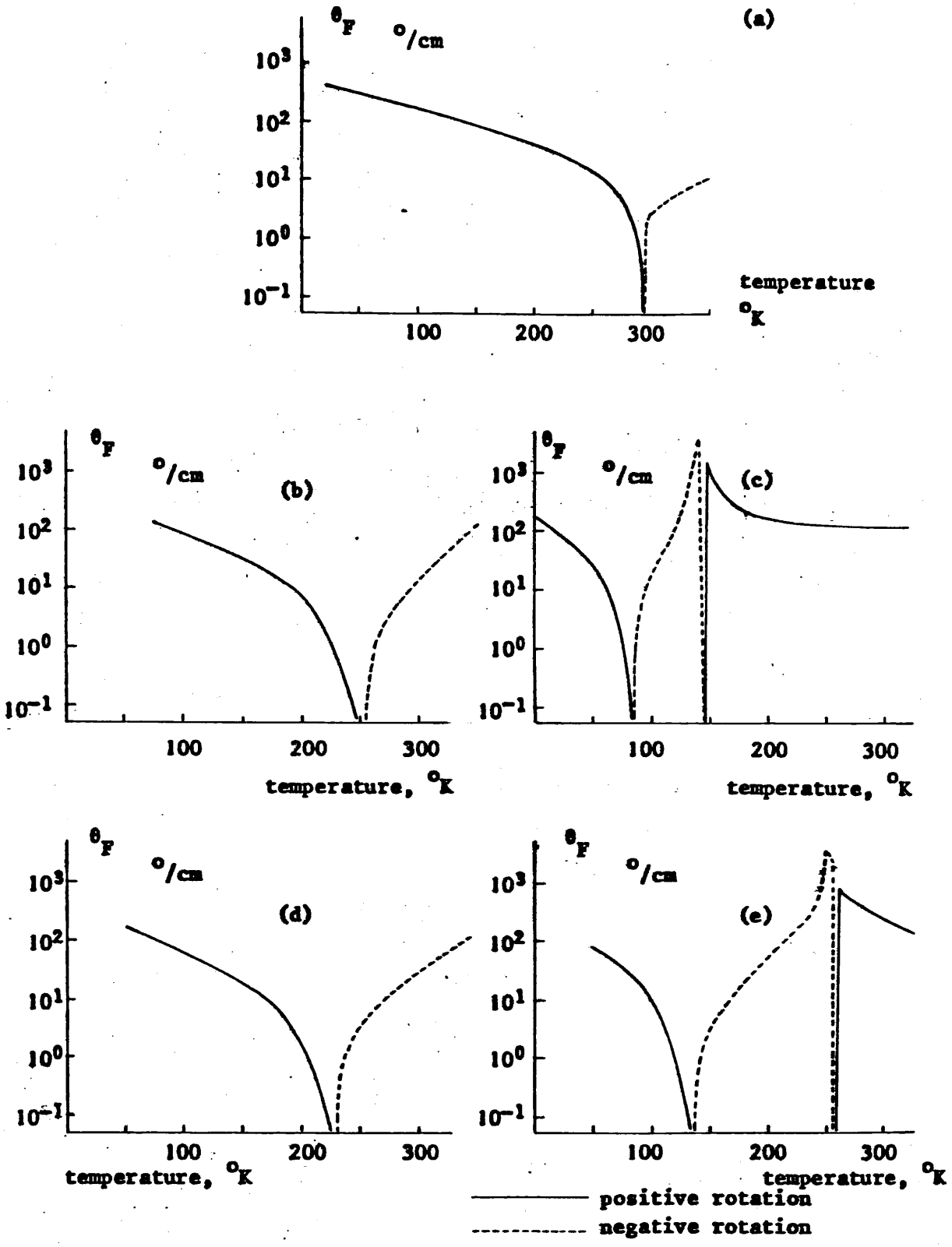

Figure 11.5. Theoretical temperature dependence of the specific Faraday rotation θ_F in the ferromagnetic mode for (a) gadolinium, (b) terbium, (c) erbium, (d) dysprosium, and (e) holmium iron garnets employing values for the rare-earth g factors in Table 11.1. $g_{Fe} = 2$.

calculations is highlighted by a reversal point above the magnetic compensation temperature in erbium and holmium iron garnets and by the absence of a reversal point below the magnetic compensation temperature in terbium and dysprosium iron garnets. To investigate this further, the temperature-dependence of the Faraday rotation in dysprosium iron garnet has been taken to be characteristic of the other iron garnets under investigation, except for the case of gadolinium and yttrium iron garnets.

The magnetic data have been used to demonstrate the variation of γ_{EFF} for the cases where the splitting factor of the dysprosium ion is less than and also greater than the splitting factor of the ferric ions. Plotting γ_{EFF} against the nett magnetisation, Figure 11.6(a) shows that for the case of $g_{Fe} = 2.0$ and $g_{Dy} = 2.5$, a discontinuity exists at negative $\underline{M}$ and so is above the magnetic compensation temperature; however, reducing g_{Dy} to 1.5, a continuous curve is obtained over the range investigated. The two curve shapes presented in Figure 11.5 are now seen to result from the values chosen for the g factors by using the values of γ_{EFF} in Figure 11.6(a) to plot $\gamma_{EFF}(M_{Fe} - M_{Dy})$, a quantity proportional to the Farady rotation, against $M_{Fe} - M_{Dy}$. These are shown in Figure 11.6(b).

An examination of the Faraday rotation occurring in the high frequency mode of precession is undertaken by inserting the magnetic data of Bertaut and Pauthenet and the g factors displayed in Table 11.1 into equation 11.2. Shown in Figure 11.7, the general features of reversal of the sense of rotation at the magnetic compensation point and a second reversal at a lower temperature are similar to those obtained experimentally. The temperature at which the reversal points occur is in good agreement with experiment; however, the magnitude of the predicted rotation is considerably less than the measured values. Rotation of the correct magnitude may be obtained by adjustment of the assigned values of the splitting factors, but if the accurately known value for the ferric ions of $g_{Fe} = 2$ is retained, then alteration of the g factor of the rare-earth predicts an incorrect position of the low temperature reversal point. Corrections can be made by allowing the g factors to vary with temperature as described earlier, but then difficulty exists in relating such data to measurements made at microwave frequencies. An alternative approach is to examine the effects of damping on the Faraday rotation.

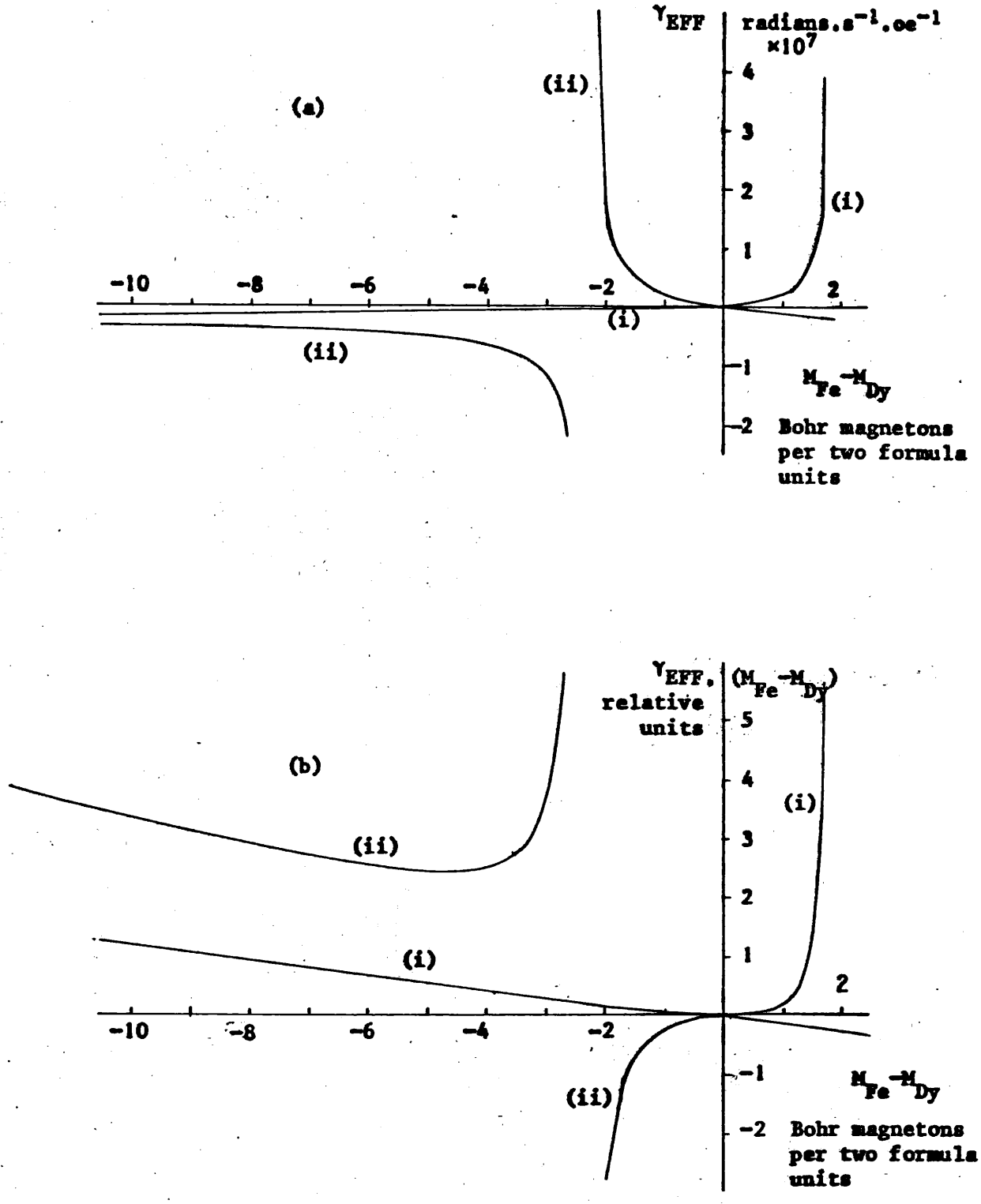

Figure 11.6. (a) γ_{EFF} and (b) $\gamma_{EFF} \cdot (M_{Fe}-M_{Dy})$ against $(M_{Fe}-M_{Dy})$ for (i) $g_{Dy} = 1.5$ and (ii) $g_{Dy} = 2.5$. $g_{Fe} = 2$.

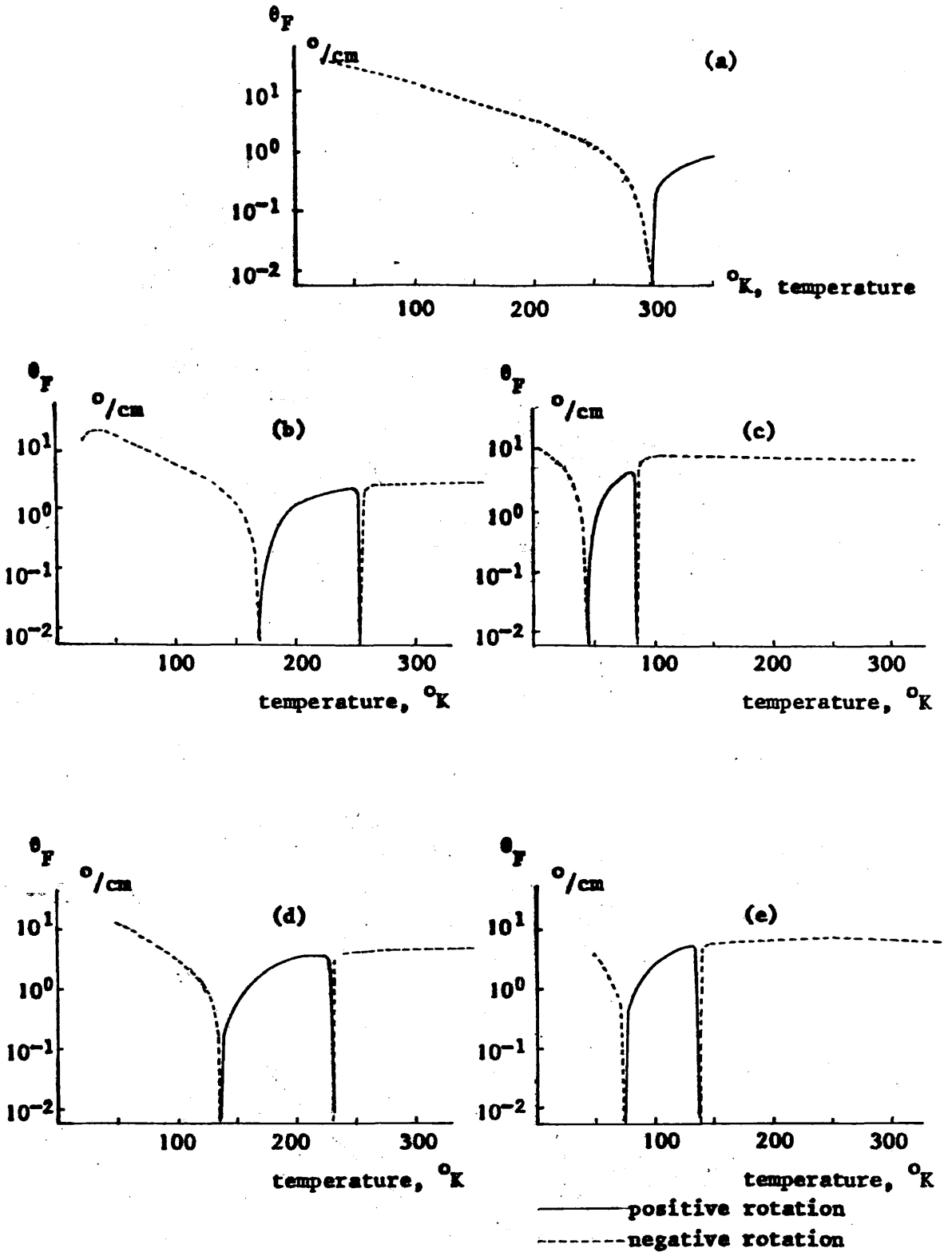

Figure 11.7. Theoretical temperature dependence of the specific Faraday rotation θ_F in the exchange mode for (a) gadolinium, (b) terbium, (c) erbium, (d) dysprosium, (e) holmium iron garnets employing values for the rare-earth g factors in Table 11.1. $g_{Fe} = 2$.

11.3. Damping

Expressions for the susceptibility elements listed in Figure 8.4 involve the damping parameters α_1, α_2 for each sublattice as introduced in the Landau-Lifshitz equation. Expressing $\alpha_{1,2}$ as functions of the relaxation times $T_{1,2}$ described by equation 8.19, enables calculations of the susceptibilities to be made in terms of linewidth data using the relationship 8.23. Data exist primarily at frequencies up to X-band by excitation of ferromagnetic modes within garnet specimens placed in microwave cavities. It has been suggested by Vittoria and Wilsey[123] that $\alpha\gamma^2M^2$ is independent of frequency, implying that T is a function of $1/\omega$. However, this must be assumed to be an over-simplified relationship when extrapolating data from the microwave to the sub-millimetre region, as the ferromagnetic resonance condition is no longer excited, ferrimagnetic precession being the dominant mode.

Using the equations listed in Figure 8.4 for a damped double sublattice system, Frayne has calculated the frequency variation of the elements of the susceptibility tensor of europium iron garnet at $297^{o}K$ in an applied field 5 koe. A value of $T_1 = 3.9 \times 10^{-7}$ seconds, obtained from microwave measurements, was employed for the relaxation time of the iron subsystem and the susceptibility elements were calculated for a range of values of the rare-earth relaxation time, T_2. These are reproduced in Figure 11.8 for the case of $T_2 = 10^{37}$, which represents a situation where the rare-earth ion is effectively undamped, and for $T_2 = 10^{-12}$ and $T_2 = 10^{-13}$ seconds. With the exception of χ'_{xx}, structures corresponding to both the low and high frequency resonance conditions are evident. No significance is attached to the absence of the ferrimagnetic resonance in χ'_{xx} as this is probably due to the large scale on which these figures are plotted. The susceptibility curves represent conditions of constant relaxation times with varying frequency, a situation that cannot be assumed to occur. The plots of the dissipative elements χ''_{xx} and χ''_{xy} show ferrimagnetic absorption to be a strong function of T_2. Hence, in principle, experimental data on the ferrimagnetic linewidth would enable the relaxation times to be found for submillimetre wavelengths. In the absence of such information, evaluation of the measurements of Faraday rotation against temperature was carried out for a range of values of T_2 in order to attain an agreement with the experimental results.

Because of the difficulties involved in allowing both the ferric and the rare-earth sublattices to have a wide range of values of relaxation

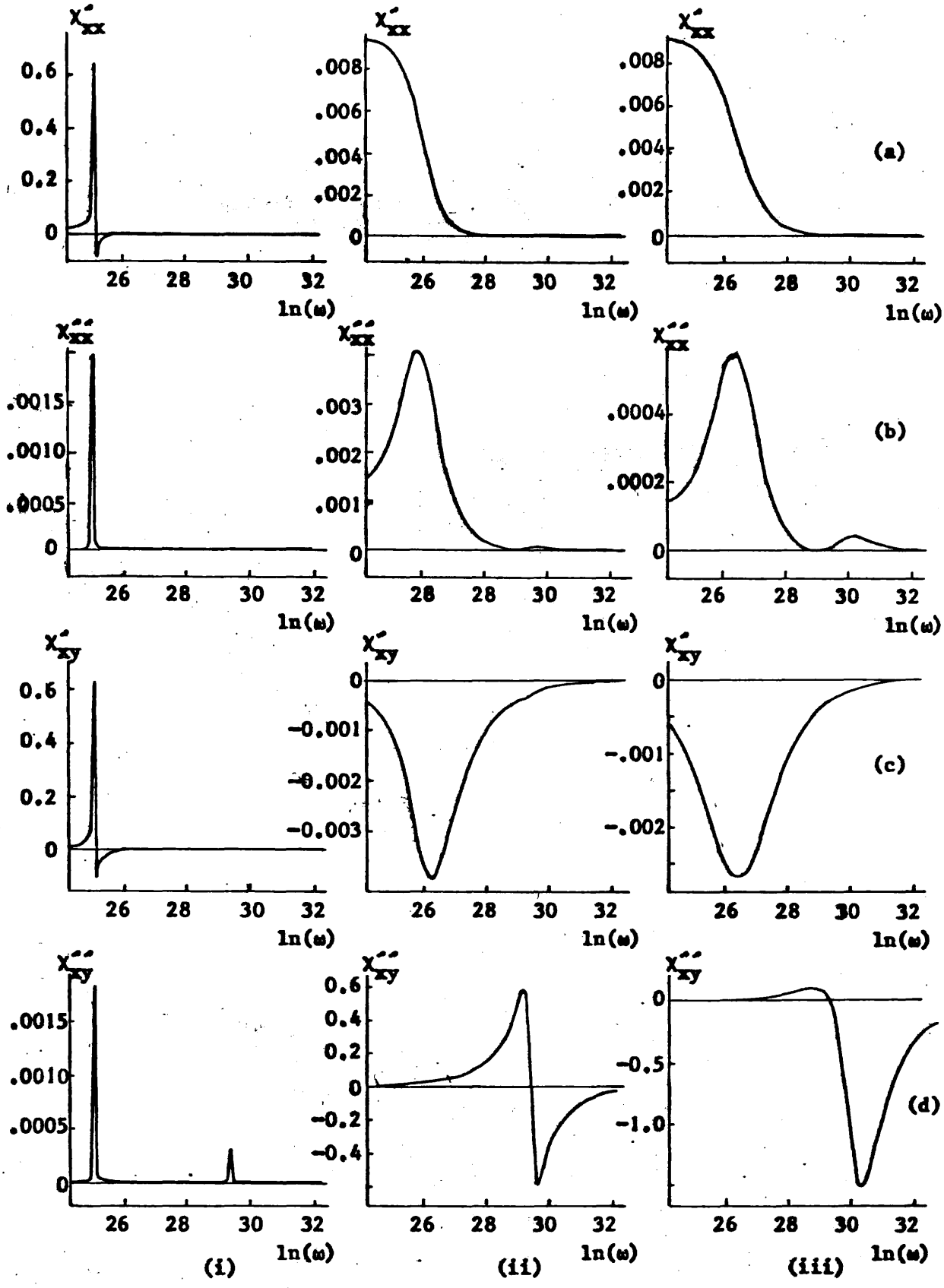

Figure 11.8. Theoretical frequency variation of the elements of the susceptibility tensor of europium iron garnet at 297°K calculated by Frayne. χ'_{xx}, χ''_{xx}, χ'_{xy} and χ''_{xy} are shown respectively in rows (a),(b),(c) and (d) for rare-earth relaxation times of 10^{37}, 10^{-12} and 10^{-13} s in columns (i),(ii) and (iii) respectively. Ferric sublattice relaxation time is 3.9×10^{-7} s. Angular frequency ω.

time, the same value that was used in Frayne's calculations was used for the T parameter of the iron subsystem. The susceptibility elements displayed in Figure 8.4 have been used with equations 8.8, 8.9, 8.10 and 8.28 to calculate the specific Faraday rotation for a range of values of the relaxation time of the rare-earth ions. Some results of these calculations, performed using the computer programme described in Appendix VI, are shown in Figures 11.9 and 11.10. The value of the g factors at absolute zero in Table 11.1 have been used for a range of rare-earth relaxation times from 10^{37} to 10^{-13} seconds. Figure 11.10 shows that for rare-earth ion T parameters of 10^{-11} seconds and higher, discontinuities occur at points other than at the magnetic compensation point. These structures arise when the term occurring in the susceptibility elements

$$\omega^2 - \omega_e\{\omega + \omega_0\}$$

becomes small, indicating that these features result from the action of the exchange field. Figures 11.9 and 11.10 also show that for the values used for the g factors, the shape of the curves has a greater dependence on the relaxation times for values of T less than 10^{-11} seconds. However, the choice of both g and T greatly affects the predicted rotations, as demonstrated by Figures 11.11 and 11.12. Faraday rotation in dysprosium iron garnet with a relaxation time for the rare-earth ion of 10^{-12} seconds is shown in Figure 11.11 for g_{Dy} equal to the average value indicated in Table 11.2 of 0.96, and for the higher values of 1.65. Neither graph represents the rotation obtained experimentally; however, it is seen that for $g_{Dy} = 1.65$, damping effects become dominant at larger dysprosium ion relaxation times than were found for the value given in Table 11.1 of $g_{Dy} = 1.33$. The predicted rotation corresponding to $T_{Dy} = 10^{-2}$ and $T_{Dy} = 10^{-6}$ seconds are displayed in Figure 11.12 for $g_{Dy} = 1.65$, and it is observed that the longer relaxation time produces a rotation that more accurately represents the experimental results, with the addition of a discontinuity at a temperature lower than that of the two reversal points. Similar results are shown in Figures 11.13 and 11.14 for terbium iron garnet and erbium iron garnet respectively where values of g for the rare-earth ion have been chosen to give the correct position of the reversal point of the rotation below magnetic compensation. It is seen that the magnitude of the rotation away from the reversal points does not agree with experiment over the full extent of the curves. In addition to a temperature variation of the g factors, this is thought to be due to

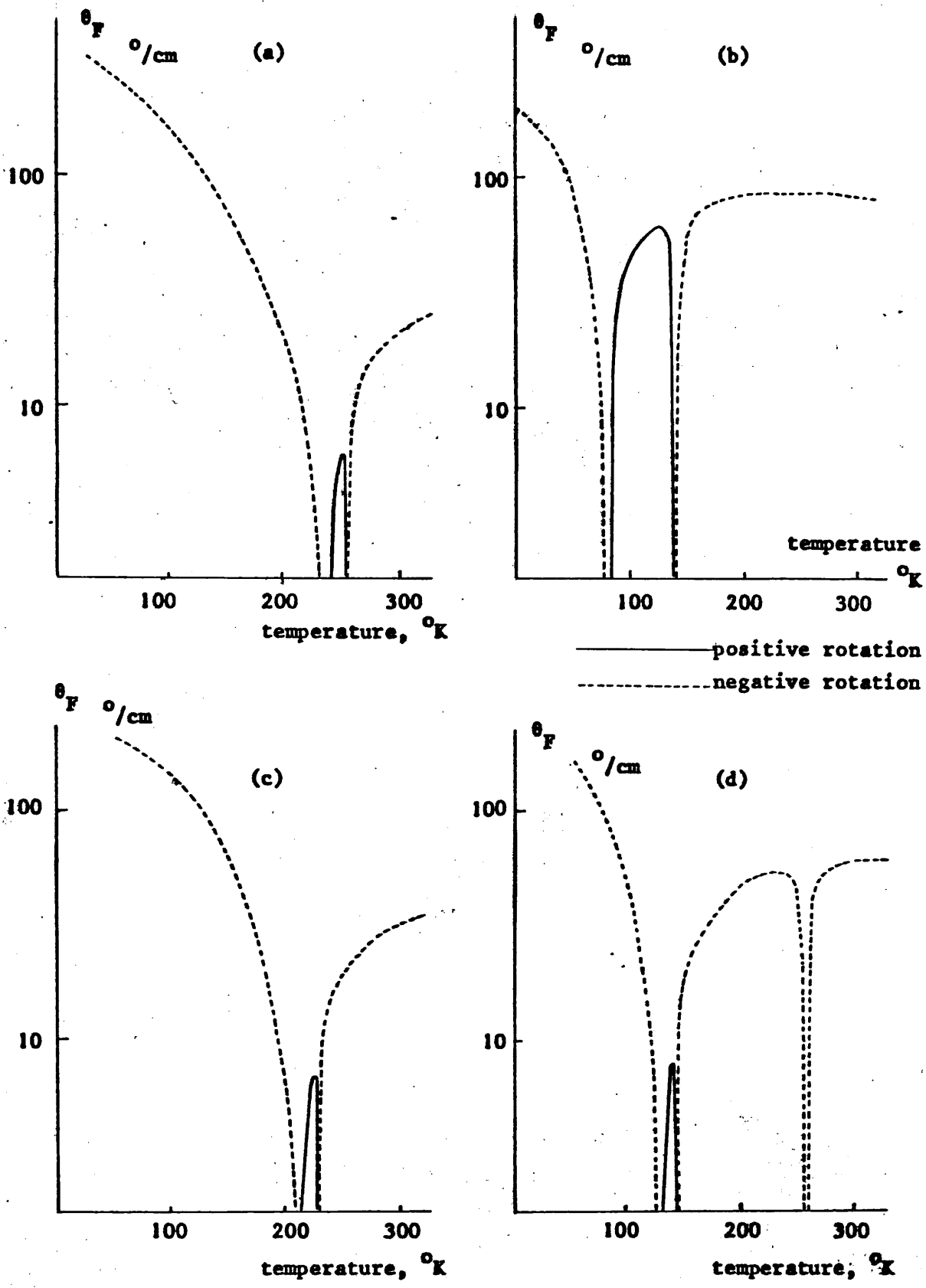

Figure 11.9. Theoretical temperature dependence of the specific Faraday rotation θ_F at 891 GHz in (a) terbium, (b) erbium, (c) dysprosium, and (d) holmium iron garnets for a rare-earth relaxation time $\tau_{RE}=10^{-13}$ s and a ferric relaxation time $\tau_{Fe} = 3.9\times10^{-7}$ s. Values for the rare-earth g factors are from Table 11.1, $g_{Fe} = 2$.

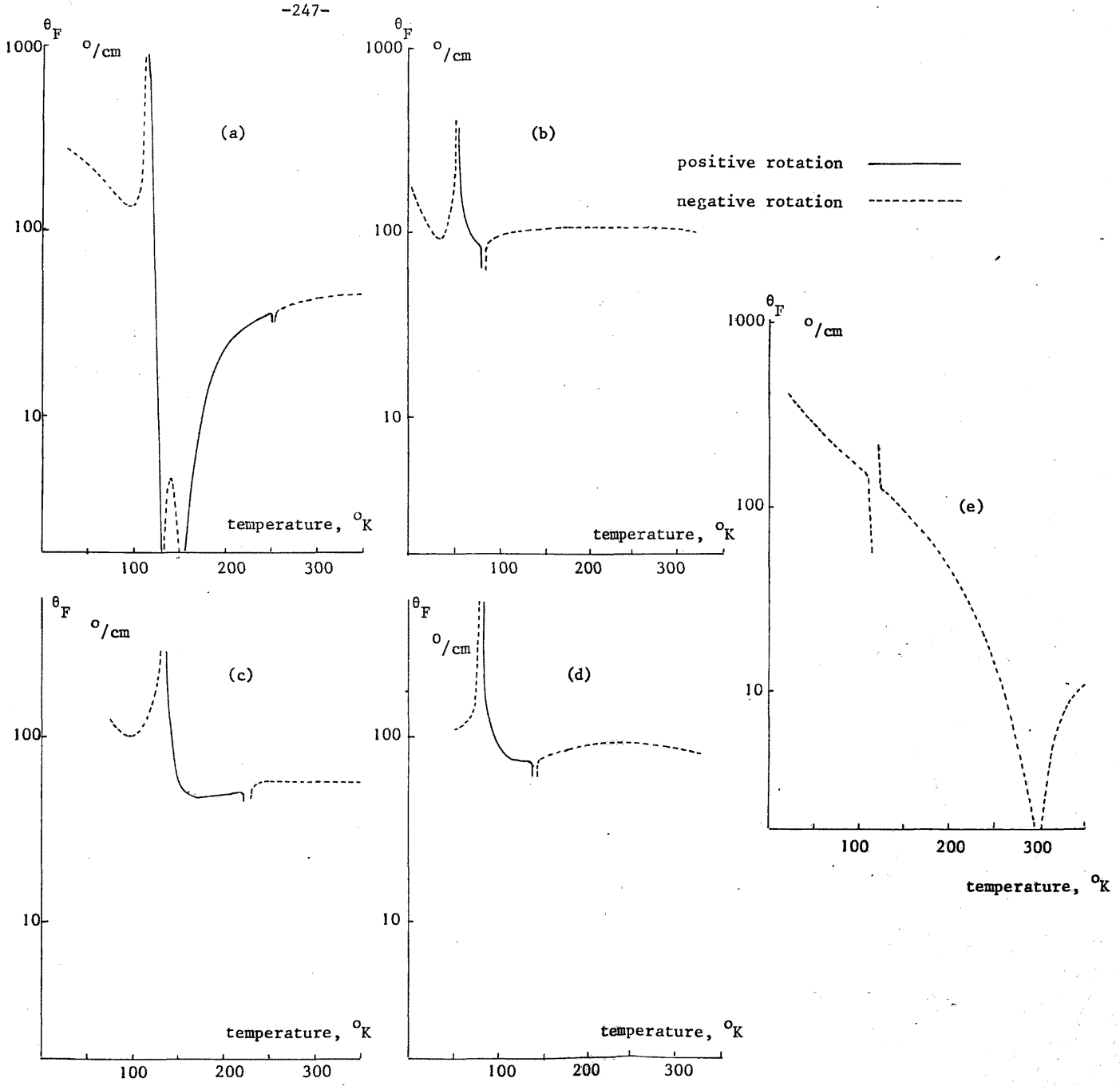

Figure 11.10. Theoretical temperature dependence of the specific Faraday rotation θ_F at 891 GHz in (a) terbium, (b) erbium, (c) dysprosium, (d) holmium, and (e) gadolinium iron garnets. For (a), (b), (c) and (d) the curves represent values for the rare-earth relaxation time T_{R_E} of 10^{37} to 10^{-11} s and for (e) $T_{R_E} = 10^{37}$ to 10^{-13} s. $T_{Fe} = 3.9 \times 10^{-7}$ s, and the g factors of the rare-earth ions are given in Table 11.1.

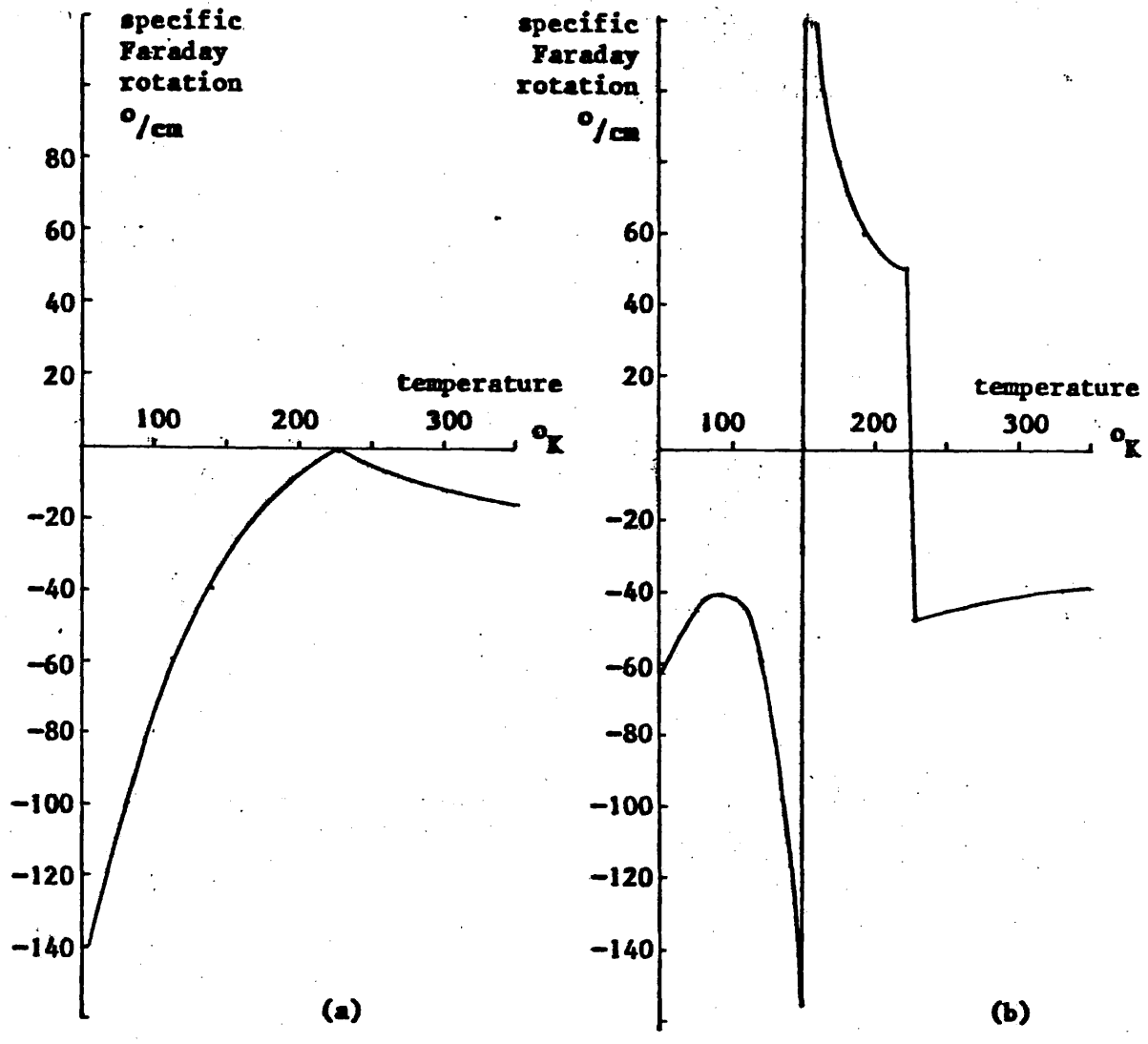

Figure 11.11. Theoretical temperature dependence of the specific Faraday rotation in dysprosium iron garnet at 891 GHz for g_{Dy} = (a) 1.65 and (b) 0.96. g_{Fe} = 2.0, $T_{Fe} = 3.9 \times 10^{-7}$ s and $T_{Dy} = 10^{-12}$ s.

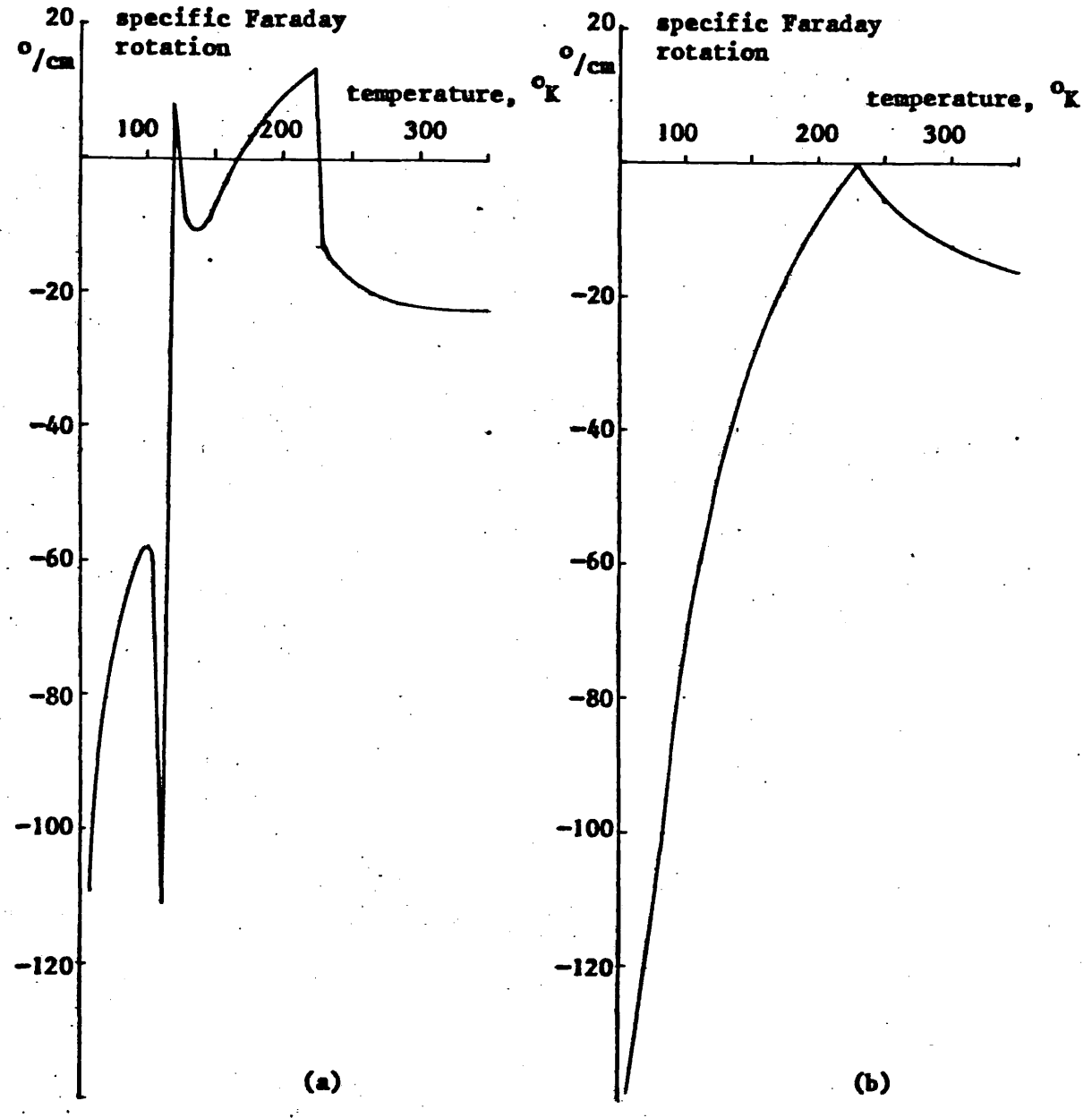

Figure 11.12. Theoretical temperature dependence of the specific Faraday rotation at 891 GHz in dysprosium iron garnet for values of the dysprosium ion relaxation time T_{Dy} = (a) 10^{-2} s and (b) 10^{-6} s.
$T_{Fe} = 3.9 \times 10^{-7}$s, $g_{Fe} = 2.0$, $g_{Dy} = 1.65$.

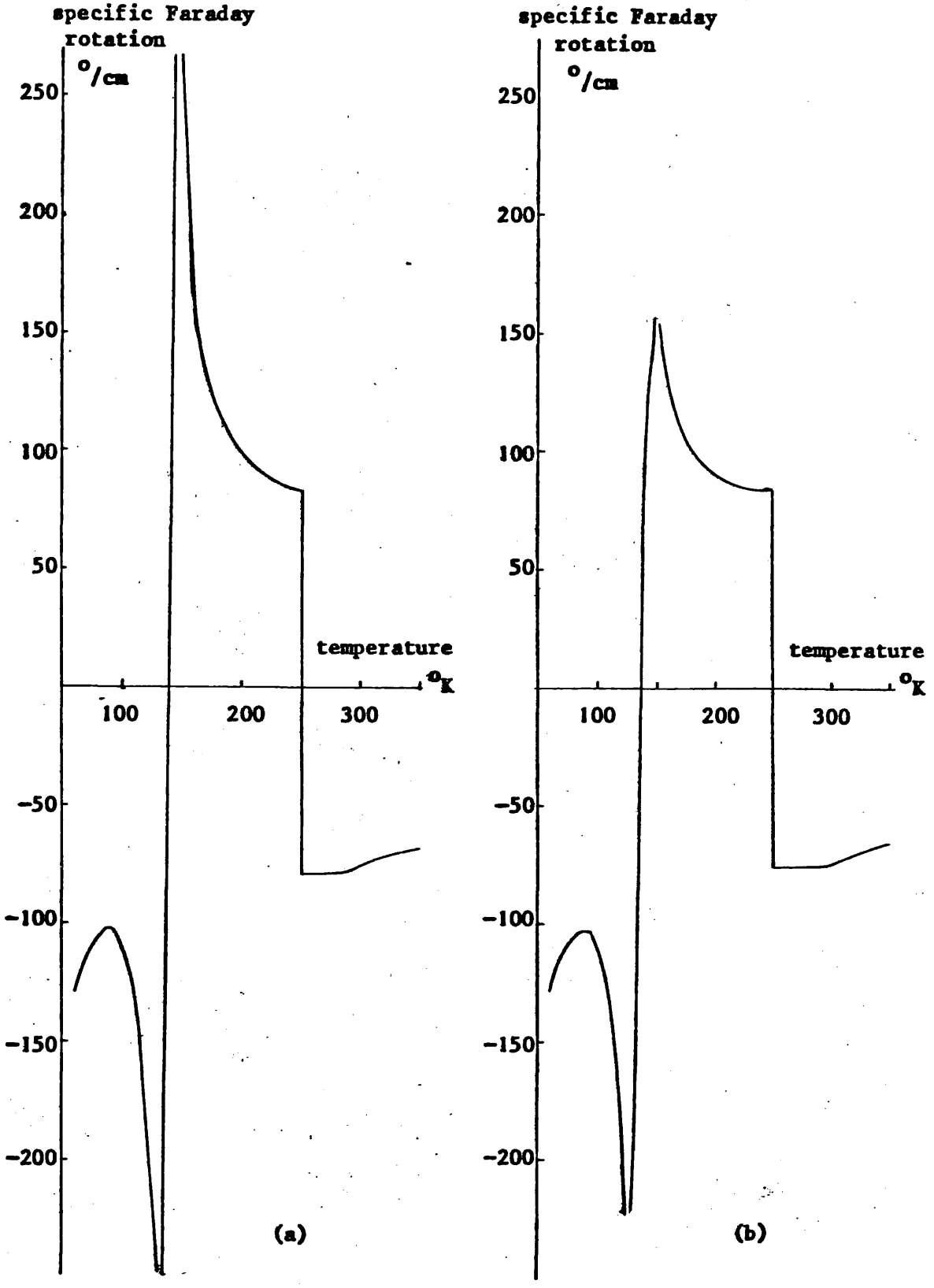

Figure 11.13. Theoretical temperature dependence of the specific Faraday rotation at 891 GHz in terbium iron garnet for values of the terbium ion relaxation time T_{Tb} = (a) 10^{-7} s and (b) 10^{-12} s. $T_{Fe} = 3.9 \times 10^{-7}$ s, $g_{Fe} = 2.0$ and $g_{Tb} = 0.99$.

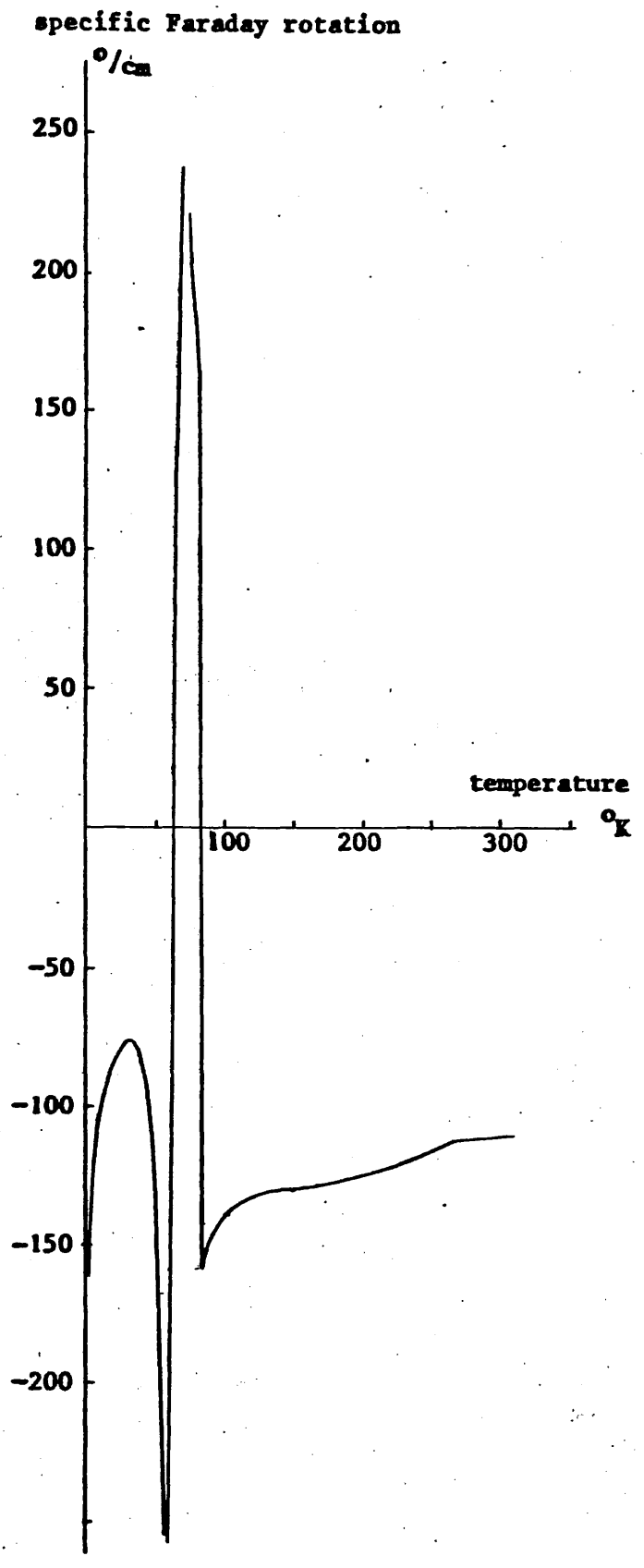

Figure 11.14. Theoretical temperature dependence of the specific Faraday rotation in erbium iron garnet at 891 GHz. The curve represents a range of values for the erbium ion relaxation time of 10^{-7} to 10^{-12} s. $T_{Fe} = 3.9 \times 10^{-7}$ s, $g_{Fe} = 2.0$, $g_{Er} = 0.83$.

the limitation of maintaining constant relaxation parameters over the range for both sublattices. Even for the case of gadolinium iron garnet where the two g factors are well documented, Figure 11.15, which shows the occurrence of ferrimagnetic resonance to be a sensitive function of the rare-earth relaxation time, also displays some disagreement with the magnitude of the measured rotation. A further investigation involving temperature-dependent relaxation parameters has not been carried out as this should involve more accurate knowledge of the damping of the ferric lattice. However, a study of T_{Fe} has been made which necessitated introducing anisotropy and is discussed in section 11.5.

With regard to gadolinium iron garnet, it is informative to note that the equations for the susceptibility elements in Figure 8.4 were used with equations 8.8, 8.9, 8.12 and 8.28 to calculate ellipticity. The experimental measurements displayed in Figure 10.24 showed that ellipticity was observed in only two garnet types, yttrium and gadolinium iron garnets. A theoretical account of ellipticity in yttrium iron garnet is not given; however, the calculated values for gadolinium iron garnet are shown in Figure 11.16 against temperature. It is seen that the ferrimagnetic resonance occurring at 115^{o}K, which had little effect on the Faraday rotation for $T_{Gd} < 10^{-12}$ seconds, perturbs the shape of ellipticity curves at all the values of the gadolinium ion relaxation time plotted. For the values shown for $T_{Gd} = 10^{-12}$ and 10^{-13} seconds, a dip in the ellipticity against temperature occurs at the ferrimagnetic resonance. However, the situation is different at $T_{Gd} = 10^{-11}$ and 10^{-10} seconds, as the general trend of increasing temperature causing reduced ellipticity is maintained across the measured range except for a peak at the resonance. Figure 10.24 shows that a dip was also observed experimentally in the [111] direction and so combined with the evaluation of the Faraday rotation measurements, the theoretical calculations give further confirmation that the gadolinium relaxation time is equal to or less than 10^{-12} seconds. The experimental data are only sufficient to state the temperature at which the minimum in the ellipticity occurred as 130 ± 10^{o}K. This discrepancy with the theoretical position is again thought to be due largely to the temperature-dependent parameters mentioned above being kept constant throughout the calculations.

No theoretical curves of Faraday rotation in holmium iron garnet with a corrected g_{Ho} value have been plotted as a lower reversal point was not found within the experimental temperature range.

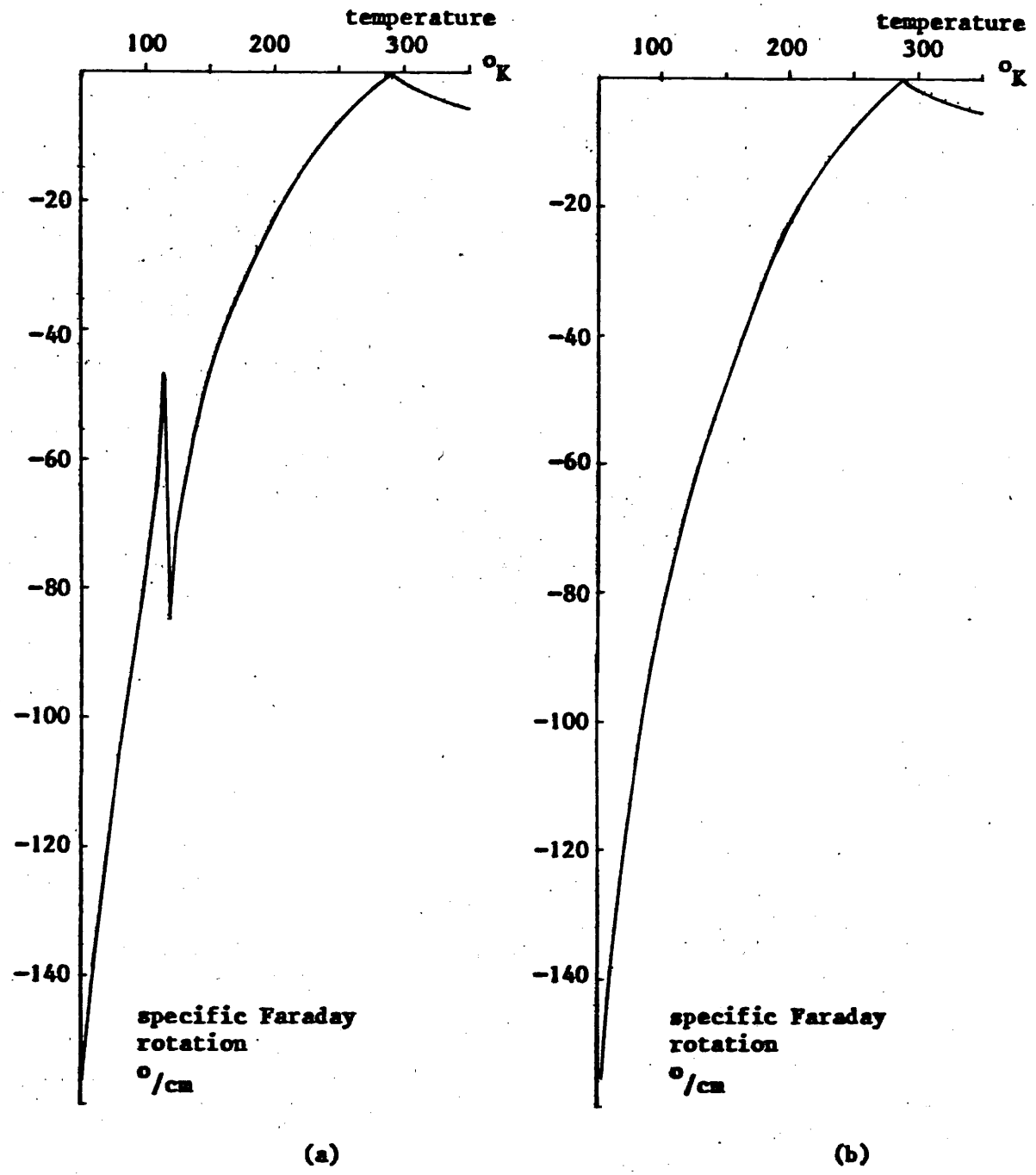

Figure 11.15. Theoretical temperature dependence of the specific Faraday rotation at 891 GHz in gadolinium iron garnet for values of the gadolinium ion relaxation time T_{Gd} = (a) 10^{-11} s and (b) 10^{-12} s. $T_{Fe} = 3.9 \times 10^{-7}$ s, $g_{Fe} = g_{Gd} = 2.0$.

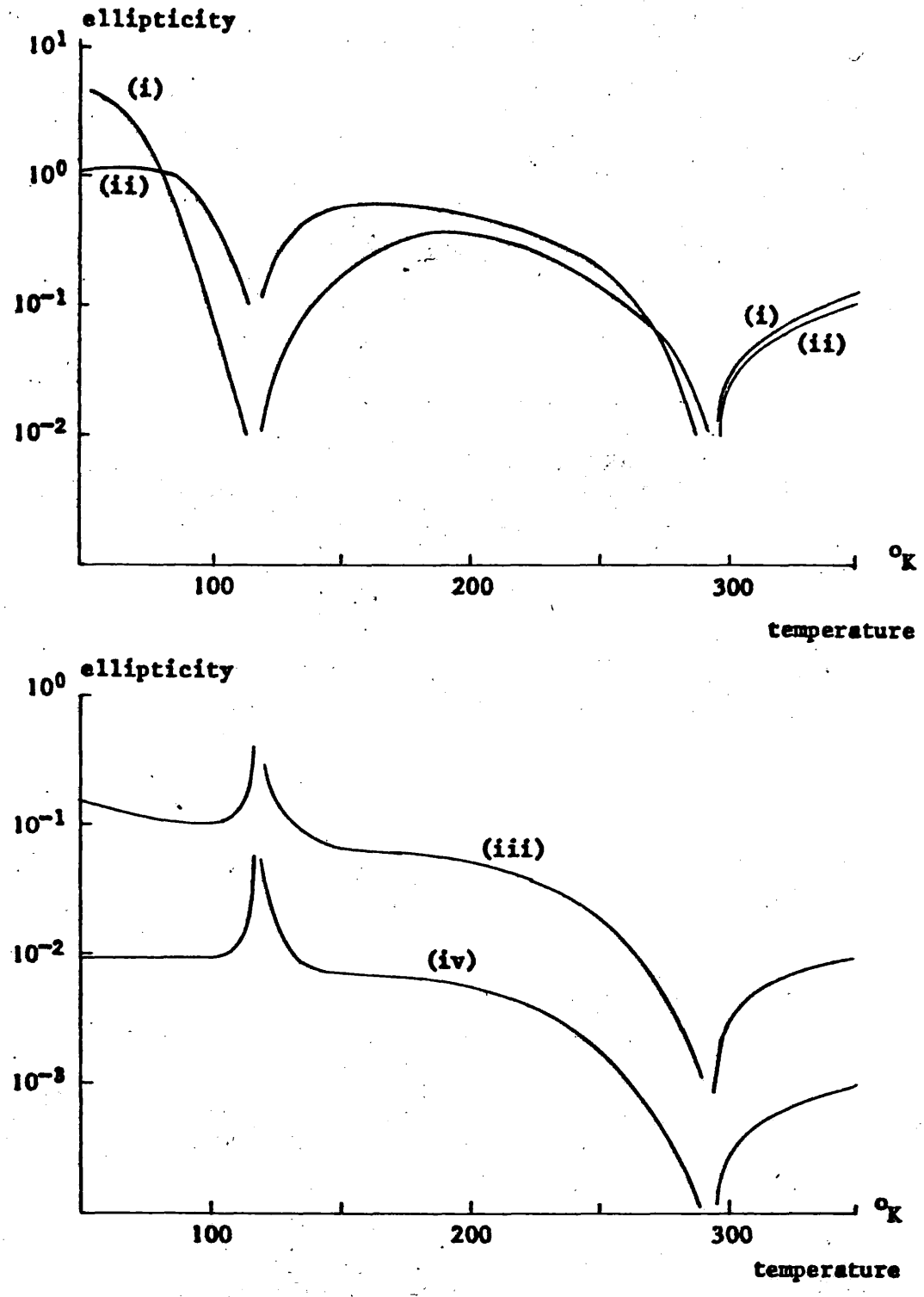

Figure 11.16. Theoretical ellipticity in gadolinium iron garnet at 891 GHz against temperature for values of T_{Gd} of (i) 10^{-13} s, (ii) 10^{-12} s, (iii) 10^{-11} s and (iv) 10^{-10} s. $T_{Fe} = 3.9 \times 10^{-7}$ s and $g_{Gd} = g_{Fe} = 2$.

11.4. Anisotropic damped systems

A feature of the Faraday rotation measurements displayed in Figures 10.3 to 10.7 that has not been considered in the analysis so far is the difference in the rotation in each crystal orientation. Differences occur in the magnitude of the rotation, which is most pronounced at the lower temperatures, and for the materials in which two reversal points were observed, in the temperature at which the lower temperature reversal takes place. To attain an insight into the mechanism producing these differences, the expressions for the phase constant derived in section 8.2 are used together with the matrix equation originated in section 8.4.3.2. These expressions represent a condition where the magnetic dipoles are at an arbitrary orientation to both the applied magnetic field and to the propagation direction of the radiation. A situation where the magnetic dipoles are not orientated along the external field can arise through the existence of magnetic anisotropy and, in double sublattice systems, can occur under the influence of large applied magnetic fields. This latter effect has been studied by Clark and Callen[124] who, neglecting anisotropy, calculated that two sublattice moments M_R and M_{Fe} are not collinear when the applied field H_0 is in the range

$$\lambda(M_R + M_{Fe}) > H_0 > \lambda|M_R - M_{Fe}|$$

λ being the molecular field constant. Throughout the present work the maximum field applied to the garnet specimen was 4.3 koe. The above condition is therefore only applicable near a compensation point and corresponds to a range of $\pm 1^{o}K$ about the compensation temperature in terbium iron garnet; this being the widest inverval in the garnets currently under investigation. With the magnetic data available, the theoretical calculations were not performed for such a limited temperature range and so this mechanism of dipole canting will not be considered. An analysis involving magnetic dipoles orientated away from the applied field will therefore only involve that due to anisotropy.

Calculations performed for the double sublattice system in dysprosium iron garnet illustrated in Figure 11.12 showed that at a fixed value of the relaxation parameter of the ferric sublattice, the lower reversal point of the Faraday rotation could be accounted for by a relaxation time of 10^{-2} seconds. However, the resonance predicted at $125^{o}K$ with this T parameter was not observed experimentally, indicating that the relaxation time at this point had changed. Examination of the anisotropic

properties of a double sublattice system will therefore be made near the lower compensation point for a range of T_{Dy} shown by the previous analysis to give a realistic value of rotation.

The elements of the matrix equation 8.26 were seen to contain demagnetisation factors representing the anisotropic contribution to the lattice field. These are calculated from the first order anisotropy constant K_1 and the magnetisation of the lattice M using the expressions of Clarricoats[125]

$$N_x^{a_1} = \frac{K_1}{M^2} \left[2 - \sin^2 \theta - 3 \sin^2 2\theta\right]$$

and

$$N_y^{a_1} = \frac{K_1}{M^2} \left[1 - 2 \sin^2 \theta - \frac{3}{8} \sin^2 2\theta\right]$$

where θ is the angle between the applied magnetic field and the [100] axis. When this field is directed along the [111] axis, $\theta = 54^o44'$ giving

$$N_x^{a_1} = (-1.55) \frac{K_1}{M^2} \quad ; \quad N_y^{a_1} = (-0.69) \frac{K_1}{M^2} \qquad \ldots(11.3)$$

and when along the [110] direction, $\theta = 90^o$ so that

$$N_x^{a_1} = \frac{K_1}{M^2} \quad ; \quad N_y^{a_1} = -\frac{K_1}{M^2} \qquad \ldots(11.4)$$

The elements of the matrices of equations 8.26 are listed in Appendix VII and the technique to obtain the susceptibility elements and hence the Faraday rotation is described. Using the value for the splitting factor of the ferric sublattice of $g_{Fe} = 2$, and the best value for the dysprosium sublattice found previously as $g_{Dy} = 1.65$, the Faraday rotation was calculated for a range of rare-earth relaxation times, while fixing the ferric sublattice parameter at $T_{Fe} = 3.9 \times 10^{-7}$ seconds. Results are shown in Figure 11.17 for rotation in the [111] and [110] directions at 175^oK, a temperature between the experimentally determined lower reversal points of the two orientations. It is seen that in the range of values of relaxation time indicated as being applicable to this garnet by the previous analysis of $\lesssim 10^{-2}$ seconds, different senses of rotation in each crystal direction have been calculated which correspond to the observed rotations. Evaluation of a wider temperature range has not been carried out, but it is considered to be informative at this stage that a study should be described of the properties of the ferric lattice.

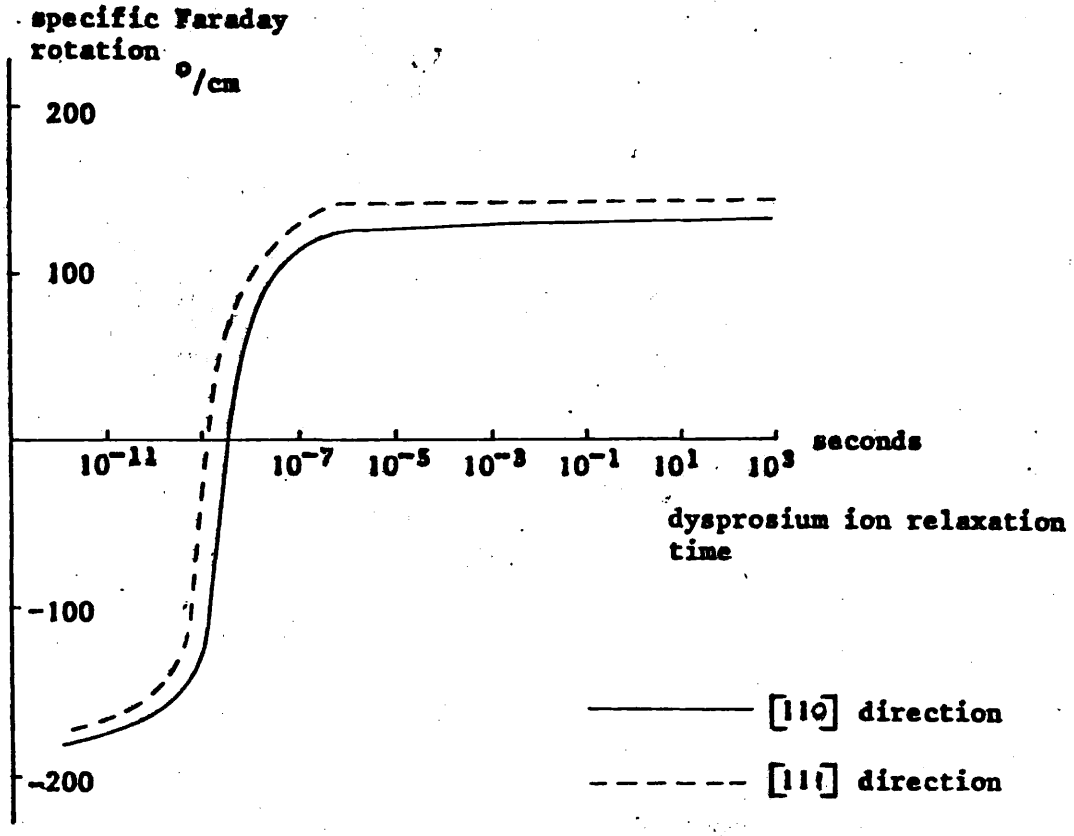

Figure 11.17. Theoretical specific Faraday rotation at 891 GHz in dysprosium iron garnet at 175°K against the value of the relaxation time of the dysprosium ion. Anisotropic terms are included. $g_{Dy} = 1.65$, $g_{Fe} = 2$ and $T_{Fe} = 3.9 \times 10^{-7}$ s.

11.5. Ferromagnetic treatment of anisotropic damped single lattice systems

The Weiss model of the exchange field implies that ions of zero magnetic moment do not enter into exchange interaction, and so an investigation was undertaken in which both yttrium iron garnet and samarium iron garnet are treated as ferromagnetic systems. The above analysis for double sublattice garnets has kept the T parameter constant with changing temperature. A study of yttrium and samarium iron garnets, for which the ferric g factor is well documented, enables an investigation to be made of the damping of the iron sublattice at the laser frequency. However, no correspondence between the characteristics of the relaxation times gained in this way and those of the other garnets in which the ferric sublattice enters into super-exchange interaction with the rare-earth subsystem is inferred.

The complex susceptibility components of a ferromagnetic system are given by Lax and Button[88] which includes demagnetisation factors and the relaxation time. A simplified form of these equations expressed in Appendix 4.1 of Lax and Button is usually adopted for microwave applications by assuming a near-resonance condition and by stipulating a lower limit to the degree of damping. To investigate the relaxation parameters encountered in the submillimetre region, neither of these restrictions is desirable. Therefore the expressions shown in Figure 11.18 have been used which are the ferromagnetic susceptibility elements of Lax and Button derived without making approximations and separated into their real and imaginary parts.

Evidence that more than the simple precession described by equation 8.16 takes place in yttrium and samarium iron garnets is found by plotting the measured values of Faraday rotation displayed in Figures 10.3 and 10.12 against the corresponding value for the magnetisation in Figure 9.2. Figures 11.19 and 11.20 show that interpolation of these graphs does not pass through the origin, a contradiction of the simple ferromagnetic expression 11.1. The equations of Figure 11.18 have therefore been used to investigate the effect of the relaxation time and the anisotropy on the Faraday rotation, as described in Appendix VIII. The model described in Chapter Eight, in which the demagnetisation and anisotropy fields are both expressed in terms of demagnetisation factors, enables the two terms to be grouped together by replacing the parameters $N_{x,y,z}$ by $N^{a}_{x,y,z} + N_{x,y,z}$. The interpretation of microwave data that the gyromagnetic ratios have little

$$\chi'_{xx} = \frac{\frac{\omega_M}{T^2}\left[\{\omega_r{}^2-\omega^2\}\{\omega_0+N_y\omega_M\}T^2+\{2\omega_0+N_x-N_y\}\omega_M\right]}{\{\omega_r{}^2-\omega^2\}^2+\{\frac{2}{T}\}^2\left[\omega_0+\frac{\{N_x-N_y\}}{2}\omega_M\right]^2}$$

$$\chi''_{xx} = \frac{\frac{\omega_M}{T}\left[\{\omega_0+\omega_M N_y\}\{2\omega_0+N_x-N_y\}\omega_M-\{\omega_r{}^2-\omega^2\}\right]}{\text{DENOMINATOR}}$$

$$\chi'_{xy} = \frac{-\omega\omega_M\left[2\omega_0+\{N_x-N_y\}\omega_M\right]\left[\frac{1}{T}\right]}{\text{DENOMINATOR}}$$

$$\chi''_{xy} = \frac{\omega\omega_M\{\omega_r{}^2-\omega^2\}}{\text{DENOMINATOR}}$$

where $\omega_0 = \gamma(H_0-N_z\omega_M)$

$$\omega_r = \left[\{\gamma H_0+(N_x-N_z)\omega_M\}\{\gamma H_0+(N_y-N_z)\omega_M\}\right]^{\frac{1}{2}}$$

$\omega_M = 4\pi M.\gamma$

N_x, N_y, N_z are the demagnetisation factors in the x, y and z directions respectively

ω is the angular frequency of the radiation

γ is the gyromagnetic ratio

H_0 is the applied magnetic field, applied in the z direction

Figure 11.18. Elements of the susceptibility tensor for the ferromagnetic mode obtained from Lax and Button[88] and separated into real and imaginary parts

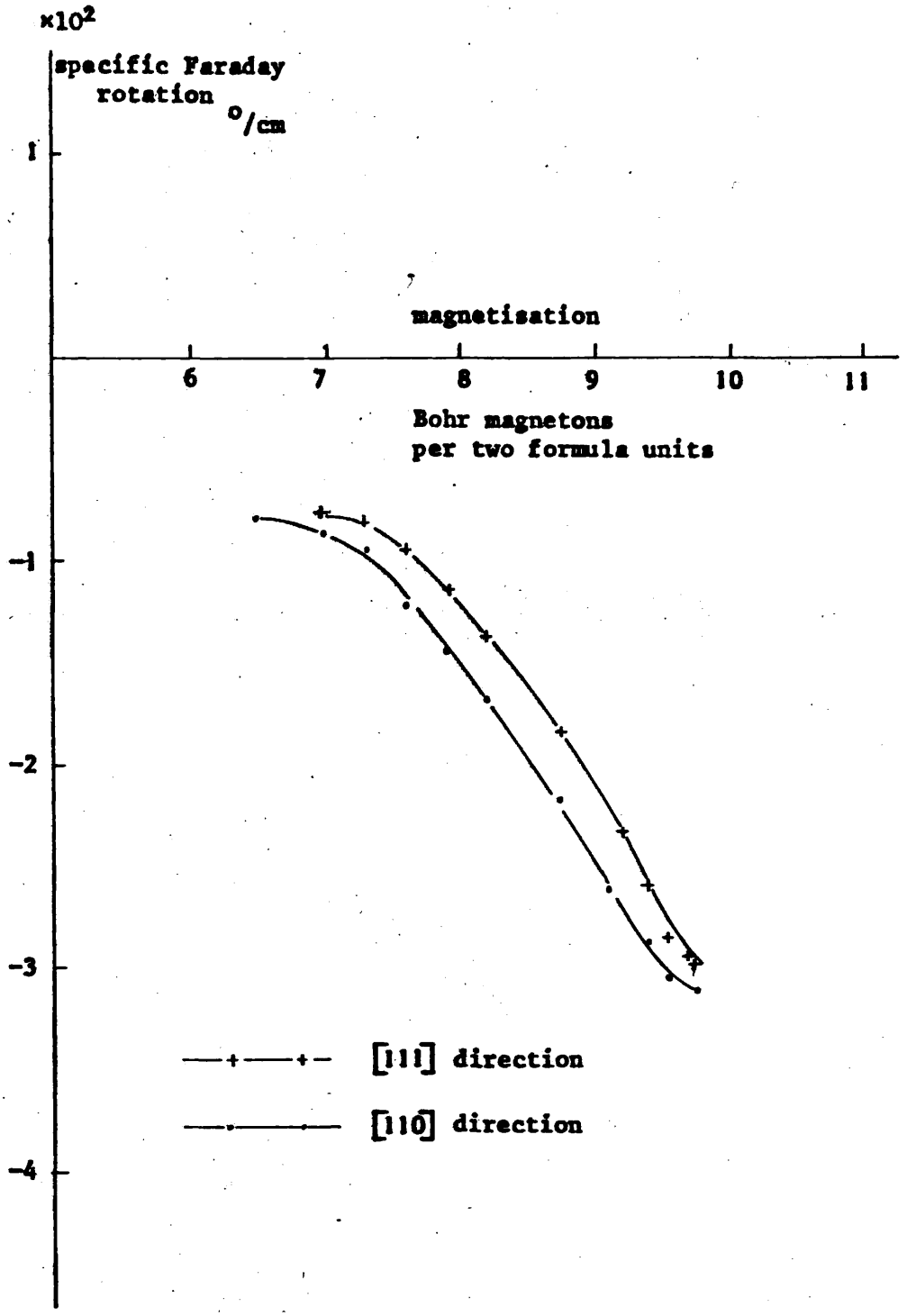

Figure 11.19. Experimentally measured specific Faraday rotation at 891 GHz in yttrium iron garnet against the corresponding magnetisation

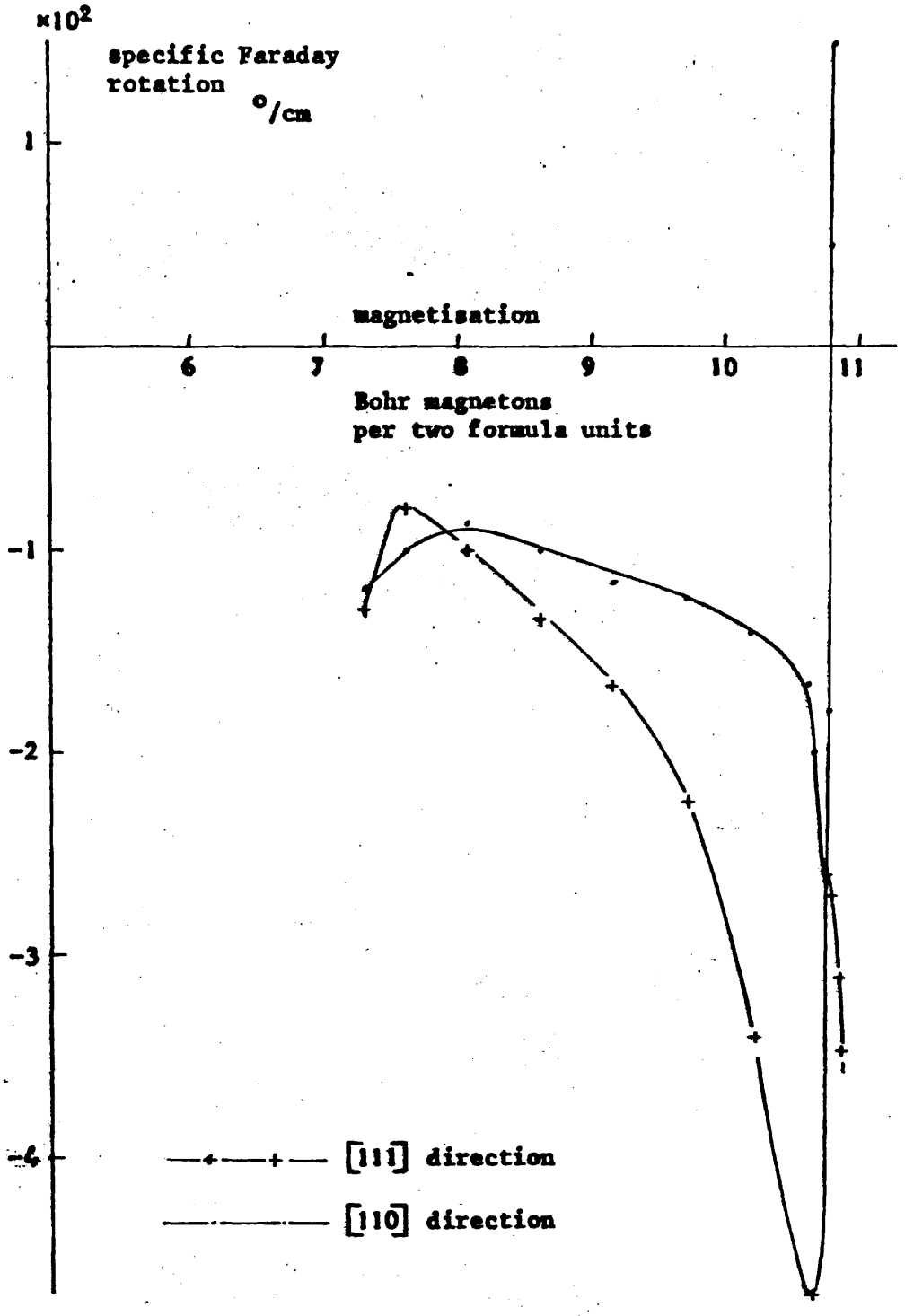

Figure 11.20. Experimentally measured specific Faraday rotation at 891 GHz in samarium iron garnet against the corresponding magnetisation. Measurements made by Frayne.

variation with temperature has again been assumed. Using the anisotropy data shown in Figure 9.4, the Faraday rotation in the [111] direction of a thin parallel-sided specimen of yttrium iron garnet has been calculated and is displayed in Figure 11.21. The calculations show that little change in the rotation occurs between the undamped case and that shown for $T = 10^{-10}$ seconds. Rotation at these low damping values is found to have a linear variation with magnetisation, that passes through the origin and has a magnitude considerably greater than that found experimentally. Lower values are calculated at shorter relaxation times with, as Figure 11.21 shows, a linear extrapolation that no longer passes through the origin. However, it is clear that the experimental observations are not explained if constant damping takes place. A situation has therefore been investigated where a linear variation of the relaxation time with temperature is allowed. The calculated rotation for propagation in the [111] and [1$\bar{1}$0] directions is shown in Figure 11.22. The proposed variation of T, also displayed in Figure 11.22, is seen to increase with increasing magnetisation, a trend partially supported by the experimental data where transmission in yttrium iron garnet was found to be greatest at low temperatures.

A similar process was carried out to calculate the Faraday rotation in samarium iron garnet by again proposing a linear variation of the relaxation time with temperature. The temperature range over which the experimental measurements were made descended lower than the range of the available data on anisotropy in Figure 9.4. Two situations have therefore been studied where the rate of increase of the anisotropy quickly reduces in the low temperature region in curve (a) of Figure 11.23, and again when the rate of increase is maintained in curve (b). The Faraday rotation calculated for the [111] and [1$\bar{1}$0] directions using values for the anisotropy constant in curve (b), together with the relaxation parameter, are shown in Figure 11.24. The model only accounts for the experimentally observed rapid reduction in the rotation at low temperature when using the postulated data of curve (b) of Figure 11.23. The calculated Faraday rotation in the [111] direction is seen to reverse sign at low temperatures, whereas the experimental observations showed rotation in the [1$\bar{1}$0] direction to reverse sign. However, the work of Harrison et al.[108] illustrated in Figure 9.3, showed that the rôle of the easy direction of magnetisation changes between 81°K and 58.6°K from the [111] to the [1$\bar{1}$0] direction. This property has not been taken into account in this analysis, neither has the further observation of Harrison that at 23.6°K the [111] axis

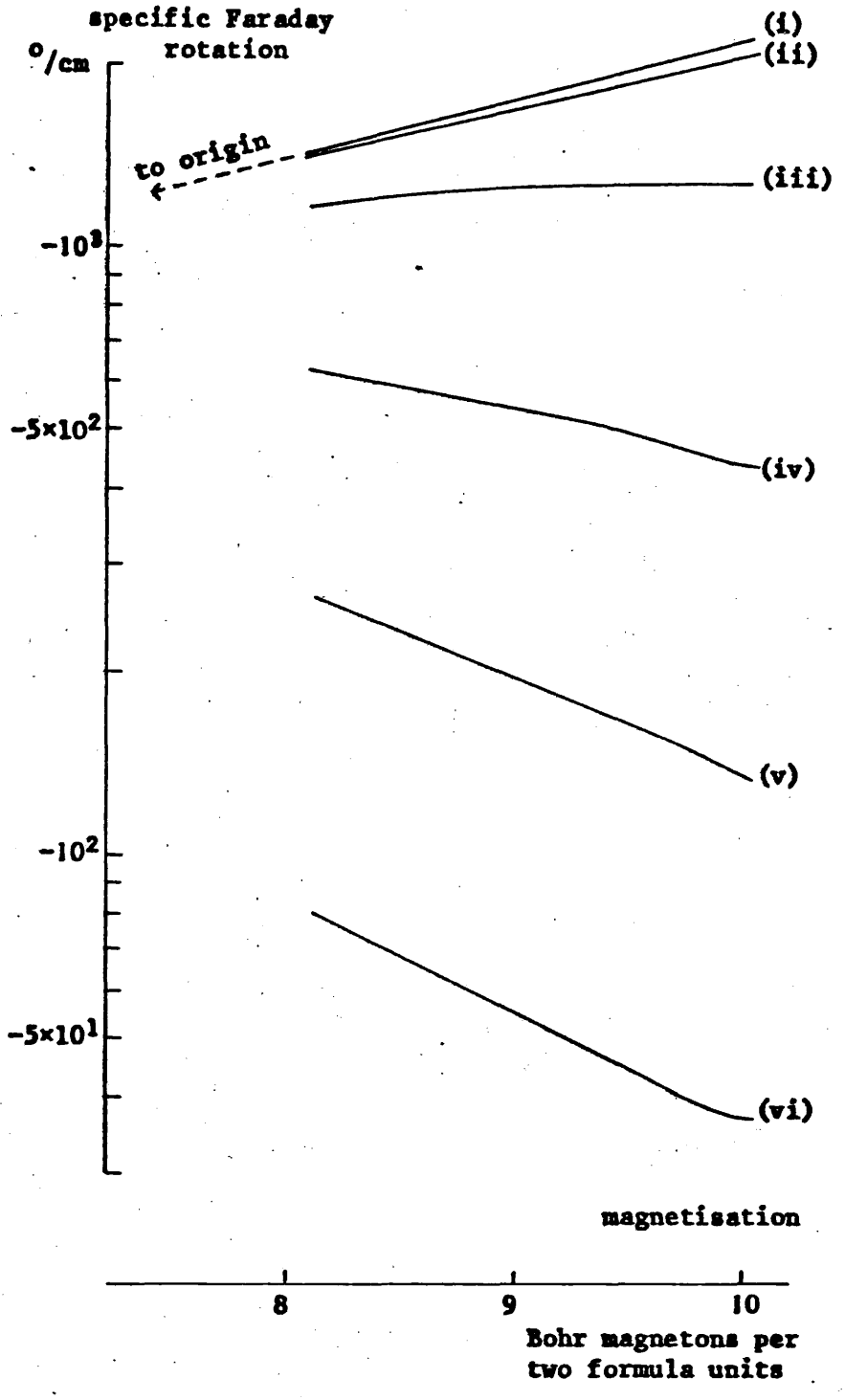

Figure 11.21. Theoretical specific Faraday rotation against magnetisation for a [111] direction in yttrium iron garnet for constant values of the ferric relaxation time of T_{Fe} = (i) 10^{-12} s, (ii) 10^{-13} s, (iii) 2.5×10^{-14} s, (iv) 10^{-14} s, (v) 5×10^{-15} s, and (vi) 2.5×10^{-15} s.

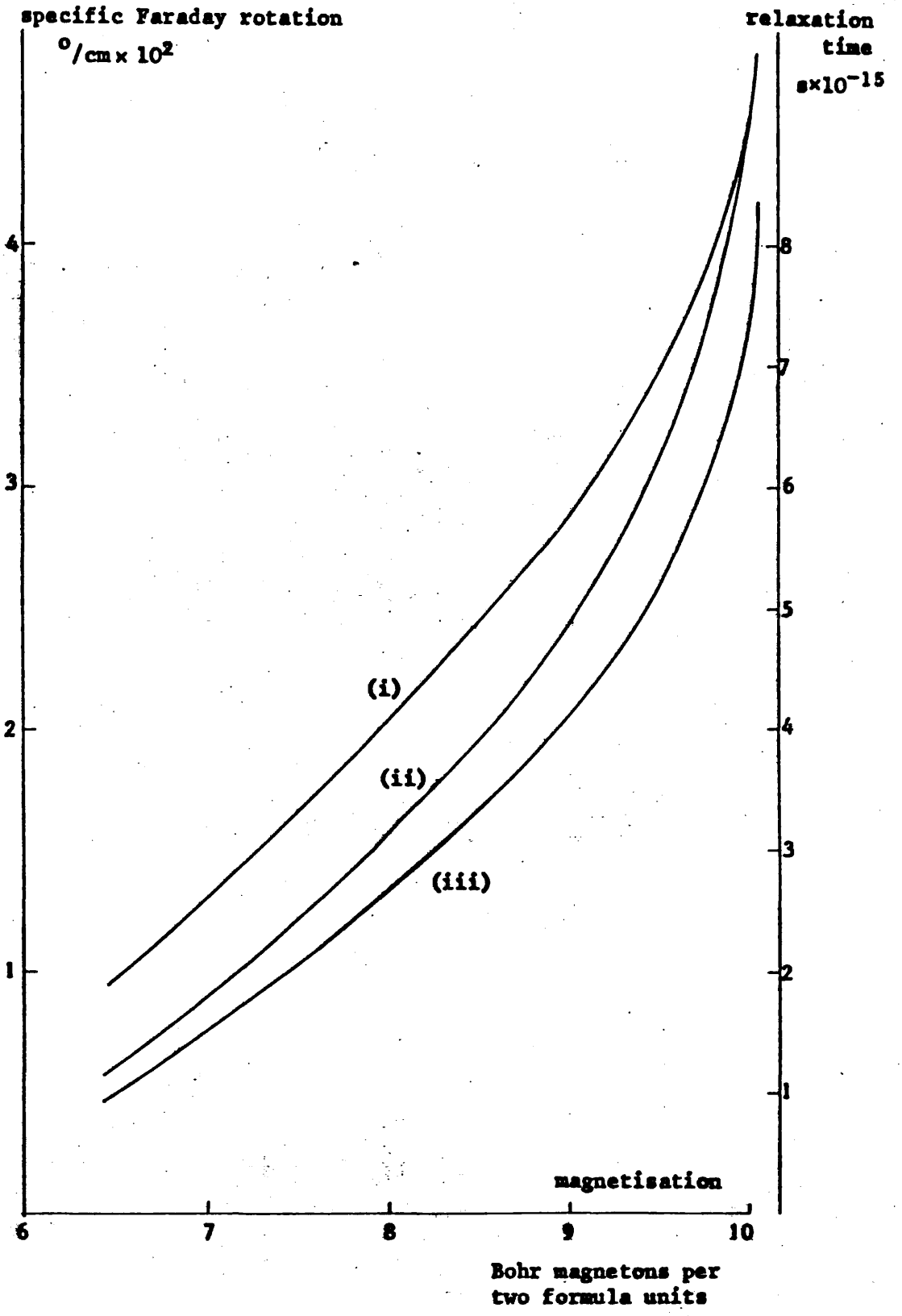

Figure 11.22. (i) Proposed relaxation time and the corresponding theoretical specific Faraday rotation in (ii) the [110] direction and (iii) the [111] direction against magnetisation for yttrium iron garnet

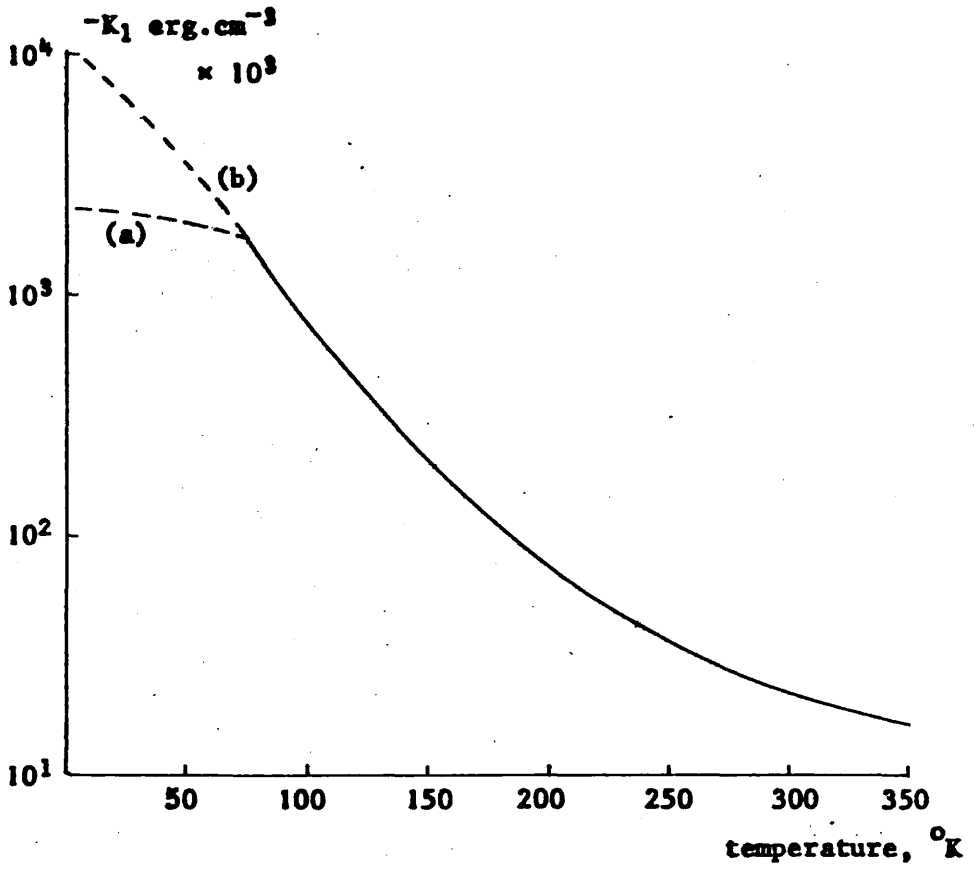

Figure 11.23. First anisotropy constant for samarium iron garnet against temperature; after Pearson[109]. Two extrapolations of the curve, shown as broken lines (a) and (b), are introduced to extend the calculations to 5°K.

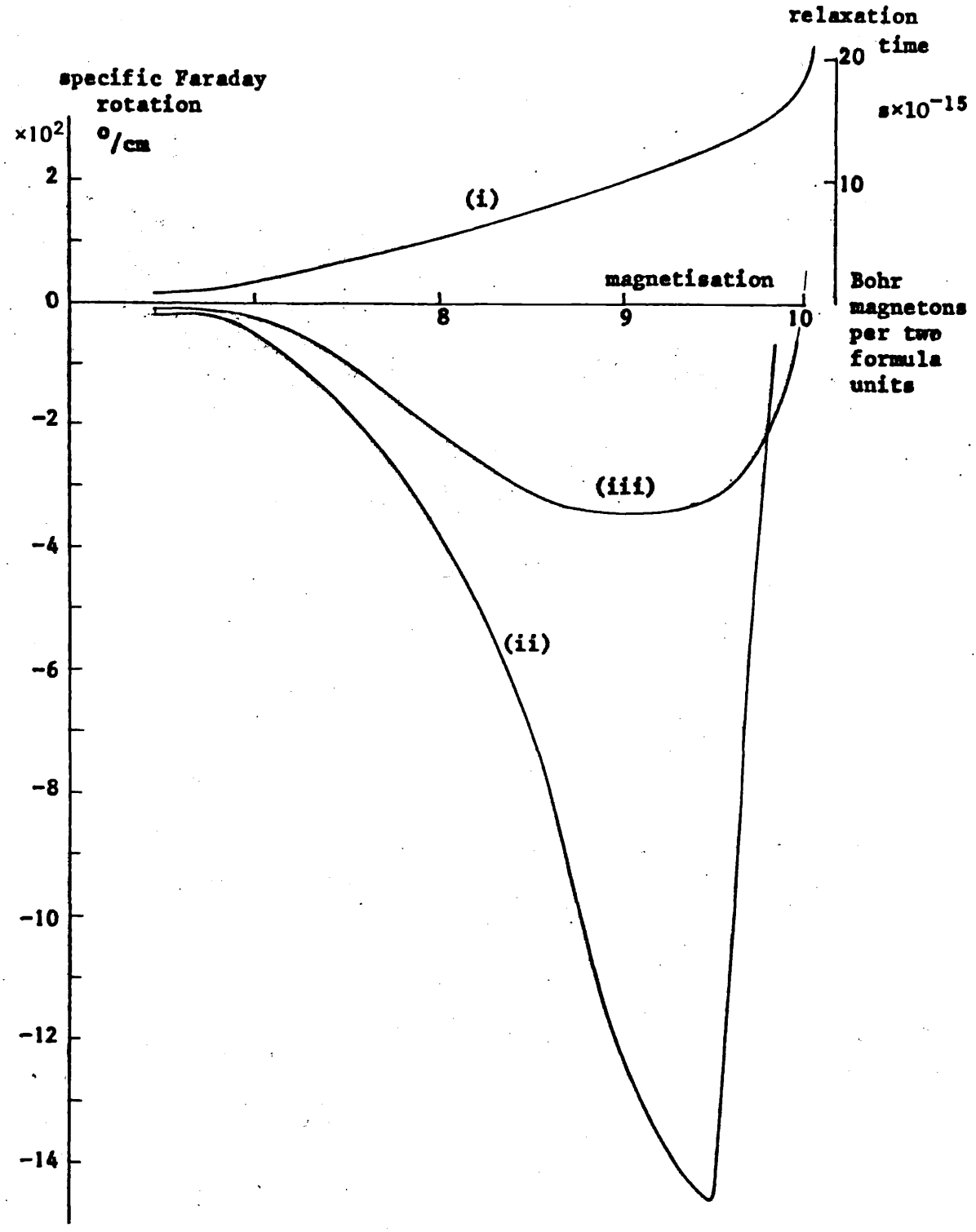

Figure 11.24. (i) Proposed relaxation time and the corresponding theoretical specific Faraday rotation in (ii) the [1$\bar{1}$0] direction and (iii) the [11$\bar{1}$] direction against magnetisation for samarium iron garnet

was in the process of becoming the hard direction of magnetisation. It is noted that this temperature is close to the point at which a second change occurs in the gradient of the experimental curve of rotation in the [111] direction against magnetisation.

The magnitude of the ferric lattice relaxation time inferred from this analysis is very different from the value used in the earlier investigations. When considering a magnetic rare-earth iron garnet, it is difficult to assess the effect on T_{Fe} when the iron subsystem is situated in a different lattice. However, it is encouraging to note that the values obtained for both yttrium and samarium iron garnets are similar. It would therefore be instructive in a future evaluation to include these temperature-dependent values for T_{Fe} and find a curve of best fit for the rare-earth relaxation time. A more rigorous evaluation should also include temperature-dependent g factors and molecular field coefficients using independently obtained relaxation parameters from a sufficiently detailed study of the far infra-red spectrum of the garnets. Spectroscopic data have not been taken into account in the present analysis and it is evident that if available, these should be included in a future programme.

Using the currently documented spectra, a brief assessment is given as to whether any serious perturbation to the Faraday rotation is expected.

11.6. Far infra-red spectra

The magneto-optical analysis described in this chapter has been developed using the classical approach of Wangsness. As a consequence any effects resulting from interband transitions have been ignored. A brief examination of the far infra-red spectra of the garnets is therefore made in order to assess the effect of strong absorption lines at the temperatures, magnetic fields and frequency employed in the current experiments.

The main mechanisms producing absorption of far infra-red radiation in rare-earth iron garnets are magnetic resonance, electronic absorption and lattice vibration[110]. These processes may be identified because magnetic resonances are expected to be temperature-dependent, while electronic lines are usually magnetic field dependent and phonon absorption should be unaffected by either parameter[110]. In this manner Yamamoto et al.[110] and Sievers and Tinkham[111] have tentatively identified the origin of the spectra displayed in Figures 9.5, 9.6 and Table 9.3.

Considering first gadolinium iron garnet, it is seen to have a simple far infra-red spectrum consisting of one line at approximately 83 cm^{-1}. This line, which is considered to be sufficiently remote from the 29.7 cm^{-1} emission line of the HCN laser to be unimportant in the present study, was identified by Sievers and Tinkham as a phonon transition and is part of a series of phonon lines which are characteristic of all the rare-earth iron garnets. Specific heat measurements[112] predict a splitting of the ground state of the gadolinium ion, at 27.8 cm^{-1}, in the exchange field. This is not observed and is attributed by Sievers and Tinkham to the crystal field being small as L = 0 for a free gadolinium ion. Also, no exchange resonance was observed because the absorption strength depends on $(g_{Gd} - g_{Fe})$ which is approximately zero.

Of the other crystals studied, samarium, erbium and dysprosium iron garnets all possess absorption lines that can, under certain conditions of temperature and applied magnetic field, become close to the laser frequency. At zero applied field, Figures 9.5 and 9.6 show that the lines in erbium and dysprosium iron garnets shift, by some small amount, away from the laser frequency as the temperature is raised, while the absorption line in samarium iron garnet passes through the radiation frequency at approximately 25°K. The measurements of Frayne in Figure 10.21 show that at certain temperatures, strong attenuation at 891 GHz occurs in samarium and erbium iron garnets when applying a 6.5 koe magnetic field. Figure 9.5 shows that at 4.2°K, the absorption feature in dysprosium iron garnet becomes coincident with the laser emission at an applied magnetic field of 20 koe. Fields of not more than 4.3 koe were produced in the present experiments and although the range of temperatures over which the spectrum was measured does not extend to those of the present measurements, the general trend shown in Figure 9.5 indicates that such pulling of the absorption line would not become important at the temperatures employed. This premise is supported by Figure 10.15 where there is no indication of entering an absorption band.

A reasonable account of the Faraday rotation in samarium iron garnet is given by the ferromagnetic treatment of section 11.5 which includes damping. However, a discrepancy exists between the theroetical and experimental results for the [111] direction below approximately 20°K. It is therefore significant to note that Figure 10.21(b) shows an absorption feature in this range which indicates that the classical analysis is insufficient in this temperature region.

The absorption lines in dysprosium and erbium iron garnets have been

identified as ferrimagnetic resonance[110,111]. The analysis of section 11.3 indicates that the occurrence of ferrimagnetic resonance at the discrete frequency of 891 GHz is a function of the relaxation parameter of the rare-earth ion. This is consistent with the theoretical characteristics of the dissipative component of the susceptibility tensor in Figure 11.8(b)(ii) and 11.8(b)(iii) which show that the frequency of the absorption line is also dependent on the relaxation time.

Electronic transitions have been identified in terbium iron garnet at 36 cm^{-1} and in holmium iron garnet at 29.4 cm^{-1}. The experiments of Yamamoto et al. on terbium iron garnet were performed at a maximum temperature of 4.2°K. It can only be assumed therefore that because the absorption line is electronic in origin, its frequency is unaltered at the temperatures used in the present experiments. In contrast, the 29.4 cm^{-1} line in holmium iron garnet is shown to be measurable at 70°K. In both cases no information was attained on the behaviour of the spectral lines with applied magnetic field. It is difficult therefore to assess the effect of such transitions on the Faraday rotations. However, reference can again be made to the measurements of Chapter Ten displayed in Figure 10.20(b) for terbium iron garnet and in Figure 10.17 for holmium iron garnet. This data, which represents conditions of both zero and 4.3 koe applied field, does not indicate the presence of an electronic transition.

A further indication that these absorption lines have little effect on Faraday rotation at the HCN laser frequency is obtained from the fit of the classical curve to the experimental data. Perturbation due to an electronic transition is expected to be greatest at the lower temperatures where thermal depopulation is most pronounced. The values of the g factors and relaxation times chosen for each garnet enabled a good fit of the theoretical curve to the experimental results both at high and at low temperatures. The presence of a significantly strong interband transition would be expected to alter the Faraday rotation in a manner similar to that described by Halpern et al.[126]. From a quantum-mechanical analysis Halpern et al. calculated the Faraday rotation introduced by an interband transition in a semiconductor. Reproduced in Figure 11.25, the variation of this rotation is shown as the radiation frequency is swept through that of the transition. Plotted against $(\omega-\omega_n)\tau$, the rotation is shown for several values of $\gamma H\tau$. Here ω is the radiation frequency, ω_n the transition frequency, τ the phenomenological relaxation time and γ the gyromagnetic ratio of the

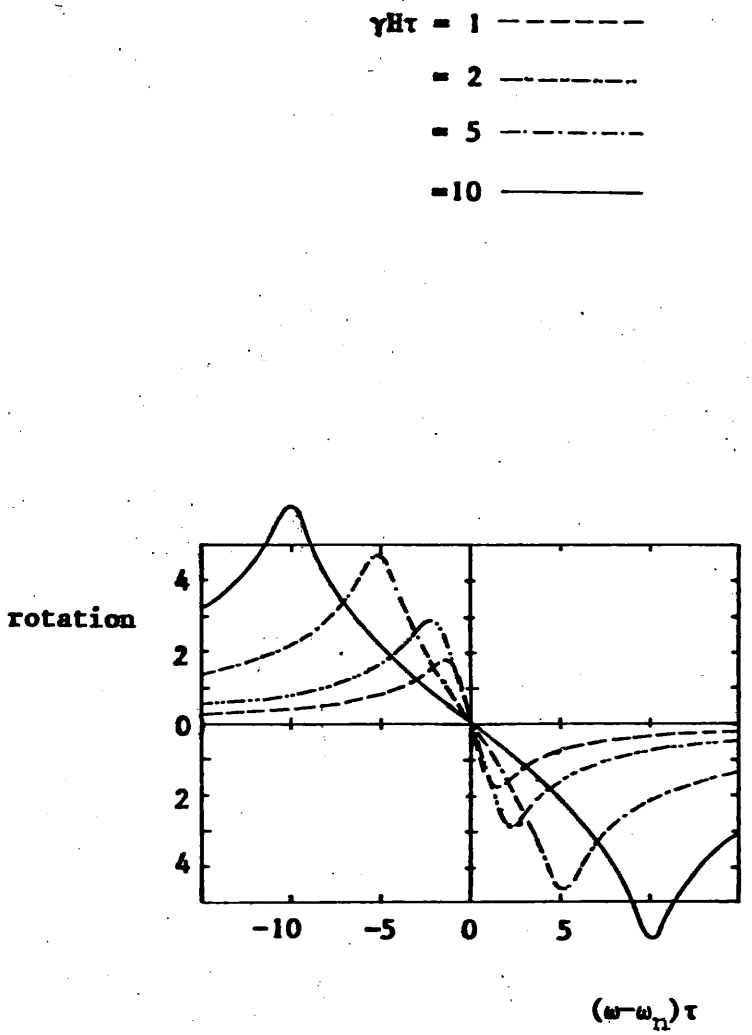

Figure 11.25. Plots of calculated Faraday rotation, indirect transition, as a function of frequency for different values of $\gamma H\tau$. After Halpern, Lax and Nishina[126].

attenuating ion situated in a field H. Low values of $\gamma H\tau$ represent conditions at room temperature or low field, while high values correspond to low temperatures or high field. The value of $\gamma H\tau$ is seen to have a considerable effect on the shape of the curve. Hence for conditions of fixed radiation frequency it is therefore expected that a significant contribution to the Faraday rotation from a transition would vary as the temperature is altered and be resolved from the classical curve shape.

CHAPTER TWELVE

CONCLUSIONS AND FURTHER WORK

The investigations carried out in this programme of work were approached with the aim of developing techniques for modulating submillimetre radiation, either for the purpose of impressing information on to the beam or for generating higher powers, this latter aspect being supplemented by an investigation into improving the performance of detectors.

Considering first the internal modulation of the laser, some enhancement of the laser output power was obtained by Q-switching and the prediction was made in section 6.4 that the pumping rate in the 15 cm diameter laser was sufficient to enable further improvements to be made by using a suitable Q-switch. However, the value of pump rate calculated from the pulsed laser output used the assumption that the peak absorption cross-section for pulsed excitation is unaltered from that for d.c. excitation. This inference is based on the observations of low electron temperature and that the ion conversion process appears to be unaltered throughout the entire range of electron densities produced. The validity of the calculations of pump rate would be supported by a more direct measurement of the peak absorption cross-section during pulsed ionisation and by a better theoretical understanding of the mechanism of excitation of the HCN molecule. As reported in section 6.4.2, Schötzau and Kneubühl[52] proposed that energy is transferred to the HCN molecule from an H_2 molecule. However, it was noted in section 6.5 that Figures 6.5 and 6.11(b) together imply that the pump rate is greater than the overall recombination rate. The hydrogen molecules must therefore donate energy to the active species many times during their lifetimes. This suggests that the H_2 particles in the lasers studied in this work are de-excited through a series of equally spaced levels on repeated collision with other particles. A mass spectroscopic analysis to determine the densities of the particle species occurring during the pulse ionisation of the active medium would enable a calculation of the H_2 - HCN collision rate to be made and indicate the feasibility of such a pumping mechanism.

It is evident that further improvements can be made to the Q-switching techniques studied. The losses incurred by placing a Melinex window across the cavity degraded the Q-switching process. A further investigation may benefit by orientating the window at the Brewster

angle. Melinex film was also used as the beam divider in the Michelson arrangement of the laser. Ionising the side arm of such an interferometer showed that it is possible to Q-switch a d.c. excited laser by this technique, but generation of high powers requires modulating a pulse-excited laser. The lack of success with this was also attributed to the Melinex film, in this case to its flexibility. Vibrations in the film, initiated by the pulsed discharge, occur and vary the relative phase between the two superimposed output beams. It is therefore suggested that future experiments should incorporate rigid beam splitters. TPX and PTFE have been found to possess low transmission losses at 337 μm[127] and an investigation by Frank[6] suggests that quartz and sapphire crystals, which were grown to a diameter of 10 cm, would form good beam splitters at this wavelength.

The aim of the theoretical and experimental evaluation of point-contact diodes was to produce a detector with an improved performance. Some success was obtained with the tungsten to gallium arsenide diode, but the advantage of low output impedance of metal-insulator-metal structures may warrant continued investigation. It is considered that the formulation of the model of a point-contact diode went some way to explaining the characteristics of these devices and indicated that further improvement in the output from M-I-M diodes is possible. The theoretical curves of Figure 7.9 indicate that a moderate increase in the difference between the work functions of the two electrodes would produce a large increase in the output voltage. It would therefore be informative in future studies to select metals with a greater difference in work function from that of tungsten than were employed in the present work. Barium, potassium, lithium and sodium have been found to possess low values of work function[128] but would be inconvenient for diode fabrication as they are highly reactive in elemental form. Certain commercially manufactured cathode materials have low work functions and might be used for a diode substrate. However, these are produced from tungsten with less than a monolayer of caesium at the surface and it cannot be certain that the macro-surface properties are representative of localized areas of the dimensions of a point-contact. A further approach is to use a rare-earth. Gadolinium is known to have a low work function[129] and the measurements of Chandler[130] have shown thin films of gadolinium, terbium and dysprosium grown and aged in ultra high vacuum to possess the low work function values displayed in Table 12.1. On exposure to air, the resistances of these films were found to be little different to those measured inside the vacuum system

Table 12.1

Values of the work functions of rare-earth thin films grown and aged in ultra high vacuum. After Chandler[130]. Errors represent spread in readings. Only one film of dysprosium was measured.

Rare-earth	Work function (eV)	
	Fresh	Aged
Gadolinium	3.545 ± 0.37	3.467 ± 0.405
Terbium	3.151 ± 0.335	3.081 ± 0.385
Dysprosium	3.077	2.97

indicating that the surface becomes passivated and that sufficient metal remains to form an electrode.

Two aspects of the development of diode detectors that have not been considered in this work are those of coupling the radiation into the antenna and of improving the fabrication technique to produce a more mechanically rugged device. It is suggested that strengthened low capacity diodes may be constructed by inserting a metal or semiconductor material into a transparent substrate and growing a transparent dielectric medium on the substrate. Removal of the dielectric by, for example, ion beam etching, in a small region over the electrode as illustrated in Figure 12.1(a) would enable a second electrode to be sputtered on to the upper surface of the dielectric. The steep sides of the trough etched into the insulator ensure a low capacity between the two electrodes. A technique for producing a rigid antenna was suggested by Faris and Gustafson[131] where a fine line is deposited on to a glass or quartz slide by sputtering tungsten through a shadow mask. By partially immersing the slide in an electrolyte, they electrochemically etched the tungsten by the same method as that used for a wire. A taper was formed at the miniscus of the liquid as illustrated in Figure 12.1(b) which could easily be reduced to a tip size of 3000 Å. Faris and Gustafson felt that by increasing the thickness of the line and the grain size of the tungsten to reduce preferential etching at the grain boundaries, microstructures of less than 500 Å could be formed. They proposed that such a technique could lead to the construction of mechanically stable high frequency diodes. It is now suggested that

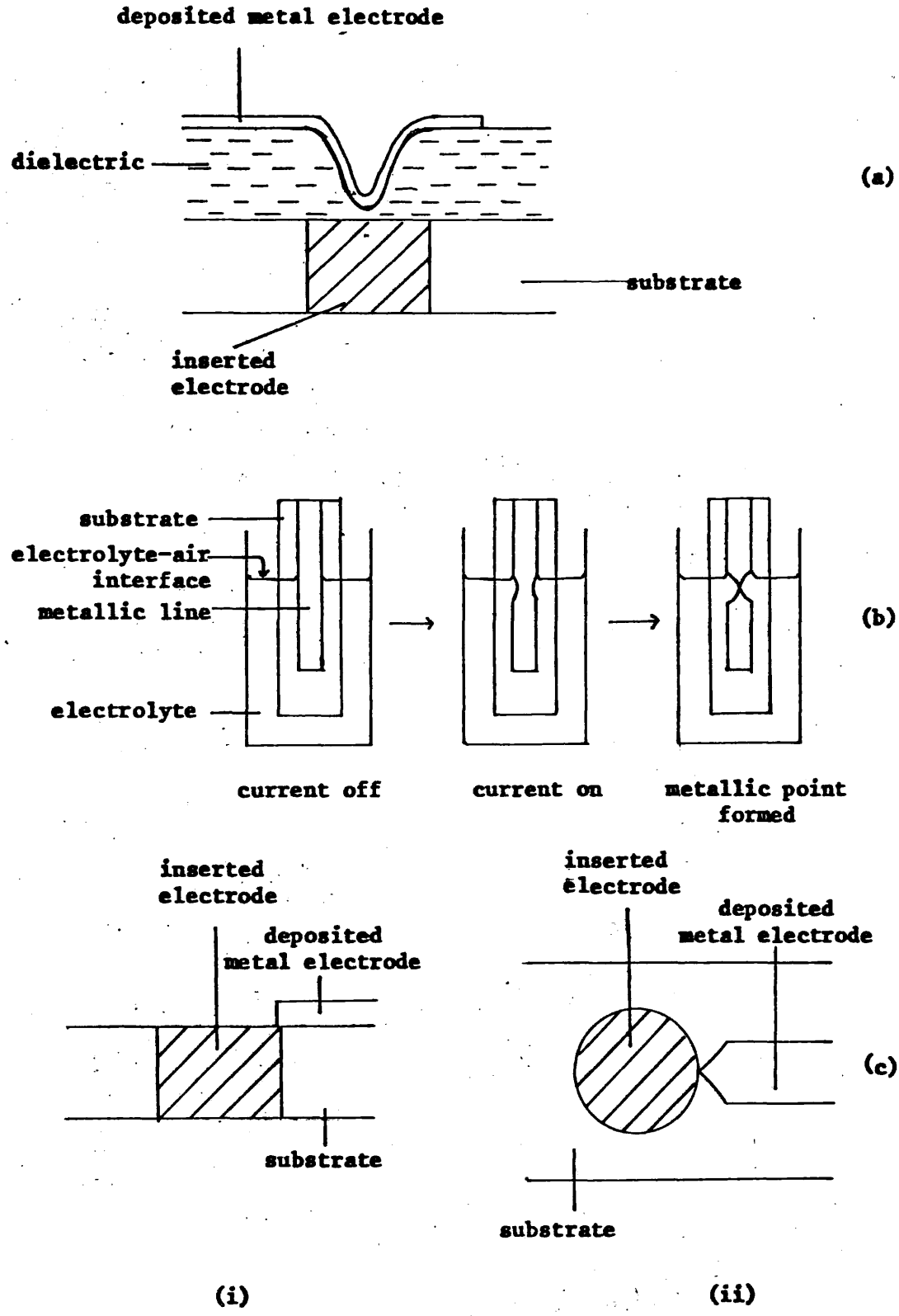

Figure 12.1. (a) Cross-section of a low capacity diode formed by etching away a dielectric medium deposited on an electrode inserted into a substrate, (b) formation of a point of a metallic film deposited on a substrate; after Faris and Gustafson[191], and (c)-(i) cross-section and (ii) plan view of an electrode inserted into a substrate with a sputtered electrode etched to form a low capacity junction

sputtering such a line on to the surface of a transparent substrate and across an inserted electrode as described above would form a rugged integrated diode and antenna. As a cheaper alternative to ion beam etching, it is feasible that the dielectric may be omitted and the antenna sputtered on to the oxidised surface of the inserted electrode and etched in the manner of Faris and Gustafson. By monitoring a current passing between the antenna and the electrode, the etching process would be terminated when a sufficiently small junction is formed between the antenna edge of the inserted electrode, as shown in Figure 12.1(c).

Whisker antennae have been mounted in free space as adopted in this programme, and have been mounted transversely to the direction of propagation in O-band waveguide. However, the most successful arrangement has been shown by Kräutle et al.[132] to be to mount the antenna in the right-angle corner of a pair of mirrors, as illustrated in Figure 12.2(a). With a whisker placed 1.2 wavelengths from the corner, this system was found to have a gain of 12 dB relative to an antenna in free space. For further development of this system, it is proposed that an integrated diode and antenna be constructed on the broad face of a right-angled prism of transparent dielectric, and the other two faces be metallised. The prism may then be inserted into the apex of two mirrors, as shown in Figure 12.2(b). Such an arrangement can, in principle, lend itself to an investigation involving other mirror profiles.

It may be assumed that the development of improved far infra-red sources and detectors may lead to an increase in activity at submillimetre wavelengths and create a requirement for modulators and non-reciprocal devices. The theoretical evaluation of the garnets showed that in the region of negligible anisotropy, the Faraday rotation may be predicted provided that magnetisations, the Landé g factors and the relaxation times are known. Hence the analysis of Chapter Eleven may provide an aid to the design of magnetic components. Of the five garnets shown in Figure 10.22, samarium iron garnet is seen to possess the best figure of merit but it is evident that further work is required to determine the transmission properties of the other garnets. However, the figure of merit is only one parameter to be considered in the design of a modulator. Although modulation frequencies are theoretically possible up to the inverse of the relaxation time of the magnetic specimen[11], practical difficulties limit the generation of high power high frequency magnetic fields[133]. To produce an analogue signal, a high value of

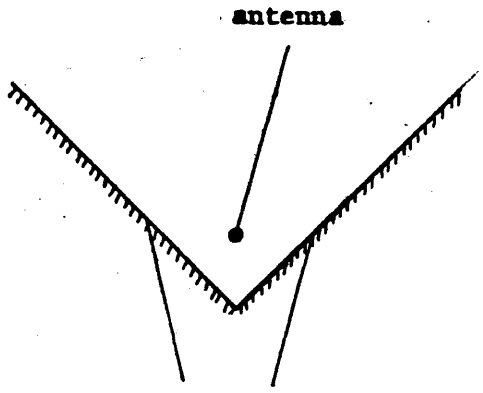

(a)

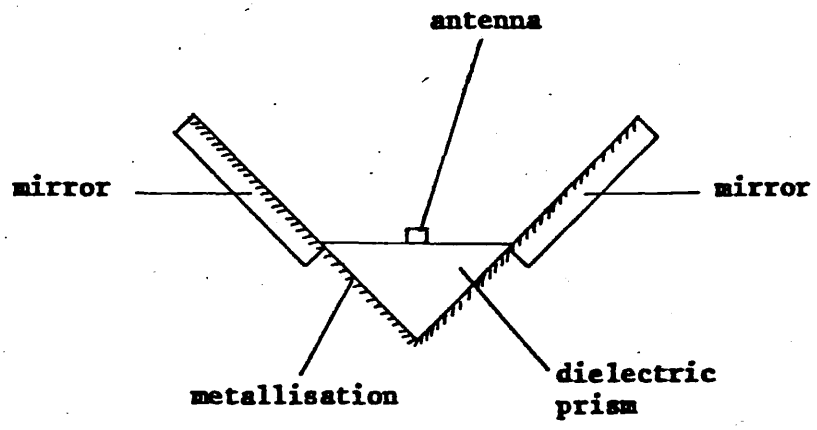

(b)

Figure 12.2. (a) Whisker antenna mounted in the corner of a pair of mirrors mutually at right angles. Antenna shown orientated perpendicularly to the plane of the page. (b) Antenna deposited on the broad face of a dielectric prism, the other faces being metallised. The prism is mounted in the apex of two mirrors.

the gradient $d\theta_F/dH_0$ is needed in order to keep the required modulation depth of the magnetic field to a minimum. θ_F and H_0 are the Faraday rotation and the magnitude of the applied field repsectively. To obtain reproducible modulation of the type necessary for Q-switching, the polarisation should be switched between conditions of 'saturated rotation' where $d\theta_F/dH_0 = 0$, and this condition should be attained at a low value of applied magnetic field. The work of Frayne[13] and Birch and Jones[11] show the polycrystalline spinel ferrites 5E1 and 8C1 to have figures of merit at room temperature of 260° and 150° respectively at 891 GHz which are superior to those of the garnets measured in this work. However, Figures 10.8 to 10.11 show saturation in the rare-earth iron garnets to occur at room temperature at a field of approximately 450 oe, while the curves of Birch and Jones, reproduced in Figure 12.3, show that a field approaching 4 koe is necessary to produce this condition in 5E1 and 8C1. It is therefore possible to obtain higher modulation frequencies than the 2 MHz value achieved by Birch and Jones by using a rare-earth iron garnet.

Figure 10.22 shows that a requirement for an improved figure of merit could, with the choice of the appropriate material, be met by cooling the specimen. Although the higher field required to saturate the garnet would not necessarily inhibit its use for non-reciprocal devices, the performance of a modulator would be impaired. The experimental graphs in Figures 10.8 to 10.11 show that, as the temperature is reduced, the effect of anisotropy becomes more pronounced. For yttrium iron garnet and samarium iron garnet, these conditions have been simulated theoretically with some success by the single lattice model, but the double sublattice model of the other rare-earth iron garnets has not been tested sufficiently to confirm its use as a tool for the design of components. It is therefore suggested that further evaluation using the computer programme described in Appendix VIII should be carried out over a wider range of magnetisations, relaxation times and g factors.

It has been suggested by Moss[133] that the difficulties incurred in producing high frequency magnetic fields could be overcome by using the magnetic component of r.f. electromagnetic fields. The practicability of such a technique is shown to be limited by considering an example for 10 cm wavelength radiation in which the peak field in a waveguide of a 1 MW beam is only 40 gauss. Nevertheless, a future programme of work could include an investigation of electro-optic effects at sub-millimetre wavelengths as such a process could render feasible

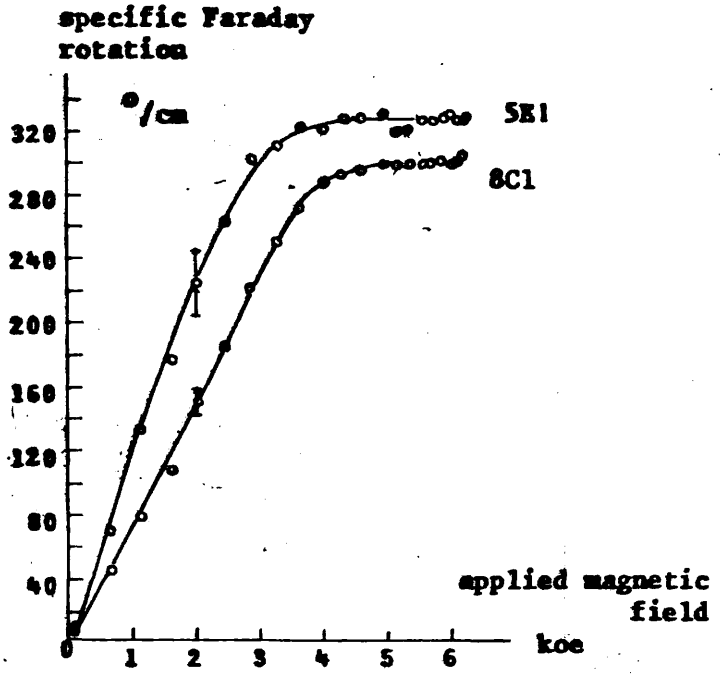

Figure 12.3. Specific Faraday rotation at 891 GHz against applied magnetic field in the polycrystalline spinel ferrites 5E1 and 8C1. After Birch and Jones[11].

modulation at microwave frequencies. Work carried out using near infra-red radiation[133] has shown that the capacity of the electrodes in a Kerr cell, together with the high voltages required, inhibit the use of a direct modulation technique. However, Kaminow[134] found that 0.85 μm wavelength radiation, when passed through a crystal of potassium dihydrogen phosphate in a suitable cavity, can be modulated at 9 GHz by the electric field of an electromagnetic wave and that only 760W of r.f. power is needed to produce a half wavelength of relative retardation.

In Chapter One it was stated that a contributory factor to the slow development of the submillimetre wavelength region was the lack of a high power source. Notable advances have been made with the invention of the optically pumped methyl fluoride and deuterium oxide lasers, both of which have been reported as being capable of producing a mega-watt of submillimetre power[6]. Large laser systems are required to generate such powers, the active medium being energised from a giga-watt CO_2 source, and are usually employed for specialized purposes as, for example, scattering from plasmas in order to measure the ion temperature[6]. For more general use, smaller lasers can be constructed as shown by Cohn et al.[135], who operated a methyl fluoride laser with a 1.85 metre long submillimetre cavity. This produced 9 kW of far infra-red power when pumped from a 6 MW CO_2 laser. It appears, however, that the output power from optically pumped far infra-red lasers is primarily limited by the volume of the active medium. The lifetimes of the rotational energy levels of the laser molecules are essentially equal and so no increase in power can be obtained by Q-switching. In contrast to this, the HCN laser has been shown to have the potential for further improvement of its output and the Michelson arrangement proposed for modulating a pulse-excited laser would provide a mechanically simple system. It is therefore felt that a successful completion of the proposals described above would ensure that many of the applications outlined in Chapter One will benefit from the range of submillimetre emission lines produced from both gas discharge and optically pumped lasers.

REFERENCES

1. Rubens, H., and Aschkinass, E. Wied. Ann., lxvii, p.459
2. Gebbie, H.A., Stone, N.W.B., and Findlay, F.D. Nature, vol.202, 1964, p.685
3. Rubens, H., and Wood, R.W. Phil. Mag., vol.21, 1911, p.249-261
4. Happ, H., Eckhardt, W, Genzel, L., Sperling, G., and Weber, R. Z. Naturfortsch, vol.12A, 1957, p.522-524
5. First International Conference on Submillimetre Waves and their Applications, reported in IEEE on MTT, vol.MTT-22, no.12, December 1974
6. Third International Conference on Submillimetre Waves and their Applications, reported in Infrared Physics, vol.18, no.5/6, December 1978
7. Symposium on Submillimetre Waves, New York, March 31, April 1,2, 1970. Conference Proceedings reported in Microwave Research Inst. Symposia Series, vol.20, Polytechnic Press of the Polytechnic Inst. of Brooklyn, Brooklyn, N.Y. Ed. J. Fox
8. Williams, N., and Foster, P.R. Elect. Eng., vol.50, no.604, 1978, p.77-81
9. Putley, E.H. Proc. Phys. Soc., vol.76, 1960, p.802-805
10. Kinchm, A., and Rollin, B.V. Brit. J. Appl. Phys., vol.14, 1963, p.672
11. Birch, J.R., and Jones, R.G. Infrared Phys., vol.10, 1970, p.217-224
12. Melngailis, I., and Tannenwald, P.E. Proc. IEEE, vol.57, 1969, p.806
13. Frayne, P.G. Brit. J. Appl. Phys. (J. Phys. D), ser.2, vol.1, 1968, p.741-751
14. McCaul, B.W. Appl. Opt., vol.9, no.3, 1970, p.653-663
15. Bradley, C.C. Infrared Phys., vol.12, 1972, p.287-299
16. Chamberlain, J.E., Chantry, G.W., Findlay, F.D., Gebbie, H.A, Gibbs, J.E., Stone, N.W.B., and Wright, A.J. Infrared Phys., vol.6, 1966, p.195-203

17. Wells, J.S., Evenson, K.M., Matarrese, L.M., Jennings, D.A., and Wichman, G.L. NBS Technical Note, no.395, 1971

18. Birch, J.R., and Bradley, C.C. Infrared Phys., vol.13, 1973, p.99-108

19. Fox, A.G., and Li T. The Bell System Tech. J., vol.40, 1961, p.453-488

20. Kneubühl, F.K., and Steffen, H. Phys. Lett., vol.25A, 1967, p.639

21. Kogelnik, H., and Li T. Appl. Opt., vol.5, no.10, 1966, p.1550-1567

22. Heald, M.A., and Wharton, C.B. Plasma diagnostics with microwaves. New York: J. Wiley, 1965

23. Mountjoy, J.H. PhD thesis, University of Cork

24. Whitbourn, L.B., Robinson, L.C., and Tait, G.D. Phys. Lett., vol.38A, no.5, 1972, p.315-317

25. Newton, A.A., and Sexton, M.C. J. Phys. B (Proc. Phys. Soc.), ser.2, vol.1, 1968, p.669-680

26. Brown, S.C. Basic data of plasma physics. New York: The Technology Press of MIT and J. Wiley, 1959

27. Frayne, P.G. J. Phys. B (Atom. Molec. Phys.), ser.2, vol.2, 1969, p.247-259

28. McClung, F.J., and Hellworth, R.W. Proc. IEEE, vol.51, 1963, p.46-53

29. Gebbie, H.A., Stone, N.W.B., Slough, W., Chamberlain, J.E., and Sheraton, W.A. Nature, vol.211, 1966, p.62

30. Stafsudd, O.M., Haak, F.A., and Radisavljevic, K. IEEE J. Quant. Elect., vol.QE-3, no.11, 1967, p.618-620

31. Lide, D.R., and Maki, A.G. Appl. Phys. Lett., vol.11, no.2, 1967, p.62-64

32. Hocker, L.O., and Javan, A. Phys. Lett., vol.25A, no.7, 1967, p.489-490

33. Proc. of Joint Conf. on Infra-red Tech., Institution of Elect. and Radio Eng., University of Reading, 21-23 Sept., 1971. IERE

34. Hocker, L.O., Javan, A., Ramachandra Rao D., Frenkel, L., and Sullivan, T. Appl. Phys. Lett., vol.10, no.5, 1967, p.147-149

35. Stafsudd, O.M., and Yeh,Y.C. IEEE J. Quant. Elect., vol.QE-5, no.7, 1969, p.377-380

36. Sharp, L.E., and Wetherell, A.T. Appl. Opt., vol.11, no.8, 1972, p.1737-1741

37. Arams, F., Allen, C., Wang, M., Button, K., and Rubin, L. Proc. IEEE, vol.55, 1967, p.420

38. Kon, S., Yamanaka, M., Yamamoto, J., and Yoshinaga, H. Japan J. Phys., vol.6, 1967, p.612

39. Kon, S., Otsuka, M., Yamanaka, M., and Yoshinaga, H. Japan J. Appl. Phys., vol.7, 1968, p.434

40. Sochor, V., and Brannen, E. Appl. Phys. Lett., vol.10, 1967, p.232

41. Steffen, H., Keller, B., and Kneubühl, F.K. Electronic Lett., vol.3, 1967, p.562

42. Jones, R.G., Bradley, C.C., Chamberlain, J., Gebbie, H.A., Stone, N.W.B., and Sixsmith, H. Appl. Opt., vol.8, no.3, 1969, p.701-705

43. Brannen, E., Sochor, V., Sarjeant, W.J., and Froelich, H.R. Proc. IEEE, vol.55, 1967, p.562

44. Yamanaka, M., Kon, S., Yamamoto, J., and Yoshinaga, H. Japan J. Appl. Phys., vol.7, 1968, p.554

45. Steffen, H., and Kneubühl, F.K. IEEE J. Quant. Elect., vol.QE-4, 1968, p.992

46. Mathias, L.E.S., Crocker, A., and Wills, M.S. IEEE J. Quant. Elect., vol.QE-4, 1968, p.205

47. Turner, R., and Poehler, T.O. J. Appl. Phys., vol.39, 1968, p.5726

48. Lam, M.F., Jassby, D.L., and Casperson, L.W. IEEE J. Quant. Elect., vol.9, 1973, p.851-852

49. Tait, G.D., Robinson, L.C., and Bartlett, D.V. IEEE Trans. on MTT, vol.MTT-22, 1974, p.1109-1111

50. Bradley, C.C., Burroughs, W.J., Gebbie, H.A., and Slough, W. Infrared Phys., vol.7, 1967, p.129

51. Duxbury, G., and Burroughs, W. J. Phys. B, vol.3, 1970, p.98

52. Schötzau, H.J., and Kneubühl, F.K. Appl. Phys., vol.6, 1975, p.25-30

53. Belland, P., Ciura, A.I., and Whitbourn, L.B. Optics Comm., vol.11, no.1, 1974, p.21-26

54. Tolansky, S. An introduction to interferometry. Longmans, 1966

55. Robinson, L.C., and Whitbourn, L.B. Proc. IREE Australia, October 1971, p.355-360

56. Schötzau, H.J., and Kneubühl, F.K. IEEE J. Quant. Elect., vol.QE-11, no.10, 1975, p.817-822

57. Anisimov, A.I., Vinogradov, N.I., Golant, V.E., and Konstantinov, B.P. Sov. Phys. - Tech. Phys., vol.7, no.10, 1963, p.884-889

58. Delcroix, J.L. Introduction to the theory of ionized gases. New York: Interscience, 1960

59. Spitzer, L. Physics of fully ionized gases. New York: Interscience, 1956

60. D'Angelo, N. Phys. Rev., vol.140, 1965, p.A1488

61. Cronin, J.C., and Sexton, M.C. Brit. J. Appl. Phys. (J. Phys. D), ser.2, vol.1, 1968, p.889-893

62. Unicam SP50, Golay Radiation Detector System, ser.IVA, Unicam Instruments Ltd., 1966

63. Matarrese, L.M., and Evenson, K.M. Appl. Phys. Lett., vol.17, no.1, 1970, p.8-10

64. Green, S.I. J. Appl. Phys., vol.42, no.3, 1971, p.1166-1169

65. Payne, C.D., and Prewer, B.E. The Radio and Electronic Eng., vol.39, no.3, 1970, p.167-171

66. Becklake, E.J., Payne, C.D., and Prewer, B.E. J. Phys. D: Appl. Phys., vol.3, 1970, p.473-481

67. Evenson, K.M., Wells, J.S., Matarrese, L.M., and Elwell, L.B. Appl. Phys. Lett., vol.16, 1970, p.159

68. Evenson, K.M., Wells, J.S., and Matarrese, L.M. Appl. Phys. Lett., vol.16, 1970, p.251

69. Hartman, T.E. J. Appl. Phys., vol.33, 1962, p.3427

70. Becklake, E.J.S., Cram, L.A., and Prewer, B.E. Elect. Lett., vol.4, no.26, 1968, p.601-602

71. Pollack, S.R., and Morris, C.E. J. Appl. Phys., vol.35, 1964, p.1503

72. Simmons, J.G. J. Appl. Phys., vol.34, no.9, 1963, p.2581-2590

73. Simmons, J.G. J. Appl. Phys., vol.35, no.8, 1964, p.2472-2481

74. Marhic, M.E., and Jassby, D.L. Report No. UCLA-34P157, PELR-3, UCLA-ENG-7204, January 1972

75. Chow, C.K. J. Appl. Phys., vol.34, no.9, 1963, p.2599-2602

76. Frayne, P.G., Chandler, N., and Booton, M.W. J. Phys. D: Appl. Phys., vol.11, 1978, p.2391-2399

77. Haas, G.A., and Thomas, R.E. Surface Sci., vol.4, 1966, p.64-88

78. Zisman, W.A. Rev. Sci. Instrum., vol.3, 1932, p.367

79. Surplice, N.A., and D'Arcy, R.J. J. Phys. E.(Sci. Instrum.), vol.3, 1970, p.477

80. Reviere, J.C. Solid State Surf. Sci., vol.1, ch.4. Ed. M. Green. Dekker, 1969

81. Thanailakis, A. Conference on metallic-semiconductor contacts, UMIST, April 1974

82. Dobson, P.J., and Hopkins, B.J. Brit. J. Appl. Phys.(J. Phys. D), ser.2, vol.1, 1968, p.1241

83. Chen, T.T., and Adler, J.G. Solid State Comm., vol.8, 1970, p.1965

84. Pitt, C.W. Microelectronics and Reliability, vol.9, 1970, p.239-266

85. Roberts, G.G., and Polanco, J.I. Phys. Stat. Sol.(a), vol.1, 1970, p.409-420

86. Kaye, G.W.C., and Laby, T.H. Tables of physical and chemical constants. Longmans, 1966

87. Polder, D. Phil. Mag., vol.40, 1949, p.99-115

88. Lax, B., and Button, K.J. Microwave ferrites and ferrimagnetics. New York: McGraw-Hill, 1962

89. Weiss, P. J. Phys., ser.4, vol.6, 1907, p.661

90. Heisenberg, W. Physical principles of the quantum theory. Chicago: Chicago Univ. Press, 1930

91. Néel, L. Propriétés magnétiques des ferrites; ferrimagnetisme et antiferromagnétisme. Reviewed by J.S. Smart. Am. J. Phys., vol.23, 1955, p.356

92. Kittel, C. Phys. Rev., vol.73, 1948, p.155

93. Kittel, C. Phys. Rev., vol.71, 1947, p.270-271

94. Néel, L. Ann. Phys., vol.3, 1948, p.137

95. Landau, L., and Lifshitz, E. Physik Z. Sowjetunion, vol.8, 1935, p.153

96. Wangsness, R.K. Phys. Rev., vol.111, no.3, 1958, p.813-816

97. Bertaut, F., and Forrat, F. C.R. Acad. Sci., vol.242, 1956, p.382

98. Geller, S., and Gilleo, M.A. Acta Cryst., vol.10, 1957, p.239

99. Gilleo, M.A., and Geller, S. Phys. Rev., vol.110, 1958, p.73

100. Craik, D.J., and Tebble, R.S. Ferromagnetism and ferromagnetic domains from selected topics in solid state physics series, vol.IV. Ed. E.P. Wohlforth. Amsterdam: North Holland Publ. Co., 1965

101. Kramers, H.A. Physica, vol.1, 1934, p.182

102. Anderson, E.E. Proc. of the International Conference on Magnetism, Sept. 1964, held at Nottingham, UK, p.660-663

103. Pauthenet, R. Compt. Rend., vol.242, 1956, p.1859

104. Aléonard, R., Barbier, J.C., and Pauthenet, R. Compt. Rend., vol.242, 1956, p.2531

105. Bertaut, F., Forrat, F., Herpin, A., and Meriel, P. Compt. Rend., vol.243, 1956, p.898

106. Smit, J., and Wijn, H.P.J. Ferrites. New York: J. Wiley, 1959

107. Bertaut, F., and Pauthenet, R. Proc. Inst. Elect. Eng. (London) vol.104B, 1957, p.261

108. Harrison, F.W., Thompson, J.F.A., and Lang, G.K. J. Appl. Phys., vol.36, no.3, 1965, p.1014-1015

109. Pearson, R.F. J. Appl. Phys. Suppl., vol.33, no.3, 1962, p.1236-1242

110. Yamamoto, J., Smith, B.T., and Bell, E.E. J. Opt. Soc. Am., vol.64, no.6, 1974, p.880-883

111. Sievers, A.J., and Tinkham, M. Phys. Rev., vol.129, no.5, 1963, p.1995-2004

112. Harris, A.B., and Meyer, H. Phys. Rev., vol.127, 1962, p.101-118

113. Borets, A.N., and Grineva, S.I. Optics and Spect., vol.18, no.5, 1965, p.462-464

114. Oswald, F. Optik, vol.16, 1959, p.527-537

115. Wangsness, R.K. Phys. Rev., vol.95, no.2, 1954, p.339-345

116. Landé, A. Phys. Rev., vol.46, 1934, p.477

117. Johnson, B., and Tebble, R.S. Proc. Phys. Soc., vol.87, 1966, p.935-944

118. Chetkin, M.V., and Shalygin, A.N. J. Appl. Phys., vol.39, no.2, 1968, p.561-562

119. Rodrigue, G.P., Meyer, H., and Jones, R.V. J. Appl. Phys. Suppl., vol.31, 1960, p.376-382.

120. Weiss, M.T. J. Appl. Phys., vol.30, 1959, p.2014

121. Geschwind, S., and Walker, L.R. J. Appl. Phys. Suppl., vol.30, 1959, p.163S-170S

122. Handbook of microwave ferrite materials. Ed. W.H. Aulock. New York: Academic Press, 1965

123. Vittoria, C., and Wilsey, N.D. J. Appl. Phys., vol.45, no.1, 1974, p.414-420

124. Clark, A.E., and Callen, E. J. Appl. Phys., vol.39, no.13, 1968, p.5972-5982

125. Clarricoates, P.J.B. Microwave ferrites. Chapman and Hall, 1961

126. Halpern, J., Lax, B., and Nishina, Y. Phys. Rev., vol.134, no.1A, 1964, p.A140-A153

127. Becklake, E.J., and Smith, M.A. The Radio and Elect. Eng., vol.39, no.3, 1970, p.161-166

128. Handbook of chemistry and physics. Ed. in chief R.C. West. The Chemical Rubber Co., 1964

129. Eastman, D.E. Phys. Rev. B, vol.2, 1970, p.1

130. Chandler, N. PhD thesis. University of London, Royal Holloway College, 1978

131. Faris, S.M., and Gustafson, T.K. J. Vac. Sci. Technol., vol.12, no.6, 1975, p.1356-1358

132. Kräutle, H., Sauter, E., and Schultz, G.V. Infrared Phys., vol.17, 1977, p.477-483

133. Moss, T.S. Infrared Phys., vol.2, 1962, p.129-139

134. Kaminow, I.P. Phys. Rev. Lett., vol.6, no.10, 1961, p.528-530

135. Cohn, D.R., Fuse, T., Button, K.J., Lax, B., and Drozdowicz, Z. Appl. Phys. Lett., vol.27, no.5, 1975, p.280-282

136. Simmons, J.G. J. Appl. Phys., vol.34, no.6, 1963, p.1793-1803

ACKNOWLEDGEMENTS

Grateful thanks are due to Dr. P.G. Frayne for his advice and encouragement and especially for the use of his unpublished data on transmission and Faraday rotation in samarium and erbium iron garnets.

My appreciation is conveyed to Mr. N. Chandler for his collaboration on the theoretical aspect of the evaluation of point-contact diodes and for the fabrication and work function measurements of several of the planar electrodes.

For his helpful assistance with the construction of much of the equipment, I am indebted to Mr. T. Tedder.

Gratitude is also expressed to Mrs. M. Guy for typing the thesis, to the late Professor S. Tolansky for providing a research studentship, and to the Science Research Council for sponsoring the project.

APPENDIX I

A numerical solution of the differential equations 4.1 and 4.2 was obtained using the Fortran IV computer programme QSWTCH. In order to store data required to represent a Lorentzian profile, the parameter AB is declared as a 1 × 10000 array. Parameters necessary for the computation are entered with numerical values as displayed in the listing in Figure A1.1(a) and represent

RO - the laser mirror radii

CD - the critical plasma density for the laser radiation as defined in equation 2.6

R - the radii of curvature of the laser mirrors

R1 and R2 - the reflectivity of the laser mirrors

ABB - the peak absorption cross-section

PU - the pumping fraction

WAVE - the wavelength of the laser radiation

C - the velocity of light in vacuum

VL - the length of the unexcited region in the laser cavity

PL - the length of excited region in the laser cavity

TOR337 - the spontaneous lifetime of the upper level of the laser transition

DT - a parameter defining the time lapse between successive calculations

MUL - a parameter defining the number of locations of AB shifted by the change in optical path length of the laser cavity

Data representing a normalized, approximate Lorentzian profile is calculated inside the DO 700 loop shown in Figure A1.1(a). To simulate cavity mode scanning through more than one gain profile, the 1000 data points forming the curve are fed into a further 9000 locations in the array AB by the loops DO 703 and DO 702.

In order to plot a Q-switched output as a function of the cavity decay time, the cavity decay time, denoted by the Fortran variable TOR, is calculated according to equation 2.18. The interval between successive

```
PROGRAM QSWTCH(INPUT,OUTPUT,TAPE1=INPUT,TAPE3=OUTPUT)
COMMON AB(10000)
RO=7.6
CD=0.984E+16
R=750.
R1=0.95
R2=0.95
ABB=0.1E-09
PU=1.E-04
WAVE=0.0337
C=0.3E+11
VL=50.
PL=600.
DA=2.4E+03
RECOMB=1.E-10
TOR337=5.E-03
DT=4.E-09
MUL=1000
W=3./891.
W=W*W
Y=1./W
DO 700 I=1,1000
X=FLOAT(I)
X=X/1000.
X=0.012*X
X=0.994+X
X=X-1.
X=4.*X*X
X=1./(X+W)
X=X/Y
AB(I)=X
700 CONTINUE
DO 703 K=1,9
J=1000*K
DO 702 I=1,1000
M=J+I
702 AB(M)=AB(I)
703 CONTINUE
W=FLOAT(MUL)
WRITE(3,77)
DO 302 JK=1,2
NN=1
53 WRITE(3,77)
DE=1.E+13
WRITE(3,801)JK
WRITE(3,77)
```

Figure A1.1(a) Listing of the programme QSWTCH

```
POP=2.
DD=1.E+9
57 ZZ=1.-D/CD
WRITE(3,1007)ZZ
Z=1./(R1*R2)
REFRAC=SQRT(ZZ)
WRITE(3,1007)REFRAC
TRAN=PL*REFRAC/C
WRITE(3,1007)TRAN
TOR=2.*((VL+PL)/C)/(ALOG(Z))
WRITE(3,1007)TOR
PN=TRAN/(TOR*PL*ABB)
WRITE(3,1007)PN
ALFA=ABB*POP
WRITE(3,1007)ALFA
FI=(ALFA*PL/TRAN)/PN
WRITE(3,1007)FI
THRESH=FI
TT=DT/TOR
LL=1
E=1.
MM=0
DO 301 III=2,5001
DP=DE
DE=DE-DD
CON=-DT/TOR337
IF(NN.EQ.1)GO TO 50
GO TO 51
50 LL=500
51 CONTINUE
GAMA=1.
DFI=FI*(POP-GAMA)
FI=(FI+DFI*TT)*AB(LL)
IF(FI.LT.THRESH)GO TO 709
GO TO 708
709 FI=THRESH
708 DN=(DE-DP)/DT
IF(JK.EQ.1)GO TO 602
PUMP=(DE-DD)/TT*PU/PN
GO TO 603
602 PUMP=1.
603 DPOP=-2.*FI*POP+PUMP
POP=POP+DPOP*(TT)-POP*(1.-(EXP(CON)))
MM=MM+1
IF(MM.EQ.500)GO TO 9
GO TO 501
9 WRITE(3,1005)POP,FI,PUMP,DE,GAMA,L,LL,III
MM=0
```

Figure A1.1(b) Listing of the programme QSWTCH continued

```
501 RHO=1.E+10
RHP=1.E+10
ZZ1=1.-RHP/CD
ZZ2=1.-RHO/CD
XX1=1.-DP/CD
XX2=1.-DE/CD
X=2.*((VL)*(SQRT(ZZ1))+(PL)*(SQRT(XX1)))/WAVE
U=2.*((VL)*(SQRT(ZZ2))+(PL)*(SQRT(XX2)))/WAVE
E=(U-X)*W+E
LL=IFIX(E)
IF(POP.LT.0.)GO TO 509
IF(FI.LE.0.)GO TO 509
GO TO 301
509 POP=0.
FI=0.
301 CONTINUE
NN=NN+1
IF(NN.EQ.2)GO TO 53
302 CONTINUE
STOP
801 FORMAT(1X,I5)
77 FORMAT(1X)
1005 FORMAT(1X,5(E9.2),1X,3(I5,1X))
1007 FORMAT(1X,E12.5)
END
```

Figure A1.1(c) Listing of the programme QSWTCH continued

calculations of the Q-switched output is expressed in terms of the cavity decay time TT=DT/TOR. Also calculated is the threshold population inversion PN, given in equation 2.21, after first obtaining a figure for the cavity transit time TRAN. The cavity transit time is in turn a function of the refractive index of the laser medium which is denoted as REFRAC. An approximate value of TRAN is obtained by considering the cavity to be filled with a plasma of density DE equal to 10^{13} particles cm^{-3}, the value chosen for the commencement of the electron decay. This enables the refractive index of the laser medium to be obtained using equation 2.5. Also calculated is the threshold level THRESH of the photon density FI which is the value used to initiate the Q-switching calculations.

With a DO 301 III=2,5001 loop, the variable DP is equated to the plasma density DE, and then the value of DE reduced by an amount previously introduced as DD. From these two quantities the refractive index and thus the optical path length of the cavity for each plasma density, X and U, are obtained. The change in position on the gain profile produced by the reduced electron density is calculated by multiplying the difference in optical path by W, which had previously been set equal to MUL by W=FLOAT(MUL). The variable E is increased by the difference in position on the Lorentzian curve by stating

```
E = (U - X)*W + E
```

E having been set to unity outside the DO 301 loop. The magnitude of the gain curve corresponding to the new plasma density is found by generating an integer variable

```
LL = IFIX(E)
```

which locates the appropriate location on the array AB(LL).

The increase in photon density corresponding to the time lapse between successive calculations is written

```
DF = FI*(POP-GAMA)
```

POP and GAMA being the normalized population inversion and the loss factor expressed in equation 4.1. The photon density can then be found as

```
FI = (FI+DFI*TT)*AB(LL)
```

LL is derived near the end of the DO 301 loop so the statement LL=1 is inserted before the loop for the first calculation of FI. The change of population inversion given by equation 4.2 is obtained from

```
DPOP = -2.*FI*POP+PUMP
```

The normalized pump rate PUMP is expressed in the form discussed in section 4.3 by a pumping fraction PU multiplied by the plasma decay rate. Hence

```
PUMP = ((DE-DD)/TT)*PU/PN
```

The photon density is calculated as

```
POP = POP+DPOP*(TT)-POP*(1.-(EXP(CON)))
```

The quantity POP*(1.-(EXP(CON))) represents the total losses incurred by the population inversion through processes other than stimulated emission, the variable CON having previously been defined in terms of the spontaneous lifetime of the laser transition as shown in the figure.

The loop DO 302 JK=1,2 stipulates that the programme simulates conditions of low continuous pump rate as illustrated in Figure 4.1, or high pump rate controlled by the decaying plasma shown in Figure 4.2. For JK=1, the statement

```
IF(JK.EQ.1) GO TO 602
```

by-passes the expression for the pump rate described above and sets PUMP equal to the nominally low value of one. When JK=2, a further GO TO statement jumps the programme past the 602 PUMP=1. statement.

After the first line of the DO 302 loop, the integer variable NN is equated to 1. After the termination of the DO 301 loop, NN is increased by the statement

```
NN = NN+1
```

When NN=2, the statement

```
IF(NN.EQ.2)GO TO 53
```

returns the computation to the line below the statement NN=1. This loop allows the programme to simulate two conditions, one in which the

laser cavity is resonant at all times, and secondly one in which mode scanning takes place. The statement

```
IF(NN.EQ.1)GO TO 50
```

placed inside the DO 301 loop sets LL=500 when NN=1. This corresponds to a value of AB=1 and the mechanism for varying LL described above is not utilized. However, for NN=2, the LL=500 line is by-passed and the gain profile is scanned.

The statement

```
IF(MM.EQ.500)GO TO 9
```

ensures that the output write statement is only incurred every 500 loops of the DO 301 loop. Having been set to zero before entering the DO loop, the integer variable MM is increased by 1 before the IF statement, and when equal to 500, MM is reset to zero immediately after the write statement.

For an analysis of the Michelson switching arrangement described in section 4.5, a statement is inserted into the programme outside the DO 302 loop setting the variable GAMA to zero. Inside the loop, an IF statement is introduced which equates GAMA to unity when III is greater than a chosen value.

APPENDIX II

Numerical values of the fraction of radiation refracted out of the cavity by the plasma, described in section 4.4, were calculated using programme GAUS written in Fortran IV and listed in Figure A2.1. Parameters describing the laser were entered into the programme as

R = radius of curvature of the mirrors

RO = radius of the mirrors

CD = the 'cut-off' density of the plasma

WAVE = wavelength of the stimulated radiation

X = length of the cavity

CONST = the constant β describing the parabolic radial distribution of the electron density

The square of the beam radius expressed in equation 2.4 is represented as W2 and calculated in statements 8 to 11. This parameter is then used in lines 12 to 14 to obtain the power of a non-refracted beam, VTOT, as described in the text by setting $r = r_0$ in equation 4.4.

Calculation of the refracted energy is performed inside two nested loops. The outer loop varies the plasma length PL in multiples of 50 cm while the inner loop adjusts the electron density, D. The terms αL and $-\alpha L$ are then calculated as CC and DD respectively and used to obtain the matrix elements

COH $\equiv \alpha_{11} = \alpha_{22}$

SIH $\equiv \alpha_{21}$

A12 $\equiv \alpha_{12}$

The parameter r_1 in equation 4.5 is then calculated as RR and used in equation 4.4 to obtain the unrefracted power, VINT, in the cavity after one transit. The fractional loss is then calculated from the ratio

RAT = VINT/VTOT

as

F = 1.-RAT

```
      PROGRAM GAUS(INPUT,OUTPUT,TAPE1=INPUT,TAPE2=OUTPUT)
      DIMENSION F(5),D(5)
      NIN=1
      NOUT=2
      PI=3.1415926535898
      R=750.0
      CD=0.984E+16
      WAVE=0.0337
      X=750.0
      RO=3.8
      A=R*WAVE/PI
      B=1.0/(2.0*R/X-1.0)
      B=SQRT(B)
      W2=A*B
      Z=-2.0*RO*RO/W2
      VTOT=1.0-EXP(Z)
      DO 10 J=1,3
      U=FLOAT(J)
      CONST=0.25*U
      WRITE(NOUT,400)CONST
      BBB=CONST/(CD*RO*RO)
      DO 40 I=1,15
      W=FLOAT(I)
      PL=50.0*W
      VL=X-PL
      WRITE(NOUT,300)PL
      WRITE(NOUT,77)
      WRITE(NOUT,200)
      WRITE(NOUT,77)
      DO 30 II=7,15
      DO 20 K=1,5
      H=FLOAT(K)
      D(K)=2.0*H*10.0**II
      BB=BBB*D(K)
      B=SQRT(BB)
      CC=B*PL
      DD=-CC
      COH=0.5*(EXP(CC)+EXP(DD))
      SIH=0.5*(EXP(CC)-EXP(DD))
      A12=SIH/B
      A21=B*SIH
      RR=RO/((COH-A12/R)+VL*(A21-COH/R))
      Z=-2.0*RR*RR/W2
      VINT=1.0-EXP(Z)
      RAT=VINT/VTOT
      F(K)=1.0-RAT
   20 CONTINUE
      WRITE(NOUT,100)(D(L),F(L),L=1.5)
   30 CONTINUE
   40 CONTINUE
   10 CONTINUE
      STOP
   77 FORMAT(1X)
  100 FORMAT(1X,5(E8.1,1X,E10.3))
  200 FORMAT(4X,5(1HD,9X,1HF,9X))
  300 FORMAT(1X,3HPL=,F5.1)
  400 FORMAT(1X,6HCONST=,F5.2)
      END
```

Figure A2.1. Listing of the programme GAUS

APPENDIX III

The power supply used to pulse-ionise the gas discharge lasers is the 10 MW Blumlein modulator supply shown in Figure A3.1. Three phase, 50 Hz power is delivered from a Variac to a high voltage (10 kV) transformer. The output from the transformer is rectified and then smoothed by a L-C circuit and fed to the anode of a series diode through a charging choke. The EHT line then charges a number of capacitors which form part of a L-C network of characteristic impedance Z_0, the common side of the capacitors being connected to earth. The output from the network is then fed to a second network, also of impedance Z_0, the common capacitor terminal of which is taken to the load. The capacitors of the second network are then charged to the d.c. EHT potential, the load forming the path to ground. An output pulse is initiated by ionising the gas in a thyratron from a separate pulse generator which, connected to the input of the first network, shorts the input to ground. This puts the two networks in series so that twice the charging voltage appears across the load during their discharge. In this way 20 kV pulses are produced from the 10 kV d.c. supply across a matched resistive load of $2Z_0$ = 40 ohms. Because the charging choke prevents a rapid recharging, the input to the first network falls to a low potential causing the ionisation in the thyratron to cease. Across a matched resistive load, square output pulses of 40 μs duration are produced, as shown in the example of Figure A3.2. This is followed by a second pulse of opposite polarity due to the second network being charged through the load. When exciting a laser, the unmatched conditions cause a series of diminishing recharging pulses to occur.

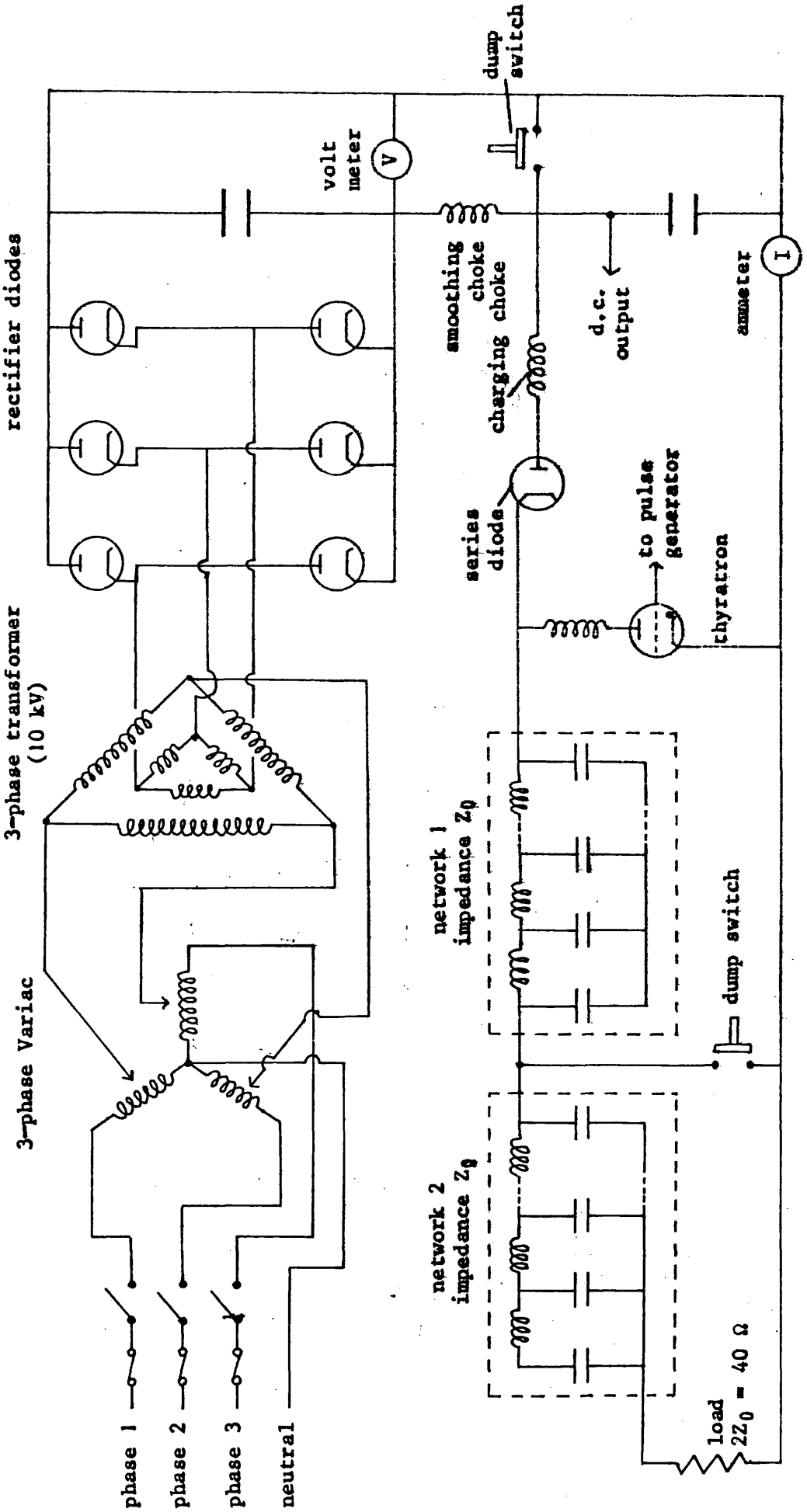

Figure A3.1. Simplified circuit diagram of the 10 MW Blumlein modulator power supply

horizontal scale, 10 μs per large division

Figure A3.2. Current pulse delivered by the Blumlein modulator supply into a 40 Ω load

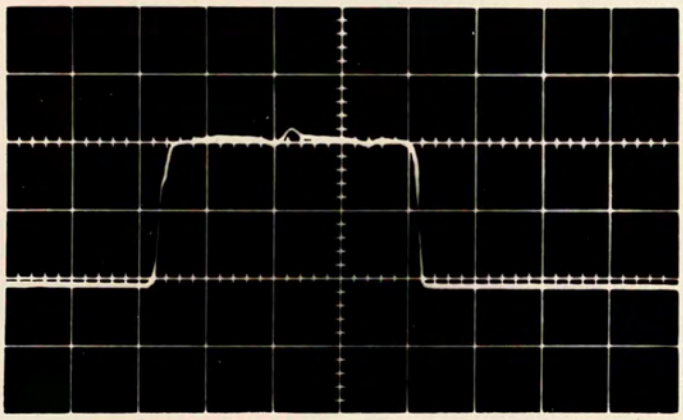

APPENDIX IV

Following the method of Simmons[136], equations for tunnel and thermionic currents are arranged such that current density is expressed in amperes per square centimetre, potential barrier heights and bias potential in MKS volts, and distances in Ångström units. Using the conversions described in reference 136, equation 7.8 for tunnel current density becomes

$$J_1 = J_0\{\bar{\phi}_1 \exp(-1.025.\Delta S.\phi_1^{-\frac{1}{2}}) - (\bar{\phi}_1+V)\exp\left[-1.025.\Delta S(\bar{\phi}_1+V)^{\frac{1}{2}}\right]\} \quad \ldots(A4.1)$$

equation 7.9 becomes

$$\bar{\phi}_1 = \phi_1 + \left[\frac{S_1+S_2}{2S}\right]\left[\Delta\Psi-V\right] - \left[\frac{5.75}{K.\Delta S}\right]\log_e\left[\frac{S_2(S-S_1)}{S_1(S-S_2)}\right] \quad \ldots(A4.2)$$

equation 7.10 becomes

$$S_1 = \left(9.2\left[\frac{5.75}{1.15K}\right]\left[3\phi_1 + \frac{20}{KS} - (V-\Delta\Psi)\right]^{-1}\right) - \frac{6}{K\{\phi_2-\Delta\Psi\}} \quad \ldots(A4.3)$$

and

$$S_2 = S - \left\{\frac{6}{K}\right\}\{\phi_2-V\}^{-1} \quad \ldots(A4.4)$$

By the same process, the density of the tunnel current for the opposite bias condition expressed in equation 7.12 becomes

$$J_2 = J_0\{\bar{\phi}_2 \exp(-1.025.\Delta S.\phi_2^{-\frac{1}{2}}) - (\bar{\phi}_2+V)\exp\left[-1.025.\Delta S(\bar{\phi}_2+V)^{\frac{1}{2}}\right]\} \quad \ldots(A4.5)$$

where equation 7.13 becomes

$$\bar{\phi}_2 = \phi_2 + \left[\frac{S_1+S_2}{2S}\right]\left[\Delta\Psi+V\right] - \left[\frac{5.75}{K.\Delta S}\right]\log_e\left[\frac{S_2(S-S_1)}{S_1(S-S_2)}\right] \quad \ldots(A4.6)$$

equation 7.14 becoming

$$S_1 = \frac{6}{K\phi_2} \quad \ldots(A4.7)$$

and equation 7.15 becomes

$$S_2 = S - \left(\frac{46}{K}\right)\left(3\phi_2 + \frac{20}{KS} - 2(V+\Delta\Psi)\right)^{-1} + S_1 \quad \ldots(A4.8)$$

For both bias conditions J_0 is expressed as

$$J_0 = 6.2 \times 10^{10}.\ (\Delta S)^{-2} \quad \ldots(A4.9)$$

ΔS being a function of S_1 and S_2 which in turn are expressed for the appropriate sense of bias.

Units of amperes per square centimetre, MKS volts and angstroms can be used in equations 7.16 and 7.17 for thermionic emission by making the conversion

$$eV \rightarrow V$$

and substituting $AT^2 = 10.8 \times 10^6$ and $kT = 0.025$ for a temperature of $T = 300^{o}K$.

A computer programme, written in Fortran IV, is described to numerically calculate the integrals expressed in equation 7.19 using the above equations for J_1 and J_2. The parameters in the current equations will be represented in the programme by the following symbols:-

RR = radius of the hemispherical whisker tip, A

S = distance between plain electrode and the closest point of the whisker tip

U = V

PHI = $\Delta\Psi$

P = K

AT2 = AT^2

D = thickness of the dielectric layer, d

Z1 = ϕ_1

Z2 = ϕ_2

U and RR are declared as arrays by the dimension statement in line two of the programme, and three values for each parameter are entered in data statements. Values for PHI, AT2, Z1, P and D are entered on individual lines and the potential barrier at the interface of the second electrode is calculated by declaring

```
Z2 = Z1 + PHI
```

Variation of the hemispherical tip radius, the applied bias and the dielectric spacing is performed by three nested DO loops as:

```
                .
                .
                .
DO 90    II=1,3
A=RR(II)
                .
                .
                .
DO 5      M=1,3
                .
                .
                .
V=U(M)
                .
                .
                .
DO 2      J=1,10
S(J)=10.*(FLOAT(J))
                .
                .
                .
```

The current integrals are evaluated by dividing the surface area of the hemisphere into flat annuli centred about the line YY′ of Figure 7.5 and parallel to the plain electrode, and then summating the current flow through each ring. The incremental increase in the radius of each ring is made a one-thousandth part of the integration limit, equation 7.20, and is introduced after calculation of S(J) as

```
RADIUS = (SQRT(2.0*A*(D-S(J))-(D-S(J))**2))/1000.0
```

By declaring the next statement as

```
DR = 2.0*3.1416*RADIUS
```

the area of each annulus is seen to be

```
DR*R(I)
```

in which R(I) is the radius of the ring. This radius is calculated in a central DO loop as

```
DO 1 I=1,1000
  R(I)=RADIUS*(FLOAT(I))
```

The thermionic and tunnel contributions to the current flow through each ring are found within this loop having first calculated the distance

of each annulus from the opposite electrode in the next statement as

SS=A+S(J)-SQRT(A*A-R(I)*R(I))

Figures A4.1(a) and (b) show the listing of the computer programme in which equations A4.1 to A4.9 are written in Fortran notation. For the case when negative bias is applied to the electrode of lower work function

S11 = S_1 of equation A4.3

S12 = S_2 of equation A4.4

DS1 = ΔS for this sense of bias

G1 = argument of the natural logarithm appearing in equation A4.2

PI1 = $\bar{\phi}_1$ of equation A4.2

CON1 = argument of the first logarithm in equation A4.1

CCC1 = argument of the second logarithm in equation A4.1

ZERO1 = J_0 of equation A4.9 for ΔS represented by DS1

Similarly, for negative bias applied to the electrode of higher work function

S21 = S_1 of equation A4.7

S22 = S_2 of equation A4.8

DS2 = ΔS for this sense of bias

G2 = argument of the natural logarithm appearing in equation A4.6

PI2 = $\bar{\phi}_2$ of equation A4.6

CON2 = argument of the first logarithm in equation A4.5

CCC2 = argument of the second logarithm in equation A4.5

ZERO2 = J_0 of equation A4.9 for ΔS represented by DS2

CUR1 and CUR2 represent the tunnel current flow through the annulus for each sense of applied bias by calculating the current densities J_1 and J_2 of equations A4.1 and A4.5 respectively and multiplying by the area of the ring DR*R(I).

Computation of the thermionic currents by representing

```
PROGRAM DETECR(INPUT,OUTPUT,TAPE1=INPUT,TAPE3=OUTPUT)
DIMENSION U(3),W(5),S(100),R(1000),RR(3),DD(2)
DATA U/0.9,0.5,0.09/
DATA W/0.1,0.25,0.5,0.75,1.0/
DATA RR/1000000.,10000.,100./
DATA DD/101.,10101./
AT2=10.8E+06
Z1=1.0
P=8.
DO 90 II=1,3
A=RR(II)
WRITE(3,85)A
WRITE(3,77)
DO 4 L=1,5
PHI=W(L)
WRITE(3,80)PHI
Z2=Z1+PHI
ARG1=-Z2*40.
DO 5 M=1,3
V=U(M)
CONST=-V*40.
ARG3=(V-Z2)*40.
WRITE(3,70)V
WRITE(3,77)
WRITE(3,20)
WRITE(3,77)
DO 2 MM=1,5
J=MM*20
S(J)=FLOAT(J)
DO 33 KK=1,2
D=DD(KK)
RADIUS=(SQRT(2.0*A*(D-S(J))-(D-S(J))**2))/1000.0
DR=2.0*3.1416*RADIUS
SUM1=0.0
SUM2=0.0
THERM1=0.0
THERM2=0.0
DO 1 I=1,1000
R(I)=RADIUS*(FLOAT(I))
SS=A+S(J)-SQRT(A*A-R(I)*R(I))
S21=6./(P*Z2)
S22=SS-(46./P)/(3.*Z2+20./(P*SS)-2.0*(V+PHI))+S21
DS2=S22-S21
G2=S22*(SS-S21)/(S21*(SS-S22))
PI2=Z2-((S21+S22)/(2.*SS))*(V+PHI)-(5.75/(P*DS2))*(ALOG(G2))
CCC2=-1.025*(S22-S21)*(SQRT(PI2+V))
CON2=-1.025*(S22-S21)*(SQRT(PI2))
ZERO2=(6.2E+10)/(DS2*DS2)
CUR2=(PI2*(EXP(CON2))-(PI2+V)*(EXP(CCC2)))*DR*R(I)
CUR2=CUR2*ZERO2
S11=(46./P)/(3.*Z1+(20./(P*SS)-(V-PHI)))-(6./P)/(Z2-PHI)
S12=SS-(6./P)/(Z2-V)
DS1=S12-S11
G1=S12*(SS-S11)/(S11*(SS-S12))
PI1=Z1+(S11+S12)*(PHI-V)/(2.*SS)-(5.75/(P*DS1))*(ALOG(G1))
CON1=-1.025*(S12-S11)*(SQRT(PI1))
```

Figure A4.1(a). Listing of programme DETECR

```
      CCC1=-1.025*(S12-S11)*(SQRT(PI1+V))
      ZERO1=(6.2E+10)/(DS1*DS1)
      CUR1=(PI1*(EXP(CON1))-(PI1+V)*(EXP(CCC1)))*DR*R(I)
      CUR1=CUR1*ZERO1
      SUM1=SUM1+CUR1
      SUM2=SUM2+CUR2
      ARG2=SQRT(14.4*(V+PHI)*1600.0/(P*SS))
      ARG4=(SQRT(14.4*(7.+P*SS*(PHI-V))))*40./(P*SS)
      TOTAL1=EXP(ARG4)*DR*R(I)
      TOTAL2=EXP(ARG2)*DR*R(I)
      RUNTH1=RUNTH1+TOTAL1
      RUNTH2=RUNTH2+TOTAL2
    1 CONTINUE
      RATIO1=(EXP(CONST))*RUNTH2/RUNTH1
      RATIO2=SUM2/SUM1
      CURTH1=AT2*(EXP(ARG3))*RUNTH1
      CURTH2=AT2*(EXP(ARG1))*RUNTH2
      SUM2=SUM2/1.E+16
      SUM1=SUM1/1.E+16
      CURTH2=CURTH2/1.E+16
      CURTH1=CURTH1/1.E+16
      TOT2=CURTH2+SUM2
      TOT1=CURTH1+SUM1
      RATIO3=TOT2/TOT1
      WRITE(3,100)J,RATIO2,RATIO1,RATIO3,SUM2,SUM1,CURTH2,CURTH1,TOT2,
     CTOT1
      R1=V*(1.0/CURTH2+1.0/CURTH1)/2.
      R2=V*(1.0/SUM2+1.0/SUM1)/2.
      R3=V*(1.0/TOT2+1.0/TOT1)/2.
      GAMA1=((RATIO1-1.)/(2.*V))*R1
      GAMA2=((RATIO2-1.)/(2.*V))*R2
      GAMA3=((RATIO3-1.)/(2.*V))*R3
      WRITE(3,105)GAMA2,GAMA1,GAMA3
      WRITE(3,77)
   33 CONTINUE
    2 CONTINUE
    5 CONTINUE
    4 CONTINUE
      WRITE(3,88)
   90 CONTINUE
      STOP
  100 FORMAT(1X,I2,1X,9(E11.4,1X))
   70 FORMAT(1X,2HV=,E12.5)
   80 FORMAT(1X,4HPHI=,E12.5)
   20 FORMAT(2X,1HS,6X,6HRATTUN,6X,6HRATTHM,6X,6HRATCOM,5X,7HTUNNEL2,5X,
     C7HTUNNEL1,4X,8HTHERMAL2,4X,8HTHERMAL1,4X,8HCOMBINE2,4X,8HCOMBINE1)
   77 FORMAT(1X)
  105 FORMAT(4X,3(E11.4,1X))
   85 FORMAT(1X,2HA=,F9.1)
   88 FORMAT(1H1)
      END
```

Figure A4.1(b). Listing of programme DETECR continued

$$\left[\frac{14.4(eV - \Delta\Psi)}{KSkT}\right]^{\frac{1}{2}}$$ of equation 7.17

and

$$\left[\frac{14.4(7 + KS\{\Delta\Psi - eV\})}{KSkT}\right]^{\frac{1}{2}}$$ of equation 7.16

by `ARG2=SQRT(14.4*(V+PHI)*1600.0/(P*SS))`

and `ARG4=SQRT(14.4*(7.+P*SS*(PHI-V)))*40./(P*SS)`

respectively enables quantities proportional to the current flow to be found by

```
TOTAL1=EXP(ARG4)*DR*R(I)
```

and `TOTAL2=EXP(ARG2)*DR*R(I)`

Summation of the values of the current flow through each ring is performed by setting

```
SUM1=0.
SUM2=0.
THERM1=0.
THERM2=0.
```

before the commencement of the central DO loop, and then before the termination of the loop stating

```
SUM1=SUM1+CUR1
```

and `SUM2=SUM2+CUR2`

for the tunnel currents and

```
THERM1=THERM1+TOTAL1
```

and `THERM2=THERM2+TOTAL2`

for the thermionic contribution. The full values of the thermal currents are calculated after the central loop by the statements

```
CURTH1=AT2*(EXP(ARG3))*THERM1
CURTH2=AT2*(EXP(ARG1))*THERM2
```

ARG1 represents $-\phi_2/_{kT}$ in equation 7.17 by

ARG1=-Z2*40.

and is entered before the outer loop, and

$$\frac{eV - \phi_2}{kT}$$

in equation 7.16 is calculated inside the second loop as

ARG3=(V-Z2)*40.

Outside the central loop, the current ratios are calculated for each of the tunnel and thermionic processes and for the combined case in which the constituent currents of the two effects are added together as TOT2 and TOT1. By calculating the average resistance for each of the three cases R1,R2,R3, three corresponding responsivities are found using equation 7.5 as GAMA1, GAMA2 and GAMA3.

Accuracy of Numerical Technique

Numerical evaluation of the integrals constituting equation 7.19 gave the current flow from the portion of the hemispherical whisker tip embedded in the oxide. The restriction was imposed to avoid the necessity to take into account any effects introduced by a dielectric-dielectric interface between the electrodes. By using a lower value of dielectric constant, K=3, in the programme, the calculations displayed in Figure A4.2 are obtained and, when compared with Figure 7.7, show γ to have only a minor dependence on K. In order to obtain an estimate of the error caused by terminating the summation at the oxide surface, the programme was re-run with the oxide thickness increased by 10,000 Å. The values of responsivity obtained were compared with those calculated previously and, for conditions in which the tunnel currents dominate, were found to differ only in the fourth significant figure. This close agreement is seen to be due to a rapid decrease in tunnel current with increased electrode spacing. Placing a WRITE statement for SUM1 and SUM2 inside the central loop of the programme showed the summation of the current through the incremental rings to approach an asymptotic value before reaching the oxide surface. An example is shown in Figure A4.3(a) for K=8, ϕ_1=1, $\Delta\Psi$=1, A=10^4 and V=0.9 at a minimum spacing of S=60 Å. However, plotting the monotonically increasing values of RUNTH1 and RUNTH2 in Figure A4.3(b) for the same conditions, showed that for the thin oxide the dominant thermionic current RUNTH1 does not attain its full value. The error thus introduced into the calculation

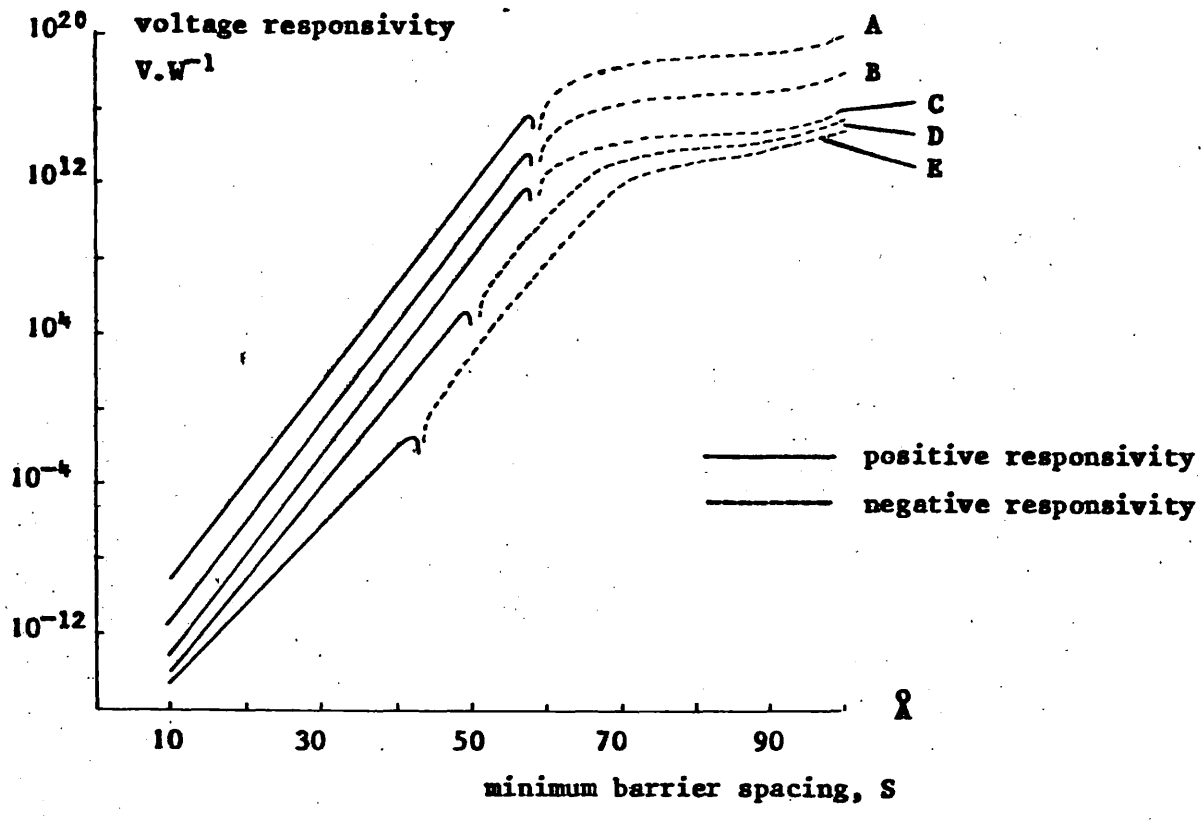

Figure A4.2. Theoretical voltage responsivity of a M-O-M point-contact diode detector against minimum barrier spacing. K=3, ϕ_1=1 eV, ϕ_2=2 eV

Curve	A	B	C	D	E
V_B(V)	0.09	0.09	0.09	0.5	0.9
A_w(Å)	10^2	10^4	10^6	10^6	10^6

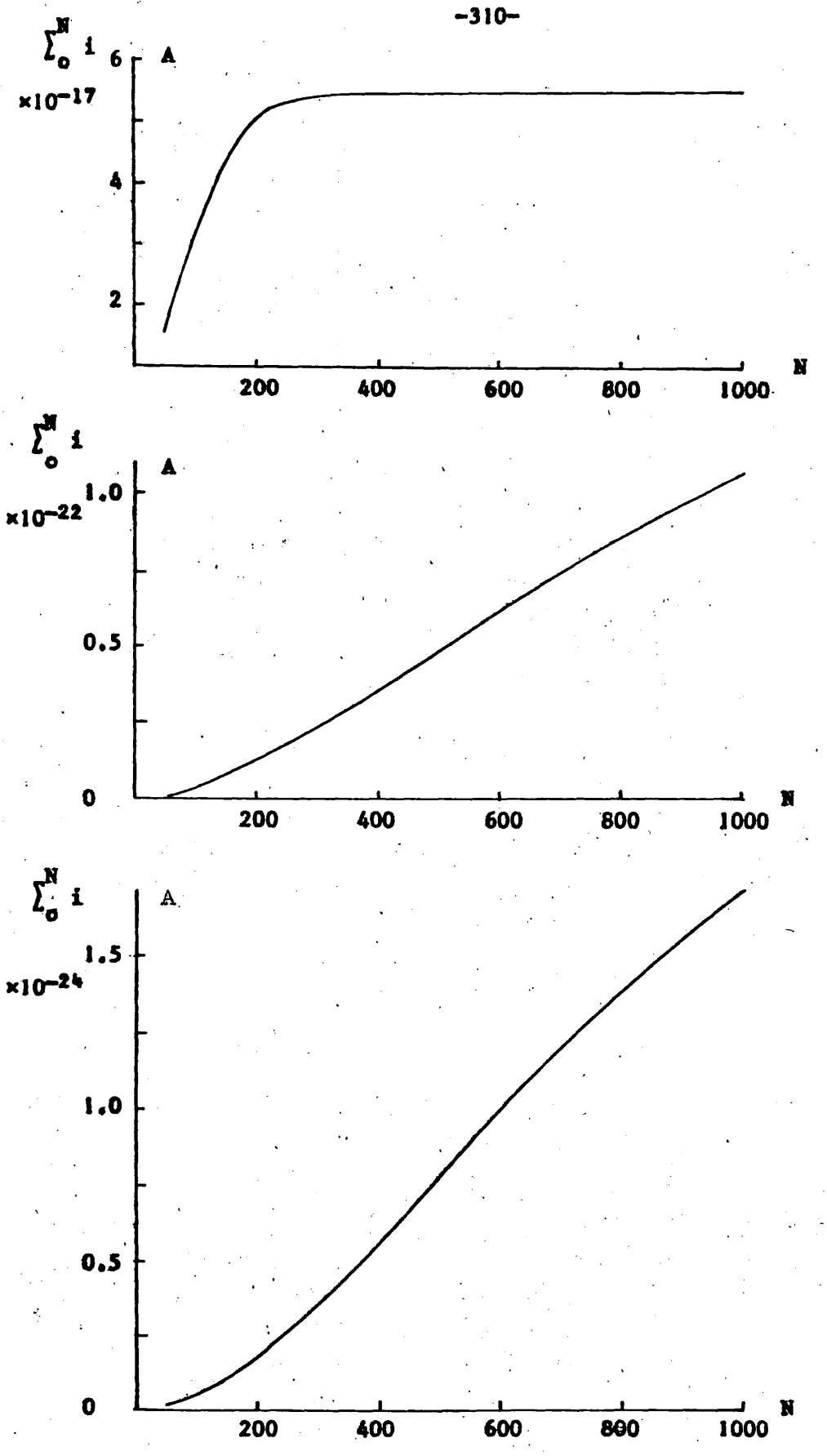

Figure A4.3. Summation of the current $\sum_0^N i$ against the annuli number N for (a) the tunnel currents and (b) and (c) the thermal contribution of RUNTH1 and RUNTH2 respectively, and appropriately scaled. S=60 Å, ϕ_1=1 eV, ϕ_2=2 eV, K=8, $A_w=10^4$ Å, V_B=0.09V.

of responsivity in the thermally dominated region is demonstrated in Figure A4.4 by plotting responsivity for both thicknesses of oxide against S. The divergence of the two curves becomes greater at larger S, as an increased proportion of the conduction is expected to occur above the oxide.

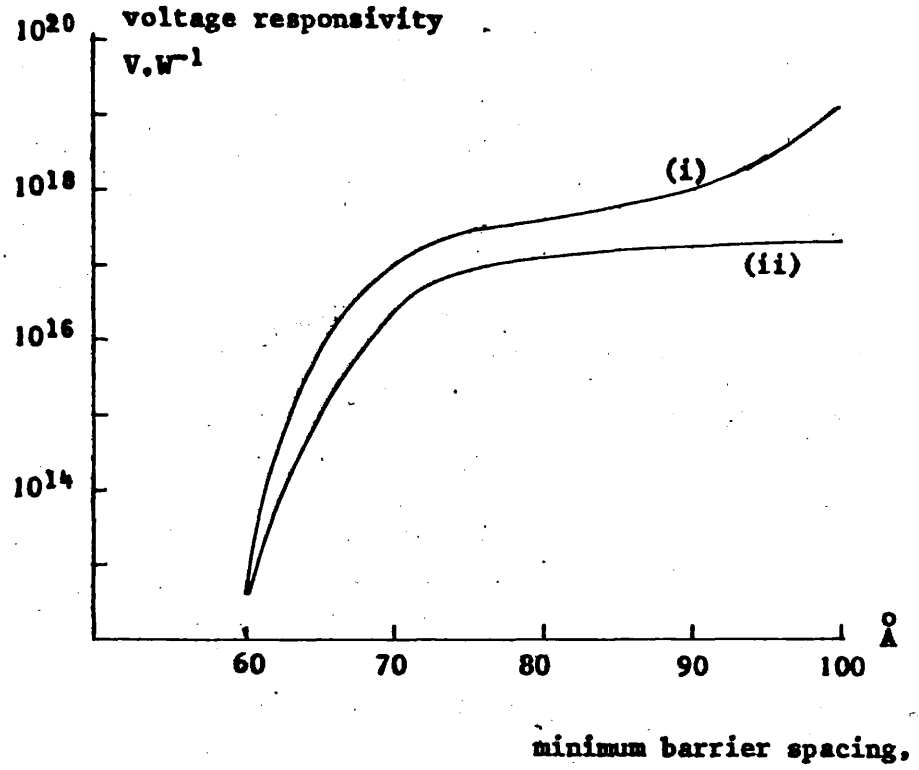

Figure A4.4. Comparison of calculated voltage responsivity of a M-O-M diode detector against minimum barrier spacing for oxide thicknesses of (i) 101 Å and (ii) 10101 Å. ϕ_1 = 1 eV, ϕ_2 = 2 eV, K = 8, A_w = 10^4 Å and V_B = 0.9V.

APPENDIX V

Data from the transmission experiments of section 10.4 were used in Programme ABSORB to calculate the reflection and attenuation coefficients and the refractive index of the various iron garnets. In the Fortran IV programme listed in Figure A5.1, each garnet would be assigned a number N which is entered into the file from a data card by the first read statement and then written on the output for identification. A calibration factor CAL, the ratio of the monitor signal to the non-attenuated signal from the cryostat, and the thickness in millimetres of the two garnet specimens X1, X2, were entered by the next two read statements. The measured signals from the monitor and from the cryostat containing the crystal of thickness X1 would then be entered as A1 and B1. At this point, two IF statements were inserted. If A1 was to be given a value of 0.2, the programme would go to the statement labelled 200, a further value of N would be read and evaluation of a second garnet type would commence. For a value of 0.3 for A1, the programme would be terminated by jumping to the STOP statement labelled 300. 0.2 and 0.3 were chosen because signal values were not recorded at these levels. The crystal and monitor signals corresponding to the garnet of thickness X2 were then entered by a read statement as A2 and B2.

The transmission through each crystal T1 and T2 was obtained by dividing the signal from the cryostat by the appropriate monitor signal and dividing by CAL. The attenuation constant ALFA was obtained from T2, T1, X2 and X1 as indicated by equation 10.2. Rearrangement of equation 10.1 now eanbles the reflection coefficient to be calculated for each sample as R1 and R2. Following equation 10.3, a value of refractive index is calculated from each reflectivity as REFR1 and REFR2. However, two IF statements by-pass the refractive index calculations if R1 and R2 are less than zero due to inaccurate data. After writing out ALFA, R1, R2, REFR1 and REFR2, a GO TO statement moves the programme back to the READ A1,B1 statement.

```
      PROGRAM ABSORB(INPUT,OUTPUT,TAPE1=INPUT,TAPE3=OUTPUT)
  200 READ(1,40)N
      WRITE(3,80)N
      READ(1,10)CAL
      READ(1,20)X1,X2
      X1=X1/10.
      X2=X2/10.
  100 READ(1,30)A1,B1
      IF(A1.EQ.0.2)GO TO 200
      IF(A1.EQ.0.3)GO TO 300
      READ(1,30)A2,B2
      T1=(A1/B1)/CAL
      T2=(A2/B2)/CAL
      Z=T2/T1
      ALFA=(ALOG(Z))/(X1-X2)
      Q1=-X1*ALFA
      Q2=-X2*ALFA
      P1=T1/EXP(Q1)
      P2=T2/EXP(Q2)
      P1=SQRT(P1)
      P2=SQRT(P2)
      R1=1.0-P1
      R2=1.0-P2
      IF(R1.LT.0.0)GO TO 2
      IF(R2.LT.0.0)GO TO 2
      REFR1=(SQRT(R1)+1.)/(1.-SQRT(R1))
      REFR2=(SQRT(R2)+1.)/(1.-SQRT(R2))
      GO TO 1
    2 REFR1=0.0
      REFR2=0.0
      WRITE(3,90)ALFA,R1,R2,REFR1,REFR2
      GO TO 100
  300 STOP
   70 FORMAT(1X)
   40 FORMAT(I2)
   80 FORMAT(1X,2HN=,I2)
   10 FORMAT(F5.3)
   20 FORMAT(F7.5,2X,F7.5)
   30 FORMAT(2(F4.1,2X))
   90 FORMAT(1X,E10.3,2X,F7.3,1X,F7.3,2X,F7.3,1X,F7.3)
      END
```

Figure A5.1. Listing of programme ABSORB

APPENDIX VI

Calculation of Faraday rotation from the susceptibility elements given in Figure 8.4 was carried out using the programme RIG which was written in Fortran IV and is listed in Figures A6.1(a) and A6.1(b). For each temperature, defined by the magnetisation of the two sublattices, values of rotation are obtained corresponding to five different values of the relaxation time of the rare-earth ion.

The programme commences with a dimension statement declaring the relaxation time of the rare-earth sublattice, TT, as a 1 × 5 array. Physical parameters necessary for the calculation are entered into the file from data cards by a series of read statements and are itemized as

REIG ≡ a number identifying the garnet type

G1,G2 ≡ the 'g factors' of the iron and rare-earth sublattices respectively

RHO ≡ the density of the material

H ≡ the laboratory magnetic field in oersteds, applied to the garnet

WW ≡ the molecular field constant

TTT ≡ the relaxation time of the iron sublattice

TT(1→5) ≡ five separate values for the relaxation time of the rare-earth sublattice

UU ≡ the refractive index of the garnet

TMW ≡ twice the molecular weight of the garnet

After writing the above constants, the gyromagnetic ratios Y1 and Y2 are calculated from their respective g factors and the angular frequency corresponding to 891 GHz is expressed as W3.

The values of the saturated magnetisation of the two ions are entered into the file by a read statement from a data card as Z4 and Z5. Expressed in Bohr magnetons per two formula units, the two parameters are converted to oersteds and labelled Z1 and Z2 respectively. Data cards for Z4 and Z5 are supplied giving values of magnetisation corresponding to $5^{o}C$ intervals of temperature. After the required computation, a GO TO statement would return the programme to the

```
      PROGRAM RIG  (INPUT,OUTPUT,TAPE1=INPUT,TAPE3=OUTPUT)
      DIMENSION G(2),TT(5),YY(2)
  500 READ(1,75)REIG
      READ(1,80)DEMZ
      READ(1,60)G(1),G(2)
      READ(1,10)RHO
      READ(1,20)H
      READ(1,20)WW
      READ(1,40)TTT
      READ(1,45)TT(1),TT(2),TT(3),TT(4),TT(5)
      READ(1,10)UU
      READ(1,20)TMW
      WRITE(3,70)
      WRITE(3,70)
      WRITE(3,70)
      WRITE(3,85)REIG
      WRITE(3,95)G(1),G(2),RHO,H,WW,TMW,UU
      Y1=-1.76*10.0**7/2.0*G(1)
      Y2=-1.76*10.0**7/2.0*G(2)
      W3=2.0*3.1416*891.0*10.0**9
  200 READ(1,30)Z4,Z5
      WRITE(3,70)
      IF (Z5.EQ.0.0)GO TO 500
      IF(Z4.EQ.0.0)GO TO 100
      Z1=5587.0*RHO*Z4/TMW
      Z2=5587.0*RHO*Z5/TMW
      A1=Y1(Z1*TTT*W3)
      I=1
  300 A2=Y2/(Z2*TT(I)*W3)
      S1=Z1/Y1
      S2=Z2/Y2
      W2=WW*(Y2*Z1+Y1*Z2)
      Z3=Z1+Z2
      N=1
      YY(1)=Y1*Y2*Z3/(Y2*Z1+Y1*Z2)
  600 W4=YY(N)*Z3
      W1=YY(N)*H
      V=(W3**2-W2*(W3+W1))*(W3**2+W2*(W3-W1))
      B=S1*S2/(S1+S2)
      C=((S1**2)*A1+(S2**2)*A2)/(S1*S2)
      E=(W3**2)*(Y1*Z1+Y2*Z2)
      F=(A1*S1**2+A2*S2**2)
      T=(A1+A2)*W3**2
      U=(A1*Z1**2+A2*Z2**2)*W3**2
      P=A1*Y2+A2*Y1
      Q=Z1*Y1**2+Z2*Y2**2
      R=A1/Y1+A2/Y2
      D=V+(4.0*(W3**2)*(W2**2)*(B**2)*(W2*W1*C-T)**2)/V
      X1=(W3*(Z3*YY(N)*(W2**2)-E)+4.0*(W3**3)*(W2**2)*Z3*P*(B**2)*(W2*W1
     C*C-T)/V)/D
      X2=((W2**2)*(YY(N)**2)*Z3*H-(W3**2)*H*Q+2.0*(W3**2)*W2*B*(W2*W1*C-
     CT)*((W3**2)*(YY(N)**2)*F-U)/V)/D
      X3=-(2.0*(W3**2)*R*YY(N)*W2*Z1*Z2+2.0*(W3**2)*W2*B*(W2*W1*C-T)*(YY
     C(N)*(W2**2)*Z3-E)/V)/D
      X4=-(W3*(W2**2)*(YY(N)**2)*F-W3*U-2.0*W3*(W2**3)*B*W1*W4*(W2*W1*C-
     CT)/V)D
      PSI1=(1.0+4.0*3.1416*(X2-X1))**2
```

Figure A6.1(a). Listing of programme RIG

```
      PSI2=(1.0+4.0*3.1416*(X2+X1))**2
      PSI3=(4.0*3.1416*(X4-X3))**2
      PSI4=(4.0*3.1416*(X4+X3))**2
      PSI5=1.0+4.0*3.1416*(X2-X1)
      PSI6=1.0+4.0*3.1416*(X2+X1)
      ZETA=W3*UU/(3.0E+10)
      BETA2=ZETA/1.414*SQRT(SQRT(PSI2+PSI4)+PSI6)
      BETA1=ZETA/1.414*SQRT(SQRT(PSI1+PSI3)+PSI5)
      GAMMA1=ZETA/1.414*SQRT(SQRT(PSI1+PSI3)-PSI5)
      GAMMA2=ZETA/1.414*SQRT(SQRT(PSI2+PSI4)-PSI6)
      THETA=(BETA1-BETA2)/2.0
      DICRO=(GAMMA1-GAMMA2)/2.0
      WRITE(3,50)X1,X2,X3,X4,THETA,DICRO,Z5,I,N
      IF (I.EQ.5)GO TO 700
      I=I+1
      GO TO 300
  700 CONTINUE
      THETAF=UU*YY(1)*(W3**2)*2.0*3.1416*Z3/(3.0*(10.0**10)*(W1**2-W3**2
     C))
      THETAE=UU*(Y1*Z1+Y2*Z2)/(6.0*(10.0**10))
      THETAI=UU*((W2**2)*YY(1)*Z3-(W3**2)*(Y1*Z1+Y2*Z2))/(6.0*(10.0**10)
     C*(W2**2-W3**2))
      WRITE(3,65)THETAF,THETAE,THETAI
      WRITE(3,25)YY(1),YY(2)
      GO TO 200
  100 CONTINUE
      STOP
   10 FORMAT(F4.2)
   20 FORMAT(F6.1)
   25 FORMAT(1X,6HYY(1)=,E12.5,10X,6HYY(2)=,E12.5)
   30 FORMAT(F6.2,2X,F6.2)
   40 FORMAT(E9.2)
   45 FORMAT(E9.2,2X,E9.2,2X,E9.2,2X,E9.2,2X,E9.2)
   50 FORMAT(1X,3HX1=,E12.5,2X,3HX2=,E12.5,2X,3HX3=,E12.5,2X,3HX4=,E12.5
     C,2X,6HTHETA=,E12.5,2X,6HDICRO=,E12.5,2X,3HZ5=,F12.5,2X,2HI=,I1,2X,
     C2HN=,I1)
   55 FORMAT(E12.5)
   60 FORMAT(F4.2,2X,F4.2)
   65 FORMAT(1X,7HTHETAF=,E12.5,2X,7HTHETAE=,E12.5,2X,7HTHETA=,E12.5)
   70 FORMAT(1X)
   75 FORMAT(F3.1)
   80 FORMAT(F3.1)
   85 FORMAT(1X,5HREIG=,F3.1)
   95 FORMAT(1X,5HG(1)=,F4.2,2X,5HG(2)=,F4.2,2X,4HRHO=,F4.2,2X,2HH=,F7.1
     C,2X,3HWW=,F7.1,2X,4HTMW=,F7.1,2X,3HUU=,F4.2
      END
```

Figure A6.1(b). Listing of programme RIG continued

```
200 READ(1,30)Z4,Z5
```

line for evaluation using the next pair of magnetisation parameters. By entering either Z4 or Z5 as zero, IF functions respectively terminate the programme by jumping to the STOP function, or return to the beginning and read in parameters for another garnet.

After calculating the damping factor of the iron sublattice as A1, an integer I=1 is declared and then the damping factor of the rare-earth ions is expressed as A2. A2 is written in terms of TT(I) and given the statement label 300. This line commences the central loop of the programme which is returned by a GO TO 300 command. Before the GO TO statement, the line I=I+1 causes the calculations to be performed for each value of TT. After the fifth parameter has been inserted into the computations, the programme is taken out of the loop by the line

```
IF(I.EQ.5)GO TO 700
```

Inside this central loop, groups of parameters which recur in the equations of Figure 8.4 are equated to individual variables and used to calculate X1,X2,X3 and X4 which respectively represent the components of the susceptibility tensor χ'_{xy}, χ'_{xx}, χ''_{xy} and χ''_{xx}. Equations 8.28 and 8.9 enable a relationship between the elements of the susceptibility tensor and the permeabilities of the rotational modes to be obtained as

$$\mu'_{\pm} = 1 + 4\pi\{\chi'_{xx} \mp \chi'_{xy}\}$$

and

$$\mu''_{\pm} = 4\pi\{\chi''_{xx} \mp \chi''_{xy}\}$$

so that

$$\alpha^{\pm} = \frac{\omega}{c}\left[\frac{\varepsilon}{2}\right]^{\frac{1}{2}}\left[\left(\left\{1+4\pi(\chi'_{xx}\mp\chi'_{xy})\right\}^2+\left\{4\pi(\chi''_{xx}\mp\chi''_{xy})\right\}^2\right)^{\frac{1}{2}}-\left\{1+4\pi(\chi'_{xx}\mp\chi'_{xy})\right\}\right]^{\frac{1}{2}}$$

and

$$\beta^{\pm} = \frac{\omega}{c}\left[\frac{\varepsilon}{2}\right]^{\frac{1}{2}}\left[\left(\left\{1+4\pi(\chi'_{xx}\mp\chi'_{xy})\right\}^2+\left\{4\pi(\chi''_{xx}\mp\chi''_{xy})\right\}^2\right)^{\frac{1}{2}}+\left\{1+4\pi(\chi'_{xx}\mp\chi'_{xy})\right\}\right]^{\frac{1}{2}}$$

Hence compounding X1,X2,X3 and X4 into PSI1 to PSI6 as shown in the listing, the imaginary parts of the propagation constant β^+ and β^- are calculated as BETA1 and BETA2 and the real parts α^+ and α^- as GAMMA1 GAMMA2. The Faraday rotation THETA and the ellipticity DICRO are calculated according to equations 8.10 and 8.12 respectively and written

on the output with the susceptibility elements and Z5.

Once out of the central loop, the Faraday rotation for the ferromagnetic and exchange modes of precession described by equations 11.1 and 11.2 are calculated as THETAF and THETAE respectively and written out. The effective gyromagnetic ratio YY is also placed on the output file by a separate write statement.

APPENDIX VII

Calculation of the specific Faraday rotation produced by a double sublattice system in which anisotropy terms are included was performed using the programme GARNET. Physical parameters describing the garnet are entered into the input file in the same format as that used for programme RIG with the addition of DEMX, DEMY and DEMZ which represent demagnetisation constants in the x, y and z directions respectively. Values of the anisotropy constant are read in as CONST1 for the ferric sublattice and CONST2 for the garnet and the difference calculated to obtain the anisotropy constant of the rare-earth CONSTR.

Parameters defined for specific crystal directions are itemized as

X1(1→2), X2(1→2) and X3(1→2)

which are the three direction cosines for the x, y and z directions respectively, and

AX1(1→2), AY1(1→2), AX2(1→2) and AY2(1→2)

which represent the anisotropic demagnetisation factors given in equations 11.3 and 11.4. The symbols X and Y denote the crystal direction and 1 and 2 in the variable name refer to the ferric and rare-earth ion respectively.

Components of the externally applied field in the x, y and z directions are represented by HOX, HOY and HOZ respectively. For this calculation, HOX and HOY are both equated to zero and HOZ is made equal to the value of H previously entered.

The anisotropic demagnetisation factors for the ferric and rare-earth ions in the Z direction are entered as ANIZ1 and ANIZ2 and set equal to zero.

To perform separate calculations for the (111) and (110) directions, the loop

```
DO 700 M=1,2
```

is introduced. Inside this loop, the direction cosines CO1, CO2 and CO3 and the anisotropic demagnetisation factors for each ion in the x and y directions ANIX1, ANIY1, ANIX2 and ANIY2 are in turn set equal to the values appropriate to the [111] and [110] directions as entered previously and shown in Figure A7.1(a). Parameters defined in

```
      PROGRAM GARNET(OUTPUT,TAPE1,TAPE3=OUTPUT)
      DIMENSION A(6,6),B(6,6),HX(6),HY(6),HZ(6),D(6,6),WKSP(6),C(6),
     CTT(5),G(2),X1(2),X2(2),X3(2),AX1(2),AY1(2),AX2(2),      AY2(2)
      COMPLEX D,C,HX,HY,HZ,XX,YX,ZX,XY,YY,ZY,XZ,YZ,ZZ,BB,CC,ARG,UPOS,
     CUMIN
      REDUC=1.E+06
      READ(1,75)REIG
      READ(1,80)DEMX,DEMY,DEMZ
      READ(1,60)G(1),G(2)
      READ(1,10)RHO
      READ(1,20)H
      READ(1,20)WW
      READ(1,40)TTT
      READ(1,45)TT(1),TT(2),TT(3),TT(4),TT(5)
      READ(1,10)UU
      READ(1,20)TMW
      WRITE(3,85)REIG
      WRITE(3,95)G(1),G(2),RHO,H,WW,TMW,UU
      Y1=-1.76*10.0**7/2.0*G(1)
      Y2=-1.76*10.0**7/2.0*G(2)
      WRITE(3,35)Y1,Y2
      W=2.0*3.1416*891.0*10.0**9
      CON=UU*W/(6.0E+10)
      ANIZ1=0.
      ANIZ2=0.
  200 READ(1,30)Z4,Z5
      IF(Z4.EQ.0.0)GO TO 100
      Z1=5587.*RHO*Z4/TMW
      Z2=5587.*RHO*Z5/TMW
      AF1=Y1/(Z1*TTT*W)
      AF1=ABS(AF1)
      II=0
      WRITE(3,70)
      WRITE(3,36)Z4
      WRITE(3,70)
      READ(1,16)CONST2
      READ(1,15)CONST1
      CONSTR=CONST1-CONST2
      CC=CONST1*(10.0**3)
      CCC=CONSTR*(10.0**3)
      X1(1)=.5774
      X2(1)=.5774
      X3(1)=.5774
      X1(2)=0.
      X2(2)=.7071
      X3(2)=.7071
      AX1(1)=-1.55*CC/(Z1*Z1)
      AY1(1)=-.6933*CC/(Z1*Z1)
      AX2(1)=-1.55*CCC/(Z2*Z2)
      AY2(1)=-.6933*CCC/(Z2*Z2)
      AX1(2)=CC/(Z1*Z1)
      AY1(2)=-CC/(Z1*Z1)
      AX2(2)=CCC/(Z2*Z2)
      AY2(2)=-CCC/(Z2*Z2)
```

Figure A7.1(a) Listing of programme GARNET

```
      ANIZ1=0.
      ANIZ2=0.
      DO 700 M=1,2
      CO1=X1(M)
      CO2=X2(M)
      CO3=X3(M)
      ANIX1=AX1(M)
      ANIY1=AY1(M)
      ANIX2=AX2(M)
      ANIY2=AY2(M)
      P1=-(DEMX+ANIX1)
      P2=-(DEMX+ANIX2)
      Q1=-(DEMY+ANIY1)
      Q2=-(DEMY+ANIY2)
      R1=-(DEMZ+ANIZ1)
      R2=-(DEMZ+ANIZ2)
      BX=WW-DEMX
      BY=WW-DEMY
      BZ=WW-DEMZ
      HOZ=H
      HOY=0.
      HOX=0.
      Z1=12.56*Z1
      Z2=12.56*Z2
      DE1=(-ANIX1*Z1*CO1-DEMX*(Z1+Z2)*CO1+WW*Z2*CO1+HOX)*CO1
      DE1=DE1+(-ANIY1*Z1*CO2-DEMY*(Z1+Z2)*CO2+WW*Z2*CO2+HOY)*CO2
      DE1=DE1+(-ANIZ1*Z1*CO3-DEMZ*(Z1+Z2)*CO3+WW*Z2*CO3+HOZ)*CO3
      DE2=(-ANIX2*Z2*CO1-DEMX*(Z1+Z2)*CO1+WW*Z1*CO1+HOX)*CO1
      DE2=DE2+(-ANIY2*Z2*CO2-DEMY*(Z1+Z2)*CO2+WW*Z1*CO2+HOY)*CO2
      DE2=DE2+(-ANIZ2*Z2*CO3-DEMZ*(Z1+Z2)*CO3+WW*Z1*CO3+HOY)*CO3
      I=1
  300 AF2=Y2/(Z2*TT(I)*W)
      AF2=ABS(AF2)
      A(1,1)=AF1*Z1*(DE1-Z1*P1)*(CO2*CO2+CO3*CO3)
      B(1,1)=W
      A(1,2)=AF1*Z1*Z1*BX*(CO2*CO2+CO3*CO3)*(-1)
      B(1,2)=0.
      A(1,3)=-(Y1*CO3*(DE1-Q1*Z1)-AF1*Z1*CO1*CO2*(Z1*Q1-DE1))
      B(1,3)=0.
      A(1,4)=Z1*BY*(Y1*CO3+AF1*Z1*CO1*CO2)
      B(1,4)=0.
      A(1,5)=-(Y1*CO2*(R1*Z1-DE1)+AF1*Z1*CO1*CO3*(DE1-R1*Z1))
      B(1,5)=0.
      A(1,6)=Z1*BZ*(-Y1*CO2+AF1*Z1*CO1*CO3)
      B(1,6)=0.
      A(2,1)=-(AF2*Z2*Z2*BX*(CO2*CO2+CO3*CO3))
      B(2,1)=0.
      A(2,2)=AF2*Z2*(DE2-Z2*P2)*(CO2*CO2+CO3*CO3)
      B(2,2)=W
      A(2,3)=Z2*BY*(Y2*CO3+AF2*Z2*CO1*CO2)
      B(2,3)=0.
      A(2,4)=-(Y2*CO3*(DE2-Q2*Z1)-AF2*Z2*CO1*CO2*(Z2*Q2-DE2))
      B(2,4)=0.
      A(2,5)=Z2*BZ*(-Y2*CO2+AF2*Z2*CO1*CO3)
```

Figure A7.1(b) Listing of programme GARNET continued

```
B(2,5)=0.
A(2,6)=-(Y2*CO2*(R2*Z2-DE2)+AF2*Z2*CO1*CO3*(DE2-R2*Z2))
B(2,6)=0.
A(3,1)=-(Y1*CO3*(P1*Z1-DE1)+AF1*Z1*CO1*CO2*(DE1-P1*Z1))
B(3,1)=0.
A(3,2)=Z1*BX*(Z1*AF1*CO1*CO2-Y1*CO3)
B(3,2)=0.
A(3,3)=AF1*Z1*(DE1-Q1*Z1)*(CO2*CO2+CO3*CO3)
B(3,3)=W
A(3,4)=-(AF1*Z1*Z1*BY*(CO2*CO2+CO3*CO3))
B(3,4)=0.
A(3,5)=-(Y1*CO1*(DE1-R1*Z1)-AF1*Z1*CO2*CO3*(R1*Z1-DE1))
B(3,5)=0.
A(3,6)=BZ*Z1*(Y1*CO1+AF1*Z1*CO2*CO3)
B(3,6)=0.
A(4,1)=Z2*BX*(Z2*AF2*CO1*CO2-Y2*CO3)
B(4,1)=0.
A(4,2)=-(Y2*CO3*(P2*Z2-DE2)+AF2*Z2*CO1*CO2*(DE2-P2*Z2))
B(4,2)=0.
A(4,3)=-(AF2*Z2*Z2*BY*(CO1*CO1+CO3*CO3))
B(4,3)=0.
A(4,4)=AF2*Z2*(DE2-Q2*Z2)*(CO1*CO1+CO3*CO3)
B(4,4)=W
A(4,5)=BZ*Z2*(Y2*CO1+AF2*Z2*CO2*CO3)
B(4,5)=0.
A(4,6)=-(Y2*CO1*(DE2-R2*Z2)-AF2*Z2*CO2*CO3*(R2*Z2-DE2))
B(4,6)=0.
A(5,1)=-(Y1*CO2*(DE1-P1*Z1)-AF1*Z1*CO1*CO3*(P1*Z1-DE1))
B(5,1)=0.
A(5,2)=Z1*BX*(Y1*CO2+AF1*Z1*CO1*CO3)
B(5,2)=0.
A(5,3)=-(Y1*CO1*(Q1*Z1-DE1)+AF1*Z1*CO2*CO3*(-Q1*Z1+DE1))
B(5,3)=0.
A(5,4)=BY*Z1*(-Y1*CO1+AF1*Z1*CO2*CO3)
B(5,4)=0.
A(5,5)=AF1*Z1*(DE1-R1*Z1)*(CO1*CO1+CO2*CO2)
B(5,5)=W
A(5,6)=-(AF1*Z1*Z1*BZ*(CO1*CO1+CO2*CO2))
B(5,6)=0.
A(6,1)=Z2*BX*(Y2*CO2+AF2*Z2*CO1*CO3)
B(6,1)=0.
A(6,2)=-(Y2*CO2*(DE2-P2*Z2)-AF2*Z2*CO1*CO3*(P2*Z2-DE2))
B(6,2)=0.
A(6,3)=BY*Z2*(-Y2*CO1+AF2*Z2*CO2*CO3)
B(6,3)=0.
A(6,4)=Y2*CO1*(Q2*Z2-DE2)+AF2*Z2*CO2*CO3*(-Q2*Z2+DE2)
B(6,4)=0.
A(6,5)=-(AF2*Z2*Z2*BZ*(CO1*CO1+CO2*CO2))
B(6,5)=0.
A(6,6)=AF2*Z2*(DE2-R2*Z2)*(CO1*CO1+CO2*CO2)
B(6,6)=W
```

Figure A7.1(c) Listing of programme GARNET continued

```
      HX(1)=AF1*Z1*Z1*(CO2*CO2+CO3*CO3)
      HX(2)=AF2*Z2*Z2*(CO2*CO2+CO3*CO3)
      HX(3)=Z1*(Y1*CO3-AF1*Z1*CO1*CO2)
      HX(4)=Z2*(Y2*CO3-AF2*Z2*CO1*CO2)
      HX(5)=(-1)*(Z1*(Y1*CO2+AF1*Z1*CO1*CO3))
      HX(6)=(-1)*Z2*(Y2*CO2+AF2*Z2*CO1*CO3)
      HY(1)=(-1)*Z1*(Y1*CO3+AF1*Z1*CO1*CO2)
      HY(2)=(-1)*Z2*(Y2*CO3+AF2*Z2*CO1*CO2)
      HY(3)=AF1*Z1*Z1*(CO1*CO1+CO3*CO3)
      HY(4)=AF2*Z2*Z2*(CO1*CO1+CO3*CO3)
      HY(5)=Z1*(Y1*CO1-AF1*Z1*CO2*CO3)
      HY(6)=Z2*(Y2*CO1-AF2*Z2*CO2*CO3)
      HZ(1)=Z1*(Y1*CO2-AF1*Z1*CO1*CO3)
      HZ(2)=Z2*(Y2*CO2-AF2*Z2*CO1*CO3)
      HZ(3)=(-1)*Z1*(Y1*CO1+AF1*Z1*CO2*CO3)
      HZ(4)=(-1)*Z2*(Y2*CO1+AF2*Z2*CO2*CO3)
      HZ(5)=AF1*Z1*Z1*(CO1*CO1+CO2*CO2)
      HZ(6)=AF2*Z2*Z2*(CO1*CO1+CO2*CO2)
      DO 11 J=1,6
      DO 12 I=1,6
      D(J,I)=CMPLX(A(J,I),B(J,I))
   12 CONTINUE
   11 CONTINUE
      CALL F04ADF(D,6,HX,6,6,1,C,1,WKSP,0)
      XX=C(1)+C(2)
      XP=REAL(XX)
      XPP=-(AIMAG(XX))
      XX=1.      *(C(1)+C(2))+1.
      YX=1.      *(C(3)+C(4))
      ZX=1.      *(C(5)+C(6)
      CALL F04ADF(D,6,HY,6,6,1,C,1,WKSP,0)
      XY=C(1)+C(2)
      YP=REAL(XY)
      YPP=-(AIMAG(XY))
      XY=1.      *(C(1)+C(2))
      YY=1.      *(C(3)+C(4)+1.
      ZY=1.      *(C(5)+C(6)
      CALL F04ADF(D,6,HZ,6,6,1,C,1,WKSP,0)
      XZ=1.      *(C(1)+C(2))
      YZ=1.      *(C(3)+C(4))
      ZZ=1.      *(C(5)+C(6))+1.
      BB=YY*ZZ+XX*ZZ-XZ*ZX-YZ*ZY
      CC=XX*YY*ZZ+XX*YZ*ZY-XZ*YX*ZY+XZ*YY*ZX+XY*YX*ZZ-XY*YZ*ZX
      ARG=BB*BB+4.*CC
      ARG=CSQRT(ARG)
      UPOS=BB+ARG
      UMIN=BB-ARG
      UPR=REAL(UPOS)
      UPI=AIMAG(UPOS)
```

Figure A7.1(d) Listing of programme GARNET continued

```
      UNR=REAL(UMIN)
      UNI=AIMAG(UMIN)
      BETAP=CON*(SQRT(SQRT(UPR*UPR+UPI*UPI)+UPR))
      BETAN=CON*(SQRT(SQRT(UNR*UNR+UNI*UNI)+UNR))
      THETA=(BETAN-BETAP)/2.
      WRITE(3,36)THETA
      IF(I.EQ.5)GO TO 700
      I=I+1
      GO TO 300
  700 CONTINUE
      GO TO 200
  100 CONTINUE
      STOP
   90 FORMAT(1X,5(E12.5,2X))
   93 FORMAT(F6.0)
   10 FORMAT(F4.2)
   15 FORMAT(F5.2)
   16 FORMAT(F6.1)
   20 FORMAT(F6.1)
   30 FORMAT(F6.2,2X,F6.2)
   35 FORMAT(1X,2(E12.5,2X))
   36 FORMAT(1X,E12.5)
   45 FORMAT(5(E8.1,2X))
   40 FORMAT(E9.2)
   50 FORMAT(1X,3HX1=,E12.5,2X,3HX2=,E12.5,2X,3HX3=,E12.5,2X,3HX4=,E12.5
     C,2X,6HTHETA=,E12.5,2X,6HDICRO=,E12.5,2X,3HZ5=,F12.5,2X,2HI=,I1)
   55 FORMAT(E12.5)
   60 FORMAT(F4.2,2X,F4.2)
   70 FORMAT(1X)
   75 FORMAT(F3.1)
   80 FORMAT(3(F5.2,2X))
   85 FORMAT(1X,5HREIG=,F3.1)
   95 FORMAT(1X,5HG(1)=,F4.2,2X,5HG(2)=,F4.2,2X,4HRHO=,F4.2,2X,2HH=,F7.1
     C,2X,3HWW=,F7.1,2X,4HTMW=,F7.1,2X,3HUU=,F4.2)
      END
```

Figure A7.1(e) Listing of programme GARNET continued

equation 8.25 are represented by the variables

$$\left.\begin{matrix} P1 \\ \\ P2 \end{matrix}\right\} a_i x \text{ ,} \qquad \left.\begin{matrix} Q1 \\ \\ Q2 \end{matrix}\right\} a_i y \text{ ,} \qquad \left.\begin{matrix} R1 \\ \\ R2 \end{matrix}\right\} a_i z$$

and $\quad BX - b_x$, $\quad BY - b_y$, $\quad BZ - b_z$

and again are shown in Figure A7.1(a) where the numerals 1 and 2 in the variable names correspond to i=1 and i=2 respectively.

The magnitude of the static component of the magnetic field at each sub-lattice ion (i), expressed in equation 8.24, is calculated as DE1 for the ferric ion and DE2 for the rare-earth ion.

Nested within the DO 700 loop is a GO TO 300 loop where the rare-earth relaxation time TT(I) is introduced and the corresponding damping parameter AF2 calculated. An integral increase in I is produced in the same manner as in programme RIG.

The real and imaginary parts of the elements of the 6 × 6 matrix (D) in equation 8.26 are expressed as $A(1\rightarrow6,1\rightarrow6)$ and $B(1\rightarrow6,1\rightarrow6)$ respectively in Figures A7.1(b) and (c). Similarly $E_{1\rightarrow6}$, $F_{1\rightarrow6}$ and $G_{1\rightarrow6}$ of equation 8.26 are displayed respectively as $HX(1\rightarrow6)$, $HY(1\rightarrow6)$ and $HZ(1\rightarrow6)$. A 6 × 6 complex array D is then formed from A and B by the statement

```
D(J,I)=CMPLX(A(J,I),B(J,I))
```

which is contained within the DO 11 and DO 12 loops shown in the figure.

Manipulation of the array elements into a form represented by equation 8.27 is performed by treating $E_{1\rightarrow6}$, $F_{1\rightarrow6}$ and $G_{1\rightarrow6}$ of equation 8.26 as separate column matrices and calling the NAG routine F04ADF. Illustrating the routine as

```
F04ADF(A,IA,B,IB,N,M,C,IC,WKSP,IFAIL)
```

then for a complex set of linear equations AX=B, the parameters within the parentheses represent:-

A - the name of a complex two-dimensional array of at least (N,N) complex elements

IA - an integer quantity, the first dimension of A, IA≥N

B - the name of a complex two-dimensional array of at least (N,M) complex elements

IB - an integer quantity, the first dimension of B, IB≥N

N - an integer quantity, the order of matrix A

M - an integer quantity, the number of right-hand side elements

C - the name of a two-dimensional complex array. On exit it contains the M solution vectors

IC - an integer quantity, the first dimension of C, IC≥N

WKSP - the name of a one-dimensional real array of at least N elements, used as work space

IFAIL - an integer variable. On entry it determines the mode of failure of the routine and on exit acts as an error indicator or shows successful use of routine

Inserting the complex array D into A and HX into B, elements corresponding to the first column of the susceptibility tensor are obtained from the output of the routine as the 1 × 6 array C. Equation 8.28 shows that the elements of the permeability tensor can be expressed in terms of those of the susceptibility tensor as

$$\mu_{xx} = 1 + \chi_{xx} \quad , \quad \mu_{xy} = \chi_{xy} \quad , \quad \mu_{xz} = \chi_{xz}$$

$$\mu_{yx} = \chi_{yx} \quad , \quad \mu_{yy} = 1 + \chi_{yy} \quad , \quad \mu_{yz} = \chi_{yz}$$

$$\mu_{zx} = \chi_{zx} \quad , \quad \mu_{zy} = \chi_{zy} \quad , \quad \mu_{zz} = 1 + \chi_{zz}$$

Using the subscripts of the permeability elements to denote the elements themselves as Fortran variable names, the first column of the permeability tensor is calculated in the manner shown in the figure. Repeating the process by insertin HY and then HZ into the routine parameter B, enables the complete matrix to be calculated. The permeability elements are then arranged in the form described by equation 8.7 so that the real and imaginary parts of the permeabilities of the rotational modes are obtained. The phase constants β^+ and β^- are thus obtained from equation 8.8 and are represented as BETAP and BETAN respectively. The Faraday rotation THETA is then calculated and written on to the output file.

APPENDIX VIII

Values for the specific Faraday rotation produced by a single lattice system, calculated from the expressions for the susceptibility elements given in Figure 11.18, were obtained from the Fortran IV computer programme YIGDAM. Parameters required for the computation are fed into the input file from the data statement of line two of the listing of the programme displayed in Figure A8.1. The same parameter names as those used in the programme RIG described in Appendix VI were employed. This is followed by calculating the gyromagnetic ratio Y, inserting the velocity of light in vacuum C, the angular frequency of the radiation W and calculating CON which represents the factor $\frac{1}{2}(\mu_0\omega^2\varepsilon)^{\frac{1}{2}}$ in equation 8.8. Demagnetisation factors in the x, y and z directions are represented respectively by DEX, DEY and DEZ. For the situation in which a thin slab with its parallel sides perpendicular to the direction of propagation of the radiation, DEX and DEY were set to zero and DEZ set to 4π.

A 200 READ statement, which forms part of a GO TO loop, is used to read in data representing the magnetisation Z4, and the anisotropy constant CONS of the garnet. The relaxation time T is introduced by a further read statement. The anisotropic demagnetisation constants are represented by ANIX in the x direction and ANIY in the y direction and are calculated for specific crystal directions. Calculations for a different orientation were performed by modifying the statements. The corresponding parameter for the z direction ANIZ was set equal to zero. Demagnetising constants and anisotropic demagnetising constants for similar orientations are added together to obtain single effective demagnetising constants DEMX, DEMY and DEMZ for the x, y and z directions respectively.

Further calculations are performed to obtain values for the Fortran variable names that correspond to parameters listed in Figure 11.18 as

WM - ω_m , WO - ω_0 , WR - ω_r

DEN - the denominator of the susceptibility elements

XXPP - χ''_{xx} , XYPP - χ''_{xy} , XYP - χ'_{xy} , XXP - χ'_{xx}

In a similar manner to that described in Appendix VI, the phase constants are calculated from the susceptibility elements and the specific Faraday rotation, THETA, obtained and written on to the output file.

```
PROGRAM YIGDAM(INPUT,OUTPUT,TAPE1=INPUT,TAPE3=OUTPUT,TAPE5,TAPE6)
DATA REIG,G1,G2,RHO,H,UU,TMW/8.,2.,2.,5.17,4500.,4.2,1476./
Y=-1.76*1.E7*G1/2.
C=3.E10
W=2.*3.1416*891.E9
CON=W*UU/3.E10
CON=CON/1.414
DEX=0.
DEY=0.
DEZ=12.5664
200 READ(5,30)Z4,CONS
IF(Z4.EQ.0.0)GO TO 100
READ(6,10)TT
T=TT*1.E-13
Z1=5587.*RHO*Z4/TMW
CONS =CONS*1.E+3
ANIX=1.0*CONS/(Z1*Z1)
ANIY=-1.0*CONS/(Z1*Z1)
ANIZ=0.
DEMX=ANIX+DEX
DEMY=ANIY+DEY
DEMZ=ANIZ+DEZ
WM=4.*3.1416*Y*Z1
WO=Y*H-DEMZ*WM
WR=SQRT((Y*H+(DEMX-DEMZ)*WM)*(Y*H+(DEMY-DEMZ)*WM))
A=WR*WR-W*W
B=2.*(WO+((DEMX-DEMY)/2.)*WM)/T
DEN=A*A+B*B
XXPP=-((WR*WR-W*W)/T-2.*(DEMY*WM+WO)/T*(WO+((DEMX-DEMY)/2.)*WM))*
+ WM/DEN
XYPP=W*WM*(WR*WR-W*W)/DEN
XYP=-W*WM*2.*(WO+((DEMX-DEMY)/2.)*WM)/DEN
XYP=XYP/T
XXP=((WO+DEMY*WM)*(WR*WR-W*W)+2.*(WO+((DEMX-DEMY)/2.)*WM)/(T*T))
+ *WM/DEN
F=XYP
E=XYPP
XYP=-E
XYPP=F
U1=1.+12.56*(XXP-XYP)
U2=12.56*(XXPP-XYPP)
U3=1.+12.56*(XXP-XYP)
BP=CON*(SQRT(SQRT(U1*U1+U2*U2)+U3))
U4=1.+12.56*(XXP+XYP)
U5=12.56*(XXPP+XYPP)
U6=1.+12.56*(XXP+XYP)
BN=CON*(SQRT(SQRT(U4*U4+U5*U5)+U6))
THETA=(BN-BP)/2.
DEG=THETA*180./3.1416
WRITE(3,25)DEG
GO TO 200
100 STOP
```

Figure A8.1(a). Listing of programme YIGDAM

```
90 FORMAT(6E12.3)
25 FORMAT(1X,E12.5)
75 FORMAT(F3.1)
60 FORMAT(F4.2,2X,F4.2)
20 FORMAT(F6.1)
16 FORMAT(F6.1)
15 FORMAT(F6.2)
70 FORMAT(1X)
30 FORMAT(F5.2,1X,F5.0)
10 FORMAT(F6.2)
END
```

Figure A8.1(b). Listing of programme YIGDAM continued

J. Phys. D: Appl. Phys., Vol. 11, 1978. Printed in Great Britain

Point-contact diode submillimetre detectors

PG Frayne, N Chandler† and MW Booton‡
Physics Department, Royal Holloway College, Egham, Surrey

Received 30 May 1978

Abstract. Point-contact whisker diodes have been used to detect 337 μm radiation giving responsivities up to 1000 V W^{-1}. The respective merits of metal–insulator–metal and metal–insulator–semiconductor diodes are examined. To explain the characteristics of responsivity with electrical and mechanical variations, a model is presented based on thermionic and tunnel currents flowing between a hemispherical and a plane electrode.

1. Introduction

The use of point-contact diodes as detectors in the submillimetre region has some advantages over other infrared detectors. Unlike the bulk InSb detector (Putley 1960), liquid helium is not required, and because of the low capacitance of its junction a point-contact diode has an inherently fast response, in contrast to room-temperature thermal detectors such as the Golay cell. The ability to rectify at far IR frequencies was demonstrated by Frayne (1967) with commercially produced diodes. However, these and devices made by contacting a pointed wire antenna on to a metal or semiconductor surface (Daneu *et al* 1969, Matarrese and Evenson 1970, Becklake *et al* 1970) possess lower responsivities than more conventional detectors. For this reason a programme was undertaken to produce a device with increased sensitivity, and to propose a model of the mechanism taking place at a point-contact to aid future development.

2. Experimental details

Diode detectors were produced by electrolytically etching to a point one end of a straight length of 20 μm diameter tungsten wire, and bringing this point into contact with the atmospherically contaminated surface of a metal or semiconductor. By orienting the tungsten wire antenna in the beam of an HCN laser operating at 891 GHz and by suitably applying pressure to the contact, a DC potential was generated across the junction. For both metal and semiconductor devices it was found that the greatest output from the diode was obtained on initial contact between the tungsten and the insulating layer. Increasing the pressure on the wire resulted in reduction of the responsivity, with ultimate reversal of the polarity of the output voltage. The output obtained, once reversal had taken place, was less than that produced on initial contact. The high responsivity could

† Present address: Marconi Research Laboratories, GEC–Marconi Electronics Ltd, Great Baddow.
‡ Present address: GEC Hirst Research Centre, Wembley.

0022-3727/78/0017–2391 $02.00

be recovered, however, as the output voltage was reproducible with cyclic variation of the contact pressure.

Although some exceptions did occur, making contact on to various samples of a particular material usually resulted in the same polarity of output on initial contact. The experimental observation of polarity reversal by Green *et al* (1970) was explained by variation of the difference between the work-functions of the two electrodes as the tip of the antenna contacted different areas of the substrate. To investigate this situation, tungsten ribbon and evaporated films of gold and aluminium were used as plane metal electrodes. By virtue of the large surface areas, the Kelvin vibrating capacitor technique (Zisman 1932, Surplice and D'Arcy 1970) was used to measure the average value of the work-function of each polycrystalline film. Measurements were also made on silicon, but the samples of the other semiconductors investigated, germanium and gallium arsenide, were not large enough for the method employed.

An indication of the possible deviation of the work-function over the surface of a material has been given by Hass and Thomas (1966). This variation was explained by the metal surface being composed of regions of different crystal orientation. The work-function of the point of the tungsten wire was unknown. However, the measured values for the plane electrodes given in table 1 are sufficiently close to the documented values for the different crystallographic orientations of tungsten in table 2 (Riviere 1969), that

Table 1. Measured average work-functions of substrate materials.

Substrate material	Work-function (eV)
Silicon	4·85±0·02
Gold	5·39±0·03
Aluminium	4·26±0·02

Table 2. Work-functions of crystal orientations in tungsten (after Riviere 1969).

Tungsten orientation	Work-function (eV)
110	5·3±0·12
111	4·4±0·03
116	4·3±0·03
100	4·6±0·08

polarity reversal of the work-function difference was experimentally possible. The situation therefore exists in which successive contacts of a whisker could yield devices with a range of work-function differences, due either to the patchy nature of the plane electrodes or to different crystal faces of the tungsten wire being exposed, either by repeated etching or by mechanical deformation. However, the repeatability and reversibility of the variation of the responsivity with applied pressure implied that, once contact had been made, the patches were large enough and the antenna drive accurate enough to eliminate random work-function changes through lateral movement of the whisker tip. The voltage responsivities of the various detectors were found after optimisation, by dividing the DC output voltage from the diode by the CW power incident on the antenna, measured using a calibrated Golay cell.

The responsivities of detectors formed by contacting tungsten antennae on to aluminium, gold, tungsten and doped silicon and germanium electrodes are shown in figure 1 as a function of the resistive load. The variation of detector performance against load was investigated by placing a shunt resistor across the diode. This is a useful method for reducing the response time of the output circuit. The output impedances derived from the curves given in table 3 are in good agreement with the zero-bias resistances estimated from the current–voltage characteristics of figure 2. These curves, which were measured by applying short pulses of current to the diode from a differentiated 900 Hz square wave, in order to limit power dissipation, show reasonable asymmetry between the forward and reverse bias conditions for the tungsten–semiconductor devices. However, only a small

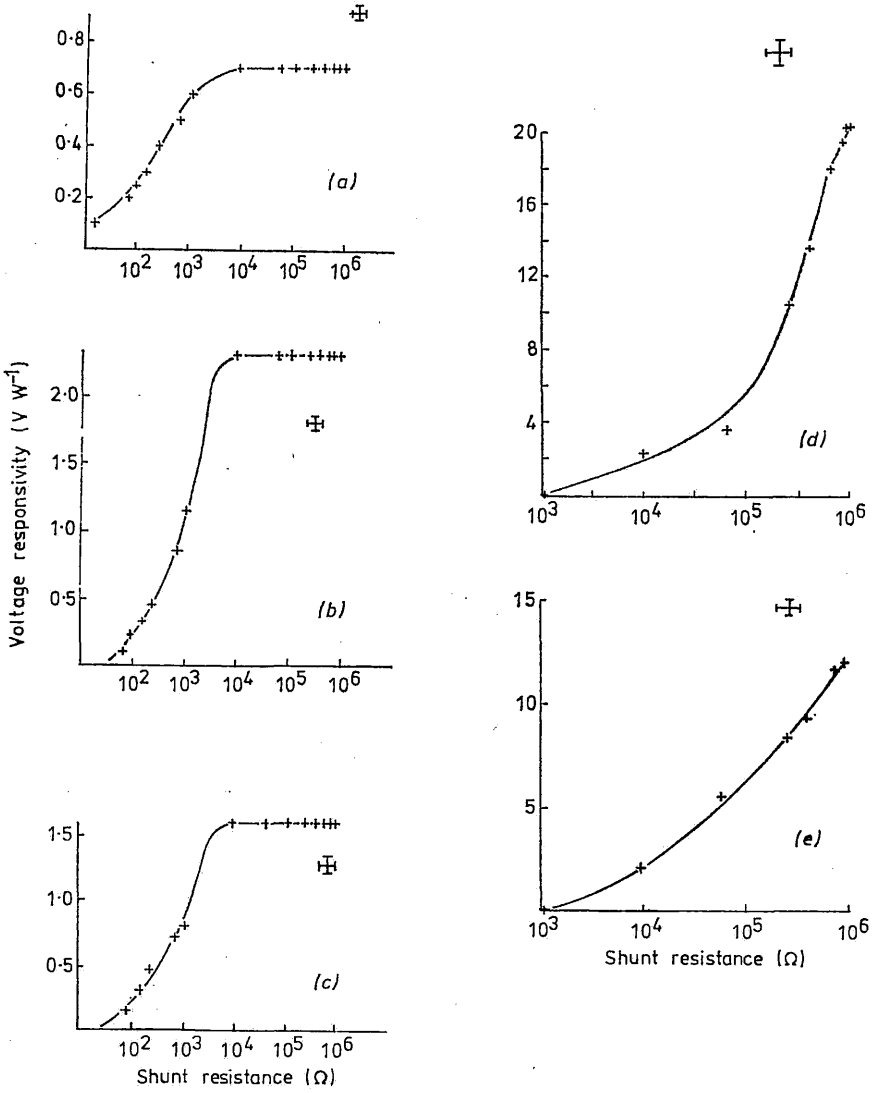

Figure 1. Experimentally observed voltage responsivities of point-contact diode detectors: tungsten to (*a*) gold, (*b*) aluminium, (*c*) tungsten, (*d*) germanium, (*e*) silicon. Crossed bars indicate uncertainty.

Table 3. Measured zero-bias resistance and output impedance of point-contact diodes.

Diode	Zero-bias resistance (Ω)	Output impedance (Ω)
Tungsten–silicon	$(2{\cdot}3\pm0{\cdot}3)\times10^4$	$(7{\cdot}8\pm0{\cdot}1)\times10^5$
Tungsten–germanium	$(4{\cdot}5\pm0{\cdot}3)\times10^4$	$(3{\cdot}2\pm0{\cdot}1)\times10^5$
Tungsten–gold	220 ± 25	200 ± 15
Tungsten–aluminium	930 ± 65	1100 ± 100
Tungsten–tungsten	770 ± 30	900 ± 30

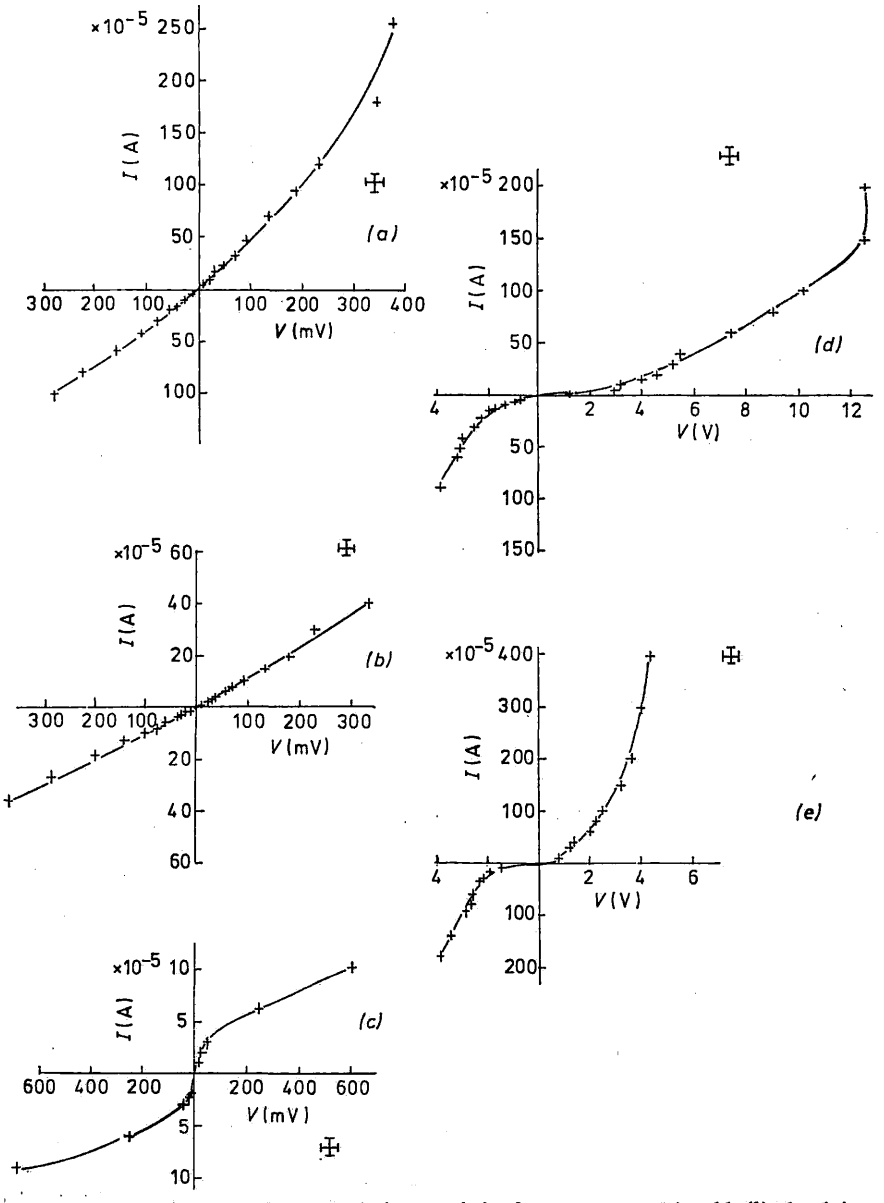

Figure 2. Current–voltage (I–V) characteristics for tungsten to (*a*) gold, (*b*) aluminium, (*c*) tungsten, (*d*) germanium, (*e*) silicon. Crossed bars indicate uncertainty.

difference is observed for the tungsten–metal diodes, hence the poorer responsivity. The nearly linear characteristic of the metal–insulator–metal (MIM) diodes also explains the observation that enhancement of the detector output was not achieved by applying DC bias to the diode.

In contrast, the metal–insulator–semiconductor (MIS) detectors showed a useful increase in responsivity with, as shown in figure 3, the application of the appropriate bias

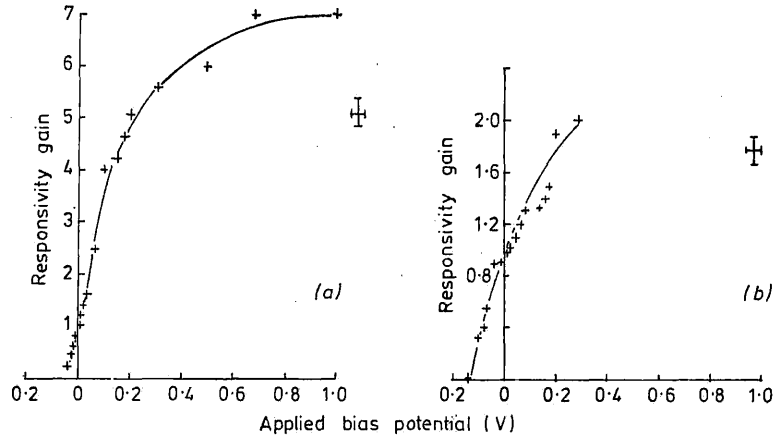

Figure 3. Responsivity gain versus applied bias for (*a*) tungsten–germanium, (*b*) tungsten–silicon. Crossed bars indicate uncertainty.

potential. The most notable result was produced by contacting a tungsten antenna on to a crystalline sample of undoped GaAs. This diode produced no rectified output in the unbiased state, but with the application of a small DC potential, a responsivity was obtained which was far greater than observed in either silicon or germanium. Figure 4 shows the response of this detector as a function of applied bias, together with the noise equivalent power. It was only with this tungsten–GaAs diode that the noise was sufficiently large to be measured without additional preamplification.

3. Theory

The simple potential distribution existing between two plane parallel electrodes separated by an insulating material and connected by an external circuit is represented diagrammatically by figure 5(*a*). Simmons (1963a,b, 1964) has explained current flow through such a structure in terms of thermionic and electronic tunnelling mechanisms, while taking into account distortion of the field by image forces which produce a potential barrier of the type illustrated in figure 5(*b*). The operation of a point-contact diode cannot adequately be explained using the analysis derived for two plane parallel electrodes, for Chow (1963) has shown that a non-uniform spacing can significantly alter the current–voltage characteristic. The diode will be represented by a planar electrode coated with a uniform dielectric layer, into which is partially inserted the sharpened hemispherical tip of the antenna. This geometry is shown in figure 6 where the interface between the plane metal and the insulator is clearly defined. Using the convention of Simmons (1963b) that J_1 represents the current density when the electrode of lower work-function is negatively biased and J_2

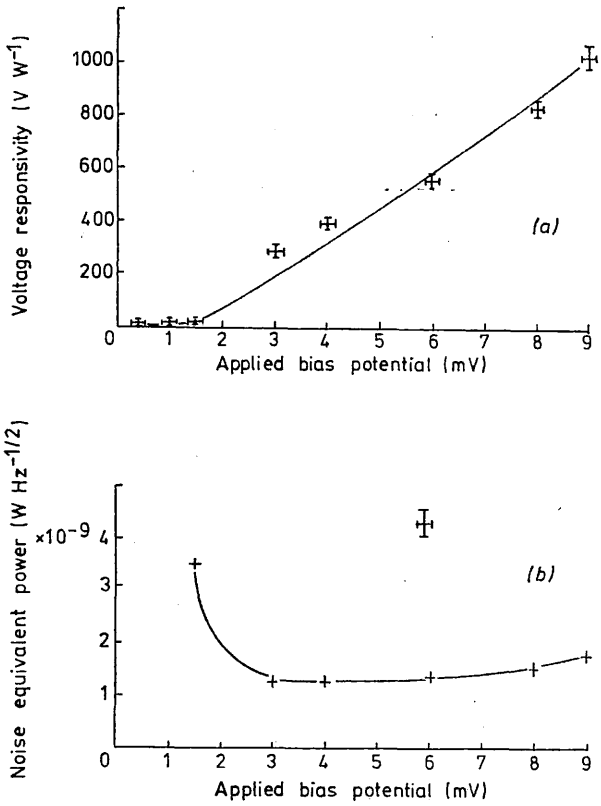

Figure 4. Tungsten–GaAs diode: (*a*) voltage responsivity versus applied bias potential, (*b*) noise equivalent power versus applied bias potential. Crossed bars indicate uncertainty.

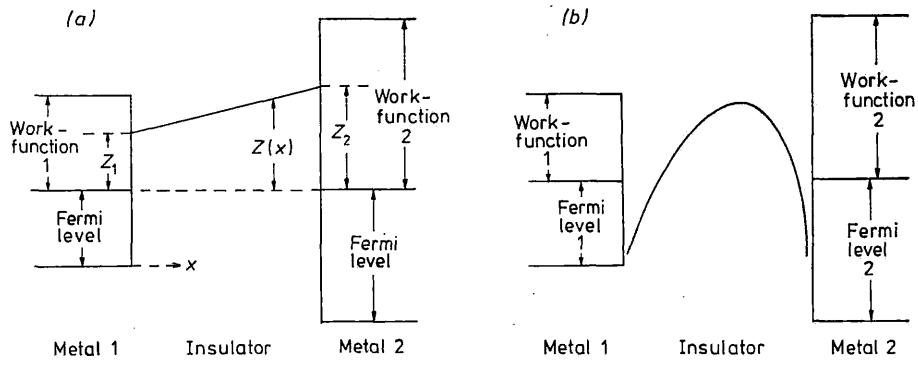

Figure 5. Energy diagram of potential barriers between dissimilar electrodes: (*a*) image forces neglected; (*b*) image forces included.

the current density for the opposite sense of applied voltage, then the rectification ratio of the diode may be expressed as

$$\eta=\frac{\int_0^R 2\pi J_2(r)r\,\mathrm{d}r}{\int_0^R 2\pi J_1(r)r\,\mathrm{d}r}.$$

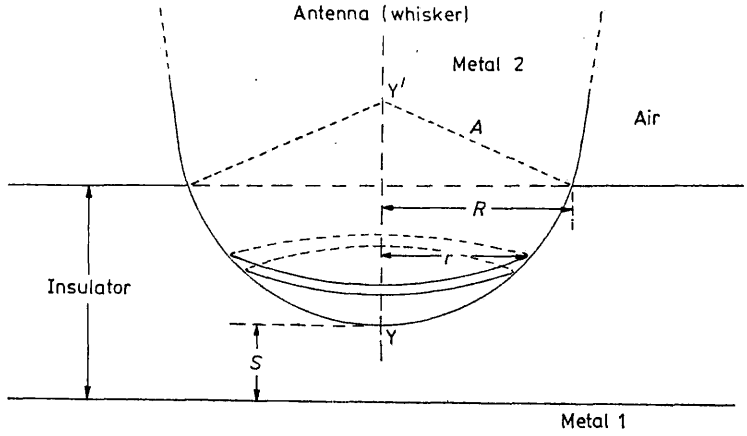

Figure 6. Diagrammatic representation of a hemispherical whisker tip partially embedded in the insulating surface layer of a plane electrode.

In this equation, r represents the perpendicular distance from the line of symmetry YY' in figure 6 to the circumference of the sphere, and $r=R$ at the insulator–air interface. Using Simmons' equations for the current density for tunnel (1963b) and thermionic (1964) conduction, the above expression for η has been evaluated numerically. Similarly, the resistance of the barrier R_B has been calculated so that the voltage responsivity expressed by Green (1971) as

$$\gamma=\frac{(\eta-1)\,R_B}{2V}$$

may be plotted against the minimum electrode spacing S. Values of the current flow between the electrodes used to calculate η and R_B were the summation of the currents arising from the tunnel and thermionic effects. The responsivity curves displayed in figure 7 show a polarity reversal due to a change in dominance from tunnel currents at small electrode spacing to thermionic processes at higher S. The figure also shows the dependence of γ on the radius A_w of the whisker tip, on the detected voltage V_D and on the minimum barrier height Z_1. For clarity, the curves for the lowest chosen value of Z_1 are shown separately in figure 8, with curve F of figure 7 included to facilitate comparison. The higher values of V_D have been omitted to comply with the theoretical assumption that $eV \leqslant Z_1$. The difference between the work-functions of the two electrodes and hence between the heights Z_1 and Z_2 of the barriers at the metal–insulator interfaces has been taken as 1 eV for these examples.

4. Discussion

The theoretical model shows qualitative agreement with the experimental observation that the voltage responsivity of point-contact diodes is greatest at large electrode separation and then decreases and finally reverses polarity as the spacing is reduced.

The poor quantitative agreement may be attributed to the imperfect efficiency of the antenna and to the simplifications in the model. It has been shown (Chow 1963) that local perturbations in the insulator thickness can change the resistance by several orders of magnitude. Imperfections in the dielectric would also reduce the resistance significantly

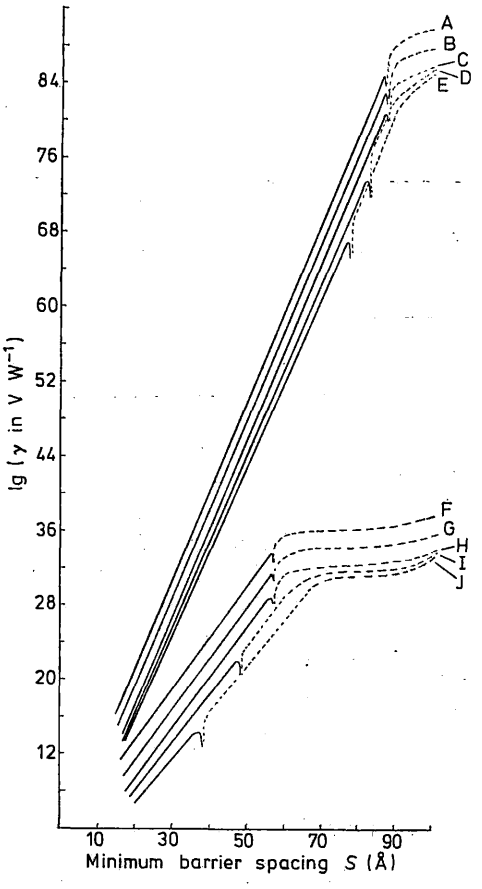

Figure 7. Theoretical voltage responsivity of a MIM point-contact diode detector. The dielectric constant of the barrier is 8.

Curve	A	B	C	D	E	F	G	H	I	J
V_D(V)	0·09	0·09	0·09	0·5	0·9	0·09	0·09	0·09	0·5	0·9
A_w (Å)	10^2	10^4	10^6	10^6	10^6	10^2	10^4	10^6	10^6	10^6
Z_1 (eV)	4	4	4	4	4	1	1	1	1	1
Z_2 (eV)	5	5	5	5	5	2	2	2	2	2

(Chen and Adler 1970). Since it is possible to produce rectification with nominally symmetrical devices (Pollack and Morris 1964) there may also be an effect due to an asymmetry caused by, for example, a poorly defined transition from metal to dielectric at one or both interfaces, resulting in reductions of barrier heights and of effective barrier thickness.

The significant factor is that the experimental characteristics are both reversible and repeatable, indicating a mechanistic rather than a random variation. Green (1971) has expressed the current–voltage characteristics of a MIM diode as

$$I=aV+bV^2+\ldots$$

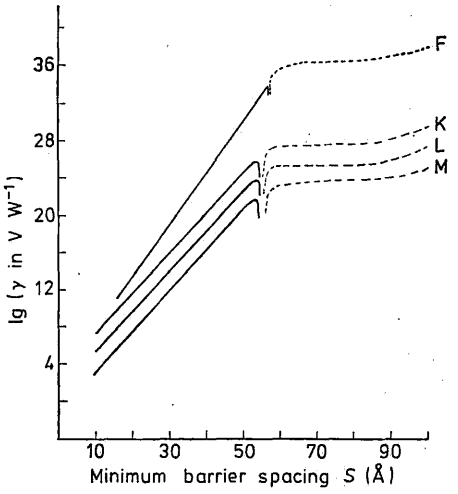

Figure 8. Theoretical voltage responsivity of a MIM point-contact diode detector. The dielectric constant of the barrier is 8; $V_D = 0{\cdot}09$ V; ——— positive γ, — — — negative γ.

Curve	F	K	L	M
A_w (Å)	10^2	10^3	10^4	10^6
Z_1 (eV)	1	0·5	0·5	0·5
Z_2 (eV)	2	1·5	1·5	1·5

where a and b are constants, and the instantaneous voltage across the diode is

$$V=(2PR_B)^{1/2}\sin\omega t=\left(2V_D\frac{a}{b}\right)^{1/2}\sin\omega t$$

where V_D can be seen to depend on the RF power P coupled into the device. Figure 7 also indicates that at a fixed dielectric thickness, variation of and, at some barrier spacings, reversal of the polarity of the responsivity occurs with changing V_D and hence incident power. This property has been demonstrated experimentally by Green *et al* (1970).

The high impedance of the MIS diodes when compared to the MIM structures indicates a relatively slow response. Assuming a typical device to have a junction diameter of 0·1 μm (Green 1971), an insulating layer of dielectric constant 8 (Pollack and Morris 1964) and a thickness 50 Å, then the measured impedances of the MIM diodes in table 3 indicates that the upper 3 dB output point for such devices can be between 45 and 100 THz. For a tungsten–silicon diode with a similar barrier resistance, a series resistance approximately equal to the output impedance indicated in table 3 and a dielectric constant of 4·5 (Kaye and Laby 1966), then the upper 3 dB point is in the region of 15 THz. Although the use of MIS detectors at higher frequencies is restricted by the limited bandwidth, figure 1 shows that they have a distinct advantage over MIM devices at 337 μm by possessing greater responsivities.

The theoretical model of the point-contact diode has been developed for an MIM barrier. However, it is interesting to note that the performance characteristics of the tungsten–semiconductor diodes with variation of whisker pressure are similar to that of the tungsten–metal diodes. A possible explanation is that the mechanism described by the MIM model contributes to a DC bias voltage across the depletion layer near the semi-

conductor surface. The polarity of this component will vary accordingly and the rectification ratio of the semiconductor device will be modified, becoming greater with forward bias and smaller with reverse. The MIS devices may therefore be expected to behave in a similar qualitative manner to the MIM diodes but to exhibit higher rectification ratios, and therefore higher responsivities as observed experimentally.

5. Conclusions

The experimental behaviour of MIM point-contact diode detectors can be explained in terms of thermionic and electron tunnelling processes taking into account the geometrical shape and dimensions of the insulating barrier between the antenna tip and the base electrode.

Responsivities of 1000 V W^{-1} have been obtained at 337 μm from biased tungsten–GaAs detectors. However, the inherent high resistivities of semiconductor devices indicate that for the highest frequencies MIM diodes must be used and these may operate up to 100 THz.

Acknowledgments

The authors wish to thank the Science Research Council for a support grant. The investigation was undertaken as partial fulfilment for higher degrees while two of the authors (NC and MWB) were in receipt of research studentships.

References

Becklake E J, Payne C D and Prewer B E 1970 *J. Phys. D: Appl. Phys.* **3** 473–81
Chen T T and Adler J G 1970 *Solid St. Commun.* **8** 1965
Chow C K 1963 *J. Appl. Phys.* **34** 2599–602
Daneu V, Sokoloff D, Sanchez A and Javan A 1969 *Appl. Phys. Lett.* **15** 398
Frayne P G 1967 *Electron. Lett.* **3** 338–9
Green S J 1971 *J. Appl. Phys.* **42** 1166
Green S J, Coleman P D and Baird J R 1970 *Proc. Submillimetre Wave, Microwave Res. Inst. Symp.* Vol. 20 (New York: Brooklyn Polytechnic Press)
Hass G A and Thomas R E 1966 *Surface Sci.* **4** 64–88
Kaye G W C and Laby T H 1966 *Tables of Physical and Chemical Constants* (London: Longmans)
Matarrese L M and Evenson K M 1970 *Appl. Phys. Lett.* **17** 8–16
Pollack S R and Morris C E 1964 *J. Appl. Phys.* **35** 1503
Putley E H 1960 *Proc. Phys. Soc.* **76** 802–5
Riviere J C 1969 *Solid State Surface Science* ed M Green (New York: Dekker)
Simmons J G 1963a *J. Appl. Phys.* **34** 1793–803
—— 1963b *J. Appl. Phys.* **34** 2581–90
—— 1964 *J. Appl. Phys.* **35** No. 8, pp 2472–81
Surplice N A and D'Arcy R J 1970 *J. Phys. E: Sci. Instrum.* **3** 477
Zisman W A 1932 *Rev. Sci. Instrum.* **3** 367